CONTENTS

Revista Mexicana de Astronomía y Astrofísica, **46**, 191–214 (2010)

THE SAN PEDRO MÁRTIR PLANETARY NEBULA KINEMATIC CATALOGUE: EXTRAGALACTIC PLANETARY NEBULAE[1]

M. G. Richer,[2] J. A. López,[2] E. Díaz-Méndez,[3] H. Riesgo,[2] S.-H. Báez,[4] Ma.-T. García-Díaz,[2] J. Meaburn,[5] D. M. Clark,[2] R. M. Calderón Olvera,[6] G. López Soto,[6] and O. Toledano Rebolo[7]

Received 2009 October 14; accepted 2010 April 17

RESUMEN

Presentamos datos cinemáticos para 211 nebulosas planetarias brillantes en once galaxias del Grupo Local: M31 (137 NPs), M32 (13), M33 (33), Fornax (1), Sagittarius (3), NGC 147 (2), NGC 185 (5), NGC 205 (9), NGC 6822 (6), Leo A (1), y Sextans A (1). Adquirimos los datos en el Observatorio Astronómico Nacional en la Sierra de San Pedro Mártir con el telescopio de 2.1 m y el espectrómetro Manchester Echelle en la línea de [O III]λ5007 con una resolución de 11 km s^{-1}. Observamos algunos objetos en Hα. La cinemática de nebulosas planetarias brillantes no depende fuertemente de la metalicidad o la edad de la población estelar progenitora en sus galaxias huéspedes, aunque existen pequeñas diferencias sistemáticas. La cinemática y la luminosidad en Hβ de las cáscaras nebulares requieren la aceleración de las cáscaras durante la evolución temprana de las estrellas centrales. Así, la cinemática representa otro argumento a favor de estrellas progenitoras similares para las nebulosas planetarias brillantes en todas galaxias.

ABSTRACT

We present kinematic data for 211 bright planetary nebulae in eleven Local Group galaxies: M31 (137 PNe), M32 (13), M33 (33), Fornax (1), Sagittarius (3), NGC 147 (2), NGC 185 (5), NGC 205 (9), NGC 6822 (5), Leo A (1), and Sextans A (1). The data were acquired at the Observatorio Astronómico Nacional in the Sierra de San Pedro Mártir using the 2.1 m telescope and the Manchester Echelle Spectrometer in the light of [O III]λ5007 at a resolution of 11 km s^{-1}. A few objects were observed in Hα. The internal kinematics of bright planetary nebulae do not depend strongly upon the metallicity or age of their progenitor stellar populations, though small systematic differences exist. The nebular kinematics and Hβ luminosity require that the nebular shells be accelerated during the early evolution of their central stars. Thus, kinematics provides an additional argument favoring similar stellar progenitors for bright planetary nebulae in all galaxies.

Key Words: ISM: kinematics and dynamics — Local Group — planetary nebulae: general — stars: evolution

1. INTRODUCTION

Planetary nebulae are the immediate descendants of asymptotic giant branch (AGB) stars of low and intermediate masses (1 $M_\odot < M < 8$ $M_\odot$). The mass lost on the AGB (or part of it) is seen as the ionized nebular shell in planetary nebulae. The composition of these nebular shells is extremely useful in studying the nucleosynthetic production of their precursor stars. The cycling of matter through these stars and its transformation is part of the chemical evolution of galaxies, since the progenitors of planetary nebulae are responsible for much of the helium,

[1]Based on observations obtained at the Observatorio Astronómico Nacional at San Pedro Mártir, Baja California, Mexico.

[2]Instituto de Astronomía, Universidad Nacional Autónoma de México, Mexico.

[3]Texas Christian University, Fort Worth, Texas, USA.

[4]Facultad de Física e Inteligencia Artificial, Universidad Veracruzana, Mexico.

[5]Jodrell Bank Observatory, University of Manchester, UK.

[6]Universidad Nacional Autónoma de México, Mexico.

[7]Instituto de Ciencias Físicas, Universidad Nacional Autónoma de México, Mexico.

carbon, nitrogen, and some s-process elements in the universe.

The luminosity function of bright extragalactic planetary nebulae (PNLF) has been used extensively as a distance indicator for about two decades (Jacoby 1989; Ciardullo et al. 1989b). While some progress has been made in understanding the nature of the progenitor stars of bright planetary nebulae (e.g., Richer & McCall 2008), the comments made by Pottasch (1990) are still largely valid: "It may seem rather strange to determine the distance to the galactic centre by calibrating against the much more distant galaxy M31, but it is no stranger than the idea of using PN as standard candles in the first place, since individual distances to PN are so poorly known."

Bright extragalactic planetary nebulae have two key advantages for evolutionary studies with respect to their Galactic counterparts. First, their distances are known, so their absolute luminosities are studied easily. Second, in galaxies more distant than the Magellanic Clouds, planetary nebulae are unresolved for ground-based observations, making it easy to study their integrated spectral properties, even at high spectral resolution. The drawback, of course, is the lack (usually) of spatial resolution available for Galactic planetary nebulae that is so useful in studying physical processes.

Over the past decade, a substantial quantity of low resolution spectroscopy has been acquired (e.g. Jacoby & Ciardullo 1999; Walsh et al. 1999; Roth et al. 2004; Méndez et al. 2005; Peña, Richer, & Stasińska 2007; Richer & McCall 2008; Magrini & Gonąlves 2009). On the other hand, the only high resolution spectroscopy of extragalactic planetary nebulae suitable for studying their internal kinematics is that of Zijlstra et al. (2006) and Arnaboldi et al. (2008), apart from the pioneering efforts of Dopita et al. (1985, 1988). Here, we present our high resolution spectroscopic observations of 211 planetary nebulae in 11 Local Group galaxies. For the first time, these data allow redundant comparisons across different stellar populations. This study is part of a larger effort to understand the systematics of planetary nebula kinematics within our Milky Way and the Local Group. López et al. (2010, in preparation) present our results for Galactic planetary nebulae.

We present our observations and the data reduction in § 2. We explain the analysis as well as its limitations in § 3. The results follow in § 4. We argue that the [O III]λ5007 line width is an adequate description of the kinematics of the majority of the ionized gas. We demonstrate that our radial velocities are accurate and in agreement with extant data. We find that the average line widths for bright planetary nebulae in all galaxies are similar, though there is a trend of decreasing line width with nuclear distance in the disc of M31. In § 5, we consider the implications of the foregoing, the most important being that the progenitor stars of bright planetary nebulae in all galaxies span a relatively small range in mass and that the central star plays an important role in accelerating the ionized shells of these objects. § 6 summarizes our conclusions.

Here, we focus on what we can learn of the evolution of bright extragalactic planetary nebulae and their progenitor stars from their [O III]λ5007 line widths. We make no attempt to investigate the kinematics of individual objects nor to interpret the line widths in terms of internal kinematics, as our spatially-integrated line profiles make this very difficult.

TABLE 1

OBSERVING RUNS

Run	Dates
2001sep	2001 Sep 21–26
2002jul	2002 Jul 23–24
2002oct	2002 Oct 31–2002 Nov 05
2003oct	2003 Oct 14–19
2004jun	2004 Jun 10–16 and 20–26
2004nov	2004 Nov 19–25
2004dec	2004 Dec 17–18
2005jul	2005 Jul 22–31
2005sep	2005 Sep 10–15
2006sep	2006 Sep 05–12
2007feb	2007 Feb 01–08
2007aug	2007 Aug 18–27

2. OBSERVATIONS AND DATA REDUCTION

The observations were obtained during twelve observing runs between 2001 September and 2007 August (see Table 1). All of the data were acquired with the 2.1 m telescope at the Observatorio Astronómico Nacional in the Sierra de San Pedro Mátir (OAN-SPM) and the Manchester Echelle Spectrometer (MES-SPM; Meaburn et al. 1984, 2003). The MES-SPM is a long slit echelle spectrometer, but uses narrow-band filters, instead of a cross-disperser, to isolate the orders containing the emission lines of interest. In our case, filters isolated orders 87 and 114 containing the Hα and [O III]λ5007 emission lines, respectively. All observations used a 150 μm

TABLE 2

[O III]λ5007 DATA FOR EXTRAGALACTIC PLANETARY NEBULAE

Galaxy	Object	Flux[a] (10^3 ADU)	FWHM (Å)	$V_{\rm helio}$[b] (km/s)	$\Delta V_{0.5}$ (km/s)	Run
Fornax	PN1	40.5 ± 0.4	0.353 ± 0.004	51.2 ± 0.1	8.4 ± 0.1	2004nov
Leo A	PN1	16.5 ± 0.4	0.65 ± 0.02	32.4 ± 0.4	18.3 ± 0.5	2004jun, 2004nov
M31	f08n04	6.9 ± 0.2	0.53 ± 0.02	-381.7 ± 0.5	14.6 ± 0.6	2005sep
M31	f08n05	10.2 ± 0.3	0.79 ± 0.03	-148.0 ± 0.7	22.7 ± 0.8	2004nov
M31	f08n08	7.0 ± 0.2	0.67 ± 0.02	-229.2 ± 0.5	18.9 ± 0.6	2005sep
M31	f08n09	8.1 ± 0.2	0.424 ± 0.009	-54.5 ± 0.2	10.9 ± 0.3	2004nov
M31	f08n10	7.8 ± 0.3	0.85 ± 0.03	-50.9 ± 0.8	24.6 ± 0.9	2005sep
M31	f15n12002	9.2 ± 0.2	0.50 ± 0.01	-90.8 ± 0.3	13.6 ± 0.3	2005sep
M31	f29n2065	4.2 ± 0.2	0.76 ± 0.04	-474 ± 1	22 ± 1	2007aug
M31	f29n9178	5.5 ± 0.1	0.52 ± 0.02	-524.1 ± 0.4	14.1 ± 0.5	2007aug
M31	f32n1	5.9 ± 0.2	0.59 ± 0.03	-371.8 ± 0.6	16.4 ± 0.7	2004nov
M31	fjchp51	3.7 ± 0.2	0.54 ± 0.03	-503.0 ± 0.8	15 ± 1	2007jan
M31	fjchp57	5.2 ± 0.2	0.54 ± 0.03	-141.9 ± 0.7	14.7 ± 0.8	2007aug
M31	M0050	13.7 ± 0.2	0.549 ± 0.008	-35.7 ± 0.2	15.1 ± 0.2	2005sep
M31	M0273	8.9 ± 0.2	0.84 ± 0.02	-132.0 ± 0.5	24.2 ± 0.7	2005sep
M31	M0319	14.5 ± 0.2	0.546 ± 0.009	-137.2 ± 0.2	15.0 ± 0.3	2005sep
M31	M0442	12.8 ± 0.2	0.597 ± 0.009	-86.0 ± 0.2	16.7 ± 0.3	2005sep
M31	M1232	2.9 ± 0.2	0.85 ± 0.06	-174 ± 1	25 ± 2	2006sep
M31	M1296	1.6 ± 0.2	0.68 ± 0.08	-90 ± 2	19 ± 2	2001sep
M31	M1558	12.2 ± 0.2	0.59 ± 0.01	-349.7 ± 0.3	16.5 ± 0.4	2005sep
M31	M1596	8.0 ± 0.2	0.76 ± 0.02	-374.5 ± 0.5	21.7 ± 0.7	2007aug
M31	M1980	7.5 ± 0.2	0.67 ± 0.02	-417.1 ± 0.4	18.9 ± 0.5	2005sep
M31	M2357	5.8 ± 0.2	0.58 ± 0.02	-561.7 ± 0.5	16.1 ± 0.7	2004nov
M31	M2371	8.6 ± 0.2	0.67 ± 0.02	-463.5 ± 0.4	19.0 ± 0.5	2004nov
M31	M2401	9.1 ± 0.2	0.56 ± 0.01	-437.0 ± 0.3	15.5 ± 0.3	2004nov
M31	M2404	21.0 ± 0.3	0.65 ± 0.01	-379.6 ± 0.3	18.2 ± 0.4	2004nov
M31	M2410	13.1 ± 0.5	0.92 ± 0.04	-436.2 ± 0.9	27 ± 1	2004nov
M31	M2437	12.2 ± 0.3	0.74 ± 0.02	-73.8 ± 0.5	21.2 ± 0.6	2004nov
M31	M2466	4.8 ± 0.2	0.46 ± 0.02	-412.5 ± 0.5	12.2 ± 0.6	2005sep
M31	M2496	11.7 ± 0.2	0.534 ± 0.009	-353.7 ± 0.2	14.6 ± 0.3	2004nov
M31	M2501	3.2 ± 0.2	0.66 ± 0.06	-386 ± 1	19 ± 1	2004nov
M31	M2502	3.6 ± 0.2	0.65 ± 0.04	-428.5 ± 0.9	19 ± 1	2004nov
M31	M2507	9.8 ± 0.3	0.61 ± 0.02	-184.7 ± 0.4	16.9 ± 0.5	2004nov
M31	M2512	6.6 ± 0.3	0.61 ± 0.03	-315.6 ± 0.8	17 ± 1	2004nov
M31	M2514	4.1 ± 0.3	0.61 ± 0.04	-453 ± 1	17 ± 1	2004nov
M31	M2519	6.0 ± 0.2	0.55 ± 0.02	-480.4 ± 0.4	15.2 ± 0.5	2004nov
M31	M2538	11.5 ± 0.1	0.434 ± 0.006	-444.3 ± 0.1	11.3 ± 0.2	2007aug
M31	M2694	10.2 ± 0.2	0.53 ± 0.01	-240.5 ± 0.3	14.6 ± 0.4	2005sep
M31	M2860	9.2 ± 0.2	0.68 ± 0.02	-413.4 ± 0.4	19.3 ± 0.5	2005sep
M31	M2943	8.9 ± 0.2	0.53 ± 0.01	-329.4 ± 0.3	14.6 ± 0.3	2007aug
M31	M2985	6.7 ± 0.2	0.46 ± 0.01	-431.9 ± 0.3	12.2 ± 0.4	2004nov
M31	M2988	5.0 ± 0.2	0.49 ± 0.02	-116.7 ± 0.6	13.0 ± 0.7	2004nov
M31	M3246	7.8 ± 0.2	0.68 ± 0.02	-542.9 ± 0.4	19.3 ± 0.5	2005sep
M31	PN001	7.0 ± 0.3	0.66 ± 0.03	-418.8 ± 0.8	19.0 ± 1	2001sep
M31	PN003	4.9 ± 0.3	0.56 ± 0.04	-273 ± 1	15 ± 1	2006sep
M31	PN008	5.7 ± 0.3	0.65 ± 0.04	-241 ± 1	18 ± 1	2006sep
M31	PN010	4.5 ± 0.3	0.61 ± 0.05	-157 ± 1	17 ± 2	2001sep
M31	PN012	4.7 ± 0.3	0.79 ± 0.06	-236 ± 2	23 ± 2	2007jan
M31	PN015	10.5 ± 0.6	0.99 ± 0.06	-351 ± 2	29 ± 2	2001sep, 2005sep
M31	PN017	2.1 ± 0.2	0.61 ± 0.05	-495 ± 1	17 ± 1	2001sep
M31	PN018	3.9 ± 0.3	0.62 ± 0.05	-507 ± 1	17 ± 1	2001sep
M31	PN023	7.1 ± 0.3	0.72 ± 0.03	-231.2 ± 0.8	20 ± 1	2006sep

TABLE 2 (CONTINUED)

Galaxy	Object	Flux[a] (10^3 ADU)	FWHM (Å)	V_{helio}[b] (km/s)	$\Delta V_{0.5}$ (km/s)	Run
M31	PN024	4.9 ± 0.2	0.69 ± 0.04	-273.5 ± 0.9	20 ± 1	2001sep, 2005sep
M31	PN026	6.3 ± 0.3	0.56 ± 0.03	-400.2 ± 0.7	15.4 ± 0.9	2001sep
M31	PN027	6.4 ± 0.2	0.89 ± 0.03	-135.3 ± 0.8	26 ± 1	2006sep
M31	PN028	4.5 ± 0.3	0.80 ± 0.07	-256 ± 2	23 ± 2	2001sep
M31	PN029	5.8 ± 0.4	0.97 ± 0.06	-456 ± 2	28 ± 2	2001sep, 2005sep
M31	PN030	11.4 ± 0.4	1.03 ± 0.04	-279 ± 1	30 ± 1	2001sep, 2007jan
M31	PN031	6.2 ± 0.2	0.57 ± 0.02	-226.5 ± 0.6	15.8 ± 0.7	2001sep
M31	PN032	16.8 ± 0.6	0.90 ± 0.03	-119.5 ± 0.8	26 ± 1	2001sep, 2005sep
M31	PN033	4.8 ± 0.2	0.63 ± 0.03	131.7 ± 0.8	18 ± 1	2007jan
M31	PN035	4.4 ± 0.3	0.71 ± 0.05	-372 ± 1	20 ± 1	2001sep, 2005sep
M31	PN036	1.9 ± 0.2	0.58 ± 0.07	-183 ± 2	16 ± 2	2001sep
M31	PN037	1.9 ± 0.3	0.8 ± 0.1	-346 ± 3	23 ± 4	2001sep
M31	PN038	5.2 ± 0.2	0.71 ± 0.03	-319.1 ± 0.8	20 ± 1	2007jan
M31	PN042	8.7 ± 0.2	0.55 ± 0.01	-390.1 ± 0.3	15.2 ± 0.3	2005jul
M31	PN043	5.8 ± 0.2	0.63 ± 0.02	-93.3 ± 0.5	17.7 ± 0.7	2006sep
M31	PN045	14.8 ± 0.3	0.55 ± 0.01	-255.0 ± 0.3	15.1 ± 0.4	2001sep
M31	PN046	14.6 ± 0.4	0.57 ± 0.02	-457.2 ± 0.4	15.7 ± 0.5	2005jul
M31	PN047	14.2 ± 0.4	0.61 ± 0.02	-316.7 ± 0.5	17.2 ± 0.6	2005jul
M31	PN048	14.6 ± 0.2	0.76 ± 0.01	-237.5 ± 0.3	21.8 ± 0.3	2005sep
M31	PN049	3.2 ± 0.2	0.59 ± 0.04	-334 ± 1	17 ± 1	2005jul
M31	PN052	4.8 ± 0.2	0.59 ± 0.03	-153.4 ± 0.6	16.5 ± 0.8	2005sep
M31	PN053	7.1 ± 0.2	0.45 ± 0.01	-270.3 ± 0.4	11.8 ± 0.4	2001sep
M31	PN054	8.3 ± 0.2	0.48 ± 0.01	-499.7 ± 0.3	13.0 ± 0.4	2005sep
M31	PN055	4.1 ± 0.2	0.75 ± 0.04	-492.8 ± 0.9	22 ± 1	2005sep
M31	PN056	7.6 ± 0.2	0.54 ± 0.01	-252.1 ± 0.4	14.7 ± 0.4	2005sep
M31	PN058	5.5 ± 0.3	0.74 ± 0.04	-420 ± 1	21 ± 1	2006sep
M31	PN061	8.7 ± 0.3	0.67 ± 0.02	-183.4 ± 0.6	19.0 ± 0.7	2001sep, 2005sep
M31	PN062	8.3 ± 0.3	0.69 ± 0.02	-570.2 ± 0.6	19.6 ± 0.7	2006sep
M31	PN064	2.3 ± 0.2	0.61 ± 0.07	-609 ± 2	17 ± 2	2001sep
M31	PN067	19.0 ± 0.3	0.498 ± 0.008	-410.6 ± 0.2	13.4 ± 0.2	2005sep
M31	PN069	3.8 ± 0.2	0.76 ± 0.05	-522 ± 1	22 ± 2	2005sep
M31	PN071	2.5 ± 0.2	0.71 ± 0.05	-229 ± 1	20 ± 2	2007jan
M31	PN072	5.4 ± 0.4	0.54 ± 0.04	-351 ± 1	15 ± 1	2005sep
M31	PN075	5.6 ± 0.4	0.81 ± 0.06	-398 ± 1	23 ± 2	2007jan
M31	PN080	11.0 ± 0.3	0.73 ± 0.02	-299.7 ± 0.5	20.9 ± 0.6	2007jan
M31	PN087	3.4 ± 0.3	0.70 ± 0.07	-381 ± 2	20 ± 2	2001sep, 2007jan
M31	PN091	6.5 ± 0.2	0.80 ± 0.03	-182.0 ± 0.7	23.0 ± 0.8	2007jan
M31	PN092	8.0 ± 0.2	0.49 ± 0.01	-275.0 ± 0.3	13.1 ± 0.3	2005sep
M31	PN093	4.5 ± 0.2	0.85 ± 0.05	-546 ± 1	25 ± 1	2006sep
M31	PN095	4.4 ± 0.1	0.42 ± 0.02	-394.3 ± 0.4	10.8 ± 0.4	2006sep
M31	PN097	8.4 ± 0.2	0.64 ± 0.01	-480.0 ± 0.3	17.9 ± 0.4	2005sep
M31	PN116	8.9 ± 0.2	0.66 ± 0.02	-350.1 ± 0.4	18.8 ± 0.5	2005sep
M31	PN125	5.0 ± 0.2	0.55 ± 0.03	-227.6 ± 0.7	15.1 ± 0.8	2006sep
M31	PN131	5.0 ± 0.1	0.53 ± 0.02	-339.3 ± 0.4	14.4 ± 0.5	2005sep
M31	pn136	3.4 ± 0.3	0.73 ± 0.06	-329 ± 2	21 ± 2	2007jan
M31	PN142	3.1 ± 0.2	0.62 ± 0.04	-259 ± 1	17 ± 1	2005jul
M31	PN143	1.6 ± 0.2	1.0 ± 0.1	-267 ± 3	28 ± 4	2005sep
M31	PN150	5.4 ± 0.2	0.64 ± 0.02	-136.2 ± 0.6	18.2 ± 0.7	2005sep
M31	PN151	6.8 ± 0.2	0.76 ± 0.02	-562.1 ± 0.6	22.0 ± 0.7	2005sep
M31	PN154	7.3 ± 0.2	0.55 ± 0.01	-349.3 ± 0.3	15.2 ± 0.4	2005sep
M31	PN155	9.8 ± 0.2	0.69 ± 0.01	-241.6 ± 0.3	19.5 ± 0.4	2005sep
M31	PN172	8.9 ± 0.2	0.82 ± 0.02	-247.2 ± 0.5	23.6 ± 0.6	2005sep
M31	PN177	4.1 ± 0.2	0.58 ± 0.04	-300.3 ± 0.9	16 ± 1	2007jan
M31	PN178	11.8 ± 0.2	0.58 ± 0.01	-213.8 ± 0.3	16.1 ± 0.3	2005sep

TABLE 2 (CONTINUED)

Galaxy	Object	Flux[a] (10^3 ADU)	FWHM (Å)	$V_{\rm helio}$[b] (km/s)	$\Delta V_{0.5}$ (km/s)	Run
M31	pn179	4.0 ± 0.2	0.62 ± 0.04	-124.6 ± 0.9	17 ± 1	2007jan
M31	PN190	4.8 ± 0.2	0.48 ± 0.02	-113.2 ± 0.5	12.9 ± 0.7	2007jan
M31	PN209	6.1 ± 0.2	0.47 ± 0.01	-320.9 ± 0.3	12.6 ± 0.4	2005sep
M31	PN216	7.2 ± 0.2	0.43 ± 0.01	-229.1 ± 0.3	11.2 ± 0.3	2005sep
M31	PN219	5.1 ± 0.2	0.71 ± 0.03	-140.9 ± 0.7	20.2 ± 0.8	2005sep
M31	PN237	5.3 ± 0.2	0.87 ± 0.04	-64.7 ± 0.9	25 ± 1	2005sep
M31	PN240	11.0 ± 0.2	0.61 ± 0.01	-95.1 ± 0.3	17.2 ± 0.4	2005sep
M31	PN278	4.2 ± 0.3	0.75 ± 0.05	-135 ± 1	21 ± 2	2005sep
M31	PN290	3.4 ± 0.2	0.57 ± 0.03	-658.6 ± 0.7	15.7 ± 0.9	2007jan
M31	PN335	3.5 ± 0.2	0.74 ± 0.04	-446.1 ± 0.9	21 ± 1	2004nov
M31	PN344	8.5 ± 0.2	0.60 ± 0.01	-505.2 ± 0.3	16.7 ± 0.4	2004nov
M31	PN345	9.8 ± 0.2	0.60 ± 0.02	-490.4 ± 0.4	16.8 ± 0.5	2004nov
M31	PN349	6.4 ± 0.2	0.47 ± 0.01	-494.5 ± 0.3	12.6 ± 0.4	2004nov
M31	PN353	6.9 ± 0.2	0.74 ± 0.02	-257.3 ± 0.5	21.1 ± 0.6	2004nov
M31	PN363	7.2 ± 0.2	0.75 ± 0.02	-95.6 ± 0.5	21.6 ± 0.6	2007aug
M31	PN364	6.8 ± 0.1	0.309 ± 0.006	-102.5 ± 0.1	6.6 ± 0.2	2005sep
M31	PN370	5.7 ± 0.2	0.41 ± 0.01	-91.0 ± 0.3	10.4 ± 0.4	2004nov
M31	PN375	11.5 ± 0.2	0.71 ± 0.02	-410.6 ± 0.4	20.1 ± 0.4	2005sep
M31	PN380	13.3 ± 0.2	0.66 ± 0.01	-297.1 ± 0.3	18.7 ± 0.3	2005sep
M31	PN387	7.5 ± 0.2	0.66 ± 0.02	-254.6 ± 0.4	18.6 ± 0.5	2005sep
M31	PN390	9.8 ± 0.2	0.83 ± 0.02	-578.7 ± 0.5	23.9 ± 0.6	2005sep
M31	PN410	6.1 ± 0.2	0.82 ± 0.03	-530.3 ± 0.7	23.7 ± 0.8	2005sep
M31	PN413	10.5 ± 0.3	0.52 ± 0.01	-317.6 ± 0.4	14.2 ± 0.4	2005sep
M31	PN414	5.1 ± 0.2	0.73 ± 0.03	37.6 ± 0.8	20.7 ± 0.9	2005sep
M31	PN450	2.3 ± 0.2	0.86 ± 0.06	-361 ± 1	25 ± 2	2005sep
M31	PN478	5.6 ± 0.2	0.47 ± 0.02	-115.9 ± 0.5	12.6 ± 0.6	2007jan
M31	PN537	7.8 ± 0.1	0.425 ± 0.009	-154.8 ± 0.2	11.0 ± 0.3	2005sep
M31	PN555	11.2 ± 0.2	0.80 ± 0.02	-98.5 ± 0.4	23.1 ± 0.6	2005sep
M31	PN557	7.1 ± 0.2	0.66 ± 0.02	-70.2 ± 0.5	18.8 ± 0.6	2005sep
M31	PN559	11.9 ± 0.1	0.520 ± 0.007	-113.0 ± 0.2	14.2 ± 0.2	2005sep
M31	PN563	8.8 ± 0.3	0.87 ± 0.03	-157.5 ± 0.7	25.1 ± 0.9	2005sep
M31	PN568	7.9 ± 0.2	0.69 ± 0.02	-118.7 ± 0.5	19.8 ± 0.7	2005sep
M31	PN569	2.7 ± 0.2	0.87 ± 0.06	-148 ± 2	25 ± 2	2005sep
M32	PN1	10.6 ± 0.3	0.56 ± 0.02	-206.7 ± 0.4	15.3 ± 0.5	2001sep, 2006sep
M32	PN2	6.6 ± 0.2	0.66 ± 0.02	-218.0 ± 0.6	18.8 ± 0.7	2006sep
M32	PN3	5.6 ± 0.2	0.46 ± 0.02	-169.3 ± 0.5	12.3 ± 0.6	2001sep
M32	PN5	5.5 ± 0.4	0.80 ± 0.06	-245 ± 1	23 ± 2	2001sep, 2006sep
M32	PN6	4.8 ± 0.3	0.84 ± 0.06	-206 ± 1	24 ± 2	2001sep, 2006sep
M32	PN7	5.6 ± 0.2	0.42 ± 0.02	-194.4 ± 0.5	10.8 ± 0.6	2001sep, 2006sep
M32	PN8	4.0 ± 0.3	0.83 ± 0.06	-168 ± 2	24 ± 2	2001sep
M32	PN21	10.1 ± 0.5	0.90 ± 0.05	-192 ± 1	26 ± 1	2001sep, 2006sep
M32	PN23	3.5 ± 0.2	0.87 ± 0.05	-231 ± 1	25 ± 2	2006sep
M32	PN24+PN25	7.8 ± 0.2	0.77 ± 0.03	-171.1 ± 0.6	22.2 ± 0.7	2006sep
M32	PN24	3.8 ± 0.2	0.82 ± 0.04	-166.8 ± 0.9	24 ± 1	2006sep
M32	PN25	4.1 ± 0.2	0.72 ± 0.03	-174.8 ± 0.7	20.5 ± 0.9	2006sep
M32	PN26	3.5 ± 0.2	0.91 ± 0.06	-229 ± 2	26 ± 2	2006sep
M32	PN29	2.4 ± 0.2	0.63 ± 0.06	-646 ± 2	18 ± 2	2006sep
M33	M002	5.0 ± 0.3	0.56 ± 0.03	-126.9 ± 0.8	16 ± 1	2003oct
M33	M005	4.0 ± 0.2	0.38 ± 0.02	-125.5 ± 0.6	9.5 ± 0.7	2003oct
M33	M008	4.4 ± 0.2	0.45 ± 0.02	-115.7 ± 0.5	11.9 ± 0.6	2003oct
M33	M013	3.2 ± 0.1	0.44 ± 0.02	-106.9 ± 0.6	11.5 ± 0.7	2002nov
M33	M017	7.0 ± 0.3	0.57 ± 0.03	-195.9 ± 0.7	15.8 ± 0.8	2002nov
M33	M018	13.4 ± 0.3	0.55 ± 0.01	-155.2 ± 0.3	15.3 ± 0.4	2002nov
M33	M028	5.0 ± 0.2	0.54 ± 0.03	-161.4 ± 0.7	15.0 ± 0.9	2002nov

TABLE 2 (CONTINUED)

Galaxy	Object	Flux[a] (10^3 ADU)	FWHM (Å)	$V_{\rm helio}$[b] (km/s)	$\Delta V_{0.5}$ (km/s)	Run
M33	M042	14.4 ± 0.5	0.79 ± 0.03	-136.1 ± 0.7	22.7 ± 0.8	2002nov
M33	M046	5.0 ± 0.2	0.37 ± 0.02	-127.7 ± 0.4	8.9 ± 0.5	2002nov
M33	M059	5.1 ± 0.2	0.40 ± 0.02	-113.3 ± 0.4	10.0 ± 0.5	2003oct
M33	M061	6.8 ± 0.3	0.66 ± 0.03	-115.3 ± 0.8	18.7 ± 0.9	2002nov
M33	M062	4.4 ± 0.2	0.53 ± 0.03	-98.3 ± 0.8	15 ± 1	2002nov
M33	M063	8.2 ± 0.3	0.68 ± 0.03	-111.5 ± 0.7	19.2 ± 0.8	2002nov
M33	M065	4.9 ± 0.2	0.54 ± 0.03	-170.7 ± 0.7	14.7 ± 0.9	2002nov
M33	M067	11.0 ± 0.3	0.64 ± 0.02	-128.0 ± 0.5	18.1 ± 0.6	2002nov
M33	M068	7.1 ± 0.3	0.50 ± 0.03	-170.7 ± 0.6	13.4 ± 0.8	2002nov
M33	M069	10.5 ± 0.5	0.84 ± 0.05	-168 ± 1	24 ± 1	2002nov
M33	M072	3.8 ± 0.2	0.53 ± 0.03	-267.5 ± 0.8	14.5 ± 0.9	2002nov
M33	M074	4.0 ± 0.3	0.72 ± 0.06	-168 ± 2	21 ± 2	2003oct
M33	M075	5.8 ± 0.2	0.46 ± 0.02	-259.8 ± 0.4	12.3 ± 0.5	2002nov
M33	M079	6.1 ± 0.3	0.75 ± 0.04	-165 ± 1	21 ± 1	2003oct
M33	M089	4.1 ± 0.3	0.69 ± 0.05	-272 ± 1	20 ± 2	2003oct
M33	M091	24.0 ± 0.5	0.70 ± 0.01	-137.6 ± 0.4	19.8 ± 0.4	2002nov, 2003oct
M33	M093	14.2 ± 0.4	0.66 ± 0.02	-171.6 ± 0.6	18.8 ± 0.7	2002nov, 2003oct
M33	M094	13.4 ± 0.4	0.57 ± 0.02	-168.3 ± 0.5	15.8 ± 0.5	2002nov, 2003oct
M33	M095	4.1 ± 0.2	0.46 ± 0.03	-262.5 ± 0.7	12.1 ± 0.8	2002nov
M33	M096	8.6 ± 0.2	0.44 ± 0.01	-151.7 ± 0.3	11.5 ± 0.4	2003oct
M33	M101	7.1 ± 0.2	0.51 ± 0.02	-132.7 ± 0.4	13.9 ± 0.5	2003oct
M33	M111	8.9 ± 0.3	0.70 ± 0.03	-241.3 ± 0.7	20.0 ± 0.8	2003oct
M33	M119	8.1 ± 0.3	0.81 ± 0.04	-231.4 ± 0.9	23 ± 1	2003oct
M33	M125	3.3 ± 0.2	0.64 ± 0.04	-182 ± 1	18 ± 1	2003oct
M33	M128	4.8 ± 0.2	0.34 ± 0.01	-260.1 ± 0.3	8.0 ± 0.4	2002nov
M33	newPN	6.2 ± 0.2	0.35 ± 0.01	-112.5 ± 0.2	8.1 ± 0.3	2003oct
NGC147	PN04	2.8 ± 0.1	0.34 ± 0.02	-192.2 ± 0.5	7.7 ± 0.6	2007jan
NGC147	PN07	3.8 ± 0.2	0.53 ± 0.03	-182.5 ± 0.9	15 ± 1	2007jan
NGC185	PN01	10.5 ± 0.3	0.73 ± 0.02	-232.7 ± 0.6	20.9 ± 0.7	2001sep
NGC185	PN02	4.3 ± 0.1	0.37 ± 0.01	-206.0 ± 0.4	8.8 ± 0.4	2001sep
NGC185	PN03	6.2 ± 0.3	0.60 ± 0.03	-213.1 ± 0.7	16.8 ± 0.8	2001sep, 2006sep
NGC185	PN04	3.5 ± 0.3	0.71 ± 0.07	-215 ± 2	20 ± 2	2006sep
NGC185	PN05	7.1 ± 0.4	0.88 ± 0.05	-245 ± 1	26 ± 1	2001sep, 2006sep
NGC205	PN1	4.5 ± 0.2	0.31 ± 0.02	-291.2 ± 0.4	6.7 ± 0.4	2001sep
NGC205	PN2	5.2 ± 0.3	0.74 ± 0.04	-230 ± 1	21 ± 1	2007aug
NGC205	PN4	4.7 ± 0.2	0.47 ± 0.03	-251.1 ± 0.6	12.6 ± 0.7	2001sep
NGC205	PN5	6.7 ± 0.3	0.58 ± 0.03	-240.6 ± 0.6	16.0 ± 0.8	2001sep
NGC205	PN6	4.8 ± 0.3	0.57 ± 0.04	-210.1 ± 0.9	16 ± 1	2001sep
NGC205	PN7	5.2 ± 0.2	0.33 ± 0.01	-243.7 ± 0.3	7.6 ± 0.3	2001sep
NGC205	PN8	3.7 ± 0.2	0.58 ± 0.04	-259.2 ± 0.9	16 ± 1	2001sep
NGC205	PN9	3.6 ± 0.2	0.36 ± 0.02	-241.4 ± 0.4	8.5 ± 0.5	2001sep
NGC205	PN10	5.4 ± 0.3	0.79 ± 0.04	-220 ± 1	23 ± 1	2007aug
NGC6822	PN1	4.5 ± 0.2	0.48 ± 0.02	-73.0 ± 0.4	12.9 ± 0.5	2005jul
NGC6822	PN19	4.4 ± 0.2	0.48 ± 0.03	-69.0 ± 0.7	12.8 ± 0.8	2005jul
NGC6822	S14	5.0 ± 0.3	0.62 ± 0.04	-100.7 ± 0.9	17 ± 1	2002jul
NGC6822	S16	11.3 ± 0.5	0.60 ± 0.03	-78.7 ± 0.7	16.7 ± 0.8	2002jul
NGC6822	S30	4.2 ± 0.2	0.97 ± 0.06	-60 ± 1	28 ± 2	2005jul
NGC6822	S33	7.5 ± 0.4	0.85 ± 0.05	-43 ± 1	25 ± 2	2002jul
Sagittarius	He 2-436	1480 ± 20	0.474 ± 0.006	131.6 ± 0.1	12.6 ± 0.2	2004juna
Sagittarius	StWr 2-21	218 ± 3	0.94 ± 0.01	116.7 ± 0.3	27.2 ± 0.4	2004junc
Sagittarius	Wray 16-423	3200 ± 30	0.727 ± 0.007	131.6 ± 0.2	20.8 ± 0.2	2004juna
Sextans A	PN1	5.0 ± 0.3	0.88 ± 0.06	31 ± 1	26 ± 2	2004nov

[a]The fluxes are not calibrated. See § 2 and § 3.
[b]The uncertainties listed are formal uncertainties. See § 4.3.

TABLE 3

Hα DATA FOR EXTRAGALACTIC PLANETARY NEBULAE

Galaxy	Object	Flux[a] (10^3 ADU)	FWHM (Å)	$V_{\rm helio}$[b] (km s^{-1})	$\Delta V_{0.5}$ (km s^{-1})	Run
Fornax	PN1	35.4 ± 0.2	0.723 ± 0.005	47.95 ± 0.09	11.4 ± 0.1	2004nov
M32	PN3	4.0 ± 0.4	0.9 ± 0.1	-157 ± 2	17 ± 2	2001sep
M32	PN6	4.3 ± 0.5	1.5 ± 0.2	-185 ± 3	33 ± 4	2001sep
M33	M059	2.2 ± 0.3	0.8 ± 0.1	-119 ± 2	13 ± 2	2003oct
NGC6822	PN19	4.8 ± 0.2	0.82 ± 0.03	-70.5 ± 0.5	14.3 ± 0.7	2005jul
NGC6822	S14	3.1 ± 0.3	0.97 ± 0.09	-104 ± 2	19 ± 2	2002jul
NGC6822	S16	3.7 ± 0.3	0.93 ± 0.09	-76 ± 2	18 ± 2	2002jul
NGC6822	S30	6.7 ± 0.2	1.32 ± 0.04	-64.1 ± 0.7	27.7 ± 0.9	2005jul
NGC6822	S33	7.0 ± 0.4	1.17 ± 0.08	-44 ± 1	24 ± 2	2002jul
Sagittarius	He 2-436	364 ± 1	0.820 ± 0.003	129.16 ± 0.05	14.43 ± 0.06	2004juna
Sagittarius	StWr 2-21	171.4 ± 0.7	1.248 ± 0.005	131.1 ± 0.1	25.9 ± 0.1	2004junc
Sagittarius	Wray 16-42	804 ± 4	1.057 ± 0.005	128.8 ± 0.1	21.0 ± 0.1	2004juna

[a]The fluxes are not calibrated. See § 2 and § 3.

[b]The uncertainties listed are formal uncertainties. See § 4.3.

TABLE 4

[O III]λ5007 DATA FOR COMPACT H II REGIONS

Galaxy	Object	Flux[a] (10^3 ADU)	FWHM (Å)	$V_{\rm helio}$[b] (km s^{-1})	$\Delta V_{0.5}$ (km s^{-1})	Run
NGC6822	S10	8.4 ± 0.4	0.59 ± 0.03	-88.1 ± 0.8	16 ± 1	2002jul
NGC3109	PN07	6.9 ± 0.2	0.47 ± 0.02	385.7 ± 0.4	12.6 ± 0.5	2004nov
NGC3109	PN10	2.7 ± 0.2	0.60 ± 0.06	409 ± 2	17 ± 2	2004dec

[a]The fluxes are not calibrated. See § 2 and § 3.

[b]The uncertainties listed are formal uncertainties. See § 4.3.

wide slit, equivalent to 1″.9 on the sky. When coupled with a SITe 1024×1024 CCD with 24 μm pixels binned 2×2, the resulting spectral resolutions were approximately 0.077 Å/pix and 0.100 Å/pix at [O III]λ5007 and Hα, respectively (equivalent to 11 km s^{-1} for 2.6 pix FWHM). Immediately before or after every object spectrum, exposures of a ThAr lamp were taken to calibrate in wavelength. The internal precision of the arc lamp calibrations is better than ± 1.0 km s^{-1}.

All spectra were of 30 minutes duration. Depending upon the resulting signal-to-noise, up to four spectra were acquired, occasionally during more than one observing run. With very few exceptions (PN24 and PN25 in M32), the spectrometer slit was always oriented north-south over the object(s) of interest.

Table 2 presents our entire sample of extragalactic planetary nebulae. In total, we observed 211 extragalactic planetary nebulae in 11 Local Group galaxies. More than half of the sample is drawn from M31 (137 objects), with M33 providing the second largest sample (33 objects). The remaining galactic hosts are dwarfs and their planetary nebula populations are smaller: one planetary nebula was observed in each of Fornax, Leo A, and Sextans A, 2 in NGC 147, 3 in Sagittarius, 5 in NGC 185, 6 in NGC 6822, 9 in NGC 205, and 13 in M32. Most of the objects we observed are within two magnitudes of the peak of the PNLF, though we did try to observe fainter objects if low-resolution spectra existed in the literature. Table 3 presents our few Hα spectra. In Table 4, we present observations of three objects whose classifications as planetary nebulae are dubious.

The object names we adopt in Tables 2–4 come from the following sources: Leo A and Sextans A from Jacoby & Lesser (1981); Fornax from Danziger et al. (1978); M31 from Ford & Jacoby (1978), Lawrie & Ford (1982), Nolthenius & Ford (1987),

TABLE 5

NEW PLANETARY NEBULAE IN M31 AND M33

Galaxy	Object	$\alpha(2000)$	$\delta(2000)$
M31	f08n04	00 49 50	42 31 40
M31	f08n05	00 49 32	42 37 38
M31	f08n08	00 50 13	42 29 48
M31	f08n09	00 48 48	42 51 36
M31	f08n10	00 47 54	42 14 58
M31	f15n12002	00 47 46.8	42 12 15
M31	f29n2065	00 33 41.1	39 31 51
M31	f29n9178	00 37 21.1	39 50 51
M31	f32n1	00 49 55	38 32 49
M33	NewPN	01 32 56	30 25 56

The objects in M31 are from Richer et al. (2004).

Ciardullo et al. (1989b), Richer, Lee, & Hwang (2004), and Merrett et al. (2006); M32 from Ford & Jenner (1975) and Ford (1983); M33 from Magrini et al. (2000); NGC 147 from Corradi et al. (2005); NGC 185 from Ford, Jacoby, & Jenner (1977); NGC 205 from Ford, Jenner, & Epps (1973), Ford (1978), and Ciardullo et al. (1989b); NGC 3109 from Peña et al. (2007); NGC 6822 from Killen & Dufour (1982) and Leisy et al. (2005); and Sagittarius from Acker et al. (1992). The names follow strict historical precedent, except for NGC 147, NGC 3109 (we do not use Richer & McCall 1992), and perhaps some objects in M31 from Nolthenius & Ford (1987) whose identifications are taken from Merrett et al. (2006). Coordinates for the objects from Richer et al. (2004) and a new planetary nebula candidate that we discovered in M33 are given in Table 5.

All of the spectra were reduced using the SPECRED package of the Image Reduction and Analysis Facility[8] (IRAF) following Massey, Valdes, & Barnes (1992). We edited each spectrum for the presence of cosmic rays. We then extracted the source spectra and used these apertures to extract ThAr spectra from the lamp spectra. The latter were used to calibrate in wavelength. If more than one object spectrum was obtained, they were co-added after being calibrated in wavelength. If they did not coincide exactly in wavelength, likely the result of centering differently or low signal-to-noise (S/N), they were shifted to a common wavelength and then co-added.

[8]IRAF is distributed by the National Optical Astronomical Observatories, which is operated by the Associated Universities for Research in Astronomy, Inc., under contract to the National Science Foundation.

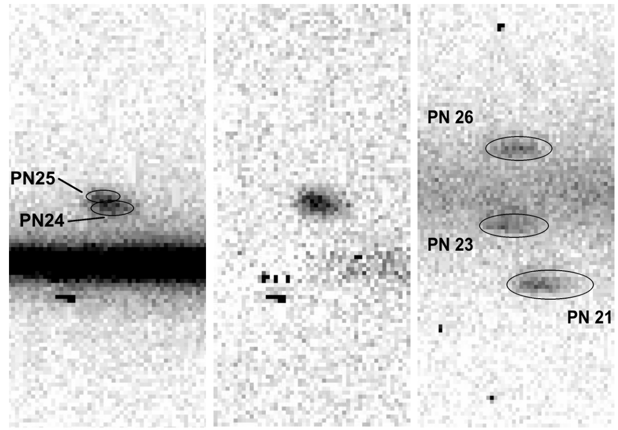

Fig. 1. The left panel presents the raw two-dimensional spectrum for PN24 and PN25 in M32 (east is up, bluer wavelengths to the left). The continuous emission below them (to the west) is from M32's nuclear region. The planetary nebulae are sufficiently close together that their emission is merged into a single teardrop-shaped profile. The middle panel presents the same spectrum for PN24 and PN25 once M32's continuous emission had been filtered out. For comparison, the right panel presents the two-dimensional spectrum for PN26, PN23, and PN21 in M32 (ordered north to south; north is up, bluer wavelengths to the left) at the same spatial scale and taken immediately prior to the spectrum of PN24 and PN25 (continuous emission from M32 is again visible). The two-dimensional (spatially-merged) spectrum of PN24 and PN25 is clearly more complex than the spectra of PN26, PN23, or PN21. PN25 is to the east (above) of PN24, has a more blueshifted radial velocity, and a narrower line profile (see Table 2), the two effects explaining the tilted teardrop shape of the combined profile. The "individual" profiles for PN24 and PN25 were obtained by splitting the combined emission at the spatial centre.

Note that shifting the spectra before co-adding minimizes the eventual line width that we measure. We did not calibrate in flux.

Except for PN24 and PN25 in M32, all of the objects were observed as spatially distinct sources. However, there were occasions when multiple objects fell within the spectrometer slit, particularly for M31 and M32 (see Figure 1, right panel). PN24 and PN25 in M32 required special treatment, since their images were not clearly resolved spatially by the spectrometer (the spectrometer slit was oriented east-west in the hope of better separating them). Fortunately, both their radial velocities and line widths are distinct, which helps separating their spectra. Figure 1 presents the two-dimensional spectrum of PN24 and PN25 (both raw and filtered so as to remove M32's continuous spectrum) and compares it with the two-dimensional spectrum of PN26, PN23, and PN21 (in M32) taken immediately before. It is clear that the two-dimensional spectrum of PN24 and PN25 is more complicated in the spatial direction (vertical in Figure 1) than those of the other PNe. The "individual" profiles for PN24 and PN25 were obtained by splitting the combined profile at the spatial centre since the two PNe are similarly bright (Ciardullo et al. 1989b). Table 2 presents the analysis of both the combined and split profiles for PN24 and PN25.

3. DATA ANALYSIS

The line profiles of extragalactic planetary nebulae usually cannot be distinguished statistically from a Gaussian shape because of their limited S/N (e.g., Dopita et al. 1985, 1988; Arnaboldi et al. 2008). We analyzed the one-dimensional line profiles with a locally-implemented software package (INTENS) (McCall, Rybski, & Shields 1985) to determine the radial velocity, flux, and profile width (FWHM; full width at half maximum intensity) as well as the uncertainties (1σ) in these parameters. INTENS fits the emission line profile with a sampled Gaussian function and models the continuum as a straight line. Thus, this analysis assumes that the lines have a Gaussian shape and that they are superposed on a flat continuum. Figures 2–4 present examples of the line profiles. Excepting the planetary nebulae in the Fornax and Sagittarius dwarf spheroidals, the line profiles in Figures 2–4 do not deviate significantly from a Gaussian shape, even though they are among our profiles with the highest S/N. For the [O III]λ5007 observations, we typically fit a 10 Å spectral interval more or less centered on the emission line, though as little as 6 Å was used in some cases to avoid cosmic rays. For the Hα observations, a 15 Å interval was used. For the observations of StWr 2-21 and Wray 16-423 in the light of Hα, the He II λ6560 line is also present, so we fit both lines simultaneously, but assuming that the widths of both lines are identical.

For each object we observed, Tables 2–4 present the flux, the observed line width, the heliocentric radial velocity (from IRAF's RVCORRECT), *half* of the intrinsic line width (see below, equation 1), and the corresponding uncertainties in all of these quantities. The uncertainties are formal, one-sigma uncertainties and pertain to the final (sometimes summed) spectra.

As already noted (§ 2), we did not attempt a flux calibration. The vast majority of the objects in our catalogue (Table 5 contains the few exceptions) already have published photometry that is undoubtedly more precise that our spectroscopic fluxes would have been. In practice, our fluxes provided a guide as to the need for additional observations. We found that the accumulation of 4000–5000 counts was sufficient to provide adequate line profiles for analysis, provided that the line profiles were not too wide. These fluxes allow the reader to judge the quality of the line profiles independently of the uncertainties attached to the line widths and central wavelengths.

The radial velocities and the observed line widths in Tables 2–4 are obtained as a result of fitting a Gaussian function to the line profile. Their *formal* uncertainties will depend upon the S/N and shape of the line profile. Given line shapes that are nearly Gaussian and reasonable S/N, we commonly obtain formal uncertainties in the line widths and radial velocities that are substantially smaller than the instrument's absolute internal precision (§ 2). While these formal uncertainties are relevant for the line widths (observed and intrinsic), it is no surprise that the uncertainties in the radial velocities are dominated by systematic calibration issues (§ 4.3).

To compute the intrinsic line widths, the observed line widths are corrected for instrumental, Doppler/thermal, and fine structure broadening, supposing that all add in quadrature, i.e.,

$$\sigma^2_{\mathrm{obs}} = \sigma^2_{\mathrm{true}} + \sigma^2_{\mathrm{inst}} + \sigma^2_{\mathrm{th}} + \sigma^2_{\mathrm{fs}}\,, \tag{1}$$

where σ_{true} is the intrinsic line width resulting from the kinematics of the planetary nebula while σ_{inst}, σ_{th}, and σ_{fs} represent the instrumental, thermal, and fine structure broadening, respectively. The instrumental profile is very nearly Gaussian with the pixel binning used and has a measured FWHM of 2.5–2.7 pixels, so we adopted a FWHM of 2.6 pixels for all objects (~ 11 km s^{-1} FWHM). We compute the thermal broadening from the usual formula (Lang 1980, equation 2-243), adopting rest wavelengths of 6562.83 Å and 5006.85 Å for Hα and [O III]λ5007, respectively, assuming an electron temperature of 10^4 K and zero turbulent velocity. The only exceptions were the planetary nebulae in the Fornax and Sagittarius dwarf spheroidal galaxies, for which the electron temperatures were adopted from the literature (Dudziak et al. 2000; Zijlstra et al. 2006; Kniazev et al. 2007). The resulting thermal broadening (FWHM) at 10^4 K amounts to 0.47 Å (21.4 km s^{-1}) and 0.089 Å (5.3 km s^{-1}) for Hα and [O III]λ5007, respectively. The fine structure broadening (Meaburn 1970), σ_{fs}, was taken to be 3.199 km s^{-1} (FWHM 7.53 km s^{-1}) for Hα and zero for [O III]λ5007 (García-Díaz et al. 2008).

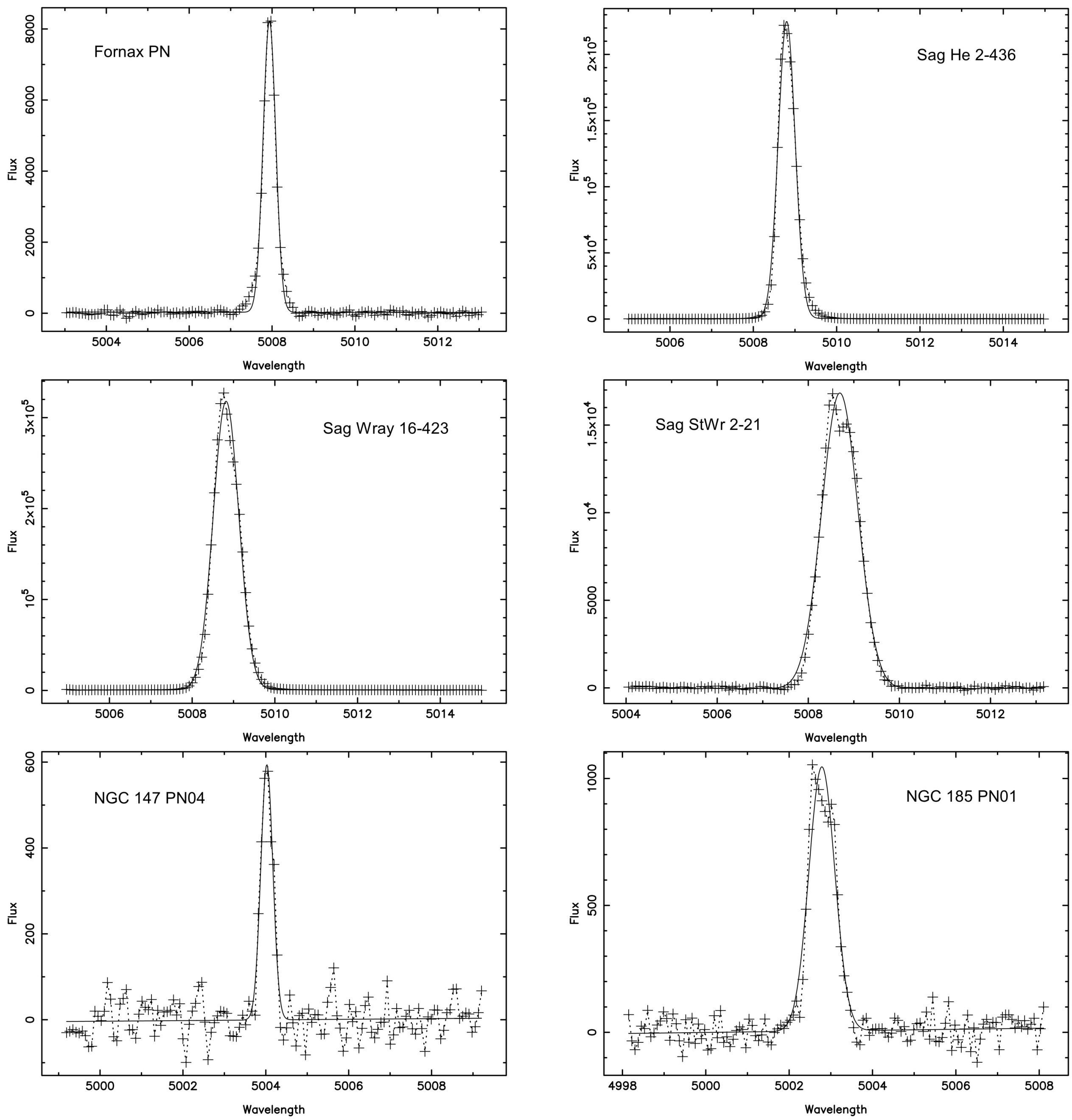

Fig. 2. This and the following two figures present a gallery of representative line profiles for extragalactic planetary nebulae. Here, the line profiles for planetary nebulae in four dwarf spheroidals are shown. The light-colored symbols are the data and the solid line is the Gaussian fit. In all cases, a 10 Å spectral interval is plotted. The line profiles for the planetary nebulae in Fornax and Sagittarius are those with the highest S/N. Even so, deviations from a Gaussian profile are small, though real (8–11% of the total flux). For the remaining objects, the deviations are usually insignificant.

For a homogeneous, spherical, thin shell that fits entirely within the spectrometer slit, the resulting corrected line width,

$$\Delta V = 2.3556\sigma_{\rm true}\,, \qquad (2)$$

is twice the expansion velocity. Only StWr 2-21 in the Sagittarius dwarf spheroidal is larger than our slit (Zijlstra et al. 2006). Departures from these assumptions in real objects affect the interpretation of

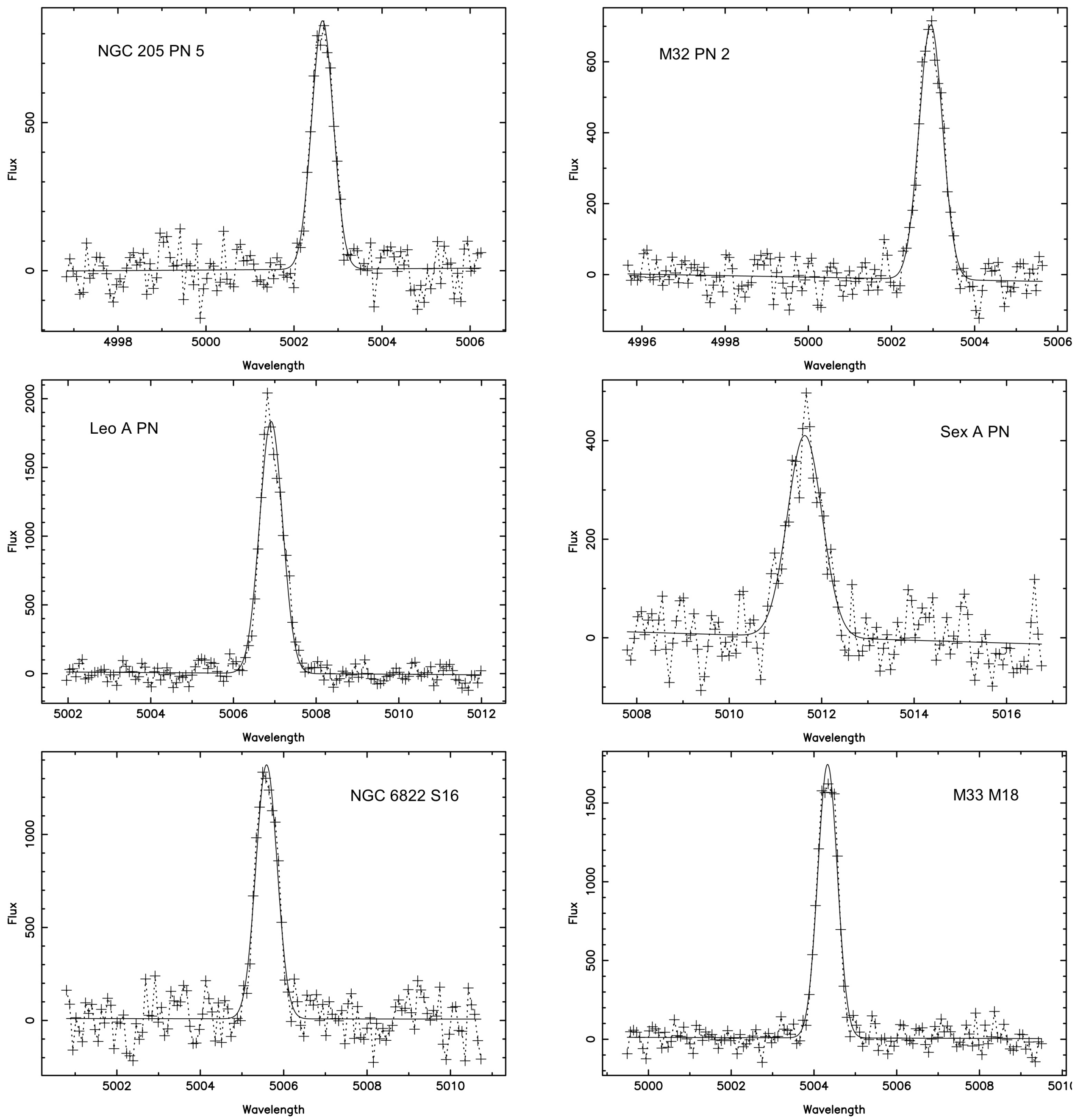

Fig. 3. The line profiles are shown for planetary nebulae in NGC 205, M32, the dwarf irregular galaxies Leo A, Sex A, and NGC 6822, and the spiral galaxy M33. Deviations of the data about the Gaussian fit are insignificant, even though these are among the profiles with the best S/N in these galaxies. See Figure 2 for further details.

ΔV (Schönberner et al. 2005a). The ionized shells of planetary nebulae are neither infinitely thin, uniformly expanding, nor perfectly spherically symmetric. Furthermore, velocity gradients within the ionized shell are relatively common (see Wilson 1950, for early examples). In practice, it is clear that ΔV will be approximately twice the typical luminosity-weighted projected velocity at which the mass of the O^{2+} zone is flowing away from the central star. The pattern velocity of the shock or ionization front that corresponds to the expansion velocity is substantially larger (Marten, Gesicki, & Szczerba 1993; Steffen et

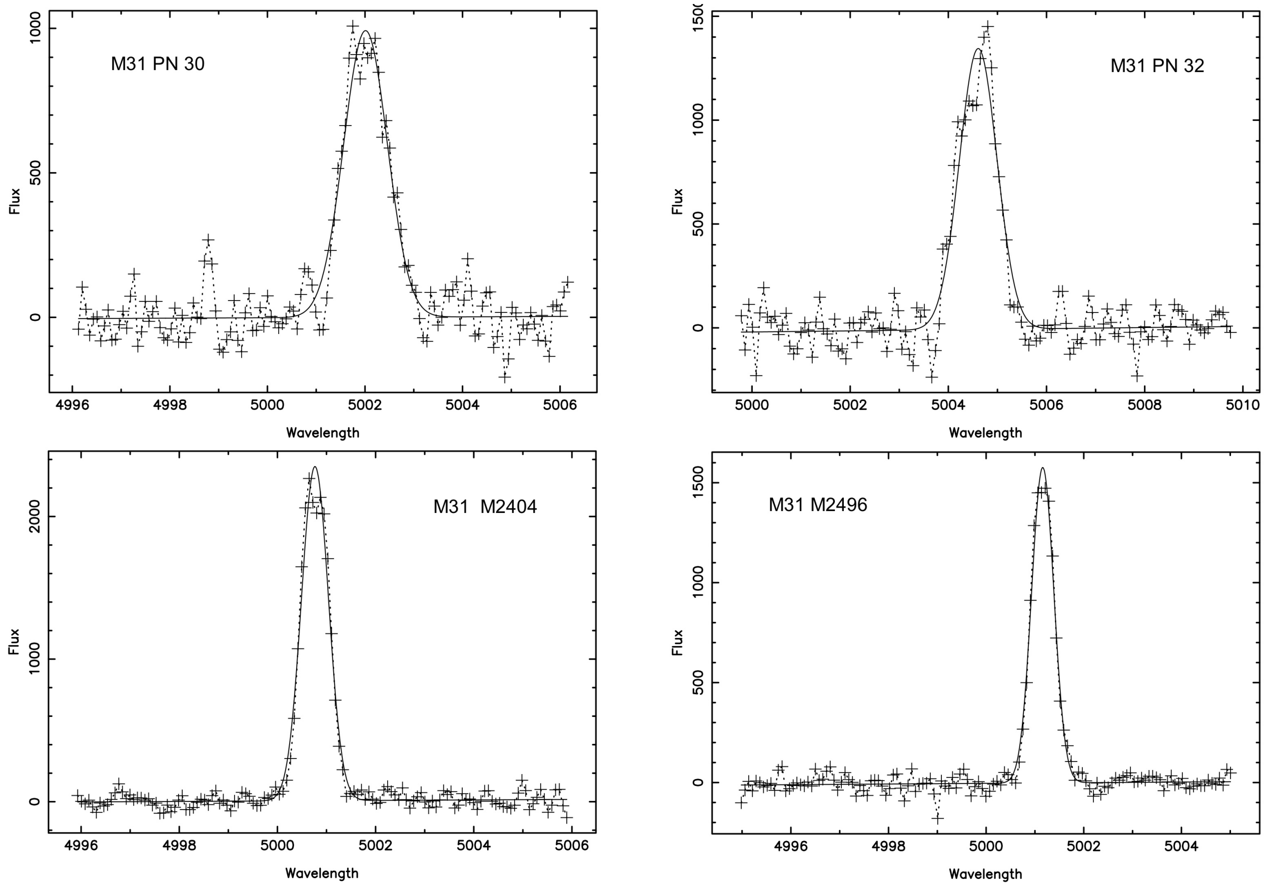

Fig. 4. The line profiles for four planetary nebulae in M31 are shown. PN 30 and PN 32 belong to the bulge, M2404 to the disk, and M2496 to the halo. Deviations of the data about the Gaussian fit are insignificant, even though these are among the profiles with the best S/N in M31 (PN 30 excepted). See Figure 2 for further details.

al. 1997; Schönberner et al. 2005a). Given that, we adopt

$$\Delta V_{0.5} = 0.5\Delta V = 1.1778\sigma_{\rm true}\,, \qquad (3)$$

as our measure of the kinematics of the matter in the O^{2+} zone. It is this line width that is tabulated in Tables 2–4. Since $\Delta V_{0.5}$ is obtained by fitting a Gaussian function, the line width at any other intensity may be derived from it. Richer et al. (2009) further discuss the limitations of this analysis.

4. RESULTS

4.1. *Line Profiles*

As expected, Figures 2–4 demonstrate that the spatially-integrated line profiles for bright extragalactic planetary nebulae are Gaussian in shape, or nearly so, in agreement with previous results (Dopita et al. 1985, 1988; Zijlstra et al. 2006; Arnaboldi et al. 2008). Our deepest profiles, however, show some additional structure. Based upon observations of bright, compact planetary nebulae in the Milky Way bulge, Richer et al. (2009) found that the Gaussian component represented more than 75% of the [O III]λ5007 emission in 89% of all cases. Therefore, it is clear that the Gaussian component is an adequate representation of most of the line emission. Richer et al. (2009) also found that the line width of the Gaussian component was recovered reliably at the flux levels typical of bright extragalactic planetary nebulae.

4.2. *Line Widths: Hα Versus [O III]λ5007*

Figure 5 compares the Hα and [O III]λ5007 line widths for those few objects for which both lines were observed. As already noted by Richer et al. (2009), the line widths for the two lines are similar in bright planetary nebulae in the Milky Way bulge that were selected to mimic samples of bright extragalactic planetary nebulae in environments without star formation. Taken with the result previously presented, the line width measured from the

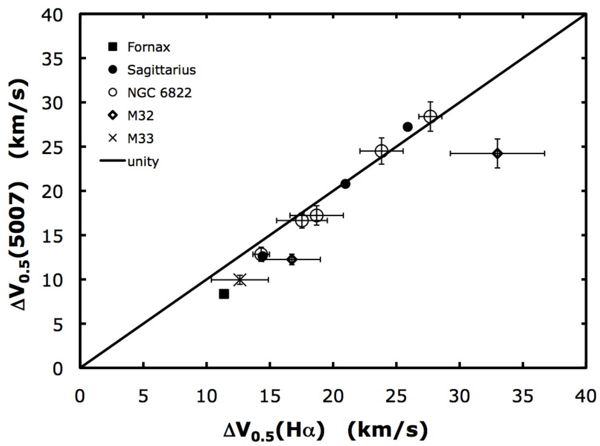

Fig. 5. We compare the line widths measured in the lines of Hα and [O III]λ5007. The solid line indicates the locus of identical line widths. The error bars show the formal uncertainty in line widths from the INTENS fit, which is smaller than the symbol for the planetary nebulae in Fornax and Sagittarius. The intrinsic widths of the two lines are similar, as is also found for planetary nebulae in the Milky Way bulge (Richer et al. 2009).

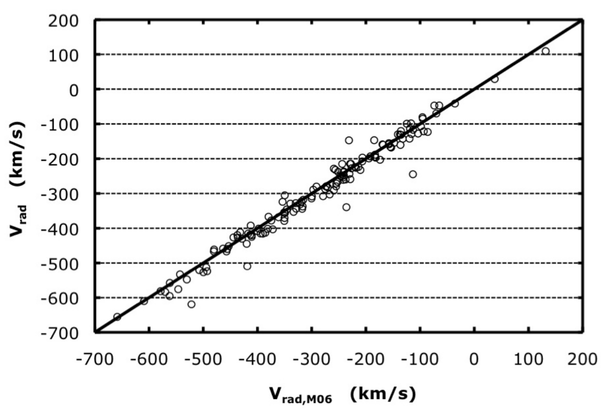

Fig. 6. We compare our radial velocities with those measured by Merrett et al. (2006, M06) for planetary nebulae in M31, M32, and NGC 205. The solid line indicates the locus of identical radial velocities. Our velocities are offset slightly, by –3.3 km s^{-1}.

[O III]λ5007 line should be an adequate and reliable description of the kinematics of the entire ionized shell in bright extragalactic planetary nebulae.

4.3. *Radial Velocities*

Although we made no effort to obtain precise absolute radial velocities, i.e., we observed no radial velocity standards, our heliocentric radial velocities turn out to be reasonably precise. In computing the radial velocities, we adopt the same rest wavelengths as for the analysis of thermal broadening

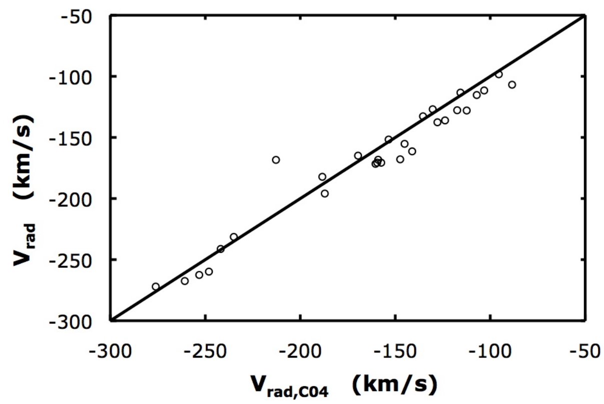

Fig. 7. We compare our radial velocities with those measured by Ciardullo et al. (2004) for planetary nebulae in M33. The solid line indicates the locus of identical radial velocities. Our velocities are offset, by –13.8 km s^{-1}.

(§ 3). The largest sample with which we can compare our radial velocities is that reported by Merrett et al. (2006, M06) with which we have 136 objects in common in M31, M32, and NGC 205. (Note that M06 adopt their absolute velocity scale from Halliday et al. 2006). Figure 6 presents the correlation between the heliocentric radial velocities for the two data sets. Clearly, the correlation is very good, with the exception of five objects (PN1, PN12, PN23, PN69, and PN190 in M31). Excluding these objects, a linear least squares fit finds

$$V_{\rm rad} = (1.005 \pm 0.010)V_{\rm M06} + (-3.3 \pm 3.2)\ {\rm km\ s^{-1}}\,. \quad (4)$$

Thus, our heliocentric radial velocities differ only marginally from those of M06, with a possible offset of only –3.3 km s^{-1}. The dispersion about this relation is 16.7 km s^{-1}. Considering that M06 claim an intrinsic dispersion of approximately 14 km s^{-1} for their measurements, our radial velocities should then have an intrinsic dispersion of about 9 km s^{-1}.

We can also compare our heliocentric radial velocities for planetary nebulae in M33 with those of Ciardullo et al. (2004, C04). Figure 7 presents the correlation for the 29 objects common to the two data sets, which is again very good, with M074 being the only deviant data point. A linear least squares fit finds

$$V_{\rm rad} = (0.956 \pm 0.027)V_{\rm C04} + (-13.8 \pm 4.7)\ {\rm km\ s^{-1}}\,. \quad (5)$$

Again, there is only a marginal difference, apart from an offset of –13.8 km s^{-1}. The dispersion about the above relation is 8.0 km s^{-1}. From Table 5 in Ciardullo et al. (2004), their typical uncertainty should be about 5.5 km s^{-1}, implying that our radial velocities should have an intrinsic dispersion of about 5.8 km s^{-1}.

It is no coincidence that the intrinsic dispersion in our radial velocities is slightly less than the FWHM (11 km s^{-1}) we measure for the arc lamp. Objects are centered in the slit via the spectrometer's imaging mode using short double exposures (sky and then slit) before the spectroscopic exposure. While this guarantees that the object is centered in the slit during the acquisition exposure, small differential guiding errors between the acquisition and spectrosocpic exposures can result in it being displaced from the centre of the slit towards one side during the spectroscopic exposure. Since the spectrometer resolves the slit used for these observations (§ 2), the resulting radial velocities will be dispersed over a range somewhat less than the FWHM of the arc lines.

We find slightly different offsets with respect to M06 and C04. This either reflects differences between their velocity scales or slight systematic changes in our radial velocity zero points from one observing run to the next. Given that neither we nor C04, M06, or Halliday et al. (2006) observed any radial velocity standards, the small offsets noted are not surprising. We therefore conclude that our radial velocities have an absolute precision on the order of 10 km s^{-1}.

4.4. *Line Width Versus Stellar Population*

A perusal of Tables 2–4 reveals that the typical line widths, $\Delta V_{0.5}$, span a limited range in all galaxies. Typically, $\Delta V_{0.5}$ is between 13 and 24 km s^{-1}, though the total range extends from 6 to 30 km s^{-1}. Considering other similar data in the literature, the foregoing changes relatively little, though the example of SMP83 in the LMC demonstrates that occasionally larger line widths may be found among planetary nebulae within 2.5 mag of the peak of the PNLF (Dopita et al. 1985, 1988; Zijlstra et al. 2006; Arnaboldi et al. 2008).

Figure 8 presents the average line width, $\Delta V_{0.5}$, observed for the planetary nebula populations in each of the galaxies in our sample. The "error bars" indicate the standard deviation of the $\Delta V_{0.5}$ distribution. In this figure, the star-forming systems are on the left while those without active, ongoing star formation are on the right. M31 is a mixed system in this diagram, with ongoing star formation in its disc, but with the bulge having ceased this activity long ago. The data points for the Magellanic Clouds are taken from the data published by Dopita et al. (1985, 1988) for planetary nebulae within 2.5 mag of the PNLF peak, but using the same line width definition as for our data. The data point for the Virgo Cluster is based upon the data published by Arnaboldi et al. (2008) for its *intracluster* planetary nebulae. Our only modification of their results was to correct for thermal broadening as we did for our data. Obviously, the progenitor stellar population for these intracluster planetary nebulae is unknown.

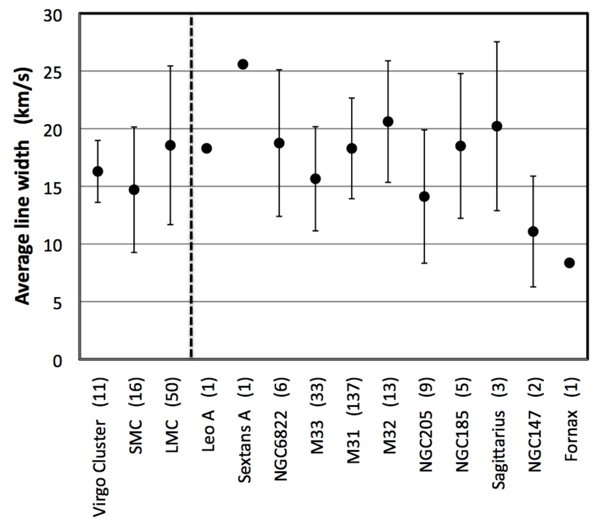

Fig. 8. We compare the average [O III]λ5007 line width from Table 2, $\Delta V_{0.5}$, found for the planetary nebulae in different galaxies. The "error bars" indicate the standard deviations of the line width distributions. The number in parentheses indicates the number of planetary nebulae observed in each galaxy. Clearly, the average line width does not vary much among different galaxies. The data for the Magellanic Clouds are taken from Dopita et al. (1985, 1988) for planetary nebulae within 2.5 mag of the PNLF peak. The data for the Virgo Cluster are taken from Arnaboldi et al. (2008).

The average line width ($\Delta V_{0.5}$) falls in a narrow range in Figure 8. For all galaxies with at least three planetary nebulae observed, the average $\Delta V_{0.5}$ falls in the range of 14–21 km s^{-1}. There is no obvious difference between galaxies with and without ongoing star formation. This velocity range also includes the average line width (16.3 km s^{-1}) for intracluster planetary nebulae in the Virgo cluster core (Arnaboldi et al. 2008).

Likewise, the range of line widths ($\Delta V_{0.5}$) is also similar among galaxies. There is a tendency to find a slightly larger range of line widths in the dwarf galaxies compared to M31 and M33. If this tendency is statistically significant, it occurs for both dwarf irregulars and dwarf spheroidals, so it would appear to be due to the metallicity rather than the age of the progenitor stars. The line widths for the intracluster

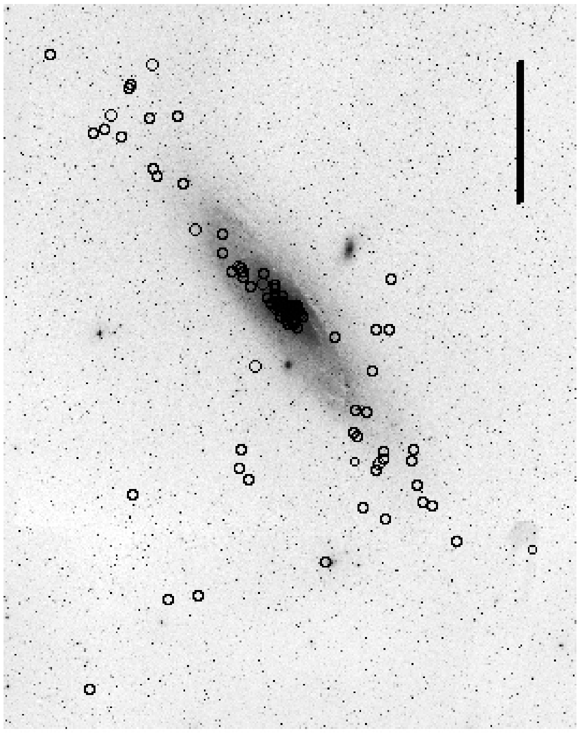

Fig. 9. The planetary nebulae observed in M31 are shown overplotted on a DSS image of M31, M32, and NGC 205. The bar is one degree in length. North is up and east is to the left.

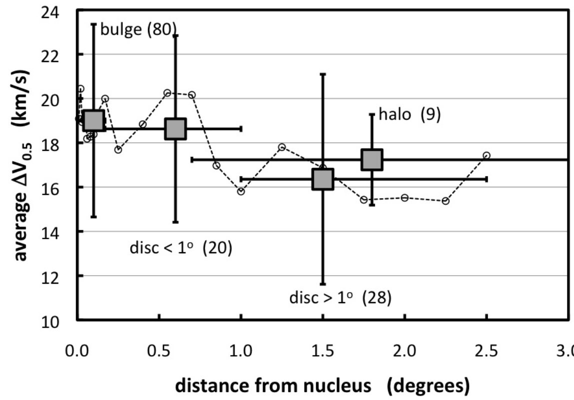

Fig. 10. For the planetary nebulae in M31, we plot the average of $\Delta V_{0.5}$ for different samples as a function of distance from the nucleus. The large symbols denote averages for the bulge, disc, and halo planetary nebulae (as defined in the text). The numbers next to the labels indicate the number of objects in each sample. The vertical error bars indicate the standard deviation within each group while the horizontal error bars denote the ratial extent. The small symbols show the local average $\Delta V_{0.5}$ for bulge and disc planetary nebulae. There is a clear tendency towards lower line widths at greater radial distances.

planetary nebulae in the Virgo cluster have a very narrow distribution, perhaps a result of the effects studied by Villaver et al. (2006).

4.5. *M31*

We observed planetary nebulae in several stellar subsystems in M31 (bulge, disk, halo) as may be appreciated from Figure 9. For the purposes of the analysis here, we assign planetary nebulae to a given subsystem based upon their position within the galaxy alone. This will clearly not be perfect, but adopting a more complex scheme, such as including kinematic information, would not necessarily provide a perfect solution either. We designate as halo objects the nine planetary nebulae lying more than 0.5° from the major axis, since this implies an inclination-corrected disc radius $> 2.2°$, or > 30.3 kpc for our adopted distance of 789 kpc (Lee et al. 2003). Note that these nine planetary nebulae all have inclination-corrected, projected disc radii in excess of 3.2°/44 kpc (adopting the scheme from Huchra, Brodie, & Kent 1991), so it is very unlikely that they are disc objects. We designate as bulge planetary nebulae the 80 objects within the effective radius of the bulge (0.17°: Walterbos & Kennicutt 1988). The remaining 48 planetary nebulae are assigned to the disk. Note that M32-PN29 has a radial velocity indicating that it belongs to M31 (the disk in our scheme). Our bulge-disc division will produce a bulge sample that is truly dominated by bulge planetary nebulae, but the disc sample will be contaminated by bulge objects near the cut-off radius.

While Figure 8 demonstrates that, to first order, the typical outflow velocity is not especially sensitive to either the metallicity or age of the progenitor stellar population, differences are noticeable within M31. In Figure 10, we plot the average outflow velocity for the bulge, inner disc ($< 1°$), outer disc ($> 1°$), and halo samples as well as a local average for bulge and disc planetary nebulae. Clearly, the line width, $\Delta V_{0.5}$, is lower for planetary nebulae at greater distances from the nucleus, though the inner disc and bulge have similar values. On the other hand, the width of the velocity distribution does not vary with nuclear distance.

The robustness of this trend can be tested via statistical tests. The simplest comparison is to consider the distribution of line widths for planetary nebulae in the bulge and disk. Applying the U-test to these subsamples (Wall & Jenkins 2003), there is only a 2.4% probability of obtaining the two line width distributions by chance from a single progenitor population. If the disk subsample is restricted to those objects at separations greater than 1° from the nucleus, thereby minimizing the contamination of the disc sample by bulge objects, the probability of obtaining the two distributions by chance from a single parent population drops to 0.5%. Therefore, the trend of lower average line width ($\Delta V_{0.5}$) at greater radial distances is statistically significant.

5. DISCUSSION

Figure 5 indicates that the line widths in the lines of Hα and [O III]λ5007 are similar, a result found for planetary nebulae in the Milky Way bulge (Richer et al. 2009). Hence, the line width observed for the brighter [O III]λ5007 line is a reasonable approximation of the line width for the entire ionized nebular shell. In all likelihood, this result arises because the intrinsically brightest planetary nebulae in the [O III]λ5007 line, such as those observed here, probably have O^{2+} zones that occupy a large fraction of the volume of the ionized shell.

Figure 5 also implies that, for planetary nebulae that are intrinsically bright in [O III]λ5007, ionization stratification (e.g., Wilson 1950) does *not* strongly bias the width of the [O III]λ5007 line. Ionization stratification might explain the trend of systematically lower [O III]λ5007 line widths at small Hα line widths, but even this effect is small. Therefore, in spite of ionization stratification, for it undoubtedly must occur, the [O III]λ5007 line width is a good estimator of the line width for the entire ionized shell, as measured by Hα. The large volume of the O^{2+} zone plays an important role in establishing this result and is a product of our sample selection (high [O III]λ5007 luminosity). For objects in other evolutionary phases, our result may not hold, as is commonly found in highly evolved objects where ionization stratification is regularly seen (e.g., Meaburn, López, & Richer 2008).

The individual planetary nebulae in Figure 5 arise from galaxies both with and without ongoing star formation. Although the sample is small, there is no obvious indication that the relation between Hα and [O III]λ5007 line widths differs between galaxies with and without ongoing star formation. Therefore, it appears that the [O III]λ5007 line width is an equally good estimate of the line width for the entire ionized shell in the brightest planetary nebulae in all galaxies.

Interpreting Figure 8 is challenging given present knowledge. The hydrodynamical models of Perinotto et al. (2004) and Schönberner et al. (2005a,b) appear to be the most relevant, given their experiments with the AGB mass-loss rate, wind velocity, and metallicity. *Only* Schönberner et al. (2005b) consider the effect of metallicity on hydrodynamical models of planetary nebula evolution, and they find a greater acceleration of the nebular shell at lower metallicity because of the higher electron temperature achieved in the ionized shell. Both observation and the theory of dust-driven winds concur in that lower metallicity produces lower AGB wind velocities, though not necessarily lower mass-loss rates (e.g., Wood et al. 1992; Marshall et al. 2004; Mattsson et al. 2008; Wachter et al. 2008; Groenewegen et al. 2009; Lagadec et al. 2010). Also, the circumstellar shells of low-mass OH/IR stars have lower expansion velocities than those surrounding their higher mass counterparts (Lewis, Eder, & Terzian 1990). Finally, though theoretical studies commonly find that the final white dwarf mass depends upon the metallicity of the progenitor star (e.g., Domínguez et al. 1999; Weidemann 2000), to date, observation has been unable to substantiate this prediction (e.g., Catalán et al. 2008).

If we consider separately the star-forming or non-star-forming galaxies from Figure 8, each group approximates a metallicity sequence, though possibly with progenitor stellar populations of different ages. There is no obvious correlation of the line width with metallicity in either group. Since lower metallicity produces progenitor AGB stars with lower wind velocities, which translate into lower expansion velocities in the resulting planetary nebula (Perinotto et al. 2004), other parameters being equal, the effect of metallicity must be compensated. Schönberner et al. (2005b) suggest that the higher electron temperatures at lower metallicities, with their consequently larger thermal pressures, provide greater acceleration of the nebular shell. Another possibility is that the progenitors of bright planetary nebulae with lower metallicity are slightly more massive, with their higher AGB wind velocities compensating for their lower metallicities. Greater acceleration is the simpler solution. Qualitatively, higher progenitor masses at lower metallicity allow the spectral differences noted in the past (Stasińska, Richer, & McCall 1998; Richer 2006), but the variation cannot be too great, in order to comply with the small range needed to maintain the similar chemical abundance ratios and the variation of the PNLF peak luminosity with metallicity that are observed (Ciardullo et al. 2002; Richer & McCall 2008).

There is no clear difference between the line widths of planetary nebulae in galaxies with and

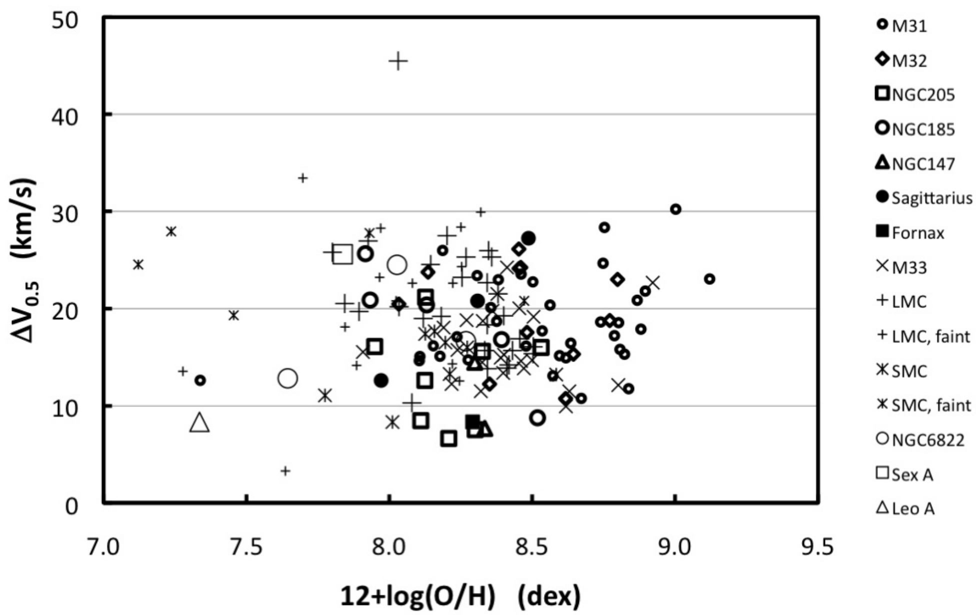

Fig. 11. We plot the [O III]λ5007 line width as a function of the oxygen abundance for the planetary nebulae with low resolution spectra. The symbols for galaxies without star formation are in bold or filled while the symbols for galaxies with ongoing star formation are light and unfilled. Bright and faint planetary nebulae in the Magellanic Clouds are distinguished by large and small symbols, respectively. For M31, the planetary nebulae come overwhelmingly from the bulge. Galactic systems with and without star formation cover the abundance range from $7.9 < 12 + \log(\mathrm{O/H}) < 8.5$, but planetary nebulae from the bulge of M31 dominate higher abundances. There is no strong variation in line width with abundance or between galactic systems with and without star formation. The oxygen abundances are taken from Richer & McCall (2008) and Magrini, Stanghellini, & Villaver (2009); the former adopting data from Jacoby & Ford (1986), Aller et al. (1987), Barlow (1987), Monk, Barlow, & Clegg (1988), Wood et al. (1987), Dopita et al. (1988), Meatheringham, Dopita, & Morgan (1988), Henry, Liebert, & Boroson (1989), Meatheringham & Dopita (1991a,b), Dopita & Meatheringham (1991), Vassiliadis et al. (1992), Jacoby & Kaler (1993), Leisy & Dennefeld (1996), Walsh et al. (1997), Jacoby & Ciardullo (1999), Richer, Stasińska, & McCall (1999), Roth et al. (2004), Kniazev et al. (2005), Magrini et al. (2005), van Zee, Skillman, & Haynes (2006), Zijlstra et al. (2006), Gonçalves et al. (2007), Kniazev et al (2007), and Richer & McCall (2007, 2008).

without star formation in Figure 8. Given the foregoing, the implication is that the stellar progenitors of bright planetary nebulae in all galaxies have similar masses, assuming that some mechanism exists to compensate for the lower velocities of the winds of AGB stars at lower metallicities. If so, at a given metallicity, bright planetary nebulae represent stars formed at similar epochs in galaxies with and without star formation. This may only be understood if the progenitor stars of bright planetary nebulae in all galaxies are of relatively low mass, since significant star formation stopped long ago (several Gyr) in many of the galaxies without star formation considered here. Another option is that the denser ISM in star forming galaxies provides a greater impediment to the nebular outflow than does its counterpart in galaxies without star formation (e.g., Oey & García-Segura 2004). If so, progenitor stars of higher masses would be feasible in galaxies with ongoing star formation. Clearly, the issue must still be investigated in detail.

In galaxies with ongoing star formation, bright planetary nebulae usually have chemical abundances similar to those in the interstellar medium (ISM) in their host galaxies (Richer & McCall 2007; Magrini & Gonąlves 2009; Bresolin et al. 2010). While this may be interpreted to suggest that the progenitors of their planetary nebulae are relatively young because the composition of the ISM has not evolved significantly since their formation, the ease with which the ISM composition can be changed decreases as the metallicity increases (and only the galaxies Leo A and Sextans A have very low metallicity). Thus, even in star-forming galaxies, the bright planetary nebulae need not arise from very recent star formation. Indeed, the chemical composition of bright planetary nebulae is very similar in galaxies with and without star formation (Richer & McCall 2008),

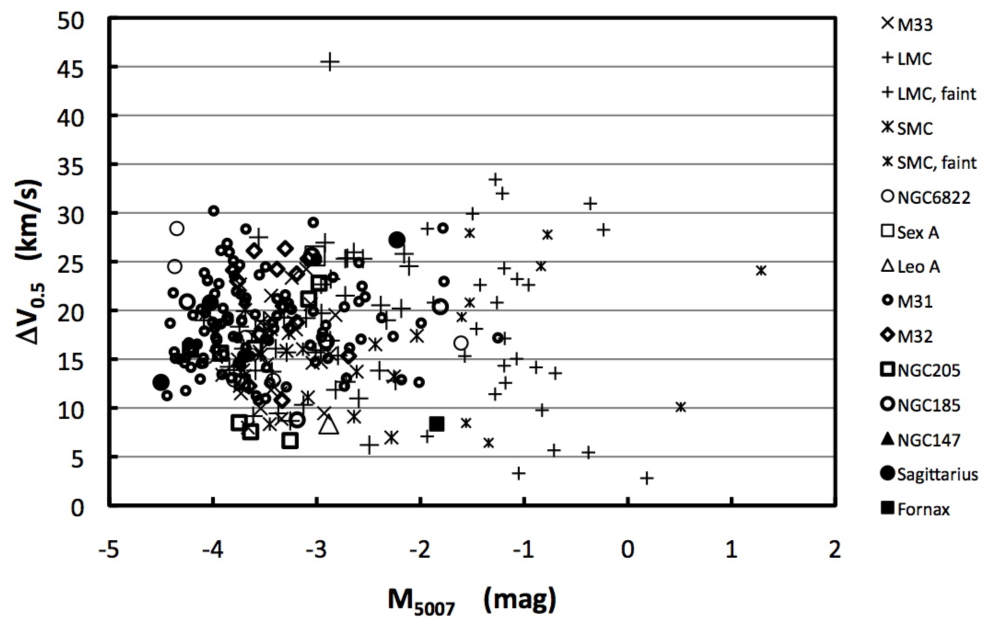

Fig. 12. We plot the [O III]λ5007 line width as a function of the absolute [O III]λ5007 magnitude, M_{5007}, for those objects with appropriate data from the literature (for M_{5007} references, see § 2 for photometry and Figure 11 for spectroscopy). The distances are adopted from Richer & McCall (1995) and Lee et al. (2003), except for M33 and NGC 147, for which we adopt distance moduli from McConnachie et al. (2005) since their distances (tip of red giant branch) for M31, NGC 185, and NGC 205 are consistent with those we adopt. The symbols follow the same scheme as in Figure 11. Note, however, that this figure includes many planetary nebulae from M31's disk. As in Figure 11, no strong trend with line width is seen. The only systematic effect is an increased dispersion for $M_{5007} > -2$ mag.

again suggesting that their progenitor stars were of similar masses.

The planetary nebulae that descend from massive progenitor stars need not be among the brightest planetary nebulae because of their rapid evolution (e.g., Villaver, Manchado, & García-Segura 2002). On the other hand, they can produce the planetary nebulae with the largest outflow velocities for the ionized shell (e.g., Villaver et al. 2002; Perinotto et al. 2004). SMP83 in the LMC, the high point in Figures 11–14 may be an example of a planetary nebula descended from a relatively massive progenitor that is also among the brightest.

Figure 8 can therefore be understood if two conditions are met. First, some mechanism must exist that compensates the slower winds of low metallicity AGB stars. The greater thermal pressure resulting from ionization is the most natural explanation (Schönberner et al. 2005b), though it is not the only possibility. Second, the masses of the progenitor stars of the brightest planetary nebulae in all galaxies should not differ too much, though some variation is feasible and even necessary to explain the differences in their low resolution spectra (Stasińska et al. 1998; Richer 2006).

The trend of line width ($\Delta V_{0.5}$) within M31 agrees with these results (Figure 10). The chemical abundances in young stars and H II regions indicate that the disc has a shallow oxygen abundance gradient (e.g., Dennefeld & kunth 1981; Blair, Kirshner, & Chevalier 1982; Venn et al. 2000; Trundle et al. 2002), with the oxygen abundance falling by less than a factor of 3 between nuclear distances of 0.5° and 2°. Since Figure 10 implies that the line width decreases only slightly as metallicity decreases, it is again necessary to invoke some mechanism to compensate for the drop in AGB wind velocity at lower metallicity.

In Figure 11, we plot the [O III]λ5007 line width as a function of the oxygen abundance. Clearly, the [O III]λ5007 line width does not vary strongly as a function of oxygen abundance. There may be greater dispersion among line widths for abundances below $12 + \log(\mathrm{O/H}) \sim 7.8$ dex. Likewise, there may be a deficit of narrow line widths above $12 + \log(\mathrm{O/H}) \sim 8.7$ dex. However, the statistics are poor in both cases.

In Figure 12, we plot the line width as a function of the absolute [O III]λ5007 magnitude, M_{5007}. Again, there is no clear variation of the line width

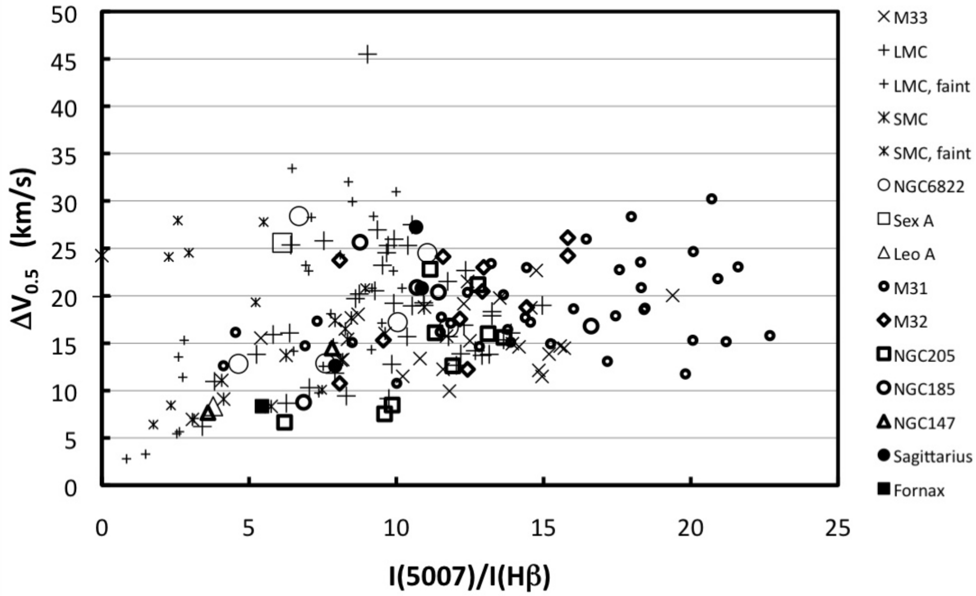

Fig. 13. We plot the [O III]λ5007 line width as a function of the $I(5007)/I(\mathrm{H}\beta)$ ratio for the planetary nebulae with low resolution spectra (see the literature cited in Figure 11). The symbols follow the same scheme as in Figure 11. Here, most of the M31 planetary nebulae are from its bulge. In part, the higher oxygen abundances for the planetary nebulae in M31's bulge allow them to achieve higher $I(5007)/I(\mathrm{H}\beta)$ ratios than those for planetary nebulae elsewhere. However, the planetary nebulae in M32 and the dwarf spheroidals tend to have systematically larger ratios than their counterparts in the dwarf irregulars, even though they have similar oxygen abundances, so nebular structure or the distribution of central star temperatures also likely play a role in elevating the $I(5007)/I(\mathrm{H}\beta)$ ratios for planetary nebulae in systems without star formation.

with M_{5007}, nor is there any obvious difference between systems with and without ongoing star formation. It is unfortunate that there are not more data for fainter planetary nebulae ($M_{5007} > -2$ mag), especially for systems without ongoing star formation, as it would be useful to determine whether the increased dispersion observed for fainter planetary nebulae in the Magellanic Clouds is a more general result (Figure 12).

When the line width is plotted as a function of the $I(5007)/I(\mathrm{H}\beta)$ ratio, there is a systematic difference in the distribution of line widths for the planetary nebulae from *dwarf* galaxies with and without star formation. In Figure 13, there is an offset between the planetary nebulae in systems with and without ongoing star formation, with those from galaxies without star formation having larger $I(5007)/I(\mathrm{H}\beta)$ ratios at a given line width. Based upon the U-test (Wall & Jenkins 2003), the difference between galaxies with and without star formation is significant at the 90% level when only bright planetary nebulae in *dwarf galaxies* are included. Since this happens even though the dwarf galaxies with and without star formation have similar oxygen abundances (Figure 11), it is not an abundance effect, so it presumably arises as a result of differences in ionization structure or in the distribution of central star temperatures. The slight difference in progenitor masses proposed to explain Figure 8 could conceivably produce this difference.

In Figure 13, the planetary nebulae in M31 extend to much higher $I(5007)/I(\mathrm{H}\beta)$ ratios than their counterparts in other galaxies. These are the most oxygen-rich planetary nebulae and simulations indicate that the $I(5007)/I(\mathrm{H}\beta)$ ratio varies as the square root of the oxygen abundance (Dopita, Jacoby, & Vassiliadis 1992; Méndez et al. 2005). However, the difference between the planetary nebulae in M31 and their counterparts in other galaxies is greater than this. The median value of the oxygen abundances for planetary nebulae in M31 differs from that for the planetary nebulae in the dwarf galaxies by less than a factor of two, but the difference in $I(5007)/I(\mathrm{H}\beta)$ ratios is greater than 50%, which suggests that the change in ionization structure may accentuate at higher oxygen abundances.

The most obvious trend that we find as a function of line width is with Hβ luminosity (Figure 14). The line widths define a broad swath in this diagram, but there are deficits of both large line widths at the

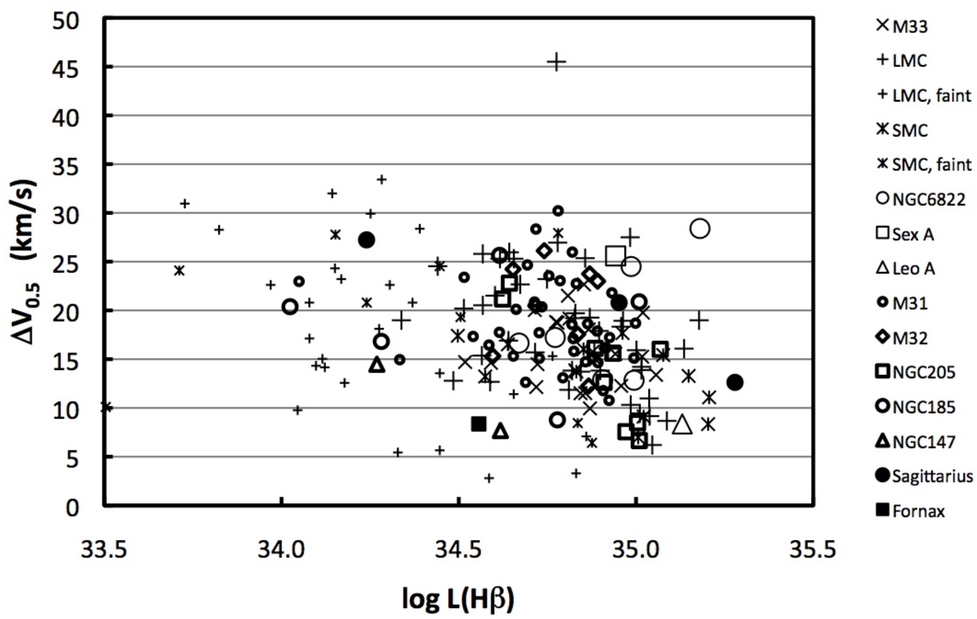

Fig. 14. We plot the [O III]λ5007 line width as a function of the Hβ luminosity of the planetary nebula for those objects with low resolution spectra from the literature. The luminosities are based upon the distances and photometry from the references given in Figure 12 and § 2, respectively, and the [O III]λ5007/Hβ ratios from the literature cited in Figure 11. The symbols follow the same scheme as in Figure 11. Again, most of the M31 planetary nebulae are from its bulge. At the brightest Hβ luminosities there is a lack of the largest line widths. Conversely, at the faintest Hβ luminosities, the opposite occurs and there is a lack of the smallest line widths.

highest Hβ luminosities and narrow line widths at the lowest Hβ luminosities. These deficits, especially that at high Hβ luminosity, are not likely to be a selection effect, since young planetary nebulae rapidly achieve their maximum luminosity (Schönberner et al. 2007), so they should be found on the right side of Figure 14. If there exist planetary nebulae that have very low Hβ luminosities when young (with low [O III]λ5007/Hβ), they could conceivably help fill in the deficit of low line widths at low Hβ luminosity.

The existence of a trend of line width with Hβ luminosity (Figure 14), but not with M_{5007} magnitude (Figure 12), has important implications for the temporal evolution of bright planetary nebulae. Objects may be intrinsically bright in [O III]λ5007 if the $I(5007)/I(\mathrm{H}\beta)$ ratio is low or modest and the Hβ luminosity is high, or if the $I(5007)/I(\mathrm{H}\beta)$ ratio is high and the Hβ luminosity is at least modest. Thus, on average, [O III]λ5007-bright planetary nebulae fade monotonically in the light of Hβ. On the other hand, their evolution in [O III]λ5007 luminosity may be double-valued. In order to reproduce the tendency found between line width and Hβ luminosity, the line width evolution should also be monotonic, on average, increasing as the Hβ luminosity decreases. Recent hydrodynamical models concur with these three evolutionary trends, at least for stellar progenitors of lower masses (Villaver et al. 2002; Perinotto et al. 2004; Schönberner et al. 2005a, 2007).

Supposing that Figure 14 represents an evolutionary sequence, it offers insight into the positions of Fornax, NGC 147, and NGC 205 in Figure 8. For the planetary nebula in Fornax as well as PN04 in NGC 147 and PN01, PN07, and PN09 in NGC 205, low-resolution spectra find very weak He II λ4686, indicating that their central stars have not yet become very hot (Gonçalves et al. 2007; Kniazev et al. 2007; Richer & McCall 2008). These two lines of evidence then imply that we observe these objects early in the planetary nebula phase and that, for Fornax and NGC 147, they bias their positions in Figure 8 to unusually low values.

Metallicity likely plays a role in the tendency to find a larger range of line widths ($\Delta V_{0.5}$) in the dwarf galaxies as compared to M31 and M33. The dwarf galaxies have lower metallicities and the peak luminosity of the PNLF is lower at lower metallicity (Ciardullo et al. 2002). This might allow progenitor stars spanning a wider range of masses to contribute to the bright end of the PNLF at lower metallicity. Alternatively, planetary nebulae in a wider range of evolutionary states might contribute to the peak of the

PNLF (Figure 14). Either possibility would produce a wider range in line width at lower metallicity.

Hydrodynamical models have consistently predicted that the velocities of nebular shells should increase with time for planetary nebulae arising from progenitors of modest masses ($M \lesssim 2.5\ M_\odot$; e.g., Schmidt-Voigt & Köppen 1987; Kahn & Breitschwerdt 1990; Mellema 1994; see also previous paragraph). Dopita et al. (1985, 1988) first proposed such an evolutionary scheme for the kinematics of planetary nebulae in the Magellanic Clouds. Richer et al. (2008, 2010) have found similar evolution for the bright planetary nebulae in the Milky Way bulge. Figure 14 indicates that the acceleration of nebular shells is a general phenomenon, at least for the intrinsically brightest planetary nebulae (in the light of [O III]λ5007). Thus, there is now excellent qualitative agreement between theory and observation regarding the ionized shell's kinematic evolution for intrinsically bright planetary nebulae: with time, the shells are accelerated. The central star's important effect upon the nebular shell is clear. A more quantitative comparison must await the arrival of spatially-integrated line profiles from hydrodynamical models that may be directly compared with observations.

For the PNLF to be a useful distance indicator, it must not be sensitive to the underlying stellar populations, a result found early in its use (Ciardullo et al. 1989a). Merrett et al. (2006) confirm this, finding that the PNLF does not vary significantly with position in M31. Meanwhile, Richer & McCall (2008) find that the progenitors of bright planetary nebulae in all galaxies have undergone similar chemical enrichment processes. These results argue that the progenitor stellar populations of intrinsically bright planetary nebulae are similar in all galaxies, though they are clearly not identical (e.g., Stasińska et al. 1998; Ciardullo et al. 2002). Likewise, the similar kinematics we find for the brightest planetary nebulae in all galaxies would appear to argue that there is not a large range in the masses of the stellar progenitors of these objects in different galaxies, whether star-forming or not. Their internal kinematics, therefore, add a third argument favoring progenitor stellar populations for the brightest planetary nebulae that are similar in all galaxies.

6. CONCLUSIONS

We present kinematic data for 211 bright extragalactic planetary nebulae in 11 Local Group galaxies. We present line profiles in the line of [O III]λ5007 for all objects and in the Hα line for a small minority. At the signal-to-noise of our data, the line profiles are Gaussian, or nearly so, in all cases. The intrinsic line widths in [O III]λ5007 and Hα are also similar. Thus, the line widths in [O III]λ5007 are an adequate description of the kinematics of most of the matter in the entire ionized shell in these objects.

We find that the average line widths for the bright planetary nebulae in all galaxies are similar (where we observed at least three objects). Given our current understanding, this result implies that the progenitors of bright planetary nebulae at lower metallicity are either slightly more massive or that the higher plasma temperatures at lower metallicities produce larger acceleration of the nebular shell. The approximate constancy of the line width also implies that there cannot be a large difference in the masses of the progenitors of bright planetary nebulae among galaxies, whether star-forming or not, though small variations are possible. Within M31, the line width decreases with increasing distance from the nucleus, in agreement with these deductions.

As a general rule, the range of line widths is larger in dwarf galaxies than in M31 or M33. Presumably, this arises because, at lower metallicity, either a larger range of progenitor masses contribute bright planetary nebulae or bright planetary nebulae encompass a wider range of evolutionary states. On the other hand, there is no obvious correlation between the line width in [O III]λ5007 and either the oxygen abundance or the absolute [O III]λ5007 magnitude, M_{5007}.

The most significant correlation is that between line width and the Hβ luminosity. Since [O III]λ5007-bright planetary nebulae represent a monotonic fading sequence in the light of Hβ, this correlation implies that the ionized shells of bright planetary nebulae are accelerated during their early evolution, independently of the age or metallicity of the progenitor stellar population. Theory has long predicted this result, so our data are consistent with its general validity.

More generally, our measurements of the kinematics of bright planetary nebulae are in good accord with the results derived from photometry and low resolution spectroscopy. All three lines of reasoning require that intrinsically bright planetary nebulae descend from progenitor stellar populations spanning a relatively small range of masses.

We thank the telescope operators during our runs, Gabriel García, Gustavo Melgoza, Salvador Monrroy, and Felipe Montalvo, for their help. We thank M. Arnaboldi for kindly providing the line widths for the planetary nebulae in the Virgo Cluster that are shown in Figure 8. We thank the referee for helpful comments and suggestions. We gratefully acknowledge financial support throughout this project from Conacyt grants 37214, 43121, 49447, and 82066 and from DGAPA-Universidad Nacional Autónoma de México grants 108406-2, 108506-2, 112103, and 116908-3. We acknowledge the use of NASA's *SkyView* facility (`http://skyview.gsfc.nasa.gov`) located at NASA Goddard Space Flight Center in generating Figure 9.

REFERENCES

Acker, A., Marcout, J., Ochsenbein, F., Stenholm, B., & Tylenda, R. 1992, Strasbourg-ESO Catalogue of Galactic Planetary Nebulae (Garching: ESO)

Aller, L. H., Keyes, C. D., Maran, S. P., Gull, T. R., Michalitsianos, A. G., & Stecher, T. P. 1987, ApJ, 320, 159

Arnaboldi, M., et al. 2008, ApJ, 674, L17

Barlow, M. J. 1987, MNRAS, 227, 161

Blair, W. P., Kirshner, R. P., & Chevalier, R. A. 1982, ApJ, 254, 50

Bresolin, F., Stasińska, G., Vílchez, J. M., Simon, J. D., & Rosolowsky, E. 2010, MNRAS, 404, 1679

Catalán, S., Isern, J., García-Berro, E., & Ribas, I. 2008, MNRAS, 387, 1693

Ciardullo, R., Durrell, P. R., Laychak, M. B., Herrmann, K. A., Moody, K., Jacoby, G. H., & Feldmeier, J. J. 2004, ApJ, 614, 167 (C04)

Ciardullo, R., Feldmeier, J. J., Jacoby, G. H., Kuzio de Naray, R., Laychak, M. B., & Durrell, P. R. 2002, ApJ, 577, 31

Ciardullo, R., Jacoby, G. H., & Ford, H. C. 1989a, ApJ, 344, 715

Ciardullo, R., Jacoby, G. H., Ford, H. C., & Neill, J. D. 1989b, ApJ, 339, 53

Corradi, R. L. M., et al. 2005, A&A, 431, 555

Danziger, I. J., Dopita, M. A., Hawarden, T. G., & Webster, B. L. 1978, ApJ, 220, 458

Dennefeld, M., & Kunth, D. 1981, AJ, 86, 989

Domínguez, I., Chieffi, A., Limongi, M., & Straniero, O. 1999, ApJ, 524, 226

Dopita, M. A., Ford, H. C., Lawrence, C. J., & Webster, B. L. 1985, ApJ, 296, 390

Dopita, M. A., Jacoby, G. H., & Vassiliadis, E. 1992, ApJ, 389, 27

Dopita, M. A., & Meatheringham, S. J. 1991, ApJ, 367, 115

Dopita, M. A., Meatheringham, S. J., Webster, B. L., & Ford, H. C. 1988, ApJ, 327, 639

Dudziak, G., Péquignot, D., Zijlstraa, A. A., & Walsh, J. R. 2000, A&A, 363, 717

Ford, H. C. 1978, in IAU Symp. 76, Planetary Nebulae, ed. Y. Terzian (Dordrecht: Reidel), 19

__________. 1983, in IAU Symp. 103, Planetary Nebulae, ed. D. R. Flower (Dordrecht: Reidel), 443

Ford, H. C., & Jacoby, G. H. 1978, ApJS, 38, 351

Ford, H. C., Jacoby, G. H., & Jenner, D. C. 1977, ApJ, 213, 18

Ford, H. C., & Jenner, D. C. 1975, ApJ, 202, 365

Ford, H. C., Jenner, D. C., & Epps, H. W. 1973, ApJ, 183, L73

García-Díaz, Ma. T., Henney, W. J., López, J. A., & Doi, T. 2008, RevMexAA, 44, 181

Gonçalves, D. R., Magrini, L., Leisy, P., & Corradi, R. L. M. 2007, MNRAS, 375, 715

Groenewegen, M. A. T., Sloan, G. C., Soszyńsky, I., & Petersen, E. A. 2009, A&A, 506, 1277

Halliday, C., et al. 2006, MNRAS, 369, 97

Henry, R. B. C., Liebert, J., & Boroson, T. A. 1989, ApJ, 339, 872

Huchra, J. P., Brodie, J. P., & Kent, S. M. 1991, ApJ, 370, 495

Jacoby, G. H. 1989, ApJ, 339, 39

Jacoby, G. H., & Ciardullo, R. 1999, ApJ, 515, 169

Jacoby, G. H., & Ford, H. C. 1986, ApJ, 304, 490

Jacoby, G. H., & Kaler, J. B. 1993, ApJ, 417, 209

Jacoby, G. H., & Lesser, M. P. 1981, AJ, 86, 185

Kahn, F. D., & Breitschwerdt, D. 1990, MNRAS, 242, 505

Killen, R. M., & Dufour, R. J. 1982, PASP, 94, 444

Kniazev, A. Y., Grebel, E. K., Pustilnik, S. A., & Pramskij, A. G. 2007, A&A, 468, 121

Kniazev, A. Y., Grebel, E. K., Pustilnik, S. A., Pramskil, A. G., & Zucker, D. B. 2005, AJ, 130, 1558

Lagadec, E., Zijlstra, A. A., Mauron, N., Fuller, G., Josselin, E., Sloan, G. C., & Riggs, A. J. E. 2010, MNRAS, 403, 1333

Lang, K. R. 1980, Astrophysical Formulae (Berlin: Springer)

Lawrie, D. G., & Ford, H. C. 1982, ApJ, 256, 120

Lee, H., McCall, M. L., Kingsburgh, R. L., Ross, R., & Stevenson, C. C. 2003, AJ, 125, 146

Leisy, P., Corradi, R. L. M., Magrini, L., Greimel, R., Mampaso, A., & Dennefeld, M. 2005, A&A, 436, 437

Leisy, P., & Dennefeld, M. 1996, A&AS, 116, 95

Lewis, B. M., Eder, J., & Terzian, Y. 1990, ApJ, 362, 634

Magrini, L., Corradi, R. L. M., Mampaso, A., & Perinotto, M. 2000, A&A, 355, 713

Magrini, L., & Gonąlves, D. R. 2009, MNRAS, 398, 280

Magrini, L., Leisy, P., Corradi, R. L. M., Perinotto, M., Mampaso, A., & Vílchez, J. M. 2005, A&A, 443, 115

Magrini, L., Stanghellini, L., & Villaver, E. 2009, ApJ, 696, 729

Marten, H., Gesicki, K., & Szczerba, R. 1993, in IAU Symp. 155, Planetary Nebulae, ed. R. Weinberger & A. Acker (Dordrecht: Kluwer), 315

Marshall, J. R., van Loon, J. Th., Matsuura, M., Wood, P. R., Zijlstra, A. A., & Whitelock, P. A. 2004, MNRAS, 355, 1348

Massey, P., Valdes, F., & Barnes, J. 1992, A User's Guide to Reducing Slit Spectra with IRAF (Vol. 2B; Tucson: NOAO)

Mattsson, L., Wahlin, R., Höfner, S., & Eriksson, K. 2008, A&A, 484, L5
McCall, M. L., Rybski, P. M., & Shields, G. A. 1985, ApJS, 57, 1
McConnachie, A. W., Irwin, M. J., Ferguson, A. M. N., Ibata, R. A., Lewis, G. F., & Tanvir, N. 2005, MNRAS, 356, 979
Meaburn, J. 1970, Nature, 228, 44
Meaburn, J., Blundell, B., Carling, R., Gregory, D. F., Keir, D., & Wynee, C. G. 1984, MNRAS, 210, 463
Meaburn, J., López, J. A., Gutiérrez, L., Quiroz, F., Murillo, J. M., Valdéz, J., & Pedrayez, M. 2003, RevMexAA, 39, 185
Meaburn, J., López, J. A., & Richer, M. G. 2008, MNRAS, 348, 497
Meatheringham, S. J., & Dopita, M. A. 1991a, ApJS, 75, 407
__________. 1991b, ApJS, 76, 1085
Meatheringham, S. J., Dopita, M. A., & Morgan, D. H. 1988, ApJ, 329, 166
Mellema, G. 1994, A&A, 290, 915
Méndez, R. H., Thomas, D., Saglia, R. P., Maraston, C., Kudritzki, R. P., & Bender, R. 2005, ApJ, 627, 767
Merrett, H. R., et al. 2006, MNRAS, 369, 120 (M06)
Monk, D. J., Barlow, M. J., & Clegg, R. E. S. 1988, MNRAS, 234, 583
Nolthenius, R., & Ford, H. C. 1987, ApJ, 317, 62
Oey, M. S., & García-Segura, G. 2004, ApJ, 613, 302
Peña, M., Richer, M. G., & Stasińska, G. 2007, A&A, 466, 75
Perinotto, M., Schönberner, D., Steffen, M., & Calonaci, C. 2004, A&A, 414, 993
Pottasch, S. R. 1990, A&A, 236, 231
Richer, M. G. 2006, in IAU Symp. 234, Planetary Nebulae in our Galaxy and Beyond, ed. M. J. Barlow & R. H. Méndez (Cambridge: Cambridge Univ. Press), 317
Richer, M. G., Báez, S.-H., López, J. A., Riesgo, H., & García-Díaz, Ma. T. 2009, RevMexAA, 45, 239
Richer, M. G., Lee, M. G., & Hwang, N. 2004, J. Korean Astron. Soc., 37, 269
Richer, M. G., López, J. A., García-Díaz, Ma. T., Clark, D. M., Pereyra, M., & Díaz-Méndez, E. 2010, ApJ, 716, 857
Richer, M. G., López, J. A., Pereyra, M., Riesgo, H., & García-Díaz, Ma. T. 2008, ApJ, 689, 203
Richer, M. G., & McCall, M. L. 1992, AJ, 103, 54
__________. 1995, ApJ, 445, 642
__________. 2007, ApJ, 658, 328
__________. 2008, ApJ, 684, 1190
Richer, M. G., Stasińska, G., & McCall, M. L. 1999, A&AS, 135, 203
Roth, M. M., Becker, T., Kelz, A., & Schmoll, J. 2004, ApJ, 603, 531
Schmidt-Voigt, M., & Köppen, J. 1987, A&A, 174, 223
Schönberner, D., Jacob, R., & Steffen, M. 2005a, A&A, 441, 573
Schönberner, D., Jacob, R., & Steffen, M., & Roth, M. M. 2005b, in AIP Conf. Proc. 804, Planetary Nebulae as Astronomical Tools, ed. R. Szczerba, G. Stasińska, & S. Górny (new York: AIP), 269
Schönberner, D., Jacob, R., Steffen, M., & Sandin, C. 2007, A&A, 473, 467
Stasińska, G., Richer, M. G., & McCall, M. L. 1998, A&A, 336, 667
Steffen, M., Schönberner, D., Kifonidis, K., & Stahlberg, J. 1997, in IAU Symp. 180, Planetary Nebulae, ed. H. J. Habing & H. J. G. L. M. Lamers (Dordrecht: Kluwer), 368
Trundle, C., Dufton, P. L., Lennon, D. J., Smartt, S. J., & Urbaneja, M. A. 2002, A&A, 395, 519
van Zee, L., Skillman, E. D., & Haynes, M. P. 2006, ApJ, 637, 269
Vassiliadis, E., Dopita, M. A., Morgan, D. H., & Bell, J. F. 1992, ApJS, 83, 87
Venn, K. A., McCarthy, J. K., Lennon, D. J., Przybilla, N., Kudritzki, R. P., & Lemke, M. 2000, ApJ, 541, 610
Villaver, E., Manchado, A., & García-Segura, G. 2002, ApJ, 581, 1204
Villaver, E., Manchado, A., García-Segura, G., & Stanghellini, L. 2006, in IAU Symp. 234, Planetary Nebulae in our Galaxy and Beyond, ed. M. J. Barlow & R. H. Méndez (Cambridge: Cambridge Univ. Press), 333
Wachter, A., Winters, J. M., Schröder, K.-P., & Sedlmayr, E. 2008, A&A, 486, 497
Wall, J. V., & Jenkins, C. R. 2003, Practical Statistics for Astronomers (Cambridge: Cambridge Univ. Press)
Walsh, J. R., Dudziak, G., Minniti, D., & Zijlstra, A. A. 1997, ApJ, 487, 651
Walsh, J. R., Walton, N. A., Jacoby, G. H., & Peletier, R. F. 1999, A&A, 346, 753
Walterbos, R. A. M., & Kennicutt, R. C., Jr. 1988, A&A, 198, 61
Weidemann, V. 2000, A&A, 363, 647
Wilson, O. C. 1950, ApJ, 111, 279
Wood, P. R., Meatheringham, S. J., Dopita, M. A., & Morgan, D. H. 1987, ApJ, 320, 178
Wood, P. R., Whiteoak, J. B., Hughes, S. M. G., Bessell, M. S., Gardner, F. F., & Hyland, A. R. 1992, ApJ, 397, 552
Zijlstraa, A. A., Gesicki, K., Walsh, J. R., Péquignot, D., van Hoof, P. A. M., & Minniti, D. 2006, MNRAS, 369, 875

Sol-Haret Báez: Facultad de Física e Inteligencia Artificial, Universidad Veracruzana, Circuito G. Aguirre Beltrán s/n, Zona Universitaria, Xalapa, Veracruz, Mexico (solharet@hotmail.com).

Roxana Marisol Calderón Olvera, Giovanni López Soto: Universidad Nacional Autóma de México, Ciudad Universitaria, 04510 México, D.F., Mexico (roxanama@msn.com, blackhole_mx@yahoo.com.mx).

David M. Clark, María-Teresa García-Díaz, José Alberto López, Michael G. Richer, Hortensia Riesgo: Instituto de Astronomía, Universidad Nacional Autónoma de México, Apdo. Postal 877, 22830, Ensenada, B. C., Mexico (tere, jal, richer, hriesgo@astrosmo.unam.mx).

Enrique Díaz-Méndez: Dept. of Physics and Astronomy, Texas Christian University, Fort Worth, Texas, US. 76109 (e.d.mendez@tcu.edu).

John Meaburn: Jodrell Bank Observatory, Dept. of Physics & Astronomy, University of Manchester, Macclesfield, Cheshire SK11 9DL, UK (jm@ast.man.ac.uk).

Oswaldo Toledano Rebolo: Instituto de Ciencias Físicas, Universidad Nacional Autónoma de México, Av. Universidad s/n, 62210, Cuernavaca, Morelos, Mexico (oswaldotoledano@hotmail.com).

Revista Mexicana de Astronomía y Astrofísica, **46**, 215–219 (2010)

ON THE SIZE OF THE NON-THERMAL COMPONENT IN THE RADIO EMISSION FROM CYG OB2 #5

Luis F. Rodríguez,[1] Yolanda Gómez,[1] Laurent Loinard,[1] and Amy J. Mioduszewski[2]

Received 2010 January 11; accepted 2010 May 19

RESUMEN

Cyg OB2 #5 es un sistema binario de contacto con emisión variable de radio. Esta emisión tiene un estado bajo de flujo dominado por el viento estelar ionizado y un estado alto de flujo, donde una componente no-térmica adicional aparece. Ahora se sabe que las variaciones tienen un período de 6.7 ± 0.2 años. La componente no-térmica ha sido atribuida a varios agentes: una envolvente en expansión eyectada periódicamente por la binaria, emisión de una región de choque de vientos, o una estrella con emisión no-térmica en órbita excéntrica alrededor de la binaria. La determinación del tamaño angular de la componente no-térmica es crucial para discriminar entre estas posibilidades. Presentamos un análisis de datos de archivo del VLA hechos a 8.46 GHz en 1994 (en estado bajo) y 1996 (en estado alto), que nos permiten sustraer el efecto de la componente térmica persistente y estimar un tamaño angular $\leq 0\rlap{.}''02$ para la componente no-térmica. Este tamaño compacto favorece la explicación en términos de una estrella con emisión no-térmica o de una región de choque de vientos.

ABSTRACT

Cyg OB2 #5 is a contact binary system with variable radio continuum emission. This emission has a low-flux state where it is dominated by thermal emission from the ionized stellar wind and a high-flux state where an additional non-thermal component appears. The variations are now known to have a period of 6.7 ± 0.2 yr. The non-thermal component has been attributed to different agents: an expanding envelope ejected periodically from the binary, emission from a wind-collision region, or a star with non-thermal emission in an eccentric orbit around the binary. The determination of the angular size of the non-thermal component is crucial to discriminate between these alternatives. We present the analysis of VLA archive observations made at 8.46 GHz in 1994 (low state) and 1996 (high state), that allow us to subtract the effect of the persistent thermal emission and to estimate an angular size of $\leq 0\rlap{.}''02$ for the non-thermal component. This compact size favors the explanation in terms of a star with non-thermal emission or of a wind-collision region.

Key Words: radio continuum: stars — stars: individual (Cyg OB2 #5)

1. INTRODUCTION

Cyg OB2 #5 (V729 Cyg, BD +40 4220) is an eclipsing, contact binary system consisting of two O-type supergiants with a 6.6-day period (Hall 1974; Leung & Schneider 1978; Rauw, Vreux, & Bohannan 1999; Linder et al. 2009). As several other luminous O-star systems in the Cyg OB2 association, this source was found to show evidence of variable radio emission (Persi et al. 1985, 1990; Bieging, Abbott, & Churchwell 1989). The radio emission appears to have two states: a low-flux state of ~ 2 mJy at 4.8 GHz where the spectral index is consistent with thermal emission from an ionized stellar wind, and a high-flux state of ~ 8 mJy at 4.8 GHz where the spectral index is flatter than in the low state. The variations were proposed to have a 7-year period (Miralles et al. 1994) and have been attributed

[1]Centro de Radioastronomía y Astrofísica, Universidad Nacional Autónoma de México, Morelia, Michoacán, Mexico.
[2]National Radio Astronomy Observatory, USA.

TABLE 1

ARCHIVE DATA USED

Epoch	Project	Frequency (GHz)	On-source Time (min)	Phase Calibrator	Bootstrapped Flux Density (Jy)	Beam Angular Size[a]
1994 Apr 09 (1994.27)	AR277	8.46	37	2007+404	2.84 ± 0.01	$0.''18 \times 0.''16$; -43°
1996 Dec 28 (1996.99)	AR277	8.46	45	2007+404	2.89 ± 0.01	$0.''30 \times 0.''21$; -85°

[a]Major axis × minor axis; position angle, for a (u, v) weighting of ROBUST = 0 (Briggs 1995).

to variable non-thermal emission from an expanding envelope arising periodically in the binary (Persi et al. 1990; Bieging et al. 1989; Miralles et al. 1994).

In addition, Abbott, Bieging, & Churchwell (1981) and Miralles et al. (1994) reported on the existence of a radio "companion" 0.8 arcsec to the NE of the main radio source (which is associated with the eclipsing binary). Observations by Contreras et al. (1997) revealed that this radio source has an elongated shape and lies in-between the short-period binary and a third star, which was first reported by Herbig (1967). Contreras et al. (1997) suggested that the proposed NE radio companion actually corresponds to the wind interaction zone between the binary system and the tertiary component. Recently, Kennedy et al. (2010) reanalysed all VLA observations of Cyg OB2 #5 and showed that the primary radio source, associated with the eclipsing binary, varies with a period of 6.7 ± 0.2 yr while the flux from the secondary NE source remains constant in time. These authors proposed that the variations in the main radio component can be represented by a simple model in which a fourth star (with constant non-thermal emission) moves around the eclipsing binary in an eccentric orbit and the varying radio emission results from the variable free-free opacity of the wind between the star and the observer (Kennedy et al. 2010). These authors estimate a major axis of 14 AU for the star with non-thermal emission. In this scenario, we have a quadruple star system: the contact binary, the star with non-thermal emission in a 6.7 yr orbit around the contact binary, and the NE component.

To advance our understanding of the nature of the time-variable non-thermal emission, a determination of the angular size of the source producing it is needed. Using VLA data taken at 8.46 GHz in 1991 October 3 (when Cyg OB2 #5 was in the high radio state), Miralles et al. (1994) estimated an angular size of $0.''046 \pm 0.''006$ for the whole (non-thermal plus thermal components) emission. Using MERLIN data taken at 4.8 GHz in 1996 November 14 (when Cyg OB2 #5 was again in the high radio state), Kennedy et al. (2010) estimated an angular size of $\sim 0.''077$ for the whole (non-thermal plus thermal components) emission associated with the primary radio component. Since the thermal contribution comes from the ionized wind that is known to be extended, these size estimates can be considered as upper limits to the size of the non-thermal emission. In this paper we present the analysis of archive 8.46 GHz continuum observations made with the Very Large Array (VLA) of the NRAO[3] in the A configuration toward Cyg OB2 #5 in two epochs. During 1994 April 9 (1994.27), the source was in the low radio state and only the thermal emission from the ionized stellar wind was present. These observations were used to estimate the characteristics of the persistent thermal component. During 1996 December 28 (1996.99), the source was in the high radio state, with both the thermal and non-thermal components present. Using the information obtained from the 1994 data, it is possible to subtract in the (u, v) plane the contribution from the thermal component and obtain a more stringent estimate of the angular size of the non-thermal emission.

2. DATA REDUCTION

The archive data were edited and calibrated using the software package Astronomical Image Processing System (AIPS) of NRAO. The parameters of the observations are given in Table 1. The absolute amplitude calbrator for both epochs was 1331+305, with an adopted flux density of 5.21 Jy. The (u, v) data were self-calibrated in amplitude and phase. An image was made with the 1994.27 (u, v) data and the clean components of this image were subtracted from the 1996.99 (u, v) data using the AIPS task UVSUB. The resulting (u, v) data, that we refer to as 1996.99-1994.27, were analyzed both in the image and in the

[3]The National Radio Astronomy Observatory is operated by Associated Universities Inc. under cooperative agreement with the National Science Foundation.

(u, v) planes. In the image plane a compact, basically unresolved source is observed. A Gaussian ellipsoid fit to this source in the image plane using the AIPS task JMFIT indicates maximum possible deconvolved angular dimensions of $0.''035 \times 0.''029$ (major axis × minor axis) for the source. However, White & Becker (1982) have shown that it is better to study the angular dimensions of marginally resolved sources directly in the (u, v) plane. We then fitted directly the (u, v) data in two dimensions using the AIPS task UVFIT and a Gaussian ellipsoid model. The fit gave $0.''023 \pm 0.''013 \times 0.''023 \pm 0.''019$ (major axis × minor axis) for the source. This result indicates that the source is very compact and that, within the error, it shows no strong departures from a circular morphology. We then adopt as an estimate of the Gaussian angular size (full width at half maximum) of the source the geometric mean of the major and minor axes, that gives $\theta_G = 0.''023 \pm 0.''012$.

The angular size determined for the non-thermal emission depends on the model assumed to fit the (u, v) data. A model of a circular disk with constant brightness gives an angular diameter of $\theta_D = 0.''019 \pm 0.''010$. Given that the errors are comparable to the measurements, we will take this determination as an upper limit, $\theta('') \leq 0.''02$, to the angular size of the non-thermal emission.

3. INTERPRETATION

The small angular size found for the non-thermal component, $\theta('') \leq 0.''02$, can be used to discuss the nature of the non-thermal component. An expanding envelope ejected periodically from the binary (Persi et al. 1990; Bieging et al. 1989; Miralles et al. 1994) would have to be bigger than the radio photosphere to be outside the optically thick region around the contact binary system. We can use the results for the 1994 data discussed in the Appendix A to estimate that the radio photosphere at 8.46 GHz has an angular size of $\theta('') \simeq 72$ milli-arcseconds. We then conclude that an envelope cannot explain the observations since the non-thermal emission would be significantly larger than observed. Recently, Pittard (2010) has proposed that the time variable emission observed in O+O binaries can come from the thermal emission from the wind-collision region between the stars. In the case of Cyg OB2 #5 the wind-collision region between the members of the contact binary is probably a strong emitter, but lies deep inside the radio photosphere of the system, although it is known that the radio photospheres can be clumpy or asymmetric, allowing the detection of sources embedded in it (e.g. WR140; White & Becker 1995). The wind-collision region could also be located between the contact binary and a third star. Kennedy et al. (2010) discussed the variations arising from non-thermal emission in a wind-collision region between the contact binary and a third star. They demonstrate that thermal emission variations that may arise in such a wind-collision region will not have sufficient amplitude to account for the variations, and conclude that the thermal-emission Pittard models would predict smaller flux changes than observed. The Kennedy et al. (2010) models also account well for the variable radio emission. We then favor the possibility of a third star with non-thermal emission in orbit around the contact binary, as proposed by Kennedy et al. (2010), or a wind-collision region.

Despite the fact that the non-thermal emission from young, low-mass stars is typically associated with gyrosynchrotron emission from Lorentz γ factors of a few (e.g. Ray et al. 1997), while the emission from massive stars is believed to be synchrotron from relativistic electrons with very large γ factors (e.g., Pittard & Dougherty 2006), we cannot rule out the possibility that the non-thermal emission from Cyg OB2 #5 is being produced by a young, low-mass star (i.e. a Tauri star) that formed coevally with the rest of the system. The non-thermal emission from young, low-mass stars is usually very compact. For the T Tau Sb star, with a mass of 0.6 $M_\odot$, Loinard et al. (2005, 2007) estimate an angular size of 0.5 mas, that at a distance of 147.6 pc corresponds to a radius of $\sim 8\ R_\odot$. For the more massive S1 star (6 $M_\odot$) in Ophiuchus, Loinard et al. (2008) estimate an angular size of 0.95 mas, that at a distance of 116.9 pc corresponds to a radius of $\sim 12\ R_\odot$. At the larger distance of 925 pc (Linder et al. 2009), we expect a non-thermal star associated with Cyg OB2 #5 to have an angular size well below a milli-arcsecond.

Cyg OB2 #5 will be again in high state during 2010 and 2011 and a very long baseline interferometry study is needed to determine accurately the angular size and morphology of the compact non-thermal emission.

4. CONCLUSIONS

We present the analysis of VLA archive data of the Cyg OB2 #5 system taken during the high (1996) and low (1994) radio states. This analysis allows the subtraction, in the (u, v) plane of the persistent thermal component and a better estimate of the angular dimensions of the non-thermal component. We obtain an upper limit, $\theta('') \leq 0.''02$ for the angular size of the non-thermal emission. Cyg OB2 #5

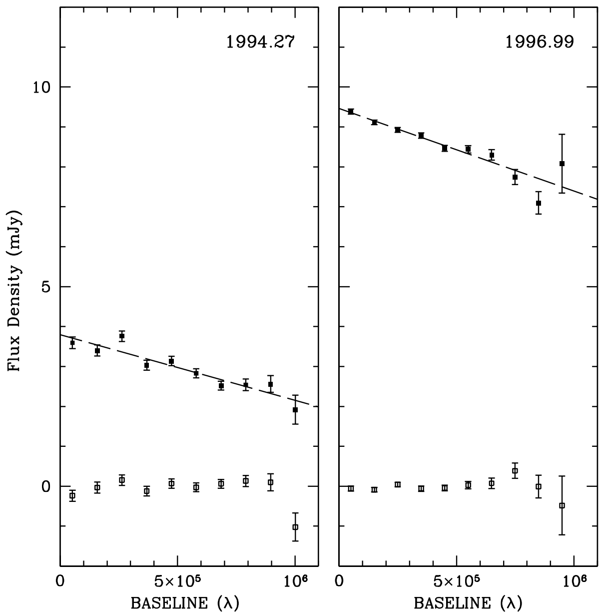

Fig. 1. (Left) Real (filled squares) and imaginary (empty squares) components of the emission at 8.46 GHz for 1994 April 9. The dashed line is the least squares fit to the real component. (Right) Same as in the left panel for 1996 December 28. The imaginary component is consistent with zero, indicating that the source is symmetric about the phase center (the origin of the visibility plane) and has no significant structure on these spatial scales.

will be again in high state during 2010 and 2011 and a very long baseline interferometry study is needed to determine the angular size and morphology of the compact non-thermal emission.

We are thankful for the support of DGAPA, Universidad Nacional Autónoma de México, and of Conacyt (Mexico). This research has made use of the SIMBAD database, operated at CDS, Strasbourg, France.

APPENDIX A. ONE-DIMENSIONAL ANALYSIS OF THE VISIBILITY FUNCTION

If the sources have approximate circular symmetry, the analysis of the (u, v) data can be made in a one-dimension approximation. To test if this was possible with the data discussed here, the NE component was subtracted in two dimensions in the (u, v) plane of both data sets using Gaussian ellipsoid models to leave only the emission from the main component, the one directly associated with the contact binary. This subtraction was performed using the AIPS task UVMOD. We then fitted the (u, v) data in two dimensions using the AIPS task UVFIT and a Gaussian ellipsoid model. The fits gave $0.''079 \pm 0.''007 \times 0.''066 \pm 0.''008$ (major axis × minor axis) for the 1994.27 data and $0.''045 \pm 0.''006 \times 0.''036 \pm 0.''005$ (major axis × minor axis) for the 1996.99 data. These results indicate that, within error, the emission at both epochs does not show strong departures from a circular assumption. We also note that at a distance of 925 pc (Linder et al. 2009), the semimajor axis of the non-thermal star (7 AU) will subtend an angle of only $0.008''$, below the upper limit of $0.020''$ found for the angular size of the non-thermal component. It is quite possible that this non-thermal star, if present, will introduce asymmetries but future VLBI observations will be needed to test this.

In Figure 1 we present the one-dimensional real and imaginary components of the amplitude as a function of baseline. These values were obtained using the AIPS task UVPLT that averages in circular rings around the origin of the (u, v) plane. Before applying this task, the source emission was centered on this origin.

For a marginally resolved wind source, the real part of the visibility, $V(b)$, can be fitted in one dimension with a linear function (Escalante et al. 1989):

$$V(b) = S_0 - Ab\,, \qquad \text{(A1)}$$

where S_0 is the flux density at zero spacing (the total flux density), given in mJy, A is the slope of the linear fit, and b is the baseline separation in wavelengths. For 1994 only the thermal (T) emission was present and we obtain $S_0(T) = 3.79 \pm 0.09$ mJy and $A(T) = (1.64 \pm 0.18) \times 10^{-6}$ mJy wavelength^{-1}. For 1996 both the thermal and non-thermal (T+N) emissions were present and we obtain $S_0(T+N) = 9.46 \pm 0.05$ mJy and $A(T+N) = (2.07 \pm 0.14) \times 10^{-6}$ mJy wavelength^{-1}. The fact that both epochs give similar slopes suggests that, as expected, most of the extended emission comes from the thermal component. Subtracting the 1994 fit to the 1996 fit we obtain the non-thermal (N) contribution alone, that is given by $S_0(N) = 5.67 \pm 0.10$ mJy and $A(N) = (0.43 \pm 0.23) \times 10^{-6}$ mJy wavelengths^{-1}. The characteristic angular size of the emitting region is given by (Escalante et al. 1989; Miralles et al. 1994):

$$\theta('') \simeq 1.44 \times 10^5 \; \frac{A}{S_0}\,, \qquad \text{(A2)}$$

which gives $\theta('') \simeq 0.''011 \pm 0.''006$ for the non-thermal component. It should be noted that our fitting of the non-thermal component to a thermal wind model may not be consistent, since the structure of the visibilities for an optically thin non-thermal source and

TABLE 2

PARAMETERS FROM FITS

Emission[a]	S_0 (mJy)	A (10^{-6} mJy λ^{-1})	θ (mas[b])
T	3.79 ± 0.09	1.64 ± 0.18	62 ± 7
N+T	9.46 ± 0.05	2.07 ± 0.14	32 ± 2
N	5.67 ± 0.10	0.43 ± 0.23	11 ± 6

[a]T = Thermal, N = Non-thermal.

[b]mas = milli-arcseconds.

a partially optically thick stellar wind are not necessarily the same. In Table 2 we summarize the parameters obtained for the thermal and thermal plus non-thermal states, as well as the subtraction that traces the non-thermal emission alone.

REFERENCES

Abbott, D. C., Bieging, J. H., & Churchwell, E. 1981, ApJ, 250, 645
Bieging, J. H., Abbott, D. C., & Churchwell, E. B. 1989, ApJ, 340, 518
Briggs, D. 1995, PhD Thesis, New Mexico Inst. of Mining and Technology, USA
Contreras, M. E., Rodríguez, L. F., Tapia, M., Cardini, D., Emanuele, A., Badiali, M., & Persi, P. 1997, ApJ, 488, L153
Escalante, V., Rodríguez, L. F., Moran, J. M., & Cantó, J. 1989, RevMexAA, 17, 11
Hall, D. S. 1974, Acta Astron., 24, 69
Herbig, G. H. 1967, PASP, 79, 502
Kennedy, M., Dougherty, S. M., Fink, A., & Williams, P. M. 2010, ApJ, 709, 632
Leung, K.-C., & Schneider, D. P. 1978, ApJ, 224, 565
Linder, N., et al. 2009, A&A, 495, 231
Loinard, L., Mioduszewski, A. J., Rodríguez, L. F., González, R. A., Rodríguez, M. I., & Torres, R. M. 2005, ApJ, 619, L179
Loinard, L., Torres, R. M., Mioduszewski, A. J., & Rodríguez, L. F. 2008, ApJ, 675, L29
Loinard, L., et al. 2007, ApJ, 671, 546
Miralles, M. P., Rodríguez, L. F., Tapia, M., Roth, M., Persi, P., Ferrari-Toniolo, M., & Curiel, S. 1994, A&A, 282, 547
Persi, P., Ferrari-Toniolo, M., Tapia, M., Roth, M., & Rodríguez, L. F. 1985, A&A, 142, 263
Persi, P., Tapia, M., Rodríguez, L. F., Ferrari-Toniolo, M., & Roth, M. 1990, A&A, 240, 93
Pittard, J. M. 2010, MNRAS, 403, 1633
Pittard, J. M., & Dougherty, S. M. 2006, MNRAS, 372, 801
Rauw, G., Vreux, J.-M., & Bohannan, B. 1999, ApJ, 517, 416
Ray, T. P., Muxlow, T. W. B., Axon, D. J., Brown, A., Corcoran, D., Dyson, J., & Mundt, R. 1997, Nature, 385, 415
White, R. L., & Becker, R. H. 1982, ApJ, 262, 657
_________. 1995, ApJ, 451, 352

Yolanda Gómez, Laurent Loinard, and Luis F. Rodríguez: Centro de Radiostronomía y Astrofísica, Universidad Nacional Autónoma de México, Apdo. Postal 3-72 (Xangari), 58089 Morelia, Michoacán, Mexico (y.gomez, l.loinard, l.rodriguez@astrosmo.unam.mx).
Amy J. Mioduszewski: National Radio Astronomy Observatory, 1003 Lopezville Road, Socorro, NM 87801, USA (amiodusz@nrao.edu).

Revista Mexicana de Astronomía y Astrofísica, **46**, 221–243 (2010)

ECHELLE SPECTROSCOPY OF THE NUCLEI OF THE HIGHLY COLLIMATED BIPOLAR PLANETARY NEBULAE M 2-9 AND M 1-91[1]

S. Torres-Peimbert,[2] A. Arrieta,[3] and M. Bautista[4]

Received 2010 January 21; accepted 2010 May 20

RESUMEN

Presentamos espectroscopía echelle del núcleo sin resolver de las nebulosas bipolares M 2-9 and M 1-91. Los espectros están dominados por líneas de emisión emitidas en un amplio intervalo de condiciones físicas. De las observaciones identificamos las líneas de emisión, las condiciones físicas y los movimientos relativos de las diferentes especies ionizadas en la región circunestelar de ambos objetos. Proponemos que las líneas prohibidas observadas se originan en la parte interior del toro extendido que rodea a cada objeto.

ABSTRACT

We present echelle spectroscopy of the unresolved nuclei of the bipolar planetary nebulae M 2-9 and M 1-91. The spectrum is dominated by emission lines emitted under a wide range of physical conditions. From the observations we identify the emission lines, derive physical conditions and relative motions of the different ionized species in the circumstellar region of both objects. We propose that the observed forbidden lines arise in the inner part of the extended torus that surrounds each object.

Key Words: planetary nebulae: individual (M 2-9, M 1-91)

1. INTRODUCTION

Among the many interesting proto-planetary nebulae and young planetary nebulae there are those with extreme bipolar shape, or "butterfly" type. M 2-9 and M 1-91 are analogous not only in morphology, but also in dusty lobes and spectral characteristics of their nuclear regions. M 2-9 has been widely studied in many of its characteristics, and yet is not fully understood; the studies on M 1-91, have been more limited because it is considerably fainter, and thus it is less well understood. We present here the result of our spectroscopic observations of their central objects in an attempt to further understand the physical conditions of the circumstellar gas. In what follows we will present each of the objects, describe the observations and their characteristics. For M 2-9 we discuss the profiles of the Balmer lines, of [O III] lines, and the intensities of the Fe lines. We also derive the reddening law and the behavior of its physical conditions as a function of velocity relative to the central star. For M 1-91 we carry out a similar study; however, as expected, the information derived for this object is more limited.

2. OBSERVATIONS

The observations were carried out at the Observatorio Astrónomico Nacional in San Pedro Mártir, Baja California with the 2.1 m telescope and the REOSC echelle spectrograph (R $\sim$ 18,000 at 5,000 Å) and a 1024×1024 Tektronix detector that yields a spectral resolution of 10.6 km s^{-1} and a spatial resolution of $0.99''$ per pixel. The 3600 to 6850 Å range was covered in 29 orders (blue spectrum) for both objects, and the 6500 to 9500 Å range in 11 orders (red spectrum) for M 2-9.

Long slit observations, $79.8'' \times 2''$, oriented along the major axis were obtained for both objects. The exposure time for the blue spectrum of M 2-9 was 600 sec and the other spectra required 900 sec.

Short window extractions (10 pixels) were performed to obtain the nuclear spectra, which will be reported here. For M 2-9 the blue spectrum was

[1]Based on observations obtained at the Observatorio Astronómico Nacional at San Pedro Mártir, Baja California, Mexico.

[2]Instituto de Astronomía, Universidad Nacional Autónoma de México, Mexico.

[3]Depto. de Física y Matemáticas, Universidad Iberoamericana, Mexico.

[4]Department of Physics, Western Michigan University, USA.

observed on 23 April 1995 and the red on 25 April 1995; while for M 1-91 the observations were carried out on 27 May 1998. The data reduction was carried out with IRAF routines. The spectra were normalized to the continuum for each spectral order with a Chebyshev polynomial.

3. M 2-9

One of the most interesting objects is M 2-9 (PN G10.8+18), a bright nebula of extreme bipolar morphology. It is seen almost face-on, with a size of approximately $12'' \times 48''$ and extensions that reach up to $60''$ from the nucleus (Schwarz et al. 1997). It has been extensively studied (cf. Allen & Swings 1972; Balick 1989; Hora & Latter 1994; Schwarz et al. 1997; Solf 2000; Doyle et al. 2000).

The evolutionary status of M 2-9 is still controversial. M 2-9 has been identified with objects which "bear the characteristics indicative for very young planetary nebulae", such as M 1-91, M 1-92 (Solf 1984), CRL 618 (Schmidt & Cohen 1981) or "protoplanetary nebulae" (Walsh 1981). Schwarz et al. (1997) derive a distance to M 2-9 of 650 pc. At this distance the bolometric luminosity is 550 $L_\odot$ and its dynamic age is 1200 years. So at least one Mira-containing symbiotic system is reminiscent of the odd behavior pattern of M 2-9 (Doyle et al. 2000).

The lobes are found to have a double shell structure; the outer shell is dominated by H_2 line emission (Hora & Latter 1994) The lobes have condensations symmetrically located relative to the equatorial plane. The weak emissions observed at $60''$ S and N of the nucleus are also located in a point-symmetric distribution. One of the more significant characteristics of this object is that the knots brighter and closer to the nucleus show motions parallel to the equatorial plane (Allen & Swings 1972; Kohoutek & Surdej 1980; Balick 1989; Doyle et al. 2000).

Polarimetric studies show that the radiation from the lobes is polarized, suggesting that the nebular emission has two components: one produced locally in the lobes and another one probably being light scattered from the bright central region (Trammell, Goodrich, & Dinerstein 1995).

Upon examination of direct HST images Balick (1999) found that the [O III] image shows a series of knots lying along the nebula's symmetry axis. Unlike other knots in the lobes, the near-nuclear [O III] knots have no counterparts in other emission lines. The enlarged [S II] image shows a network of nearly radial filaments that are not artifacts of the telescope optics. These are associated with the base of the lobes. Figure 1 shows an image of the bipolar nebula in the light of [O III] and [S II]. An enlargement of the central regions is presented (from Balick, Icke, & Mellema 1997).

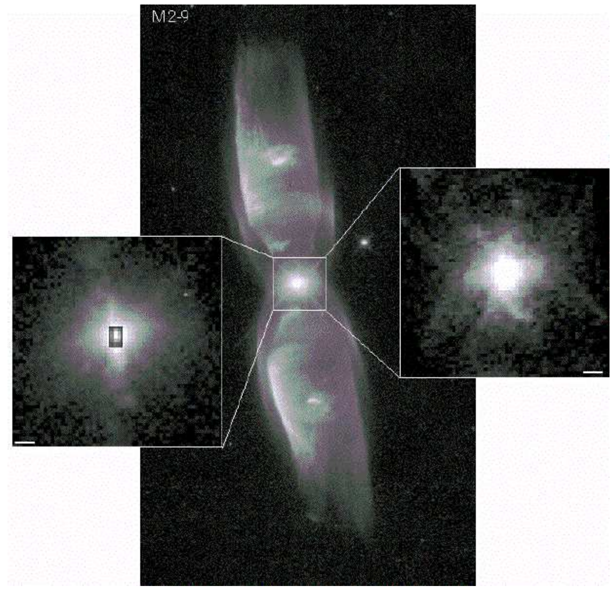

Fig. 1. HST image of the bipolar planetary nebula M 2-9 from Balick et al. (1997). Also shown are details of the internal region taken with two different filters: [OIII] on the left, and [S II] on the right.

3.1. *Nucleus of M 2-9*

M 2-9 is a very dust rich nebula. It has been found that the reddening of the nucleus is significantly different from that shown in the lobes. In the nucleus, different authors have found different reddening values; Swings & Andrillat (1979) and Calvet & Cohen (1978) determined an $A_{\rm v} \geq 5$ mag, while Hora & Latter (1994) from the hydrogen Brackett series determined an $A_{\rm v} = 2.3$ mag.

The nuclear spectrum shows nebular lines in emission over a weak continuum. No absorption lines have been observed, therefore the determination of its spectral type is very uncertain. It has been proposed that the nucleus is composed of a binary system: a hot component that ionizes the O^{++} gas and a B5 star that contributes to its visible luminosity (Calvet & Cohen 1978). Also Schwarz et al. (1997) suggest that a compact but hot component must be present; the hot component ionizes the high excitation emission lines while the B5 (or cooler) star provides part of the luminosity and the binary interaction of the pair produces the high collimation of the nebula. An accretion disk around the compact star would provide the fast disk wind.

Among other possible explanations, Livio & Soker (2001) have proposed a model to explain the apparent motion of the knots and the evolutionary stage of the exciting star. They propose that the nucleus is constituted by a binary system composed by an AGB or post-AGB star and a white dwarf.

Kwok et al. (1985) observed at five different radio continuum frequencies angular radii of the optically thick surface from 0.033″ to 22″, depending on the frequency. Adopting a value of the wind velocity of 1600 km s^{-1} they derive a mass loss rate of $3.3 \times 10^{-5}\,M_\odot$ yr^{-1} for a distance of 1 kpc. If the distance is 650 pc, then the mass loss rate is $1.1 \times 10^{-5}\,M_\odot$ yr^{-1}. This mass loss rate is much higher than the rates ($< 10^{-7}\,M_\odot$ yr^{-1}) estimated for other planetary nebulae. They propose that M 2-9 has descended from a rotating red-giant progenitor and that the bipolar morphology is the result of rapid expansion of the ionization front in the N-S directions.

Interferometric mapping of the ^{12}CO J = 1 - 0 emission from M 2-9 by Zweigle et al. (1997) indicates the existence of an expanding equatorial torus of molecular gas of about 6″ diameter around the center of M 2-9. The symmetry axis of the torus is tilted with respect to the plane of the sky by $\sim 17°$. The deprojected expansion velocity is 7 km s^{-1}, and for a distance of 650 pc, it corresponds to a kinematical age of about 1365 years.

Smith, Balick, & Gehrz (2005) using high dispersion near infrared spectra observe the 2.12 μm H_2 line and determine that the nuclear emission arises in an equatorial molecular disk or torus, consistent with the detection of a CO torus by Zweigle et al. (1997), where the H_2 emission arises closer to the central star, perhaps marking the irradiated inner edge of this larger torus.

Near-infrared color images of M 2-9 by Aspin, McLean, & Smith (1988) suggest that the central core of M 2-9 is surrounded by a dense extended equatorial disk of luminous dust. From the spectral energy distribution of the bright central core, using a 4″ diameter aperture, Smith & Gehrz (2005) fit a 260 K gray body to the unresolved central engine, although they suggest that the observed SED is actually flatter than any single temperature, perhaps indicating dust at various radii in a circumstellar disk.

3.2. *Systemic velocity*

The determination of the systemic velocity is not straightforward, since no photospheric lines are detected in the spectra of the nucleus of M 2-9. The emission lines show composite profiles or have different velocities depending on the degree of ionization,

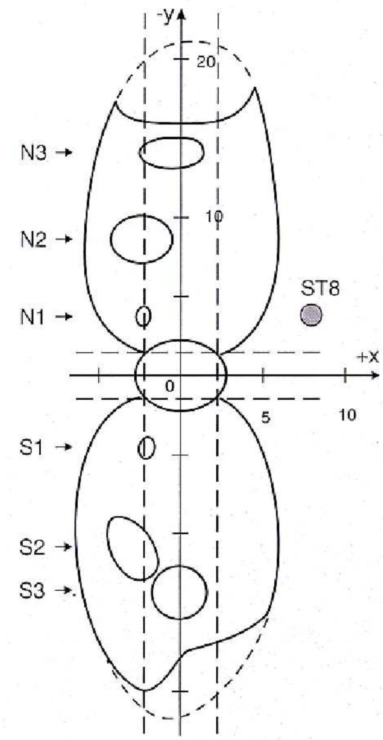

Fig. 2. Diagram of the structure of M 2-9 where the knots and nomenclature by Kohoutek & Surdej (1980) are shown. Also indicated is the position of the spectrograph slit used.

which allows us to assume that they are produced in circumstellar regions. Therefore, we determined the nuclear velocity from the kinematics of the lobes.

We show in Figure 2 the positions of the slit in the case of M 2-9, where we use the nomenclature by Kohoutek & Surdej (1980) to refer to the condensations. The detailed Hα profile was used to determine the systemic velocity.

On the long slit Hα spectral isocontours shown in Figure 3, a very bright central region with a double peak profile and two regions can be seen that correspond to the northern and southern lobes. Superimposed on the lobe emission, there are strong emissions at +15″ and –15″ relative to the nucleus, which correspond to the N3 and S3 knots, respectively. The nuclear velocity was estimated under the assumption that both knots were ejected symmetrically from the central region at the same speed.

In this figure the dashed line joins the intensity maxima of the N3 and S3 knots through the central region. The arrows indicate λ_0, the laboratory wavelength for Hα and the central part of the nebula. The velocity difference is $+40 \pm 5$ km s^{-1}, which yields a systemic heliocentric velocity of $+60 \pm 5$ km s^{-1} (cor-

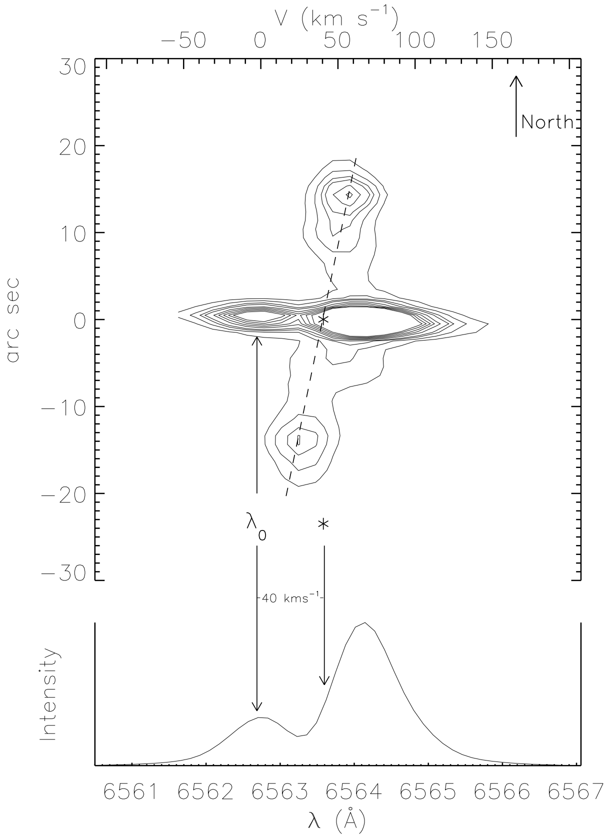

Fig. 3. Position-velocity diagram of the central part of M 2-9 from the long slit spectrum of the Hα profile. To determine the systemic velocity it has been assumed that the N3 and S3 knots were ejected symmetrically and are moving at the same speed relative to the nucleus. The dashed line joins both knots and yields the velocity of the nucleus. The laboratory wavelength of the derived velocity of the nucleus is indicated, which corresponds to a heliocentric velocity of $+60 \pm 5$ km s^{-1}.

responding to $V_{\rm LSR} = +75$ km s^{-1}). In the following sections all velocities will be referred to the systemic velocity. This value is comparable to those obtained by other authors; namely, $V_{\rm hel} = +69.2$ km s^{-1} from [Fe II] (Smith et al. 2005); and $V_{\rm LSR} = +80$ km s^{-1} from CO, (Bachiller, Martín-Pintado, & Bujarrabal 1990; Zweigle et al. 1997).

3.3. *Spectrum Description*

The nuclear spectrum is dominated by emission lines over a weak continuum, where no absorption lines can be detected; therefore it is not possible to determine directly the central star spectral type. In our data, emission lines from the following ions were identified and measured: H I, He I, C I, C II, C III, N I, N II, O I, O II, O III, Ne I, Ne II, Mg I, Mg II, Si I, Si II, Cl III, Ca I, Fe I, Fe II, Fe III, Ni II, Ni III, [N I], [N II], [N IV], [O I], [O II], [O III], [Ne III], [S II], [S III], [Cl II], [Cl III], [Ar III], [Cr II], [Cr III], [Mn II], [Fe I], [Fe II], [Fe III], [Fe IV], [Ni II], [Ni III], and [Ni IV]. To identify the lines in this very rich spectrum we used the code EMILI (Sharpee et al. 2003) under a set of different temperatures (9,000 to 11,500 K) and densities (10^4 to 10^7 cm^{-3}) to account for the different conditions that prevail in the source. The blue spectrum from 4150 to 6850 Å is presented in Figure 4, and the red spectrum from 6500 to 9400 Å in Figure 5. In both figures the most intense features have been marked.

Some of these lines are emitted in different unresolved regions of different velocities. For example, the Balmer lines have two maxima with a stronger red component. Also the profiles of the [OIII] 4959,5007 Å lines show two maxima, but in this case the blue component is brighter. The rest of the lines are approximately symmetric about a single peak; at the spectral resolution available, they are adjusted satisfactorily with Gaussian profiles. Tables 1 and 2 list the identifications of the observed lines for the 3700 to 6800 Å range and for the 6450 to 9460 Å range, respectively. They contain in Columns (1) and (2) the laboratory and observed wavelengths of the identified lines; in Columns (3) and (4) the measured intensities relative to Hβ and the extinction corrected intensity (see details of the extinction law in § 3.4); in Column (5) the measured FWHM (uncorrected for instrumental width); and in Column (6) the line identification. The blue section is normalized to Hβ, while the red section has been normalized to Hα. It was not possible to normalize the red spectrum to Hβ because the observations were carried out on different nights under different atmospheric conditions.

3.4. *Interstellar extinction*

Usually the Balmer and Paschen line ratios are used to derive interstellar extinction to any object. M 2-9 poses a difficult case, since its hydrogen lines show very complex profiles. While the Balmer lines show double peaked profiles, the Paschen lines show single component lines. Figure 6 shows these profiles normalized to maximum intensity. In this figure, lines are shown in increasing order of the upper level of the transition for each series. In the Balmer series, the Hα line shows two well separated components and the separation becomes less well defined as the energy of the upper level increases.

On the other hand, the Paschen series shows essentially a single component. A possible explanation for the single components could be that at these

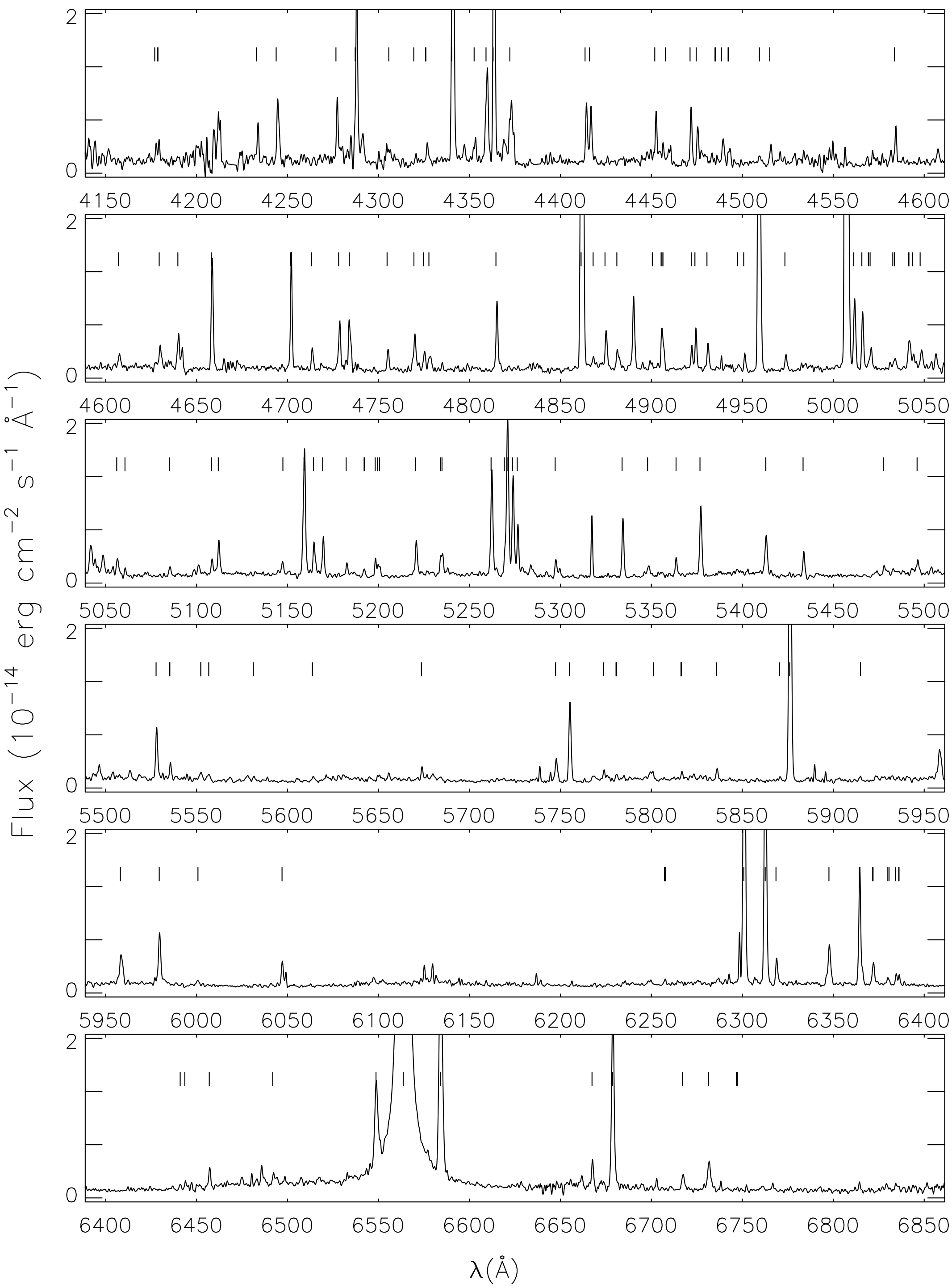

Fig. 4. Blue spectrum of the nucleus of M 2-9; it has been expanded to show the faint lines. The identified lines are indicated.

wavelengths the spectral resolution is lower than in the case of Hα. To rule out this possibility we degraded the resolution of the Balmer series to the same resolution as the Paschen series and found that the difference between the two peaks continues to be appreciable. Alternatively, if extinction were respon-

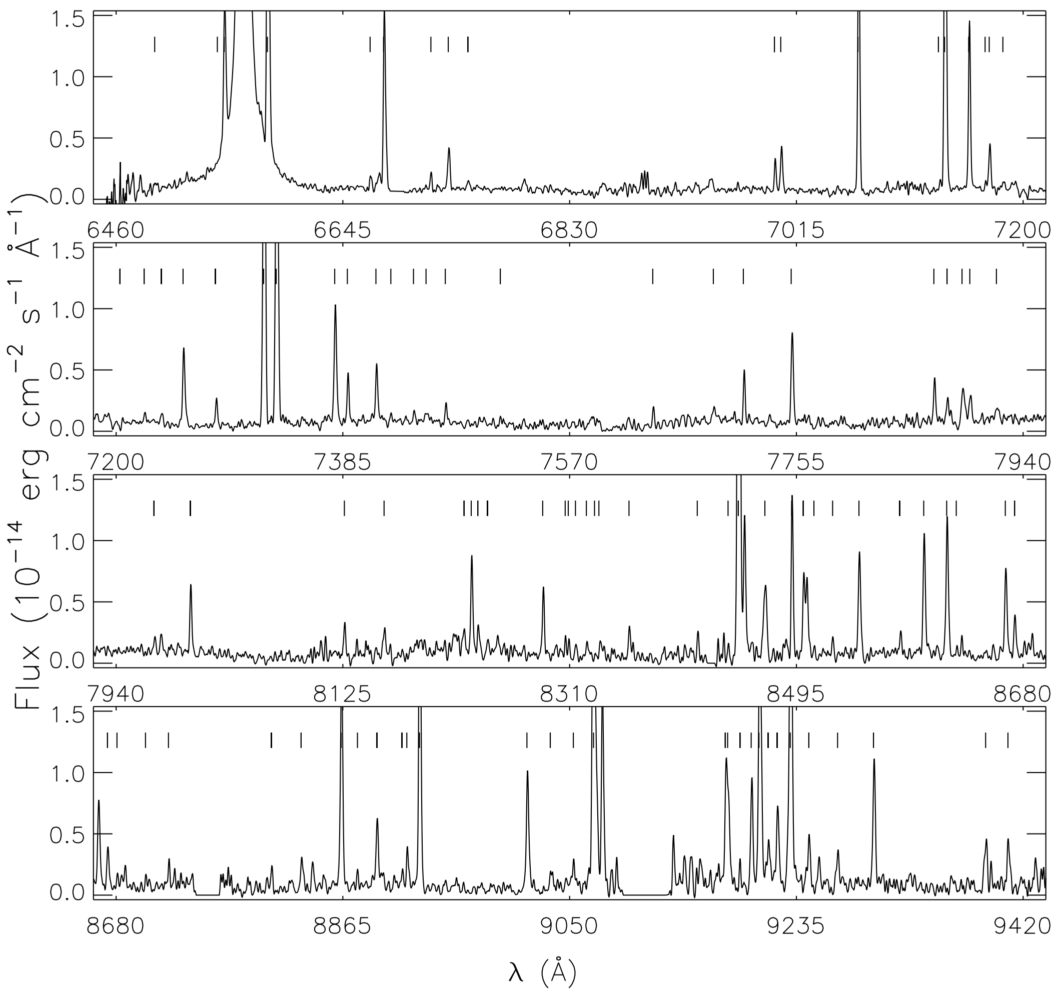

Fig. 5. Red spectrum of the nucleus of M 2-9; it has been expanded to show the faint lines. Also indicated are the identified lines. Our echelle configuration does not cover all the wavelength range, and thus there are gaps in the bottom panel.

sible for the shape of the Balmer profiles, the effect would tend to depend on the wavelength of the lines, and this effect is not observed.

In addition to the observed difference in the shape of the profile of the hydrogen lines, it should be noted that, within the uncertainties, in each series, for increasing energy of the upper level the centroid of the line approaches the systemic velocity. A possible explanation for this behavior in terms of the expected line ratios for each one of the transitions and interstellar extinction will be described in § 3.6.

We compared the hydrogen emission lines in the nucleus with the predictions for Case B recombination (Osterbrock 1989) in an attempt to derive A_V by means of a normal interstellar extinction law.

Assuming a mean density and temperature of 10^6 cm^{-3} and 10^4 K and adopting the interstellar extinction curve given by Cardelli, Clayton, & Mathis (1989) for $R_V = 3.1$, it is found that while the observed Hα to Hβ ratio suggests $A_V = 6.45$, all other Balmer lines are consistent with $A_V = 1.3 \pm 0.2$. Both estimates are quite different from the value determined by Hora & Latter (1994), $A_V = 2.3$, from the Brackett lines in the nearby IR spectrum of the nucleus. The anomalous value of extinction obtained using the Hα/Hβ ratio can be explained as an exceptionally intense Hα line.

The explanation of the discrepancy between the values of A_V determined by the other Balmer lines and the Brackett lines is less obvious. This discrepancy exceeds all the reasonable uncertainties in line intensity determinations and the possible deviation from Case B recombination. Therefore, this discrepancy suggests an unusual extinction curve.

TABLE 1

EMISSION LINES IN M 2-9 – BLUE SPECTRUM

λ_0	λ_{obs}	$I_\lambda/I_{H\beta}$[a] observed	$I_\lambda/I_{H\beta}$[b] ext correct	FWHM Å	Identification
3721.94	3722.04	0.039	0.068	0.9	H 14
3726.03	3726.62	0.058	0.101	0.8	[O II] 1F
3728.81	3729.09	0.040	0.069	1.0	[O II] 1F
3734.37	3734.76	0.013	0.023	0.9	H 13
3750.15	3750.45	0.062	0.107	1.2	H 12
3770.63	3770.87	0.045	0.077	0.8	H 11
3797.90	3798.29	0.044	0.074	0.8	H 10
3835.38	3835.75	0.051	0.086	1.2	H 9
3863.05	3863.22	0.013	0.022	0.8	Ne II
3869.06	3868.96	0.232	0.384	0.9	[Ne III] 1F
3889.05	3889.25	0.183	0.300	1.2	H8
3964.73	3965.29	0.012	0.020	0.4	He I
3967.79	3967.69	0.070	0.112	1.1	[Ne III] 1F
3970.07	3970.49	0.115	0.183	1.1	Hϵ
4026.20	4026.96	0.029	0.045	0.7	He I
4068.60	4069.02	0.038	0.057	0.9	[S II] 1F
4076.35	4076.67	0.019	0.029	1.2	[S II] 1F
4101.73	4102.24	0.230	0.343	1.1	Hδ
4143.76	4144.43	0.009	0.013	1.1	He I
4177.20	4177.82	0.016	0.022	0.7	[Fe II] 21F
4178.85	{4179.43	0.018	0.026	0.6}	N II
4178.96					[Fe II]
4233.17	4233.63	0.017	0.024	0.6	Fe II 27
4243.97	4244.68	0.067	0.093	1.4	[Fe II] 21F
4276.83	4277.33	0.045	0.062	0.7	[Fe II] 21F
4287.39	4287.93	0.111	0.151	0.8	[Fe II] 7F
4305.89	4306.36	0.016	0.022	1.0	[Fe II] 21F
4319.62	4320.17	0.032	0.042	0.8	[Fe II] 21F
4326.15	{4326.94	0.017	0.023	1.0}	[Ni II] 3F
4326.24					[Ni III]
4340.47	4326.94	0.416	0.531	-	H$\gamma^\dagger$
4352.78	4352.21	0.027	0.036	1.2	[Fe II] 21F
4359.33	4359.69	0.099	0.129	1.5	[Fe II] 7F
4363.21	4363.55	0.361	0.468	0.8	[O III] 3F
4372.43	4372.92	0.011	0.014	1.2	[Fe II] 21F
4413.78	4414.36	0.055	0.070	0.9	[Fe II] 7F
4416.27	4416.81	0.057	0.072	0.8	[Fe II] 6F
4452.10	4452.61	0.037	0.046	0.8	[Fe II] 7F
4457.95	4458.59	0.007	0.009	0.9	[Fe II] 6F
4471.50	4471.86	0.062	0.075	0.8	He I
4474.90	4475.43	0.017	0.021	0.9	[Fe II]
4485.21	{4486.11	0.006	0.008	1.0}	[Ni II] 3F
4485.57					Fe III
4488.75	4489.39	0.018	0.021	1.5	[Fe II] 6F
4492.63	{4492.08	0.008	0.010	0.6}	[Fe II] 6F
4492.41					Ne I
4509.61	4509.47	0.008	0.010	1.6	[Fe II] 6F
4515.34	4515.70	0.020	0.024	1.0	Fe II
4583.84	4584.42	0.029	0.033	0.5	Fe II 38
4607.03	4607.57	0.022	0.025	1.5	[Fe III] 3F
4629.39	4629.95	0.016	0.018	0.9	[Fe II] 37
4639.67	4640.29	0.016	0.018	0.9	[Fe II] 4
4658.05	4658.56	0.136	0.150	1.0	[Fe III] 3F
4701.53	4702.02	0.117	0.126	0.5	[Fe III] 3F
4713.14	4713.61	0.017	0.018	1.0	He I
4728.07	4728.61	0.037	0.040	0.9	[Fe II] 4F
4733.91	4734.28	0.024	0.026	1.3	[Fe III] 3F
4754.69	4755.27	0.024	0.025	1.0	[Fe III] 3F
4769.43	4769.91	0.020	0.021	1.2	[Fe III] 3F
4774.72	4775.34	0.012	0.012	1.1	[Fe II] 20F
4777.68	4778.19	0.012	0.012	1.0	[Fe III] 3F
4814.53	4815.11	0.080	0.082	0.9	[Fe II] 20F
4861.33	-	1.000	1.000	-	H$\beta^\dagger$
4867.95	{4868.12	0.008	0.008	1.0}	[Fe IV]-F
4868.00					Ne II
4874.49	4875.12	0.022	0.021	1.0	[Fe II] 20F
4881.00	4881.76	0.018	0.018	2.2	[Fe III] 2F
4900.50	4899.21	0.007	0.007	0.8	[Fe IV]-F
4905.81	4905.86	0.070	0.068	0.2	[Fe II] 20F
4906.36	{4906.94	0.029	0.029	0.7}	O II 28
4905.34					[Fe III]
4906.56					[Fe IV]
4921.96	4922.42	0.028	0.028	0.9	He I
4923.93	4924.48	0.041	0.040	0.8	Fe II 42
4930.54	4931.13	0.026	0.025	1.1	[Fe III] 1F
4947.37	4947.95	0.011	0.010	2.6	[Fe II] 20F
4950.74	4951.41	0.019	0.018	1.1	[Fe II] 20F
4958.91	-	0.833	0.795	-	[O III]1F†
4973.39	4973.05	0.007	0.006	0.3	[Fe II] 20F
5006.84	-	2.879	2.684	-	[O III] 1F†
5011.25	5011.76	0.072	0.067	1.2	[Fe III] 1F
5015.68	5016.13	0.057	0.053	1.1	He I
5019.29	5019.12	0.017	0.016	0.7	O I 15
5020.23	5020.80	0.025	0.023	0.8	[Fe II] 20F
5032.70	5033.08	0.025	0.023	-	[Fe III] 2F
5033.59	5033.93	0.010	0.009	-	[Fe IV]-F
5041.56	{5041.94	0.037	0.034	1.5}	[N IV]-F
5041.40					N I
5043.52	5044.14	0.009	0.009	0.8	[Fe II] 20F
5047.74	5048.43	0.015	0.014	1.3	He I
5055.80	5056.51	0.023	0.021	1.4	Fe I
5060.34	5060.73	0.006	0.005	0.8	[Fe III]
5084.77	5085.36	0.009	0.009	-	[Fe III] 1F
5107.95	5108.59	0.010	0.009	0.9	[Fe II] 18F
5111.63	5112.31	0.031	0.027	1.0	[Fe II] 19F
5147.16	5147.32	0.016	0.014	1.0	[Fe I] 19F
5158.77	5159.28	0.145	0.126	1.2	[Fe II] 19F
5163.95	5164.57	0.022	0.019	1.0	[Fe II]
5169.03	5169.70	0.045	0.039	0.7	Fe II 42
5181.95	5182.63	0.016	0.014	0.8	[Fe II] 18F
5191.82	{5192.15	0.015	0.013	1.1}	[Ar III] 3F
5192.01					Ni III
5197.90	5198.34	0.018	0.015	0.6	[N I] 1F
5199.18	5199.77	0.011	0.010	1.0	[Fe II] 35F?
5200.26	5200.84	0.009	0.008	0.6	[N I] 1F
5220.06	5220.80	0.024	0.020	0.8	[Fe II] 19F
5233.76	5234.24	0.014	0.012	0.8	[Fe IV]-F
5234.62	5235.37	0.015	0.013	0.8	Fe II 49?
5261.62	5262.30	0.136	0.113	1.1	[Fe II] 19F
5268.87	5269.50	0.028	0.023	0.5	[Fe II] 18F
5270.40	5270.95	0.189	0.156	1.2	[Fe III] 1F
5273.35	5274.00	0.106	0.088	1.0	[Fe II] 18F
5275.99	5276.66	0.041	0.034	0.8	Fe II 49
5296.83	5297.56	0.021	0.017	1.2	[Fe II] 19F
5333.65	5334.38	0.069	0.055	1.0	[Fe II] 19F
5347.65	5348.33	0.007	0.005	0.8	[Fe II] 18F
5363.30	5363.78	0.014	0.011	1.1	[Ni IV]-F
5376.45	5377.21	0.092	0.073	0.9	[Fe II] 19F
5412.64	5413.08	0.044	0.034	1.4	[Fe II] 17F
5433.13	5433.83	0.026	0.020	0.9	[Fe II] 18F
5477.24	5478.10	0.013	0.010	1.2	[Fe II] 34F
5495.82	5496.56	0.016	0.012	1.7	[Fe II] 17F
5527.33	5528.04	0.065	0.049	0.9	[Fe II] 17F
5534.89	{5535.55	0.014	0.011	0.9}	Fe II
5534.70					Ni II
5551.91	{5552.38	0.008	0.006	1.7}	[Mn II]
5551.96					[Cr III]
5556.29	5556.54	0.008	0.006	2.3	[Fe II] 18F
5580.82	5581.52	0.004	0.003	1.3	[Fe II] 39F
5613.27	5614.25	0.008	0.006	2.0	[Fe II] 39F
5673.21	5674.13	0.014	0.010	1.1	[Fe II]
5746.96	5747.75	0.035	0.024	1.4	[Fe II] 34F
5754.64	5755.24	0.105	0.072	1.2	[N II] 3F
5773.40	5774.06	0.004	0.002	0.7	[Fe I] 2F?
5780.20	{5780.72	0.008	0.005	1.7}	Fe II
5780.51					Ne II
5800.70	5800.81	0.012	0.008	1.6	[Fe IV]-F
5816.02	{5816.75	0.007	0.005	1.0}	S II
5816.00					Mg I
5816.08					Si I
5835.45	5836.13	0.012	0.008	1.0	[Fe II]
5870.02	5870.81	0.005	0.003	1.4	[Fe II]
5875.67	5876.29	0.595	0.391	1.3	He I 11
5914.61	5914.82	0.004	0.003	-	Ne II

TABLE 1 (CONTINUED)

λ_0	$\lambda_{\rm obs}$	$I_\lambda/I_{H\beta}$[a] observed	$I_\lambda/I_{H\beta}$[b] ext correct	FWHM Å	Identification	λ_0	$\lambda_{\rm obs}$	$I_\lambda/I_{H\beta}$[a] observed	$I_\lambda/I_{H\beta}$[b] ext correct	FWHM Å	Identification
5957.56	5958.54	0.063	0.040	2.2	Si II 4	6383.72	6384.66	0.009	0.005	0.8	Fe II
5978.93	5979.64	0.059	0.037	1.4	Si II 4	6385.45	6386.25	0.008	0.004	0.6	Fe II
6000.2	6000.60	0.008	0.005	2.0	[Ni III] 2F	6385.64					O I
6046.44	6047.14	0.039	0.024	1.3	O I 22	6440.40	6441.02	0.007	0.004	1.2	[Fe II] 15F
6256.71					Si I	6442.95	6443.82	0.005	0.003	0.98	Fe II
6256.93	6257.68	0.007	0.004	1.3	O I	6456.38	6457.31	0.018	0.010	1.1	[Fe II]
6257.20					C II	6491.28	6492.33	0.023	0.012	-	Fe II
6300.30	6301.10	0.620	0.350	1.0	[O I] 1F	6548.04	6548.82	0.187	0.097	2.0	[N II] 1F
6312.06	6312.68	0.374	0.211	1.2	[S III]	6562.80	-	33.636	17.380	-	Hα[†]
6317.98	6318.88	0.032	0.018	1.1	Fe II	6583.46	6584.20	0.541	0.277	2.0	[N II]
6347.11	6347.87	0.066	0.037	1.6	Si II (2)	6666.80	6667.60	0.034	0.017	0.7	[Ni II] (2D-2F)
6363.78	6364.57	0.166	0.092	0.9	[O I] 1F	6678.15	6678.77	0.303	0.151	1.4	He I (46)
6371.37	6372.09	0.028	0.015	1.2	Si II (2)	6700.64	6702.94	0.010	0.005	0.6	[Fe II]
6371.13					Fe II	6702.22					C II
6379.46	6380.14	0.010	0.005	0.73	Ni II	6716.44	6717.47	0.021	0.010	1.7	[S II] 2F
6380.16					O II	6730.82	6731.75	0.046	0.022	1.7	[S II] 2F

[a] $I(H\beta)_{\rm obs} = 1.50 \times 10^{-13}$ erg cm^{-2} s^{-1}.
[b] $I(H\beta)_{\rm extcorr} = 2.35 \times 10^{-12}$ erg cm^{-2} s^{-1}.
[†] Several components.

The grain distribution of a nebular gas under the presence of a strong radiation field is expected to correspond to grains of larger sizes than those in the typical interstellar medium. This is due to the fact that the small dust grains are easily photodissociated while the large ones are much less affected. A larger grain size results in a shallower extinction curve than that of the galactic interstellar medium. A well known example of this effect is the extinction curve of the Orion Nebula (Mathis & Wallenhorst 1981; Kim, Martin, & Hendry 1994), which is best fitted by $R_{\rm V} = 5.1$. Besides the $R_{\rm V}$ variations, the nebula can exhibit an uncommon extinction curve due to the reflection effect and to the mixture of dust grains along the emitting gas column. The dependence on wavelength of the modified extinction curve can be characterized by the nebular extinction parameter, $N_{\rm V}$ (Bautista, Pogge, & DePoy 1995).

An important characteristic of interstellar extinction is that for λ longer than ~ 1 μm, it is practically insensitive to $R_{\rm V}$ and $N_{\rm V}$. Then, the observations of Hora & Latter (1994) could be real indicators of the amount of extinction in the J band. Starting from their value of $A_{\rm V} = 2.3$ and $E_{B-V} = 0.75$, a value of $A_{\rm J} = 0.12$ is obtained. With this fixed value we derive $R_{\rm V} = 5.0\pm0.5$ and $A_{\rm V} = 2.7\pm0.1$ to best represent the optical spectrum. These values were used to correct the observed nuclear lines in our spectrum (Tables 1 and 2).

3.5. *Hα line – optical depth effects*

Very noticeably in this nebula is that it shows an exceptionally wide Hα profile. Balick (1989) reports a width of 11000 km s^{-1} for this line; Arrieta & Torres-Peimbert (2003) report a full width (FWZI) of 5000 km s^{-1} that they explain as the result of Raman scattering. The core of the Hα line is also anomalous in that it exhibits at least two strong components with peaks separated by ~ 70 km s^{-1} (see Figure 7).

The Hα/Hβ ratio from the extinction corrected spectrum shows two maxima near −40 and +60 km s^{-1} and a minimum at about −10 km s^{-1}. The ratio at minimum is consistent with the predictions of Case B recombination (value indicated in the bottom panel of Figure 7). On the other hand, the red shifted peak has a ratio about 6 times the value predicted by recombination theory.

Neither collisional excitation nor extinction can explain the large departure from Case B. Instead, the difference can be explained by optical depth effects for transitions to levels n=2. We estimate the optical depth effects by including an escape probability

$$P_{\rm esc} = \frac{1-\exp(-\tau)}{\tau} \qquad (1)$$

on the Balmer lines. Here

$$\tau_{\rm ul} = {\rm constant} \times \lambda f_{\rm lu}\Big(n_{\rm l} - \frac{n_{\rm u} g_{\rm l}}{g_{\rm u}}\Big)$$
$$\approx {\rm constant} \times \lambda f_{\rm lu} n_{\rm l}\,, \qquad (2)$$

where, $f_{\rm lu}$ is the oscillator strength, $n_{\rm l}$ and $n_{\rm u}$ are the populations of the levels involved and $g_{\rm l}$ and $g_{\rm u}$ the statistical weights. Then, we compute the H I recombination spectrum using the model of Bautista et al. (1998) assuming that optical depths for all the permitted transitions to level n=1 have an infinitely large value (Case B approximation) and normalizing the optical depth of the Balmer series to that of the

TABLE 2

EMISSION LINES IN M 2-9 – RED SPECTRUM

λ_0	λ_{obs}	$100\times I_\lambda/I_{H\alpha}$[a] observed	$100\times I_\lambda/I_{H\alpha}$[b] ext corrected	FWHM Å	Identification	λ_0	λ_{obs}	$100\times I_\lambda/I_{H\alpha}$[a] observed	$100\times I_\lambda/I_{H\alpha}$[b] ext corrected	FWHM Å	Identification
6548.05	6548.99	0.571	0.573	1.8	[N II] 1F	8323.42	8324.26	0.076	0.044	1.5	H I Pa25
6562.82	-	100.000	100.000	-	Hα*	8330.59	8330.92	0.029	0.017	1.4	Fe II
6583.46	6584.24	1.747	1.735	1.9	[N II] 1F	8333.78	8334.50	0.029	0.017	1.2	H I Pa24
6666.80	6668.05	0.104	0.100	1.5	[Ni II] (2D-2F)	8357.69	8359.04	0.175	0.099	2.7	[Cr II](1F) + H I Pa22
6678.15	6678.99	0.765	0.736	1.4	He I (46)	8413.32	8414.73	0.124	0.069	1.5	H I Pa19
6716.44	6717.65	0.068	0.064	1.6	[S II] 2F	8437.95	8439.88	0.114	0.063	1.85	H I Pa18
6730.81	6731.81	0.204	0.193	2.1	[S II] 2F	8446.48	8448.25	4.392	2.430	1.6	O I (4)?
6746.73	6747.81	0.020	0.018	1.0	[Fe II] (4P-2S)	8446.12					Fe II
6746.13					[Fe II]	8467.26	8469.90	0.510	0.280	2.7	H I Pa17
6997.10	6997.88	0.094	0.082	1.2	[Fe IV] 4P	8490.73	8491.73	0.525	0.287	1.5	[Fe II] (2G-2F)
6997.18					Fe I]	8499.70	8501.24	0.376	0.205	1.7	[Ni III]
7002.12	7003.07	0.149	0.129	1.6	O I (21)	8500.20					[Cl III]
7065.18	7066.10	0.933	0.792	1.4	He I (10)	8500.32					Cl III
7131.11	7131.71	0.041	0.034	1.2	[Fe II]	8509.66	8509.92	0.035	0.019	1.23	Fe II
7135.80	7136.70	1.816	1.506	1.8	[Ar III] (1F)	8523.66	8525.14	0.047	0.025	1.37	Fe II]
7155.16	7156.37	0.578	0.477	1.3	[Fe II] (14F)	8545.38	8546.67	0.490	0.264	2.0	H I Pa15
7169.24	7169.78	0.051	0.042	2.1	Fe II	8578.69	8579.84	0.075	0.040	1.6	[Cl II] (1F)
7172.00	7173.13	0.233	0.191	1.6	[Fe II] (14F)	8579.18					Fe I
7182.09	7184.26	0.053	0.043	2.5	O II	8598.39	8599.48	0.431	0.229	1.8	H I Pa14
7203.90	7203.96	0.033	0.027	1.8	N II	8616.95	8618.22	0.510	0.269	1.5	[Fe II] (13F)
7203.35					Fe I	8626.40	8626.05	0.027	0.014	0.7	[Cr II]
7222.18	7223.69	0.029	0.024	2.1	[Fe II]	8665.02	8666.07	0.343	0.179	1.9	H I Pa13
7222.80					[Fe IV] (4D-4F)	8672.32	8673.60	0.184	0.096	1.73	Fe II]
7236.19	7237.71	0.061	0.049	1.8	C I	8672.40					O III
7236.52					Fe I	8680.20	8681.34	0.067	0.035	2.0	O II
7254.44	7255.43	0.288	0.230	1.9	O I(20)	8703.87	8704.61	0.082	0.042	1.9	[Ni II]
7281.35	7281.83	0.178	0.141	1.6	He I (45)	8722.35	8723.35	0.067	0.034	1.02	Fe II
7281.63					[Fe II]	8806.76	8807.32	0.131	0.066	1.6	Mg I (7)
7131.12	7131.71	0.041	0.034	1.2	[Fe II] (2G-2G)	8805.43					Fe I
7319.99	7321.14	2.471	1.931	2.0	[O II] (2F)	8806.06					Fe I
7330.73	7331.44	2.510	1.955	2.3	[O II] (2F)	8830.50	8831.55	0.157	0.078	1.9	He I
7377.83	7379.16	0.494	0.379	1.8	[Ni II] (2F)	8830.70					[Fe III]
7388.17	7389.47	0.175	0.133	1.5	[Fe II] (14F)	8862.79	8864.18	0.827	0.409	1.9	H I Pa11
7411.61	7412.79	0.208	0.158	1.6	[Ni II] (2F)	8876.34	8877.52	0.086	0.043	1.8	Ca I
7423.64	7424.97	0.043	0.033	1.6	N I (3)	8885.62	8893.48	0.194	0.095	1.8	[Fe II]
7442.30	7443.42	0.047	0.035	1.2	N I (3)	8884.94					Si I
7452.54	7453.68	0.188	0.141	1.2	[Fe II] (14F)	8890.90					Fe II
7468.31	7469.36	0.061	0.045	1.2	N I (3)	8891.91					[Fe II]
7513.16	7514.25	0.043	0.032	1.72	Fe II	8912.63	8913.84	0.076	0.037	1.2	Fe II]
7513.21	7514.25	0.175	0.133	1.5	Ca I	8913.27					Mg II
7637.54	7638.63	0.067	0.047	1.5	[Fe II] (1F)	8916.76	8917.78	0.147	0.072	1.0	Fe I
7686.94	7688.06	0.067	0.046	1.7	[Fe II] (1F)	8926.64	8927.97	1.229	0.598	1.51	Fe II
7711.43	7712.52	0.202	0.139	1.1	Fe II	8927.40					Ne I
7751.12	7751.58	0.484	0.330	2.4	[Ar III] (1F)	9014.91	9015.80	0.471	0.224	1.7	H I Pa10
7866.55	7867.97	0.204	0.134	1.60	Fe II	9033.50	9034.82	0.076	0.036	1.5	[Fe II] (13F)
7874.25	7878.68	0.161	0.105	2.8	[Fe II]	9034.20					C II
7878.05					Mg II	9051.95	9053.66	0.118	0.055	1.7	[Fe II] (13F)
7889.90	7890.95	0.255	0.166	2.7	[Ni III] (1F)	9068.9	9070.08	1.961	0.921	2.3	[S III] (1F)
7896.29	7897.31	0.167	0.109	2.9	[Fe II]	9177.13	9177.57	0.765	0.350	1.7	Fe I
7917.80	7919.00	0.110	0.071	1.9	Fe II	9178.42					C I
7971.6	7971.51	0.071	0.045	1.4	He I	9178.05	9179.52	0.784	0.359	2.4	Fe II
7970.61					C III	9188.7	9189.64	0.127	0.058	1.6	Ne II
8000.08	8001.15	0.192	0.121	1.5	[Cr II] (1F)	9188.16					Fe II]
7999.49					[Fe II]	9197.9	9198.72	0.431	0.196	1.9	C II
8125.30	8126.87	0.061	0.037	1.4	[Cr II] (1F)	9205.30	9205.08	0.665	0.302	1.4	C II
8158.13	8159.24	0.098	0.059	1.70	Fe I	9210.24	9212.54	0.188	0.085	2.8	He I (6/9)
8223.13	8224.49	0.104	0.061	1.6	N I (2)	9210.89					Fe II
8222.04					[Fe II]	9219.80	9219.91	0.320	0.145	2.2	C II
8229.67	8230.35	0.249	0.147	1.1	[Cr II] (1F)	9218.92					Fe II
8235.35	8235.68	0.098	0.058	2.1	O I	9218.25					Mg II
8235.00					Mg I	9229.02	9230.57	1.584	0.716	2.0	Pa9
8235.69					Mg II	9244.26	9245.77	0.225	0.102	2.3	Mg II (1)
8242.39	8243.58	0.047	0.028	1.3	N I (2)	9244.74					Fe II
8242.44					Fe I	9267.56	9269.20	0.112	0.050	1.6	[Fe II] (13F)
8286.43	8288.67	0.273	0.158	1.3	H I	9297.1	9298.47	0.431	0.192	1.57	Fe I
8306.11	8306.99	0.098	0.056	1.4	H I Pa27	9297.1					Fe II
8308.49	8309.51	0.131	0.076	1.1	[Cr II] (1F)	9388.87	9389.99	0.333	0.145	2.8	Mn II
8314.26	8315.35	0.084	0.048	1.4	H I Pa26	9407.08	9408.22	0.378	0.164	2.1	Fe II

[a] $I(H\alpha)_{obs} = 6.10 \times 10^{-12}$ erg cm^{-2} s^{-1}.
[b] $I(H\alpha)_{extcorr} = 4.40 \times 10^{-11}$ erg cm^{-2} s^{-1}.
* Several components.

3s - 3p transition, which is kept as a free parameter. Figure 8 shows the value of the Hα/Hβ ratio as a function of τ(3s - 2p). It can be seen that the Hα/Hβ ratio increases monotonically by nearly an order of magnitude as τ(3s - 3p) grows from 0 to 10. The figure also shows that the Hγ/Hβ ratio increases with optical depth too, but by a much smaller factor. This explains that traces of the blue shifted compo-

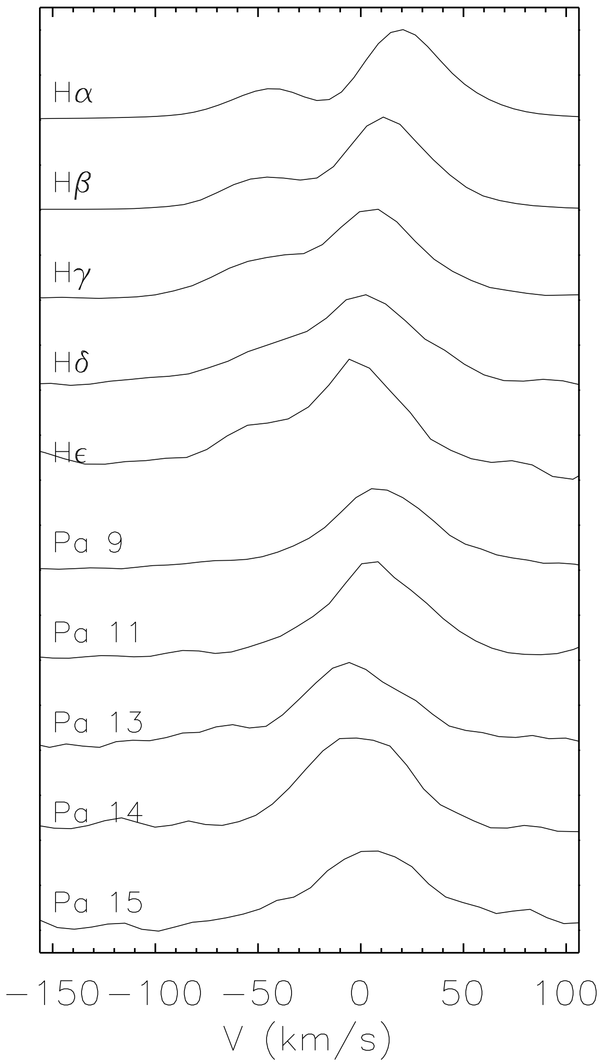

Fig. 6. Balmer and Paschen hydrogen line series in the nucleus of M 2-9. The intensities have been normalized. Hα shows a marked velocity shift, and the Balmer line profiles show two components.

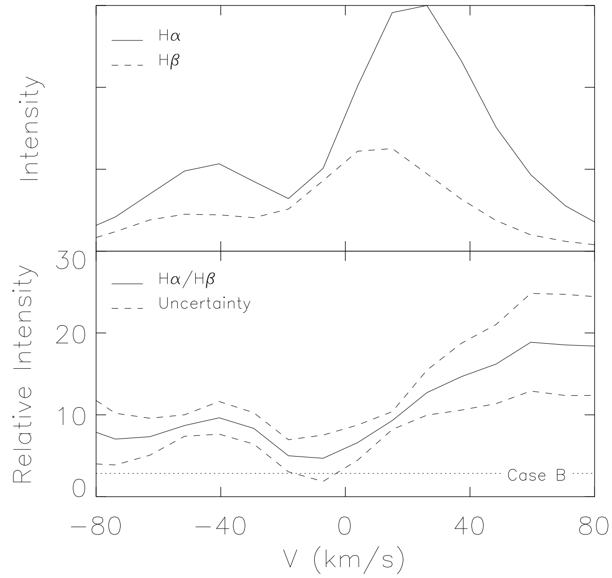

Fig. 7. Evidence that the Hα line is optically thick in the nucleus of M 2-9. In the upper panel the extinction corrected profiles Hα and Hβ ×3 lines are shown. Zero corresponds to the systemic velocity. In the lower panel the Hα/Hβ ratio of the extinction corrected spectra show excesses in Hα at –40 km s^{-1} and +60 km s^{-1}. The uncertainties and the value of the relation for Case B of recombination are shown.

nents and the red shifted components are present in Hβ. These components, however, are much smaller and closer to the center of the line that in the case of Hα.

Furthermore, the excess in Hα line intensity relative to the one predicted for case B can be explained by high optical depths for the transitions of level n=2. Therefore, it is proposed that the different observed components in these lines are the result of a single optically thick line.

Considering the total flux in the Hα, Hβ and Hγ lines it is found that Hα/Hβ = 17.3 and Hγ/Hβ = 0.531 after extinction correction. These ratios can be reproduced by two models of recombination with approximate τ(3s - 2p) values of 8.0 and 2.0 respectively. A better approximation in all the H I spectrum could require a more detailed treatment of radiation transfer of the lines. In this work we adopt a mean value of τ(3s - 2p) = 5.

The optical depth in the spectrum of H I has an important effect over the emissivities of the predicted lines and therefore also for the derived H^+ abundance. For example, for τ(3s - 2p) = 5 the emissivity of the Hβ line is reduced by a factor of 2.6 with respect to Case B recombination, then the calculated H^+ abundance increases by this same factor.

In brief, an extinction law in the nucleus characterized by $R_V = 5.0 \pm 0.5$ and $A_V = 2.7 \pm 0.1$ is used to correct the nuclear spectrum for extinction. This extinction law corresponds to larger dust grains than those of the typical interstellar medium. The exceptionally high value of the intensity of the Hα line relative to the predicted recombination by Case B is explained by a Balmer line optical depth τ(3s - 2p) ∼ 5. Further, we propose that the double peaked profile of these lines is also due to optical depth effects.

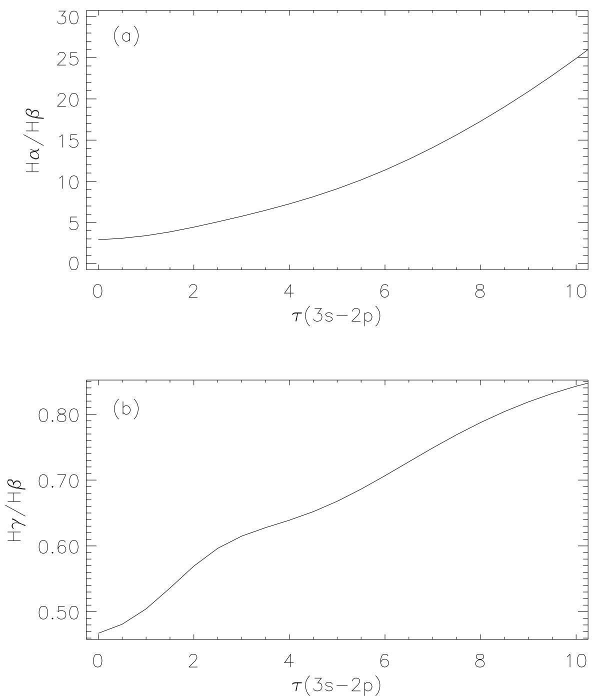

Fig. 8. Dependence on the Balmer intensity ratios on Hα optical depth in the nuclear region of M 2-9. The extinction corrected Hα/Hβ ratio is = 17.3. It is consistent with a value of τ(3s - 2p) = 8, while Hγ/Hβ = 0.531 with τ(3s - 2p) = 2. In this work a mean value of τ(3s - 2p) = 5 was adopted.

3.6. *Forbidden line profiles*

Balick (1989) found that the central region [N II] lines are well characterized by a bright central Gaussian at the systemic velocity, plus two weaker "satellite" lines at about $\pm$52 km s^{-1}. The bright [N II] emission seen towards the nucleus is "circumstellar". This conclusion is also supported by the very large ratio [N II] 5755/6583 intensities observed towards the nucleus. The circumstellar [N II] lines are spatially unresolved when the slit is oriented E-W (perpendicular to the lobes). Yet, with the slit along the lobes, the two satellite [N II] lines are offset about 0.7$''$ from the central star. Thus, the satellite lines probably arise along the nebular symmetry axis, and are unlikely to be directly associated to the 2 μm E-W disk surrounding the star observed by Aspin et al. (1988).

Solf (2000) found that [N II] and [O III] in the nuclear region show 3 components of different velocity, the central one at the systemic velocity (low velocity component) and the blue and red shifted components at about $\pm$50 km s^{-1} (high velocity components), all of which could be resolved spatially along the major axis of the nebula.

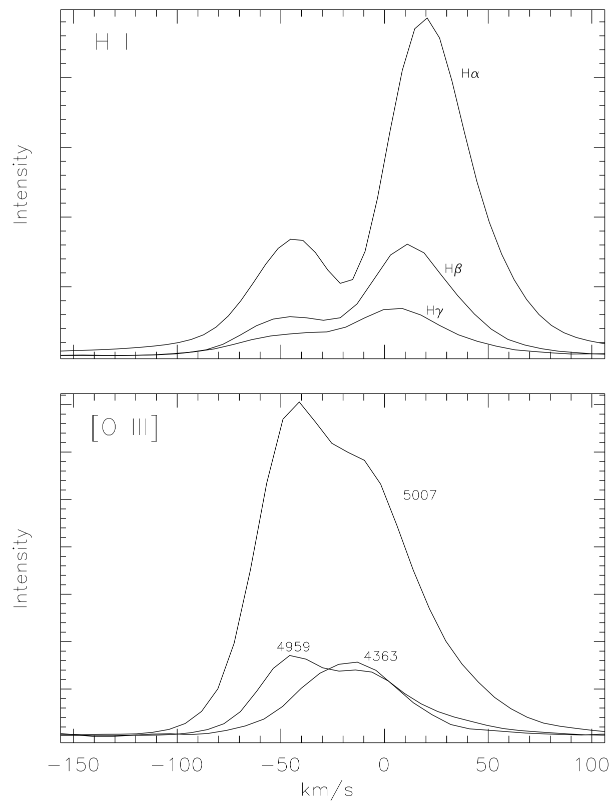

Fig. 9. Comparison of the Balmer series and [O III] profiles in the nuclear region of M 2-9. Both diagrams are on the same velocity scale and are normalized to the maximum of the bright line; on the upper panel Hβ and Hγ have been multiplied by 6. The higher [O III] density corresponds to the central Hα minimum.

We analyze the complex O^{++} emission line profiles in our spectra. While the 5007 and 4959 Å lines present double peaked profiles, with a weak component centered at –17 km s^{-1} and a bright one centered at –45 km s^{-1}, the 4363 Å line shows a single component centered at –17 km s^{-1}. The H I and [O III] profiles are different; whereas for hydrogen the red component is brighter that the blue one, in contrast for oxygen the blue component is stronger than the red one. In Figure 9 we compare the Balmer and [O III] lines on the same velocity scale. The ($\lambda\lambda$5007+4959)/λ4363 ratios in the two zones indicate that there is a region with a very high density at –17 km s^{-1} and another of lower density at –45 km s^{-1}. Due to the velocity displacement between the components, it is expected that the higher density component is associated to the region where all the single lines of the spectrum are produced. On the other hand, the blue component is formed in a different region.

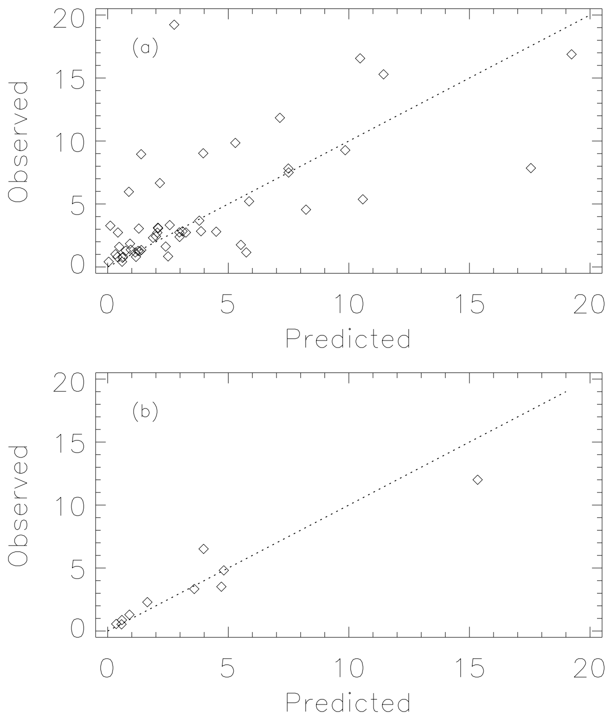

Fig. 10. Observed intensity of the permitted and forbidden Fe II lines vs. the predicted intensities in M 2-9. The predicted lines correspond to a $W = 10^{-9}$, $T_e = 10^4$ K and $N_e = 10^5$ cm^{-3} model. The upper panel corresponds to the lines in the blue spectrum and the lower panel to those of the red spectrum.

3.7. *Physical Conditions and kinematics of the emitting region*

It has been noted that the low value of [O III] 5007/4363 indicates high densities $\sim 10^{6-7}$ cm^{-3} (Allen & Swings 1972; Goodrich 1991). However, a low density region also contributes to the core; the presence of the [S II] 6717,6731 lines indicates Ne $< 10^4$ cm^{-3}. There is no significant [N I] 5200 emission in the core; the critical density of this line is ~ 2000 cm^{-3}.

In our spectra the [N II], [O II], [O III] and [S II] line ratios were used to determine the temperature and density in the nucleus; for this purpose we applied the NEBULAR tasks of the IRAF data reduction package. In addition, we used models of Bautista & Pradhan (1998) for Fe II, Fe III, and Fe IV, and the model of Bautista (2004) for Ni II.

As it has been mentioned in § 3.6 the [O III] lines also show two components: one centered at –17 km s^{-1} and another at –45 km s^{-1} (see Figure 9). From the ($\lambda\lambda$5007+4959)/λ4363 line ratio it is found that these components originate in regions of different density. The component at –17 km s^{-1} corresponds to a density $\sim 10^7$ cm^{-3} (that we associate to the nuclear emission proper) while the one at –45 km s^{-1} to $\sim 10^6$ cm^{-3} (that we associate to the micro jets emerging from the nuclear region identified by Balick 1999).

The [Fe II] and [Ni II] lines require special attention. The fact that there are permitted Fe II lines present in the spectrum indicates that this ion is undergoing fluorescence excitation (Bautista & Pradhan 1998). Fluorescence is also suggested by the [Ni II] line intensity ratios, which cannot be reproduced by collisional excitation alone. For the analysis of the [Fe II] lines, those that are less sensitive to fluorescence are selected first; they are usually on the red and infrared part of the spectrum (Bautista & Pradhan 1998). These lines indicate an electronic density of $\sim 10^5$ cm^{-3}. To model the lines affected by fluorescence, the radiation continuum from 0 to 13.6 eV is approximated by a 40,000 K black body spectrum. The intensity of the radiation in the region of the emission line is proportional to the dilution factor

$$W = \frac{1}{4}\left(\frac{R}{r}\right)^2 , \qquad (3)$$

where R is the radius of the ionizing star and r is the distance from the emission region to the star. The value of W is adjusted to find the best agreement between predicted relative line intensities and the observed fluxes of Fe II and Ni II lines. It must be noted that variations in the adopted temperature for the black body can be compensated for the most part by different values of W, such that one gets essentially identical fits to the observed spectrum and predicted line emissivities.

In Figure 10 we plot observed Fe II permitted and forbidden intensities against the intensities predicted by the model with $W = 10^{-9}$, $T_e = 10^4$ K and $N_e = 10^5$ cm^{-3}. The upper panel corresponds to the blue spectrum, the lower to the red spectrum. The agreement with the red region is very good while the agreement with the blue region is only moderately satisfactory, although acceptable, given the lower precision of the weak lines and the uncertainties in the radiation field that affects the Fe II lines. However, it should be noted that both forbidden and permitted lines are reasonably well explained with the same model.

Our Fe III model reproduces reasonably well the twelve identified [Fe III] lines in the blue spectrum. The agreement between the model predictions and the observations can be seen in Table 3. Here the mean of the dispersion between the ratio of Fe^{++}/H$^+$ abundance calculated for each line is less that 40%,

TABLE 3

COMPARISON OF OBSERVED AND THEORETICAL [FE III] INTENSITIES NORMALIZED TO $\lambda5085(A\ ^3P_1 - A\ ^5D_0)$

Wavelength	Transition	Obs.	Theoretical
		I(λ)/I(λ5085)	
4607	$a\ ^3F_3 - a\ ^5D_4$	2.87	1.84
4658	$a\ ^3F_4 - a\ ^5D_4$	17.2	18.3
4702	$a\ ^3F_3 - a\ ^5D_3$	14.5	9.85
4734	$a\ ^3F_2 - a\ ^5D_2$	2.95	4.05
4755	$a\ ^3F_4 - a\ ^5D_3$	2.91	3.43
4770	$a\ ^3F_3 - a\ ^5D_2$	2.38	3.40
4778	$a\ ^3F_2 - a\ ^5D_1$	1.40	1.96
4881	$a\ ^3H_4 - a\ ^5D_4$	2.11	2.15
4931	$a\ ^3P_0 - a\ ^5D_1$	2.96	2.26
5011	$a\ ^3P_1 - a\ ^5D_2$	7.82	5.83
5085	$a\ ^3P_1 - a\ ^5D_0$	1	1
5270	$a\ ^3P_2 - a\ ^5D_3$	18.5	11.5

which is in accordance to estimated uncertainties in the intensity of these weak lines.

The [Fe IV] lines in the optical spectrum of M 2-9 are consistent with the presence of a high density region. The effective collision strengths for optical [Fe IV] lines are very small; thus, high electron densities are required for those lines to be visible. Table 4 shows the comparison of model predictions with observations. The agreement is excellent for all the lines excepting that at 4906 Å. This disagreement can be due to blends.

We have determined the mean velocity for the different forbidden ions observed. This determination was carried out from those lines that are not ostensibly blended. The observed values are presented in Table 5, where we also include the standard deviation and the number of lines available. In the nuclear spectrum practically all lines have negative velocities relative to the systemic velocity; they lie in the −48 to +0.2 km s^{-1} range. The absence of positive velocity components is an indication of obscuration around the nucleus. The existence of a dense equatorial disk which is obscuring the inner portions of the receding matter has been suggested by Solf (2000). Thus, we can only see the front section of the circumstellar region.

TABLE 4

COMPARISON OF OBSERVED AND THEORETICAL [FE IV] INTENSITIES NORMALIZED TO $\lambda5234\ (A\ ^4F_{3/2} - A\ ^4G_{7/2})$

Wavelength	Transition	Obs.	Theoretical
		I(λ)/ I(λ5233)	
4868	$a\ ^2F_{5/2} - a\ ^4G_{9/2,11/2}$	0.70	0.72
4900	$a\ ^4F_{9/2} - a\ ^4G_{7/2}$	0.57	0.56
4906	$a\ ^4F_{9/2} - a\ ^4G_{11/2}$; $a\ ^4F_{7/2} - a\ ^4G_{5/2}$	2.40	1.72
5033	$a\ ^4F_{3/2} - a\ ^4G_{7/2}$	1	1
5034	$a\ ^4F_{5/2} - a\ ^4G_{11/2}$	0.75	0.74

TABLE 5

RADIAL VELOCITY AND PHYSICAL CONDITIONS OF DIFFERENT IONS FROM FORBIDDEN LINES IN M 2-9

Ion	Radial velocity[a]		log N_e cm^{-3}	T K	Ionization potential
[N I]	−11.± 4.	(2)	-	-	0.
[N II]	−6.± 2.	(3)	5.6	9500	14.53
[N IV]	−17.±-	(1)	-	-	47.45
[O I]	−2.± 0.	(2)	-	-	0.
[O II]	−3.±11.	(4)	5.6	9500	13.62
[O III]	−17.±-	(1)	7.0	11500	35.12
[Ne III]	−48.± 0.	(2)	-	-	40.96
[S II]	−5.± 9.	(4)	5.0	9000	9.98
[Cl II]	+0.±-	(1)	-	-	12.97
[Cl III]	−3.±-	(1)	-	-	23.81
[Ar III]	−15.± 9.	(3)	-	-	27.63
[Cr II]	−18.±21.	(4)	-	-	7.34
[Fe I]	−15.±11.	(3)	-	-	0.
[Fe II]	−1.± 8.	(76)	5.0	9000	7.87
[Fe III]	−8.± 6.	(14)	6.0	-	16.16
[Fe IV]	−18.±11.	(6)	6.6	11500	30.65
[Ni II]	−0.± 8.	(5)	-	-	7.64
[Ni III]	−10.±10.	(2)	-	-	18.17
[Ni IV]	−13.±-	(1)	-	-	35.17

[a]Radial velocity and standard deviation. The number of measured lines is shown in parenthesis.

It is also found that there is a relationship between the ionization potential and the radial velocity. This relation is presented in Table 5 and Figure 11 where only those species with more than one observed (unblended) line are displayed. That is, it was found that the velocities for different lines of the same ion are comparable, and that these velocities show a correlation with the ionization potential, where the more negative velocities correspond to higher potentials, and the positive ones to the neutral species. Furthermore, the emission lines originate in regions of a wide range of densities, as presented in this same table. The electron density varies from about 10^5 cm^{-3} in the region of low ionization ([S II] emitting region) to 10^7 cm^{-3} in the [O III] emitting region for temperatures from 9000

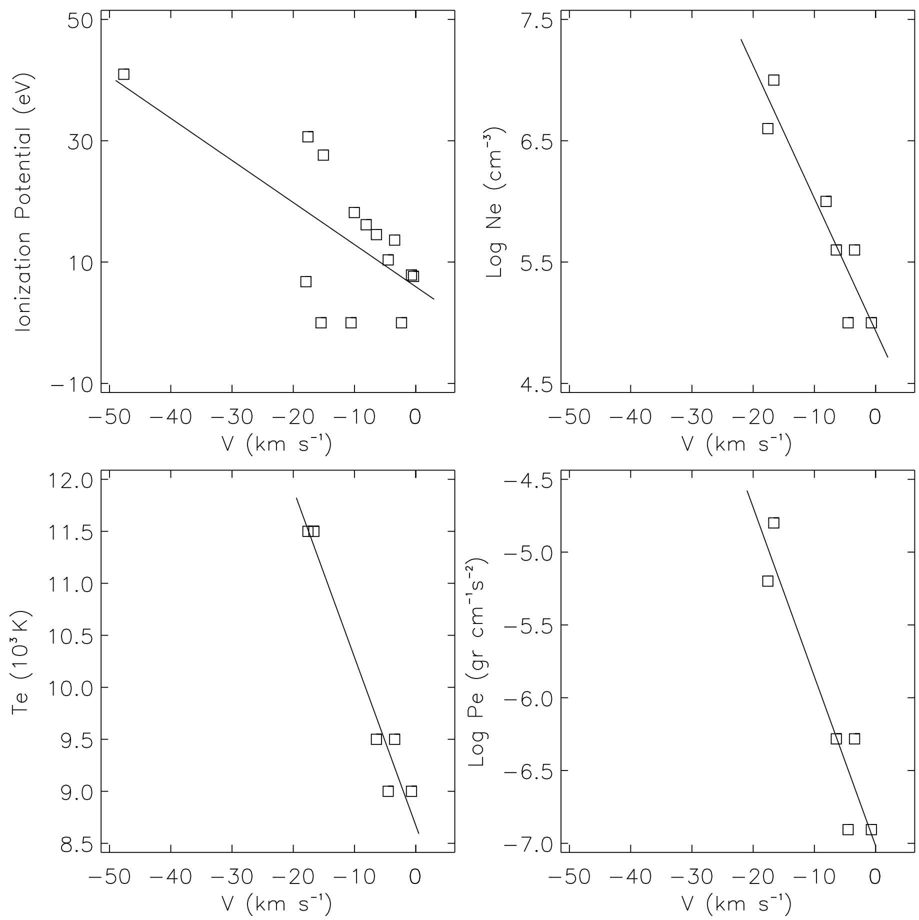

Fig. 11. Behavior of physical conditions relative to the observed radial velocity in M 2-9. On the upper left panel the velocity dependence on ionization potential is shown for those forbidden species for which more than one line was measured. On the lower left panel the electron temperature is presented; on the upper right panel, the electron density; and on the lower right panel, the electron pressure. The velocities are given relative to the systemic velocity. Solid lines indicate the best linear fit to the data.

to 11500 K, respectively. These values are also included in Table 5. This result is in agreement with the Calvet & Cohen (1978) estimates of N_e and T_e determined from the [OIII], [NII] and [OI] lines in the nucleus. They further argue the existence of ionization stratification, where a dense [OIII] zone is surrounded by a less dense [OI] zone. That is, there is also a correlation of physical conditions with radial velocity; where the lines of higher ionization species are emitted in regions of much higher density than those of the neutral species. This dependence is displayed in Figure 11, where we also show evidence of temperature and electron pressure correlation. This well defined negative gradient of ionization potential, electron density, electron temperature and gas pressure with radial velocity was already shown in a preliminary work by Arrieta & Torres-Peimbert (2000).

Although the spectral data reported here refer to a $2'' \times 10''$ window, the observed line emission is produced only in the nuclear region, which is significantly brighter than the surrounding region; that is, we are observing a circumstellar envelope. We adopt a size of the observed circumstellar envelope as that of the [S II] ($\sim 1.5''$ diameter) equatorial region imaged with HST (Figure 1), which at a distance of 650 pc corresponds to a circumstellar structure of $\sim$ 490 AU in radius. The fast moving material (high density, and high ionization), at a mean velocity of $\sim$ 30 km s^{-1}, can traverse the ionized circumstellar region in $\sim$ 80 years.

We try to describe in a very simple manner the geometry of the optical emitting circumstellar region. Comsidering that we observe only negative velocities we rule out the possibility of looking at a complete shell; next we consider the case of the front half of a spherical shell, in this case the expansion (deprojected) velocities can be 3 times larger than the observed ones; moreover, the profiles would indicate a significant contribution at the systemic velocity. Therefore we find it more likely that we are observing a toroidal geometry, an extension of the molecular torus that is present very close to the star, and extends to large enough distances to pinch the waist of the lobes.

We place the observed high ionization species ([O III], [Ne III], etc.) in the inner part of the torus that is being shocked by the fast wind, and the less ionized species ([S II], [O I], etc.) in the external part, expanding at a lower velocity, consistent with the velocity of the CO torus (~ 7 km s^{-1}). That is, the optical emission lines are produced in the inner regions of the torus that is surrounding the central star. This picture is consistent with a very extended torus where the inner region is producing the optical emission lines and the radio continuum emission (Kwok et al. 1985), followed by the warm H_2 component (observed by Smith et al. 2005), that continues to a CO torus (observed by Zweigle et al. 1997), altogether forming a warm dusty torus at 260 K (Smith & Gehrz 2005).

For the case of a quasi-steady state structure, we can estimate the width of the ionized region of the circumstellar configuration. From conservation of mass considerations the relative sizes of the emitting regions can be derived

$$r_2^2 v_2 n_2 \propto r_1^2 v_1 n_1 \,, \tag{4}$$

where r_1 and r_2 refer to the internal and external radii of the emitting region. From the values reported in Table 5 and the linear fit presented in Figure 11 we can adopt $v_1 \sim 30$ km s^{-1} and $v_2 \sim 5$ km s^{-1} as the inner and outer expanding velocities and $n_1 \sim 10^{6.7}$ and $n_2 \sim 10^5$ as the densities. We derive $r_2/r_1 \sim 4.5$. Therefore an estimate of the size of the nuclear emitting region can be determined, which corresponds to $r_2 \approx 490$ AU and therefore to $r_1 \approx 110$ AU.

On the other hand, the small scale of the emitting region ($\sim$ 490 AU, allows us to propose that observable changes in the kinematical behavior of the optical forbidden lines might take place in timescales of the order of ~ 40 years.

3.8. *Abundances*

The estimate of the nebular ion abundances is generally carried out by adopting a mean value for density and temperature and then calculating the line emissivities for all species. This approximation is reasonable in most cases where all diagnostics for each ion agree within their uncertainty. By contrast, in M 2-9 we find a clear density gradient with distance from the central star. Thus, the ionic abundances were calculated here by adopting a varying density through each emission region while the temperature is kept constant at 10^4 K. In this approximation the density diagnostic has been used for each available ion. The calculated abundances for each ion are listed in Table 6.

TABLE 6

ABUNDANCES IN THE M 2-9 NUCLEUS, AND COMPARISON TO SOLAR ABUNDANCES

X	X^0/H^+	X^+/H^+	X^{++}/H^+	X^{3+}/H^+	X/H	X/H solar[a]
He	...	1.1(−1)			1.1(−1)	8.5(−2)
N	1.0(−5)	4.1(−5)	2.9(−5)	...	8.0(−5)	8.3(−5)
O	2.5(−6)	2.2(−4)	1.3(−4)	...	3.5(−4)	6.7(−4)
Ne	...	...	2.8(−7)	...	...	
S	...	5.9(−6)	5.8(−6)	...	1.2(−5)	2.1(−5)
Ar	...	...	7.7(−7)	...		
Fe	...	5.4(−7)	6.1(−6)	2.6(−6)	9.2(−6)	3.2(−5)
Ni	...	1.8(−8)	4.2(−7)	1.4(−7)	5.8(−7)	

[a]From Grevesse & Sauval (1998).

The abundances of O^0 and N^0 were computed including the contributions of continuum fluorescence from the model of Bautista (1999). To compute the abundances of Ni III and Ni IV we adopted the models of Bautista (2001) and Meléndez & Bautista (2005), respectively.

The comparison with solar abundances yields $N/O_{\rm M\ 2-9} > N/O_{\odot}$; this value is common for this type of objects since the alpha mechanism is transforming C into N. Most of the abundances presented in Table 6 are in reasonable agreement with solar abundance values, with the exception of Fe and Ni. The low abundance of these two elements can be explained by depletion into dust (Georgiev at al. 2006).

4. M 1-91

The extreme bipolar planetary nebula M 1-91 (also known as M 4-15, He 2-437 and PN G061.3+03.6) is morphologically very similar to M 2-9. In fact is is even more extreme in its aspect ratio (3.6:1). It is among the most collimated PNe known. Although very similar to M 2-9, its surface brightness is lower and thus has been less extensively studied. A striking difference is that the knots in M 1-91 are point-symmetric, not plane-symmetric like those near the center in M 2-9 (Figure 12).

From deep images it is found that it has a size of $45 \times 4.6''$ (Machado et al. 1996). Carsenty & Solf

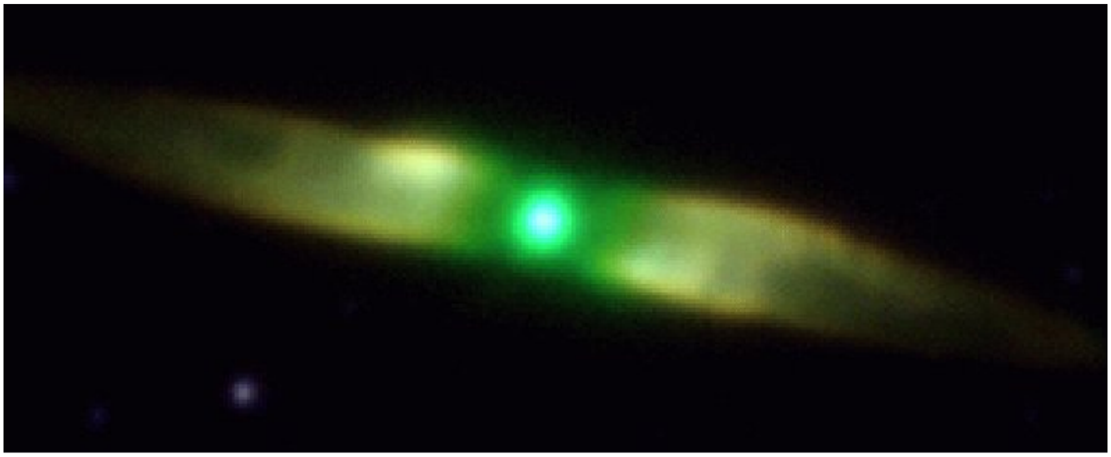

Fig. 12. Image of the planetary nebula M 1-91 (from Manchado et al. 1996). The size is $45 \times 4.6''$. Our slit covered the central $2''$ along the major axis.

(1983) estimate that the inclination angle between the bipolar axis and the plane of the sky is about 15°. M 1-91 is not only morphologically very similar to M 2-9, but its nuclear spectrum is also quite analogous. It is smaller in size and considerably fainter. Guerrero et al. (2000) detect H_2 only marginally in the lobes of the nebula.

Trammell et al. (1996) report that the lobes are significantly polarized in Hα. However the high [O III] $\lambda\lambda$ 4959,5007/4363 ratio (~ 89 is the eastern lobe, ~ 67 in the western lobe) compared to the one found in the nucleus (~ 8), indicates that part of the [O III] emission in the lobes is intrinsic and not due to dust scattered from the nucleus (Goodrich 1991).

Calvet & Cohen (1978) estimate a distance of 3.1 kpc for this object, while Cahn & Kaler (1971) and Maciel (1984) estimate a distance to the planetary nebula M 1-91, of 7.79 and 7.0 kpc, respectively; the methods used to determine these values are valid only for optically thin planetary nebulae. As will be discussed later we can conclude that the nucleus of M 1-91 is optically thick, which is another characteristic in common with M 2-9. Rodríguez, Corradi, & Mampaso (2001) adopt a distance for M 1-91 of 7.8 kpc that implies a height above the galactic plane of $z = 440 - 490$ pc, which is still rather high compared to the mean distance to the galactic plane of bipolar planetary nebulae of $<z> = 130$ pc (Corradi & Schwartz 1995); therefore, it is possible that the distance to M 1-91 has been overestimated. There are two ways to determine an approximate distance to this object: (a) by assuming that it has the same physical size as M 2-9, in which case it would be 2.7 times farther away than M 2-9, that is at 1.7 kpc, and (b) by assuming that its height above the galactic plane is 130 pc (the mean value for bipolar PNe), in which case this would correspond to 2.1 kpc. We will adopt a distance of 1.9 kpc for this object.

4.1. *Nucleus of M 1-91*

The spectrum of the core of M 1-91 closely resembles that of the M 2-9 core (Calvet & Cohen 1978) and Hα emission line also shows extended wings (Goodrich 1991). Also like M 2-9, it shows weak [S II] 6717, 6731 and a high [O III] 4363/5007 ratio. The lines of [Fe II] are also seen in M 1-91, although they are relatively weaker than in M 2-9, with somewhat weaker [O III] and iron lines, and stronger [O I] and He I lines.

Rodríguez et al. (2001) estimated densities in the nucleus of M 1-91 to be in the range of $10^{3.3}$ to $10^{6.3}$ cm^{-3} depending on the ion under consideration. They propose that the range in densities indicates that some phenomenon of mass loss or mass motion is taking place in the nucleus.

In contrast to M 2-9 and of most young PNe, the nucleus of M 1-91 does not show a molecular component. Josselin et al. (2000) do not detect CO. The absence of an intense molecular component could be due to a hotter central star in M 1-91.

The radio continuum images only show a compact core, which coincides with the optical stellar core (Lee, Lim, & Kwok 2007). Along the axis they resolve the source to be from 34 to 77 mas, depending on the frequency. The spectral index is of 0.7 which is compatible with an isothermal stellar wind with a constant expansion velocity. Lee et al. (2007) for an isotropic mass loss, derive a mass loss rate of $\dot{M} \sim 9 \times 10^{-5}\ M_\odot$ yr^{-1}. However, they revise this value by proposing that this source is elongated pos-

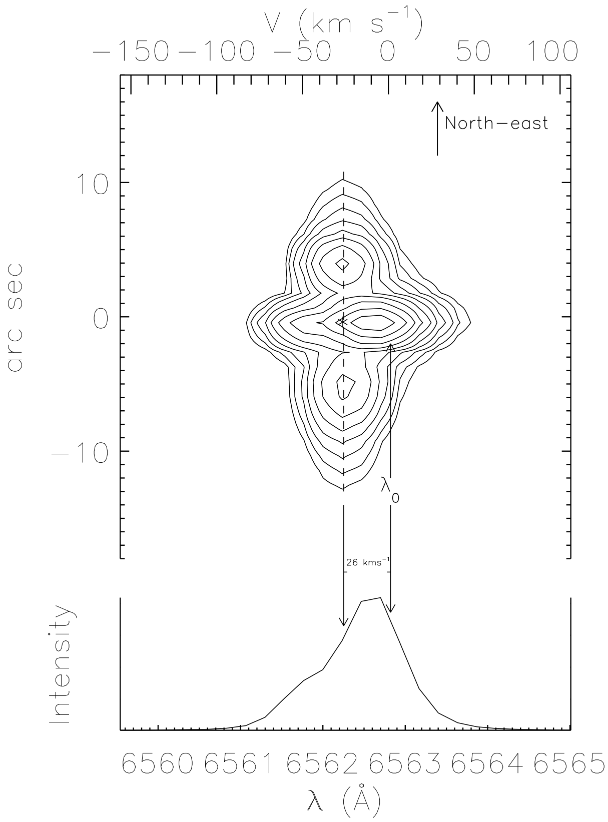

Fig. 13. Determination of the systemic velocity of M 1-91. The dashed line joins both condensations and from it we derive the velocity at the nucleus. The velocity difference is –26 km s^{-1} for the systemic velocity, which corresponds to a heliocentric velocity of -10 ± 5 km s^{-1}.

sibly by collimated winds; in this case it corresponds to $\dot{M} \sim 10^{-6}$ $M_\odot$ yr^{-1}. The mass loss rate derived is at least an order of magnitude higher than expected, which they take as an indication that the object is a symbiotic star. They suggest that the radio core represents a collimated outflow responsible for shaping the bipolar morphology of the nebula.

4.2. *Systemic velocity*

Our slit was located along the major axis, and covered most of the nebula. Also in this case, no significant continuum was measured nor any absorption lines were detected in the spectrum of the nucleus of M 1-91; therefore the systemic velocity determination was carried out under the assumption that the nucleus has the same velocity as the lobes.

Figure 13 shows isocontours on the position-velocity diagram of the long slit echelle spectrum at Hα. Here a very bright central region with a double peaked profile is seen, as well as the eastern and western lobes. The arrows indicate the laboratory wavelength of Hα, (λ_0) and the position of the central part of the nebula. The difference in velocity of the arrows is $\sim -26 \pm 5$ km s^{-1}. Correcting for the earth's motion (+16.5 km s^{-1}) it is found that the heliocentric velocity of the M 1-91 system is -10 ± 5 km s^{-1} and the $V_{\rm LSR} = +9 \pm 5$ km s^{-1}. In the following sections all the discussions of velocities are referred to the systemic velocity of the nebula.

4.3. *Spectrum description*

Motivated by the similarity of their spectra the same type of study as performed for M 2-9 and described in § 3.1 was carried out for M 1-91. Unfortunately it is significantly fainter, and thus it was not possible to derive as much information as for M 2-9. The following results are based on our spectral observations of the nuclear zone. Details of the observations and reductions have been given in § 2.

As in the case of M 2-9, the nucleus of M 1-91 shows a faint continuum without absorption lines; however the number of emission lines is more limited. The blue spectrum from 4150 to 6850 is presented in Figure 14. The emission spectrum shows permitted lines (H I, He I, N I, N II, O I, O II, Ne I, Si I, Fe I and Fe II) and forbidden lines ([N II], [O I], [O II], [O III], [Ne III], [Ar III], [S II], [S III], [Fe II], [Fe III] and [Fe IV]). It was also useful to resort to the code EMILI (Sharpee et al. 2003) to identify the faint lines. The code was used for a set of different temperatures (9000 to 11000) and densities (10^4 to $10^{6.5}$ cm^{-3}). The profiles of the Balmer lines and the [O III] 5007, 4959 lines show different unresolved regions. The M 2-9 and M 1-91 spectra are similar, as far as the signal-to-noise ratio allowed such a comparison. Practically all the M 2-9 emission lines stronger than $I_\lambda/I_{H\beta} > 0.05$ are present in M 1-91.

In Table 7 the observed spectral lines are listed: Columns (1) and (2) present the laboratory and observed wavelength of the identified lines; Column (3) shows the extinction corrected intensities relative to Hβ (the details about the extinction law are given in § 4.5); Column (4) lists the FWHI (not corrected for instrumental broadening); and in Column (5) the line identification is given.

4.4. *Balmer and [O III] profiles*

Analogously to the case of M 2-9 the Balmer and [O III] 5007 and 4959 line profiles show several components. In the Balmer series it can be noticed that Hα shows two well separated components and this separation is less defined with increasing upper level.

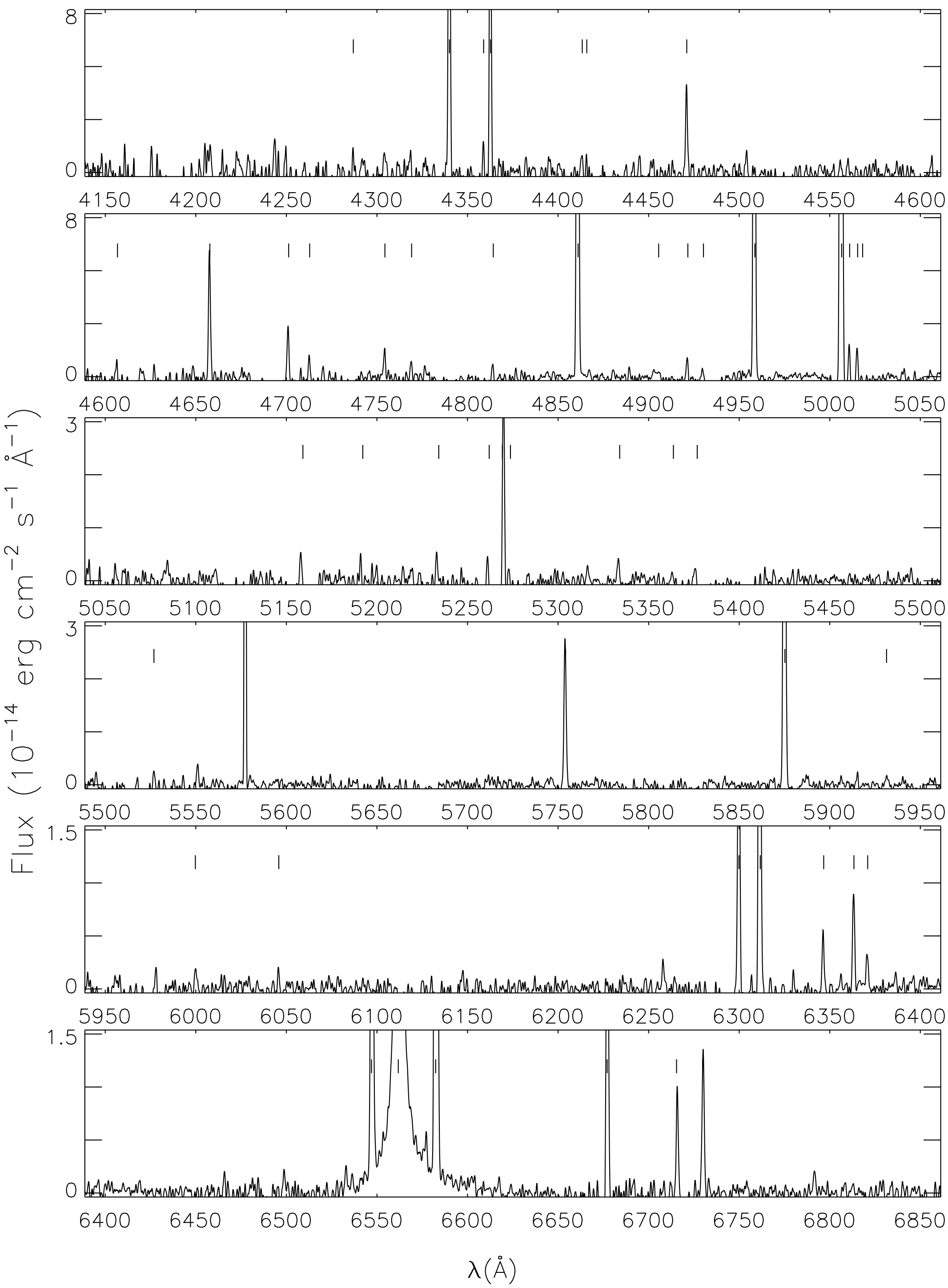

Fig. 14. Blue spectrum of the nucleus of M 1-91. The vertical scale has been expanded to show the faint lines (note that the expansion is different in each panel). The identified lines are marked.

Our M 1-91 spectrum reaches only wavelengths of 6800 Å, and therefore it was not possible to compare the observed Paschen profiles as was the case for M 2-9. In the case of the [O III] lines, the two components are not so well separated as in the hydrogen case, but it can be appreciated that the [O III] 5007 and 4959 lines have two components, while [O III] 4363 has a single component. Also, in hydrogen the

TABLE 7

EMISSION LINES IN THE NUCLEUS OF M 1-91

λ_0	$\lambda_{\rm obs}$	$I_\lambda/I_{H\beta}$[a] ext corrected	FWHM Å	Identification	λ_0	$\lambda_{\rm obs}$	$I_\lambda/I_{H\beta}$[a] ext corrected	FWHM Å	Identification
3721.94	3721.48	0.047	0.5	H14	5158.78	5158.26	0.027	2.0	[Fe II]19F
3726.03	3725.68	0.193	0.6	[O II]	5191.80	5190.99	0.012	0.9	O I bl
3728.81	3728.33	0.092	0.5	[O II]	5191.82				[Ar III]3F bl
3734.37	3733.96	0.193	1.2	H13	5233.45				O II bl
3750.15	3749.70	0.130	1.7	H12	5233.76	5232.95	0.012	1.0	[Fe IV]F bl
3797.90	3797.37	0.095	1.2	H10	5233.70				N I bl
3869.04	3868.19	0.459	0.8	[Ne III]1F	5234.03				Ne I bl
3889.05	3888.41	0.281	1.3	H8	5261.62	5261.12	0.021	1.1	[Fe II]19F
3967.79	3967.11	0.148	1.3	[Ne III]1F	5270.40	5269.92	0.092	1.1	[Fe III]
3970.07	3969.56	0.193	0.9	Hϵ	5273.35	5272.51	0.003	1.0	[Fe II]18F
4101.73	4101.20	0.311	0.9	Hδ	5333.65	5333.21	0.013	1.6	[Fe II]19F
4287.39	4286.85	0.009	0.7	[Fe II]7F	5363.80	5362.91	0.009	2.1	O II
4340.46	4339.90	0.459	0.9	Hγ	5376.45	5375.90	0.015	1.8	[Fe II]19F
4359.33	4358.79	0.011	0.7	[Fe II]7F	5527.34	5526.81	0.003	1.1	[Fe II]17F bl
4363.21	4362.58	0.361	0.8	[O III]3F	5527.57				Fe II bl
4413.78	4413.04	0.047	1.2	[Fe II]7F	5754.64	5753.85	0.061	1.3	[N II]3F
4416.27	4415.79	0.006	0.7	[Fe II]6F	5875.66	5874.95	0.308	1.2	He I
4471.50	4470.90	0.089	1.0	He I	5931.89				Si I bl
4607.03	4606.11	0.025	1.0	[Fe III]3F	5932.35	5931.49	0.008	2.1	N II bl
4658.05	4657.53	0.132	1.1	[Fe III]3F	5932.20				Si I bl
4701.53	4700.90	0.061	1.0	[Fe III]3F	6000.55	5999.94	0.006	1.5	Fe I bl
4713.22	4712.56	0.027	0.7	He I	6000.93				Ne I bl
4754.69	4754.26	0.030	0.9	[Fe III]3F	6046.39	6045.58	0.005	0.8	O I
4769.43	4768.87	0.022	1.2	[Fe III]3F	6300.30	6299.80	0.068	1.3	[O I]1F
4814.51	4813.78	0.022	1.2	O II bl	6312.10	6311.31	0.141	1.2	[S III]
4814.52				[Fe II]20F bl	6347.11	6346.31	0.012	1.1	Si II(2)
4861.32	4860.89	1.000	1.0	Hβ	6363.78	6363.17	0.021	1.2	[O I]1F
4906.00	4905.40	0.003	1.0	O I	6371.37	6370.66	0.008	1.4	Si II(1)
4921.93	4921.22	0.027	1.0	He I	6548.04	6547.30	0.133	1.3	[N II]1F
4930.53	4930.05	0.015	1.8	[Fe III]1F	6562.82	-	7.541		Hα[†]
4958.91	4958.28	0.781	1.0	[O III]1F	6583.46	6582.69	0.441	1.4	[N II]1F
5006.84	5006.20	2.325	1.1	[O III]1F	6678.15	6677.17	0.098	1.3	He I(46)
5011.25	5010.66	0.044	1.1	[Fe III]1F	6716.44	6715.81	0.022	1.2	[S II]2F
5015.68	5015.02	0.033	1.1	He I	6730.81	6730.09	0.031	1.3	[S II]2F
5018.39	5017.49	0.018	1.0	O II					

[a] $I(H\beta)_{\rm obs} = 1.85 \times 10^{-14}$ erg cm^{-2} s^{-1} and $I(H\beta)_{\rm extcorr} = 4.40 \times 10^{-11}$ erg cm^{-2} s^{-1}.
[†] Several components.

red component is stronger than the blue one, in contrast to what is observed in oxygen. These same characteristics are present in the nucleus of M 2-9 (§§ 3.5 and 3.6).

4.5. *Interstellar extinction*

To derive the visual extinction, A_V, the hydrogen emission lines were compared with predictions for Case B recombination using a normal interstellar extinction law.

Assuming a mean density and temperature of 10^6 cm^{-3} and 10^4 K, respectively, and adopting the extinction curve by Cardelli et al. (1989) with $R_V = 3.1$, it is found that while the observed ratio of Hα to Hβ suggests $A_V \sim 5$, all the other Balmer lines are consistent with $A_V = 2.4 \pm 0.3$. The low signal-to-noise ratio in these lines did not allow us to explore the case of an anomalous extinction curve, as in the case of M 2-9. Therefore, a value of $A_V = 2.4 \pm 0.3$ was adopted from the Hγ/Hβ, Hδ/Hβ, and Hϵ/Hβ ratios. This value was used to correct the spectrum for extinction.

As in M 2-9, the Hα line excess can be explained as an effect of high optical depth to levels n=2. In Figure 15 it is shown that the Hα line exhibits two strong components with peaks separated by ~ 50 km s^{-1}. Observing the Hα/Hβ ratio in this same figure, one finds two maxima of this ratio about –30 and +40 km s^{-1} and a minimum centered on the systemic velocity. This ratio in the minimum is consistent with the recombination predictions in Case B (shown in the figure). On the other hand, the highest value of the Hα/Hβ ratio is about 3 times higher than predicted from case B recombination theory.

Comparing the total extinction-corrected Hα and Hβ flux it is found that Hα/Hβ = 7.5. This ratio can

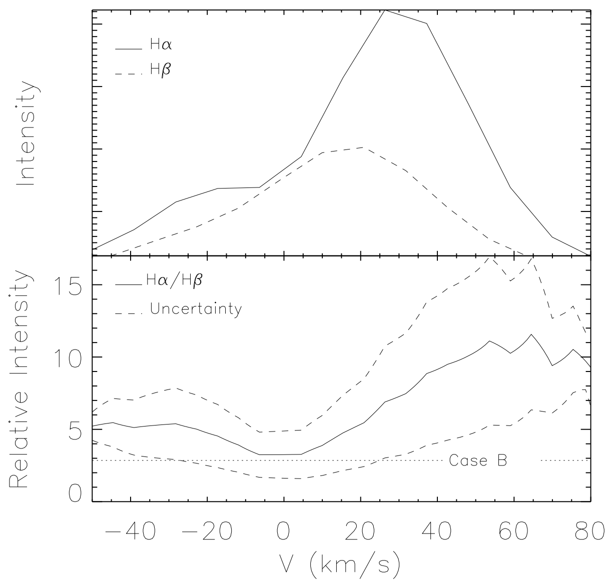

Fig. 15. Hα and Hβ ×3 in M 1-91. The extinction corrected profiles of Hα and Hβ ×3 in M 1-91 are shown in the upper panel. The velocity is given relative to the systemic velocity. In the lower panel the extinction corrected Hα/Hβ ratio is shown. At –30 km s^{-1} and +40 km s^{-1} excesses of the Hα/Hβ ratio can be appreciated. The uncertainties are marked, and the recombination case B value is also included. This diagram is evidence that the Hα line is optically thick.

be reproduced with a case B recombination model with τ(3s - 2p) ~ 4 (as derived from Figure 8).

4.6. *Physical conditions and kinematics of the emitting region*

The forbidden line ratios were used as density diagnostics, applying the NEBULAR tasks of IRAF. The [O II] and [S II] density determinations were obtained from 3729/3726 and 6717/6731 ratios, respectively. The [Fe II], [Fe III], [N II] and [O III] densities were taken from the work by Rodríguez et al. (2001).

The electron density varies from about 2200 cm^{-3} in the region of low ionization ([O II] emitting region) to 3×10^6 cm^{-3} in the [O III] emitting region (Table 8).

All of the forbidden lines show negative velocities, which are indicative of an obscuring disk around the core. The estimate of the velocity for different ions where more than one line is observed is in the -33 to 0 km s^{-1} range relative to the systemic velocity. These velocities show a correlation with the ionization potential, where the more negative velocities correspond to higher potentials, and the positive ones to the neutral species.

TABLE 8

RADIAL VELOCITY AND PHYSICAL CONDITIONS OF DIFFERENT IONS FROM FORBIDDEN LINES IN M 1-91

Ion	Radial velocity[a]		log N_e cm^{-3}	Ionization potential
[N II]	–11.± 3.	(3)	5.15[b]	14.53
[O I]	–0.± 3.	(2)	–	0.
[O II]	–7.± 5.	(2)	3.5	13.62
[O III]	–14.± 2.	(3)	6.4[b]	35.12
[Ne III]	–33.± 7.	(2)	–	40.96
[S II]	–4.± 2.	(2)	3.34[b]	10.36
[S III]	–12.± -	(1)	–	23.33
[Fe II]	–10.± 8.	(11)	6.0[b]	7.87
[Fe III]	–10.±10.	(8)	6.5[b]	16.16
[Fe IV]	–20.± -	(1)	–	30.65
[Ar III]	–22.± -	(1)	–	40.74

[a]Radial velocity and standard deviation. The number of measured lines is shown in parenthesis.

[b]Rodríguez et al. (2001).

There is a correlation between density and velocity in the nuclear spectrum of this object. Again similarly to M 2-9, we find that the behavior of density is not only correlated to the ionization potential but also to the observed radial velocity in each ion. In Figure 16 the relative velocity is plotted for the different species for which we observe more than one line as a function of ionization potential and electron density.

For this object, we also propose that the observed optical emission lines are produced on the front part of the object, while the receding part is obscured by the dense torus. We can only speculate that the ionized region is the inner part of the torus irradiated by the star. We propose that the high density emitting zones are the regions closer to the nucleus, while the neutral or those of lower degree of ionization are at larger distances from the star.

The size of the core emitting region is difficult to estimate. The 1.3 cm radio continuum observations yield a size of 0.077″ (Lee et al. 2007). However, we can conservatively assume that the total diamter of the ionized circumstellar region is 10 times this value, that is, of $\sim 0.8''$. This size is compatible with the $\sim 2''$ size of the direct images available, which are upper limits to the apparent size. At a distance of 1.9 kpc, 0.8″ corresponds to a radius $r_2 \approx 760$ AU. At the mean velocity of 33 km s^{-1} the distance from the star to the outskirts of the ionized circumstellar

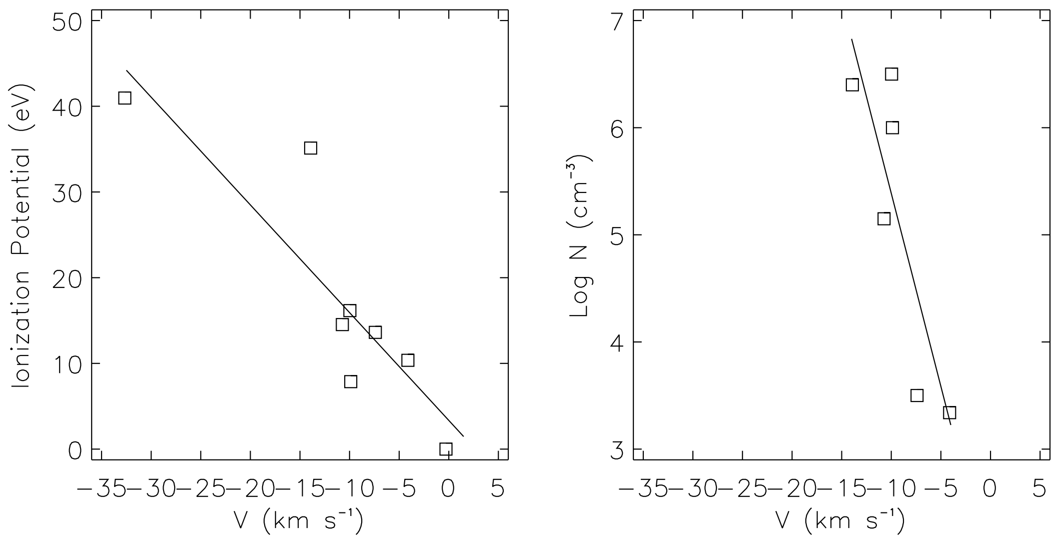

Fig. 16. Behavior of the observed radial velocity with ionization potential and density for M1-91. On the left panel is presented the kinematical behavior of the observed radial velocity with ionization potential in the observed forbidden lines, for which more than one line was measured. On the right panel the electron density behavior with observed radial velocities is displayed. The velocities are given relative to the systemic velocity. The solid line indicates the best fit to the data.

torus can be crossed in 115 years. Then it is conceivable that detectable changes in the kinematical behavior of the system can be expected in a fraction of this time. We suggest that in $\sim$ 30 years there might be significant changes in the velocity distribution of the emitting region.

Alternatively, in the case of quasi-equilibrium, where we assume that constant mass loss is occuring and deceleration of the wind takes place, we can assume that the equation 4 is valid. For the high and low velocities $v_1 \sim 33$ km s^{-1}, and $v_2 \sim 5$ km s^{-1}, and for $n_1 \sim 10^{6.5}$ cm^{-3}, and $n_2 \sim 10^{3.3}$ cm^{-3}, we can derive $r_2/r_1 \sim 32$. For $r_2 \approx 760$ AU (low ionization region) we obtain $r_1 \approx 50$ AU (high ionization region), which would be the inner region where the fast wind is impinging on the dense torus.

5. SUMMARY AND CONCLUSIONS

For M2-9 from the hydrogen Balmer and Paschen series in the nucleus, it was found that the extinction curve has unusual characteristics, different from those of a gas under the action of a strong radiation field. This curve is described by $R_V = 5.0$, $A_V = 2.7$ and explains the discrepancies reported in the literature. The double peak found in the profiles of the Balmer lines had been previously explained by accretion discs like those found in symbiotic stars. According to those models the localized condensations in the disc produces the bright peak in the profile. As the hot spot rotates about of the star, the bright peak in the profile is blue and red shifted. In this work, the possibility that a fast moving hot spot in an accretion disc produces the asymmetry found in these profiles is not favored; this is based on observations of this object carried out at different epochs, only for the purpose of monitoring the profile morphology. It was found that in all spectra (including the one reported by Balick 1989) the bright peak is always red shifted and the intensity ratio between both peaks remains unchanged. In this section it was found that the double profile can be associated to optical depth effects. From the Hα/Hβ and Hγ/Hβ line ratios an optical depth of $\tau_{H\alpha} \sim 5$ in the line Hα was estimated. In addition, from the (5007+4959)/4363 [O III] line ratio it was found that there are two different zones in the nuclear regions not spatially resolved, a component of very high density and velocity –20 km s^{-1} and another less dense with velocity of –45 km s^{-1}. Here it is proposed that the denser component is associated to the circumstellar torus, while the less dense component corresponds to the collimated structure seen in the [O III] 5007 images obtained with HST by Balick et al. (1997). The forbidden emission lines in the core present negative velocities (including [O III] that has a complex profile); that is, we are only observing the approaching side of the core, and presumably there is obscuring material that does not allow us to see the receding part. From the [S II] and [N II] narrow filter HST observations it was found that in these ions the region has an extended morphology in the equatorial direction. It is here proposed that this extended region is the one that emits with these peculiar characteristics. The upper limit to the size of the ionized region is that of the [S II] emission region in the HST image ($\sim 1.5''$ in diameter) which at a distance of 650 pc corresponds to 490 AU in radius. We can estimate that the more internal emission zones (for example [O III]) are located at about 170 AU from the exciting star. If the assumptions in this work are valid, the extended emitting zone located in the direction of the equator is composed of expanding material. We propose that the emission lines are produced in an inner extension of the molecular torus located very close to the star, and extending to large enough distances to pinch the waist of the lobes. In our scheme the optical emission lines are produced in the inner regions of the torus that is surrounding the central star. The high ionization species are located in the innermost region where the gas is being shocked by the fast wind, and the less ionized species in the external part. The expansion rate of the neutral species is consistent with the low velocity of the CO torus. This scenario corresponds to a very extended torus where the inner region is producing the optical emission lines and the radio continuum emission (Kwok et al. 1985), followed by a warm H_2 component (Smith et al. 2005), that merges into a CO torus (Zweigle et al. 1997), altogether forming a warm dusty torus at 260 K (Smith & Gehrz 2005). In principle, this scenario is in agreement to the wind interaction models (Mellema 1993; Franco, Tenorio-Tagle, & Bodenheimer 1990) at very close distance to the central star, and is compatible with the radio continuum spectral index that agrees with mass loss from the central star. The size of the circumstellar structure is small and the characteristic times are relatively short (for a structure 490 AU radius the crossing time from the central star outwards at a velocity of 30 km s^{-1} is 80 years, and at the same velocity the distance from the inner border to the outer edge of the ionized region can be reached in 53 years). Thus it would be of interest to monitor the kinematic behavior of the emission lines, for any possible changes in timescales of decades. Furthermore, we suggest that the group of pinched waist planetary nebulae should be investigated to find out if this behavior extends to all of them.

For its part, the core of M1-91 exhibits double peaked Balmer lines profiles. It is proposed that these two components can be explained by large optical depth effects in the hydrogen Balmer lines. From the Hα/Hβ ratio, an optical depth of $\tau \sim 4$ was estimated for the Hα line. For M 1-91 we again find a correlation of the kinematics of the forbidden lines similar to that of M 2-9. We further find a tendency for the atoms with higher ionization potential to correspond to denser zones, and to have higher absolute velocities relative to the nucleus, while those ions of lower ionization potential are less dense and have lower velocities relative to the nucleus. Although there are no observations of a molecular component in M 1-91, we extend our interpretation of M 2-9 to this object by proposing that the ionized region is the inner part of an extended torus that has produced such a bipolar morphology. It is estimated that the radius of the [S II] circumstellar emitting region is $\sim$ 760 AU (assuming a distance to the nebula of 1.9 kpc). On the one hand, by assuming a quasi equilibrium mass flow in this region it is found that the distance from the nucleus to the inner edge of the circumstellar torus (corresponding to the [Ne III], [O III] emitting region) is $\sim$ 50 AU.

In conclusion, as has been noted by many authors, M 2-9 and M 1-91 indeed share many characteristics: very young emission nebulae of extremely collimated morphology, undisclosed characteristics of the exciting star(s), very dusty circumstellar regions, very high density cores that give rise to Hα Raman scattering, complex Hα profiles, similar nuclear spectra with permitted and emission lines that show the same kinematic behavior, and expanding circumstellar tori that presumably extend to produce the pinched waist. The sizes of the circumstellar structures are small and the characteristic times are relatively short, such that it would be of interest to monitor the kinematic behavior of the emission lines for possible changes that could presumably take place in timescales of decades. Furthermore, we suggest that the cores of the group of pinched waist planetary nebulae should be studied spectroscopically to find out if the emission line kinematics extends to all of them, and if that is the case, to monitor their behavior in time.

ST-P and AA have received support from DGAPA-IN112708, Conacyt-60967 and Conacyt-46904 grants. We are grateful for the comments from the referee and many fruitful discussions with L. N. Georgiev.

Note added in proof: R. Corradi (private communication) kindly informed us that the distance of 650 pc assigned to M 2-9 (Schwarz et al. 1997) is not correct, and that it should be 1.3 kpc. This value, if confirmed, would modify our size and time estimates by a factor of 2.

REFERENCES

Allen, D. A., & Swings, J. P. 1972, ApJ, 174, 583

Arrieta, A., & Torres-Peimbert, S. 2000, in ASP Conf. Ser. 199, Asymmetrical Planetary Nebulae II: From Origins to Microstructures, ed. J. H. Kastner, N. Soker, & S. Rappaport (San Francisco: ASP), 255

_________. 2003, ApJS, 147, 97

Aspin, C., McLean, I. S., & Smith, M. G. 1988, A&A, 196, 227

Balick, B. 1989, AJ, 97, 476

_________. 1999, in ASP Conf. Ser. 188, Optical and Infrared Spectroscopy of Circumstellar Matter, ed. E. Guenther, B. Stecklum, & S. Klose (San Francisco: ASP), 241

Balick, B., Icke V., & Mellema, G., 1997, STScI Press Release PR97-38

Bachiller, R., Martín-Pintado, J., & Bujarrabal, V. 1990, A&A, 227, 188

Bautista, M. A. 1999, A&AS, 137, 529

_________. 2001, A&A, 365, 268

_________. 2004, A&A, 420, 763

Bautista, M. A., Kallman, T. R., Angelini, L., Liedahl, D. A., & Smits, D. P. 1998, ApJ, 509, 848

Bautista, M. A., Pogge, R. W., & DePoy, D. L. 1995, ApJ, 452, 685

Bautista, M. A., & Pradhan, A. K. 1998, RevMexAA (SC), 7, 163

Cahn, J. H., & Kaler, J. B. 1971, ApJS, 22, 319

Calvet, N., & Cohen, M. 1978, MNRAS, 182, 687

Cardelli, J. A., Clayton, G. C., & Mathis, J. S. 1989, ApJ, 345, 245

Carsenty, U., & Solf, J. 1983, IAU Symp. 103, Planetary Nebulae, ed. D. R. Flower (Dordrecht: Reidel), 510

Corradi, R. L. M., & Schwarz, H. E. 1995, A&A, 293, 871

Doyle, S., Balick, B., Corradi, R. L. M., & Schwarz, H. E. 2000, AJ, 119, 1339

Franco, J., Tenorio-Tagle, G., & Bodenheimer, P. 1990, ApJ, 349, 126

Georgiev, L. N., Richer, M. G., Arrieta, A., & Zhekov, S. A. 2006, ApJ, 639, 185

Goodrich, R. W. 1991, ApJ, 366, 163

Grevesse, N., & Sauval, A. J. 1998, Space Sci. Rev., 85, 161

Guerrero, M. A., Villaver, E., Machado, A., García-Lario, P., & Prada, F. 2000, ApJS, 127, 125

Hora, J. L., & Latter, W. B. 1994, ApJ, 437, 281

Josselin, E., Bachiller, R., Manchado, A., & Guerrero, M. A. 2000, A&A, 353, 363

Kim, S., Martin, P. G., & Hendry, P. D. 1994, ApJ, 422, 164

Kohoutek, L., & Surdej, J. 1980, A&A, 85, 161

Kwok, S., Purton, C. R., Matthews, H. E, & Spoelstra, T. A. T. 1985, A&A, 144, 321

Lee, T.-H., Lim, J., & Kwok, S. 2007, ApJ, 665, 341

Livio, M., & Soker, N. 2001, ApJ, 552, 685

Maciel, W. J. 1984, A&AS, 55, 253

Manchado, A., Guerrero, M. A., Stanghellini, L., & Serra-Ricart, M. 1996, The IAC Morphological Catalog of Northern Galactic Planetary Nebulae (La Laguna, España: Instituto de Astrofísica de Canarias)

Mathis, J. S., & Wallenhorst, S. G. 1981, ApJ, 244, 483

Meléndez, M., & Bautista, M. A. 2005, A&A, 436, 1123

Mellema, G. 1993, Ph.D. Thesis, University of Leiden

Osterbrock, D. E. 1989, Astrophysics of Gaseous Nebulae and Active Galactic Nuclei (Mill Valley: Univ. Science Books)

Rodríguez, M., Corradi, R. L. M., & Mampaso, A. 2001, A&A, 377, 1042

Schmidt, G. D., & Cohen, M., 1981, ApJ, 246, 444

Schwarz, H. E., Aspin, C., Corradi, R. L. M., & Reipurth, B. 1997, A&A, 319, 267

Sharpee, B., Williams, R., Baldwin, J. A., & van Hoof, P. A. M. 2003, ApJS, 149, 157

Smith, N., Balick, B., & Gehrz, R. D. 2005, AJ, 130, 853

Smith, N., & Gehrz, R. D. 2005, AJ, 129, 969

Solf, J. 1984, A&A, 139, 296

_________. 2000, A&A, 354, 674

Swings, J. P., & Andrillat, Y. 1979, A&A, 74, 85

Trammell, S. R., Goodrich, R. W., & Dinerstein, H. L. 1995, ApJ, 453, 761

Trammell, S. R., Kartje, J. F., Hill, J. G., & Dinerstein, H. L. 1996, in ASP Conf. Ser. 97, Polarimetry of the Interstellar Medium, ed. W. G. Roberge & C. B. Doug (San Francisco: ASP), 217

Walsh, J. R. 1981, MNRAS, 194, 903

Zweigle, J., Neri, R., Bachiller, R., Bujarrabal, V., & Grewing, M. 1997, A&A, 324, 624

A. Arrieta: Universidad Iberoamericana, Depto. de Física y Matemáticas, Prol. Paseo de la Reforma 880, Lomas de Santa Fe, México D. F. 01219, Mexico (anabel.arrieta@uia.mx).

M. Bautista: Department of Physics, Western Michigan University, Kalamazoo, MI 49008, USA.

S. Torres-Peimbert: Instituto de Astronomía, Universidad Nacional Autónoma de México, Apdo. Postal 70-264, México, D. F. 04510, Mexico (silvia@astroscu.unam.mx).

Revista Mexicana de Astronomía y Astrofísica, **46**, 245–251 (2010)

SPECKLE INTERFEROMETRY AT THE OBSERVATORIO ASTRONÓMICO NACIONAL. II

V. G. Orlov, V. V. Voitsekhovich, J. L. Rivera, C. A. Guerrero, and F. Ortiz

Instituto de Astronomía, Universidad Nacional Autónoma de México, Mexico

Received 2010 March 27; accepted 2010 May 27

RESUMEN

Presentamos mediciones interferométricas de motas para estrellas binarias, obtenidas en junio de 2009 en el telescopio de 1.5 m del Observatorio Astronómico Nacional en San Pedro Mártir (México). Nuestros datos comprenden 189 mediciones de ángulos de posición y separaciones de 144 sistemas. Las separaciones angulares medidas abarcan desde $0''.16$ hasta $3''.64$. La magnitud máxima de la componente más brillante es de 10.96. El error medio en las separaciones es de $0''.02$ y en los ángulos de posición de 1.5°. Algunos ángulos de posición se determinaron con la ambigüedad usual de 180°.

ABSTRACT

We present speckle interferometric measurements of binary stars made during June of 2009 with the 1.5 m telescope of the Observatorio Astronómico Nacional at SPM (Mexico). The data contain 189 position angle and separation measures of 144 systems. The measured angular separations range from $0''.16$ to $3''.64$. The maximum magnitude of the brighter component is 10.96. The mean error in separation is $0''.02$ and in the position angles 1.5°. Some of the position angles were determined with the usual 180° ambiguity.

Key Words: binaries: visual — stars: fundamental parameters — techniques: high angular resolution — techniques: interferometric

1. INTRODUCTION

In our previous paper (Orlov et al. 2009) we reported results of speckle observations of binary stars obtained at the 1 m telescope of Observatorio Astronómico Nacional at Tonanzintla (OAN-Tonanzintla), Mexico. The telescope is located at a site with moderate seeing. As it is well known the resolution of speckle interferometry (SI) does not depend on seeing. However, the limiting magnitude of stars which can be resolved by SI does depend on seeing. The Instituto de Astronomía has a total of four telescopes. Three of them are situated at Observatorio Astronómico Nacional at San Pedro Mártir, Mexico (OAN-SPM). The OAN-SPM is located in one of the best astronomical sites (Ávila, Cruz-González, & Tapia 2003). Included at the SPM site are 3 telescopes: 84 cm, 1.5 m and 2.1 m.

In this paper we present results from four observing nights in June 2009. The observations were performed at the 1.5 m telescope of the OAN-SPM.

2. OBSERVATIONS

The observations were performed at the 1.5 m telescope of the Observatorio Astronómico Nacional which is located at the San Pedro Mártir (Mexico). For these observations we used the DRAGON equipment (Voitsekhovich et al. 2005), which was slightly modified to be able to record speckle interferograms (Orlov et al. 2007). During the observations we had good seeing conditions. We estimated that the seeing was between 0.7 to 1 arcsec. Unfortunately, aberrations introduced by the telescope had a larger effect. It can be clearly seen on a centered image of one of the stars (Figure 1). Aberrations of the 1.5 m mirror cannot be corrected because the telescope is not equipped with an active optics system.

After calibration we determine the Pixel Scale = $0.024''$/px and detector orientation. For calibration we used 40 wide pairs with very slow orbital motions and some of them with known orbital parameters.

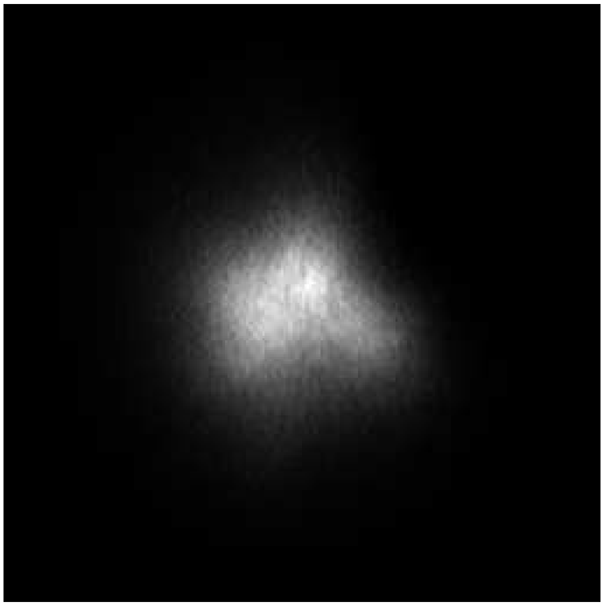

Fig. 1. The centered image of the binary star COU 1581. It was obtained by averaging 700 previously centered speckle interferograms. The window is $6''.3 \times 6''.3$.

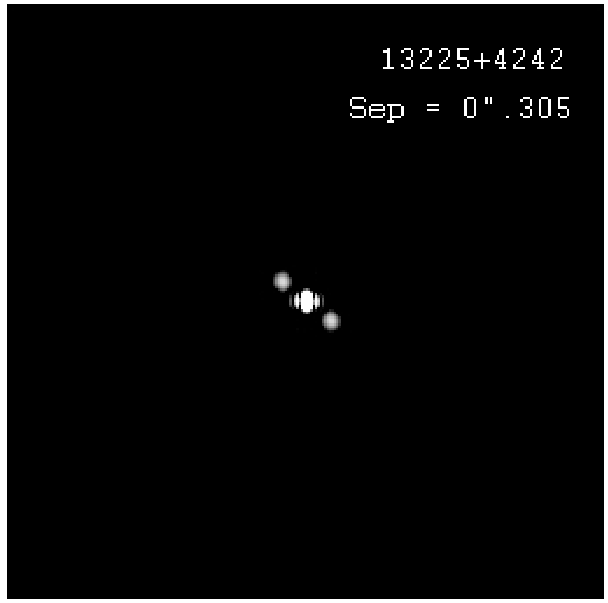

Fig. 2. Reconstructed ACF of the binary star COU 1581. Separation $= 0''.305$.

During four nights of observations we made 189 measurements of 144 pairs. Most of observed binaries have separations less than $1''$. Table 1 shows how these 144 pairs are distributed according to their separations.

3. DATA PROCESSING AND RESULTS

For each binary star, a typical observing procedure involved the accumulation of one set of 700 short exposure images on hard disk. One short exposure image consists of a two-dimensional 582×584 array of 8-bit numbers. The volume of one set on the hard disk is 226 MB. The data were processed by the algorithm which was explained in detail by Tokovinin, Mason, & Hartkopf (2010). This algorithm permits derivation of the binary star parameters without using the reference star. The resulting autocorrelation function (ACF) of one binary star COU 1581 calculated by this algorithm is shown in Figure 2. The position of the secondary is calculated as the center of weight of values of the ACF in a region around the maximum value.

TABLE 1

DISTRIBUTION OF PAIRS BY THEIR SEPARATIONS

$> 1''.5$	$1''.5 - 1''$	$1'' - 0''.5$	$0''.5 - 0''.25$	$< 0''.25$
18	23	38	57	12

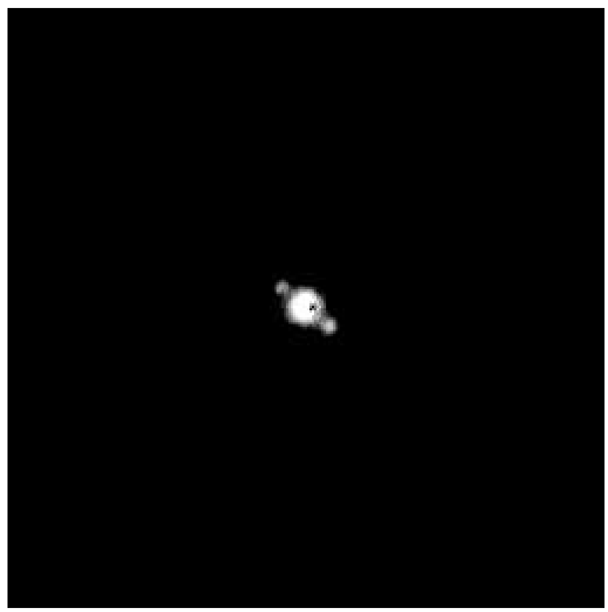

Fig. 3. Result of self-calibrating shift-and-add technique for the binary star COU 1581.

As is well known, the ACF has no information about the Fourier phase of the image; therefore, the position angle is determined only modulo 180°. To avoid this inconvenience we also used Christou's self-calibrating shift-and-add technique (Christou et al. 1986). Figure 3 shows an image which was calculated using this technique. We have to admit that the

TABLE 2

SPECKLE MEASUREMENTS ON THE 1.5 M TELESCOPE

WDS ($\alpha, \delta J2000.0$)	Disc. Name	Date Besselian	P.A (deg)	Sep. (arcsec)	P.A. Orb. (deg)	Sep. Orb. (arcsec)	Reference
12154+4008	A 1999	2009.4326	62.2	0.29	40.9	0.53	Seymour et al. 2002
12182+2718	HDS1733	2009.4410	241.9	0.32			
12244+4305	STT 250	2009.4327	351.2	0.33			
12306+3431	HDS1759	2009.4327	203.3	0.27			
12328+2301	AG 179	2009.4327	142.0	0.99			
12510+3129	HDS1804	2009.4300	256.8	0.75			
12510+3129	HDS1804	2009.4327	257.2	0.75			
12575+2457	COU 397	2009.4300	60.6	0.68			
12575+2457	COU 397	2009.4410	60.6	0.68			
12575+2457	COU 397	2009.4327	61.1	0.69			
13004+3545	HU 1141	2009.4327	343.5	0.49			
13037+2339	STF1714	2009.4410	307.2	3.12			
13037+2339	STF1714	2009.4327	307.2	3.13			
13063+2044	HU 739	2009.4327	204.1	1.37	207.3	1.39	Seymour et al. 2002
13063+2044	HU 739	2009.4410	204.1	1.37			
13091+2127	HU 572	2009.4411	344.6	0.46	10.1	0.35	Zulevic 1969
					105.5	0.52	Baize 1981
					50.7	0.35	Baize 1986
13128+4030	A 1606	2009.4328	195.9	1.29			
13128+4030	A 1606	2009.4411	196.5	1.30			
13221+3952	HDS1876	2009.4300	88.9	0.26			
13225+4242	COU1581	2009.4411	157.5	0.33			
13266+3235	COU 787	2009.4300	147.4	0.34			
13280+3235	A 1856	2009.4411	343.5	1.08			
13280+3235	A 1856	2009.4328	343.7	1.07			
13305+3430	A 1857	2009.4301	340.9	0.48			
13305+3430	A 1857	2009.4328	341.4	0.47			
13348+4242	HDS1908	2009.4411	24.1	0.48			
13387+3823	COU1429AB	2009.4411	64.0	0.66			
13387+3823	COU1429AB	2009.4301	64.4	0.66			
13465+1545	A 2063	2009.4411	136.9	0.23			
13465+1545	A 2063	2009.4328	136.9	0.19			
13465+1545	A 2063	2009.4301	137.4	0.25			
13509+3555	COU1132	2009.4301	147.5	0.79			
13509+4422	A 1613AB	2009.4328	259.9	3.08			
13571+3426	BU 937	2009.4301	135.0	1.04			
14082+3645	STT 276AB	2009.4301	206.9	0.44			
14087+3341	HU 742	2009.4329	354.0	0.24	67.0	0.29	Popovic 1972
14087+3341	HU 742	2009.4412	355.6	0.25			
14109+1513	HDS1989Aa,Ab	2009.4412	358.7	0.43			
14109+2412	HDS1988	2009.4329	150.2	3.29			
14113+3013	COU 605	2009.4412	163.5	0.26			
14113+3013	COU 605	2009.4329	164.4	0.27			
14124+2843	STT 277AB	2009.4301	64.3	0.19			
14164+2539	HDS2006	2009.4412	249.2	0.70			
14184+3412	HU 901	2009.4301	32.6	0.61			
14276+2037	HO 542	2009.4329	213.6	0.98			
14278+3257	STF1848	2009.4302	356.2	3.09			
14278+3257	STF1848	2009.4412	356.3	3.08			
14295+3612	HU 1268	2009.4412	345.2	0.30	313.0	0.38	Erceg 1975
14436+3745	STF1875	2009.4329	128.5	3.06			
14485+2445	COU 304	2009.4329	300.8	0.46			

TABLE 2 (CONTINUED)

WDS ($\alpha, \delta J2000.0$)	Disc. Name	Date Besselian	P.A (deg)	Sep. (arcsec)	P.A. Orb. (deg)	Sep. Orb. (arcsec)	Reference
15002+2129	HU 907	2009.4413	277.3	0.24			
15002+2129	HU 907	2009.4329	278.0	0.21			
15049+3428	STF1908AB	2009.4413	151.4	1.33			
15075+1541	A 2228	2009.4330	12.2	3.29			
15136+3453	HO 60	2009.4413	68.1	0.18	72.7	0.16	Baize 1993a
15136+3453	HO 60	2009.4330	73.5	0.16	72.7	0.16	Baize 1994
15151+3650	STT 295	2009.4413	150.3	0.30			
15192+4329	A 1630	2009.4330	244.8	0.78			
15208+4242	A 573	2009.4413	171.9	0.71			
15257+2638	STF1941	2009.4330	212.6	1.38			
15271+2355	A 82	2009.4330	351.0	0.83			
15272+4133	COU1443	2009.4413	172.8	0.49			
15307+3810	HU 1163	2009.4413	168.1	0.22	189.1	0.17	Couteau 1990
15307+3810	HU 1163	2009.4330	169.3	0.21	191.9	0.21	Zulevic 1995
					191.9	0.21	Zulevic 1996
					169.4	0.21	Hartkopf et al. 2000
15390+2545	COU 612	2009.4413	177.5	0.29	326.6	0.15	Baize 1992a
					326.6	0.15	Baize 1993b
					176.2	0.26	Docobo & Ling 1998a
					173.2	0.30	Aristidi et al. 1999
15404+2123	HU 579	2009.4414	136.5	0.70			
15498+4431	BU 621	2009.4302	26.4	0.67			
15554+2932	HO 399	2009.4302	117.3	3.59			
15574+4140	STF1991AB	2009.4331	195.5	3.02			
15574+4140	STF1991AB	2009.4414	195.8	3.01			
15574+4140	STF1991AB	2009.4302	196.4	2.99			
16115+1507	A 1799	2009.4414	117.6	0.76			
16128+3922	STF2028	2009.4302	144.7	0.39	140.8	0.33	Alzner 2001
16156+1944	HU 480	2009.4331	261.9	1.61			
16161+2936	A 348	2009.4302	149.2	1.04			
16192+4140	STT 309	2009.4302	307.4	0.28	306.6	0.28	Seymour et al. 2002
16199+2341	COU 108	2009.4414	255.1	0.63			
16199+2341	COU 108	2009.4331	255.9	0.62			
16248+3925	HU 1276	2009.4302	270.3	0.39			
16248+3925	HU 1276	2009.4414	270.4	0.42			
16273+2653	A 226	2009.4331	94.1	1.01			
16273+2653	A 226	2009.4415	94.3	1.02			
16309+3804	STF2059	2009.4303	186.3	0.36			
16326+2314	BU 817	2009.4303	327.9	0.94			
16326+2314	BU 817	2009.4331	328.1	0.94			
16384+3514	COU 985	2009.4415	69.4	0.30	79.4	0.20	Baize 1993c
16384+3514	COU 985	2009.4331	70.1	0.30	82.8	0.21	Docobo & Ling 1998b
					82.8	0.20	Docobo et al. 2000
16412+1714	HDS2366	2009.4331	95.8	0.53			
16422+3753	HDS2372	2009.4303	252.1	0.18			
16422+4112	STF2091	2009.4303	325.9	0.40			
16476+4255	COU1452	2009.4415	103.5	0.26			
16476+4255	COU1452	2009.4332	108.6	0.29			
16539+2547	COU 492	2009.4332	91.9	0.52			
16539+2547	COU 492	2009.4415	91.9	0.52			
17063+2631	A 228	2009.4388	185.7	0.46			
17075+3810	COU1291	2009.4303	301.1	0.28	0.6	0.15	Baize 1993c
					356.3	0.07	Docobo & Ling 1998a
					348.0	0.07	Docobo & Ling 2002

TABLE 2 (CONTINUED)

WDS ($\alpha, \delta J2000.0$)	Disc. Name	Date Besselian	P.A (deg)	Sep. (arcsec)	P.A. Orb. (deg)	Sep. Orb. (arcsec)	Reference
17094+1901	A 2086	2009.4332	204.3	3.14			
17116+3916	HU 1178AB	2009.4332	9.5	0.36			
17116+3916	HU 1178AB	2009.4303	10.4	0.36			
17116+3916	HU 1178AB	2009.4303	10.7	0.36			
17184+3240	BU 628	2009.4303	267.1	0.52	255.4	0.39	Zulevic 1986
17215+2845	KUI 80AB	2009.4388	169.9	0.62			
17221+2310	COU 415	2009.4388	249.3	0.24	174.5	0.27	Baize 1992a
					174.5	0.27	Baize 1993b
17239+3627	STF2162	2009.4304	284.5	1.35			
17250+4306	COU1454	2009.4304	148.0	0.98			
17251+3444	HU 922	2009.4304	225.4	0.21	6.8	0.31	Heintz 1982
17275+1627	A 2184	2009.4388	30.4	1.87			
17377+4250	HDS2489	2009.4304	346.7	0.55			
17377+4250	HDS2489	2009.4332	347.1	0.55			
17412+4139	STF2203	2009.4416	293.7	0.73			
17434+3357	HO 560	2009.4304	263.3	1.32			
17434+3357	HO 560	2009.4416	263.3	1.33			
17434+3357	HO 560	2009.4388	265.2	1.37			
17486+2339	BAR 8	2009.4416	237.8	1.16			
17504+3526*	STF2236	2009.4389	18.9	0.31			
17504+3526*	STF2236	2009.4304	22.6	0.32			
17504+3526	STF2236	2009.4389	97.0	3.39			
17504+3526	STF2236	2009.4304	97.1	3.37			
17506+3932	COU1301	2009.4389	84.3	1.74			
17506+3932	COU1301	2009.4416	85.0	1.74			
17541+2949	AC 9	2009.4389	240.6	1.09			
17577+2815	HO 424	2009.4389	203.0	1.42			
17584+3524	COU1000	2009.4416	153.3	0.89			
17591+3228	HU 1185	2009.4416	138.5	0.36	148.4	0.27	Heintz 1975
18017+4011	STF2267	2009.4304	271.1	0.55			
18017+4011	STF2267	2009.4389	271.7	0.56			
18025+4414	BU 1127AB	2009.4332	52.9	0.73	65.4	1.15	Popovic 1970
					62.6	1.02	Popovic & Pavlovic 1995a
					62.6	1.02	Popovic & Pavlovic 1995b
18033+3921	STF2275	2009.4416	297.2	0.27	300.0	0.26	Popovic 1998
					299.9	0.26	Popovic et al. 2000
18063+3824	HU 1186	2009.4304	115.6	0.25	141.3	0.09	Heintz 1965
18063+3824	HU 1186	2009.4416	123.3	0.30	119.0	0.22	Baize 1992b
					121.1	0.20	Heintz 1995
18126+3836	BU 1091	2009.4305	320.7	0.72			
18126+3836	BU 1091	2009.4416	320.7	0.72			
18178+4351	A 578 AB	2009.4332	157.2	1.75			
18178+4351	A 578 Aa,Ab	2009.4332	247.0	0.31			
18264+4326	HDS2606	2009.4417	49.3	1.02			
18432+3822	HDS2651	2009.4305	50.8	0.44			
18450+4239	HDS2657	2009.4305	37.1	0.21			
19018+3448	COU1612	2009.4305	318.7	0.82			
19072+4451	A 703	2009.4305	188.4	0.54			
19072+4451	A 703	2009.4390	189.3	0.56			
19089+3404	COU1462	2009.4306	204.7	0.19	225.1	0.62	Mante 1994
					203.0	0.20	Mante 1997
					203.0	0.20	Mante 1999
19122+3215	HU 941	2009.4333	146.1	1.08			
19131+2154	A 153	2009.4306	267.7	0.71			

TABLE 2 (CONTINUED)

WDS ($\alpha, \delta J2000.0$)	Disc. Name	Date Besselian	P.A (deg)	Sep. (arcsec)	P.A. Orb. (deg)	Sep. Orb. (arcsec)	Reference
19214+1948	HO 637	2009.4333	27.6	1.20			
19251+2213	COU 513	2009.4333	2.6	0.25			
19266+3120	HDS2762	2009.4306	214.6	0.35			
19272+1626	HDS2765	2009.4333	177.5	0.36			
19331+3254	HU 948AB	2009.4306	149.9	0.26			
19331+3254	HU 948AB	2009.4333	152.2	0.27			
19350+2947	A 368	2009.4306	153.4	0.50			
19356+4002	A 1400	2009.4390	122.5	0.35	134.3	0.24	Seymour et al. 2002
19358+2316	A 163	2009.4333	20.8	0.23	1.7	0.18	Baize 1981
19466+4346	HDS2810	2009.4390	49.5	0.34			
19532+4238	COU2635	2009.4390	157.5	0.54			
19538+2237	COU 825AB	2009.4334	32.0	1.23			
19575+2018	BU 425AB	2009.4334	239.7	1.35			
19583+2208	AG 244AB	2009.4334	273.2	1.51			
20016+3435	COU1947	2009.4307	88.4	0.27			
20082+2105	J 1168	2009.4334	192.6	0.88			
20109+2237	HDS2877	2009.4334	201.4	0.45			
20157+4339	A 2095AB	2009.4390	155.9	0.26	146.7	0.21	Zulevic 1997
					146.8	0.24	Ling 1999
20157+4339	STF2659AC	2009.4390	314.0	3.03			
20172+2415	HDS2893	2009.4334	168.4	0.31			
20177+4030	HDS2897	2009.4390	269.0	0.33			
20302+2651	WOR 9AB	2009.4334	256.4	0.51			
20333+2727	HDS2935	2009.4334	114.1	0.48			
20477+4204	BU 268	2009.4391	199.3	0.39			
20506+3024	STT 415	2009.4280	232.2	3.68			
20531+2909	STT 417AB	2009.4280	27.7	0.90			
20564+4308	COU2544	2009.4391	160.4	0.32			
20564+4308	COU2544	2009.4280	160.5	0.33			
20582+3510	COU1813	2009.4335	308.9	1.16			
21000+4004	KUI 103AB	2009.4335	356.2	0.42	182.6	0.64	Lippincott 1975
21000+4004	KUI 103AB	2009.4280	357.1	0.43	44.0	0.54	Baize 1989
					44.0	0.54	Baize 1991
					40.5	0.60	Heintz 1994
					32.8	0.31	Docobo & Ling 1994
					336.9	0.23	Soderhjelm 1999
					12.4	0.35	Mante 2000
					12.4	0.43	Pourbaix 2000
21018+3916	STF2746	2009.4391	321.1	1.19			
21089+1748	HU 365	2009.4335	19.9	1.03			
21111+1704	HEI 187	2009.4335	255.7	1.13			
21115+4115	STT 431AB	2009.4391	125.2	2.62			
21115+4115	STT 431AB	2009.4281	125.3	2.61			
21143+4109	STT 432	2009.4391	114.8	1.33			
21161+4101	COU2229	2009.4281	272.1	0.78			
21171+4312	A 401	2009.4391	219.7	0.41			
21328+3904	A 1443	2009.4391	240.4	0.27			
21328+3904	A 1443	2009.4281	240.7	0.25			
21334+3058	COU 732Aa,Ab	2009.4336	264.8	0.49			
21356+3446	COU1481	2009.4281	171.7	0.64			
21363+1627	HDS3076	2009.4336	262.5	0.34			
21380+4153	A 402	2009.4281	45.9	0.85			
21421+4414	A 403	2009.4281	77.7	0.48			

technique doesn't work for weak objects when single photon events are strongly dominant in the speckle image.

Table 2 contains 189 measurements pertaining to 144 binary or multiple stars. The format for presentation of these measurements is not the same as in our previous publication (Orlov et al. 2009). We include three new columns for ephemerides of binaries with known orbital elements. Column 1 contains the epoch-2000 coordinates in the format used in the Washington Double Star (WDS) Catalog (Worley & Douglass 1997). The second column gives the name of the star or discoverer designation. The third column gives the epoch of the observation in fractional Besselian year. The two following columns contain the measured position angles θ given in degrees and angular distances ρ in arcseconds. The last three columns show ephemerides calculated for the date of observation and references to publications in which orbital elements can be found. As one can see, some orbits give very discrepant position of the secondary.

4. CONCLUSION

A program of speckle observations has been started at the Observatorio Astronómico Nacional telescopes, with the goal of obtaining astrometric data of double stars. This study started with well-known binaries from the WDS catalogue. One hundred seventy five position angle and separation measures for one hundred sixty three binaries have been presented, a subset of which has been used to determine measurement precision. We only present here the cases where the binary was clearly resolved. The results on binaries which demand more detailed analysis will be reported in subsequent publications.

The speckle interferometry program at the OAN telescopes is supported by the Direccion General de Asuntos del Personal Académico (Universidad Nacional Autónoma de México, Mexico) under projects IN104910 and IN113308 (PAPIIT).

REFERENCES

Alzner, A. 2001, IAUDS, Inf. Circ. 144
Aristidi, E., et al. 1999, A&AS 134, 545
Ávila, R., Cruz-González, I., & Tapia, M. 2003, RevMexAA (SC), 19, 121
Baize, P. 1981, A&AS, 44, 199
_________. 1986, A&AS, 65, 551
_________. 1989, IAUDS, Inf. Circ. 107
_________. 1991, A&AS, 87, 49
_________. 1992a, IAUDS, Inf. Circ. 116
_________. 1992b, IAUDS, Inf. Circ. 117
_________. 1993a, IAUDS, Inf. Circ. 120
_________. 1993b, A&AS 99, 205
_________. 1993c, IAUDS, Inf. Circ. 121
_________. 1994, A&AS 106, 267
Couteau, P. 1990, IAUDS, Inf. Circ. 112
Christou, J. C., Hege, E. K., Freeman, J. D., & Ribak, E. 1986, J. Opt. Soc. Am., A, 3, 204
Docobo, J. A., & Ling, J. F. 1994, IAUDS, Inf. Circ. 124
_________. 1998a, IAUDS, Inf. Circ. 136
_________. 1998b, IAUDS, Inf. Circ. 135
_________. 2002, IAUDS, Inf. Circ. 147
Docobo, J. A., Balega, Y. Y., Ling, J. F., Tamazian, V., & Vasyuk, V. A. 2000, AJ, 119, 2422
Erceg, V. 1975, Bull. Obs. Astron. Belgr., 126, 50
Hartkopf, W. I., et al. 2000, AJ, 119, 3084
Heintz, W. D. 1965, Veroff. Sternw. Munchen, 7, 7
_________. 1975, ApJS, 29, 331
_________. 1982, A&AS, 47, 569
_________. 1994, AJ, 108, 2338
_________. 1995, ApJS, 99, 693
Ling, J. F. 1999, IAUDS, Inf. Circ. 137
Lippincott, S. L. 1975, AJ, 80, 833
Mante, R. 1994, Obs. Trav. Soc. Astron. France, 39, 21
_________. 1997, Obs. Trav. Soc. Astron. France, 52, 44
_________. 1999, IAUDS, Inf. Circ. 138
_________. 2000, IAUDS, Inf. Circ. 142
Orlov, V. G., Voitsekhovich, V. V., Mendoza-Valencia, G. A., Svyryd, A., Rivera, J. L., Ortiz, F., & Guerrero, C. A. 2009, RevMexAA, 45, 155
Orlov, V. G., Voitsekhovich, V. V., Sánchez, L. J., & Garfias, F. 2007, RevMexAA, 43, 137
Popovic, G. M. 1970, Bull. Obs. Astron. Belgr., 28, 141
_________. 1972, Bull. Obs. Astron. Belgr., 29, 31
_________. 1998, IAUDS, Inf. Circ. 136
Popovic, G. M., & Pavlovic, R. 1995a, Bull. Obs. Astron. Belgr., 151, 45
_________. 1995b, IAUDS, Inf. Circ. 125
Popovic, G. M., Pavlović, R., & Zivkov, V. 2000, A&AS, 144, 211
Pourbaix, D. 2000, A&AS, 145, 215
Seymour, D., Mason, B. D., Hartkopf, W. I., & Wycoff, G. L. 2002, AJ, 123, 1023
Soderhjelm, S. 1999, A&A, 341, 121
Tokovinin, A., Mason, B. D., & Hartkopf, W. I. 2010, AJ, 139, 743
Voitsekhovich, V. V. Sánchez, L. J., Orlov, V. G., Garfias, F., & Benitez, R. 2005, RevMexAA, 41, 399
Worley, C. E., & Douglass, G. G. 1997, A&AS, 125, 523
Zulevic, D. J. 1969, Bull. Obs. Astron. Belgr., 27, 55
_________. 1986, IAUDS, Inf. Circ. 98
_________. 1995, IAUDS, Inf. Circ. 127
_________. 1996, Bull. Obs. Astron. Belgr., 153, 79
_________. 1997, Bull. Obs. Astron. Belgr., 155, 109

C. A. Guerrero, V. G. Orlov, F. Ortiz, J. L. Rivera, and V. V. Voitsekhovich: Instituto de Astronomía, Universidad Nacional Autónoma de México, Apdo. Postal 70-264, Cd. Universitaria, 04510 México D. F., Mexico (cguerrero, orlov, fortiz, jrivera, voisteko@astroscu.unam.mx).

Revista Mexicana de Astronomía y Astrofísica, **46**, 253–262 (2010)

COMPACT RADIO SOURCES IN THE VICINITY OF THE ULTRACOMPACT HII REGION G78.4+2.6

Citlali Neria, Yolanda Gómez, and Luis F. Rodríguez

Centro de Radioastronomía y Astrofísica
Universidad Nacional Autónoma de México, Morelia, Mexico

Received 2010 January 26; accepted 2010 June 4

RESUMEN

Utilizando el Very Large Array (VLA) a 3.6 cm, hemos identificado cuatro nuevas fuentes compactas de radio en los alrededores de la región HII con morfología cometaria G78.4+2.6 (VLA 1). Las cuatro fuentes compactas de radio (denominadas VLA 2 a 5), tienen contrapartes en el infrarrojo cercano, como se muestra en la imagen del Spitzer a 3.6 μm. Una de estas fuentes (VLA 5) claramente muestra evidencia de radio-variabilidad en una escala de tiempo de horas. Hemos explorado la posibilidad de que estas radio-fuentes están asociadas con estrellas de pre-secuencia principal (PMS) en la vecindad de la región HII ultracompacta G78.4+2.6. Nuestros resultados favorecen una distancia corta de 1.7 kpc para G78.4+2.6. Además de la detección de radio-fuentes en los alrededores de G78.4+2.6, detectamos otro grupo de cinco fuentes, localizado aproximadamente 3′ al noroeste de la región HII. Algunas de estas fuentes presentan emisión extendida.

ABSTRACT

Using the Very Large Array (VLA) at 3.6 cm we identify four new compact radio sources in the vicinity of the cometary HII region G78.4+2.6 (VLA 1). The four compact radio sources (named VLA 2 to VLA 5), have near-infrared counterparts, as seen in the 3.6 μm Spitzer image. One of them (VLA 5) clearly shows evidence of radio variability in a timescale of hours. We explore the possibility that these radio sources are associated with pre-main sequence (PMS) stars in the vicinity of the UC HII region G78.4+2.6. Our results favor the smaller distance value of 1.7 kpc for G78.4+2.6. In addition to the detection of the radio sources in the vicinity of G78.4+2.6, we detected another group of five sources which appear located about 3′ to the northwest of the HII region. Some of them exhibit extended emission.

Key Words: HII regions — ISM: individual (G78.4+2.6, IRAS 20178+4046) — radio continuum: stars

1. INTRODUCTION

Although our understanding of star forming regions has progressed in recent years, many aspects of the early evolution stages are still unclear. Observationally, pre-main sequence (PMS) stars are among the most difficult to study because they are usually heavily obscured by their parental molecular cloud. Observations at radio wavelengths of young clusters are of considerable relevance because a fraction of these stars appear to be undetectable even in the infrared. In this sense radio observations can provide unique information. Radio clusters of non-thermal PMS stars have been found in several star forming regions. Gómez et al. (2000, 2002) reported centimeter wavelength observations of the GGD14 star forming region. In this study, they found a radio cluster of PMS stars made of eight extremely compact and faint radio sources around a compact HII region that seems to be ionized by a B0.5 zero age main sequence (ZAMS) star. Similar radio clusters have been studied toward HH 124 IRS by Reipurth et al. (2002), NGC 2024 (Orion B) by Rodríguez, Gómez, & Reipurth (2003) and toward the Orion Nebula (M42) by Zapata et al. (2004), among others. Some members of the radio clusters mentioned above are characterized by compact non-thermal emission, time variability, and in some cases circular polarization. All these characteristics suggest that most likely their radio emission is due to the gyrosynchrotron mechanism from an active magnetosphere in a PMS star (e.g. Gómez et al. 2002).

The identification of more such PMS clusters can provide valuable information of the star forming processes. Here we present the identification of new members that surround the HII region G78.4+2.6. This is an ultracompact (UC) HII region whose estimated kinematic distances range from 1.7 kpc (Wilking et al. 1989; Schneider et al. 2006) to 3.3 kpc (Kurtz, Churchwell, & Wood 1994). It has a cometary morphology (Kurtz et al. 1994) and it is associated with the IRAS source 20178+4046 with a far-infrared luminosity of 7×10^4 $L_\odot$ (assuming a distance of 3.3 kpc). From the radio continuum emission the HII region seems to be ionized by a B0–B0.5 ZAMS star (Kurtz et al. 1994; Tej et al. 2007). No maser emission of OH (6035 MHz), H_2O (22.2 GHz) or CH_3OH (6.7 GHz) or thermal emission of NH_3 (23.6–23.9 GHz) has been detected toward this region (Baudry et al. 1997; Codella, Felli, & Natale 1996; Kurtz & Hofner 2005; Sunada et al. 2007; Slysh et al. 1999). In the mid-infrared images the UC HII region appears single (Crowther & Conti 2003), but the presence of a stellar group/cluster around it is clear in the near-infrared images (Tej et al. 2007).

Recently, Tej et al. (2007) presented a multi-wavelength study toward IRAS 20178+4046. They used the Giant Metrewave Radio Telescope (GMRT) to map the radio continuum emission at 1280 and 610 MHz. Available archival data from the Two Micron All Sky Survey (2MASS), the Midcourse Space Experiment (MSX), and the James Clerk Maxwell Telescope (JCMT) were used to study the complex in the near-infrared (NIR) JHK bands, the mid-infrared at 8.3, 12.13, 14.65 and 21.34 μm and the sub-mm at 450 and 850 μm, respectively. From their analysis of the NIR 2MASS data, they proposed the presence of nine early type sources with spectral types $\sim$ B0.5 or earlier around IRAS 20178+4046. Their multiwavelength study led Tej et al. (2007) to conclude that a scenario with possible different evolutionary stages of star formation is present toward IRAS 20178+4046 (G78.4+2.6).

In this paper we present sensitive high resolution radio continuum observations at 3.6 cm in order to search for faint compact radio continuum sources around this UC HII region.

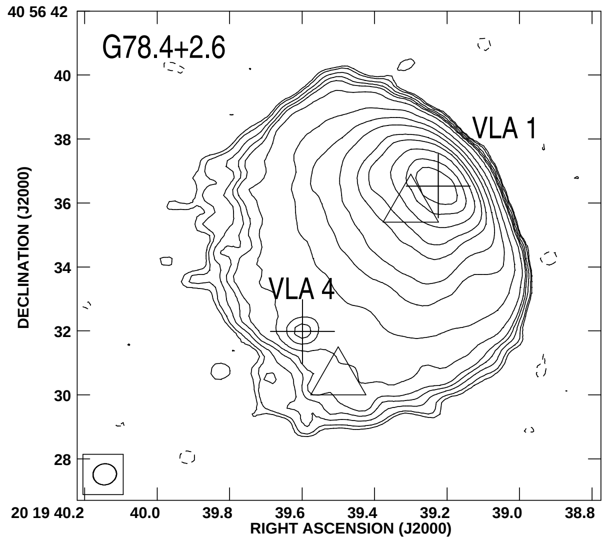

Fig. 1. Contour image of the 3.6 cm continuum emission from the UC HII region G78.4+2.6. The contours are –3, 3, 4, 6, 8, 10, 15, 30, 50, 70, 100, 120, 150, 180 and 200 times 10 μJy beam^{-1}, the rms noise of the image. The synthesized beam (0.″76 × 0.″67 with a position angle of $-79°$) is shown in the bottom left corner of the image. The dynamic range achieved in the 3.6 cm image is approximately 200. The crosses mark the peak position of the 3.6 cm radio sources VLA 1 and VLA 4. The triangles mark the positions of the NIR sources number 1 (bottom left) and number 2 (top right) of Tej et al. (2007).

2. OBSERVATIONS

G78.4+2.6 was observed with the VLA of the NRAO[1] at 3.6 cm (8.4 GHz) in the B configuration during 2002 August 6 and 7 for a total on-source time of $\sim$ 10 hrs. The data were taken using two IFs each with an effective bandwidth of 50 MHz and both circular polarizations. The flux density scale was determined from observations of the amplitude calibrator 1331+305, for which we assumed a flux density of 5.22 and 5.20 Jy, for IF=1 (8.4351 GHz) and IF=2 (8.4851 GHz), respectively. The source 2007+404 was used as the phase calibrator, with bootstrapped flux densities of 2.704 ± 0.003 and 2.708 ± 0.003 Jy for the first and second IF, respectively. The data were edited and calibrated using the standard procedures of the Astronomical Image Processing System (AIPS) of NRAO. The data were also self-calibrated

[1]The National Radio Astronomy Observatory (NRAO) is operated by Associated Universities Inc. under cooperative agreement with the National Science Foundation.

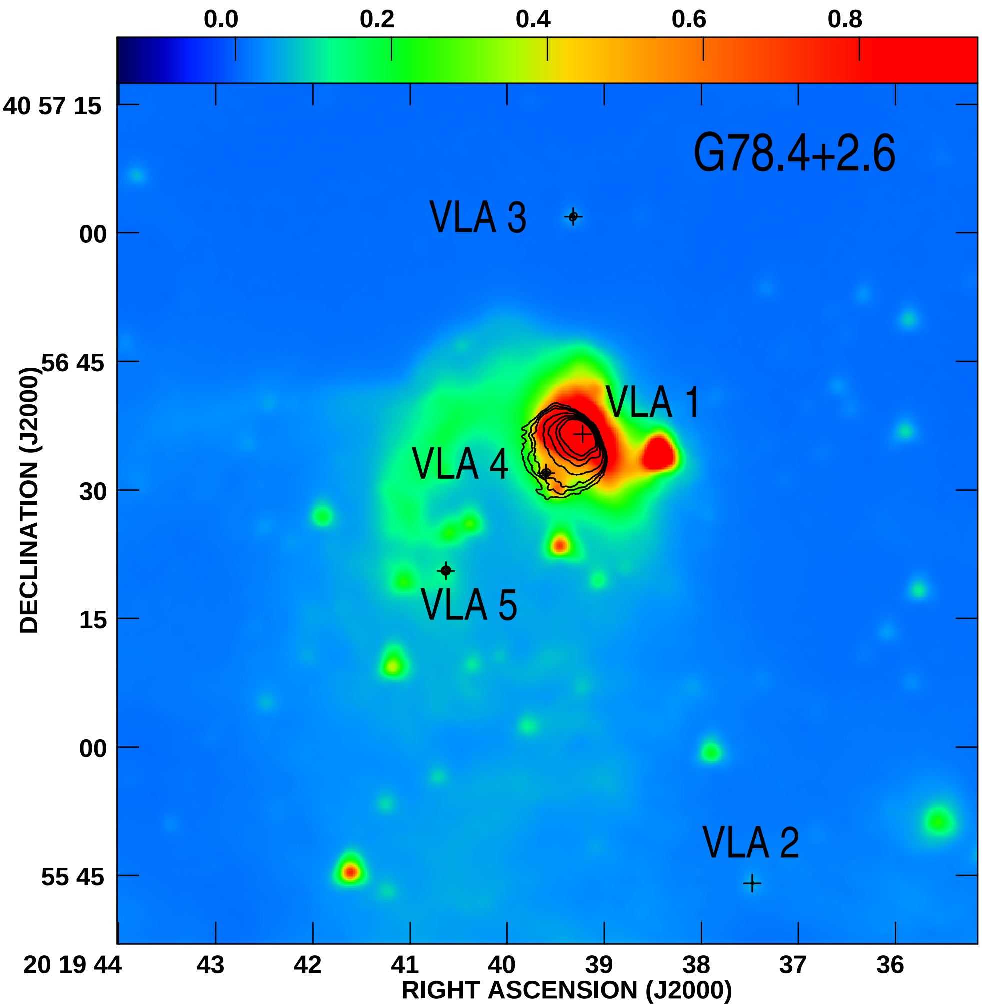

Fig. 2. The image shows the Spitzer 3.6 μm band emission in color for the region around G78.4+2.6. Color scale goes from -0.15 to 0.95 GJy sr^{-1}. The contours represent the 3.6 cm continuum emission from G78.4+2.6 showing the four compact radio sources. The contours are –5, 5, 10, 15, 30, 50, 70 and 90 times 10 μJy beam^{-1}, the average rms noise of the image. The crosses mark the peak position of the 3.6 cm radio sources listed in Table 1. The synthesized beam is $0\farcs76 \times 0\farcs67$ with a position angle of $-79°$.

in phase and for sources far away from the center we applied a primary beam correction to the images (with the task PBCOR). The synthesized beam is $0\farcs76 \times 0\farcs67$ with a position angle of $-79°$, and the rms noise is 10 μJy beam^{-1}.

3. RESULTS

3.1. *Compact radio sources toward G78.4+2.6*

Figures 1 and 2 show the radio continuum emission at 3.6 cm toward the UC HII region G78.4+2.6. In addition to the UC HII region, which we hereafter call VLA 1, it is possible to identify emission from four fainter compact radio continuum sources above the 5σ level; they are called VLA 2 through VLA 5 by us. Figure 1 shows VLA 1 and the compact source VLA 4, which appears inside the extended emission region of the cometary source VLA 1. The source VLA 4 could be physically embedded in the cometary HII region. Unfortunately, our data do not have enough angular resolution to ascertain the nature of this radio source. Figure 2 exhibits a larger area where all the compact radio sources in the vicinity of VLA 1 can be identified.

For these compact sources, we looked for near-infrared counterparts using the Spitzer 3.6 μm band image and the 2MASS Point Source Catalog (PSC), within a radius of 2$''$ around each VLA source. The parameters of the radio continuum sources, and their

TABLE 1

PARAMETERS OF THE RADIO SOURCES TOWARD G78.4+2.6

Source	α(2000)	δ(2000)	Flux Density[a] (mJy)	NIR Counterpart (2MASS PSC)	Spitzer Counterpart[b] α(2000)	Spitzer Counterpart[b] δ(2000)	Time Variable?
VLA 1	20 19 39.224	40 56 36.53	62.26±0.14	20193932+4056358[d]	20 19 39.12	40 56 37.84	N
VLA 2	20 19 37.475	40 55 44.11	0.06±0.02	20193748+4055441	20 19 37.48	40 55 44.14	N
VLA 3	20 19 39.318	40 57 01.91	0.11±0.02	20193931+4057018	20 19 39.34	40 57 01.85	N
VLA 4	20 19 39.599	40 56 31.98	0.48±0.02	20193949+4056305[e]	20 19 39.56	40 56 32.18	N
VLA 5	20 19 40.630	40 56 20.57	0.24±0.02[c]	–	20 19 40.64	40 56 20.19	Y

[a]Flux densities at 3.6 cm. The flux densities for sources VLA 2 to 5 were measured from an image where extended emission was suppressed using only $(u,\, v)$ data with baselines larger than 100 kλ.

[b]Peak position associated with the 3.6 μm Spitzer image.

[c]Time-averaged flux density.

[d]NIR source number 2 of Tej et al. (2007).

[e]NIR source number 1 of Tej et al. (2007).

possible counterparts, are listed in Table 1. Of the nine NIR 2MASS sources reported by Tej et al. (2007), only one (source 2) clearly coincides in position with a VLA source (VLA 1). There is another NIR source reported by Tej (source number 1) that could be associated with a VLA source (VLA 4; within 1.″5). In Figure 1 we plot the peak position of the NIR source number 1 of Tej et al. (2007), where the shift in position with respect to the radio source VLA 4 is evident. Further observations at different frequencies and higher angular resolution are required to confirm or reject the association. Tej et al. (2007) have noted that their NIR source number 1 coincides in position with the source IRAS 20178+4046, one of the brightest infrared sources in the region.

To study the time-variability of the four fainter compact radio continuum sources (see Figure 2) during the approximately 12 hours of the total observing session (of which 10 hours were on-source), we proceeded as follows. The precise position of each source was determined from the image shown in Figure 2. The (u, v) data were then recentered at the position of the source considered and the real and imaginary parts of its flux density were plotted as a function of time, averaged over the (u, v) plane and in 10 time bins. A detailed description of this technique is given in the Appendix A. To avoid contamination from extended emission, we use only (u, v) data with baselines larger than 100 kλ, suppressing emission from scales larger than $\sim$ 0.″5. The technique did not work in a reliable way in the case of VLA 4, which is embedded in the much brighter UC HII (VLA 1). In the case of the remaining sources, we found clear

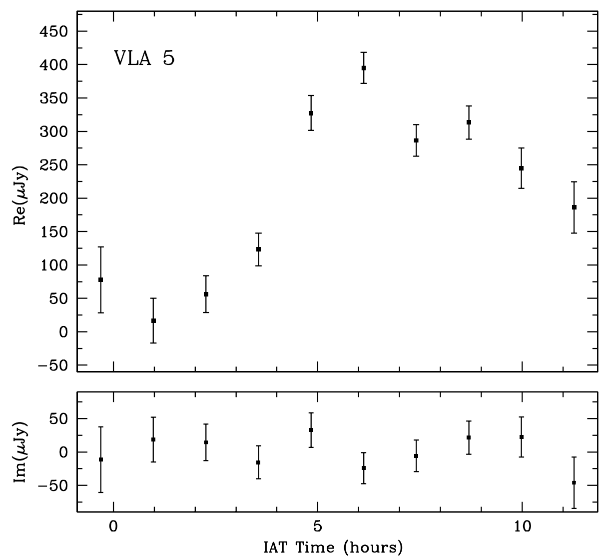

Fig. 3. Real (top) and imaginary (bottom) components of the flux density of VLA 5 as a function of time (IAT = International Atomic Time).

evidence of variability for VLA 5. In Figure 3 we show the real and imaginary parts of its flux density as a function of time, where it can be appreciated that the source was very weak during the first half of the run and that, in a timescale of about an hour, it rose to a much stronger flux density. No evidence of variability was found for VLA 2 and VLA 3. In the last column of Table 1, we list if the sources were time-variable or not.

The variability observed in VLA 5 has been observed in other low-mass PMS stars (e.g., Gómez et

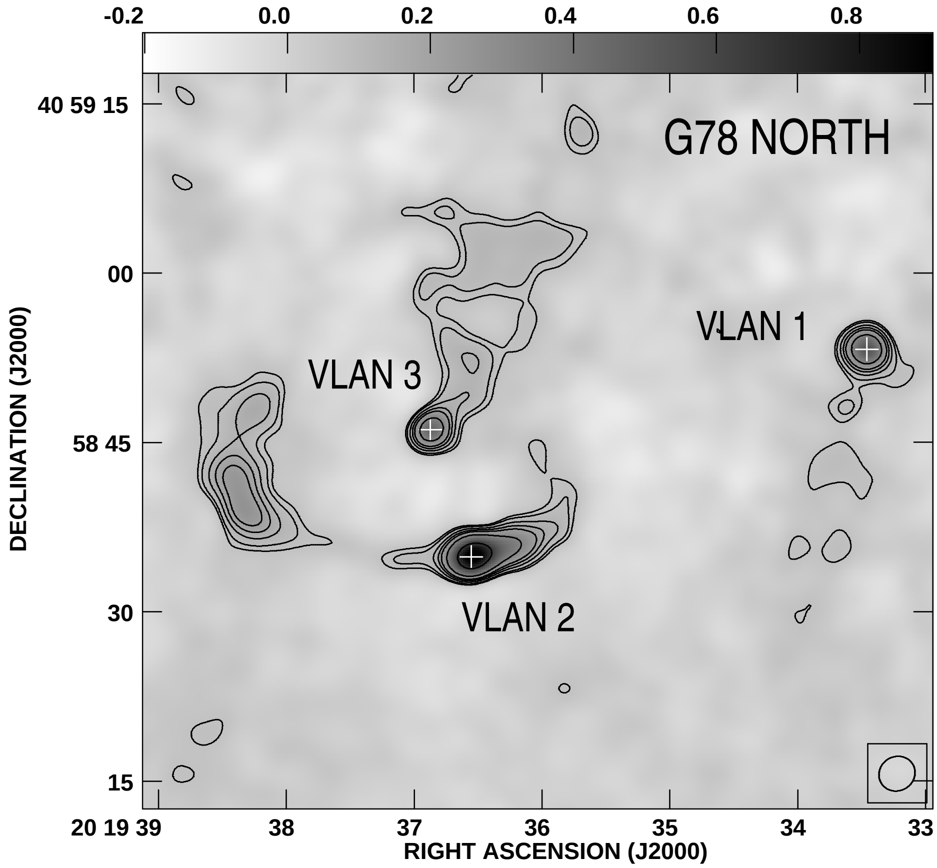

Fig. 4. Contour image overlapped on a grayscale image at 3.6 cm of VLAN 1, VLAN 2 and VLAN 3 toward the G78-North region. Contour levels are 3, 4, 6, 8, 10, 15, 30 and 50 times 21.8 μJy beam^{-1}, the average rms noise of the image. The grayscale flux goes from -0.2 to 0.9 mJy beam^{-1}. The synthesized beam, after applying UVTAPER = 50 kλ (3.″26 × 3.″02 with a position angle of $-60°$), is shown in the bottom right corner of the image. The crosses mark the peak position of the 3.6 cm radio sources listed in Table 2.

al. 2002; Bower et al. 2003; Gómez et al. 2008; Forbrich, Menten, & Reid 2008) and it can be attributed to gyrosynchrotron emission from an active magnetosphere. For UC HII regions or externally-ionized globules variability at such short time scales is not expected.

3.2. *Other radio sources in the field*

Toward the north of the UC HII region G78.4+2.6, we detect another cluster of five compact radio sources (designated as VLAN 1 to VLAN 5) above 5σ level. After we applied UVTAPER (50 kλ, resulting in a beam size of 3.″26×3.″02, P.A. = $-60°$) to this image we noted that two of these sources (VLAN 2 and 3) have diffuse extended emission associated with them. The extended radio emission toward the east of VLAN 2 is more likely an extension of a possible jet. VLAN 1 also displays some signs of extended emission though the morphology is more compact. Figure 4 shows a close-up of the north region showing these three radio sources. The compact sources VLAN 4 and VLAN 5 were not included in this close-up, because they do not exhibit significant extended emission and lie far away from the main group (> 10″). Figure 5 shows the sources VLAN 4 and VLAN 5. As for the four fainter compact radio continuum sources in the vicinity of the UC HII (VLA 2 to 5), we also looked for any counterparts in order to gain understanding about their nature. The search in the Strasbourg Astronomical Data Center (CDS) and the Spitzer 3.6 μm band image does not show any counterpart within one arcsec. We also searched for 1.4 GHz radio emission using the NRAO VLA Sky Survey (NVSS), which does not show any source above $\sim$ 1.2 mJy (3σ). The morphology of VLAN 1 to 3 resembles that of a cluster of radio galaxies, but the extended emission could alternatively be HII regions surrounding massive stars.

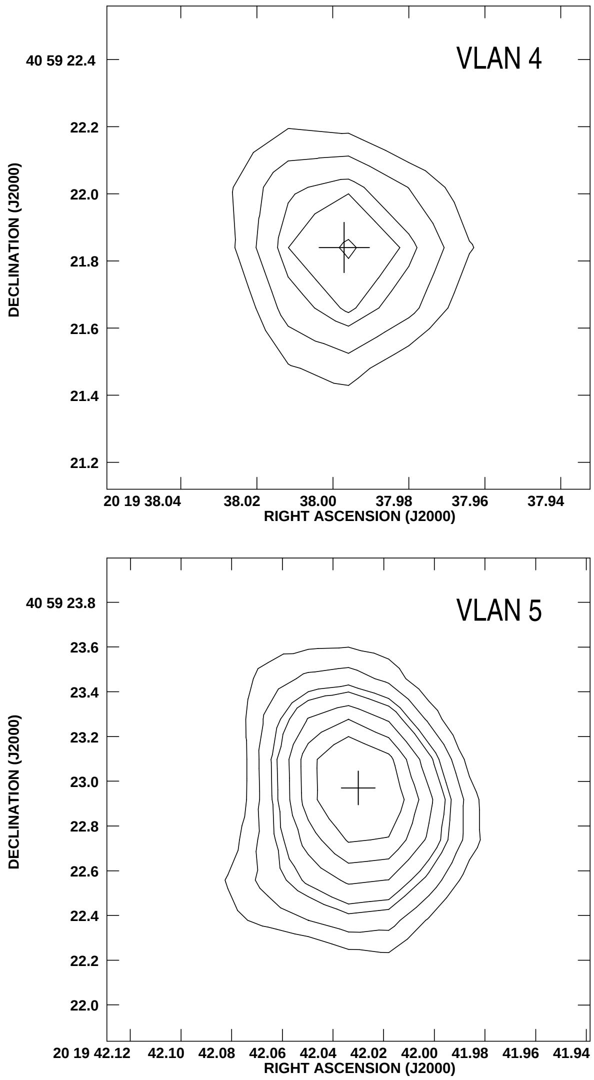

Fig. 5. Contour image of the 3.6 cm continuum emission from VLAN 4 (top) and VLAN 5 (bottom) toward the G78-North region. The contours are −5, 5, 7, 9, 10, 12, 14 and 16 times 10 μJy beam^{-1}, the average rms noise of the image. The synthesized beam is $0\rlap{.}''76 \times 0\rlap{.}''67$, with a position angle of -79°. The crosses mark the peak position of the 3.6 cm radio sources listed in Table 2.

Such varied morphologies of HII regions are not uncommon (e.g., Kurtz et al. 1994, 1999). However, more observations are needed in order to clarify the nature of these sources. The main parameters of the five compact radio sources to the north of G78.4+2.6 are listed in Table 2.

4. DISCUSSION

The high sensitivity continuum observations toward the region G78.4+2.6 (IRAS 20178+4046), have resulted in the identification of four new compact radio sources in the vicinity ($< 1'$) of the cometary HII region (VLA 1) (see Table 1). These sources could be associated with pre-main sequence (PMS) stars, but multiwavelength observations are required to confirm this.

TABLE 2

PARAMETERS OF THE RADIO SOURCES TOWARD THE NORTH OF G78.4+2.6

Source	α(2000)	δ(2000)	Flux Density[a] (mJy)
VLAN 1	20 19 33.457	40 58 53.25	0.57 ± 0.05
VLAN 2	20 19 36.554	40 58 34.86	0.87 ± 0.04
VLAN 3	20 19 36.874	40 58 46.14	0.49 ± 0.04
VLAN 4	20 19 37.997	40 59 21.84	0.09 ± 0.03
VLAN 5	20 19 42.030	40 59 22.97	0.28 ± 0.05

[a]Flux densities at 3.6 cm corrected for the primary beam response.

Tej et al. (2007), based on the analysis of the 850 μm emission, have reported the presence of two regions at different evolutionary stages toward this star-forming region, the northern and southern cores. The southern core traces a later stage of evolution and is associated with the UC HII region, and an earlier stage of evolution is proposed for the northern core, which does not have radio or NIR emission. Tej et al. (2007) have analyzed the nature of the near-infrared sources detected in the 2MASS JHK observations around the UC HII G78.4+2.6 region and, by using color-magnitude diagrams and assuming a distance of 3.3 kpc (Kurtz et al. 1994), they proposed the presence of nine B0.5 or earlier type candidates, all mainly located toward the southern core. However, only one (VLA) of the five radio sources reported by us in this paper (Table 1) clearly coincides in position with one of the nine B0.5 or earlier type sources proposed by Tej et al. (2007).

The UC HII region (VLA 1) is excited at least by a B0.5 ZAMS star (see discussion below) and radio emission is clearly detected. We believe that if more B0.5 stars were present in the surroundings they should have been detected in our deep radio image. The non-detection of the rest of the NIR sources could be due to a factor already considered by Tej et al. (2007): there is considerable uncertainty in the distance to G78.4+2. Indeed, if instead of the large value of 3.3 kpc we consider the smaller value of 1.7 kpc (Wilking et al. 1989; Schneider et al. 2006) then the B0.5 candidates will become less luminous stars, with no expected detectable HII region.

In the particular case of VLA 4, if it is associated with the NIR source number 1 of Tej et al. (2007), and the radio continuum reported in this work at 3.6 cm is produced by an optically thin homogeneous spherical HII region, following Mezger & Henderson (1967), we can estimate the number of ionizing photons per second, $N_{\rm i}$, produced by the exciting star as,

$$\left[\frac{N_{\rm i}}{\rm s^{-1}}\right] = 7.7\ \times 10^{43}\left[\frac{S_\nu}{\rm mJy}\right]\left[\frac{\nu}{\rm GHz}\right]^{0.1}\left[\frac{D}{\rm kpc}\right]^2,$$

where S_ν is the flux density of the compact source, ν is the observing frequency and D is the distance from the Sun. Adopting a distance of 1.7 kpc, we estimate for VLA 4 $N_{\rm i} = 1.3 \times 10^{44}$ s^{-1}, implying an exciting star type B3 ZAMS (Panagia 1973), while for a distance of 3.3 kpc, $N_{\rm i} = 5.0 \times 10^{44}$ s^{-1}, then the spectral type will be $\sim$ B2 ZAMS. In both cases the exciting star for the VLA 4 source should be later than a B2 ZAMS and does not reach the ionizing rate of a B0.5 ZAMS or earlier star. As mentioned above, Tej et al. (2007) had already pointed out that there is a discrepancy seen in their determination of the spectral types by using the NIR color-magnitude diagrams due to the distance uncertainty, to the possible presence of IR excess and to the 2MASS resolution limit.

It is possible to plot the $(H-K)$ colors and K magnitudes from our VLA sources with NIR counterparts in a color-magnitude diagram to derive the spectral types of the sources in the same way as was done by Tej et al. (2007). Assuming that VLA 1 is ionized by the NIR source number 2 of Tej et al. (2007), a B0.5 ZAMS star at a distance of 1.7 kpc is needed to provide the ionization. Then, if we apply a similar distance correction in the color-magnitude diagram (Figure 3 of Tej et al. 2007) for all the other sources, we find that VLA 4 (source number 1 of Tej) is associated with a B3 ZAMS star (consistent with our previous estimate from the radio continuum flux density). VLA 2 and VLA 3 will correspond to a spectral type between F and G ZAMS. Only one source clearly shows evidence of fast (hours) radio variability (VLA 5), a physical characteristic of low-mass PMS stars. Unfortunately, this source does not have a NIR counterpart, although it does have a Spitzer (mid-infrared) counterpart (see Table 1). We then propose that VLA 1 is an HII region excited by a B0.5 ZAMS star, VLA 4 is possibly an HII region excited by a B3 ZAMS star and that the remaining three compact radio sources (VLA 2, VLA 3 and VLA 5) are low-mass PMS stars embedded in the star forming region.

The non-detection in our data of radio continuum counterparts to the NIR sources number 3 to 9 from Tej et al. (2007), favors the smaller value of 1.7 kpc fot the distance to G78.4+2.6. Also we notice that four of our radio sources are located toward the southern core, where radio and 3.6 μm emission is present (see Figure 2), which suggests their association with a later evolutionary stage core where massive stars have formed an UC HII region.

The compact radio source VLA 3 is displaced $\sim 16''$ from the center of the northern core. The northern core is traced by the submillimeter emission at 850 μm (see Figure 5 of Tej et al. 2007) and it is not associated with radio or NIR emission, suggesting an early stage of evolution (Klein et al. 2005; Tej et al. 2006, 2007). We propose that VLA 3 may be a PMS star embedded in the early evolutionary stage northern core. Alternatively, VLA 3 could simply be an outer component of the southern core that appears projected in the line-of-sight toward the northern core. If the association with the northern core is confirmed, it will support the idea that the less massive objects are among the first ones to form in a cluster (Klein et al. 2005; Molinari et al. 2008).

In order to be sure that the four compact radio sources identified in this paper are new members of the PMS cluster toward G78.4+2.6 and not background sources, we now estimate the number count probability following Windhorst et al. (1993). The expected number of background sources per square arcmin, N, with a flux density at 8.3 GHz above S, is given by

$$\left[\frac{N}{(\rm arcmin)^2}\right] = 0.0024\left[\frac{S}{\rm mJy}\right]^{-1.3}.$$

Using S = 0.05 mJy (5σ of the radio continuum image), within a solid angle of $1'.5 \times 1'.5$ we obtain that the expected number of background sources is $\sim$ 0.3, which suggests that the four compact radio sources are members of the star forming region.

Finally, following the formulation of Mezger & Henderson (1967) and Rodríguez et al. (1980) for a homogeneous and spherically symmetric region, we estimate the physical parameters of the UC HII region G78.4+2.6, assuming that the gas has constant electron density, an electron temperature of 8000 K (Tej et al. 2007) and a kinematic distance of 1.7 kpc. At 3.6 cm we measure a total flux density of $\sim$ 62.3 mJy (see Table 1), and an angular size of $4''.5 \times 3''.5$ ($\sim$ 0.03 pc at a distance of 1.7 kpc). This flux density is in agreement with other radio estimates (Wilking et al. 1989; McCutcheon et al. 1991; Kurtz et al. 1994; Tej et al. 2007) in the 0.6–

8.5 GHz frequency range, which is consistent with an optically thin region. Under these conditions we estimate an electron density $n_e = 6.4 \times 10^3$ cm^{-3}, an ionized mass $M_{\rm HII} = 8.5 \times 10^{-3}$ $M_\odot$, and an emission measure EM of 1.3×10^6 cm^{-6} pc. Using the ionizing rates of Panagia (1973) and assuming that the logarithm of the ionizing rate has an approximate linear behavior with the spectral subtype (Vacca, Garmany, & Shull 1996), we estimate for the ionizing star of VLA 1 a spectral type of B0.5 ZAMS (for a distance of 1.7 kpc) or of B0.3 ZAMS (for a distance of 3.3 kpc). The latter result is in agreement with Kurtz et al. (1994) and Tej et al. (2007) who estimated a spectral type for the exciting source of VLA 1 between B0 and B0.5 (assuming a distance of 3.3 kpc).

5. CONCLUSIONS

We present high angular resolution VLA observations at 3.6 cm toward the star-forming region G78.4+2.6. In addition to the cometary UC HII region VLA 1, a group of four compact radio sources was found (VLA 2 to 5). One of them (VLA 5) shows evidence of radio variability in a timescale of hours. The four new compact radio sources, reported by us, coincide in position with Spitzer 3.6 μm peaks. From the five radio sources reported at 3.6 cm, one is clearly associated with the NIR source number 2 of Tej et al. (2007) with a spectral type B0.5. Another VLA source (VLA 4) seems to be associated with the NIR source number 1 of Tej et al. (2007) and corresponds to a spectral type B3 ZAMS star. The rest of the radio sources (VLA 2, VLA 3 and VLA 5) are probably PMS stars with spectral types between F and G ZAMS. Our results favor the smaller distance of 1.7 kpc (Wilking et al. 1989; Schneider et al. 2006) proposed for the star forming region G78.4+2.6.

Another group of five radio sources is found about 3′ to the NW of the HII region G78.4+2.6 whose nature is still undetermined.

We thank an anonymous referee for comments and suggestions that helped to improve this paper. CN, YG, and LR are thankful for the support of DGAPA, Universidad Nacional Autónoma de México, and of Conacyt (Mexico). This research has made use of the SIMBAD database, operated at CDS, Strasbourg, France. This publication has also made use of the Spitzer Space Telescope and NASA/IPAC Infrared Science Archive, which is operated by the Jet Propulsion Laboratory, California Institute of Technology, under contract with the National Aeronautics and Space Administration.

APPENDIX A. MEASURING THE FLUX DENSITY AS A FUNCTION OF TIME IN THE (u, v) PLANE

In some cases, the observer is interested in determining the flux density of a source in the field as a function of time. This can be achieved by making images from data on small time intervals, but it is faster (since no images have to be made) to explore in the (u, v) plane different time intervals to search for variability at different timescales. As it is the case in the image plane (x, y), it is possible to isolate the emission from a source also in the (u, v) plane, as described below.

The visibility $V(u, v)$ for a given point (u, v) is (Thompson, Moran, & Swenson 1986):

$$V(u,v) = \int_{-\infty}^{+\infty}\int_{-\infty}^{+\infty} I(x,y)\exp[i2\pi(ux+vy)]dxdy\,, \tag{A1}$$

where $V(u, v)$ is the visibility, in general a complex function, u and v are the projections of the baseline of a given antenna pair along the sky coordinates x and y, respectively, given in units of wavelengths, and $I(x, y)$ is the intensity of the source or sources as a function of the position (x, y) with respect to the phase center. A point source located at the phase center, $(x, y) = (0, 0)$, can be described by

$$I(x,y) = S\ \delta^2(x,y)\,, \tag{A2}$$

where S is the flux density of the source and δ^2 is Dirac's delta function in two dimensions. The integral of equation (1) then becomes:

$$V(u,v) = S\,. \tag{A3}$$

In this case, the real, Re(u), and imaginary, Im(u), parts of the visibility are given by:

$$\mathrm{Re}(u,v) = S\,, \tag{A4}$$

$$\mathrm{Im}(u,v) = 0\,. \tag{A5}$$

Finally, the real and imaginary parts are averaged over the range of values of u and v for which one has measurements, $-u_m \le u \le u_m$, $-v_m \le v \le v_m$:

$$\mathrm{Re} = \frac{1}{2u_m}\frac{1}{2v_m}\int_{-u_m}^{+u_m}\int_{-v_m}^{+v_m}\mathrm{Re}(u,v)du\ dv = S\,, \tag{A6}$$

$$\mathrm{Im} = \frac{1}{2u_m}\frac{1}{2v_m}\int_{-u_m}^{+u_m}\int_{-v_m}^{+v_m}\mathrm{Im}(u,v)du\ dv = 0\,. \tag{A7}$$

That is, the average over (u, v) of the real and imaginary components of the visibility of a point source at the phase center are simply S and 0, respectively.

What happens if there is an additional source in the field, that is centered at a position different from the phase center? Assuming again that this source is pointlike and that it is located at the point $(x, y) = (x_1, 0)$, it can be described by

$$I(x, y) = S_1\ \delta^2(x - x_1, y)\,, \tag{A8}$$

where S_1 is its flux density. Again using equation (1) we have that the real, $\mathrm{Re}_1(u, v)$, and imaginary, $\mathrm{Im}_1(u, v)$, parts of the visibility are in this case given by:

$$\mathrm{Re}_1(u, v) = S_1\ \cos(2\pi u x_1)\,, \tag{A9}$$

$$\mathrm{Im}_1(u, v) = S_1\ \sin(2\pi u x_1)\,. \tag{A10}$$

Averaging over (u, v), we obtain

$$\begin{aligned}\mathrm{Re}_1 &= \frac{1}{2u_m}\frac{1}{2v_m}\int_{-u_m}^{+u_m}\int_{-v_m}^{+v_m}\mathrm{Re}_1(u, v)dudv\\ &= \frac{1}{2u_m}\int_{-u_m}^{+u_m} S_1\ \cos(2\pi u x_1)du\\ &= S_1\ \frac{\sin(2\pi u_m x_1)}{2\pi u_m x_1} = S_1\ \mathrm{sinc}(2\pi u_m x_1)\,, \end{aligned}\tag{A11}$$

where $\mathrm{sinc} = (\sin\ x)/x$,

$$\begin{aligned}\mathrm{Im}_1 &= \frac{1}{2u_m}\frac{1}{2v_m}\int_{-u_m}^{+u_m}\int_{-v_m}^{+v_m}\mathrm{Im}_1(u, v)dudv\\ &= \frac{1}{2u_m}\int_{-u_m}^{+u_m} S_1\ \sin(2\pi u x_1)du = 0\,.\end{aligned}\tag{A12}$$

We conclude that, in this case, the average over (u, v) of the imaginary component is 0, as in the previous case of the source at the phase center. The real component is now the flux density of the source, multiplied by a sinc function. For a well-designed interferometer we can assume that $u_m \simeq v_m$, and that the angular resolution of the data is given approximately by

$$\theta \simeq \frac{1}{u_m} \simeq \frac{1}{v_m}\,. \tag{A13}$$

We then conclude that as long as this source is several resolution elements away from the phase center and is not very bright, its contribution to the real component is small. In brief, as long as the condition

$$S \ll \frac{S_1}{2\pi(x_1/\theta)}\,, \tag{A14}$$

is fulfilled, we can take the real component of the averaged visibility as dominated by the flux density of the source at the phase center.

In the case of the source VLA 5, we have that $S \simeq 0.1 - 0.3$ mJy. The other compact sources in the field of G78.4+2.6 have flux densities comparable to that of VLA 5 and are at angular distances of $15''$ or more away from it. Since the angular resolution of the data is $\theta \simeq 0.''7$, we have that the angular separation is $x_1 \simeq\ 20\ \theta \simeq 20/u_m$, and that an upper limit to the contribution of these sources is given by

$$|\mathrm{Re}_1| \leq 0.003 \text{ mJy}\,. \tag{A15}$$

So, the other point sources in the field contribute less than 1% to the real component measured after centering the (u, v) data at the position of VLA 5.

We have, however, to consider the effect of the extended source VLA 1, that is quite bright, $S_1 \simeq$ 60 mJy. In this case it can be shown that the condition given by equation (14) approximately becomes

$$S \ll \left[\frac{\theta}{\theta_S}\right]^2\ \frac{S_1}{2\pi(x_1/\theta)}\,, \tag{A16}$$

where S_1 is the flux density of the extended source, and θ_S is its angular diameter, $\theta_S \simeq 4''$ in the case of VLA 1. In this case $x_1 \simeq 20''$. Evaluating the contribution of VLA 1 at the position of VLA 5 we obtain

$$|\mathrm{Re}_1| \leq\ 0.01 \text{ mJy}\,, \tag{A17}$$

$$\mathrm{Im}_1 =\ 0\,. \tag{A18}$$

We then conclude that the contribution of VLA 1 at the position of VLA 5 does not affect significantly the flux density determinations of the latter source. The contribution of extended sources in the field is further suppressed by not including in the averaging the short baselines of the (u, v) data, where most of the extended emission is present.

REFERENCES

Baudry, A., Desmurs, J. F., Wilson, T. L., & Cohen, R. J. 1997, A&A, 325, 255
Bower, G. C., et al. 2003, ApJ, 598, 1140
Codella, C., Felli, M., & Natale, V. 1996, A&A, 311, 971
Crowther, P. A., & Conti, P. S. 2003, MNRAS, 343, 143
Forbrich, J., Menten, K. M., & Reid, M. J. 2008, A&A, 477, 267
Gómez, Y., Rodríguez, L. F., & Garay, G. 2000, ApJ, 531, 861
_________. 2002, ApJ, 571, 901
Gómez, L., Rodríguez, L. F., Loinard, L., Lizano, S., Allen, C., Poveda, A., & Menten, K. M. 2008, ApJ, 685, 333

Klein, R., Posselt, B., Schreyer, K., Forbrich, J., & Henning, T. 2005, ApJS, 161, 361
Kurtz, S., Churchwell, E., & Wood, D. O. S. 1994, ApJS, 91, 659
Kurtz, S., & Hofner, P. 2005, AJ, 130, 711
Kurtz, S. E., Watson, A. M., Hofner, P., & Otte, B. 1999, ApJ, 514, 232
McCutcheon, W. H., Sato, T., Dewdney, P. E., & Purton, C. R. 1991, AJ, 101, 1435
Mezger, P. G., & Henderson, A. P. 1967, ApJ, 147, 471
Molinari, S., Pezzuto, S., Cesaroni, R., Brand, J., Faustini, F., & Testi, L. 2008, A&A, 481, 345
Panagia, N. 1973, AJ, 78, 92
Reipurth, B., Rodríguez, L. F., Anglada, G., & Bally, J. 2002, AJ, 124, 1045
Rodríguez, L. F., Gómez, Y., & Reipurth, B. 2003, ApJ, 598, 1100
Rodríguez, L. F., Moran, J. M., Ho, P. T. P., & Gottlieb, E. W. 1980, ApJ, 235, 845
Schneider, N., et al. 2006, A&A, 458, 855
Slysh, V. I., Val'tts, I. E., Kalenskii, S. V., Voronkov, M. A., Palagi, F., Tofani, G., & Catarzi, M. 1999, A&AS, 134, 115
Sunada, K., Nakasato, T., Ikeda, N., Hongo, S., Kitamura, Y., & Yang, J. 2007, PASJ, 59, 1185
Tej, A., Ghosh, S. K., Kulkarni, V. K., Ojha, D. K., Verma, R. P., & Vig, S. 2007, A&A, 468, 1001
Tej, A., Ojha, D. K., Ghosh, S. K., Kulkarni, V. K., Verma, R. P., Vig, S., & Prabhu, T. P. 2006, A&A, 452, 203
Thompson, A. R., Moran, J. M., & Swenson, G. W. 1986, Interferometry and Synthesis in Radio Astronomy (New York: Wiley-Interscience)
Vacca, W. D., Garmany, C. D., & Shull, J. M. 1996, ApJ, 460, 914
Wilking, B. A., Blackwell, J. H., Mundy, L. G., & Howe, J. E. 1989, ApJ, 345, 257
Windhorst, R. A., Fomalont, E. B., Partridge, R. B., & Lowenthal, J. D. 1993, ApJ, 405, 498
Zapata, L., Rodríguez, L. F., Kurtz, S., & O'Dell, C. R. 2004, ApJ, 127, 2252

Citlali Neria, Yolanda Gómez, and Luis F. Rodríguez: Centro de Radiostronomía y Astrofísica, Universidad Nacional Autónoma de México, Apdo. Postal 3-72 (Xangari), 58089 Morelia, Michoacán, Mexico (c.neria, y.gomez, l.rodriguez@crya.unam.mx).

Revista Mexicana de Astronomía y Astrofísica, **46**, 263–277 (2010)

ORBITAL ELEMENTS FOR EIGHT BINARIES. STUDY OF THE NATURE OF WIDE COMPONENTS. I

F. M. Rica Romero[1,2]

Received 2010 March 25; accepted 2010 June 5

RESUMEN

Se calcularon nuevos parámetros orbitales y masas para ocho binarias. Las órbitas, en la mayoría de estas binarias, mostraron grandes residuos que aconsejaban obtener nuevos parámetros orbitales. Para determinar los parámetros orbitales iniciales se usó el método de Thiele-van den Bos modificado, para posteriormente usar el método de corrección diferencial de Heintz para obtener los parámetros orbitales finales. El método Thiele-van den Bos fue modificado para que un valor aproximado de la constante areal permitiera obtener buenos resultados. La naturaleza de las componentes distantes fue estudiada mediante fotometría $BVIJHK$ y datos cinemáticos y astrométricos. Se realizó una búsqueda de nuevas compañeras alrededor de las binarias estudiadas.

ABSTRACT

New orbital parameters and masses for eight binaries were determined. Most of these were noted as being in need of correction due to large residuals to the previous best orbit. A modified Thiele-van den Bos method was used to obtain initial orbits which were improved using the differential correction method of Heintz. The Thiele-van den Bos method was modified so that an approximate value of the areal constant allowed good results to be obtained. The nature of wide components was studied using $BVIJHK$ photometry, historical astrometry and kinematical data. A search for new unreported companions around the binaries was carried out.

Key Words: binaries: general — binaries: visual — instrumentation: high angular resolution — techniques: high angular resolution

1. INTRODUCTION

As a result of part of the work on visual double stars carried out by the Double Star Section of Liga Iberoamericana de Astronomía (LIADA) I present orbital parameters and other data (residuals, ephemerides, masses, parallaxes, apparent orbits, etc.) for eight visual binary systems: WDS03272+0944 (HDS 433), WDS 04070-1000 (HDS 521), WDS06345-1114 (HO 234), WDS09228-0950 AB (A 1342 AB), WDS12274-2843 (B 228), WDS18410+2450 (A 2988), WDS 21459+1153 AB (A 1223 AB) and WDS 23026+4245 AB (BU 1147 AB). For HDS 433 this is the first orbit published.

Initial orbits were calculated using the method of Thiele-van den Bos and were then improved using the differential correction method of Heintz (1978). Dynamical parallaxes were calculated using the Baize-Romani algorithm (1946). Bolometric corrections were taken from Allen's tables (1973). The nature of wide components was studied using $BVIJHK$ photometry, historical astrometry and kinematical data.

The astrophysical properties of the binaries were determined and discussed. All the orbits presented here, except that of HDS 521, have previously been announced in the Information Circulars of IAU Commission 26 (hereafter IAUDS). The orbital parameters listed in this paper are the final corrected versions and are slightly different from those announced in IAUDS.

2. METHOD OF ORBITAL CALCULATION

Before using any analytical method θ was corrected for precession and proper motion. θ and ρ

[1]Agrupación Astronómica de Mérida, Spain.
[2]Liga Iberoamericana de Astronomía (LIADA), Argentina.

TABLE 1

ORBITAL PARAMETERS, PARALLAXES AND RESIDUALS

Name	HDS 433	HDS 521	HO 234	A1342
WDS	03272+0944	04070-1000	06345-1114	09228-0950
ADS	...	...	5212	7334
HIP	16083	19206	31356	45999
Disc. date	1983.7134	1991.25	1888.64	1905.99
P [years]	51.923 ± 15.054	22.467 ± 1.812	374.882 ± 153.887	53.199 ± 0.193
T [BY]	2008.282 ± 0.502	1996.723 ± 0.230	1912.738 ± 1.133	1957.346 ± 0.572
e	0.568 ± 0.077	0.678 ± 0.044	0.345 ± 0.068	0.038 ± 0.037
a [$''$]	0.441 ± 0.027	0.221 ± 0.017	0.694 ± 0.048	0.165 ± 0.011
i [$^\circ$]	22.7 ± 5.1	123.1 ± 5.1	55.8 ± 3.0	67.1 ± 4.1
ω [$^\circ$]	3.0 ± 6.3	255.0 ± 4.6	179.3 ± 1.7	173.6 ± 4.6
Ω [$^\circ$]	112.1 ± 4.4	37.0 ± 3.1	35.9 ± 3.4	23.7 ± 3.6
Residuals:				
RMS(θ)[$^\circ$]	1.06	2.83	1.35	3.59
RMS(ρ) [$''$]	0.007	0.006	0.013	0.009
MA(θ)[$^\circ$]	0.77	0.57	0.92	1.86
MA(ρ)[$''$]	0.005	0.001	0.005	0.005
a^3/P^2	7.21370×10^{-5}	10.59844×10^{-5}	4.42712×10^{-6}	9.61969×10^{-6}

Name	B 228	A 2988	A 1223 AB	BU 1147
WDS	12274-2843	18410+2450	21459+1153	23026+4245
ADS	8555	11574	15300	16467
HIP	60775	91609	107461	113788
Disc. date	1926.77	1916.43	1905.53	1889.54
P [years]	44.483 ± 6.249	57.172 ± 1.168	44.046 ± 1.374	73.997 ± 0.509
T [BY]	1952.295 ± 1.251	1941.464 ± 1.520	1972.549 ± 1.175	1870.280 ± 0.595
e	0.666 ± 0.077	0.688 ± 0.101	0.324 ± 0.107	0.800 ± 0.056
a [$''$]	0.173 ± 0.107	0.102 ± 0.019	0.123 ± 0.018	0.225 ± 0.011
i [$^]circ$]	63.6 ± 12.0	154.7 ± 19.0	160.7 ± 40.4	21.7 ± 46.0
ω [$^\circ$]	164.9 ± 12.6	306.8 ± 11.5	154.1 ± 8.8	356.4 ± 3.0
Ω [$^\circ$]	137.8 ± 10.6	329.6 ± 9.7	14.8 ± 8.3	159.5 ± 2.0
Residuals:				
RMS(θ)[$^\circ$]	4.15	4.54	4.89	2.40
RMS(ρ) [$''$]	0.011	0.018	0.023	0.016
MA(θ)[$^\circ$]	2.73	3.27	3.71	1.48
MA(ρ)[$''$]	0.007	0.011	0.011	0.007
a^3/P^2	1.51253×10^{-5}	3.18298×10^{-6}	7.78058×10^{-6}	9.24564×10^{-6}

were plotted against time which allowed the detection of measures with important errors or quadrant problems. Measures with the largest errors were assigned zero weight.

Preliminary orbits were determined by the method of Thiele-van den Bos which was then improved by the author. Three base points and a crude value of the areal constant c are needed. A set of Keplerian orbits changing the initial value of the areal constant in an appropiate range (i.e., 50 percent of the initial value of c) was calculated. All the apparent orbits pass through the three given points. Only periodic orbits were considered. The step size and the search range for c are customizable by the user.

The orbit with minimum RMS residuals was retained. In the next iteration the search range and

TABLE 2

EPHEMERIDES

	03272+0944		04070-1000		06345-1114		09228-0950	
DATE	θ (deg)	ρ (arcsec)	θ (deg)	ρ (arcsec)	θ (deg)	ρ (arcsec)	θ (deg)	ρ (arcsec)
2010.0	160.9	0.207	357.7	0.240	0.8	0.597	199.6	0.156
2011.0	182.5	0.231	278.6	0.169	1.4	0.604	202.5	0.158
2012.0	199.5	0.262	6.2	0.236	2.1	0.611	205.3	0.158
2013.0	212.7	0.296	294.6	0.179	2.8	0.617	208.2	0.156
2014.0	223.1	0.332	15.5	0.220	3.4	0.624	211.2	0.152
2015.0	231.5	0.367	308.8	0.191	4.0	0.630	214.5	0.146
2016.0	238.4	0.401	27.3	0.182	4.6	0.637	218.0	0.138
2017.0	244.3	0.434	321.2	0.204	5.2	0.643	222.0	0.129
2018.0	249.4	0.464	52.4	0.098	5.8	0.650	226.7	0.118
	12274-2843		18410+2450		21459+1153		23026+4245	
DATE	θ (deg)	ρ (arcsec)	θ (deg)	ρ (arcsec)	θ (deg)	ρ (arcsec)	θ (deg)	ρ (arcsec)
2010.0	254.8	0.036	236.7	0.113	312.5	0.105	13.3	0.207
2011.0	108.1	0.146	233.5	0.118	301.9	0.099	16.8	0.190
2012.0	127.1	0.265	230.5	0.123	289.9	0.093	20.8	0.172
2013.0	137.5	0.271	227.8	0.128	276.4	0.088	25.6	0.154
2014.0	156.2	0.138	225.2	0.132	261.6	0.084	31.6	0.135
2015.0	67.6	0.062	222.8	0.136	245.6	0.082	39.9	0.114
2016.0	121.1	0.226	220.6	0.140	229.2	0.082	53.8	0.089
2017.0	132.9	0.283	218.4	0.143	212.8	0.083	82.3	0.062
2018.0	144.8	0.220	216.4	0.146	197.1	0.085	137.7	0.046

the step size for the new value of c were reduced. The process was repeated until the result for two iterations did not show a significant difference. Two or three iterations were sufficient for most of the binaries. The difference between the initial estimate of c and the final value of c was less than 15 percent for most binaries.

If a set of Keplerian orbits showed a flat gradient for the RMS residuals then those orbits were rejected by comparing of the mass calculated by dynamical parameters, with that determined using spectral types.

The three base points have to be chosen carefully where the observational data seem most reliable considering instrumentation, data density, or critical arc coverage. I also tried to cover as much of the observed arc as possible. This may allow the area around a single observation to represent a base point without additional observational coverage.

Initial orbits determined by the Thiele-van den Boss method were improved using the Heintz differential correction method (1978). The initial weights for measures were assigned using a data weighting scheme based on Hartkopf, McAlister, & Franz (1989), Mason, Douglass, & Hartkopf (1999a), Seymour et al. (2002), Docobo & Ling (2003). The initial θ weights were 5 times larger than the ρ weights (Heintz 1978) for visual measures. After several iterations in the differential correction process the measures with residuals larger than 3σ were assigned zero weight. Later, the non-zero weight measures were reassigned following the work of Irwin, Yang, & Walker (1996).

3. RESULTS

Table 1 lists, for each binary, the date of its discovery, the final orbital elements, the root mean square (RMS) residuals and the mean absolute (MA) residuals. These are in both cases weighted averages calculated using the data-weighting scheme described in § 2.

TABLE 3

STELLAR DATA

Star		WDS			Present Work	Hipparcos			
WDS	HIP	m_A	m_B	Spectral Type	π (Dynamical) (arcsec)	H_{pA}	H_{pB}	π (Trigonometric) (arcsec)	$\sum M_\odot$
03272+0944	16083	3.74	7.55	B9Vn	...	3.74	7.55	0.01468 ± 0.00101	10.1 ± 6.4
04070-1000	19206	7.29	8.60	G0	0.0240	7.29	8.60	0.02400 ± 0.00092	1.55 ± 0.43
06345-1114	31356	7.73	9.05	F0	0.0093	8.22	8.31	0.01046 ± 0.00200	2.08 ± 2.11
09228-0950	45999	6.99	7.84	A3V	0.0069	6.99	7.84	0.00720 ± 0.00080	4.25 ± 1.66
12274-2843	60775	8.18	8.39	A9V	0.0095	8.18	8.39	0.00988 ± 0.00096	2.71 ± 5.15
18410+2450	91609	8.08	9.08	F0V	0.0042	8.08	9.08	0.00441 ± 0.00085	3.79 ± 3.07
21459+1153	107461	9.77	9.60	G0	0.0071	9.77	9.60	0.00723 ± 0.00135	2.54 ± 6.78
23026+4245	113788	5.19	7.70	A3Vn	0.0070	5.26	7.43	0.00774 ± 0.00051	4.49 ± 1.11

TABLE 4

STATISTICAL RESULTS

Star		Authors	RMS		MA	
WDS	Name		$\delta\theta(^\circ)$	$\delta\rho('')$	$\delta\theta(^\circ)$	$\delta\rho('')$
03272+0944	HDS 433	Rica (this paper)	1.06	0.007	0.77	0.005
04070-1000	HDS 521	Rica (this paper)	2.83	0.006	0.57	0.001
		Balega et al. (2006)	4.29	0.007	0.97	0.002
06345-1114	HO 234	Rica (this paper)	1.35	0.013	0.96	0.005
		Heintz (1979)	5.85	0.099	3.06	0.088
		Baize (1958)	45.38	0.177	39.44	0.170
09228-0950	A 1342 AB	Rica (this paper)	3.59	0.009	1.86	0.005
		Starikova (1981)	5.00	0.022	4.12	0.019
		Finsen (1976)	45.52	0.018	21.14	0.015
		Ekenberg (1945)	121.04	0.032	107.12	0.023
12274-2843	B 228	Rica (this paper)	4.15	0.011	2.73	0.007
		Heintz (1981)	42.89	0.069	18.72	0.058
18410+2450	A 2988	Rica (this paper)	4.54	0.018	3.27	0.011
		Starikova (1981)	5.69	0.033	4.40	0.028
		Baize (1955)	85.88	0.036	61.84	0.032
21459+1153	A 1223 AB	Rica (this paper)	4.89	0.023	3.71	0.011
		Baize (1955)	6.17	0.043	3.89	0.018
		Voronov (1934)	103.49	0.077	92.39	0.030

The a^3/P^2 values are also listed. Errors for the elements were calculated from the covariance matrix and the residuals of all observations.

Table 2 presents ephemerides for the period 2010–2018. Table 3 lists stellar data for binaries: WDS magnitudes in Columns (3) and (4) and WDS spectral types in Column (5); in Column (6), the dynamical parallaxes calculated using the orbital periods and semimajor axes obtained in this work; in Columns (7) and (8) the apparent magnitudes published in the *Hipparcos* and *Tycho* catalogs (ESA 1997), in Column (9) the corresponding trigonometric parallaxes (with their standard errors); and in Column (10) the total mass of the binary (with an estimated standard error), as calculated from the *Hipparcos* parallax. I summarize in Table 4 some statistical results concerning the orbits computed in this work and other orbits previously calculated. The RMS and MA residuals for θ and ρ also are listed.

Figures 1–8 show the new apparent orbits drawn together with the observational data; the x and y scales are arcseconds. The solid ellipse represents

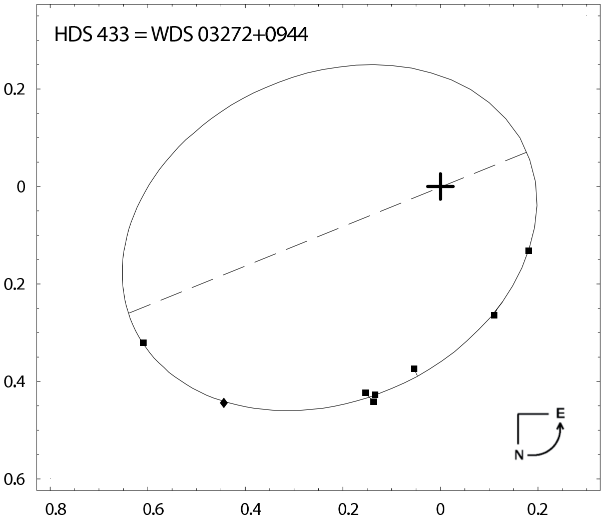

Fig. 1. Apparent orbit for HDS 433.

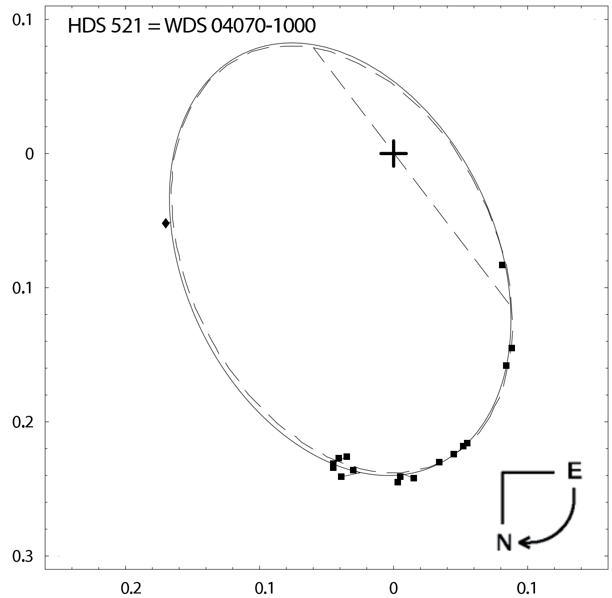

Fig. 2. Apparent orbit for HDS 521.

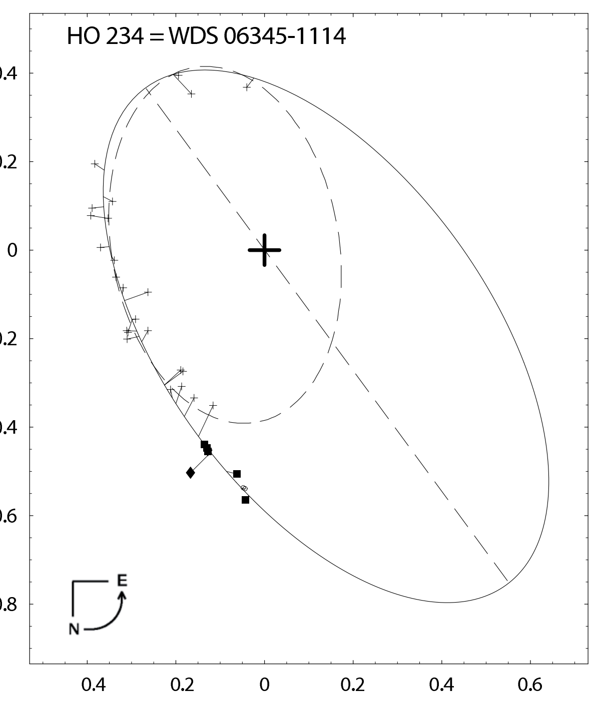

Fig. 3. Apparent orbit for HO 234.

the newly determined orbit, while the dashed ellipse represents previous orbit. The line passing through the origin is the line of nodes. Speckle measures are shown as filled squares, visual interferometric observations as open circles, visual measures as plus signs, and measures from the ESA *Hipparcos* instrument as filled diamonds. The rejected observations are shown as crosses. All measures were connected to their predicted positions on the new orbit by O-C lines.

The absolute magnitudes were calculated using the tables published by Zombeck (1990), which relate the spectral types to the absolute magnitudes. For red stars Henry et al.'s (1997) work was used, which relates optical-infrared colors to absolute magnitudes. I expect that most of these stars have near solar metallicity

4. NOTES FOR INDIVIDUAL SYSTEMS

Next, photometric, astrometric, spectroscopy and kinematical data were analysed. Spectral types and luminosity classes, masses and dynamical parallaxes were obtained. The dynamical parallaxes were calculated using the Baize-Romani method (1946).

The tables published in Montes et al. (2001) and Soderblom & Mayor (1993) were consulted to check the membership of the binaries included in this paper to young kinematic groups.

In the next paragraphs we adopt the grading scheme used in the Sixth Catalog of Orbits of Visual Binary Stars (Hartkopf & Mason 2001).

4.1. *WDS 03272+0944 = HDS 433*

Since the first measure in 1983.7134 (Mason et al. 1999b) 8 additional measures for this binary have been obtained, which cover an arc of about 116 degrees. The orbit presented in this work is the first orbit published.

HDS 433 (2 Tau, ξ Tau) is composed of stars of magnitudes 3.74 and 7.55 (ESA 1997). The main

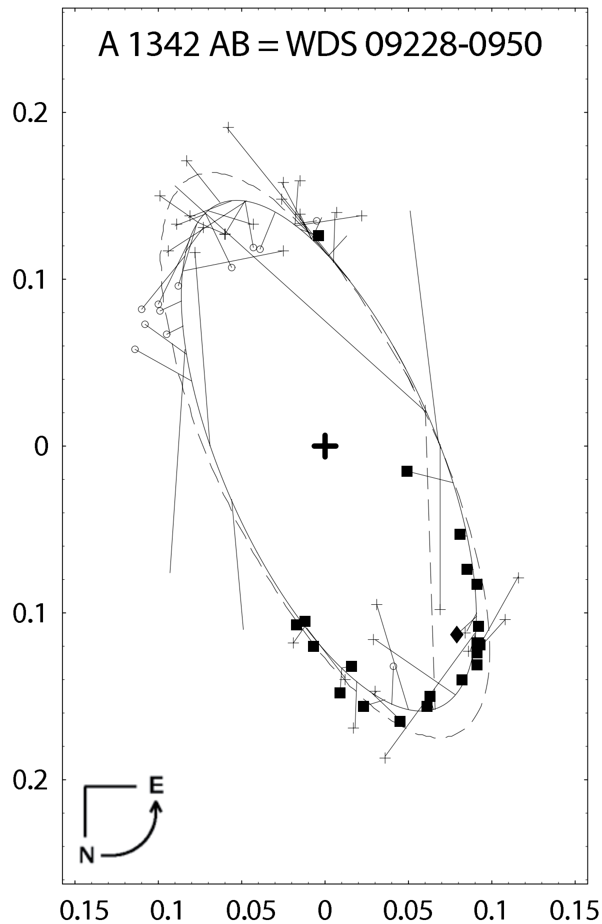

Fig. 4. Apparent orbit for A 1342 AB.

component is a short period triple spectroscopic system. There are several unresolved observations of this system. The high Δm undoubtedly is the reason for the many unsuccessful attempts at resolution (Mason et al. 1999b). The *Hipparcos* catalog lists a proper motion of $+53.61 \pm 1.02$ mas yr^{-1} in RA and -38.12 ± 1.01 mas yr^{-1} in DEC and a trigonometric parallax of 14.68 ± 1.01 mas, which corresponds to a distance of $68.11^{+5.1}_{-4.4}$ pc.

In the astronomical literature HDS 433 has been classified as a B9V star (Jaschek 1978; Kennedy 1983; Buscombe & Foster 1995). From the apparent magnitudes and the *Hipparcos* parallax, the absolute magnitude for the secondary is +3.4 which corresponds to a spectral type F5V.

Tokovinin (1997) obtained masses of 3.20 $M_\odot$ for Aa, 3.10 $M_\odot$ for Ab, 5.50 $M_\odot$ for Ac and 1.24 $M_\odot$ for B. The sum of the masses is 13.04 $M_\odot$. A total mass of 10.1 ± 6.4 $M_\odot$ was obtained, using the orbit of this work and the errors in the trigonometric parallax, P and a.

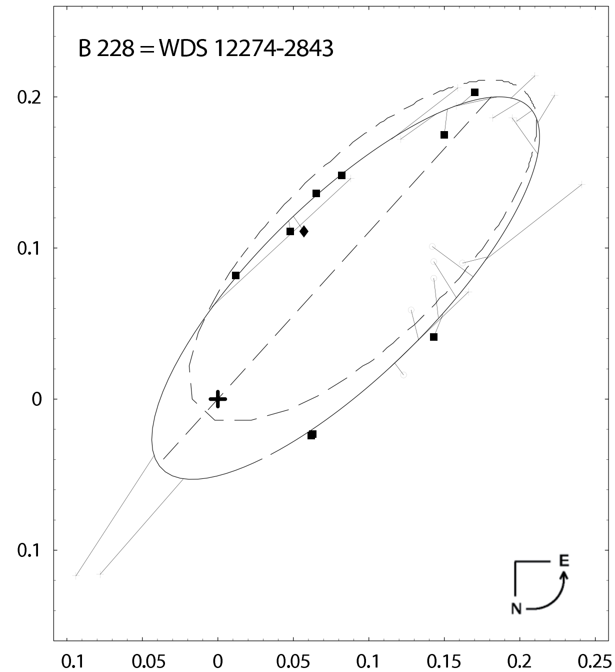

Fig. 5. Apparent orbit for B 228.

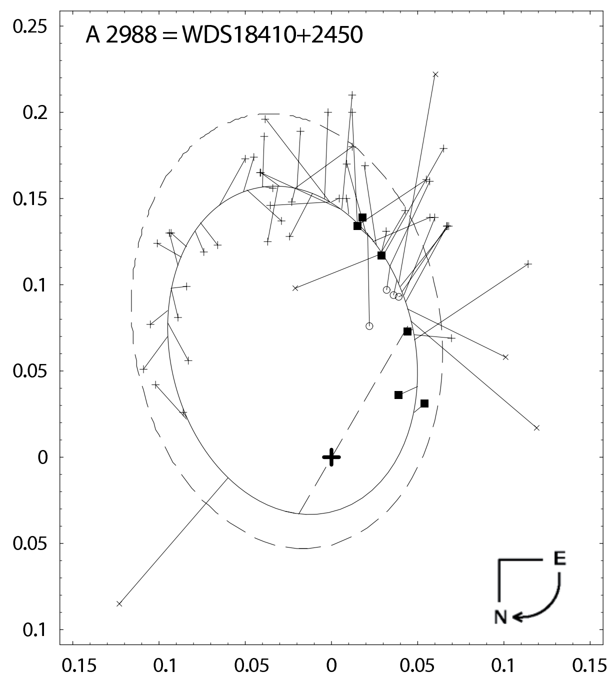

Fig. 6. Apparent orbit for A 2988.

Age and Stellar Population. Using the *Hipparcos* proper motion, parallax and a radial velocity of $+22.0 \pm 6.6$ km s^{-1} as given by Duflot, Figon, & Meyssonnier (1995), in this work a peculiar velocity

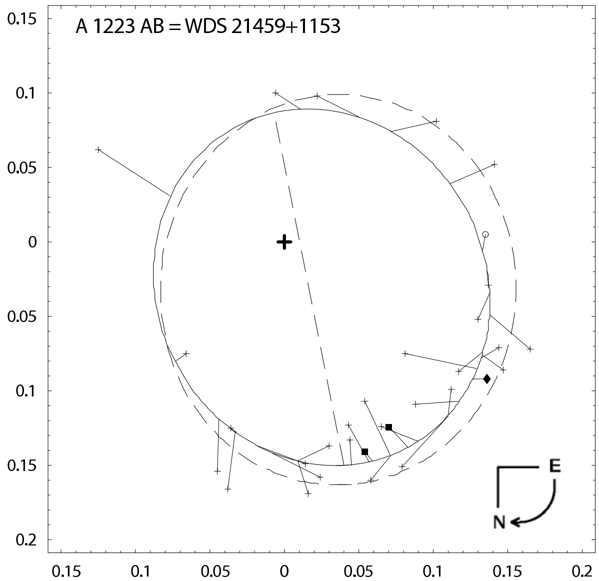

Fig. 7. Apparent orbit for A 1223 AB.

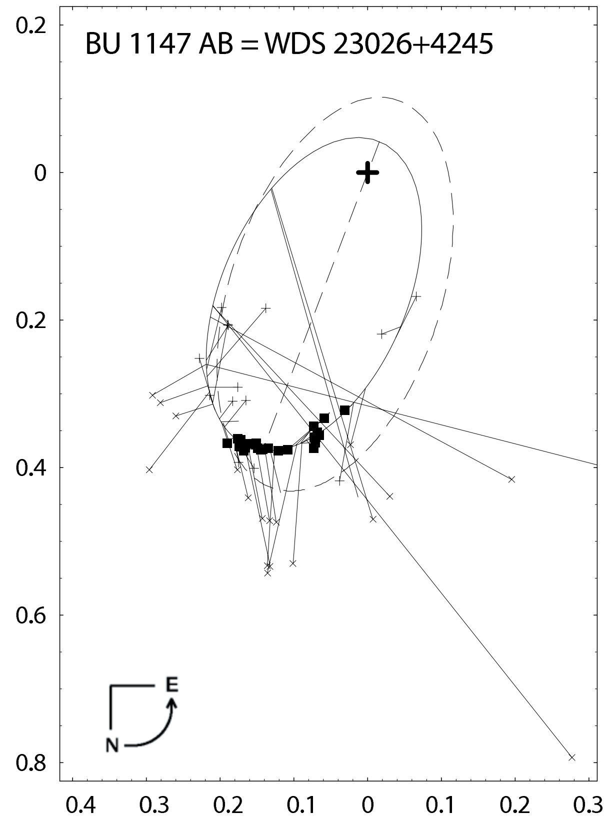

Fig. 8. Apparent orbit for BU 1147 AB.

(U,V,W) = (-5, $+4$, -30) km s^{-1} was calculated. According to Eggen's diagrams (1969a,b) this system is a member of the young galactic disk. A value of 0.19 for the kinematic age parameter of Grenon (1987), fG, was obtained in this work, corresponding to young-middle age thin disk stars of age $3-4$ Gyr. However, Strom, Wolff, & Dror (2005) determined an age of only $12-15$ Myr.

4.2. *WDS 04070-1000 = HDS 521*

The *Hipparcos* satellite discovered this system in 1991.25. HDS 521 has 18 measures which cover an arc of 295 degrees.

Balega et al. (2002) used the 6 m telescope at the Special Astrophysical Observatory in Celenchuk to obtain a measure in 1998. B. Mason et al. (in preparation) used a 4 m telescope to perform a measure in 2001. Balega et al. (2006) recently calculated the orbital parameters for this binary. Later, Horch et al. (2008) obtained 11 speckle measures in 2002 to 2004, which cover 12–13 degrees. HDS 521 is composed of stars of magnitudes 7.29 and 8.60 with a combined spectral type of G1/2V (Houk & Swift 1999).

The *Hipparcos* satellite determined a high proper motion of -127.56 ± 1.02 mas yr^{-1} in RA and -141.56 ± 1.05 mas yr^{-1} in DEC, and a trigonometric parallax of 24.00 ± 0.92 mas (which corresponds to a distance of $41.6^{+1.7}_{-1.4}$ pc).

Using the orbital parameters calculated in this work, masses were calculated taking into account the standard deviation for the *Hipparcos* trigonometric parallax, and for P and a. A total mass of 1.55 ± 0.43 $M_\odot$ was obtained. The dynamical parallax turns out to be 24.00 mas, in excellent agree with the *Hipparcos* data.

Differential photometry from *Hipparcos* gives $\Delta m = +1.31$. The individual spectral types inferred from the differential photometry are F9V and G8V. In this work, individual spectral types of F7V and G6V were also obtained using $BVIJHK$ photometry and a combined proper motion.

From the spectral types, stellar masses of 1.14 $M_\odot$ and 0.84 $M_\odot$ were calculated using Allen's tables (1973). If the spectral types determined in this work are used, then stellar masses of 1.23 $M_\odot$ and 0.90 $M_\odot$ are obtained. So the sum of the masses ranges from 1.98 $M_\odot$ to 2.13 $M_\odot$, consistent within the error margins.

Absolute magnitudes of +4.20 and +5.40 were determined using the apparent magnitudes and the *Hipparcos* trigonometric parallax. These values correspond to F9V and G7/8V stars.

Age and Stellar Population. Nordstrom et al. (2004) obtained a metallicity [Fe/H] = -0.27, an age of 8.0 ± 1.2 Gyr, a radial velocity of +10.2 ± 3.3 km s^{-1} and a peculiar heliocentric velocity (U,V,W) = (+34, −2, −20) km s^{-1}. Nordstrom et al. (2004) determined that HDS 521 describes a galactic orbit with an excentricity of 0.13, a periastron of 7,700 pc and an apoastron of 9,360 pc.

According to Eggen's diagrams (1969a,b) HDS 521 is a member of the young Galactic disk. A value of 0.17 for Grenon's (1987) parameter fG was obtained in this work, corresponding to young-middle age thin disk stars of age 3 − 4 Gyr.

4.3. *WDS 06345-1114 = HO 234*

Hough (1890) discovered this binary in 1888.64 and it has 33 measures which cover about 170 degrees. Baize (1958) calculated the first orbit with a period of 169 years ($a = 0.38''$; $e = 0.18$) more than twice shorter that the orbit calculated in this work. Heintz (1979) calculated the next orbit which is a grade 4 orbit. At the same time of my publication in IAU Circ. Inf. of the orbit published in this work, Hartkopf, Mason, & Rafferty (2008) published new orbital parameters with residuals slightly smaller than those for the orbit presented in this work. Hartkopf et al. used a new measure not used in this work. HO 234 is composed by stars of 8.22 and 8.31 magnitudes (ESA 1997). *Tycho*-2 catalog proper motions are −27.4 mas yr^{-1} in RA and −1.5 mas yr^{-1} in DEC. The *Hipparcos* trigonometric parallax of 10.46 ± 2.00 mas corresponds to a distance of $95.6^{+22.6}_{-15.3}$ pc.

The orbit calculated in this work has a period more than two times larger and a major semiaxis about 60 percent greater than the previous orbit. A total mass of 2.08±2.11 $M_\odot$ was obtained. In the astronomical literature HO 234 has been classified as a F3V star (Buscombe 1998) and F2V (Houk & Swift 1999). In this work a combined spectral type of F4V (F4V+F5V) was obtained using $BVIJHK$ photometry and the combined proper motion. From the apparent magnitudes and the *Hipparcos* parallax, the absolute magnitudes for the components were determined, which correspond to spectral types F4/5V. Using the historical measures, the photometric difference is 0.13 magnitudes. Stellar masses of 1.39 and 1.35 $M_\odot$ were calculated using Allen's tables (1973). The sum of the masses is 2.74 $M_\odot$.

The dynamic parallax obtained, 9.3 mas, is in agreement with the *Hipparcos* parallax. Nordstrom et al. (2004) obtained a metallicity [Fe/H] = −0.30, and an age of $1.9^{+0.4}_{-0.3}$ Gyr. The projected rotational velocity is 20 km s^{-1} (Glebocki, Gnacinski, & Stawikowski 2000). However these data were not useful to estimate the age for the stellar system. The orbital elements have previously been announced in the Information IAUDS No. 162 (Rica 2007).

4.4. *WDS 09228-0950 = A 1342 AB*

This system is KU Hya, a magnetic $\alpha\,CVn$ variable star in which brightness changes of 0.05 magnitudes in a period of 33.97 days have been observed (Hensberge et al. 1981). Aitken (1929) discovered this binary in 1905.99 and it has 72 measures which cover two revolutions.

Ekenberg (1945) calculated the first orbit (P = 15.0 yr; $e = 0.10$; $a = 0.166''$). Finsen (1976) calculated another orbit with a period of 25.4 years ($e = 0.962$; $a = 0.28''$). Starikova (1981) also calculated an orbit, graded 2. Since then, 15 new measures have been made, covering about 161 degrees.

Using the historical measures listed in the WDS database, the photometric difference is 0.04 magnitudes. So the *Hipparcos* apparent magnitudes were not used for this system. A 1342 AB is composed of stars of 7.3 and 7.3 magnitudes (this work). According to the *Tycho*-2 catalog the proper motion is −28.8 mas yr^{-1} in RA and −16.0 mas yr^{-1} in DEC. The *Hipparcos* trigonometric parallax of 7.20± 0.80 mas corresponds to a distance of $138.9^{+17.4}_{-13.9}$ pc.

Using the orbital parameters, a total mass of 4.25 ± 1.66 $M_\odot$ was obtained. In the astronomical literature A 1342 AB has been classified as an A5 star (Cowley et al. 1969; Buscombe & Foster 1995), an A3V star (Abt 1981) and an F1 star (Abt & Morrell 1995). In this work, a combined spectral type of A5V was obtained using $BVIJHK$ photometry and a combined proper motion. From the apparent magnitudes and *Hipparcos* parallaxes the absolute magnitudes for the components were determined, which correspond to spectral types A3/4V.

Grenier et al. (1999) calculated a radial velocity of +19.6 ± 5.0 km s^{-1}.

Stellar masses of 2.07 and 2.05 $M_\odot$ were calculated from Allen's tables (1973) using the absolute magnitudes. The sum of the masses is 4.12 $M_\odot$. The dynamic parallax obtained is 6.9 mas, in agreement with the *Hipparcos* parallax.

Age and Stellar Population. In this work a peculiar velocity of (U,V,W) = (−15, −22, −6) km s^{-1} was calculated. According to Eggen's diagrams (1969a,b) A 1342 AB is a member of the young galactic disk. A value of 0.13 for Grenon's fG was obtained in this work, corresponding to young-middle age thin disk stars of age 3 − 4 Gyr.

4.5. *WDS 12274-2843 = B 228*

Van den Bos (1928) discovered this double in 1926.77. B 228 has 28 measures which cover about two revolutions. Van den Bos and Finsen obtained more than half of the historical measures.

The only existing orbit for B 228 was calculated by Heintz (1981) and it is of grade 4. Since then, 11 new measures have been made (9 of them were speckle measures, one measure is micrometrical, and the other measure was made by *Hipparcos*) covering about 326 degrees. B 228 is composed of stars of 8.18 and 8.39 magnitudes (ESA 1997). *Tycho*-2 determined a proper motion of -53.8 mas yr^{-1} in RA and -5.7 mas yr^{-1} in DEC. The *Hipparcos* trigonometric parallax of 9.88 ± 0.96 mas corresponds to a distance of $101.2^{+10.9}_{-9.0}$ pc.

The orbit calculated in this work is less excentric and more inclined than the previous orbit. The semimajor axis is larger by about 14 percent. A total mass of 2.71 ± 5.15 $M_\odot$ was obtained.

Cannon & Pickering (1918-1924) classified B 228 as an F0 star and Houk (1982) as an A9V star. In this work a combined spectral type of F3V was obtained using $BVIJHK$ photometry and a combined proper motion.

From *Tycho*-2 apparent magnitudes and *Hipparcos* parallaxes, the absolute magnitudes for the components were determined, which correspond to individual spectral types F3V and F4V.

Stellar masses of 1.45 and 1.38 $M_\odot$ were calculated using Allen's tables (1973). The sum of the masses is 2.83 $M_\odot$ is good agreement with the sum of masses obtained by the use of dynamical parameters.

The dynamic parallax obtained is 9.5 mas, in good agreement with the *Hipparcos* parallax.

4.6. *WDS 18410+2450 = A 2988*

Aitken (1918) discovered this system in 1916.43. A 2988 has 60 measures which cover nearly two revolutions.

Baize (1955) calculated an orbit with a dynamic parallax of 0.0074″. Starikova (1981) also calculated an orbit with a dynamic parallax of 0.006″. Since then, 27 new measures have been obtained (nearly half of the historic measures).

A 2988 is composed of stars of 8.08 and 9.08 magnitudes (ESA 1997). *Tycho*-2 lists a proper motion of $+1.9$ mas yr^{-1} in RA and $+8.5$ mas yr^{-1} in DEC. The *Hipparcos* trigonometric parallax of 4.41 ± 0.85 mas, corresponds to a distance of $226.8^{+54.1}_{-36.6}$ pc.

The orbit calculated in this work is more excentric and inclined than the previous one. The semimajor axis is smaller by about 22 percent. A total mass of 3.79 ± 3.07 $M_\odot$ was obtained.

In the astronomical literature A 2988 has been classified as an A5 star (Cannon & Pickering 1918–1924), an A7 star (Grenier et al. 1999), an A8V (Christy & Walker 1969) and an F0V star (Cowley & Cowley 1965; Kennedy 1983). In this work a combined spectral type of F1V was obtained using $BVIJHK$ photometry and a combined proper motion. From the apparent magnitudes and *Hipparcos* parallaxes the absolute magnitudes for the components were determined, which correspond to spectral types F0V.

Rufener (1981) determined that A 2988 is a Delta Scuti variable star. It is catalogued as NSV 24547. Grenier et al. (1999) calculated a radial velocity of -36.3 ± 7 km s^{-1}.

Using the historical measures listed in the WDS, the photometric difference is 0.0. *Hipparcos* obtained a difference in magnitude of 1.0. A more accurate value for the differential photometry is needed.

Assuming a zero photometric difference, stellar masses of 1.64 $M_\odot$ and 1.64 $M_\odot$ were calculated using Allen's tables (1973) and spectral types F1V for both components. The sum of the masses is 3.28 $M_\odot$.

The dynamic parallax obtained is 4.2 mas, in excellent agreement with the *Hipparcos* parallax. The orbital elements have previously been announced in the Information IAUDS No. 160 (Rica 2006b).

Age and Stellar Population. Bartkevicius & Gudas (2002) calculated a peculiar velocity (U,V,W) = $(-19.9, -16.9, -0.8)$ km s^{-1} and classified it as a intermediate age thin disk star.

4.7. *WDS 21459+1153 = A 1223 AB*

Since Aitken (1906) discovered it in 1905.53, A 1223 AB has been measured on 32 occasions. These measures cover more than two revolutions. Tokovinin (1985) performed an interferometric measure and two speckle measures were made (Hartkopf et al. 2000; Scardia et al. 2000). *Hipparcos* obtained a measure in 1991.

Voronov (1934) calculated the first orbit (P = 23.9 yrs; $e = 0.21$; $a = 0.12''$). Another orbit was calculated by Baize (1955) and graded 4. Since then 13 measures have been made covering nearly a revolution.

A 1223 AB is composed of stars of 9.77 and 9.60 magnitudes (ESA 1997) with a combined spectral type of G0V (Kennedy 1983).

Tycho-2 (Høg et al. 2000) determined a proper motion of -83.4 mas yr^{-1} in RA and -85.6 mas yr^{-1}

in DEC. The *Hipparcos* trigonometric parallax of 7.23 ± 1.35 mas corresponds to a distance of $138.3^{+31.8}_{-21.8}$ pc.

Masses were calculated taking into account the standard deviation for the *Hipparcos* trigonometric parallax and the errors of P and a. A total mass of $2.54 \pm 6.78\ M_\odot$ was obtained.

Eggen (1969c) obtained a spectral type of G2V while Christy & Walker (1969) obtained G1V with individual spectral types of G0V and G2V. In this work, a spectral type of G3V was obtained using $BVIJHK$ photometry and a combined proper motion. From the apparent magnitudes and *Hipparcos* parallaxes the absolute magnitudes for the components were determined, which correspond to spectral types of F7/8V and F8/9V.

Differential photometry from *Hipparcos* yields -0.17. A mean differential photometry using the five last historical results from WDS catalog yields $+0.14$. From the spectral types of the literature, stellar masses of 1.09 and 1.09 $M_\odot$ were calculated using Allen's tables (1973). The sum of the masses is 2.18 $M_\odot$ in agreement, within errors, with the total mass obtained using orbital parameters.

The dynamic parallax is 7.1 mas in excellent agreement with the *Hipparcos* parallax. Individual masses of 1.13 and 1.12 $M_\odot$ were determined using the Baize-Romani method (1946).

The orbital elements have previously been announced in the Information IAUDS No. 159 (Rica 2006a).

Age and Stellar Population. Bartkevicius & Gudas (2002) obtained a peculiar velocity of $(U,V,W) = (+73, -45, +24)$ km s^{-1}.

According to Eggen's diagrams (1969a,b) A 1223 AB is a member of the old Galactic disk. A value of 0.37 for fG was obtained in this work corresponding to old age thin disk stars, or to thick disk stars of age about 10 Gyr.

4.8. *WDS 23026+4245 = BU 1147 AB*

Since Burnham (1894) discovered it in 1889.54, BU 1147 AB (= 2 And = HD 217782 = BD+41 4665) it has collected 66 measures which cover nearly two revolutions. A previous orbit was calculated by Baize (1974) and graded 4. Since the previous orbit, 39 measures, many of which are speckle measurements, have been made, covering 26 degrees.

BU 1147 AB is composed of stars of 5.26 and 7.43 magnitudes (ESA 1997) with a combined spectral type of A0V (Kennedy 1983).

The *Tycho*-2 catalog (Høg et al. 2000) proper motion is $+58.9 \pm 1.0$ mas yr^{-1} in RA and $+6.3 \pm 1.0$ mas yr^{-1} in DEC. The *Hipparcos* trigonometric parallax (van Leeuwen 2007) of 7.74 ± 0.51 mas corresponds to a distance of $129.2^{+9.1}_{-8.0}$ pc.

The total stellar mass was calculated taking into account the standard deviation for the *Hipparcos* trigonometric parallax and the errors of the orbital parameters. A total mass of $4.49 \pm 1.11\ M_\odot$ was obtained.

According to different references, the combined spectral type is A0V (Palmer et al. 1968; Kennedy 1983; Bartkevicius & Lazauskaite 1997), A1V (Abt & Morrell 1995) or A3Vn (Cowley et al. 1969). Since in the literature the individual spectral types were not found, I determined them from the differential magnitude (+2.17 from *Hipparcos*) and the combined spectral type of Cowley et al. (1969) using the tables published by Christy & Walker (1969) and Edwards (1976). Spectral types of B8V/A2V and F1V/F4V were determined for the primary and secondary.

From *Hipparcos* apparent magnitudes and parallaxes, the absolute magnitudes, corrected for the reddening calculated in this paper ($E(B-V) = 0.06$) were determined (-0.48 ± 0.14 and $+1.49 \pm 0.14$). The primary component could be a subgiant star of an age of about 500 Myr and it has been suspected to be a spectroscopic binary but not confirmed. The absolute magnitude of the secondary is about 1.5 magnitudes brighter than that of an F1V/F4V star.

From the spectral types of the literature, stellar masses of 2.61 and 1.40 $M_\odot$ were calculated using Allen's tables (1973). The sum of the masses is 4.01 $M_\odot$ in agreement, within errors, with the total mass calculated using orbital parameters and the *Hipparcos* parallax.

The dynamic parallax is 7.0 mas. Individual masses of 3.32 and 1.87 $M_\odot$ were determined using the Baize-Romani method (1946).

The secondary component is catalogued as the suspected variable star NSV14396. Frolov (1970) included it in a list of Delta Scuti stars, although is not clear if the variable is the main or the secondary component.

Age and Stellar Population. Bartkevicius & Gudas (2002) obtained a peculiar velocity of $(U,V,W) = (-13.94, -1.26, -7.44)$ km s^{-1}. According to Eggen's diagrams (1969a,b) BU 1147 AB is a member of the young Galactic disk. A value of 0.07 for fG corresponds to young-medium age thin disk stars about 3 – 4 Gyr old.

5. STUDY OF WIDE COMPANIONS

The astronomical literature was consulted in order to obtain photometric, astrometric and kinematic data. VizieR, Simbad (Wenger et al. 2003) and the "services abstract" tools were used from the website of Centre De Données Astronomiques de Strasbourg. Photometry in the B, V and I bands came from the *Hipparcos* (ESA 1997) and *Tycho*-2 catalogs (Høg et al. 2000). Infrared J, H and K photometry came from the Two Micron All Sky Catalogue (Cutri et al. 2000), hereafter 2MASS. The proper motions were taken from the *Tycho*-2 Catalogue. This catalog was chosen because the *Hipparcos* proper motions could be affected by Keplerian motion due to its smaller baseline. Historical astrometric data were kindly supplied by Mason. Spectral types and other astrophysical data were taken from other sources.

The details about the process to estimate spectral types and luminosity classes for the companions, the calculation of interstellar reddening, determination of the nature for the stellar systems, the expected semiaxis major and the orbital period were explained in detail in Rica (2008) and Benavides et al. (2010).

5.1. *The criterion of Halbwachs*

Several criteria were used to determine if the wide components are gravitationally bound. These criteria were commented in detail in Rica (2008) and Benavides et al. (2010). In this paper we use also the criterion of Halbwachs (1986) who presented a search of common proper motion systems among AGK 3 star. The selection of physical systems was based upon the ratio between the angular separation (ρ), and the proper motion (μ), which he called T. T is the time after which a system has covered on the sky a distance equal to ρ. Because of the inaccuracy in proper motion of the AGK 3 catalog, Halbwachs studied pairs with $\mu \geq +50$ mas yr^{-1} and listed all the pairs with $T < 1000$ years in a table, where optical pairs were estimated to be 1 percent.

5.2. *A 1223 C*

The component C is a star with a 13.5 magnitude (Rapaport et al. 2001) which was measured for the first time by Aitken (1906) in 1905 when the angular separation was $1.60''$ (in direction of $349°$) from the AB close pair. Since 1905 it has been measured on 10 occasions, last in 2000 from the 2MASS catalog when the angular separation was $11.87''$ (in direction of $39.4°$).

Using magnitude r from the Carlsberg Meridian Catalog Number 14 (CMC 2006, hereafter CMC14) and JHK from 2MASS, I determined the V magnitude for C using the following relation (John Greaves, private communication):

$$V = 0.6 \times (J - K) + r'_{\rm CMT} - 0.03\,. \qquad (1)$$

Greaves took a large number of V magnitudes from the catalog "$UBVRI$ photometry of faint field stars" (Skiff 2007),[3] and matched them against CMC14 plotting $V - r'_{\rm CMT}$ and $J - K_{\rm s}$. The expression (1) is only valid for $-0.2 < J - K < 1.2$ and $9 < r'_{\rm CMT} < 14$. The standard deviation for V calculated in this way is 0.06 magnitudes. A V magnitude of 13.32 was calculated for component C in agreement with Rapaport's value.

The Catalog of Rectilinear Elements (Hartkopf et al. 2006) lists a relative motion of C with respect to AB of $\Delta x = +87.9 \pm 0.7$ mas yr^{-1} and $\Delta y = +79.5 \pm 1.0$ mas yr^{-1}. The proper motion of C is not listed in the literature so I calculated it using the proper motion of AB and the relative motion of C: $\mu(\alpha) = +4.5 \pm 1.4$ mas yr^{-1} and $\mu(\delta) = -6.1 \pm 1.6$ mas yr^{-1}.

In this work a spectral type of F2 was obtained based on $VJHK$ photometry. No spectral type information was founded in literature.

According to the very different proper motions (much greater than 3σ) of C and AB, this component is not gravitationally bound to AB system and so it is an optical companion. This pair must be flagged with "U" code ("*Proper motion or other technique indicates that this pair is non-physical*") in the Note column of the WDS Index Catalog.

5.3. *RST 5568 C*

This is a star with 11.66 magnitude (average of historical photometries from WDS catalog) at about $2.0''$ from A 1342 AB. It was measured first in 1938 by van den Bos (1938) when the angular separation was $1.88''$ from the AB close pair. Since then, it has been measured 12 times, last in 1976 by Worley (1978) when the angular separation was $1.96''$.

I calculated the relative motion of C with respect to AB: $\Delta x = -2.8 \pm 1.3$ mas yr^{-1} and $\Delta y = -0.8 \pm 1.3$ mas yr^{-1}. The baseline of the 12 measures used was only 38 years. The proper motion of C was not listed in the literature so we calculated it using the proper motion of AB and the relative motion: $\mu(\alpha) = -31.6 \pm 2.4$ mas yr^{-1} and $\mu(\delta) = -16.8 \pm 2.5$ mas yr^{-1}.

No spectral type was found in the literature and I did not estimate it due to the lack of photometric and astrometric data. If this wide companion were gravitationally bound to AB then it would be a K2V star.

In order to determine the nature of the wide C component, two tests, based on probability theory were used. Using the work of Ciardullo et al. (1999)

[3] `http://cdsarc.u-strasbg.fr/viz-bin/Cat?II/277`.

the probability P that a star of 11.66 magnitude could be located by chance at a distance of 1.9″ from another star is 0.003 percent. In a list of optical pairs studied by LIADA, no optical double was found with $P < 0.09$, so component C is likely bound to the AB pair.

Grocheva & Kiselev (1998) propose to use the real distribution of proper motions for estimating P. In this work if $P < 0.01$ the pair is considered physical. The value of P for RST 5568 AB-C is 0.002, and so the component C is surely bound to the AB close pair.

Based on a normal distribution there is a probability of 55 percent that RST 5568 AB-C is a common proper motion pair. The parameter T of Halbwachs is 56 years and so this system is likely be physical according to this criterion.

I calculated a hypotetical parallax, $\pi_{\rm hyp}$, for the stellar system of 0.0062 mas (160.2 pc) in good agreement with the *Hipparcos* parallax of 0.0072 ± 0.0008 mas ($138.9^{+17.4}_{-13.9}$ pc). So the C component is likely bound to the AB close binary.

The expected semimajor axis would be 260 UA and the orbital period $\sim 1,900$ yrs (assuming a circular and face-on orbit). The expected semimajor axis was calculated using the expression obtained by Fischer & Marcy (1992) The arc covered by this component is only 2.7 degrees. If we take into account this angular motion this binary completes a orbit in about $\sim 5,000$ yrs.

5.4. *BU 1147 C*

The component C was added to the system BU 1147 AB in 1911 by Burnham (1913) when he observed a star of 13.6 magnitude at 90.55″ from the close pair, in direction 191.6°. Since 1911 it has been measured only 4 times, last in 1998 (195.1° and 91.53″, from 2MASS).

In order to obtain a modern estimate for the magnitude of C, photographic catalogs were used. The photometric data of the Guide Star Catalogue 1.2 (hereafter GSC) was calibrated, using *Tycho*-2 stars for the region of the sky where the component C is located. In this part of the sky, GSC photometry is 0.15 magnitude brighter than the V band. A magnitude $V = 13.17 \pm 0.16$ was calculated. From B and R photometric data of the USNO-B1.0 catalog, a value of $V = 13.35 \pm 0.30$ was obtained using the expression

$$V = B_j - 0.46 \times (B_j - R_f)\,, \qquad (2)$$

cited in Lépine, Rich, & Shara (2005). From $B1$ and $R1$ photometry of USNO-B1.0 a magnitude $V = 13.0 \pm 0.5$ was obtained. In this case I used the expression determined by Greaves (2008),[4]

$$V = 0.444 \times B1 + 0.556 \times R1\,. \qquad (3)$$

A weighted mean gave a $V = 13.19 \pm 0.21$.

No spectral type information was found in the literature. From the V magnitude and the J, H and K magnitudes listed in 2MASS, I determined a spectral type of K2-4. A giant nature was rejected because then the tangential velocity would be about 280 km s^{-1} and this is an unlikely value. So I conclude that the C component is a K3V dwarf at about 175 pc. I estimated an interstellar reddening of 0.08 for the $B - V$ color. The spectral type of K3V is corrected for this effect.

The proper motion of C listed in the UCAC-2 catalog is $\mu(\alpha) = -5.3 \pm 5.6$ mas yr^{-1} and $\mu(\delta) = -5.1 \pm 5.6$ mas yr^{-1}. The USNO-B1.0 catalog lists $\mu(\alpha) = -6 \pm 1$ mas yr^{-1} and $\mu(\delta) = -4 \pm 2$ mas yr^{-1}.

Using historical measures, a weighted linear fit was performed to calculate a relative motion of C with respect to AB of $\Delta x = -70.7 \pm 2.7$ mas yr^{-1} and $\Delta y = -2.9 \pm 2.3$ mas yr^{-1}. The baseline of the 4 measures used was 87 years. From the proper motion of AB and relative motion of C, I calculated a proper motion $\mu(\alpha) = -11.8 \pm 2.9$ mas yr^{-1} and $\mu(\delta) = -9.2 \pm 2.5$ mas yr^{-1} for C.

In view of the very different proper motions (much greater than 3σ) of C and AB, this component is not gravitationally bound to the AB system and so it is an optical companion. This pair must be flagged with "U" code (*"Proper motion or other technique indicates that this pair is non-physical."*) in the Note column of the WDS Index Catalog.

5.5. *LYS 25 D*

The component D was added to the system BU 1147 AB in 1984 by Louys (1987) when he took a photograph with an astrograph and observed a star of 12.1 magnitude (inferred from the differential magnitude obtained by Louys) at 142.79″ from the close pair, in direction 282.7°. Three more measures were added to WDS from the Washington Fundamental Catalog (WFC) and 2MASS. The most recent measure has an epoch of 1998.78 (282.9° and 142.48″).

In order to obtain a more accurate estimate for the magnitude of D, the photometric data from the GSC catalog were calibrated using *Tycho*-2 stars, for the region of the sky where component D is located.

[4] `http://www.aerith.net/astro/color_conversion.html`.

In this part of the sky, GSC photometry is 0.15 magnitude brighter than V band and thus a magnitude $V = 10.68 \pm 0.16$ was calculated.

From the magnitude r from CMC14 and JHK from 2MASS, I determined the V magnitude for D using the relation of John Greaves (private communication) commented in this work for A 1223 C. A V magnitude of 10.87 ± 0.06 was calculated for component D.

The *TASS Mark IV Photometric Survey of the Northern Sky* (Droege et al. 2006) lists 30 photometric points in the V and I bands for component D with mean magnitudes $V = 10.97 \pm 0.21$ and $I = 9.57 \pm 0.26$. From the three values for V, a weighted mean gave $V = 10.85 \pm 0.08$.

No spectral type information was found in the literature. From the V and I magnitudes from TASS and the J, H and K magnitudes listed in 2MASS (in addition to kinematic data), I determined that component D is a K1III giant located at a distance of about 950 pc. This spectral type was corrected for the reddening ($E(B-V) = 0.19$) which was calculated in this work.

The TASS catalog lists a Welch-Stetson (Welch & Stetson 1993, hereafter WS) variability index of 40.28. The WS index is a normalized measure of the degree of correlation of V-band and I-band variations from their mean values. The variability index will be close to zero for stars with random variations which are independent in each passband, or stars which vary by less than the uncertainty of each measurement. It will be a large (greater than 2 or 3) positive value for stars which really do change significantly in brightness. Nothing is listed in *The International Variable Star Index (VSX)* so component D is likely to be an uncatalogued variable star.

The proper motion of D listed in the UCAC-2 catalog is $\mu(\alpha) = +6.8 \pm 1.0$ mas yr^{-1} and $\mu(\delta) = -1.4 \pm 0.8$ mas yr^{-1}.

Tycho-2 lists for the close AB pair a proper motion of $\mu(\alpha) = +58.9 \pm 1.0$ mas yr^{-1} and $\mu(\delta) = -6.3 \pm 1.0$ mas yr^{-1}. In view of the very different proper motions (much greater than 3σ) D is not gravitationally bound to the AB system and so it is an optical companion. This pair must be flagged with "U" code (*"Proper motion or other technique indicates that this pair is non-physical."*) in the Note column of the WDS Index Catalog.

6. SEARCH FOR NEW BOUND COMPANIONS

SIMBAD and VizieR tools were used to find uncatalogued bound companions consulting astrometric catalogs and photographics plates. First I searched for common proper motion companions. For nearby stars I searched for bound companions by plotting the neighbour stars in a color-magnitude diagram where apparent 2MASS $J-K$ and K data are plotted. A dwarf sequence at the distance of the target was also plotted. So dwarf companion candidates must be located on or near this dwarf sequence. Subdwarf or white dwarf companions will not be detected unless we use reduced proper motion diagrams. Giant companions will be bright enough to be detected and they will be located well above the dwarf sequence.

The expression of Abt (1988) which relates stellar masses of the primary with the maximum projected separation (in AU) was used to define the sky region to search. I selected companion candidates consulting 2MASS where only stars located within the search region and with a $S/N > 10$ were selected.

6.1. *Two Stars in the Vicinity of HDS 433*

In the search for uncatalogued companions I found two red dwarfs with high proper motion. Although these two stars are not bound to HDS 433 AB I studied their astrophysical properties. At coordinates AR $= 03^h\,26^m\,59.66^s$ and DEC $= +9^\circ\,49'\,04''$ I found an M1.5V dwarf of magnitude $V = 15.36$ (from the catalog GSC-2.3) located at 125 pc. Using astrometry from USNO-A2.0 and 2MASS for the epochs 1949.882 and 1999.935 I calculated a proper motion $\mu(\alpha) = +16$ mas yr^{-1} and $\mu(\delta) = +94$ mas yr^{-1}. At coordinates AR $= 03^h\,27^m\,40.17^s$ and DEC $= +09^\circ\,44'\,58''$ I found a M3V dwarf of magnitude $V = 14.84$ (from the catalog GSC-2.3) located at 46 pc. The USNO-B1.0 catalog lists a proper motion $\mu(\alpha) = +44 \pm 1$ mas yr^{-1} and $\mu(\delta) = -112 \pm 2$ mas yr^{-1}.

7. CONCLUSIONS

I have presented the first orbital solution for HDS 433 (8 measures covering 116 degrees) and updated orbital solutions for 7 binaries in addition to the masses.

Data from the literature were consulted and an astrophysical study was carried out. The B9V primary component of HDS 433 is a short period triple spectroscopic system. The sum of the masses for this young stellar system is 13.4 $M_\odot$. Strom et al. (2005) determined an age of only $12-15$ Myr.

A 1342 AB is the magnetic α CVn variable star cataloged as KU Hya while A 2988 is a Delta Scuti cataloged as NSV 24547.

Wide components were studied astrophysically. For A 1223 C, a value for the V magnitude of 13.32

was obtained. The proper motion and spectral type (F2) of C were determined for the first time. Based in the large difference in the proper motions, the component C is not bound to AB close binary.

RST 5568 C, the wide component of A 1342 AB, has not been resolved since 1976. The relative motion of C with respect AB was calculated. The proper motion of C was determined for the first time. According to the same tests, I concluded that C is likely to be bound to the AB close binary. The orbital period ranges from $1900 - 5000$ years.

I searched for new bound companions to the close binaries. No new companion was detected. However, two uncatalogued red dwarfs with high proper motion were discovered.

REFERENCES

Abt, H. A. 1981, ApJS, 45, 437

———. 1988, ApJ, 331, 922

Abt, H. A., & Morrell, N. I. 1995, ApJS, 99, 135

Aitken, R. G. 1906, Lick Obs. Bull., 4, 4

———. 1918, Lick Obs. Bull., 9, 132

———. 1929, Lick Obs. Bull., 14, 62

Allen, C. W. 1973, Astrophysical Quantities (London: Athlone Press)

Baize, P. 1955, J. Obs., 38, 37

———. 1958, J. Obs., 41, 163

———. 1974, A&AS, 13, 65

Baize, P., & Romani, L. 1946, Ann. d'Astrophys., 9, 13

Balega, I. I., Balega, Y. Y., Hofmann, K.-H., Malogolovets, E. V., Schertl, D., Shkhagosheva, Z. U., & Weigelt, G. 2006, A&A, 448, 703

Balega, I. I., et al. 2002, A&A, 385, 87

Bartkevicius, A., & Gudas, A. 2002, Baltic Astron., 11, 153

Bartkevicius, A., & Lazauskaite, R. 1997, Baltic Astron., 6, 499

Benavides, R., Rica, F., Reina, E., Castellanos, J., Naves, R., Lahuerta, L., & Lahuerta, S. 2010, JDSO, 6, 30

Burnham, S. W. 1894, Publ. Lick Obs., 2, 153

———. 1913, Measures of Proper Motion Stars Made with the 40-Inch Refractor of the Yerkes Observatory in the Years 1907 to 1912 (Washington: Carnegie Institution of Washington)

Buscombe, W. 1998, 13th General Catalogue of MK Spectral Classification (Evanston: Northwestern Univ.)

Buscombe, W., & Foster, B. E. 1995, 12th General Catalogue of MK Spectral Classification (Evanston: Northwestern Univ.)

Cannon, A. J., & Pickering, E. C. 1918–1924, The Henry Draper Catalogue and Extension 1, Ann. Astron. Obs. Harvard College, Vols. 91–100

Christy, J. W., & Walker, R. L. 1969, PASP, 81, 643

Ciardullo, R., Bond, H., Sipior, M. S., Fullton, L. K., Zhang, C.-Y., & Schaefer, K. G. 1999, AJ, 118, 488

CMC (Copenhagen Univ. Obs., Inst. of Astronomy Cambridge, UK, & Real Instituto y Observatorio de La Armada, F. E. S.) 2006, VizieR Online Data Catalog, 1304, 0 (CMC14)

Cowley, A., & Cowley, C. 1965, PASP, 77, 184

Cowley, A., Cowley, C., Jaschek, M., & Jaschek, C. 1969, AJ, 74, 375

Cutri, R. N., et al. 2000, Explanatory Supplement to the 2MASS Second Incremental Data Release, `http://www.ipac.caltech.edu/2mass/releases/second/doc/explsup.html`

Docobo, J. A., & Ling, J. F. 2003, A&A, 409, 989

Droege, T. F., Richmond, M. W., Sallman, M., & Creager, R. P. 2006, PASP, 118, 1666

Duflot, M., Figon, P., & Meyssonnier, N. 1995, A&AS, 114, 269

Edwards, T. S. 1976, AJ, 81, 245

Eggen, O. J. 1969a, PASP, 81, 741

———. 1969b, PASP, 81, 553

———. 1969c, R. Greenwich Obs. Bull., 137, 165

Ekenberg, B. 1945, Lund Medd. Astron. Obs. Ser. II, 116, 130

ESA 1997, The Hipparcos and Tycho Catalogues ESA sp-1200 (Noordwijk: ESA)

Finsen, W. S. 1976, IAUDS, Inf. Circ., 69

Fischer, D. A., & Marcy, G. W. 1992, AJ, 396, 178

Frolov, M. S. 1970, Inf. Bull. Variable Stars, 427, 1

Glebocki, R., Gnacinski, P., & Stawikowski, A. 2000, Acta Astron., 50, 509

Grenier, S., et al. 1999, A&AS, 137, 451

Grenon, M. 1987, J. Astrophys. Astron., 8, 123

Grocheva, E., & Kiselev, A. 1998, in ASP Conf. Ser. 145, Astronomical Data Analysis Software and Systems VII, ed. R. Albrecht, R. N. Hook & H. A. Bushouse (San Francisco: ASP), 15

Halbwachs, J. L. 1986, A&AS, 66, 131

Hartkopf, W. I., & Mason, B. D. 2001, Sixth Catalog of Orbits of Visual Binary Stars, `http://ad.usno.navy.mil/wds/orb6.html`

Hartkopf, W. I., Mason, B. D., & Rafferty, T. J. 2008, AJ, 135, 1334

Hartkopf, W. I., Mason, B. D., Wycoff, G. L., & Kang, D. 2006, Catalog of Rectilinear Elements, `http://ad.usno.navy.mil/wds/lin1.html`

Hartkopf, W. I., McAlister, H. A., & Franz, O. G. 1989, AJ, 98, 1014

Hartkopf, W. I., et al. 2000, AJ, 119, 3084

Heintz, W. D. 1978, Double Stars (Dordrecht: Kluwer)

———. 1979, ApJS, 41, 549

———. 1981, ApJS, 45, 559

Hensberge, H., et al. 1981, A&AS, 46, 151

Henry, T. J., Ianna, P. A., Kirkpatrick, J. D., & Jahreiss, H., 1997, AJ, 114, 388

Høg, E., et al. 2000, AJ, 355, L27

Horch, E. P., van Altena, W. F., Cyr, W. M., Kinsman-Smith, L., Srivastava, A., & Zhou, J. 2008, AJ, 136, 312

Hough, G. W. 1890, Astron. Nachr., 125, 1

Houk, N. 1982, Michigan Catalogue of Two-Dimensional Spectral Types for the HD Stars, Vol. 3 (Ann Arbor: Univ. Michigan Dept. Astron.)
Houk, N., & Swift, C. 1999, Michigan Catalogue of Two-Dimensional Spectral Types for the HD Stars, Vol. 5 (Ann Arbor: Univ. Michigan Dept. Astron.)
Irwin, A. W., Yang, S. L. S, & Walker, G. A. H. 1996, PASP, 108, 580
Jaschek, M. 1978, Bull. Inf. CDS, 15, 121
Kennedy, P. M. 1983, MK Classification Catalog Extension (Weston Creek: Mt. Stromlo & Siding Spring Obs.)
Lépine, S., Rich, R. M., & Shara, M. M. 2005, ApJ, 633, L121
Louys, L. 1987, Bull. Astron. Obs. R. Belg., 10, 129
Mason, B. D., Douglass, G. G., & Hartkopf, W. I. 1999a, AJ, 117, 1023
Mason, B. D., et al. 1999b, AJ, 117, 1890
Montes, D., López-Santiago, J., Gálvez, M. C., Fernández-Figueroa, M. J., De Castro, E., & Cornide, M. 2001, MNRAS, 328 ,45
Nordstrom, B., et al. 2004, A&A, 419, 989
Palmer, D. R., Walker, E. N., Jones, D. H. P., & Wallis, R. E. 1968, R. Obs. Bull., 135, 385
Rapaport, M., et al. 2001, A&A, 376, 325
Rica, F. 2006a, IAUDS, Inf. Cir., 159
__________. 2006b, IAUDS, Inf. Circ., 160
__________. 2007, IAUDS, Inf. Circ., 162
__________. 2008, RevMexAA, 44, 137
Rufener, F. 1981, A&AS, 45, 2, 207
Scardia, M., Prieur, J.-L., Aristidi, E., & Koechlin, L. 2000, ApJS, 131, 561
Seymour, D. M., Mason, B. D., Hartkopf, W. I., & Wycoff, G. L. 2002, AJ, 123, 1023
Soderblom, D. R., & Mayor, M. 1993, AJ, 105, 226
Starikova, G. A. 1981, Sov. Astron. Lett., 7, 130
Strom, S. E., Wolff, S. C., & Dror, D. H. A. 2005, AJ, 129, 809
Tokovinin, A. A. 1985, A&AS, 61, 483
__________. 1997, A&AS, 124, 75
van den Bos, W. H. 1928, Ann. Leiden Obs., 14, 4
__________. 1938, Tashkent Union Obs. Circ., 24, 481
van Leeuwen, F. 2007, A&A, 474, 653
Voronov, N. 1934, TashKent Obs. Circ. N 24
Welch, D. L., & Stetson, P. B. 1993, AJ, 105, 1813 (WS)
Wenger, M., et al. 2003, SIMBAD Astronomical Database, http://simbad.u-strasbg.fr/simbad/
Worley, C. E. 1978, Publ. US Naval Obs., 24, Part 6
Zombeck, M. V. 1990, Handbook of Space Astronomy and Astrophysics (Cambridge: Cambridge Univ. Press)

Francisco Rica Romero: Agrupación Astronómica de Mérida, C/José Ruiz Azorín, 14, 4 D, 06800, Mérida, Spain and Liga Iberoamericana de Astronomía (LIADA), Av. Almirante Guillermo Brown, 4998, 3000 Santa Fe, Argentina (frica0@gmail.com).

Revista Mexicana de Astronomía y Astrofísica, **46**, 279–290 (2010)

SPECTRAL VARIABILITY OF ROMANO'S STAR

O. Maryeva,[1, 2] and P. Abolmasov[3]

Received 2010 February 3; accepted 2010 June 10

RESUMEN

Combinamos observaciones espectroscópicas de archivo de la estrella LBV V532 (conocida como Estrella de Romano) con fotometría en la banda B. Los datos espectroscópicos cubren un intervalo de 15 años, desde 1992 hasta 2007. Mostramos que en máximo de brillo el objeto se comporta como una supergigante con líneas de emisión, mientras que en mínimo V532 se mueve a lo largo de la secuencia de las estrellas WN tardías. En este sentido, la estrella tiene un comportamiento similar al de las bien conocidas variables luminosas azules (LBV: luminous blue variables) AG Car y R 127, pero es un poco más caliente en mínimo. Identificamos unas 100 líneas espectrales en el intervalo 3700–7300 Å. Nuestra espectroscopía para este objeto es la más completa en la actualidad. Obtenemos la velocidad del viento usando las líneas del triplete de He I (300 ± 30 km s^{-1}). También estimamos los parámetros físicos de la nebulosidad que rodea a V532.

ABSTRACT

We combine archival spectral observations of the LBV star V532 (Romano's star) together with existing photometric data in the B band. Spectroscopic data cover 15 years of observations (from 1992 to 2007). We show that the object in maximum of brightness behaves as an emission line supergiant while in minimum V532 moves along the sequence of late WN stars. In this sense, the object behaves similarly to the well-known Luminous Blue Variable (LBV) stars AG Car and R127, but is somewhat hotter at the minima. We identify about 100 spectral lines in the $3700 - 7300$ Å wavelength range. As of today, our spectroscopy is the most comprehensive for this object. The velocity of the wind is derived using the He I triplet lines (360 ± 30 km s^{-1}). Physical parameters of the nebula around V532 are estimated.

Key Words: galaxies: individual (M33) — stars: individual (Romano's star) — stars: Wolf-Rayet — supergiants

1. INTRODUCTION

Luminous Blue Variables (LBVs) are a class of rare astrophysical objects introduced by Conti (1984) and remain a subject of intense interest. LBVs are broadly accepted to be very massive and energetic stars emitting close to the Eddington limit, evolving from Of toward Wolf-Rayet stars. However, contemporary evolutionary models do not answer the question about the exact relations between LBV, nitrogen-rich Wolf-Rayet (WN) and hydrogen-rich WN (WNH) stars. Numerical simulations show that the objects may pass the LBV evolutionary stage either before or after the WNH stage (Smith & Conti 2008). Currently, only 35 LBV and LBV candidates are known in our Galaxy (Clark, Larionov, & Arkharov 2005). Studying LBVs in nearby galaxies is very important for understanding stellar evolution and the evolution of the interstellar medium perturbed and contaminated by massive stars at various evolutionary stages.

The object V532 ($\alpha = 01^h35^m09.^s71$, $\delta = +30^\circ41'57''.1$) is located in the outer spiral arm of the M33 galaxy. Giuliano Romano was the first to recover its light curve (Romano 1978) and to find irregular magnitude variations between $16^{\rm m}.7$ and $18^{\rm m}.1$. Romano classified V532 as a variable of the Hubble-Sandage type by the shape of the light curve and

[1]Stavropol State University, Russia.
[2]Special Astrophysical Observatory, Russia.
[3]Sternberg Astronomical Institute, Russia.

TABLE 1

OBSERVATIONAL LOG FOR MPFS DATA. S/N IS SIGNAL-TO-NOISE RATIO PER RESOLUTION ELEMENT

Date	Exposure time (s)	Seeing ($''$)	S/N	Spectral standard star	Spectral range (Å)
05 10 2002	900	3.8	16	BD25d4655	4250–6700
13 11 2004	4200	1.5	20	HZ44	4000–7000
17 01 2005	3600	1.5	18	G248	4000–7000

its colour index. Humphreys & Davidson (1994) on the basis of its light variations classified the star as an LBV candidate. Two maxima of brightness were detected during the last half of the century (Kurtev et al. 2001). The first was observed around 1970 and the second in the early 1990s (Kurtev et al. 2001). Long-term variability has an amplitude of about $1^{\rm m}$ and seems to be superimposed on an even stronger downward trend. Short-timescale variability with amplitude $\sim 0\overset{\rm m}{.}5$ was discovered in addition to the longer-timescale variability (Kurtev et al. 2001; Sholukhova et al. 2002). Such photometric behavior is typical for an LBV star.

The first optical spectrum was obtained by T. Szeifert (1996) at the 3.5 m Calar Alto telescope in 1992. In this spectrum, “few metal lines are visible, although a late B spectral type is most likely (faint HeI)”. This spectrum, obtained with the TWIN spectrograph of the Calar Alto telescope, is unique in being obtained in a profound flare state. It is drastically different from the hot spectra observed at the minima of brightness (see below).

Another spectrum was obtained by O. Sholukhova at the 6 m telescope of the Special Astrophysical Observatory (SAO) of the Russian Academy of Sciences (RAS) in 1994 (Sholukhova et al. 1997). Another spectrum was obtained at SAO with the Multi-Pupil Fiber Spectrograph (MPFS) in September 1998. This spectrum was classified as WN10–WN11 Fabrika et al. (2005). Polcaro et al. (2003) estimated the bolometric absolute magnitude of the object as $M_{\rm bol} \simeq -10\overset{\rm m}{.}4$, using a bolometric correction “of at least –3 mag” and the distance modulus $m - M = 24\overset{\rm m}{.}8$. They classify V532 as an LBV because the object fulfills all the criteria of Humphreys & Davidson (1994). Using five spectra obtained in 2003–2006, Viotti et al. (2006, 2007) find an anti-correlation between equivalent widths of the Wolf-Rayet blue bump at 4630–4686 Å and visual luminosity.

Comparing the spectra published by Szeifert (1996), Fabrika et al. (2005) and Viotti et al. (2007), we find that the object changes its spectral properties significantly.

Here we combine the spectral observations (both new and already published) with the light curve of the object to trace the spectral variability of the star. We describe the data and data reduction process in the next section. Results are presented in § 3 and discussed in § 4. In § 5, we present the conclusions.

2. OBSERVATIONS AND DATA REDUCTION

In this work, we use archival data from the 6m SAO telescope[4] and the SUBARU telescope, which is operated by the National Astronomical Observatory of Japan. The 6 m telescope data were obtained with the Multi Pupil Fiber Spectrograph (MPFS) (Afanasiev, Dodonov, & Moiseev 2001) and with the SCORPIO multi-mode focal reducer in the long-slit mode (Afanasiev & Moiseev 2005). The data from SUBARU were obtained with the Faint Object Camera (FOCAS) (Kashikawa et al. 2002) in the Cassegrain focus. Uncertainties are everywhere dominated by statistical Poissonian noise (readout noise and round-off errors are significantly smaller).

2.1. *MPFS Data*

MPFS obtains simultaneously the spectra from 240 (16×15) or 256 (16×16) spatial sampling elements arranged in the form of a rectangular array of square lenses. In 2002 and 2004–2005, the data were obtained in the 240-element and 256-element configurations, respectively. Spatial sampling of $1'' \times 1''$ was used. Light from individual sampling elements is collected by microlenses and transmitted by means of optical fibers reorganized in the form of a pseudo-slit toward the spectral camera. Grating # 4 (600 Å pix^{-1}) providing a spectral resolution of about 6 Å was used for all the observations. Detectors CCD TK 1024 (1024×1024 pixels) and EEV42-40 (2048×2048 pixels) were used in 2002 and 2004–2005, respectively. A sky background spectrum at a distance of $4''$ away from the

[4] Available via ASPID database `http://alcor.sao.ru/db/aspid/`.

TABLE 2

OBSERVATIONAL LOG FOR THE SCORPIO DATA. α IS SEEING, PA IS POSITION ANGLE, S/N IS SIGNAL-TO-NOISE RATIO

Date	Exposure time (s)	Grism	Spectral range (Å)	$\delta\lambda$ (Å)	S/N	$\alpha('')$	Spectral standard star	PA (°)
06 02 2005	600				8	1.7	G248	−136
30 08 2005	1200	VPHG550G	3500–7200	10	30	1.9	G191-B2B	210
08 11 2005	3300				45	1.9	BD25d4655	145
03 08 2006	1500				20	2	GD248	200
10 08 2007	1800	VPHG1200G	4000–5700	5	24	2	BD33d2642	252
05 10 2007	2700				40	1.1	BD25d4655	−141
08 01 2008	1800	VPHG1200R	5700–7500	5	20	2.1	BD25d4655	48
10 01 2008	1800	VPHG1200G	4000–5700	5	20	1.4	BD25d4655	18

object is taken simultaneously with the object by 17 (for 16 × 16 field size) or 16 (for 16 × 15 configuration) additional fibres. We summarize the relevant information on the MPFS data in Table 1.

The data reduction system was written in the IDL environment and makes use of procedures written by V. Afanasiev, A. Moiseev and P. Abolmasov. The reduction process consists of the standard steps for panoramic data reduction (see for example Sánchez 2006): bias subtraction, flat-fielding, removal of cosmic-ray hits, extraction of the individual spectra from the frames and their wavelength calibration using the spectrum of a He-Ne-Ar lamp. At every wavelength, we calculate the median sky level using the offset fibres and subtract from the spectra of the field. Spectra of spectrophotometric standard stars were used for absolute flux calibration.

Three emission-line spectra obtained with MPFS in 2002–2005 were used. We estimate the signal-to-noise ratio in continuum as 10–30 per resolution element (see Table 1 for details). Integral spectra were extracted in an annular aperture 2″ in radius. Up to the instrumental resolution, the object is point-like. Note that, unlike long-slit spectrographs, MPFS being free from slit losses and absolute flux calibration, is much more reliable.

2.2. *SCORPIO Data*

Observational data from SCORPIO are summarized in Table 2. All the spectra were reduced using the `ScoRe` package for long-slit data reduction, written in IDL[5]. CCD frames were de-biased, cosmic

[5]Available at `http://narod.ru/disk/24196358000/Score_v1.2.tar.html`.

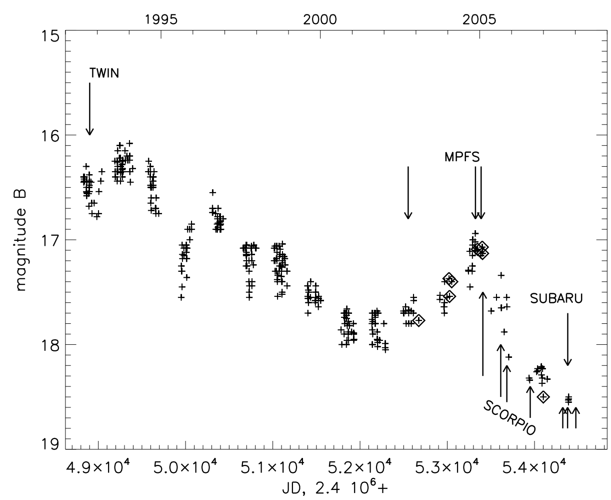

Fig. 1. *B*-band light curve of V532. Arrows indicate when spectroscopic observations were made. Data from (Viotti et al. 2007) are shown by diamonds.

particle hits were removed from all types of exposures except bias. Save for the single 10 minute long exposure obtained in February 2005, several object exposures are present for every day, which simplifies the removal of cosmic hits. Then we divide object and spectral standard exposures over the normalized mean flat-field frame. After wavelength calibration using He-Ar-Ne lamps and night sky OI (λ 5577 or λ 6300 depending on grism) emission lines, the CCD data were flux-calibrated using standard stars from Oke's (1990) spectrophotometric standard list (see Table 2). Spectra were extracted by fitting the profiles of slices across dispersion with a Gaussian function.

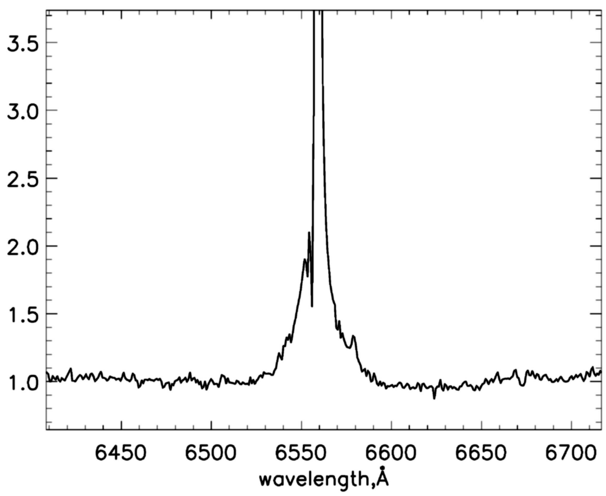

Fig. 2. Hα line profile in the Calar Alto spectrum obtained in 1992. The spectrum is normalized by the local continuum level.

In total, eight spectra were obtained with SCORPIO in 2005–2008 (dates of observations are shown by upward arrows in Figure 1). The spectral resolution is 10 Å (for VPHG550G grism) and 5 Å (for VPHG1200G and VPHG1200R grisms), the signal-to-noise ratios of the continuum vary from about 10 to about 50 for larger total exposures.

2.3. *Data from SUBARU*

One exposure 1200s in length was obtained with the SUBARU telescope on October 2007. The VPHG450 grism was used providing the spectral range of 3750–5250 Å. A slit width of $0\farcs5$ implies a spectral resolution of about 1.7 Å (currently, it is the best resolution achieved for this object) in the extracted spectrum. Data were reduced using IDL-based software. The CCD frames were bias-subtracted and flat-fielded. We used the Th-Ar arc spectrum for wavelength calibration. Star BD40d4032 from the SUBARU spectrophotometric standard list was used to calibrate the stellar spectra. We extracted the spectrum in the same way we did for SCORPIO (see above § 2.2).

If we degrade the spectral resolution to 5 Å, the spectrum becomes practically identical to the spectrum obtained with SCORPIO on the same date. Though the spectral shapes are similar, the spectra differ in normalization (by about a factor of three) connected to slit losses.

2.4. *Photometric Data*

The light curve (see Figure 1) was provided by Vitalij Goranskij and consists of the CCD data obtained by Goranskij and Zharova with the 1 m SAO telescope and two instruments of the Crimean laboratory of the Sternberg Astronomical Institute (SAI), and photographic plates from the SAI collection. CCD data were reduced with MaxIm DL software[6]. The joint light curve will be published by A. V. Zharova et al. (in preparation) in a separate paper, all the details of the data reduction process will be given there. Photographic B-band magnitudes were identified with the B-band magnitudes obtained by CCD observations. CCD data uncertainties are of the order of 0.05 mag, plate data have larger errors depending on the source brightness, usually of the order 0.1–0.2 mag.

The joint curve contains the data of Viotti et al. (2007) but complements them with much larger photometric material and primarily allows to trace the recent evolution of the object.

3. RESULTS

3.1. *Spectral Evolution*

The first optical spectrum of V532 was obtained during the rise of brightness, when the object was $16\fm4$ in the V band. This spectrum covers two spectral ranges $\lambda\lambda$ $4400-5000$ and $\lambda\lambda$ $5800-6750$, as it was obtained with the two-channel TWIN spectrograph[7]. In this spectrum, two strong lines are present, Hα (shown in Figure 2) and Hβ, having complex profiles consisting of a narrow line with P Cyg profile and broad wings. FWHM (Full Width at Half Maximum intensity) of the wings is $\sim$ 15 Å for Hβ and $\sim$ 20 Å for Hα. Such wings were first found for LBVs in the spectrum of P Cygni by Bernat & Lambert (1978). These wings are explained by scattering of line photons by free electrons in the stellar wind. Similar line profiles were observed for the LBV stars R127 and AG Car during the initial rise to maximum (Stahl et al. 1983, 2001).

Emission lines of He I λ 5876 and Si II λ 5957.612, 5978.970, 6347.091, 6371.359 are also present in the red spectrum. Szeifert (1996) mentions these SiII lines as "weak metal emissions".

Figure 3 shows all the spectra of V532 in the blue range (4000–5500 Å) analysed in this article, obtained at different spectral resolutions. All the spectra are normalised to continuum level in a uniform way. In order to get a reasonable normalisation for our spectra, we chose several wavelength intervals practically free from Wolf-Rayet emissions (4250–4270, 5100–5200, 5520–5620, 5750–5800 and

[6]`http://www.cyanogen.com/maxim_main.php`.
[7]A comprehensive description is present at `http://www.caha.es/CAHA/Instruments/TWIN/HTML/twin.html`.

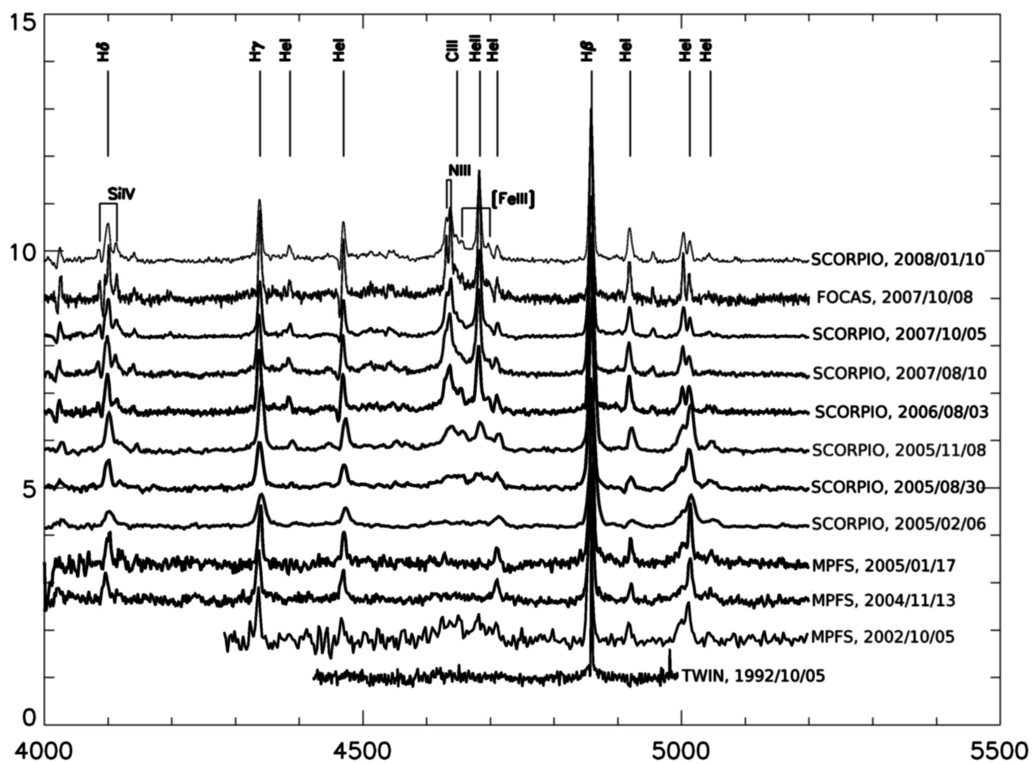

Fig. 3. Optical spectrum evolution in the blue spectral range (4000–5200 Å). Spectra are normalized by the local continuum level and vertically shifted for clarity.

TABLE 3

SPECTRAL CLASSES IDENTIFIED VIA THE SCHEME OF SMITH, CROWTHER, & PRINJA (1994)

B, mag	Spectral subtype	Date
17.5	WN10.5	2002/10/05
16.9	WN11	2004/11/13
17.1	WN11	2005/01/17
17.15	WN11	2005/02/06
17.3	WN10	2005/08/30
17.6	WN9	2005/11/08
18.3	WN8	2006/08/03
18.4	WN8	2007/08/10
18.5	WN8	2007/10/05–08
	WN8	2008/01/08–10

6950–6970 Å) and reconstructed the continuum using a second-order polynomial. Below, for spectral classification we use characteristic equivalent width ratios, which makes our results practically independent of spectral resolution.

The spectral appearance of the spectra of V532 obtained in 2002–2008 resembles that of late WN stars. It allows us to apply a classification scheme used for WN stars, bearing in mind that abundances of individual elements may differ, but physical conditions are similar. All the spectra obtained between 2002 and 2008 were classified using the classification of Smith, Crowther, & Prinja (1994) for WN6-11 stars based primarily on relative strengths of N V $\lambda\lambda$ 4604 − 20, N IV λ 4058, N III $\lambda\lambda$ 4634 − 41 and N II λ 3995 emission lines. The method has low dependence on elemental abundances, though only helium and nitrogen lines (preferably, ratios of the lines of one element) are used. The results of the spectral classification are given in Table 3.

The light curve exhibits a local maximum in 2004 and early 2005. In the spectra obtained in this period, one may observe strong emission lines of hydrogen and neutral helium. The spectral appearance of V532 shows strong similarities with a spectrum of a WN11 star. He I λ 4713 line is stronger than the N II blend, and He II λ 4686 is absent. In the spectrum obtained in 2002, the N II λ 3995 line is outside the spectral range; therefore we carry out the classification comparing N III $\lambda\lambda$ 4634 − 41 and

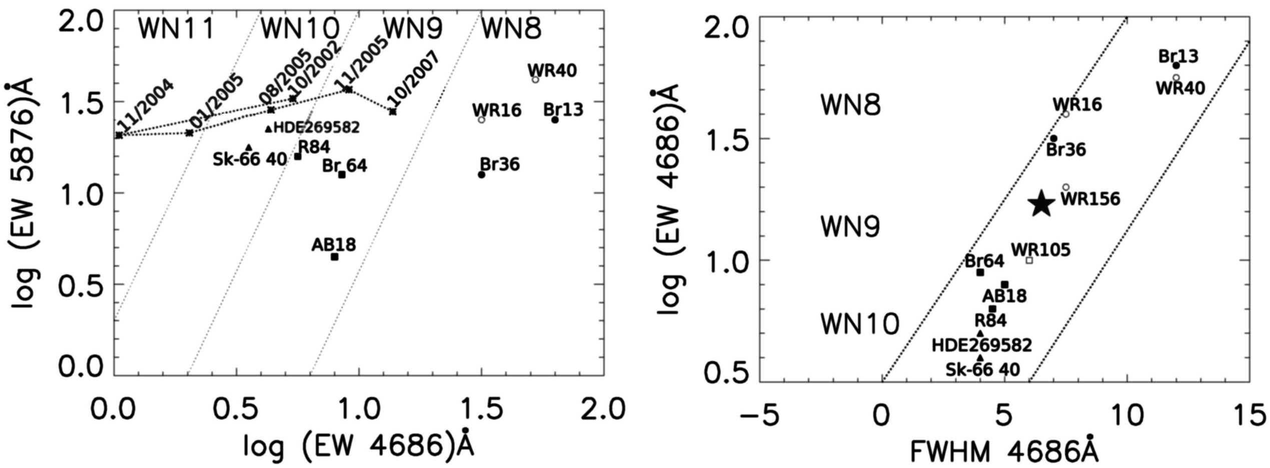

Fig. 4. Left panel: V532 location on the equivalent width diagram of He I λ 5876 versus He II λ 4686 for different dates of observation. The points are connected with dotted lines in chronological order. Right panel: V532 location in October 2007 (FOCAS data) on the equivalent width versus FWHM diagram for the He II λ 4686 line. In both graphs, known Galactic (open symbols) and LMC (filled) WN stars are shown for comparison: WN8 by circles, WN9 by squares, and WN10 by triangles. Data for these objects were taken from Smith et al. (1995).

N II $\lambda\lambda$ 4601 − 43 blends having similar intensity to the N II λ 3995 emission. N III $\lambda\lambda$ 4634 − 41 lines appear, but are weaker than N II $\lambda\lambda$ 4601 − 43. He II λ 4686 line is approximately as bright as the N II $\lambda\lambda$ 4634 − 41 emission; hence we classify the object as WN10.5.

Starting from the middle of 2005, Romano's star weakens in the optical range; its visible magnitude falls from 17 to $18^{\rm m}\!.8$. During this period its spectrum evolves from WN10 (August 2005) through WN9 (November 2005) to WN8 (August 2007) by three spectral sub-classes. In October 2007, He II λ 4686 line is stronger than N III $\lambda\lambda$ 4634 − 41. However, the N IV lines do not appear in the spectrum. We also classify the spectrum as WN8.

The evolution of V532 on the equivalent width diagram of He I λ 5876 versus He II λ 4686 is shown in the left panel of Figure 4. Locations of well-proven Galactic and Large Magellanic Cloud (LMC) Wolf-Rayet stars R84 (WN9), Sk-60 40 (WN10), LBV HDE 269582 (WN10) and some other objects are shown for comparison with our object. The figure shows that in the period between 2002 and 2005, when the star brightened by about one magnitude, its spectrum changed from WN9.5 to WN11. Since 2005, the spectrum has changed smoothly according to the sequence established by Smith, Shara, & Moffat (1996).

We used a quantitative chemistry-independent criterion based on the FWHM of the He II λ 4686 line for an alternative spectral classification. In Figure 4, we show the location of V532 on the diagram of the equivalent width of He II λ 4686 versus the FWHM of this line. We have measured equivalent width and FWHM of the He II line in the FOCAS spectrum. For this, we approximate the Wolf-Rayet blue bump by 7 Gaussians. The position of V532 is fully consistent with its Galactic and LMC WN9 analogues. The spectral class defined from the diagram is consistent with that determined from the relative strengths of N II, N III and He I with an accuracy of about one subclass.

Table 4 shows the lines detected in the spectra obtained with FOCAS (October 2007) and with SCORPIO (January 2008, with grisms 1200G and 1200R). Three spectra are used in order to cover the maximal wavelength range at maximal possible spectral resolution. The spectrum of V532 does not change noticeably from October 2007 to January 2008. Equivalent widths of the principal lines (absorptions, emissions and P Cyg) are given with errors of approximation. Uncertainties due to the choice of the continuum level are smaller than the errors of approximation. Lines with P Cygni profiles were resolved by fitting with the models described in the next subsection.

3.2. *Line Profiles and Terminal Wind Velocity*

In Figure 5 we show the FOCAS spectrum in the optical blue range 3800 − 5100 Å. The Wolf-Rayet blue bump (consisting primarily of N III $\lambda\lambda$ 4634, 4640, C III λ 4650, He II λ 4686 and He I λ 4713) is clearly seen in this spectrum.

TABLE 4

LIST OF EMISSION LINES DETECTED IN THE FOCAS AND SCORPIO (JANUARY 2008) SPECTRA OF V532[a]

λ, Å	Ion	EW emission Å	EW absorption Å	λ, Å	Ion	EW emission Å	EW absorption Å
3770.60	H11+HeII			4613.90	NII		
3797.90	H10+HeII			4621.40	NII		
3819.76	HeI			4630.54	NII		
3835.39	H9+HeII			4634.00	NIII	6.2 ± 1.0	
3871.82	HeI			4640.64	NIII	7.4 ± 0.5	
3889.05	H8+HeI	11 ± 1	3.7 ± 1.3	4643.09	NII		
3964.73	HeI			4650.16	C III	5.0 ± 0.5	
3970.08	Hϵ+HeII			4658.10	[FeIII]	2.5 ± 1.0	
3994.99	NII			4685.81	HeII	15.2 ± 0.2	
4009.00	HeI			4701.50	[FeIII]	2.9 ± 1.0	
4025.60	HeI+HeII	2.5 ± 0.5	1.2 ± 0.2	4713.26	HeI	1.6 ± 0.2	
4088.90	SiIV			4861.33	Hβ	22.5 ± 1.5	
4097.31	N III			4921.93	HeI	4.3 ± 0.2	
4101.74	Hδ+HeII	7.6 ± 1.0		4958.91	[O III]	1.3 ± 0.2	
4103.40	NIII			5006.84	[O III]	3.9 ± 0.6	
4116.10	SiIV			5015.67	HeI	2.6 ± 0.3	
4120.99	HeI			5411.50	HeII	6.2 ± 0.2	
4143.76	HeI			5666.60	NII		
4199.80	HeII			5676.02	NII		
4236.93	NII			5679.56	NII		
4241.79	NII			5686.21	NII		
4241.79	NII			5710.76	NII		
4340.47	Hγ+HeII	8.0 ± 0.3		5875.79	HeI	25.5 ± 0.7	
4387.93	HeI	1.4 ± 1.0		6548.00	[N II]		
4471.69	HeI	5.0 ± 0.3	1.7 ± 0.2	6562.82	Hα+HeII	107 ± 3	
4481.13	MgII			6583.00	[N II]		
4510.90	NIII			6678.15	HeI	18 ± 3	
4514.90	NIII			6683.20	HeII		
4518.20	NIII			7065.44	HeI	18 ± 3	
4523.60	NIII			7135.73	ArIII	3.2 ± 0.3	
4530.80	NIII			7281.35	HeI		
4534.60	NIII						
4541.60	HeII						
4547.30	NIII						
4601.50	NII						
4607.20	NII						

[a]For higher signal-to-noise ratios, equivalent widths (EW) are given. For lines with P Cyg profiles, we give both emission and absorption component EWs.

We suppose that the lines near 4658 and 4701 Å are nebular lines of [Fe III]. They cannot belong to C IV since C IV $\lambda\lambda$ 5812, 5801 lines are not present in the SCORPIO spectrum obtained simultaneously in October 2007.

Analyzing the FOCAS spectrum of V532, we found that triplet and singlet lines of HeI have different profiles (see Figure 6). Triplet lines of He I (λ 3889, 4025, 4471) show strong P Cyg profiles, while singlet lines (λ 3965, 4922, 5016) have

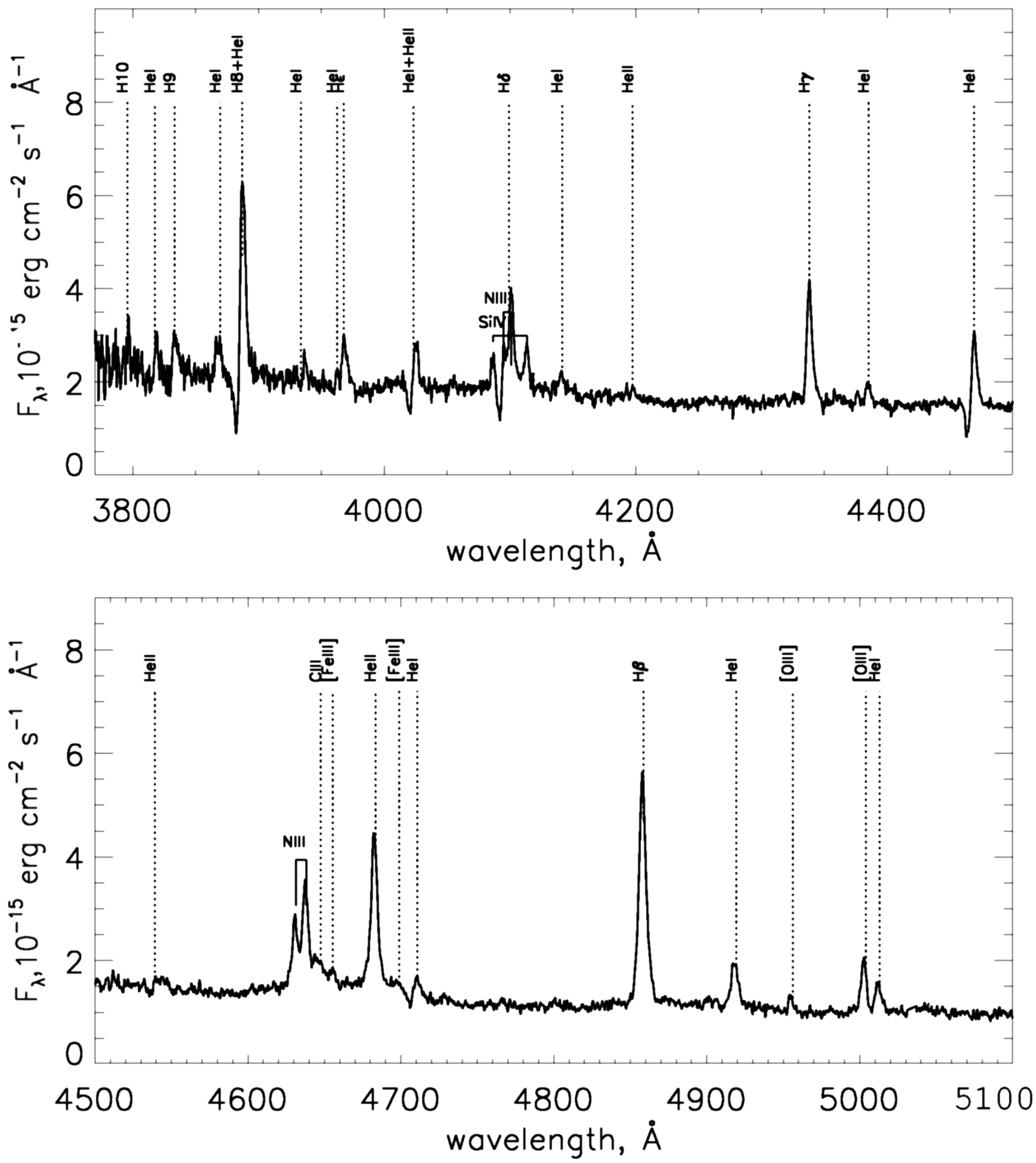

Fig. 5. Optical spectrum of V532 obtained with FOCAS in the range 3800–5100 ÅÅ.

flat-topped profiles. The widths of these lines correspond to a velocity span of about 100 km s^{-1}.

We used P Cyg profiles of triplet HeI lines to estimate the terminal wind velocity v_∞. Line profiles were fitted with a sum of two Gaussians (one representing the absorption, the other the emission component). We suppose that the widths of the emission and absorption components are equal to the instrumental profile width of 1.8 Å which is almost independent of wavelength. The instrumental profile width is determined using wavelength calibration spectrum lines of similar wavelengths. The terminal wind velocity is estimated by the velocity shift between the Gaussian centers. Even for the emission component of He I lines, we do not detect any Doppler broadening. This may mean that the profiles are not true P Cyg but wind blueshifted absorptions plus nebular emissions. This possibility does not however alter the wind velocity estimates.

Wind velocities for all the He I lines with P Cyg profiles are equal within the statistical errors. The mean wind velocity for the three triplet lines is 360 ± 30 km s^{-1}. This value is consistent with the terminal wind velocities for late WN (Crowther, Hillier, & Smith 1995; Smith, Crowther, & Willis 1995) which we give in Table 5 for comparison.

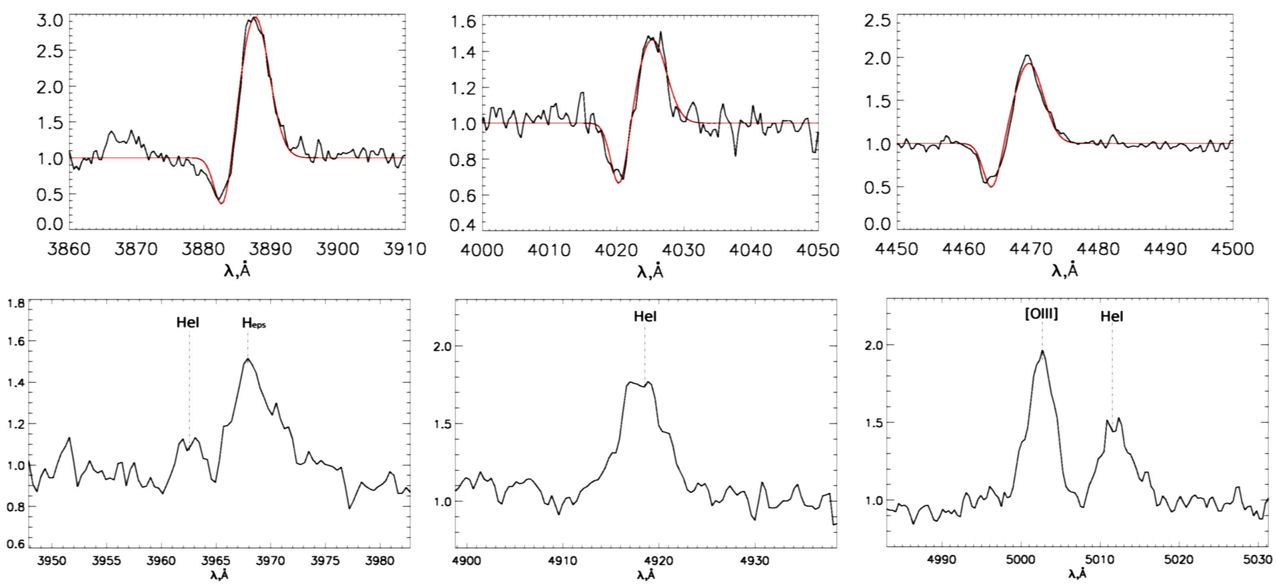

Fig. 6. Top panel: profiles of triplet He I λ 3889, 4025, 4471 lines (from left to right). Two-component model fits are shown (see text for details). Bottom panel: profiles of singlet He I λ 3965, 4922, 5016 lines. FOCAS data.

It is interesting to compare these profiles with the He II λ 5412 line in the SCORPIO spectrum obtained in October 2007. The spectrum has very high signal-to-noise ratio which allows reasonable terminal wind velocity estimates in spite of the significantly worse spectral resolution. The line has a classical low-optical-depth P Cyg profile: broad emission and blueshifted narrow absorption. We approximate this line by a classical P Cyg model profile (flat-topped emission with a narrow blueshifted absorption component) convolved with an instrumental point spread function that we consider Gaussian (the instrumental profile width is ~ 5.5 Å). Similar line profiles are produced by optically thin envelopes expanding at a constant velocity. Its fitting yields the wind speed of 200 ± 15 km s^{-1}. The expansion velocity indicates that the line is formed in the hotter inner parts of the wind that move with smaller outward velocities. Among Pickering emissions, we also detect λ 4541.6 and λ 4199.8 having similar profiles in the FOCAS spectrum, but we lack signal-to-noise to obtain reliable expansion velocity estimates for these lines.

3.3. *Nebular Lines*

The lines at 4959 and 5007 Å are clearly identified as [O III] emissions, which is consistent with their flux ratio equal to 3 and FWHMs equal within the measurement errors. In the cooler spectra of 2003 (Polcaro et al. 2003), nebular lines of [O III] are overridden by N II 4994-5005 emissions. However, in 2007, the N II lines are absent, but the [O III] λ 4959, 5007 doublet is clearly seen.

Nebular lines of [O III] $\lambda\lambda$ 4959, 5007, [N II] $\lambda\lambda$ 6548, 6583 are present in all the spectra analysed by us while the [S II] λ 6717, 6731 doublet is not. Therefore, we can estimate the electron density of the surrounding nebula. The electron density is between $10^{3.6}$ cm^{-3} and $10^{4.9}$ cm^{-3}. The former value corresponds to the critical density of the [S II] doublet, the second to that of [N II] $\lambda\lambda$ 6548, 6583 lines (see for example Osterbrock & Ferland 2006).

All the nebular lines present in the FOCAS spectrum as well as the [Ar III] λ 7135.73 emission in SCORPIO data show flat-topped or two-peaked profiles. The widths of the emission line cores are of the order of 100 km s^{-1}. Once we know the density of the emitting gas, we may estimate the size of the Strömgren region and the mass of the nebula surrounding V532. The former may be found as follows (see for example Lang 1974):

$$R_{\rm s} \simeq \left(\frac{3S}{4\pi \alpha n_{\rm e}^2} \right)^{1/3},$$

where α is the Case B recombination coefficient for hydrogen, $\alpha \simeq 2.6 \cdot 10^{-13} \left(\frac{10^4}{T}\right)^{0.85}$ cm^3 s^{-1}, $n_{\rm e}$ is the electron density, and S is the hydrogen-ionizing quanta production rate. For O9.5Ia stars, probably similar to the object in mass and luminosity, S is estimated as $10^{49.17}$ s^{-1} (Osterbrock & Ferland 2006).

TABLE 5

WIND VELOCITIES ESTIMATED THROUGH OPTICAL HEI LINES AND AMBIENT OXYGEN ABUNDANCES

Star	Galaxy	WN subtype	v_∞ km s^{-1}	$12+\log$ O/H abundance	HII region
V532 (during minimum epoch 2007)	M33	9	360	8.26 ± 0.08	
MCA1-B[a]	M33	9	420	8.315 ± 0.061	NGC588[e]
B517[b]	M33	11	275	8.334 ± 0.083	MA2[e]
Sk-66°40[a]	LMC	10	300		
R84[a]	LMC	9	400		
BE381[c]	LMC	9	280	8.37	30 Dor[f]
WR105[a]	MW	9	700		
AG Car (during minimum epoch 1985–1990)[d]	MW	11	300		
AG Car (during minimum epoch 2002)[d]	MW	11	200		

[a]Smith et al. (1995). [b]Crowther et al. (1997). [c]Crowther et al. (1995). [d]Groh et al. (2009). [e]Rosolowsky & Simon (2008). [f]Rosa & Mathis (1987).

One may estimate the size of a homogeneous nebula around V532 as:

$$R_{\rm s} \simeq 0.1 \cdot \left(\frac{S}{10^{49}{\rm s}^{-1}}\right)^{1/3} \times \left(\frac{n_{\rm e}}{10^4~{\rm cm}^{-3}}\right)^{-2/3} \times \times \left(\frac{T}{10^4{\rm K}}\right)^{0.28} {\rm pc}\,. \quad (1)$$

Note that possible inhomogeneity has little effect on the linear size: for a gas filling only some part of the nebular volume f, $R_{\rm s}$ should scale with filling factor as $\propto f^{-1/3}$. However, sizes of about 1 pc are plausible. The nebular mass may be trivially inferred as:

$$M \simeq \rho \cdot \frac{4\pi}{3} R_{\rm s}^3$$

$$\simeq 0.17 \cdot \left(\frac{S}{10^{49}{\rm s}^{-1}}\right) \left(\frac{n_{\rm e}}{10^4~{\rm cm}^3}\right)^{-1} \left(\frac{T}{10^4{\rm K}}\right)^{0.84} \cdot M_\odot\,. \quad (2)$$

The estimated size and the ionised mass of the nebula are consistent with these for ejecta of LBV stars (see Smith et al. 1994, and references therein) to order of magnitude. It is possible that the total mass lost by the object is higher, about several solar masses, but we observe only the ionized part of the envelope. The emitting gas was probably ejected during one or several outburst events at wind velocities of about 100 km s^{-1}.

4. DISCUSSION

In Table 5, terminal wind velocities for the WN9-WN11 stars in the Galaxy, LMC and M33 and LBV star AG Car (during minimum) are given. These velocities are also estimated through the optical He I lines. Because wind acceleration is tightly connected to metallicity (Massey et al. 2004; Puls, Vink, & Najarro 2008), we also give oxygen abundances ($12 + \log$ O/H) for selected H II regions adjacent to MCA1-B, B517 and BE381. They may be used as a measure for initial object metallicities.

V532 is located at a distance of about 17′ from the centre of M33. Taking the central oxygen abundance value of $12+\log {\rm O/H} = 8.36\pm0.04$ and a radial gradient of -0.027 ± 0.012 dex kpc^{-1} (Rosolowsky & Simon 2008), we may estimate the primordial oxygen abundance for V532 as 8.26 ± 0.08. The ambient metallicity is thus similar to that of the 30 Dor star-forming region. Our estimate for the terminal wind velocity of V532 is fairly consistent with that of other late WN stars in similar environments.

Wolf-Rayet stars are believed to be more evolved objects than Ofpe and Be supergiants. Information on elementary abundances may cast some light upon this issue. However, to recover reliable abundance estimates, one needs sophisticated modelling of both the moving atmosphere of the star and its structure. Here, we restrict ourselves only to some semi-qualitative estimates for the H/He abundance ratio. We compare the equivalent width ratios of Hβ to he-

TABLE 6

EQUIVALENT WIDTHS OF HELIUM LINES (IN Hβ UNITS) AND HELIUM-TO-HYDROGEN ABUNDANCE RATIOS FOR TWO LATE HYDROGEN-RICH WNS AND V532 (2007)

Object	Spectral Class	H/He	He I+H8 3889	Hγ	He II 4686	He I 4713	He I 5876
R84	WN9	2.5	3	2.3	3.5	12.6	
BE381	WN9h	2	2.1	2.4	1.9	16.6	0.8
V532			2	2.75	1.4	13.4	0.8

lium lines in the spectra obtained in 2007 to those for several WN9 (taken from Crowther et al. 1995) to estimate the relative abundances of hydrogen and helium. The equivalent width ratios are given in Table 6. The table shows that they are similar to those for BE381 (Brey 64) that has H/He=2 and is classified as WN9h by Crowther & Smith (1996). By analogy with BE381, we suppose that for V532, H/He $\sim$ 2. It places Romano's star in the region occupied by hydrogen-rich late WN stars that have atmospheres moderately contaminated by helium.

We have already mentioned the strikingly diverse behaviour of triplet lines of He I having P Cyg-like profiles and singlet emissions. Probably singlet lines have weak absorptions that we cannot detect due to insufficient signal-to-noise or spectral resolution. Besides this, He I λ 5015 is contaminated by the oxygen [O III] λ 5007 emission.

The similarity of the line profiles of singlet He I, [O III] $\lambda\lambda$ 4959, 5007 and [Ar III] λ 7136 suggests that both singlet He I and forbidden emissions are produced mainly in the low-density ejecta, expanding at velocities of about 100 km s^{-1}. Probably, singlet and triplet lines of neutral helium are formed in different places. Because the lowest possible level for triplet lines is metastable, concentrations of atoms at the lower levels of triplet transitions (and therefore the intensities of absorption line components) should be higher.

We classify the observed evolution of the object as an S Dor variability cycle. The main difference from AG Car and other LBVs is that at the optical minimum V532 becomes much hotter and may be classified as a WN9/WN8 star, while AG Car stops at about WN11. The non-monotonous spectral changes and variability timescales indicate that these spectral changes hardly correspond to any real stellar evolution, rather being connected to the ordinary LBV variability. It also means that LBV stars may have spectral classes as early as WN8. To our notion, there is only one example of an object that acquired even earlier spectral classes of WN6/7 during LBV variability cycle, HD5980 (Barbá, Niemela, & Morrell 1997; Koenigsberger & Moreno 2008) in the SMC. The hot spectra of this object are probably connected to lower ambient metallicity, too.

V532 is one more example of an LBV star temporarily becoming a WN. We predict that, vice versa, some of the Galactic or extra-galactic Wolf-Rayet stars may prove to be dormant LBVs. Probably, the hottest possible temperature for an LBV decreases with metallicity, but more data on the brightest stars in different environments are needed.

5. CONCLUSIONS

Our results show that the object changes from a *B* emission line supergiant at optical maximum, through Ofpe/WN (WN10,WN11) to WN9 and further towards a WN8 star at deep minimum. We confirm the result of Viotti et al. (2007) that there is an anti-correlation between the visual luminosity and the temperature of the star, with a larger amount of spectral data.

V532 spans a large range of spectral classes, becoming one of the first (probably, the second, after HD5980) LBV stars noticed to make an excursion as deep as WN8 into the Wolf-Rayet domain. It is interesting to trace further the evolution of the object. Further monitoring of V532, as well as of other late WN stars, is necessary to establish the evolutionary link between WRs and LBVs. Some WNs may prove to be dormant LBVs.

We are grateful to Vitalij Goranskij, Elena Barsukova and Alla Zharova for providing us with photometric data and Olga Sholukhova and Thomas Szeifert for the spectrum obtained with TWIN Calar Alto spectrograph in 1992. We would also like to thank the anonymous referee for valuable comments and for drawing our attention to HD5980.

REFERENCES

Afanasiev, V. L., Dodonov, S. N., & Moiseev, A. V. 2001, in Stellar Dynamics: From Classic to Modern, ed. L. P. Osipkov & I. I. Nikiforov (St. Petersburg: St. Petersburg Univ. Press), 103

Afanasiev, V., & Moiseev, A. 2005, Astron. Lett., 31, 194

Barbá, R. H., Niemela, V. S., & Morrell, N. I. 1997, in ASP Conf. Ser. 120, Luminous Blue Variables: Massive Stars in Transition, ed. A. Nota & H. Lamers (San Francisco: ASP), 238

Bernat, A. P., & Lambert, D. L. 1978, PASP, 90, 520

Clark, J. S., Larionov, V. M., & Arkharov, A. 2005, A&A, 435, 239

Conti, P. S. 1984, in IAU Symp. 105, Observational Tests of the Stellar Evolution Theory, ed. A. Maeder & A. Renzini (Dordrecht: Reidel), 233

Crowther, P. A., Hillier, D. J., & Smith, L. J. 1995, A&A, 293, 172

Crowther, P. A., & Smith, L. J. 1996, A&A, 305, 541

Crowther, P. A., Szeifert, Th., Stahl, O., & Zickgraf, F.-J. 1997, A&A, 318, 543

Fabrika, S., Sholukhova, O., Becker, T., Afanasiev, V., Roth, M., & Rossi, C. 2005, A&A, 437, 217

Groh, J. H., Hillier, D. J., Damineli, A., Whitelock, P. A., Marang, F., & Rossi, C. 2009, ApJ, 698, 1698

Humphreys, R., & Davidson, K. 1994, PASP, 106, 1025

Kashikawa, N., et al. 2002, PASJ, 54, 819

Koenigsberger, G., & Moreno, E. 2008, RevMexAA (SC), 33, 108

Kurtev, R., Sholukhova, O., Borrisova, J., & Georgiev, L. 2001, RevMexAA, 37, 57

Lang, K. R. 1974, Astrophysical Formulae (New York: Springer-Verlag)

Massey, P., Bresolin, F., Kudritzki, R. P., Puls, J. R., & Pauldrach, A. 2004, ApJ, 608, 1001

Oke, J. B. 1990, AJ, 99, 1621

Osterbrock, D. E., & Ferland, G. J. 2006, Astrophysics of Gaseous Nebulae and Active Galactic Nuclei (2nd ed.; Sausalito: University Science Books)

Polcaro, V. F., Gualandi, R., Norci, L., Rossi, C., & Viotti, R. 2003, A&A, 411, 193

Puls, J., Vink, J., & Najarro, F. 2008, A&AR, 16, 209

Romano, G. 1978, A&A, 67, 291

Rosa, M., & Mathis, J. S. 1987, ApJ, 317, 163

Rosolowsky, E., & Simon, J. D. 2008, ApJ, 675, 1213

Sánchez, S. F. 2006, Astron. Nachr., 327, 850

Sholukhova, O. N., Fabrika, S. N., Vlasyuk, V. V., & Burenkov, A. N. 1997, Astron. Lett., 23, 458

Sholukhova, O., Zharova, A., Fabrika, S., & Malinovskii, D. 2002, in ASP Conf. Proc. 259, Radial and Nonradial Pulsations as Probes of Stellar Physics, ed. C. Aerts, T. R. Bedding, & J. Christensen-Dalsgaard (San Francisco: ASP), 522

Smith, N., & Conti, P. 2008, ApJ, 679, 1467

Smith, L. J., Crowther, P. A., & Prinja, R. K. 1994, A&A, 281, 833

Smith, L. J., Crowther, P. A., & Willis, A. J. 1995, A&A, 302, 830

Smith, L. F., Shara, M. M., & Moffat, F. J. 1996, MNRAS, 281, 163

Stahl, O., Wolf, B., Klare, G., Cassatella, A., Krautter, J., Persi, P., & Ferrari-Toniolo, M. 1983, A&A, 127, 49

Stahl, O., et al. 2001, A&A, 375, 54

Szeifert, T. 1996, in Wolf-Rayet Stars in the Framework of Stellar Evolution, ed. J. M. Vreux, A. Detal, D. Fraipont-Caro, E. Gosset, & G. Rauw (Liege: Univ. Liege-Institute d'Astrophysique), 459

Viotti, R. F., Galleti, S., Gualandi, R., Montagni, F., Polcaro, V., Rossi, C., & Norci, L. 2007, A&A, 464, L53

Viotti, R. F., Rossi, C., Polcaro, V. F., Montagni, F., Gualandi, R., & Norci, L. 2006, A&A, 458, 225

O. Maryeva: Stavropol State University, Pushkina Str., 1, Stavropol, Russia 355009, Russia and Special Astrophysical Observatory, Nizhnij Arkhyz, Zelenchukskij, Karachai-Cirkassian Republic, Russia 369167 (olga.maryeva@gmail.com).

P. Abolmasov: Sternberg Astronomical Institute, Moscow State University, Universitetsky pr., 13, Moscow 119992, Russia (pavel.abolmasov@gmail.com).

Revista Mexicana de Astronomía y Astrofísica, **46**, 291–308 (2010)

$uvby - \beta$ PHOTOELECTRIC PHOTOMETRY OF CEPHEID STARS[1]

J. H. Peña,[2] A. Arellano Ferro,[2] R. Peña-Miller,[3] M. Álvarez,[4] Y. Rosas,[5] H. García,[6]
G. Muñoz,[7] B. Vargas,[8] J. P. Sareyan,[9] C. A. Guerrero,[2] and A. Rentería[2]

Received 2010 May 4; accepted 2010 June 10

RESUMEN

Presentamos fotometría fotoeléctrica $uvby-\beta$ de 41 estrellas Cefeidas clásicas. Se llevó a cabo una breve discusión de los datos comparados con observaciones análogas.

ABSTRACT

We present time-series $uvby - \beta$ photometry of 41 classical Cepheid stars. A brief discussion of a comparison between the present data and previous photometric observations is included.

Key Words: stars: variables: Cepheids — techniques: photometric

1. INTRODUCTION

The relevance of classical Cepheids in stellar astrophysics, both as distance indicators and for understanding stellar structure and pulsation, has been long acknowledged. The Strömgren ($uvby - \beta$) photometric system has proven to be very useful for the determination of fundamental physical quantities, such as reddening, effective temperature, gravity, and metallicity, for main sequence (Crawford 1975), giant (Olsen 1984), and supergiant stars (Arellano Ferro & Parrao 1989; Arellano Ferro & Mantegazza 1996). Large compilations of $uvby - \beta$ photometry for Cepheids have been published previously (Feltz & McNamara 1980; Eggen 1983, 1985; Meakes, Wallerstein, & Opalko 1991; Arellano Ferro et al. 1998). While there are several stars in common to such studies, there remain numerous Cepheids that are still poorly observed. This paper presents new $uvby - \beta$ data for 41 Cepheids, for many of which there is very little or no previous Strömgren photometry.

2. OBSERVATIONS

The observations presented here were gathered over different seasons (see Table 1) from 1989 to 2009 at the San Pedro Mártir Observatory in Baja California, Mexico. All data were obtained with the 1.5 m telescope equipped with a six-channel grating spectrophotometer. The observational procedure was the same in most seasons; each data point reported is the average of at least five 10 s integrations, and both sets of $uvby$ data and the narrow and wide bands that define the β index were observed almost simultaneously. A single measurement of the sky with an integration time of 10 s was subtracted from the star measurements. On each night several standard stars were observed to carry out transformation into the standard system of Olsen (1983) and Crawford (1975, 1979). Photometric reductions were made using the NABAPHOT package (Arellano Ferro & Parrao 1989) that corrects for atmospheric extinction, transforms the data into the standard system, and converts the sidereal time into Heliocentric Julian Day. Standard stars were taken from Grönbech, Olsen, & Stromgren (1976), Grönbech & Olsen (1977) and Olsen (1983), but some bright standard stars were also taken from the list published in the Astronomical Nautical Almanac.

The transformation equations used in this work have the following form:

$$V = \mathrm{A} + \mathrm{B}\ (b-y)(\mathrm{inst}) + y(\mathrm{inst})\,,$$

[1]Based on observations collected at the San Pedro Mártir Observatory, Mexico.

[2]Instituto de Astronomía, Universidad Nacional Autónoma de México, Mexico.

[3]Department of Mathematics, Imperial College London, UK.

[4]Observatorio Astronómico Nacional, UNAM, Mexico.

[5]Centro de Radioastronomía y Astrofísica, Universidad Nacional Autónoma de México, Mexico.

[6]Facultad de Ciencia, UNAN-Managua, Nicaragua.

[7]ESIME, Instituto Politécnico Nacional, Mexico.

[8]Instituto de Geofísica, Universidad Nacional Autónoma de México, Mexico.

[9]Lesia, Observatoire de Paris-Meudon and Observatoire de la Cote d'Azur, France.

TABLE 1

LOG OF THE OBSERVING SESSIONS

Epoch	No. of stars	Initial date year month day	Final date year month day	Observers
1989 OctNov	16	1989 10 29	1989 11 07	jhp, rpg
2005 MayJune	4	2005 05 28	2005 06 31	jhp, rpm
2006 July	7	2006 07 14	2006 07 19	ma, jps
2006 November	12	2006 11 01	2006 11 13	ma, lpl, jps, yr
2006 December	8	2006 12 09	2006 12 11	jhp, jps, hg
2007 MarchApril	8	2007 03 30	2007 04 03	jhp, gm, bv
2007 October	12	2007 10 05	2007 10 26	jhp, jps, cg
2008 October	8	2008 10 08	2008 10 14	ma, jps
2008 December	9	2008 12 09	2008 12 14	jhp, pz, vha
2009 June	9	2009 06 24	2009 06 26	jhp, hg, arl

jhp - J.H. Peña; rpg - R. Peniche; rpm - R. Peña Miller; jps - J. P. Sareyan; ma - M. Alvarez; yr - Y. Rosas; lpl - L. Parrao; hg - H. Garcia; gm - G. Muñoz; bv - B. Vargas; cg - C. Guerrero; pz - P. Zasche; vah - V. H. Alvarado and arl - A. Renteria.

TABLE 2

MEAN VALUES AND STANDARD DEVIATIONS $\langle\sigma\rangle$ FOR THE TRANSFORMATION COEFFICIENTS DURING THE OCTOBER 2008 SEASON

Season	B	D	F	J	H	I	L
2008	0.884	0.996	1.027	0.013	1.007	0.062	−1.319
$\langle\sigma\rangle$	0.026	0.015	0.081	0.031	0.054	0.074	0.065

$$
\begin{aligned}
(b-y)(\mathrm{std}) &= \mathrm{C} + \mathrm{D}\ (b-y)(\mathrm{inst})\,,\\
m_1(\mathrm{std}) &= \mathrm{E} + \mathrm{F}\ m_1(\mathrm{inst}) + \mathrm{J}\ (b-y)(\mathrm{inst})\,,\\
c_1(\mathrm{std}) &= \mathrm{G} + \mathrm{H}\ c_1(\mathrm{inst}) + \mathrm{I}\ (b-y)(\mathrm{inst})\,,\\
\beta\ (\mathrm{std}) &= \mathrm{K} + \mathrm{L}\ \beta\ (\mathrm{inst})\,.
\end{aligned}
$$

Transformations between the instrumental and literature values for a group of standard stars are illustrated in Figure 1 for the night of October 11, 2008, while Table 2 presents values for the slopes and color term coefficients averaged for seven nights from the 2008 season. Standard deviations for each coefficient are listed at the bottom of the table. Except for the May 2005 season, which was devoted entirely to data acquisition of Cepheid stars, most seasons were planned for observation of short period variable stars, and hence few data points were obtained on each night for Cepheid and standard stars. Nevertheless, some seasons were long enough to obtain data strings suitable for covering the long cycles of some Cepheid stars.

TABLE 3

PHOTON COUNTING UNCERTAINTIES FOR THE NIGHT OF OCTOBER 11, 2008

ID	V	u	b	v	y	N
BS 1430	5.4	0.0004	0.0003	0.0002	0.0003	4
RT AUR	5.2	0.0005	0.0003	0.0002	0.0003	5
SZ TAU	6.5	0.0009	0.0006	0.0004	0.0004	6
ST TAU	8.5	0.0023	0.0014	0.0010	0.0010	6
SY AUR	9.0	0.0040	0.0020	0.0020	0.0020	6
AO AUR	9.1	0.0023	0.0014	0.0010	0.0010	10
AN AUR	10.7	0.0070	0.0040	0.0020	0.0020	10
ER AUR	11.6	0.0090	0.0050	0.0030	0.0030	10

2.1. *Photometric uncertainties*

Individual uncertainties were determined by calculating standard deviations for the fluxes in each filter for each star. Bright stars were clearly observed more accurately than faint ones, although faint stars were observed long enough to obtain pho-

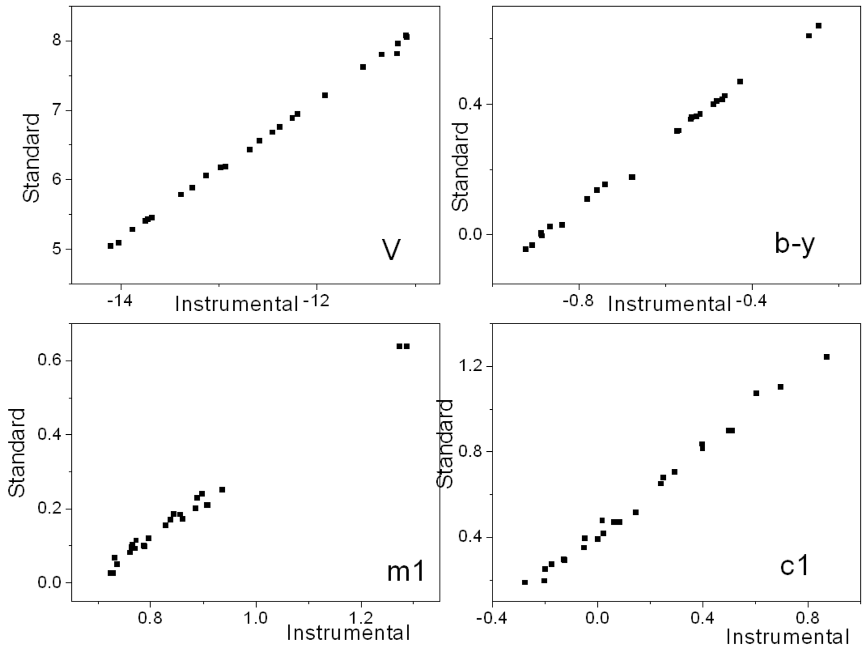

Fig. 1. A sample of transformation correlations between instrumental and standard values for a group of standard stars for the October 2008 season.

ton counts of high S/N ratio. Representative values for the photon counting uncertainties $N/\sqrt{(N)}$ derived from measurements on the night of October 11, 2008, for Cepheids with magnitudes ranging from $V = 5.2$ to 11.6 are presented in Table 3, with the standard star BS 1430 included for comparison. Given the results, the uncertainties associated with photon counting appear to be negligible.

Seasonal errors were evaluated from the differences (calculated minus observed) between magnitudes and colors for the standard stars, with ten to fifteen standard stars being observed on each night. Emphasized is the large range in magnitude and colors for the standards. Figure 1 presents for illustration standard deviations of the mean values in the differences $\langle\delta(V,\ (b-y),\ m_1,\ c_1)\rangle = (0.012,\ 0.005,\ 0.007,\ 0.018)$ for the October 2008 season.

3. RESULTS

A summary of the program objects is given in Table 4. Column 1 gives the star name, and Columns 2 and 3 the ephemerides elements employed to calculate light curve phase. The elements were taken from the General Catalogue of Variable Stars (Samus et al. 2009) in order to provide current light curve phasing. Subsequent columns in the table report the number of observations for each star by each of the previously-mentioned $uvby - \beta$ photometric observers: namely, Feltz & McNamara (1980), Eggen (1983, 1985), Meakes et al. (1991) and Arellano Ferro et al. (1998). The last column lists the number of observations from the present paper. Magnitudes and colors in the standard system obtained here for our sample of Cepheids are listed in Table 5.

4. COMPARISON WITH PREVIOUS PHOTOMETRY

The confidence level of our observations can be evaluated from the uncertainties discussed previously, and the good quality of the photometry is demonstrated by the good agreement with previously reported $uvby - \beta$ observations. The archival sources cited previously and the number of data points for each star are listed in Table 4. Of those, four stars with a large number of observations from different observers were selected to demonstrate the excellent agreement among the various data sets.

The stars considered for comparison were X Cyg, VZ Cyg, SW Tau, and SS Tau. As evident from Figure 2, the various observations are in excellent agreement with each other. A comparison was made between the data of Arellano Ferro et al. (1998) and those of the present paper for all stars, and all observations fit in either the light curve or color index diagrams, demonstrating once again the stability of the stellar pulsations and the reproducibility and good quality of the observations. Figure 3 illustrates light curves for most of the Cepheids in our sample. The

TABLE 4

OBSERVED STARS IN $uvby - \beta$

Star	Epoch	Period	AF[1] 1998	Eggen 1983	Meakes 1991	F&McN[2] 1980	This paper
SW TAU	41687.77	1.583584	6		7		5
EU TAU	41324.22	2.10248					14
SZ TAU	34628.57	3.14873	6			28	46
SS SCT	35315.625	3.671253	26	13		29	0
RT AUR	42361.155	3.728115					11
Y AUR	37203.629	3.859485	1				37
CM SCT	35111.32	3.916977					21
ST TAU	41761.963	4.034299	2				42
X SCT	34905.58	4.19807					16
VZ CYG	41705.702	4.864453	9			30	10
AS PER	41723.934	4.972516					13
BG LAC	35315.273	5.331908				26	18
UY PER	44945.845	5.365106					3
BX SCT	27901.83	6.41133					11
AW PER	42709.059	6.463589				23	11
AO AUR	42815.86	6.763006					15
CK SCT	40855.25	7.41522					13
RS ORI	42820.794	7.566881	10	21			25
VY CYG	43045.282	7.856982	2				10
RX CAM	42766.583	7.912024					4
BK AUR	17377.719	8.002432					16
CN SCT	28670.16	9.9923					7
SY AUR	36843.52	10.144698	1				36
AN AUR	36843.309	10.29056					46
Y SCT	34947.2	10.341504	27				5
Z LAC	42827.123	10.885613	5			25	15
VX PER	43758.994	10.88904					4
TY SCT	37377.09	11.05302					8
SV PER	43839.296	11.129318	1				14
RX AUR	39075.63	11.623515				21	61
Z Sct	36247.16	12.90133	27				5
TX CYG	43794.971	14.7098					10
RW CAS	35575.227	14.7949					3
SZ CYG	43306.79	15.10965	10				5
ER AUR	43861.3	15.69073					11
X CYG	43830.387	16.386332	18			53	13
RW CAM	37389.57	16.41437					4
YZ AUR	37431.141	18.193212					28
RU SCT	31174.67	19.70062	27				8
VX CYG	43783.642	20.133407	6				13

[1]Arellano Ferro et al. (1998).

[2]Feltz & McNamara (1980).

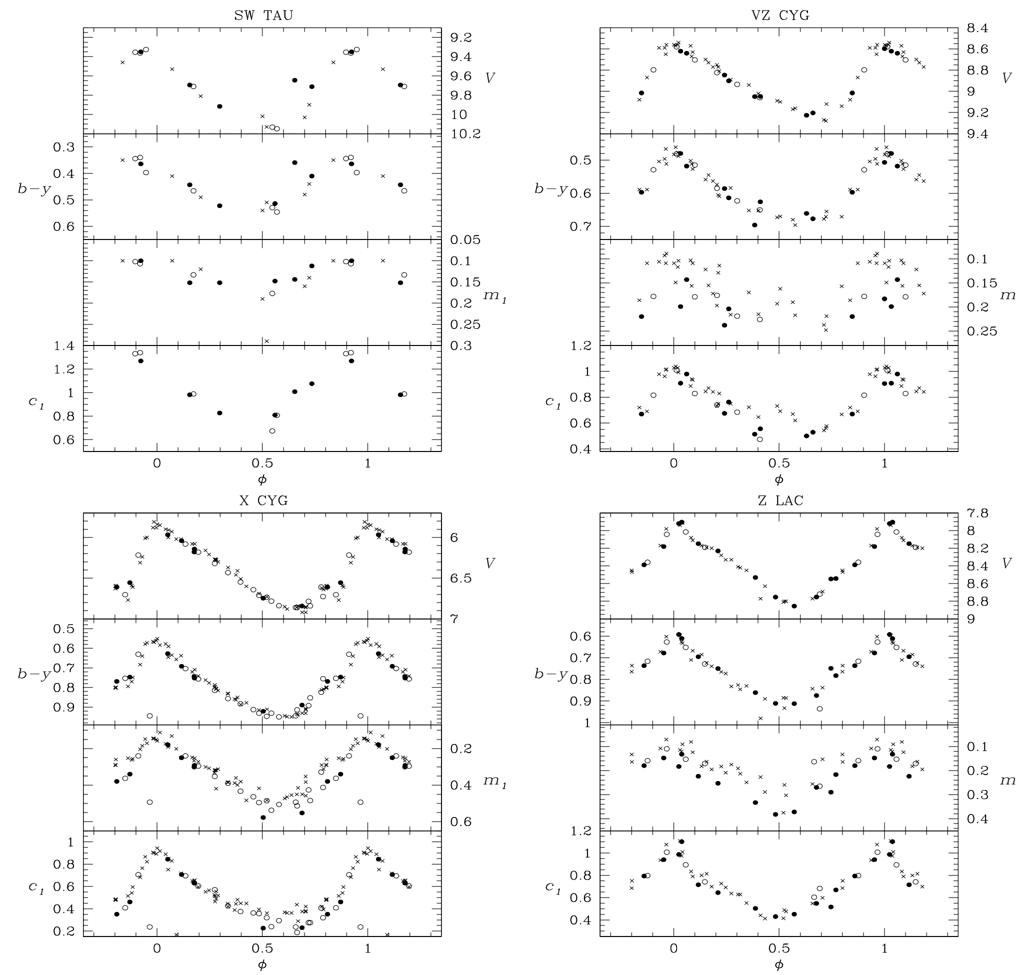

Fig. 2. Light curves in $uvby-\beta$ for four stars observed by several authors. Note the good agreement between the various sources. Open circles: Arellano Ferro et al. (1998); crosses, Feltz & McNamara (1980); filled circles, present work.

figure includes two data sets for each star, namely those of Arellano Ferro et al. (1998), represented by open circles, and those of the present paper by filled circles.

5. CONCLUSIONS

New $uvby-\beta$ photoelectric photometry has been acquired and is presented for 41 Cepheid stars. Such data can be useful for various fields of Cepheid research, such as the study of secular period changes (Szabados 1991; Arellano Ferro 1983), metallicity (Arellano Ferro & Mantegazza 1996), interstellar reddening (Chulhee 2008), and other physical parameters, for instance mean radii through applications of the Baade-Wesselink method (Arellano Ferro & Rosenzweig 2000). The photometry can also be utilized for several other purposes: to establish relationships with other basic properties, such as empirical determinations of pulsation mode like those developed for RR Lyrae stars (e.g., Kovács & Walker 2001, and references therein) through Fourier decomposition of the light curves (e.g., Peña et al. 2009); to determine metallicity photometrically from color indexes compared directly with predictions from theoretical models (e.g., Meakes et al. 1991); to support and improve knowledge of the chemical enrichment gradient in the Galaxy (e.g., the series of papers by Andrievsky et al. 2004, and references therein), among other topics.

We thank the staff of the OAN for their assistance in securing the observations, and acknowledge the help of several colleagues who participated in the observations: R. Peniche, L. Parrao, V. H. Alvarado and P. Zasche. This work was partially supported by PAPIIT IN110102 and IN108106-3. RPM, GM, BV, VHA and HG thank the IA-Universidad Nacional

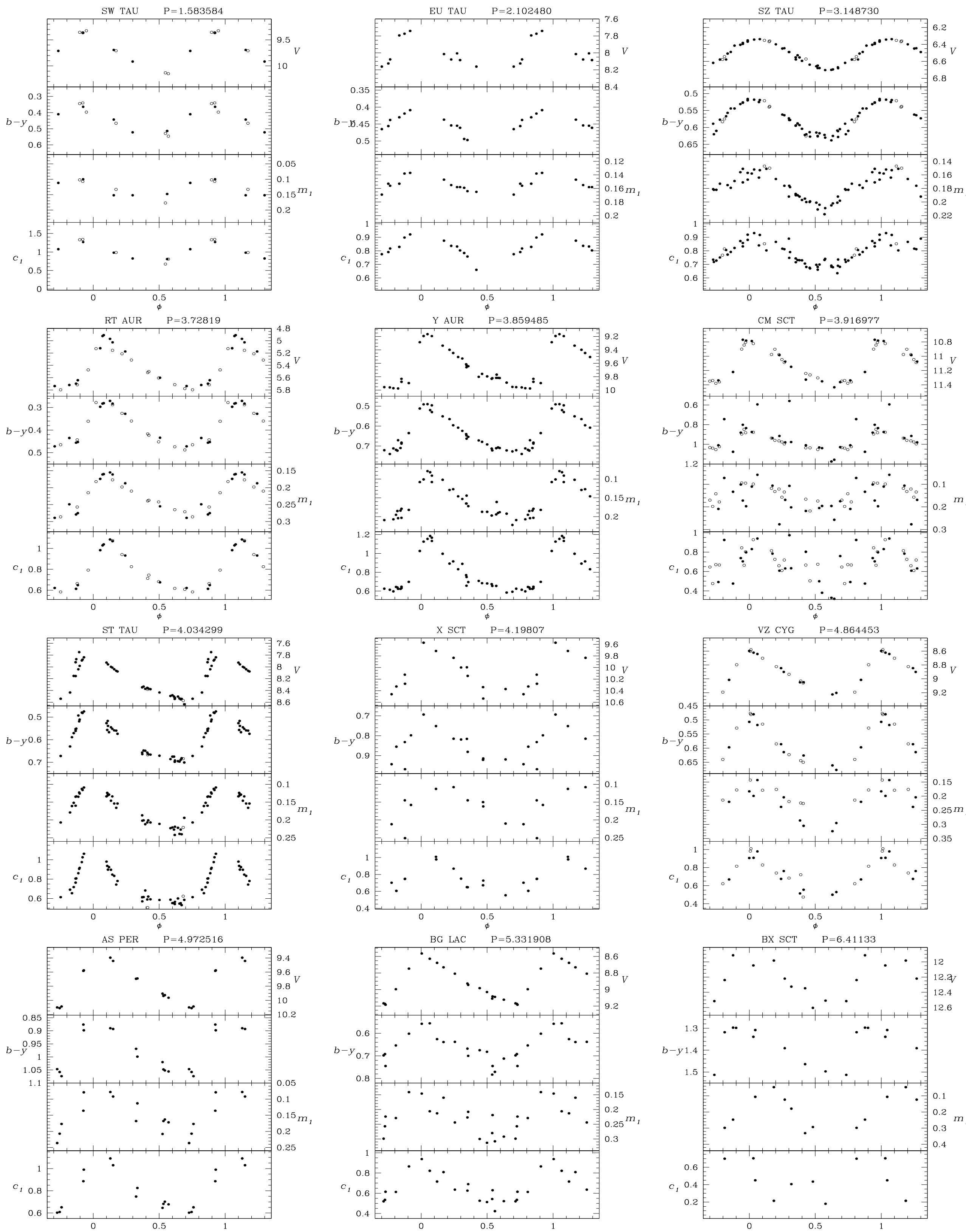

Fig. 3. $uvby-\beta$ Light curves of program Cepheids.

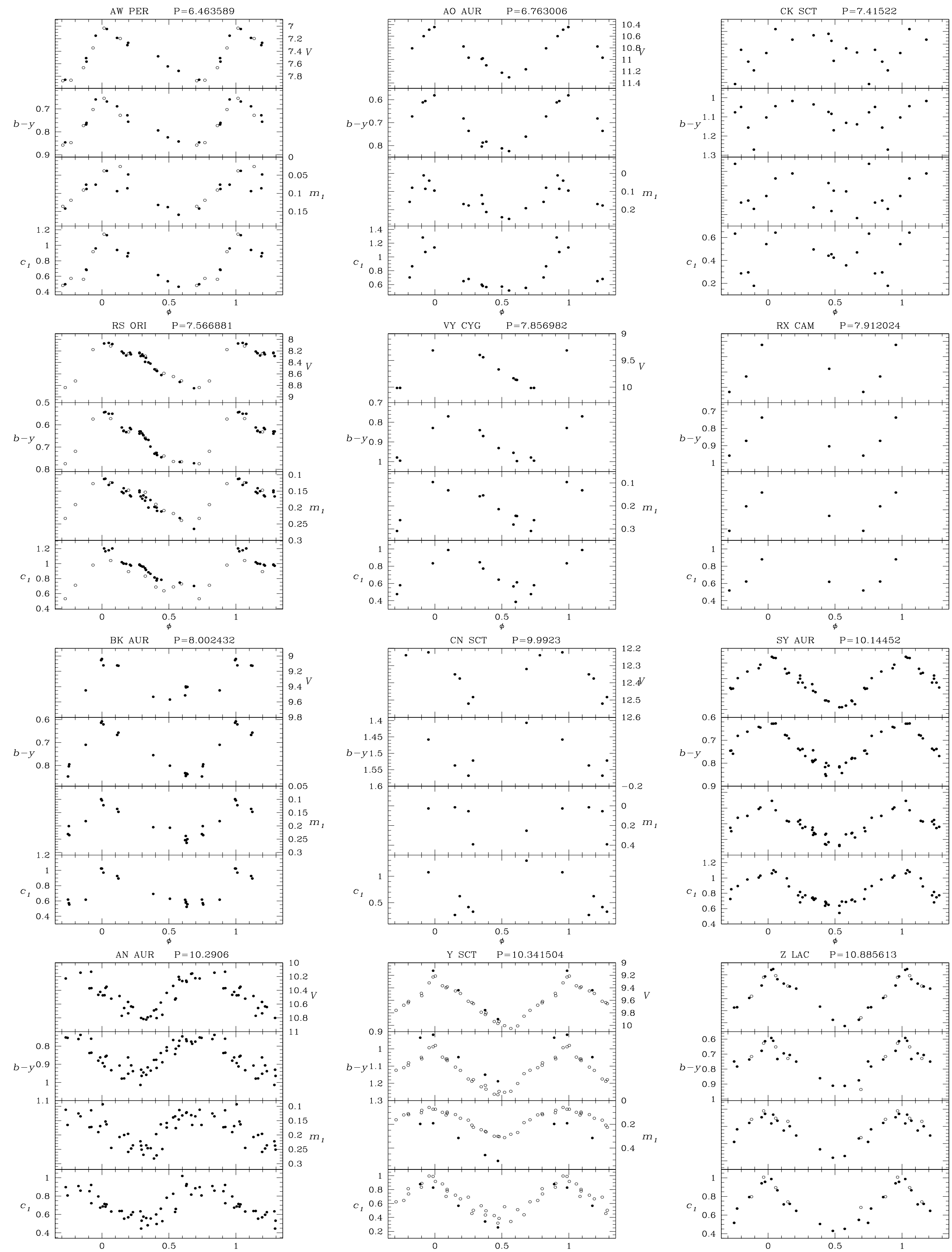

Fig. 3. Continued.

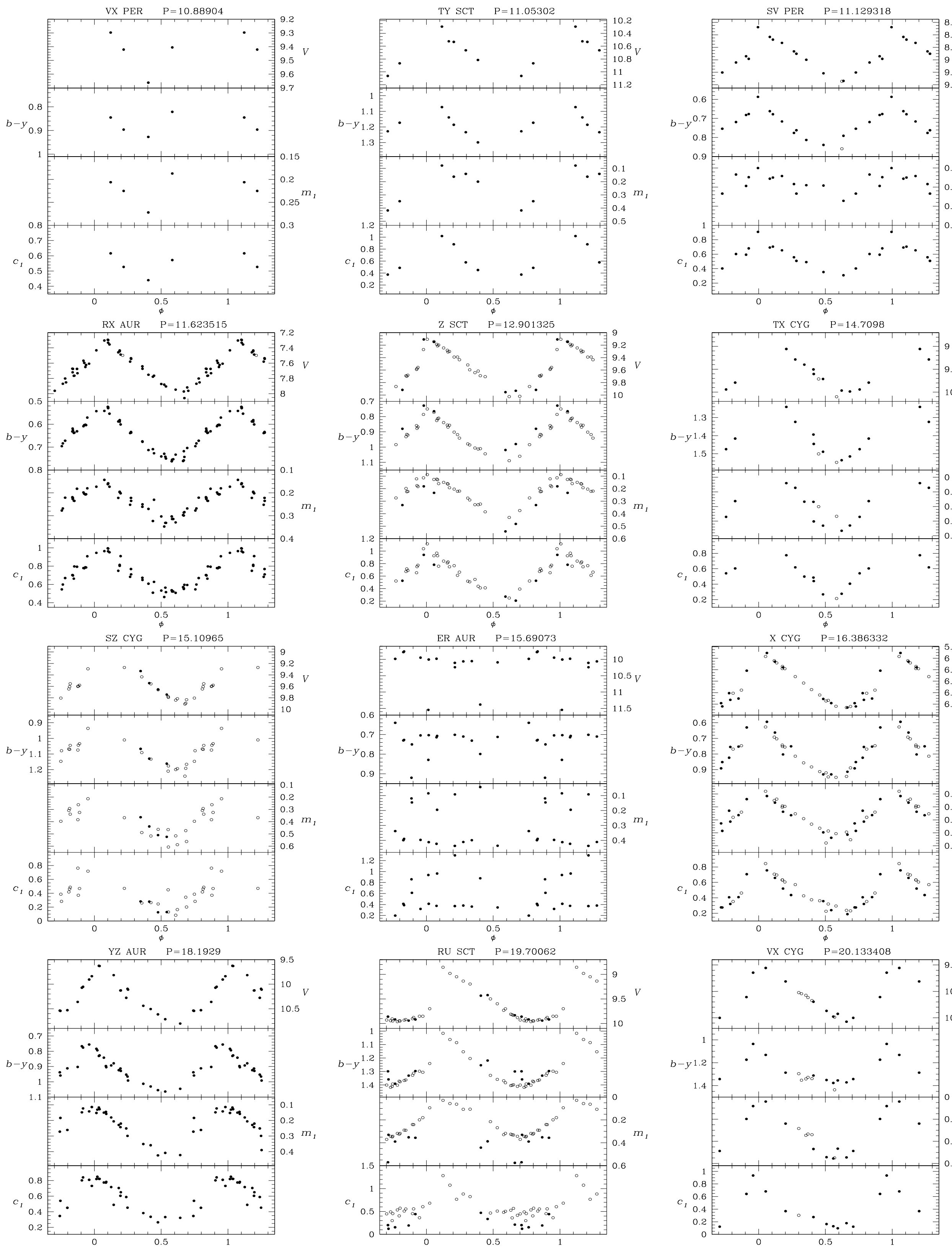

Fig. 3. Concluded.

TABLE 5

SAMPLE $uvby-\beta$ OBSERVATIONS OF CLASSICAL CEPHEIDS

Star	V	$b-y$	m_1	c_1	HJD ($uvby$)	β	HJD (β)	Epoch-2400000	P (days)
SWTAU	9.694	0.443	0.152	0.982	2447833.9053	2.713	33.9046	41687.77	1.583584
SWTAU	9.712	0.410	0.112	1.076	2447837.9903	2.729	37.9923	41687.77	1.583584
SWTAU	9.916	0.522	0.152	0.826	2454190.6381			41687.77	1.583584
SWTAU	9.366	0.364	0.100	1.269	2454191.6274			41687.77	1.583584
SWTAU		0.514	0.148	0.809	2454192.6355			41687.77	1.583584
EUTAU	8.162		0.165	0.660	2454040.8979			41324.219	2.102480
EUTAU	7.774	0.419	0.138	0.898	2454041.8543			41324.219	2.102480
EUTAU	7.741	0.409	0.137	0.921	2454041.9443			41324.219	2.102480
EUTAU		0.494	0.159	0.784	2454042.8053			41324.219	2.102480
EUTAU		0.497	0.164	0.758	2454042.8578			41324.219	2.102480
EUTAU	7.794	0.430	0.153	0.829	2454043.8737			41324.219	2.102480
EUTAU	8.006	0.455	0.158	0.832	2454044.7949			41324.219	2.102480
EUTAU	8.085	0.461	0.158	0.803	2454044.8430			41324.219	2.102480
EUTAU	8.077	0.438	0.156	0.817	2454045.8303			41324.219	2.102480
EUTAU	8.125	0.456	0.153	0.791	2454047.9038			41324.219	2.102480
EUTAU	8.078	0.454	0.155	0.837	2454048.9065			41324.219	2.102480
EUTAU	8.162	0.465	0.169	0.775	2454049.9025			41324.219	2.102480
EUTAU	8.014	0.437	0.147	0.875	2454050.8937			41324.219	2.102480
EUTAU	8.029	0.436	0.158	0.887	2454052.9347			41324.219	2.102480
CYLAC	9.010	0.497	0.210	0.750	2453931.9447			28746.219	2.786944
CYLAC	9.119	0.489	0.214	0.712	2453934.9388			28746.219	2.786944
SZTAU	6.679	0.617	0.204	0.699	2447832.8697	2.636	32.8701	34628.570	3.148730
SZTAU	6.489	0.544	0.179	0.792	2447833.9010	2.659	33.9013	34628.570	3.148730
SZTAU	6.658	0.615	0.201	0.697	2447835.9425	2.627	35.9427	34628.570	3.148730
SZTAU			0.151	0.803	2454040.8974			34628.570	3.148730
SZTAU		0.622	0.195	0.706	2454041.8169			34628.570	3.148730
SZTAU		0.620	0.200	0.681	2454041.8505			34628.570	3.148730
SZTAU		0.627	0.199	0.670	2454041.9394			34628.570	3.148730
SZTAU		0.620	0.182	0.718	2454042.7934			34628.570	3.148730
SZTAU		0.610	0.182	0.728	2454042.8510			34628.570	3.148730
SZTAU		0.525	0.164	0.840	2454043.8684			34628.570	3.148730
SZTAU	6.528	0.588	0.190	0.732	2454044.7906			34628.570	3.148730
SZTAU	6.554	0.593	0.192	0.731	2454044.8361			34628.570	3.148730
SZTAU		0.609	0.201	0.635	2454045.7401			34628.570	3.148730
SZTAU		0.605	0.198	0.682	2454045.8001			34628.570	3.148730
SZTAU			0.158		2454046.8453			34628.570	3.148730
SZTAU	6.578	0.594	0.190	0.716	2454047.8989			34628.570	3.148730
SZTAU	6.670	0.611	0.192	0.690	2454048.9024			34628.570	3.148730
SZTAU	6.352	0.516	0.167	0.881	2454049.8978			34628.570	3.148730
SZTAU	6.490	0.578	0.176	0.748	2454050.8886			34628.570	3.148730
SZTAU	6.394	0.527	0.171	0.833	2454052.9298			34628.570	3.148730
SZTAU	6.650	0.626		0.661	2454079.9074			34628.570	3.148730
SZTAU	6.578	0.567		0.806	2454379.9989			34628.570	3.148730
SZTAU	6.639	0.614	0.200	0.675	2454381.9939			34628.570	3.148730
SZTAU	6.579	0.577	0.173	0.751	2454382.9998			34628.570	3.148730
SZTAU	6.338	0.519	0.153	0.917	2454383.9522			34628.570	3.148730
SZTAU	6.594	0.604	0.197	0.730	2454384.9585			34628.570	3.148730
SZTAU	6.618	0.589	0.181	0.735	2454385.9876			34628.570	3.148730
SZTAU	6.343	0.518	0.152	0.931	2454386.9658			34628.570	3.148730
SZTAU	6.553	0.595	0.188	0.744	2454387.9579			34628.570	3.148730
SZTAU	6.681	0.628		0.736	2454388.9694			34628.570	3.148730
SZTAU	6.367	0.520	0.157	0.919	2454389.9605			34628.570	3.148730
SZTAU		0.578	0.178	0.791	2454390.9715			34628.570	3.148730
SZTAU	6.700	0.638	0.205	0.691	2454391.9569			34628.570	3.148730
SZTAU	6.405	0.531	0.156	0.872	2454392.9336			34628.570	3.148730
SZTAU	6.449	0.562		0.816	2454393.9365			34628.570	3.148730
SZTAU		0.622	0.218	0.733	2454394.9437			34628.570	3.148730
SZTAU	6.414	0.544	0.169	0.821	2454395.9437			34628.570	3.148730
SZTAU	6.399		0.166	0.866	2454396.9304			34628.570	3.148730
SZTAU	6.680	0.625	0.211	0.681	2454397.9288			34628.570	3.148730
SZTAU	6.508	0.557	0.175	0.772	2454398.9272			34628.570	3.148730
SZTAU	6.695	0.625	0.202	0.679	2454750.9489			34628.570	3.148730
SZTAU	6.382	0.526	0.151	0.858	2454751.9486			34628.570	3.148730

TABLE 5 (CONTINUED)

Star	V	$b-y$	m_1	c_1	HJD ($uvby$)	β	HJD (β)	Epoch-2400000	P (days)
SZTAU	6.445	0.564	0.176	0.812	2454752.9397			34628.570	3.148730
SZTAU	6.703	0.630	0.209	0.741	2454753.9136			34628.570	3.148730
SZTAU	6.490	0.573	0.192	0.890	2454809.7245			34628.570	3.148730
SZTAU		0.634	0.121	0.683	2454810.7411			34628.570	3.148730
RTAUR	5.719	0.435	0.249	0.505	2454040.8987			42361.155	3.72819
RTAUR	4.924	0.283	0.161	1.029	2454041.8385			42361.155	3.72819
RTAUR	4.910	0.281	0.160	1.039	2454041.8723			42361.155	3.72819
RTAUR	5.697	0.456	0.279	0.613	2454044.8182			42361.155	3.72819
RTAUR	5.641	0.453	0.275	0.648	2454044.8667			42361.155	3.72819
RTAUR	4.970	0.271	0.155	1.086	2454045.7782			42361.155	3.72819
RTAUR	5.026	0.283	0.161	1.069	2454045.8508			42361.155	3.72819
RTAUR	5.736	0.472	0.289	0.621	2454047.9423			42361.155	3.72819
RTAUR	5.175	0.328	0.187	0.932	2454049.9351			42361.155	3.72819
RTAUR	5.601	0.434	0.255	0.675	2454050.9188			42361.155	3.72819
RTAUR	5.122	0.297	0.174	0.983	2454052.9576			42361.155	3.72819
YAUR	9.629	0.663	0.144	0.749	2447833.9792	2.645	33.9798	37203.629	3.859485
YAUR	9.876	0.683	0.179	0.646	2447835.9349	2.635	35.9355	37203.629	3.859485
YAUR	9.644	0.654	0.172	0.696	2447837.8887	2.642	37.8911	37203.629	3.859485
YAUR	9.769		0.161	0.502	2454040.9108			37203.629	3.859485
YAUR		0.719	0.195	0.644	2454041.8256			37203.629	3.859485
YAUR		0.723	0.185	0.638	2454041.8652			37203.629	3.859485
YAUR		0.710	0.184	0.623	2454041.9568			37203.629	3.859485
YAUR		0.520	0.082	1.185	2454042.8232			37203.629	3.859485
YAUR		0.530	0.091	1.132	2454042.8758			37203.629	3.859485
YAUR	9.660	0.647	0.165	0.657	2454043.8871			37203.629	3.859485
YAUR	9.818	0.707	0.190		2454044.8111			37203.629	3.859485
YAUR	9.820	0.710	0.188		2454044.8578			37203.629	3.859485
YAUR	9.832	0.688	0.203	0.631	2454045.8443			37203.629	3.859485
YAUR	9.888	0.722	0.192	0.584	2454048.9203			37203.629	3.859485
YAUR	9.895	0.635	0.182	0.698	2454049.9193			37203.629	3.859485
YAUR	9.337	0.551	0.102	0.996	2454050.9089			37203.629	3.859485
YAUR	9.952	0.727	0.222	0.593	2454052.9494			37203.629	3.859485
YAUR	9.802	0.672		0.708	2454380.0205			37203.629	3.859485
YAUR	9.399	0.565	0.129	0.892	2454383.0253			37203.629	3.859485
YAUR	9.758	0.679	0.187	0.684	2454383.9782			37203.629	3.859485
YAUR	9.955	0.721	0.209	0.625	2454384.9769			37203.629	3.859485
YAUR	9.286	0.512	0.108	1.026	2454386.0158			37203.629	3.859485
YAUR	9.447	0.596	0.127	0.915	2454386.9931			37203.629	3.859485
YAUR	9.795	0.692	0.187	0.681	2454387.9858			37203.629	3.859485
YAUR	9.959	0.740		0.614	2454388.9982			37203.629	3.859485
YAUR	9.194	0.491	0.101	1.125	2454389.9869			37203.629	3.859485
YAUR	9.506	0.608	0.146	0.832	2454390.9964			37203.629	3.859485
YAUR	9.831	0.713	0.197	0.674	2454391.9776			37203.629	3.859485
YAUR	9.822	0.722		0.655	2454391.9948			37203.629	3.859485
YAUR	9.971	0.712	0.207	0.597	2454392.9614			37203.629	3.859485
YAUR	9.166	0.490	0.079	1.154	2454393.9603			37203.629	3.859485
YAUR	9.529	0.624	0.153	0.889	2454394.9784			37203.629	3.859485
YAUR	9.818	0.711	0.194	0.655	2454395.9700			37203.629	3.859485
YAUR	9.975	0.671	0.204	0.623	2454396.9589			37203.629	3.859485
YAUR	9.195	0.496	0.108	1.167	2454397.9469			37203.629	3.859485
YAUR	9.614	0.640	0.165	0.769	2454398.9499			37203.629	3.859485
CMSCT	10.769	0.801	0.172	0.704	2446963.8983	2.654	63.8987	35111.32	3.916977
CMSCT	10.781	0.835	0.197	0.797	2446967.9135	2.658	67.9140	35111.32	3.916977
CMSCT	10.985	0.915	0.277	0.608	2446968.9025			35111.32	3.916977
CMSCT	11.328	1.010	0.218	0.803	2453518.8728			35111.32	3.916977
CMSCT	11.328	1.010	0.218	0.803	2453518.8728			35111.32	3.916977
CMSCT	11.363	1.029	0.175	0.759	2453519.8934			35111.32	3.916977
CMSCT	0.881	0.101	0.738		2453520.8581			35111.32	3.916977
CMSCT	0.937	0.106	0.784		2453521.7988			35111.32	3.916977
CMSCT	1.175	0.196	0.328		2453930.9144			35111.32	3.916977
CMSCT	11.221	1.076	0.133	0.475	2453931.9108			35111.32	3.916977
CMSCT	11.435	1.157	0.257	0.318	2453934.9170			35111.32	3.916977
CMSCT	11.339	1.010	0.209	0.491	2454189.9954			35111.32	3.916977
CMSCT	10.788	0.875	0.110	0.831	2454190.9884			35111.32	3.916977
CMSCT	11.075	0.980	0.169	0.631	2454191.9809			35111.32	3.916977

TABLE 5 (CONTINUED)

Star	V	$b-y$	m_1	c_1	HJD ($uvby$)	β	HJD (β)	Epoch-2400000	P (days)
CMSCT		1.032	0.205	0.499	2454192.9901			35111.32	3.916977
CMSCT	12.654	0.559	0.107	0.974	2455006.8366	2.893	6.8360	35111.32	3.916977
CMSCT	11.352	1.039	0.196	0.380	2455007.8062	2.584	7.8072	35111.32	3.916977
CMSCT	12.553	0.744	−0.072	0.925	2455008.8173	2.769	8.8184	35111.32	3.916977
CMSCT	12.947	0.594	0.058	0.940	2455009.8037	2.921	9.8047	35111.32	3.916977
CMSCT	11.149	0.977	0.202	0.633	2455010.8039	2.630	10.8028	35111.32	3.916977
STTAU	8.435	0.630	0.179	0.691	2447832.8748	2.643	32.8753	41761.963	4.034299
STTAU	7.927	0.527	0.134	0.981	2447833.9904	2.679	33.9910	41761.963	4.034299
STTAU	8.493	0.686	0.223	0.588	2447835.9458	2.611	35.9461	41761.963	4.034299
STTAU	7.921	0.561	0.135	0.806	2454041.8312			41761.963	4.034299
STTAU	7.869	0.551	0.134	0.808	2454041.8525			41761.963	4.034299
STTAU	7.750	0.519	0.123	0.906	2454041.9411			41761.963	4.034299
STTAU		0.557	0.124	0.937	2454042.7987			41761.963	4.034299
STTAU		0.567	0.129	0.924	2454042.8540			41761.963	4.034299
STTAU		0.664	0.202	0.571	2454043.8705			41761.963	4.034299
STTAU	8.481	0.675	0.221	0.553	2454044.7920			41761.963	4.034299
STTAU	8.504	0.675	0.227	0.554	2454044.8399			41761.963	4.034299
STTAU		0.589	0.161	0.655	2454045.7543			41761.963	4.034299
STTAU	8.153	0.571	0.152	0.718	2454045.8080			41761.963	4.034299
STTAU		0.517	0.131		2454046.8478			41761.963	4.034299
STTAU	8.347	0.657	0.187	0.613	2454047.9007			41761.963	4.034299
STTAU	8.526	0.692	0.219	0.566	2454048.9038			41761.963	4.034299
STTAU	8.155	0.553	0.160	0.764	2454049.8997			41761.963	4.034299
STTAU	7.958	0.539	0.128	0.898	2454050.8907			41761.963	4.034299
STTAU	8.544	0.698	0.242	0.543	2454052.9316			41761.963	4.034299
STTAU	8.434	0.671	0.211	0.585	2454189.6307			41761.963	4.034299
STTAU	8.540	0.672	0.207	0.614	2454190.6438			41761.963	4.034299
STTAU	8.634	0.701	0.194	0.586	245438 0			41761.963	4.034299
STTAU	8.078	0.574	0.154	0.781	2454381.9947			41761.963	4.034299
STTAU	8.378	0.666	0.207	0.592	2454383.0012			41761.963	4.034299
STTAU	8.542	0.682	0.240	0.532	2454383.9539			41761.963	4.034299
STTAU	7.877	0.482	0.116	1.026	2454384.9592			41761.963	4.034299
STTAU	7.838	0.475	0.109	1.062	2454385.0014			41761.963	4.034299
STTAU	8.066	0.560	0.166	0.744	2454385.9891			41761.963	4.034299
STTAU	8.367	0.664	0.201	0.620	2454386.9676			41761.963	4.034299
STTAU	8.549	0.689	0.227	0.552	2454387.9603			41761.963	4.034299
STTAU	7.892	0.480	0.113	0.976	2454388.9715			41761.963	4.034299
STTAU	8.040	0.559	0.154	0.834	2454389.9619			41761.963	4.034299
STTAU	8.356	0.657	0.207	0.590	2454390.9734			41761.963	4.034299
STTAU	8.536	0.697	0.239	0.547	2454391.9583			41761.963	4.034299
STTAU	7.983	0.511	0.126	0.917	2454392.9393			41761.963	4.034299
STTAU	8.012	0.552	0.134	0.847	2454393.9380			41761.963	4.034299
STTAU	8.373	0.649	0.212	0.683	2454394.9455			41761.963	4.034299
STTAU	8.503	0.695	0.222	0.601	2454395.9455			41761.963	4.034299
STTAU	8.041	0.493	0.135	0.861	2454396.9334			41761.963	4.034299
STTAU	7.999	0.545	0.146	0.897	2454397.9306			41761.963	4.034299
STTAU	8.334	0.648	0.201	0.615	2454398.9288			41761.963	4.034299
XSCT	9.996	0.816		0.650	2446963.8898			34905.58	4.19807
XSCT	10.327	0.855	0.285	0.606	2446965.8430			34905.58	4.19807
XSCT	9.999	0.819		0.750	2446967.9021	2.628	67.9026	34905.58	4.19807
XSCT	10.460	0.943	0.212	0.702	2453518.8789			34905.58	4.19807
XSCT	9.571	0.694	0.051	1.326	2453519.8968			34905.58	4.19807
XSCT	9.833	0.815	0.108	0.868	2453520.8515			34905.58	4.19807
XSCT	10.338	0.921	0.150	0.672	2453521.7885			34905.58	4.19807
XSCT	10.535	0.914	0.162	0.727	2453521.7958			34905.58	4.19807
XSCT	12.511	0.798	0.158		2453930.9066			34905.58	4.19807
XSCT	10.280	0.968	0.251	0.748	2453934.9147			34905.58	4.19807
XSCT				0.977	2453935.9080			34905.58	4.19807
XSCT	10.371	0.919	0.210	0.554	2454189.9992			34905.58	4.19807
XSCT	10.123	0.832	0.145	0.746	2454190.9907			34905.58	4.19807
XSCT	9.714	0.752	0.113	1.008	2454191.9833			34905.58	4.19807
XSCT	10.144	0.881	0.145	0.649	2454192.9929			34905.58	4.19807
VZCYG	9.049	0.626	0.305	0.555	2448887.6361	2.629	87.6357	41705.702	4.864453
VZCYG	9.226	0.661	0.324	0.500	2448888.7007	2.611	88.6995	41705.702	4.864453
VZCYG	8.622	0.480	0.199	0.908	2448890.6559	2.665	90.6552	41705.702	4.864453

TABLE 5 (CONTINUED)

Star	V	$b-y$	m_1	c_1	HJD ($uvby$)	β	HJD (β)	Epoch-2400000	P (days)
VZCYG	8.846	0.586	0.238	0.675	2448891.6701	2.642	91.6694	41705.702	4.864453
VZCYG	9.204	0.677	0.295	0.529	2448893.7081	2.634	93.7086	41705.702	4.864453
VZCYG	9.016	0.597	0.220	0.669	2448894.6185	2.644	94.6182	41705.702	4.864453
VZCYG	8.641	0.518	0.143	0.979	2448895.6626	2.669	95.6631	41705.702	4.864453
VZCYG	8.901	0.614	0.204	0.762	2448896.6345	2.642	96.6341	41705.702	4.864453
VZCYG	9.051		0.286	0.514	2453931.9423			41705.702	4.864453
VZCYG	8.597	0.507	0.183	0.906	2453934.9357			41705.702	4.864453
ASPER	10.087	1.074	0.177	0.651	2447828.9884	2.623	28.9894	41723.934	4.972516
ASPER	9.937	1.048	0.168	0.682	2447832.8284	2.623	32.8290	41723.934	4.972516
ASPER	10.110	1.058	0.207	0.609	2447833.8906	2.598	33.8911	41723.934	4.972516
ASPER	9.442	0.893	0.092	1.030	2447835.9040	2.68	35.9048	41723.934	4.972516
ASPER	9.963	1.056	0.172	0.678	2447837.9943	2.604	37.9967	41723.934	4.972516
ASPER	10.100	1.047	0.236	0.603	2448887.9683	2.637	87.9677	41723.934	4.972516
ASPER	9.583	0.876	0.136	0.886	2448888.9583	2.689	88.9576	41723.934	4.972516
ASPER	9.695	0.969	0.168	0.748	2448890.9426	2.63	90.9422	41723.934	4.972516
ASPER	9.905	1.020	0.208	0.646	2448891.9408	2.615	91.9404	41723.934	4.972516
ASPER	9.575	0.898	0.079	0.990	2448893.9461	2.692	93.9458	41723.934	4.972516
ASPER	9.396	0.890	0.078	1.091	2448894.9462	2.697	94.9458	41723.934	4.972516
ASPER	9.690	0.999	0.113	0.825	2448895.9663	2.65	95.9659	41723.934	4.972516
ASPER	9.926	1.052	0.163	0.702	2448897.0010	2.647	97.0014	41723.934	4.972516
BGLAC	9.030	0.682	0.313	0.513	2448887.6383	2.616	87.6379	35315.273	5.331908
BGLAC	9.167	0.698	0.299	0.520	2448888.7919	2.627	88.7911	35315.273	5.331908
BGLAC	8.627	0.556	0.206	0.822	2448890.6585	2.665	90.6579	35315.273	5.331908
BGLAC	8.808	0.638	0.244	0.636	2448891.6725	2.633	91.6719	35315.273	5.331908
BGLAC	8.983	0.675	0.300	0.526	2448892.6764	2.619	92.6761	35315.273	5.331908
BGLAC	9.123	0.712	0.292	0.522	2448893.6520	2.62	93.6516	35315.273	5.331908
BGLAC	8.996	0.654	0.229	0.613	2448894.6197			35315.273	5.331908
BGLAC	8.564	0.558	0.146	0.938	2448895.6663	2.674	95.6667	35315.273	5.331908
BGLAC	8.731	0.639	0.160	0.809	2452500.9161			35315.273	5.331908
BGLAC	8.944	0.700	0.208	0.690	2452501.9125			35315.273	5.331908
BGLAC	9.083	0.745	0.219	0.630	2452502.8989			35315.273	5.331908
BGLAC	9.184	0.745	0.224	0.615	2452503.9046			35315.273	5.331908
BGLAC	8.747	0.602	0.141	0.865	2452504.8502			35315.273	5.331908
BGLAC	9.089	0.771	0.308	0.423	2453931.9437			35315.273	5.331908
BGLAC	8.677	0.626	0.213	0.716	2453934.9375			35315.273	5.331908
BGLAC	8.927	0.668	0.227	0.626	2455007.8790	2.628	7.8795	35315.273	5.331908
BGLAC	9.109	0.783	0.280	0.543	2455008.8802			35315.273	5.331908
BGLAC	9.173	0.692	0.257	0.535	2455009.8780	2.632	9.8784	35315.273	5.331908
UYPER	11.303	1.123	0.087	0.807	2447833.8798	2.617	33.8803	44945.845	5.365106
UYPER	11.759	1.235	0.191	0.568	2447835.8917	2.633	35.8929	44945.845	5.365106
UYPER	10.899	0.948	0.064	1.143	2447837.8443	2.709	37.8459	44945.845	5.365106
BXSCT	11.914	1.297	0.247		2446961.9231	2.753	61.9239	27901.83	6.41133
BXSCT	12.047	1.339		0.703	2446962.9098			27901.83	6.41133
BXSCT	11.983		0.046	0.214	2446963.9071	2.667	63.9077	27901.83	6.41133
BXSCT	12.239	1.318	0.298	0.699	2446967.9256	2.676	67.9260	27901.83	6.41133
BXSCT		1.308	0.106	0.450	2453521.7926				6.41133
BXSCT	12.325		0.179	0.406	2453933.8728				6.41133
BXSCT	12.604		0.293	0.435	2453934.9191				6.41133
BXSCT	12.220	1.391	0.123		2454190.0042				6.41133
BXSCT	12.347	1.464	0.331		2454190.9931				6.41133
BXSCT	12.509	1.497		0.180	2454191.9851				6.41133
BXSCT	12.515	1.513			2454192.9946				6.41133
AWPER	7.566	0.761	0.088	0.681	2447833.9387	2.664	33.9393	42709.059	6.463589
AWPER	7.303	0.728	0.086	0.858	2447835.9119	2.67	35.9122	42709.059	6.463589
AWPER	7.642	0.824	0.138	0.536	2447837.8613	2.62	37.8633	42709.059	6.463589
AWPER	7.152	0.659	0.076	0.960	2448887.9472	2.699	87.9468	42709.059	6.463589
AWPER	7.187	0.689	0.094	0.940	2448888.9791	2.68	88.9782	42709.059	6.463589
AWPER	7.481	0.794	0.132	0.616	2448890.9592	2.641	90.9588	42709.059	6.463589
AWPER	7.714	0.842	0.159	0.465	2448891.9472	2.62	91.9468	42709.059	6.463589
AWPER	7.855	0.846	0.142	0.497	2448892.9393	2.638	92.9390	42709.059	6.463589
AWPER	7.510	0.768	0.076	0.688	2448893.9506	2.653	93.9510	42709.059	6.463589
AWPER	7.045	0.668	0.038	1.131	2448894.9490	2.712	94.9494	42709.059	6.463589
AWPER	7.265	0.756	0.048	0.900	2448895.9780	2.669	95.9787	42709.059	6.463589
AOAUR	10.807	0.673	0.079	0.865	2447832.8599	2.626	32.8608	42815.86	6.763006
AOAUR	10.443	0.581	0.095	1.138	2447833.9835	2.671	33.9841	42815.86	6.763006

TABLE 5 (CONTINUED)

Star	V	$b-y$	m_1	c_1	HJD ($uvby$)	β	HJD (β)	Epoch-2400000	P (days)
AOAUR		0.612		1.283	2454041.8362			42815.86	6.763006
AOAUR		0.606	0.085	1.072	2454041.9645			42815.86	6.763006
AOAUR	10.775	0.682	0.169	0.649	2454043.8935			42815.86	6.763006
AOAUR	10.990	0.804	0.120	0.598	2454044.8153			42815.86	6.763006
AOAUR	10.978	0.787	0.168	0.579	2454044.8635			42815.86	6.763006
AOAUR		0.549	0.157	0.703	2454047.9375			42815.86	6.763006
AOAUR	10.488		0.040		2454048.9256			42815.86	6.763006
AOAUR	10.968	0.736	0.177	0.681	2454050.9152			42815.86	6.763006
AOAUR	11.304	0.824	0.251	0.513	2454052.9546			42815.86	6.763006
AOAUR	10.599		0.011		2454380.0317			42815.86	6.763006
AOAUR	11.225	0.812	0.242	0.570	2454383.9835			42815.86	6.763006
AOAUR	11.098	0.783	0.213	0.564	2454389.9548			42815.86	6.763006
AOAUR	11.166	0.761	0.192	0.551	2454391.9520			42815.86	6.763006
CKSCT	10.730	1.139	0.425	0.470	2446962.8980			40855.25	7.41522
CKSCT	10.688	1.048	0.317	0.287	2446963.8953	2.662	63.8958	40855.25	7.41522
CKSCT	10.461	1.035	0.351	0.496	2446967.9097	2.650	67.9102	40855.25	7.41522
CKSCT	10.548	1.084	0.376	0.454	2446968.8996			40855.25	7.41522
CKSCT	10.364	1.044	0.149	0.642	2453520.8547			40855.25	7.41522
CKSCT	10.529	1.017	0.114	0.731	2453521.7908			40855.25	7.41522
CKSCT	10.861	1.170	0.234	0.424	2453931.9149			40855.25	7.41522
CKSCT	11.225	1.076	0.047	0.633	2453933.8696			40855.25	7.41522
CKSCT	11.011	1.271	0.361	0.179	2453934.9109			40855.25	7.41522
CKSCT	10.437	1.074	0.181	0.441	2455006.8337	2.640	6.8336	40855.25	7.41522
CKSCT	10.666	1.131	0.239	0.357	2455007.8106	2.611	7.8113	40855.25	7.41522
CKSCT	10.874	1.156	0.303	0.296	2455009.8078	2.630	9.8085	40855.25	7.41522
CKSCT	10.739	1.103	0.271	0.542	2455010.8062	2.622	10.8070	40855.25	7.41522
RSORI		0.542	0.112	1.164	2447943.7633	2.688	43.7648	42820.794	7.566881
RSORI	8.241	0.626	0.141	1.000	2447944.7993	2.648	44.8008	42820.794	7.566881
RSORI	8.230	0.640	0.148	0.988	2447945.6936	2.638	45.6951	42820.794	7.566881
RSORI	8.545	0.726	0.200	0.774	2447946.6584	2.627	46.6597	42820.794	7.566881
VYCYG	9.398	0.840	0.158	0.846	2448885.6512	2.641	85.6520	43045.282	7.856982
VYCYG	9.834	0.955	0.281	0.566	2448887.6257	2.613	87.6253	43045.282	7.856982
VYCYG	10.016	0.979	0.309	0.476	2448888.6513	2.611	88.6506	43045.282	7.856982
VYCYG		0.770	0.132	0.988	2448891.6575	2.675	91.6568	43045.282	7.856982
VYCYG	9.441	0.870	0.154	0.773	2448893.7059	2.630	93.7063	43045.282	7.856982
VYCYG	9.669	0.931	0.214	0.644	2448894.6157	2.627	94.6161	43045.282	7.856982
VYCYG	9.865	0.997	0.244	0.613	2448895.6876	2.620	95.6887	43045.282	7.856982
VYCYG	10.014	0.995	0.262	0.579	2448896.6912	2.618	96.6916	43045.282	7.856982
VYCYG	9.861		0.243	0.386	2453931.9409			43045.282	7.856982
VYCYG	9.313	0.829	0.096	0.834	2453934.9355			43045.282	7.856982
RXCAM	7.859	0.872	0.191	0.622	2447828.9839	2.632	28.9847	42766.583	7.912024
RXCAM	7.758	0.904	0.216	0.619	2447833.8874	2.627	33.8879	42766.583	7.912024
RXCAM	8.061	0.958	0.255	0.518	2447835.9007	2.622	35.9010	42766.583	7.912024
RXCAM	7.446	0.737	0.155	0.880	2447837.8274	2.650	37.8291	42766.583	7.912024
BKAUR	9.514	0.833	0.254	0.616	2454041.8282			17377.719	8.002432
BKAUR	9.398	0.846	0.238	0.577	2454041.8678			17377.719	8.002432
BKAUR	9.411	0.839	0.255	0.590	2454041.8778			17377.719	8.002432
BKAUR	9.403	0.838	0.250	0.557	2454041.9612			17377.719	8.002432
BKAUR		0.848	0.231	0.618	2454042.8321			17377.719	8.002432
BKAUR		0.804	0.201	0.572	2454042.8827			17377.719	8.002432
BKAUR	9.449	0.710	0.182	0.617	2454043.8921			17377.719	8.002432
BKAUR	9.055	0.614	0.099	1.024	2454044.8133			17377.719	8.002432
BKAUR	9.038	0.608	0.104	1.023	2454044.8600			17377.719	8.002432
BKAUR	9.123	0.667	0.136	0.926	2454045.7736			17377.719	8.002432
BKAUR	9.127	0.657	0.147	0.894	2454045.8463			17377.719	8.002432
BKAUR	9.533	0.755	0.205	0.692	2454047.9257			17377.719	8.002432
BKAUR	9.569	0.801	0.207	0.629	2454048.9225			17377.719	8.002432
BKAUR	9.857	0.835	0.264	0.523	2454049.9218			17377.719	8.002432
BKAUR	9.831	0.795	0.235	0.553	2454050.9111			17377.719	8.002432
BKAUR	9.122	0.621	0.122	0.970	2454052.9518			17377.719	8.002432
CNSCT	12.320	1.407	0.253	1.294	2446962.9032			28670.16	9.9923
CNSCT	12.240				2446963.9005	2.774	63.9012	28670.16	9.9923
CNSCT	12.375			0.623	2446967.9151	2.655	67.9158	28670.16	9.9923
CNSCT	12.483	1.522	0.391	0.331	2446968.9039			28670.16	9.9923
CNSCT	12.223	1.458	0.027	1.074	2454190.0101			28670.16	9.9923

TABLE 5 (CONTINUED)

Star	V	$b-y$	m_1	c_1	HJD ($uvby$)	β	HJD (β)	Epoch-2400000	P (days)
CNSCT	12.351	1.537	0.015	0.269	2454191.9883			28670.16	9.9923
CNSCT	12.521	1.568	0.055	0.418	2454192.9969			28670.16	9.9923
SYAUR	9.116	0.769	0.160	0.774	2447832.8484	2.652	32.8489	36843.52	10.14452
SYAUR	9.350	0.798	0.184	0.687	2447835.9294	2.636	35.9298	36843.52	10.14452
SYAUR	8.995	0.681	0.131	0.895	2447837.8819	2.654	37.8845	36843.52	10.14452
SYAUR	9.129	0.759			2449399.7761			36843.52	10.14452
SYAUR	8.961		0.138	0.682	2454040.9054			36843.52	10.14452
SYAUR	9.073	0.789	0.170	0.739	2454041.8231			36843.52	10.14452
SYAUR		0.795	0.162	0.745	2454041.8619			36843.52	10.14452
SYAUR		0.790	0.179	0.715	2454041.9533			36843.52	10.14452
SYAUR		0.848	0.185	0.691	2454042.8181			36843.52	10.14452
SYAUR		0.855	0.182	0.679	2454042.8686			36843.52	10.14452
SYAUR		0.818	0.221	0.543	2454043.8829			36843.52	10.14452
SYAUR	9.284	0.781	0.181	0.712	2454044.8047			36843.52	10.14452
SYAUR	9.293	0.777	0.179	0.718	2454044.8511			36843.52	10.14452
SYAUR	9.121	0.746	0.163	0.726	2454045.7653			36843.52	10.14452
SYAUR	9.134	0.745	0.174	0.853	2454045.8370			36843.52	10.14452
SYAUR	8.867	0.642	0.103	1.006	2454047.9160			36843.52	10.14452
SYAUR	8.719	0.628	0.077	1.060	2454048.9148			36843.52	10.14452
SYAUR	8.874	0.677			2454049.9116			36843.52	10.14452
SYAUR	9.052	0.737	0.143	0.773	2454050.9028			36843.52	10.14452
SYAUR	9.283	0.817	0.215	0.637	2454052.9428			36843.52	10.14452
SYAUR	8.735	0.627	0.107	1.079	2454383.9687			36843.52	10.14452
SYAUR	8.926	0.692	0.143	0.890	2454384.9686			36843.52	10.14452
SYAUR	9.053	0.738	0.164	0.748	2454386.0031			36843.52	10.14452
SYAUR	9.176	0.785	0.183	0.732	2454386.9821			36843.52	10.14452
SYAUR	9.294	0.811	0.209	0.650	2454387.9744			36843.52	10.14452
SYAUR	9.370	0.843		0.692	2454388.9879			36843.52	10.14452
SYAUR	9.332	0.779	0.194	0.693	2454389.9764			36843.52	10.14452
SYAUR	8.910	0.663	0.125	0.980	2454391.9714			36843.52	10.14452
SYAUR	8.821	0.645	0.098	1.031	2454392.9513			36843.52	10.14452
SYAUR	8.732	0.628		1.101	2454393.9510			36843.52	10.14452
SYAUR	8.936	0.680	0.141	0.995	2454394.9587			36843.52	10.14452
SYAUR	9.002	0.743	0.152	0.817	2454395.9597			36843.52	10.14452
SYAUR	9.159	0.744	0.186	0.731	2454396.9492			36843.52	10.14452
SYAUR	9.283	0.799	0.217	0.665	2454397.9402			36843.52	10.14452
SYAUR	9.371	0.814	0.218	0.638	2454398.9401			36843.52	10.14452
ANAUR	10.534	0.844	0.135	0.627	2447828.9993	2.618	28.9999	36843.309	10.2906
ANAUR	10.130	0.759	0.114	0.921	2447832.8379	2.66	32.8384	36843.309	10.2906
ANAUR	10.366	0.858	0.153	0.685	2447833.9419	2.638	33.9426	36843.309	10.2906
ANAUR	10.634	0.906	0.247	0.597	2447835.9147	2.603	35.9158	36843.309	10.2906
ANAUR	10.803	0.920	0.271	0.496	2447837.8668	2.632	37.8693	36843.309	10.2906
ANAUR	10.755	0.889	0.249	0.527	2448887.9491	2.641	87.9487	36843.309	10.2906
ANAUR	10.518	0.814	0.176	0.660	2448888.9818	2.634	88.9808	36843.309	10.2906
ANAUR		0.754	0.165	0.807	2448890.9608	2.666	90.9604	36843.309	10.2906
ANAUR	10.144	0.738	0.135	0.859	2448891.9506	2.642	91.9500	36843.309	10.2906
ANAUR	10.347	0.853	0.163	0.710	2448893.9519	2.65	93.9524	36843.309	10.2906
ANAUR	10.483	0.907	0.207	0.637	2448894.9510	2.62	94.9506	36843.309	10.2906
ANAUR	10.643	0.938	0.236	0.625	2448895.9798	2.624	95.9803	36843.309	10.2906
ANAUR	10.825	0.958	0.236	0.561	2448897.0030	2.59	97.0038	36843.309	10.2906
ANAUR	10.569	0.862	0.196	0.326	2454040.9093			36843.309	10.2906
ANAUR		1.014	0.222	0.634	2454041.8574			36843.309	10.2906
ANAUR		0.964	0.251	0.532	2454041.9480			36843.309	10.2906
ANAUR		0.825	0.174	0.782	2454043.8778			36843.309	10.2906
ANAUR	10.205	0.799	0.146	2.033	2454044.8001			36843.309	10.2906
ANAUR	10.244	0.770	0.113	1.317	2454044.8461			36843.309	10.2906
ANAUR	10.161	0.775	0.131	0.816	2454045.7611			36843.309	10.2906
ANAUR	10.155	0.787	0.165	1.286	2454045.8329			36843.309	10.2906
ANAUR	10.465	0.880	0.190	0.796	2454048.9102			36843.309	10.2906
ANAUR	10.521	0.933	0.245	0.632	2454049.9067			36843.309	10.2906
ANAUR	10.657	0.978	0.200	0.554	2454050.8968			36843.309	10.2906
ANAUR	10.777	0.935	0.246	0.556	2454052.9376			36843.309	10.2906
ANAUR	10.770	0.979		0.638	2454380.0115			36843.309	10.2906
ANAUR	10.792	0.917	0.246	0.482	2454382.0012			36843.309	10.2906
ANAUR	10.578	0.838	0.163	0.663	2454383.0112			36843.309	10.2906

TABLE 5 (CONTINUED)

Star	V	$b-y$	m_1	c_1	HJD ($uvby$)	β	HJD (β)	Epoch-2400000	P (days)
ANAUR	10.336	0.766	0.139	0.825	2454383.9615			36843.309	10.2906
ANAUR	10.260	0.762	0.123	0.912	2454384.9646			36843.309	10.2906
ANAUR	10.278	0.772	0.121	0.930	2454384.9991			36843.309	10.2906
ANAUR	10.228	0.752	0.112	0.897	2454385.9982			36843.309	10.2906
ANAUR		0.761	0.125	0.909	2454386.9756			36843.309	10.2906
ANAUR	10.368	0.836	0.172	0.722	2454387.9681			36843.309	10.2906
ANAUR	10.471	0.912		0.714	2454388.9796			36843.309	10.2906
ANAUR	10.817	0.945	0.269	0.576	2454391.9662			36843.309	10.2906
ANAUR	10.677	0.875	0.197	0.600	2454392.9461			36843.309	10.2906
ANAUR					2454393.9451			36843.309	10.2906
ANAUR	10.265	0.746	0.132	1.019	2454394.9525			36843.309	10.2906
ANAUR	10.224	0.775	0.135	0.885	2454395.9538			36843.309	10.2906
ANAUR	10.423	0.862	0.169	0.674	2454398.9375			36843.309	10.2906
ANAUR	10.734	0.952	0.259	0.569	2454750.9690			36843.309	10.2906
ANAUR	10.801	0.930	0.237	0.446	2454751.9635			36843.309	10.2906
ANAUR	10.692	0.876	0.282	1.130	2454752.9489			36843.309	10.2906
ANAUR	10.437	0.806	0.158	1.539	2454753.9277			36843.309	10.2906
ANAUR	10.371	0.838	0.173	0.853	2454809.7383			36843.309	10.2906
ANAUR	10.473	0.893	0.093	0.687	2454810.7554			36843.309	10.2906
YSCT		0.935	0.197	0.879	2446962.8933			34947.2	10.341504
YSCT	9.127	0.918	0.191	0.829	2446963.8906	2.677	63.8910	34947.2	10.341504
YSCT	9.439	1.048	0.315	0.568	2446965.8418			34947.2	10.341504
YSCT	9.756	1.150	0.459	0.342	2446967.9038	2.631	67.9042	34947.2	10.341504
YSCT	9.900	1.188	0.508	0.257	2446968.8926			34947.2	10.341504
ZLAC	8.548	0.749	0.290	0.516	2448887.6472	2.629	87.6463	42827.123	10.885613
ZLAC	7.919	0.592	0.183	0.987	2448890.6705	2.675	90.6699	42827.123	10.885613
ZLAC	8.148	0.695	0.224	0.715	2448891.6806	2.647	91.6799	42827.123	10.885613
ZLAC	8.231	0.750	0.253	0.645	2448892.6924	2.634	92.6919	42827.123	10.885613
ZLAC	8.532	0.861	0.333	0.504	2448894.6258	2.624	94.6253	42827.123	10.885613
ZLAC	8.753	0.911	0.382	0.430	2448895.6721	2.629	95.6725	42827.123	10.885613
ZLAC	8.856	0.912	0.372	0.452	2448896.6355	2.63	96.6360	42827.123	10.885613
ZLAC	8.752	0.875	0.270	0.548	2452500.9199			42827.123	10.885613
ZLAC	8.542	0.783	0.217	0.670	2452501.9153			42827.123	10.885613
ZLAC	8.388	0.736	0.180	0.793	2452502.9009			42827.123	10.885613
ZLAC	8.180	0.678	0.147	0.941	2452503.9065			42827.123	10.885613
ZLAC	7.904	0.611	0.132	1.102	2452504.8451			42827.123	10.885613
ZLAC	8.028	0.614	0.127	0.957	2455007.8756	2.689	7.8752	42827.123	10.885613
ZLAC	8.075	0.733	0.167	0.866	2455008.8769	2.670	8.8773	42827.123	10.885613
ZLAC	8.195	0.706	0.199	0.720	2455009.8787	2.640	9.8791	42827.123	10.885613
VXPER	9.297	0.845	0.206	0.616	2447832.8185	2.635	32.8190	43758.994	10.88904
VXPER	9.421	0.896	0.225	0.527	2447833.8773	2.599	33.8777	43758.994	10.88904
VXPER	9.662	0.927	0.272	0.440	2447835.8890	2.625	35.8895	43758.994	10.88904
VXPER	9.405	0.821	0.187	0.572	2447837.8412	2.626	37.8423	43758.994	10.88904
TYSCT	10.524	1.139	0.315	0.565	2446961.9112	2.69	61.9116	37377.09	11.05302
TYSCT	10.972		0.294	0.208	2446963.8969	2.613	63.8974	37377.09	11.05302
TYSCT	11.063	1.228	0.418	0.374	2446967.9117	2.64	67.9125	37377.09	11.05302
TYSCT	10.867	1.173	0.348	0.487	2446968.9010			37377.09	11.05302
TYSCT	10.295	1.073	0.078	1.019	2454190.0149			37377.09	11.05302
TYSCT	10.533	1.186	0.162	0.881	2454190.9973			37377.09	11.05302
TYSCT	10.664	1.234	0.141	0.579	2454191.9907			37377.09	11.05302
TYSCT	10.815	1.299	0.200	0.450	2454192.9986			37377.09	11.05302
SVPER	9.216	0.839	0.146	0.353	2447828.9930	2.621	28.9938	43839.296	11.129318
SVPER	9.043	0.719	0.117	0.602	2447832.8319	2.638	32.8324	43839.296	11.129318
SVPER	8.985	0.677	0.124	0.680	2447833.8940	2.66	33.8946	43839.296	11.129318
SVPER	8.676	0.678	0.125	0.704	2447835.9084	2.666	35.9089	43839.296	11.129318
SVPER	8.903	0.762	0.167	0.507	2447837.8697	2.632	37.8720	43839.296	11.129318
SVPER	9.338	0.791	0.186	0.308	2448887.9449	2.65	87.9444	43839.296	11.129318
SVPER	9.203	0.754	0.167	0.402	2448888.9762	2.627	88.9754	43839.296	11.129318
SVPER	8.943	0.682	0.147	0.593	2448890.9572	2.669	90.9568	43839.296	11.129318
SVPER	8.477	0.587	0.100	0.908	2448891.9481	2.674	91.9485	43839.296	11.129318
SVPER	8.633	0.662	0.128	0.692	2448892.9367	2.671	92.9363	43839.296	11.129318
SVPER	8.729	0.716	0.121	0.653	2448893.9489	2.669	93.9493	43839.296	11.129318
SVPER	8.865	0.776	0.142	0.557	2448894.9472	2.655	94.9476	43839.296	11.129318
SVPER	8.999	0.813	0.145	0.490	2448895.9765	2.655	95.9760	43839.296	11.129318
RXAUR	7.303	0.542	0.143	0.964	2447829.0017	2.655	29.0022	39075.63	11.623515

TABLE 5 (CONTINUED)

Star	V	$b-y$	m_1	c_1	HJD ($uvby$)	β	HJD (β)	Epoch-2400000	P (days)
RXAUR	7.752	0.713	0.270	0.608	2447832.8403	2.608	32.8423	39075.63	11.623515
RXAUR	7.873	0.741	0.303	0.533	2447833.9555	2.608	33.9560	39075.63	11.623515
RXAUR	7.971	0.718	0.286	0.550	2447835.9176	2.602	35.9179	39075.63	11.623515
RXAUR	7.720	0.619	0.226	0.702	2447837.8644	2.638	37.8667	39075.63	11.623515
RXAUR		0.571	0.180	0.908	2447943.7530	2.638	43.7547	39075.63	11.623515
RXAUR	7.355	0.554	0.173	0.951	2447945.6787	2.648	45.6798	39075.63	11.623515
RXAUR	7.487	0.601	0.202	0.909	2447946.6519	2.633	46.6529	39075.63	11.623515
RXAUR	7.458	0.588	0.222	0.749	2448887.9510	2.634	87.9506	39075.63	11.623515
RXAUR	7.580	0.639	0.252	0.683	2448888.9842	2.62	88.9835	39075.63	11.623515
RXAUR	7.778	0.709	0.323	0.510	2448890.9627	2.601	90.9623	39075.63	11.623515
RXAUR	7.881	0.729	0.347	0.463	2448891.9526	2.601	91.9522	39075.63	11.623515
RXAUR	7.947	0.733	0.329	0.508	2448892.9437	2.606	92.9430	39075.63	11.623515
RXAUR	7.918	0.704	0.268	0.594	2448893.9540	2.633	93.9536	39075.63	11.623515
RXAUR	7.801	0.672	0.221	0.670	2448894.9521	2.636	94.9525	39075.63	11.623515
RXAUR	7.675	0.631	0.182	0.793	2448895.9813	2.651	95.9817	39075.63	11.623515
RXAUR		0.762	0.303	0.537	2454041.8208			39075.63	11.623515
RXAUR		0.755	0.314	0.522	2454041.8592			39075.63	11.623515
RXAUR		0.753	0.314	0.523	2454041.9501			39075.63	11.623515
RXAUR		0.761	0.297	0.571	2454042.8149			39075.63	11.623515
RXAUR		0.758	0.299	0.558	2454042.8650			39075.63	11.623515
RXAUR		0.696	0.277	0.546	2454043.8793			39075.63	11.623515
RXAUR	7.672	0.632	0.219	0.702	2454044.8019			39075.63	11.623515
RXAUR	7.675	0.627	0.223	0.698	2454044.8483			39075.63	11.623515
RXAUR	7.567	0.609	0.198	0.779	2454045.7634			39075.63	11.623515
RXAUR	7.596	0.604	0.204	0.777	2454045.8348			39075.63	11.623515
RXAUR	7.332	0.530	0.159	0.962	2454047.9136			39075.63	11.623515
RXAUR	7.445	0.589	0.195	0.814	2454048.9127			39075.63	11.623515
RXAUR	7.544	0.637	0.235	0.710	2454049.9089			39075.63	11.623515
RXAUR	7.673	0.677	0.250	0.649	2454050.8999			39075.63	11.623515
RXAUR	7.905	0.750	0.331	0.516	2454052.9400			39075.63	11.623515
RXAUR	7.870	0.684	0.268	0.599	2454078.84			39075.63	11.623515
RXAUR	7.764	0.637	0.235	0.797	2454079.837			39075.63	11.623515
RXAUR	7.623	0.604	0.206	0.785	2454080.858			39075.63	11.623515
RXAUR	8.058	0.743	0.284	0.596	2454380.0071			39075.63	11.623515
RXAUR	7.766	0.638	0.234	0.663	2454382.0050			39075.63	11.623515
RXAUR	7.650	0.602	0.207	0.788	2454383.0125			39075.63	11.623515
RXAUR	7.432	0.543	0.173	0.945	2454383.9656			39075.63	11.623515
RXAUR	7.293	0.524	0.162	0.995	2454384.9667			39075.63	11.623515
RXAUR	7.297	0.526	0.158	0.992	2454384.9957			39075.63	11.623515
RXAUR	7.433	0.582	0.197	0.803	2454386.0001			39075.63	11.623515
RXAUR	7.535	0.634	0.222	0.768	2454386.9787			39075.63	11.623515
RXAUR	7.641	0.675	0.261	0.673	2454387.9712			39075.63	11.623515
RXAUR	7.764	0.727	0.230	0.628	2454388.9848			39075.63	11.623515
RXAUR		0.742	0.331	0.565	2454389.9732			39075.63	11.623515
RXAUR		0.924	0.429	0.200	2454390.9826			39075.63	11.623515
RXAUR	7.962	0.724	0.311	0.576	2454391.9689			39075.63	11.623515
RXAUR	7.852	0.665	0.261	0.629	2454392.9488			39075.63	11.623515
RXAUR	7.732	0.627	0.208	0.730	2454393.9484			39075.63	11.623515
RXAUR	7.607	0.578	0.204	0.911	2454394.9560			39075.63	11.623515
RXAUR	7.297	0.523	0.156	1.001	2454395.9568			39075.63	11.623515
RXAUR	7.345	0.517	0.177	0.927	2454396.9465			39075.63	11.623515
RXAUR	7.475	0.601	0.211	0.808	2454397.9388			39075.63	11.623515
RXAUR	7.570	0.643	0.240	0.706	2454398.9347			39075.63	11.623515
RXAUR	7.664	0.674	0.283	0.634	2454399.9724			39075.63	11.623515
RXAUR	7.936	0.749	0.329	0.504	2454750.9718			39075.63	11.623515
RXAUR	7.976	0.731	0.304	0.546	2454751.9682			39075.63	11.623515
RXAUR	7.895	0.684	0.278	0.613	2454752.9530			39075.63	11.623515
RXAUR	7.771	0.643	0.227	0.757	2454753.9309			39075.63	11.623515
RXAUR	7.986	0.740	0.331	0.624	2454809.7424			39075.63	11.623515
RXAUR	7.938	0.715	0.188	0.623	2454810.7576			39075.63	11.623515
ZSCT	9.953	1.019	0.542	0.272	2446962.8952			36247.16	12.901325
ZSCT	9.931	0.980	0.482	0.207	2446963.8925	2.621	63.8930	36247.16	12.901325
ZSCT	9.917	0.880	0.331	0.526	2446965.8407			36247.16	12.901325
ZSCT	9.109	0.728	0.181	0.941	2446967.9055	2.676	67.9060	36247.16	12.901325
ZSCT	9.149	0.765	0.233	0.782	2446968.8955			36247.16	12.901325

TABLE 5 (CONTINUED)

Star	V	$b-y$	m_1	c_1	HJD ($uvby$)	β	HJD (β)	Epoch-2400000	P (days)
TXCYG	9.603	1.446	0.302	0.440	2448890.6327	2.653	90.6321	43794.971	14.7098
TXCYG	9.712	1.489	0.331	0.268	2448891.6517	2.63	91.6510	43794.971	14.7098
TXCYG	9.965	1.536	0.366	0.276	2448893.7043	2.651	93.7047	43794.971	14.7098
TXCYG	9.985	1.515	0.330	0.406	2448894.6140	2.636	94.6144	43794.971	14.7098
TXCYG	9.941	1.475	0.271	0.541	2448895.6849	2.642	95.6856	43794.971	14.7098
TXCYG	9.792	1.416	0.163	0.604	2448896.6891	2.67	96.6892	43794.971	14.7098
TXCYG	9.057	1.241	0.040	0.775	2455006.8867	2.680	6.8871	43794.971	14.7098
TXCYG	9.286	1.324	0.072	0.618	2455007.8740	2.669	7.8736	43794.971	14.7098
TXCYG	9.399		0.167	0.499	2455008.8692	2.649	8.8696	43794.971	14.7098
TXCYG	9.504	1.394	0.168	0.486	2455009.8693	2.664	9.8707	43794.971	14.7098
RWCAS	9.651	1.020	0.481	0.242	2447832.7477	2.622	32.7492	35575.227	14.7949
RWCAS	9.756	1.028	0.478	0.259	2447833.8739	2.656	33.8746	35575.227	14.7949
RWCAS	9.611	0.909	0.370	0.382	2447835.8862	2.632	35.8866	35575.227	14.7949
SZCYG	9.333	1.067	0.364	0.282	2455006.8807	2.632	6.8815	43306.79	15.10965
SZCYG	9.544	1.130	0.439	0.279	2455007.8654	2.608	7.8655	43306.79	15.10965
SZCYG	9.653		0.510	0.125	2455008.8562	2.592	8.8567	43306.79	15.10965
SZCYG	9.744	1.162	0.524	0.128	2455009.8417	2.608	9.8422	43306.79	15.10965
ERAUR	9.984		0.338		2454040.9171			43861.3	15.69073
ERAUR	9.778	0.730	0.399	0.412	2454041.8765			43861.3	15.69073
ERAUR	9.759	0.727	0.390	0.387	2454041.9593			43861.3	15.69073
ERAUR	9.948	0.704	0.397	0.319	2454043.8891			43861.3	15.69073
ERAUR	10.005	0.703	0.412	0.413	2454044.8559			43861.3	15.69073
ERAUR	9.980	0.714	0.423	0.375	2454045.7687			43861.3	15.69073
ERAUR		0.707			2454045.8421			43861.3	15.69073
ERAUR	10.107	0.701	0.437	0.371	2454047.9214			43861.3	15.69073
ERAUR	10.062	0.710	0.411	0.381	2454048.9185			43861.3	15.69073
ERAUR	10.055	0.731	0.399	0.362	2454049.9160			43861.3	15.69073
ERAUR	10.091	0.712		0.346	2454052.9472			43861.3	15.69073
XCYG	6.784	0.892	0.427	0.276	2449216.8791			43830.387	16.386332
XCYG	6.609	0.824	0.329	0.407	2449217.8666			43830.387	16.386332
XCYG	6.710	0.931	0.496	0.357	2449507.9857			43830.387	16.386332
XCYG	6.783	0.931	0.538	0.240	2449508.9608			43830.387	16.386332
XCYG	6.860	0.914	0.514	0.188	2449510.9498			43830.387	16.386332
XCYG	6.841	0.852	0.485	0.275	2449511.9769			43830.387	16.386332
XCYG	6.726	0.755	0.413	0.320	2449512.9663			43830.387	16.386332
XCYG	6.703	0.753	0.363	0.409	2449513.9712			43830.387	16.386332
XCYG	6.216	0.630	0.240	0.706	2449514.9814			43830.387	16.386332
XCYG	5.907	0.594	0.216	0.756	2455006.8773	2.653	6.8777	43830.387	16.386332
XCYG	6.059	0.663	0.267	0.658	2455007.8628	2.646	7.8632	43830.387	16.386332
XCYG	6.159	0.803	0.337	0.520	2455008.8542	2.642	8.8547	43830.387	16.386332
XCYG		0.751	0.364	0.436	2455009.8398	2.647	9.8399	43830.387	16.386332
RWCAM	8.251	0.846	0.091	0.696	2447828.9812	2.656	28.9824	37389.57	16.41437
RWCAM	8.600	1.016	0.162	0.327	2447833.8844	2.633	33.8856	37389.57	16.41437
RWCAM	8.741	1.059	0.154	0.219	2447835.8988	2.636	35.8991	37389.57	16.41437
RWCAM	8.918	1.063	0.158	0.136	2447837.8483	2.625	37.8505	37389.57	16.41437
YZAUR	10.543	0.959	0.184	0.540	2447832.8512	2.621	32.8508	37431.141	18.1929
YZAUR	10.053	0.776	0.123	0.840	2447835.9317	2.655	35.9322	37431.141	18.1929
YZAUR		0.794	0.131	0.849	2447837.8794	2.627	37.8819	37431.141	18.1929
YZAUR	10.538	0.938	0.272	0.346	2448887.9529	2.607	87.9525	37431.141	18.1929
YZAUR	10.530	0.912	0.261	0.451	2448888.9867	2.628	88.9860	37431.141	18.1929
YZAUR	10.072	0.767	0.148	0.802	2448890.9645	2.655	90.9641	37431.141	18.1929
YZAUR	9.905	0.756	0.142	0.809	2448891.9541	2.646	91.9537	37431.141	18.1929
YZAUR		0.784	0.152	0.819	2448892.9455	2.656	92.9452	37431.141	18.1929
YZAUR		0.842	0.150	0.775	2448893.9551	2.638	93.9416	37431.141	18.1929
YZAUR		0.893	0.181	0.716	2448894.9532	2.646	94.9536	37431.141	18.1929
YZAUR		0.924	0.229	0.704	2448895.9825	2.605	95.9829	37431.141	18.1929
YZAUR	10.278	0.953	0.251	0.589	2448897.0055	2.604	97.0060	37431.141	18.1929
YZAUR	10.361	0.903			2449399.7871			37431.141	18.1929
YZAUR	9.837		0.114	0.731	2454040.9072			37431.141	18.1929
YZAUR	9.625	0.831	0.117	0.822	2454041.8638			37431.141	18.1929
YZAUR	9.629	0.827	0.128	0.821	2454041.9551			37431.141	18.1929
YZAUR		0.897	0.145	0.773	2454042.8209			37431.141	18.1929
YZAUR		0.905	0.158	0.783	2454042.8718			37431.141	18.1929
YZAUR	9.815	0.879	0.206	0.489	2454043.8842			37431.141	18.1929
YZAUR	10.128	0.913	0.243	0.604	2454044.8066			37431.141	18.1929

TABLE 5 (CONTINUED)

Star	V	$b-y$	m_1	c_1	HJD ($uvby$)	β	HJD (β)	Epoch-2400000	P (days)
YZAUR	10.127	0.929	0.220	0.650	2454044.8532			37431.141	18.1929
YZAUR	10.093	0.966	0.299	0.452	2454045.7672			37431.141	18.1929
YZAUR	10.111	0.992			2454045.8387			37431.141	18.1929
YZAUR	10.440	1.013	0.351	0.383	2454047.9186			37431.141	18.1929
YZAUR	10.506	1.031	0.359	0.335	2454048.9167			37431.141	18.1929
YZAUR	10.615	1.055	0.424	0.265	2454049.9137			37431.141	18.1929
YZAUR	10.713	1.064	0.408	0.332	2454050.9054			37431.141	18.1929
YZAUR	10.802	1.046	0.422	0.322	2454052.9457			37431.141	18.1929
RUSCT	9.434	1.254	0.442	0.471	2446962.8966			31174.67	19.70062
RUSCT	9.422	1.219	0.387	0.336	2446963.8939	2.64	63.8943	31174.67	19.70062
RUSCT	9.833	1.300	0.575	0.213	2446967.9073	2.63	67.9078	31174.67	19.70062
RUSCT	9.862	1.299	0.570	0.202	2446968.8981			31174.67	19.70062
RUSCT		1.359	0.330	0.122	2455006.8254	2.652	6.8260	31174.67	19.70062
RUSCT	9.918	1.391	0.389	0.155	2455007.8016	2.625	7.8023	31174.67	19.70062
RUSCT	9.942	1.331	0.352	0.194	2455009.7980	2.643	9.7989	31174.67	19.70062
RUSCT	9.919	1.297	0.356	0.442	2455010.7956	2.649	10.7945	31174.67	19.70062
VXCYG	10.196	1.312	0.469	0.275	2448885.6451	2.638	85.6459	43783.641	20.133408
VXCYG	10.369	1.351	0.543	0.164	2448887.6211	2.607	87.6207	43783.641	20.133408
VXCYG	10.477	1.377	0.555	0.129	2448888.6461	2.604	88.6454	43783.641	20.133408
VXCYG	10.574	1.372	0.545	0.178	2448890.6300	2.639	90.6294	43783.641	20.133408
VXCYG	10.501	1.343	0.487	0.122	2448891.6485	2.632	91.6478	43783.641	20.133408
VXCYG	10.108	1.174	0.198	0.642	2448895.6830	2.644	95.6838	43783.641	20.133408
VXCYG	9.646	1.036	0.082	0.934	2448896.6870	2.679	96.6866	43783.641	20.133408
VXCYG	9.556	1.132	0.041	0.682	2453931.9365			43783.641	20.133408
VXCYG	9.812	1.287	0.240	0.369	2453934.9314			43783.641	20.133408
VXCYG	10.425	1.355	0.466	0.097	2455009.8666	2.632	9.8671	43783.641	20.133408

Autónoma de México for the opportunity to carry out the observations. Typing was partially done by J. Orta, and proofreading by J. Miller. C. Guzmán, F. Ruiz and A. Díaz assisted us in the computer reductions. We are indebted to an anonymous referee for a series of comments and suggestions that led to improvement of the present paper. This research has made use of the Simbad databases operated at CDS, Strasbourg, France, and the NASA ADS Astronomy Query Form.

REFERENCES

Andrievsky, S. M., Luck, R. E., Martin, P., & Lepine, J. R. D. 2004, A&A 413, 159
Arellano Ferro, A. 1983, ApJ, 274, 755
Arellano Ferro, A., & Mantegazza, L. 1996, A&A, 315, 542
Arellano Ferro, A., & Parrao, L. 1989, Reporte Técnico, 57 (México: IA-UNAM)
Arellano Ferro, A., Rojo Arellano, E., González-Bedolla, S., & Rosenzweig, P. 1998, ApJS, 117, 167
Arellano Ferro, A., & Rosenzweig, P. 2000, MNRAS, 315, 296
Chulhee, K. 2008, ApJ, 674, 1062
Crawford, D. L. 1975, AJ, 80, 955
_________. 1979, AJ, 84, 1858
Eggen, O. J. 1983, AJ, 88, 998
_________. 1985, AJ, 90, 1297
Feltz, K. A., & McNamara, D. H. 1980, PASP, 92, 609
Grönbech, B., & Olsen, E. 1977, A&AS, 27, 443
Grönbech, B., Olsen, E. H., & Stromgren, B. 1976, A&AS, 26, 155
Kovács, G., & Walker, A. R. 2001, A&A, 371, 579
Meakes, M., Wallerstein, G., & Opalko, J. F. 1991, AJ, 101, 1795
Olsen, E. H. 1983, A&AS, 54, 55
_________. 1984, A&AS, 57, 443
Peña, J. H., Arellano Ferro, A., Peña Miller, R., Sareyan, J. P., & Álvarez, M. 2009, RevMexAA, 45, 191
Samus, N. N., et al. 2009, General Catalogue of Variable Stars (Moscow: Sternberg Astronomical Institute)
Szabados, L. 1991, Comm. Konkoly Obs., 96, 123

A. Arellano Ferro, C. A. Guerrero, J. H. Peña, & A. Rentería: Instituto de Astronomía, Universidad Nacional Autónoma de México, Apdo. Postal 70-264, México D. F. CP 04510, México (jhpena@astroscu.unam.mx).
M. Álvarez: Instituto de Astronomía, Universidad Nacional Autónoma de México, Ensenada.
J. P. Sareyan: OCA, Department Gemini, Boulevard de l'Observatoire BP 4229, 06304 Nice Cedex 4, France.
R. Peña: Department of Mathematics, Imperial College London, South Kensington Campus, London SW7 2AZ, UK.

Revista Mexicana de Astronomía y Astrofísica, **46**, 309–322 (2010)

HYPERCRITICAL ACCRETION ONTO A MAGNETIZED NEUTRON STAR SURFACE: A NUMERICAL APPROACH

C. G. Bernal, W. H. Lee, and Dany Page

Instituto de Astronomía
Universidad Nacional Autónoma de México, Mexico

Received 2010 January 19; accepted 2010 June 14

RESUMEN

La acreción sobre una proto-estrella de neutrones en las horas que siguen al colapso del núcleo de la estrella masiva que le dio origen puede afectar sus propiedades observables. Este fenómeno se da en el régimen denominado hipercrítico (Chevalier 1989), donde el enfriamiento por neutrinos es crucial para la evolución termodinámica. En este trabajo presentamos un estudio en este contexto en una dimensión con simetría esférica y llevamos a cabo simulaciones numéricas en dos dimensiones dentro de una columna de acreción sobre una estrella de neutrones. Consideramos procesos microfísicos detallados, enfriamiento por neutrinos y la presencia de campos magnéticos en la aproximación de magnetohidrodinámica ideal. Comparamos nuestros resultados numéricos con las soluciones analíticas e investigamos cómo las soluciones, tanto hidrodinámicas como magnetohidrodinámicas, difieren de éstas. Iniciamos también una exploración de cómo este proceso puede afectar la aparición del remanente como un pulsar típico en radio.

ABSTRACT

The properties of a new-born neutron star, produced in a core-collapse supernova, can be strongly affected by the possible late fallback which occurs several hours after the explosion. This accretion occurs in the regime dominated by neutrino cooling, explored initially in this context by Chevalier (1989). Here we revisit this approach in a 1D spherically symmetric model and carry out numerical simulations in 2D in an accretion column onto a neutron star, considering detailed microphysics, neutrino cooling and the presence of magnetic fields in ideal MHD. We compare our numerical results with the analytic solutions and explore how the purely hydrodynamical as well as the MHD solutions differ from them, and begin to explore how this may affect the appearance of the remnant as a typical radio pulsar.

Key Words: accretion, accretion disks — hydrodynamics — magnetic fields — stars: neutron — supernovae: individual (SN1987A)

1. INTRODUCTION

The neutrino signal (Hirata et al. 1987; Bionta et al. 1987) detected from the supernova SN1987A clearly demonstrated the birth of a neutron star (Burrows & Lattimer 1986). Identification of the progenitor as the blue supergiant Sanduleak $-69°202a$ (Gilmozzi et al. 1987) and modeling of the early light curve (Hillebrandt et al. 1987; Shigeyama et al. 1987) proved that the supernova resulted from the core-collapse of a massive, $\sim 20\ M_\odot$, star. However, to date, there is no evidence for the presence of a pulsar, or even a quiet neutron star, in the remnant (see, e.g., discussion in Haberl et al. 2006 and Shternin & Yakovlev 2008). Several solutions to this dilemma have been proposed as, e.g., the delayed collapse of the neutron star into a black-hole (Ellis, Lattimer, & Prakash 1996; Brown & Bethe 1994) or a delayed turn-on of the pulsar (Michel 1994; Muslimov & Page 1995). The latter case is just an extreme case of the more mundane possibility that the

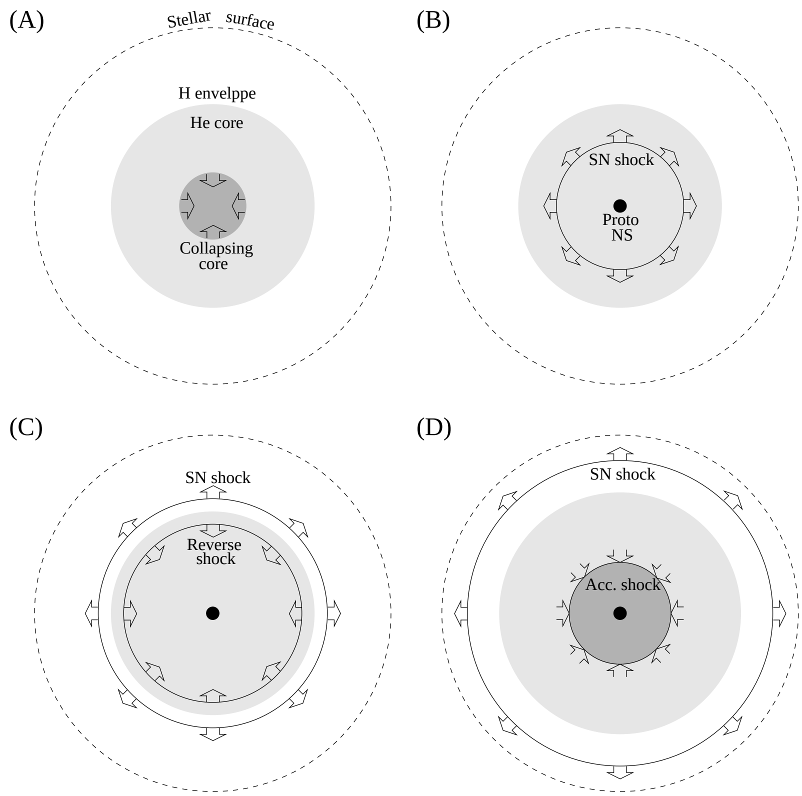

Fig. 1. Schematic evolution of a collapsing stellar core. A, the Chandrasekhar-mass iron core collapses; B, upon formation of a proto-neutron star, the equation of state stiffens and produces a bounce, launching an outwardly propagating shock; C, a reverse shock is formed at the He-H interface in the stellar envelope, moving back towards the neutron star; D, an accretion shock is established, interior to which an atmosphere close to hydrostatic equilibrium in the neutrino-cooled regime deposits mass and energy onto the neutron star in the hours following the explosion.

neutron star is weakly magnetized and/or slowly rotating, resulting in a spin-down energy that is low enough so as to be undetectable.

In recent years, several measurements of pulsar masses point toward large values approaching, or even exceeding, 2 $M_\odot$ (see, e.g., Freire 2008) which would strongly disfavor the black-hole explanation. On the other side, timing of radio quiet compact stars in young supernova remnants, usually dubbed CCOs ("Central Compact Objects", Pavlov et al. 2002) recently unveiled at least three case of weakly magnetized young neutron stars (Gotthelf & Halpern 2008): PSR J0821-4300 (in the SNR Puppis A) with a rotational period $P = 112$ ms, an upper limit on its spin-down power $\dot{E} < 2.3 \times 10^{35}$ erg s^{-1}, and a surface dipolar magnetic field strength $B_{\rm dip} < 9.8 \times 10^{11}$ G (Gotthelf & Halpern 2009); PSR 1E1207.4-5209 (in the SNR PKS 1209-51/52) with $P = 424$ ms, $\dot{E} < 1.3 \times 10^{32}$ erg s^{-1}, and $B_{\rm dip} < 3.3 \times 10^{11}$ G (Gotthelf & Halpern 2007), and finally PSR J1852+0040 (in the SNR Kes 79) with $P = 424$ ms, and measurements of $\dot{E} = 3.0 \times 10^{32}$ erg s^{-1}, and $B_{\rm dip} = 3.1 \times 10^{10}$ G (Halpern & Gotthelf 2010). The last two of these hence have an energy output well below the 0.2–10.0 keV luminosity of the SN 1987A remnant, $L < 5.7 \times 10^{34}$ erg s^{-1} (Haberl et al. 2006). If the neutron star produced by SN 1987A has similar characteristics it would presently be undetectable.

In the present paper we consider the scenario in which the initial magnetic field of the new-born neutron star is strongly modified by a phase of late, and intense, accretion, occurring a few hours after the initial explosion (Geppert, Page, & Zannias 1999). When a massive star explodes as a supernova, following the core-collapse scenario (Woosley & Janka 2005; Mezzacappa 2005; Janka et al. 2007), a large fraction of its mass expands freely and interacts with the interstellar medium. However, the central compact remnant also interacts with the inner envelope through its gravitational field. In Type II SNe (see Figure 1), the initial core-collapse (Panel A) produces a proto-neutron star when the equation of state stiffens close to nuclear density. A high-velocity (10^4 km s^{-1}) expansive shock then starts moving outward (Panel B). Flow lines bifurcate and some part of the matter falls back onto the central remnant. The rest is unbound and ends up being ejected in the explosion. This scenario produces a low density region in near free fall between the surface of the compact object and the extended atmosphere in near hydrostatic equilibrium that has formed. If the progenitor star had a low density envelope surrounding the He core a reverse shock (Panel C) decelerates the matter and causes a late fallback onto the compact object, depositing great amounts of matter onto the surface of the new-born neutron star in the hours following the explosion (Panel D). Following the ideas of Blondin (1986), Chevalier (1989), Houck & Chevalier (1991), and Brown & Weingartner (1994) about the accretion of matter onto compact objects, it is possible to develop an analytical model of accretion following core-collapse, and particularly in the case of SN1987A. One of the salient features of this analysis is that the gas, being quite dense, is unable to cool by photon emission, and the mass accretion rates are highly super-Eddington in that sense. However, at sufficiently high temperatures, cooling through neutrinos sets in, mostly through pair annihilation and pair capture onto free nucleons, and given their much lower interaction cross section with matter, they are able to remove enough energy from the flow for accretion to take place. This regime is usually termed "hypercritical" accretion, is common in the inner collapsing stellar cores and is likely to drive the central engines of Gamma Ray Bursts (Lee & Ramirez-Ruiz 2007). With this model it is formally possible to obtain the radial position of the shock as a function of the mass accretion rate from fallback, assuming steady state in spherical symmetry, as well as the structure of the envelope.

Chevalier (1989) and Houck & Chevalier (1991) computed such solutions in the context of SN1987A. Here we wish to explore the behavior of the flow under more general conditions, and we present solutions for an accretion column in two dimensions, which we compare with the analytical scalings. Neutrino cooling is a crucial ingredient in the relevant density and temperature regimes, and we consider it along with a detailed equation of state. In addition, and more importantly, we begin to explore the effects of the magnetic field on the accumulation of matter onto the neutron star surface. This is only possible through 2D simulations of the kind shown here, and we make a comparative analysis between the analytical and numerical approaches to consider the submergence of the magnetic field in the crust of the neutron star and the piling up of matter on its surface. Previously, Muslimov & Page (1995) and Geppert et al. (1999) considered in one-dimensional calculations how such accretion might delay the switch-on of a pulsar following its formation, by computing the ohmic diffusion time of the magnetic field through the accreted matter. Fryer, Benz, & Herant (1996) studied the two-dimensional accretion dynamics onto new-born neutron stars in the neutrino cooled regime, finding that in some cases, neutrino-driven convection can significantly modify the simple one-dimensional steady state solution.

Here we report on preliminary, two-dimensional numerical calculations which aim to determine if hypercritical, neutrino-cooled accretion can submerge the magnetic field into the crust of the neutron star, and if it plays an important role in the dynamics in this regime. In § 2 we develop the analytical model of the hypercritical accretion process and calculate the structure of the envelope for a two dimensional accretion column. We build a numerical model, based on these analytical consideration, in § 3. In § 4, we show numerical results for various configurations including magnetic fields at several accretion rates and present a comparative analysis between the numerical and analytical solutions for the scenario of SN1987A. Finally, in § 5 we present some preliminary conclusions.

2. ANALYTICAL MODELS

As a benchmark against which to compare our numerical simulations, we summarize below the basic results of an analytical model, based on the one developed by Chevalier (1989), and adapt them to the case of an accretion column. The essential assumptions of the model are that the neutron star is at rest within the expanding medium at infinity and rotation is neglected. For this analytical approach, we also neglect the effect of a possible magnetic field. Matter is described by a polytropic equation of state, $P = K\rho^{\gamma}$ with an index $\gamma = 4/3$, and is assumed to evolve adiabatically, except at the shock interfaces and close to the neutron star surface where neutrino emission (through $e^{\pm}$ pair annihilation) assures that the accretion energy is properly removed from the system.

2.1. *The Initial Late-Accretion Rate in SN1987A*

Spherically symmetric accretion by a compact star in an initially static, infinite, background was described by Bondi (1952) (see also, e.g., Shapiro & Teukolsky 1983). The mass accretion rate $\dot{M}$ is obtained from the density and sound velocity at infinity, ρ_∞ and c_∞ respectively, as

$$\dot{M}_{\rm B} = 4\pi\lambda \left(\frac{GM}{c_\infty^2}\right)^2 \rho_\infty c_\infty \,, \tag{1}$$

where the numerical constant $\lambda = 1/\sqrt{2} \simeq 0.707$ for the case of an ideal gas with adiabatic index $\gamma = 4/3$. In our case the medium is not strictly initially at rest but has been set into expansion by the supernova shock wave. At early times the core is in homologous expansion, with a velocity $v = r/t$ and density ρ such that $\rho t^3 = \rho_{\rm a} t_{\rm a}^3$ is constant, in terms of a reference density $\rho_{\rm a}$ at time $t_{\rm a}$. As long as the time t is smaller than the Bondi accretion time scale $\tau_{\rm B} \simeq GM/c_\infty^3$, one can still estimate $\dot{M}$ with equation (1) by allowing ρ_∞ and c_∞ to be time dependent, and obtain (Chevalier 1989)

$$\dot{M}_{\rm B} = 5.77 \frac{(GM)^2}{K^{3/2}} (\rho_{\rm a} t_{\rm a}^3)^{1/2}\, t^{-3/2} \,. \tag{2}$$

According to Woosley (1988) and Shigeyama, Nomoto, & Hashimoto (1988), $\rho_{\rm a} t_{\rm a}^3 \sim 10^9$ g cm^{-3} s^3. Now the density and sound velocity at infinity have been estimated, for SN1987A, by Woosley (1988) and Bethe & Pizzochero (1990) as being of the order of

$$\rho_\infty = \frac{2.5\ M_\odot}{(4/3)\pi(v_{\rm f} t)^3} \simeq 1.78 \times 10^{-13} \left(\frac{t}{\rm yr}\right)^{-3} \ {\rm g\ cm^{-3}}, \tag{3}$$

$$c_\infty^2 = \frac{\gamma k_{\rm B} T_\infty}{\mu m_{\rm H}} \simeq 1.24 \times 10^{12} \left(\frac{t}{\rm yr}\right)^{-\frac{3}{4}} \ {\rm cm^2\ s^{-2}}, \tag{4}$$

where $v_{\rm f} \simeq 600\,{\rm km\,s^{-1}}$ is the final expansion velocity and $T_\infty \simeq 70\,{\rm keV}\ (4 \times 10^9\,{\rm cm}/v_{\rm f} t)^{3/4}$ for a radiation dominated shock as in a supernova like SN1987A. Bethe & Pizzochero (1990) calculated that the temperature for a shock radius of 4×10^9 cm is $T_{\rm sh} \simeq 70\,{\rm keV}$. The mass of the expanding CO core is $\sim 4\ M_\odot$, but here we considered only $2.5\ M_\odot$ because $1.5\ M_\odot$ were taken to make the compact object at the center of the supernova. We hence have

$$\begin{aligned} \dot{M} \simeq&\ 2.23 \times 10^{22} \left(\frac{t}{\rm yr}\right)^{-\frac{15}{8}} {\rm g\,s^{-1}} \\ \simeq&\ 3.5 \times 10^{-4} \left(\frac{t}{\rm yr}\right)^{-\frac{15}{8}} M_\odot\,{\rm yr^{-1}}\,. \end{aligned} \tag{5}$$

Woosley (1988) calculated the time that the reverse shock takes to return to the surface of the neutron star for SN1987A as $t \simeq 7 \times 10^3$ s, giving us, for the accretion rate in SN1987A in the hypercritical regime

$$\dot{M} \simeq 1.57 \times 10^{29}\,{\rm g\,s^{-1}} = 2500\ M_\odot\,{\rm yr^{-1}}\,. \tag{6}$$

This accretion rate exceeds by an order of magnitude the value calculated by Chevalier (1989), $\dot{M} = 2.2 \times 10^{28}$ g s^{-1} = 340 $M_\odot$ yr^{-1} because of different assumed values at infinity. Now, the Eddington mass accretion rate when considering photon radiation is $\dot{M}_{\rm Edd} = 3.77 \times 10^{18}\,{\rm g\,s^{-1}}$, if one considers electron scattering in pure ionized Hydrogen as the source of opacity, $k_{\rm es} = 0.4\,{\rm cm^2\,g^{-1}}$. When $\dot{M} \gg \dot{M}_{\rm Edd}$ the flow is what we described above as *Hypercritical Flow*, studied by Blondin (1986). For the case of SN1987A, we have

$$\frac{\dot{M}}{\dot{M}_{\rm Edd}} \simeq 10^9 - 10^{10}\,, \tag{7}$$

for the two values given above, placing such flows clearly in the hypercritical, neutrino cooled, regime. Henceforth we adopt as our fiducial accretion rate the value

$$\dot{M}_0 \simeq 2.2 \times 10^{28}\,{\rm g\,s^{-1}} = 340\ M_\odot\,{\rm yr^{-1}}\,. \tag{8}$$

2.2. *The Envelope and the Shock Radius: Spherical Case*

When the reverse shock bounces against the surface of the neutron star, a third expansive shock is formed, which propagates through the infalling matter. Thus, eventually an atmosphere in quasi-hydrostatic equilibrium is formed around the compact object (see Panel D in Figure 1), whose general structure can be calculated analytically under some simplifying assumptions.

Following the formulation of Chevalier (1989), the structure of the envelope is calculated and an expression for the pressure at the surface of the neutron star, $P_{\rm ns}$, in terms of $\dot{M}$ and the shock radius, $r_{\rm sh}$, is derived. Cooling by neutrinos close to the neutron star surface, which depends on $P_{\rm ns}$, is introduced and this ultimately determines the shock radius solely as a function of the accretion rate. From the condition of hydrostatic equilibrium, $dP/dr = -\rho GM/r^2$, we obtain the integrated values for the pressure, density and velocity as a funtion of the distance from the neutron star surface. This is possible because neutrino cooling is only important near the surface of the neutron star and we can consider that the post-shock flow is adiabatic over the greater part of the volume. In addition, the flow is highly subsonic except close the shock. With this we obtain, $P \propto r^{-\gamma/(\gamma-1)} \propto r^{-4}, \rho \propto r^{-1/(\gamma-1)} \propto r^{-3}, v \propto r^{(3-2\gamma)/(\gamma-1)} \propto r$, where we have used $\gamma = 4/3$. These results also are valid in the shock and the envelope structure in hydrostatic equilibrium is given by

$$P = P_{\rm sh}\left(\frac{r}{r_{\rm sh}}\right)^{-4}, \quad (9)$$

$$\rho = \rho_{\rm sh}\left(\frac{r}{r_{\rm sh}}\right)^{-3}, \quad (10)$$

$$v = v_{\rm sh}\left(\frac{r}{r_{\rm sh}}\right), \quad (11)$$

where $P_{\rm sh}$, $\rho_{\rm sh}$, $v_{\rm sh}$ and $r_{\rm sh}$ are the values at the shock. These values can be obtained from the jump conditions when $P_{\rm sh} \gg P_0$, where P_0 and ρ_0 the pre-shock pressure and density. Under these considerations we obtain $P_{\rm sh} = (7/8)\rho_0 v_0^2$, $\rho_{\rm sh} = 7\rho_0$ and $v_{\rm sh} = -(1/7)v_0$. The pre-shock velocity is that of free-fall, $v_0 = \sqrt{2GM/r_{\rm sh}}$, and the density is $\rho_0 = \dot{M}/4\pi r_{\rm sh}^2 v_0$. From equation (8) we obtain the pressure at the surface, $P_{\rm ns} = 1.36 \times 10^{-12} \dot{M} r_{\rm sh}^{3/2}$, with $M \sim 1.44\ M_\odot$ and $r_{\rm ns} \sim 10^6$ cm. On the other hand, the energy loss by neutrinos (only pair production) by unit volume can be estimated as (Dicus 1972),

$$\dot{\varepsilon}_n = 1.83 \times 10^{-34} P^{2.25}\,{\rm erg\,cm^{-3}\,s^{-1}}\,. \quad (12)$$

In this case, we consider that $e^{\pm}$ pairs also contribute to the pressure. Now, this cooling is operative only in a small volume close to the neutron star surface, $\sim \pi r_{\rm ns}^3$ since it is a sensitive function of temperature. So, from energy conservation, the shock radius is obtained as,

$$r_{\rm sh} \simeq 7.58 \times 10^8 \left(\frac{\dot{M}}{M_\odot\,{\rm yr}^{-1}}\right)^{-\frac{10}{27}} {\rm cm}\,. \quad (13)$$

With this we have the structure of the envelope and the shock radius as a function of the accretion rate. For the case of SN1987A with our fiducial accretion rate $\dot{M} = \dot{M}_0 = 340\ M_\odot\ {\rm yr}^{-1}$, the shock radius is $r_{\rm sh} \simeq 8.77 \times 10^7$ cm.

2.3. *The Envelope and the Shock Radius: The Accretion Column*

If we consider a small rectangular accretion column of area $A_{\rm col}$ onto a fraction of the neutron star surface, with area $A = 4\pi R_{\rm NS}^2$, we can take it to be a plane-parallel surface (see Figure 2). In this case, the spherical mass accretion rate must be scaled to its value in the column. Since in the spherical case the area depends on the distance to the neutron star, while for the case of an accretion column the area is constant, the structure of the envelope and the shock radius are modified. Note that this modification causes the mass accretion rate per unit area to be independent of height in the domain. Also, since it is smaller than in the spherical case, the analytical estimate of the shock radius decreases significantly, and is now given by

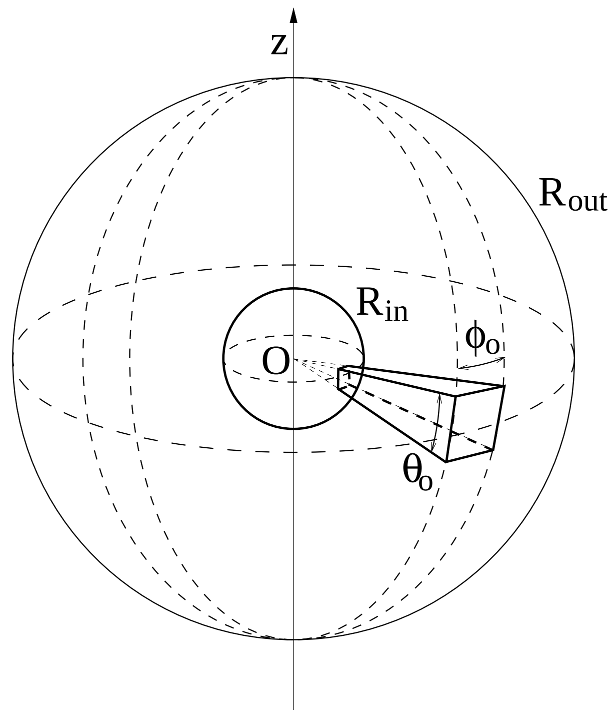

Fig. 2. Schematic geometry of the accretion column onto the neutron star surface.

$$y_{\rm sh} \simeq 7.61 \times 10^6 \left(\frac{\dot{M}/A}{M_\odot\,{\rm yr}^{-1}/A_{\rm col}}\right)^{-0.16} {\rm cm}\,, \quad (14)$$

where y measures the height above the neutron star surface. With these considerations and taking $A_{\rm col} = (3 \times 10^5)^2\ {\rm cm}^2$, the shock radius for the fiducial accretion rate, equation (8), is $y_{\rm sh} = 6.92 \times 10^6$ cm, and the structure of the envelope is given by

$$P = P_{\rm sh}\left(\frac{y}{y_{\rm sh}}\right)^{-4}, \quad (15)$$

$$\rho = \rho_{\rm sh}\left(\frac{y}{y_{\rm sh}}\right)^{-3}, \quad (16)$$

$$v = v_{\rm sh}\left(\frac{y}{y_{\rm sh}}\right)^{3}. \quad (17)$$

The velocity profile is different for the accretion column as well because the column area is constant as a function of height above the neutron star. The conditions in the shock in the SN1987A scenario are thus

$$v_0 = \sqrt{\frac{2GM}{y_{\rm sh}}} \simeq 7.53 \times 10^9\,{\rm cm\,s^{-1}}\,, \quad (18)$$

$$\rho_0 = \frac{\dot{M}}{v_0 \times {\rm A}} \simeq 2.31 \times 10^5\,{\rm g\,cm^{-3}}\,, \quad (19)$$

$$\rho_{\rm sh} = 7\rho_0 \simeq 1.62 \times 10^6\,{\rm g\,cm^{-3}}\,, \quad (20)$$

$$v_{\rm sh} = -\frac{1}{7}v_0 \simeq -1.07 \times 10^9\,{\rm cm\,s^{-1}}\,, \quad (21)$$

$$P_{\rm sh} = \frac{7}{8}\rho_0 v_0^2 \simeq 1.14 \times 10^{25}\,{\rm dyn\,cm^{-2}}\,. \quad (22)$$

Now we can build a numerical model with more refined physics to perform 2D hydrodynamics (HD) and magnetohydrodynamics (MHD) simulations, which we can compare with the 1D analytical results.

3. NUMERICAL APPROACH

For the work shown in this paper we used the numerical code AMR FLASH2.5 (Fryxell et al. 2000) to perform the 2D simulations. FLASH[1] is a modular, portable, highly scalable, adaptive-mesh simulation code for astrophysical hydrodynamics problems. It was originally developed at the DOE ASCI Alliances Center for Astrophysical Thermonuclear Flashes at the University of Chicago for the purpose of simulating Type Ia supernovae, novae, and X-ray bursts. It has since evolved to handle more general astrophysical problems, including those involving collisionless particle dynamics. FLASH is freely available from the ASCI Flash Center. This code is designed to allow users to configure initial and boundary conditions, change algorithms, and add new physics modules with minimal effort. It uses the PARAMESH library to manage a block-structured adaptative grid, placing resolution elements where they are needed most.

3.1. *The Numerical Method*

FLASH2.5 provides two main types of modules: Physics and Infrastructure Modules. In our model we used the hydro-mhd, eos-helmholtz, gravity and neutrino-cooling custom modules.

The FLASH code solves the the equations of a magnetized fluid (ideal or non-ideal), described by

$$\frac{\partial \rho}{\partial t} + \nabla\cdot(\rho\mathbf{v}) = 0\,, \quad (23)$$

$$\frac{\partial \rho\mathbf{v}}{\partial t} + \nabla\cdot(\rho\mathbf{v}\mathbf{v} - \mathbf{B}\mathbf{B}) + \nabla P_* = \rho\mathbf{g} + \nabla\cdot\tau\,, \quad (24)$$

$$\frac{\partial \rho E}{\partial t} + \nabla\cdot[\mathbf{v}\,(\rho E + P_*) - \mathbf{B}\,(\mathbf{v}\cdot\mathbf{B})] = \rho\mathbf{v}\cdot\mathbf{g} + O(\tau,\eta)\,, \quad (25)$$

$$\nabla\cdot(\mathbf{v}\cdot\tau + \sigma\nabla T) + \nabla\cdot(\mathbf{B}\times(\eta\nabla\times\mathbf{B})) = O(\tau,\eta)\,, \quad (26)$$

$$\frac{\partial \mathbf{B}}{dt} + \nabla\cdot(\mathbf{v}\mathbf{B} - \mathbf{B}\mathbf{v}) = -\nabla\times(\eta\nabla\times\mathbf{B})\,, \quad (27)$$

where

$$P_* = P + \frac{B^2}{2}, \quad (28)$$

$$E = \frac{1}{2}v^2 + \varepsilon + \frac{B^2}{2\rho}, \quad (29)$$

$$\tau = \mu\left[(\nabla\mathbf{v}) + (\nabla\mathbf{v})^{\mathbf{T}} - \frac{2}{3}(\nabla\mathbf{v})\right]. \quad (30)$$

Here P_*, E and τ are the total pressure, total specific energy and stress tensor, respectively, and the remaining symbols have their usual meaning. Units in these equations are such that no 4π and μ_0 factors appear.

We have simplified the above set of equations by restricting ourselves to the ideal hydro and MHD cases. Setting the thermal conductivity, σ, and electrical resistivity, η, to zero is justified by the fact that time scales for heat and magnetic field diffusion are many orders of magnitude larger than our simulation times. The inviscid ($\mu = 0$) approximation, i.e., neglect of momentum diffusion, is acceptable because we have not considered rotation in our models. Note that when $\mathbf{B} = 0$, the Euler equations are then obtained.

A particular complication associated with solving the MHD equations numerically lies in the solenoidality of the magnetic field. The non-existence of magnetic monopoles, $\nabla\cdot\mathbf{B} = \mathbf{0}$ is difficult to satisfy in discrete computations. Being only an initial condition of the MHD equations, it enters the equations indirectly and is not, therefore, guaranteed to be generally satisfied unless special algorithmic provisions are made. FLASH2.5 uses a simple yet very effective method to destroy the magnetic monopoles on the scale on which they are generated. In this method, a diffusive operator proportional to $\nabla\nabla\cdot\mathbf{B}$ is added to the induction equation, so that the equations become

$$\frac{\partial \mathbf{B}}{dt} + \nabla\cdot(\mathbf{v}\mathbf{B} - \mathbf{B}\mathbf{v}) = -\nabla\times(\eta\nabla\times\mathbf{B}) - \mathbf{v}\nabla\cdot\mathbf{B} + \eta_{\rm a}\nabla\nabla\cdot\mathbf{B}\,, \quad (31)$$

[1] http://flash.uchicago.edu/website/home/

with the artificial diffusion coefficient $\eta_{\rm a}$ chosen to match that of grid numerical diffusion. In the FLASH code, $\eta_{\rm a} = (\lambda/2)(1/\Delta x + 1/\Delta y + 1/\Delta z)^{-1}$, in 3D where λ is the largest characteristic speed in the flow. Since the grid magnetic diffusion Reynolds number is always on the order of unity, this operator locally destroys magnetic monopoles at the rate which they are created. All our simulations are in Cartesian coordinates: in the presence of a magnetic field polar/spherical coordinates are very troublesome and, presently, the MHD version of FLASH does not support them.

3.2. *The Physics Ingredients*

In the analytical approach an ideal gas equation of state has been used. This allows much simplification in the structure of the envelope and, in addition, the flow can be managed like an adiabatic fluid with $\gamma = 4/3$. The gas is dominated by radiation, which is trapped within the flow. Also, the neutrino losses depend on a high power of the pressure, but are only important at the base of the envelope. Nevertheless, to account for the thermodynamics more accurately and for the consequent piling up of matter on the star, it is advisable and necessary to work with a more complete and realistic equation of state. The Helmholtz EOS provided with the FLASH2.5 distribution contains more physics and is appropriate for addressing astrophysical phenomena in which electrons and positrons may be relativistic and/or degenerate and in which radiation may significantly contribute to the thermodynamic state. This EOS thus includes contributions from black-body radiation, completely ionized ideal nuclei, and free electrons and positrons. The pressure and internal energy are calculated as the sum over the components,

$$P_{\rm tot} = P_{\rm rad} + P_{\rm ion} + P_{\rm ele} + P_{\rm pos} + P_{\rm coul}\,, \qquad (32)$$

$$\varepsilon_{\rm tot} = \varepsilon_{\rm rad} + \varepsilon_{\rm ion} + \varepsilon_{\rm ele} + \varepsilon_{\rm pos} + \varepsilon_{\rm coul}\,. \qquad (33)$$

Here the subscripts "rad" , "ion", "ele", "pos" and "coul" represent the contribution from radiation, nuclei, electrons, positrons, and Coulomb corrections, respectively. The radiation portion assumes a blackbody in local thermodynamic equilibrium, the ion portion (nuclei) is treated as an ideal gas with $\gamma = 5/3$, and the electrons and positrons are treated as a non-interacting Fermi gas of arbitrary degeneracy and relativity.

Under the physical conditions of interest for the set of simulations presented here, the gas is dense enough that the optical depth for photons is $\tau_\gamma \gg 1$, and they are fully trapped in the flow. Adding the corresponding term to the pressure as $P_{\rm rad} = aT^4/3$ is thus entirely appropriate. We note that more recent versions of FLASH (upwards of 3.2) include modules for radiation transport, making them useful for a wider range of studies.

The gravity module suplied with FLASH2.5 computes gravitational source terms for the code. These can take the form of the gravitational potential $\phi(\mathbf{x})$ or the gravitational acceleration,

$$g(\mathbf{x}) = -\nabla\phi(\mathbf{x})\,. \qquad (34)$$

The gravitational field can be externally imposed or self-consistently computed from the gas density via the Poisson equation,

$$\nabla^2\phi(\mathbf{x}) = 4\pi G\rho(\mathbf{x})\,, \qquad (35)$$

where G is Newton's gravitational constant. In the latter case, either periodic or isolated boundary conditions can be applied. In our case, we used an externally applied gravitational field (*plane-parallel gravitational field*), where the acceleration vector is parallel to one of the coordinate axes, and its magnitude drops with distance along that axis as the distance squared. Its magnitude and direction are independent of the other two coordinates.

In the conditions present in both the high density part of the accretion flow and the underlying envelope neutrino emission occurs essentially through neutral currents processes. The five processes we included in the models are analogous to standard photon emission processes where the γ emission is replaced by a $\nu - \overline{\nu}$ pair. They are:

PAIR ANNIHILATION: $e^- + e^+ \rightarrow \nu + \overline{\nu}$,

PHOTONEUTRINOS: $\gamma + e^\pm \rightarrow e^\pm + \nu + \overline{\nu}$, the analogous of Compton scattering,

PLASMON DECAY: $\Gamma \rightarrow \nu + \overline{\nu}$, where Γ is a plasmon,

BREMSSTRAHLUNG: $e^\pm + N \rightarrow e^\pm + N + \nu + \overline{\nu}$, where N is a nucleus, and

SYNCHROTRON: $e^\pm + \mathbf{B} \rightarrow e^\pm + \mathbf{B} + \nu + \overline{\nu}$, where $\mathbf{B}$ represents the magnetic field.

For the first four processes we used the calculations of Itoh et al. (1996) and for the synchrotron emission we followed Bezchastnov et al. (1997). Pair annihilation is the dominant process but synchrotron can make some significant contribution when the magnetic field becomes strongly compressed. As noted above, the density in the flow is typically high enough that photons are trapped, but not neutrinos. As a rough guide, the optical depth for neutrinos under coherent scattering off free nuclei is $\tau_\nu \simeq 1$ when $\rho \simeq 10^{11}$ g cm^{-3}, which is several orders of magnitude higher than the maximum values studied here.

Thus neutrino cooling can be implemented simply as a sink in the energy equation.

3.3. *The Initial and Boundary Conditions*

We simulated a small 2D accretion column in Cartesian coordinates anchored onto the surface of the neutron star, and considered various accretion rates and magnetic field configurations. This set of simulations allows us to compare numerically obtained results in the pure hydrodynamical and MHD case with the proposed analytical approach, as well as to analyze the reaction of the magnetic field to the infalling gas. The computational domain covers $0 \leq x \leq 3\times10^5$ cm, $0 \leq y \leq 10^7$ cm. The dimensions for the column are: $A_{\rm col} = L_x \times L_z = (3\times10^5)^2\,{\rm cm}^2$ (for the base) and height$_{\rm col} = L_y = 10^7\,$cm for the height. This height is adequate because it is below the analytical shock radius value calculated for the accretion rate of SN1987A. The fluid is initially in free fall and we set a constant temperature in the gas. We considered horizontal ($B_x = 10^{12}\,$G, $B_y = 0$), vertical ($B_x = 0$, $B_y = 10^{12}\,$G, mimicking accretion onto the magnetic pole of the neutron star), diagonal ($B_x = B_y = 10^{12}\,$G) and dipolar ($B_x = 2\mu/y^3$, $B_y = 0$, representing accretion onto the neutron star equator) cases, where $\mu = 5\times10^{29}$ is the dipolar moment, fixed so that $B_x = 10^{12}\,$G at the neutron star surface. With these considerations, the initial conditions in the column for velocity, temperature and density are:

$$\rho = \frac{\dot{M}_{\rm col}}{v_{\rm ff}\times A_{\rm col}}\,, \quad (36)$$

$$T = 10^9\,{\rm K}\,, \quad (37)$$

$$v_{\rm ff} = \sqrt{\frac{2GM}{y}}\,, \quad (38)$$

$$B = 10^{12}\,{\rm G}\,, \quad (39)$$

where $\dot{M}_{\rm col} = \dot{M}A_{\rm col}/A$ is the scaled accretion rate in the column making up the domain.

For the vertical boundaries of the accretion column, $x = 0$ and $x = 3\times10^5$ cm, parallel to the y-axis, we implement standard periodic boundary conditions. Thus, any fluid element moving out of the computational domain on the right (left) boundary re-enters the domain on the left (right) edge with the same thermodynamical properties and velocity.

For the top and bottom of the computational domain, parallel to the x-axis, we implemented custom boundary conditions. The gravity vector is directed along the y-axis, and we want the lower boundary at $y = 0$ to support the fluid above against infall, mimicking the hard surface of the neutron star, and in addition to have the magnetic field anchored to it. In order to establish this boundary, we use "guard", or "ghost" numerical cells. These are cells outside the formal computational domain (e.g., at $y \leq 0$ or $y \geq 10^7$) for which we can fix the hydrodynamical and thermodynamical properties and which are not evolved along with the rest of the flow. They are useful precisely to guarantee boundary conditions of interest, depending on the setup of the problem. A layer of at least 2 such cells along the top and bottom of the domain can thus be used to compute proper gradients at the edge of the flow (e.g., a pressure or temperature gradient). In this case, along the bottom edge of the column, we fix the velocities to be null in all guard cells, ($v_x = v_y = v_z = 0$), keeping them at rest, and copy the density and the pressure of the first zone of the numerical domain to mimick the the neutron star surface: $\left(\rho = \rho(1), P = P(1) + \rho v^2 + \rho g h\right)$, where the label 1 refers to the first cell in the computational domain. The magnetic field is put in this boundary in such form that it is continuous from the guard cell to the physical domain, i.e, we anchor the magnetic field onto the neutron star surface and in the rest of the guard cells it is null. The other thermodynamics variables are calculated from the equation of state. At the top of the column, $y = 10^7$ cm, we set the velocity to be that of free fall, $v_y = -\sqrt{2GM/y}$ in all the guard cells, and set the density to fix a constant inflow mass accretion rate, $\rho = \dot{M}_{\rm col}/(|v_y|\times{\rm A}_{\rm col})$. As in the computational domain initially, the temperature in the guard cells is set to $T = 10^9$ K (at all times). The remaining variables are calculated from the equation of state.

4. RESULTS AND DISCUSSION

We now present results obtained from the 2D hydrodynamical simulations (HYDRO) as well as for the MHD case for an accretion column in cartesian coordinates, and compare these to the analytical scalings. We varied the accretion rate and magnetic field configuration (for the MHD case). The chosen rates were one, two and three orders of magnitude above our fiducial rate $\dot{M}_0 = 340\ M_\odot\,{\rm yr}^{-1}$.

4.1. *Comparison of the HYDRO and MHD solvers*

For the assumed physical parameters of SN1987A, in 200 ms the system reaches a quasi-stationary state, whereas for higher rates of accretion, this drops substantially: 60 ms at $10\ \dot{M}_0$, 20 ms at $100\ \dot{M}_0$ and 5 ms at $1000\ \dot{M}_0$. We set a level of refinement of 4, with 2 blocks along the

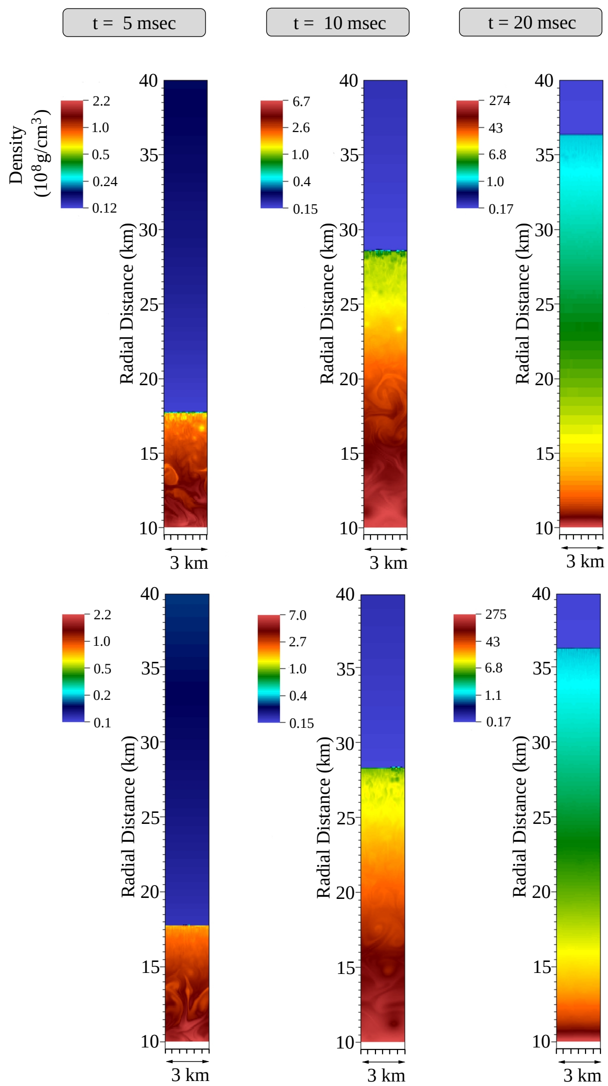

Fig. 3. Color maps of density for cases HYDRO (top) and MHD_0 (bottom) at $t = 5, 10, 20$ ms from left to right. The accretion rate is $\dot{M} = 100\ \dot{M}_0$.

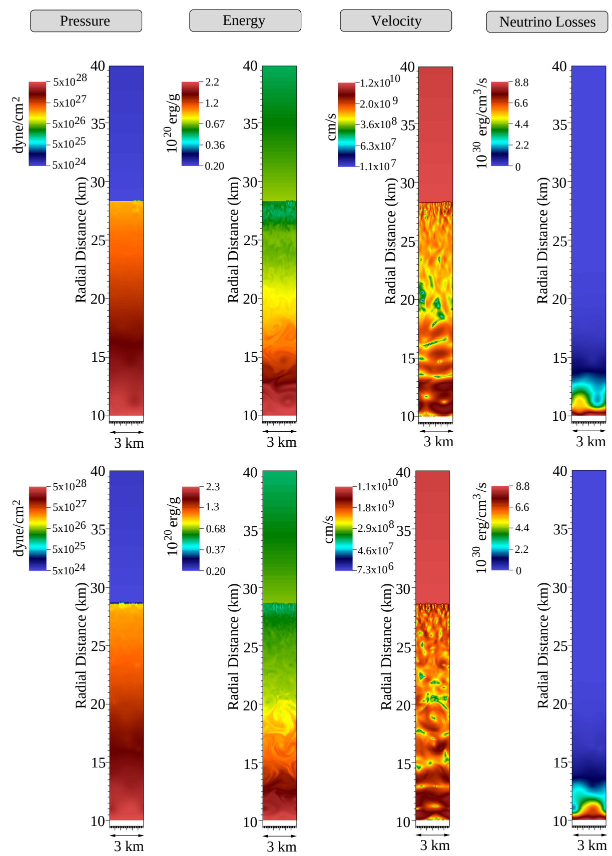

Fig. 4. Color maps of pressure, total specific energy, magnitude of velocity and neutrino emissivity, for cases HYDRO (top) and MHD_0 (bottom) at $t = 10$ ms. The accretion rate is $\dot{M} = 100\ \dot{M}_0$.

x-axis and 18 along y-axis. This implies an effective resolution of 128×1152 zones in the computational domain.

In Figure 3 we show the density contrast for the HYDRO and MHD cases with null magnetic field (MHD_0), for $\dot{M} = 100\ \dot{M}_0$. We choose this accretion rate as being representative since its associated shock radius is much smaller than that for $\dot{M} = \dot{M}_0$, and is therefore easier to visualize. In addition, it is possible to both do a comparative analysis of solvers (HYDRO and MHD) and of their response to the imposed initial conditions. This comparison allows us to determine whether the equations are being solved in both modules to a comparable accuracy. In principle, the MHD module with null magnetic field should reproduce exactly the results obtained with module HYDRO. The constrasts of pressure, specific total energy, velocity and neutrino cooling per unit volume for all the cases (at $t = 10$ ms), are shown in Figure 4. The radial profiles of density, pressure and velocity for the SN1987A accretion rate are given in Figure 5.

We note that although the system reaches a quasi-stationary state in $t = 20$ ms, there is remnant noise in the radial profile of the velocity due to the interaction of the matter with the lower boundary condition and to the fact that horizontal motions are allowed because of the periodic boundary condition. On the other hand, only the bottom section, 4×10^6 cm, of the entire accretion column, with height 10^7 cm is shown, where the most interesting processes occur. We note that the profiles, while not identical in all respects, are indeed very similar, showing that the HYDRO and MHD solvers are

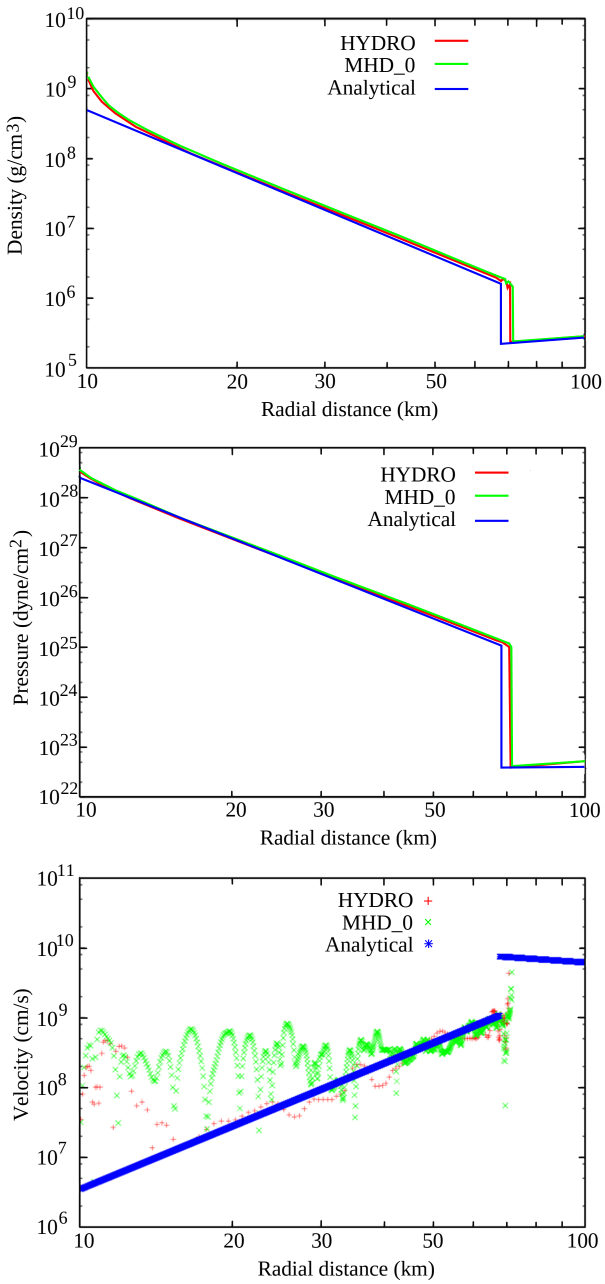

Fig. 5. Radial profiles of density (top), pressure (middle) and magnitude of velocity (bottom) at $t = 200$ ms. The accretion rate is $\dot{M} = \dot{M}_0$. The HYDRO (red), MHD_0 (green) and analytical solution (blue) are shown together. The location of the shock is reproduced with very good agreement in the two numerical cases with respect to the analytical solution. In the shocked region, the velocity is a significantly higher due in part to lateral motions of the gas. At small radii, the numerical solutions deviate from the analytical curve, since the assumption of self-similarity is no longer valid as material piles up near the star and cooling becomes relevant in the energy balance.

giving essentially the same final state, both in space and time evolution. There is some convection in the early stages of the evolution, and Rayleigh-Taylor instabilities are present, but are quickly damped as the system approaches the stationary solution. Deviations from this are most evident when one examines variations in the velocity field.

The location of the shock is reproduced quite well, to within 5% when compared to the analytical calculation. Moreover, both solvers place it essentially at the same height, indicating that the quantitative aspects are not affected from one to the other. Since the code is able to model the bottom of the column self-consistently within the imposed boundary condition, the numerical solution deviates from the self-similar scaling once neutrino cooling becomes important, and matter starts piling up near the surface.

Hereafter, unless otherwise noted we refer to calculations with $\dot{M} = \dot{M}_0$. The adiabatic and radiative gradients can be calculated from the simulations, when the system is relaxed. We find $\nabla_{\rm ad} = 1 - 1/\gamma_{\rm c} \simeq 0.26$, $\nabla_{\rm rad} = (d\ln T/d\ln P) \simeq 0.24$. In this case, the value of the adiabatic index $\gamma_{\rm c}$ has been taken directly from the simulation ($\gamma_{\rm c} = 1.35$), and the radiative gradient was calculated by building a plot of temperature vs. pressure. These gradients have almost constant values within the envelope, except in the region close to the neutron star surface. Since $\nabla_{\rm ad} > \nabla_{\rm rad}$, the system is manifestly stable to convection. Nevertheless, being so close numerically is probably indicative of marginal stability. Within the envelope the flow is fully subsonic, as expected after passing through the accretion shock front: the sound speed is $c_{\rm s} = \sqrt{\gamma_{\rm c} P/\rho} \simeq 6.9 \times 10^9\,{\rm cm\,s^{-1}}$, and $v \simeq 1.24 \times 10^7\,{\rm cm\,s^{-1}}$, giving a Mach number $m = v/c_{\rm s} \simeq 10^{-3}$. Therefore, besides confirming that the HYDRO and MHD solvers give accurate and consistent results, we are able to study the global structure of the accretion column in detail and to compare it with the analytical approach, particularly in the region where the approximations in the latter break down.

It is worthy to note the thermodynamical conditions the fluid is in as it accretes towards the protoneutron star. The Fermi temperature can be computed from the Fermi energy $E_{\rm F}$

$$T_{\rm F} = \frac{E_{\rm F}}{k_{\rm B}} = \frac{\sqrt{p_{\rm F}^2 c^2 + m_{\rm e}^2 c^4} - m_{\rm e} c^2}{k_{\rm B}} \simeq 6.48 \times 10^{10}\,{\rm K}\,, \tag{40}$$

at the base of the flow, where $p_{\rm F} = (3\pi^2 n_{\rm e})^{1/3}\hbar$ is the Fermi momentum. The temperature obtained from

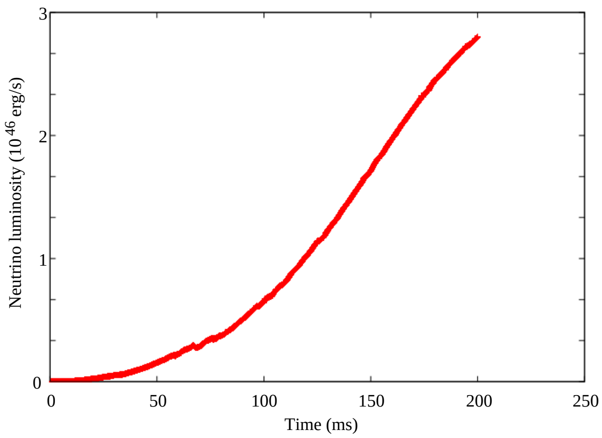

Fig. 6. Neutrino luminosity integrated over the computational domain for the fiducial accretion rate, $\dot{M} = \dot{M}_0$, up to $t = 200$ ms. Note how after an initial transient, the power output is leveling off as the system reaches a quasi-stationary state.

the simulation, close to the bottom of the accretion column in quasi-stationary state is $T \simeq 4.54 \times 10^{10}$ K, so $T/T_{\rm F} \simeq 0.7$. It is thus clear that assuming that the $e^{\pm}$ pairs are entirely degenerate is not a proper approximation, and a full expression such as the one in the Helmholtz equation of state is required if one wishes to compute the evolution of the flow accurately. It is also clear that neutrino cooling effectively turns on at a scale height $L_y \sim 2 \times 10^5$ cm. For the simulation with $\dot{M} = \dot{M}_0$, the integrated neutrino luminosity, shown in Figure 6, is $L_\nu \simeq 2.51 \times 10^{46}\,{\rm erg\,s^{-1}}$, close to the value estimated with the cooling function of Dicus (1972) scaled to the column: $L_\nu = \dot{\varepsilon}_{\rm n} \times V \simeq 1.83 \times 10^{46}\,{\rm erg\,s^{-1}}$, with $V \simeq (2 \times 10^5) \times (3 \times 10^5)^2\,{\rm cm}^3$.

Once the system reaches the quasi-stationary state, radial profiles can be compared for different accretion rates. Four different rates for each initial condition were computed. In all of these, the piling up of material close to the neutron star surface is seen. The velocity profiles remain noisy and turbulent in the shocked region, but on average the analytical profile is globally recovered. In Figure 7 these are plotted, along with density and pressure, for case MHD_0. Note also that at greater accretion rates the shock is located at lower height, as expected. For $\dot{M}/\dot{M}_0 = 1, 10, 100, 1000$, the position of the shock in the simulation is at $R_{\rm sh}/10^6{\rm cm} = 7.06, 4.96, 3.74, 2.68$, in excellent agreement with the analytical values given by $R_{\rm sh}/10^6{\rm cm} = 6.92, 4.80, 3.33, 2.31$, respectively (see Figure 8).

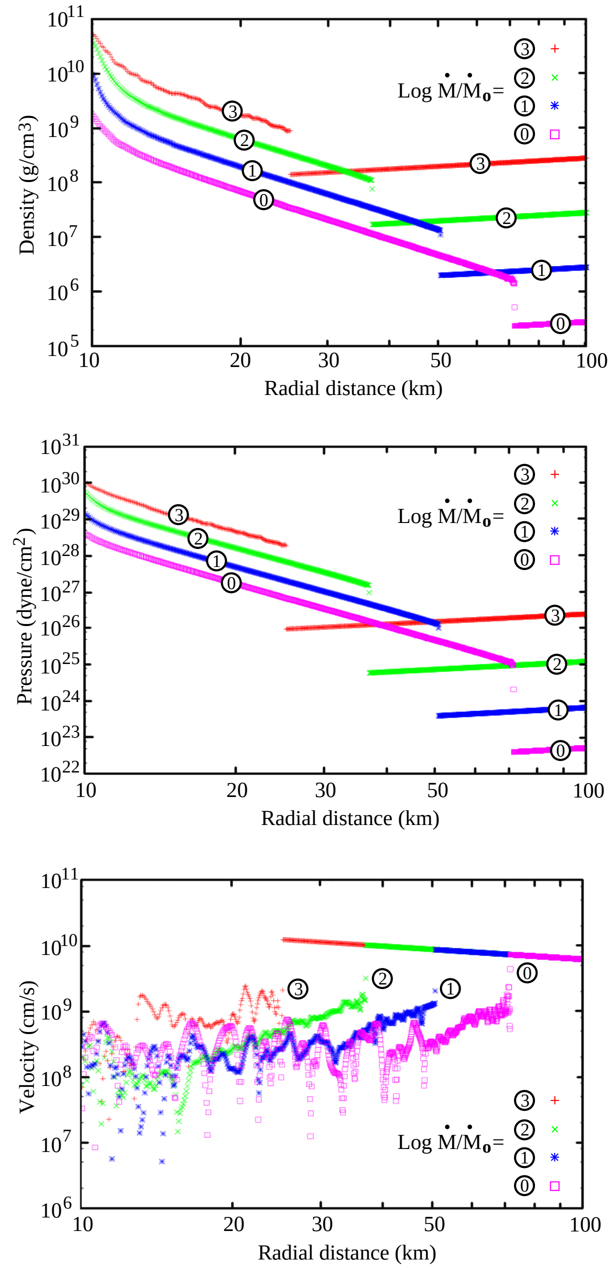

Fig. 7. Radial profiles of density (top), pressure (middle) and velocity (bottom) for the MHD_0 case after a stationary state has been reached. The accretion rates are $\dot{M}/\dot{M}_0 = 1, 10, 100, 1000$ (cyan, blue, green and red, respectively).

4.2. *Magnetic field submergence*

We now consider the case with non-zero magnetic field strength. Figure 9 shows the radial profiles of density, pressure and magnitude of the velocity for $\dot{M} = \dot{M}_0$ with several field configurations: null (MHD_0), constant horizontal (MHD_H), constant

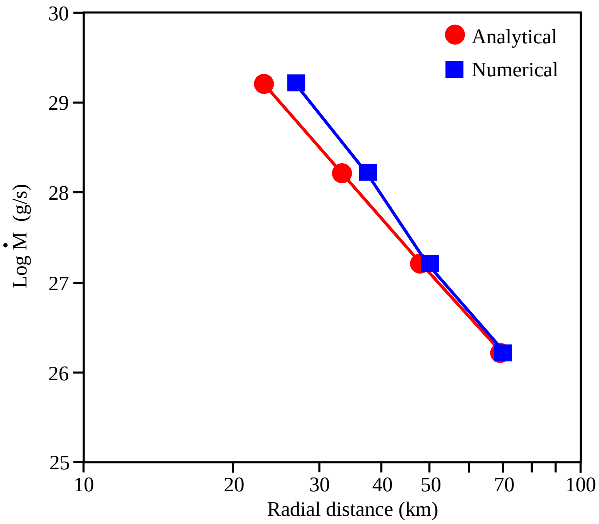

Fig. 8. Accretion rate as a function of shock radius for the hydrodynamical simulations with $\dot{M}/\dot{M}_0 = 1000, 100, 10, 1$ after a stationary state has been reached. The analytical solution given by equation 14 is shown for comparison.

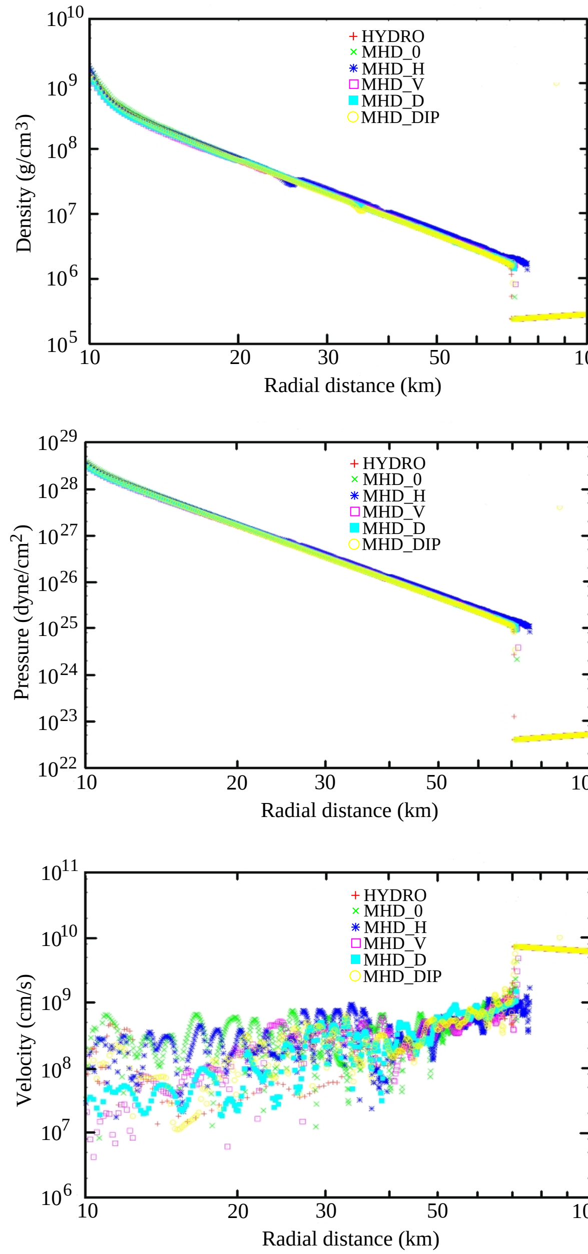

Fig. 9. Radial profiles of density (top), pressure (middle) and velocity (bottom) for $\dot{M} = \dot{M}_0$ and various field configurations (labeled).

vertical (MHD_V), constant diagonal (MHD_D) and dipolar (MHD_DIP), for comparative effects. The initial intensity of the magnetic field in all cases is 10^{12} G, except in the dipole configuration, where it is 10^{12} G at the neutron star surface. We also overplot the hydrodynamical solution for comparison. Note that the profiles are practically the same at this accretion rate indicating that the magnetic field is not playing an important role as far as the dynamics are concerned.

In all simulated cases, regardless of the magnetic field configuration, when the system has relaxed and reached the quasi-stationary state, the field is completely submerged in the neutron star crust. Its intensity rises accordingly, by up to two orders of magnitude for the highest accretion rates. Figure 10 shows the distribution of magnetic field strength after the system has relaxed, when $\dot{M} = 1000\,\dot{M}_0$, for our four initial magnetic field configurations. It is only within the first km in the column, where the matter piles up, that the magnetic field is at or above the initial value in the calculation, and the compression is quite clear.

The initial dynamics in the MHD case are somewhat more violent than in the pure hydrodynamical case. The infalling gas quickly drags the initial field towards the neutron star surface since the ram pressure, $P_{\rm ram} = \rho v^2/2$ is substantially greater than the magnetic pressure $P_{\rm mag} = B^2/8\pi$, even for the smallest accretion rate, $\dot{M} = \dot{M}_0$. The increased magnetic pressure as compression takes place is insufficient to overcome this flow, and large field strengths close to the surface result. The effect on the large scale dynamics is thus of a more transitory nature, and sensitive to the initial conditions, rather than a permanent feature. As a second point, we note that the magnetic field, advected along with the flow, strongly fluctuates in strength in the shocked region

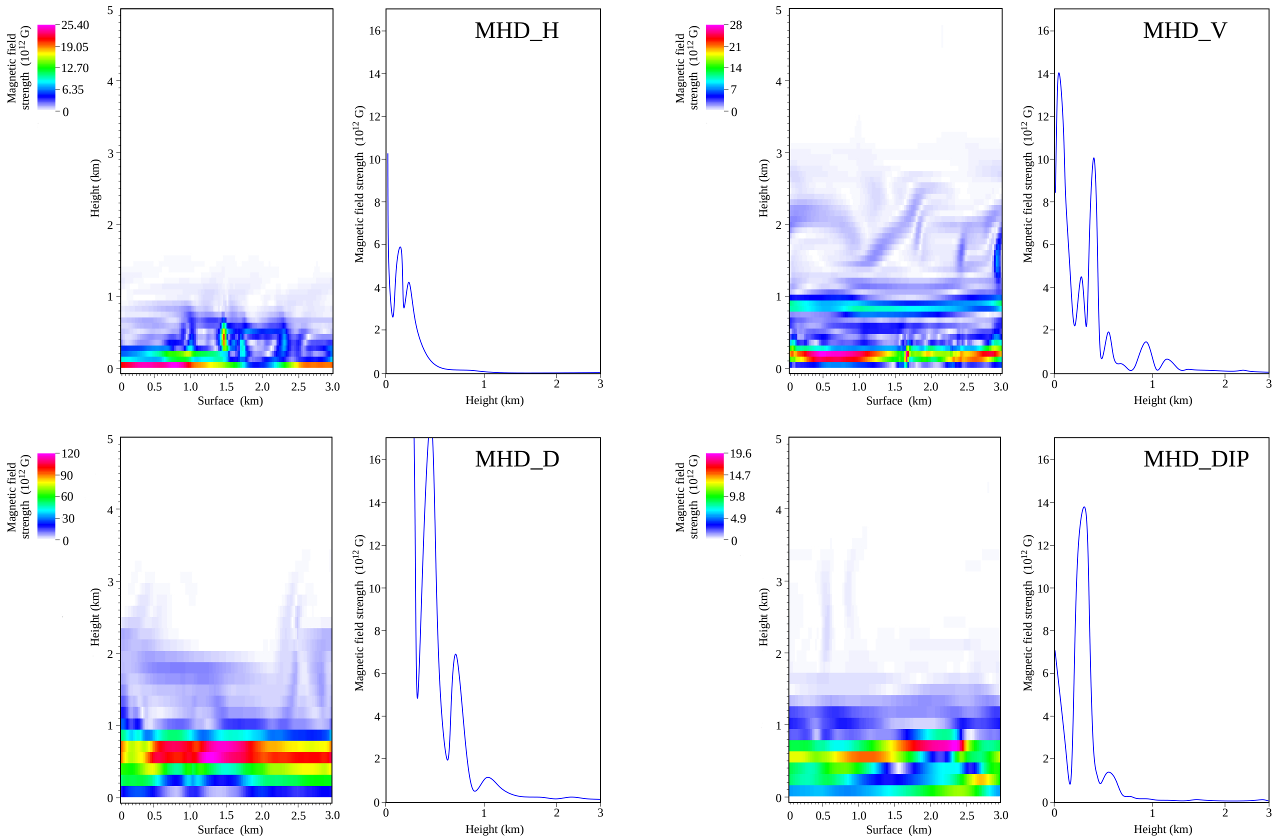

Fig. 10. Maps (left half-panel) and horizontally-averaged vertical profiles (right half-panel) of magnetic field strength for a magnetic field that is initially horizontal, case MHD_H (top left), vertical, case MHD_V (top right), diagonal, case MHD_D (bottom left), and dipolar, case MHD_D (bottom right), after the system has relaxed for $\dot{M} = 1000\dot{M}_0$. Note the submergence of the magnetic field close to the neutron star surface.

as it piles up against the lower boundary, where neutrino cooling is efficient. The additional piling up of material makes it even harder for the field to rise to significant levels as the evolution proceeds further. Nevertheless, as the system evolves the turbulent structures that form initially begin to smooth themselves until they disappear completely in the hydrodynamical case, but some small scale structure remains when magnetic fields are present.

Once the accretion rate drops significantly, it is in principle possible that the field will rise buoyantly through the envelope, playing some dynamical role as the accretion time becomes long and the balance between ram and magnetic pressure is reversed. This will occur on a much longer time scale than simulated here, and its modeling requires a different set of assumptions in terms of the present set of calculations.

5. CONCLUSIONS

We have presented the results of two-dimensional simulations of accretion in the hypercritical, neutrino-cooled regime onto the surface of a neutron star, using the FLASH code. The flow in accretion columns for a variety of initial accretion rates was simulated until a steady state was reached. We find that at this stage, the location of the accretion shock, where the flow transitions from free fall to subsonic settling onto the neutron star surface, is well reproduced when compared with the analytical estimates of Chevalier (1989). However, close to the surface, matter piles up, the solution is no longer adiabatic, and the self-similar character of the flow breaks down as expected.

We performed a detailed comparison of the hydrodynamical and ideal MHD routines in FLASH, and found excellent agreement between the two when the initial field is null. For various finite field configurations (initially horizontal, vertical, diagonal and dipolar), we find that performing the calculations in two dimensions does not allow for any additional buoyancy effects of the field to be manifested: for all accretion rates simulated, the initial field is entirely advected by the flow and submerged close to the neutron star surface. Its intensity rises accordingly, by up to two orders of magnitude in some cases. In principle, thus, it is possible for such an accretion episode following core collapse and the formation of a proto-neutron stars to effectively bury the initial field and delay the appearance of a classical radio pulsar (Muslimov & Page 1995). The simulated time scales at present do not allow us to place hard constraints on the re-diffusion of the field at late times, and a more quantitative estimation of this is left for future work.

CGB acknowledges support from a DGEP-UNAM scholarship. Financial support for this work was provided in part by Conacyt (45845E) and DGAPA-Universidad Nacional Autónoma de México (IN 122609). The software used in this work was in part developed by the DOE-supported ASC/Alliance Center for Astrophysical Thermonuclear Flashes at the University of Chicago. The numerical calculations were carried out on the KanBalam Supercomputer at DGSCA, UNAM, whose support team is gratefully acknowledged. We thank the anonymous referee for comments and criticism which helped improve this final version.

REFERENCES

Bethe, H. A., & Pizzochero, P. 1990, ApJ, 350, L33
Bezchastnov, V. G., Haensel, P., Kaminker, A. D., & Yakovlev, D. G. 1997, A&A, 328, 409
Bionta, R. M., Blewitt, G., Bratton, C. B., Caspere, D., & Ciocio, A. 1987, Phys. Rev. Lett., 58, 1494
Blondin, J. M. 1986, ApJ, 308, 755
Bondi, H. 1952, MNRAS, 112, 195
Brown, G. E., & Bethe, H. A. 1994, ApJ, 423, 659
Brown, G. E., & Weingartner, J. C. 1994, ApJ, 436, 843
Burrows, A., & Lattimer, J. M. 1986, ApJ, 307, 178
Chevalier, R. A. 1989, ApJ, 346, 847
Dicus, D. A. 1972, Phys. Rev. D, 6, 941
Ellis, P. J., Lattimer, J. M., & Prakash, M. 1996, Comments in Nuclear and Particle Physics, 22, 63
Freire, P. C. C. 2008, in AIP Conf. Ser. 983, 40 Years of Pulsars: Millisecond Pulsars, Magnetars and More, ed. C. Bassa, Z. Wang, A. Cumming, & V. M. Kaspi (Melville: AIP), 459
Fryer, C. L., Benz, W., & Herant, M. 1996, ApJ, 460, 801
Fryxell, B., et al. 2000, ApJS, 131, 273
Geppert, U., Page, D., & Zannias, T. 1999, A&A, 345, 847
Gilmozzi, R., et al. 1987, Nature, 328, 318
Gotthelf, E. V., & Halpern, J. P. 2007, ApJ, 664, L35
———. 2008, in AIP Conf. Ser. 983, 40 Years of Pulsars: Millisecond Pulsars, Magnetars and More, ed. C. Bassa, Z. Wang, A. Cumming, & V. M. Kaspi (Melville: AIP), 320
———. 2009, ApJ, 695, L35
Haberl, F., Geppert, U., Aschenbach, B., & Hasinger, G. 2006, A&A, 460, 811
Halpern, J. P., & Gotthelf, E. V. 2010, ApJ, 709, 436
Hillebrandt, W., Hoeflich, P., Weiss, A., & Truran, J. W. 1987, Nature, 327, 597
Hirata, K., Kajita, T., Koshiba, M., Nakahata, M., & Oyama, Y. 1987, Phys. Rev. Lett., 58, 1490
Houck, J. C., & Chevalier, R. A. 1991, ApJ, 376, 234
Itoh, N., Hayashi, H., Nishikawa, A., & Kohyama, Y. 1996, ApJS, 102, 411
Janka, H., Langanke, K., Marek, A., Martínez-Pinedo, G., & Müller, B. 2007, Phys. Rep., 442, 38
Lee, W. H., & Ramirez-Ruiz, E. 2007, New J. Phys., 9, 17
Mezzacappa, A. 2005, Ann. Rev. Nucl. Part. Sci., 55, 467
Michel, F. C. 1994, MNRAS, 267, L4
Muslimov, A., & Page, D. 1995, ApJ, 440, L77
Pavlov, G. G., Sanwal, D., Garmire, G. P., & Zavlin, V. E. 2002, in ASP Conf. Ser. 271, Neutron Stars in Supernova Remnants, ed. P. O. Slane & B. M. Gaensler (San Francisco: ASP), 247
Shapiro, S. L., & Teukolsky, S. A. 1983, Black Holes, White Dwarfs, and Neutron Stars (New York: John Wiley & Sons)
Shigeyama, T., Nomoto, K., & Hashimoto, M. 1988, A&A, 196, 141
Shigeyama, T., Nomoto, K., Hashimoto, M., & Sugimoto, D. 1987, Nature, 328, 320
Shternin, P. S., & Yakovlev, D. G. 2008, Astron. Lett., 34, 675
Woosley, S. E. 1988, Lect. Notes Phys., 305, 361
Woosley, S., & Janka, T. 2005, Nature Phys., 1, 147

C. G. Bernal, W. H. Lee, and D. Page: Instituto de Astronomía, Universidad Nacional Autónoma de México, Apdo. Postal 70-264, México D.F. 04510, Mexico (bernalcg, wlee, page@astroscu.unam.mx).

Revista Mexicana de Astronomía y Astrofísica, **46**, 323–330 (2010)

THE IMPORTANCE OF NUCLEUS ROTATION IN DETERMINING THE LARGEST GRAINS EJECTED FROM COMETS

A. Molina[1,2]

Received 2010 February 18; accepted 2010 June 16

RESUMEN

Se determina el valor máximo del diámetro de las partículas eyectadas de los núcleos cometarios haciendo uso del modelo clásico de expansión radial de los gases de los cometas. Se destaca la importancia de las fuerzas inerciales, principalmente de las debidas a la rotación del cometa. Se muestra una sencilla expresión indicando el valor mínimo que debe tener el periodo de rotación del cometa para que la partícula pueda levantarse de la superficie. Los resultados obtenidos son comparados con los valores determinados a partir de medidas de radar. También se analiza el cometa Churyumov-Gerasimenko, que alcanzará la misión ROSETTA en 2014, proponiendo valores para los diámetros de las mayores partículas que pueden desprenderse del cometa.

ABSTRACT

The maximum diameter of large boulders ejected from the cometary nuclei is investigated using the classical model of dust grain as dragged out by radially expanding cometary gases. The importance of the inertial forces, and particularly those due to the rotation of the comet is shown. Although a larger dust grain can be lifted from the nucleus surface if the rotation is faster, the rotation period has to be larger than a certain value. A simple expression for this critical value of rotation period is given. Our results are applied to different comets and a comparison with the maximum radius values obtained by radar measurements is made. Finally, comet Churyumov-Gerasimenko, the target of the ROSETTA mission to arrive on 2014, is going to be analyzed and a range for the maximum diameter of the dust grains that can be lifted is proposed.

Key Words: comets: general — comets: individual (Halley, Wirtanen, Hyakutake, C/2001 A2 LINEAR, IRAS-Araki-Alcock, Churyumov-Gerasimenko) — interplanetary medium — meteoroids

1. INTRODUCTION

As is known, the cometary nuclei release dust grains as the comets approach the Sun. Small grains are dominated by solar radiation pressure and leave the nucleus to form the dust tail of the comet. Large grains can produce a meteroid stream. The study of meteoroid streams can be used as a probe of cometary structure (Beech 1998). Thus, knowledge of the characteristics of meteoroids can provide us information on the composition of cometary nuclei. The large grains can be up to a few meter in diameter. Taking into account the conditions to produce electrophonic sounds, Beech (1998) obtained a lower bound of 1.24 m for the diameter of the largest meteoroids within the Leonid stream. Cometary dust trails have been observed using space-based telescopes, as in Sykes et al. (1986) who used four broad-band filters at 12, 25, 60 and 100 μm on the Infrared Astronomical Satellite. Reach, Kelley, & Sykes (2007) observed debris trails of 27 short period comets due to mm-sized or larger particles using the 24 μm camera on the *Spitzer Space Telescope*. Also, meteoroid strems have been observed by ground-based telescopes. Thus, Ishiguro et al. (2002) obtained first evidence of a cometary dust trail in optical wavelengths using the 2K CCD camera attached

[1]Departamento de Física Aplicada, Facultad de Ciencias, Universidad de Granada, Granada, Spain.

[2]Instituto de Astrofísica de Andalucía, CSIC, Granada, Spain.

to the 105 cm Schmidt telescope at the Kiso Observatory. Aside from the direct use of telescopes, these large meteoroids can be studied by means of the observations of the flashes that occur when they impact on the surface of the Moon. Ortiz et al. (2000) analyzed five impact flashes observed on the night side of the Moon on 18 November 1999, which were associated to the flux of meteoroids of the Leonid meteor shower. They derived a mass range of 1.3 kg to 9 kg for the meteoroid that produced the brightest impact. Assuming that the Leonids are the meteoroids with the lowest density values, 400 kg m^{-3}, of the all known meteoroid streams (Babadzhanov 2002), then that meteoroid was 0.18–0.35 m in diameter.

Large ejected grains can also be found around the cometary nuclei in pseudostable orbits. This constitutes a hazard for the spacecrafts visiting the neighbourhood of a comet (for physical risks of landing on a comet see Kuhrt, Knollenberg, & Keller 1997) and therefore the estimations of the size of the particles that can be orbiting around a cometary nucleus are of the greatest interest.

In this paper, I show in § 2 how the diameter of the largest ejected particle can be obtained. I use a classical outgassing theory with special attention to the rotation of the comet. I apply our expressions to comet 1P/Halley, a comet with a very low rotation period (§ 3), and to comet 46P/Wirtanen, a very fast spinning comet (§ 4). § 5 shows a comparison with results on the size of the ejected particles from several cometary nuclei obtained by radar measurements. Due to the interest in Comet 67P/Churyumov-Gerasimenko, the target of the Rossetta mission, I estimate the diameter of the largest ejected particle from the nucleus of the comet in § 6. The conclusions are presented in § 7.

2. SIZE OF THE LARGEST EJECTED GRAINS

Cometary gas of the nucleus drags dust particles from the surface of the comet. Some of those particles can be orbiting around the comet describing pseudostable orbits (Fulle 1997). Once the particles have left the nucleus surface, they suffer the gravitational forces of the nucleus and of the Sun, the solar radiation pressure force, the gas drag force and the inertial forces, which appear because a reference frame attached to the nucleus is considered. The equation of motion can be written as follows:

$$\frac{d^2\vec{r}_{\rm d}}{dt^2} = \left(\frac{3C_{\rm D}\dot{m}_{\rm g}v_{\rm g}}{16\pi C_{\rm p}Q_{\rm p}}\beta - GM_{\rm c}\right)\frac{\vec{r}_{\rm d}}{r_{\rm d}^3} + \frac{\mu M_{\rm S}G}{r_{\rm c}^3}\left(\frac{3\vec{r}_{\rm d}\cdot\vec{r}_{\rm c}}{r_{\rm c}^2}\vec{r}_{\rm c} - \vec{r}_{\rm d}\right) + \beta M_{\rm S}G\,\frac{\vec{r}_{\rm c}}{r_{\rm c}^3} + \Omega^2\vec{r}_{\rm d} - (\vec{\Omega}\cdot\vec{r}_{\rm d})\vec{\Omega} + 2\vec{v}_{\rm d}\times\vec{\Omega}\,. \quad (1)$$

Here, $\vec{r}_{\rm d}$ is the nucleus to grain vector, $C_{\rm D}$ is the drag coefficient, $\dot{m}_{\rm g}$ is the global gas mass loss rate (also appearing as Q in the literature), $v_{\rm g}$ is the gas velocity, $C_{\rm p} = 1.19 \cdot 10^{-3}$ kg m^{-2}, $Q_{\rm p}$ is the scattering efficiency of the grain, β is the ratio of radiation pressure to gravitational force of the Sun, G is the gravitational constant, $M_{\rm c}$ is the mass of the comet, $M_{\rm S}$ is the mass of the Sun, $\vec{r}_{\rm c}$ is the Sun to comet vector, $\mu = 1-\beta$, $\vec{\Omega}$ is the angular velocity of the rotation of the comet and $\vec{v}_{\rm d} = d\vec{r}_{\rm d}/dt$ where t is the time.

The drag coefficient depends on the shape of the particle and the flow conditions. Henderson (1976) presented, for spherical particles, accurate expressions for $C_{\rm D}$ varying over a wide range of flow conditions. In this paper, a spherical shape for the particle is assumed and a constant value of 2 for $C_{\rm D}$ is employed for all cases. The constant $C_{\rm p}$ is related to β by means of the expression $\beta = C_{\rm p}Q_{\rm p}(\rho_{\rm d}d)^{-1}$, where $\rho_{\rm d}$ is the density and d the diameter of the dust particle. Excluding very small grains, the radiation pressure force increases with decreasing size (Burns, Lamy, & Soter 1979). The value of $1.19\cdot10^{-3}$ kg m^{-2} is obtained from $C_{\rm p} = 3E_{\rm s}(8cGM_{\rm S})^{-1}$, where $E_{\rm s}$ is the mean total solar radiation and c the speed of light (see Finson & Probstein 1968). I also assume that the nucleus obliquity is 0. In the above expression we have used the same nomenclature as that employed by Fulle (1997) except for the last three terms, which are due to the rotation of the cometary nucleus, and are not present in the work of Fulle. However, they can be important as I show in this paper.

From equation (1), I obtain an expression for the particle with largest diameter that can be lifted from the surface (see, for example Molina, Moreno, & Jiménez-Fernández 2008):

$$d_{\rm max} = \frac{1}{\rho_{\rm d}g_{\rm eff}}\frac{3C_{\rm D}\dot{m}_{\rm g}v_{\rm g}}{16\pi R^2}\,, \quad (2)$$

where R is the radius of the cometary nucleus and $g_{\rm eff} = g - \Omega^2 R\cos^2\phi$ (g is the gravitational acceleration of the comet and ϕ is the latitude on the surface where the dust particle is located). In this paper, I show the importance of the rotation terms in the equation of motion, and, particularly, of the values obtained for $d_{\rm max}$, and I discuss the results obtained for several comets of different rotational periods. For comets rotating slowly, $\Omega^2 R\cos^2\phi \ll g$ and then $g_{\rm eff} \approx g$. As $g = G4\pi\rho_{\rm n}R/3$, it will be much larger than $\Omega^2 R\cos^2(\phi)$ for comets with $\tau^2 \gg 3\pi/\rho_{\rm n}G$,

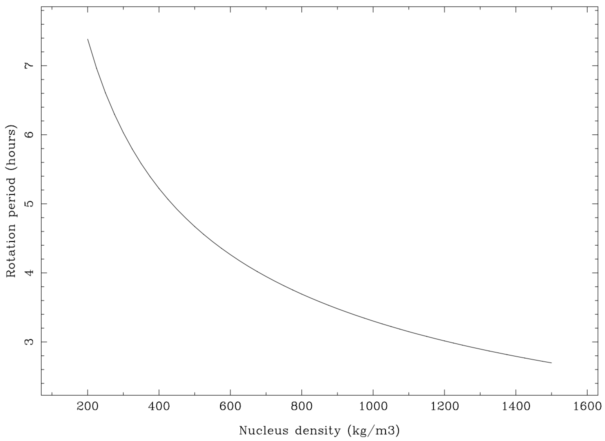

Fig. 1. Critical rotation period versus density of the cometary nucleus. Only the region above the curve is permitted.

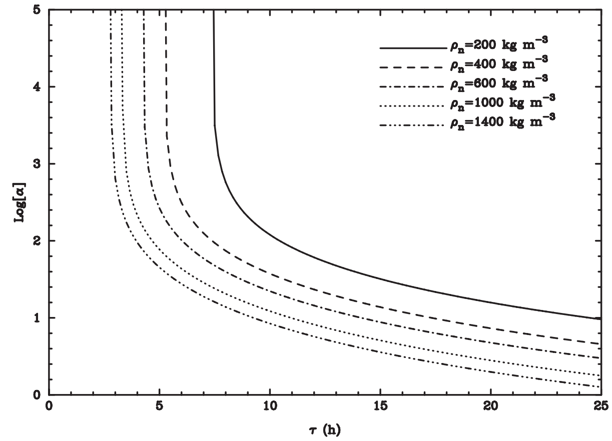

Fig. 2. Percentage relative increase in $d_{\max}$ due to cometary rotation for different values of the nucleus density.

where τ is the rotation period. For τ in seconds and $\rho_{\rm n}$ in kg m^{-3}, $d_{\max}$ will be independent of the nucleus rotation when $\tau^2 \gg 1.4\cdot 10^{11}\rho_{\rm n}{}^{-1}$. Asuming the cometary nucleus as a strengthless body, $g_{\rm eff}$ must be positive and then only rotation periods larger than a critical period $\tau_{\rm crit} = \sqrt{3\pi/\rho_{\rm n}G}$ are possible, otherwise the comet would fly apart. Thus, $\tau_{\rm crit} = 3.76\cdot 10^5\frac{1}{\sqrt{\rho_{\rm n}}}$ with τ is in seconds and $\rho_{\rm n}$ is in kg m^{-3}. A curve of $\tau_{\rm crit}$ for different values of nucleus densities is shown in Figure 1.

In order to illustrate the relative importance of the cometary rotation in the obtained values of $d_{\max}$, I introduce the parameter α as the percentage relative increase in $d_{\max}$ due to the cometary rotation. Thus, $\alpha = 100\cdot(d_{\max} - d^0_{\max}/d^0_{\max})$, where $d^0_{\max}$ is the value of $d_{\max}$ when the comet is not rotating. From equation (2), I obtain $\alpha = 100\cdot(\frac{\rho_{\rm n}G\tau^2}{3\pi} - 1)^{-1}$. In Figure 2 I show α versus τ for different values of $\rho_{\rm n}$.

The quantity $\dot{m}_{\rm g}v_{\rm g}$ in the differential equation of motion is crucial, because the grains would not lift from the surface for low values of it (that is when the attractive cometary gravitational force is greater than the other forces acting on the grains). I assume that the emission of grains from the cometary nucleus is anisotropic and suggest a strong anisotropy towards the Sun. Following Fulle (1997), $\dot{m}_{\rm g}v_{\rm g} = 0$ if $\cos(Z) < 0$ (dark hemisphere) where Z the zenith angle, and if $\cos(Z) \geq 0$, $\dot{m}_{\rm g}v_{\rm g}$ varies as the third power of the cosine of the zenith angle. Then, I can write, for illuminated hemisphere, $\dot{m}_{\rm g}v_{\rm g} = P\frac{-\cos^3(Z)}{r^\gamma}$, where P is the normalization constant, and γ is a fit constant which depends on the comet. After integration over the illuminated hemisphere, I obtain $\dot{m}_{\rm g}v_{\rm g} = 8(\dot{m}_{\rm g}v_{\rm g})_0$, where $(\dot{m}_{\rm g}v_{\rm g})_0$ is the quantity $\dot{m}_{\rm g}v_{\rm g}$ for an isotropic emission. It should be noted that equation (2) is only valid at the sub-solar point of the nucleus if an anisotropic gas emissin in considered.

3. GRAIN EJECTION FROM A COMET WITH A HIGH ROTATION PERIOD. COMET 1P/HALLEY

The state of rotation of Halley's comet has been the subject of many works. An explanation of the two observed periods is to consider Halley's nucleus to be in a complex rotation. The long-axis rotates around the total angular momentum vector with a period of 3.69 days, and the component of spin around the long-axis has a period of 7.1 days (see Belton et al. 1991, and references therein). In any case, the observed rotation is slow enough to consider $g_{\rm eff} \approx g$.

Krankowsky et al. (1986) derived a water molecule density $n_{\rm H_2O} = 4.7\cdot 10^7$ molecules cm^{-3} at 1000 km from the cometary nucleus from the neutral mass spectrometer experiment carried by the Giotto spacecraft and they estimated an uncertainty of 50%. The heliocentric distance of the comet was 0.89 AU. Since the derived water abundance was 80% by volume and since the volume mixing ratios (relative to H_2O) were 3.5% for CO_2, 10% (upper limit) for NH_3 and 7% (upper limit) for the CH_4, I obtain $Z_{\rm n} = 1.25 n_{\rm H_20}v_{\rm g}$, where $Z_{\rm n}$ is the gas mass flux expressed by the number of molecules cm^{-2} s^{-1}, and $v_{\rm g}$ is in cm s^{-1}. For an isotropic emission, I can obtain $\dot{m}_{\rm g}$ from $Z_{\rm n}$ multiplying by $4\pi R^2$. Krankowsky et al. obtained a gas expansion velocity (at distances closer than 10,000 km) of (900 ± 200) m s^{-1}. Putting this all together, and considering a strong anisotropic emission as reported by Fulle (1997), I conclude that $\dot{m}_g v_g$ ranges from $5.0 \cdot 10^7$ to $3.1 \cdot 10^8$ kg m s^{-2}.

Equation (2) can be rewritten as

$$d_{\max} = \frac{1}{\rho_d} \frac{9C_D \dot{m}_g v_g}{64\pi^2 R^3} \frac{1}{G\rho_n - \frac{3\pi}{\tau^2}\cos^2\phi} . \quad (3)$$

Using $\dot{m}_g v_g = 5.0 \cdot 10^7 - 3.1 \cdot 10^8$ kg m s^{-2} in equation (3), and considering that $\frac{3\pi}{\tau^2}\cos^2\phi \ll G\rho_n$ (in this case of comet Halley), I obtain values of $d_{\max}$ between 0.17 and 1.06 m if dust and nucleus densities are equal to 1000 kg m^{-3}.

4. GRAIN EJECTION FROM A COMET WITH LOW ROTATION PERIOD. COMET 46P/WIRTANEN

As mentioned in the introduction, a purpose of this paper is to show the importance of nucleus rotation for the values obtained for $d_{\max}$. For that reason, I apply the previous equations to the case of a comet with a short rotation period, such as comet 46P/Wirtanen. This comet was discovered by C. A. Wirtanen in January 1948 by studying its proper motion on plates obtained at the Lick Observatory with the 20 inch f/7.4 Carnegie astrograph. Although this comet is not now a target of any space mission (it was initially chosen as a target of Rosetta) it is among the best observed short period comets and has been studied from the ultraviolet to radio wavelengths from ground and from space (see Schulz & Schwehm 1999, and references therein). Furthermore, I have choosen this comet because its rotation period of 6 hours makes it one the fastest rotators among cometary nuclei having a well-determined rotational period (Lamy et al. 1998).

Comet 46P/Wirtanen is a small comet of 0.60 ± 0.02 km radius as derived by Lamy et al. (1998) from Hubble Space Telescope measurements. This radius is smaller than that reported by Crifo & Rodionov (1997) which is 1.4 km. The former authors considered their obtained values for the nucleus radius more realistic owing to the much higher contrast between nucleus and coma in the HST observation than that displayed in the ground-based observations by the latter authors.

Assuming a nucleus mass density of 1000 kg m^{-3} for Comet 46/P Wirtanen and considering a value for the rotation period of 6 hours (Lamy et al. 1998), I obtain a factor α of 43. The largest particle ejected from the nucleus due to the fast rotation of comet Wirtanen has a diameter more than 40 percent larger than the non-rotating case. This result is in agreement with Groussin & Lamy (2003), who pointed out that the maximum size must be enlarged by a factor of about 1.4 if the rotation of the comet is taken into account. In order to obtain absolute values for $d_{\max}$ I must know $\dot{m}_g v_g$. The evolution of Comet 46P/Wirtanen was investigated as a function of heliocentric distance at $r_h \leq 4.6$ AU (see, e.g., Schulz & Schwehm 1999). The composition of the emitted gas was mainly water (more than 99 percent) near perihelion. Therefore, the number of water molecules per second is essentially the gas production rate. Enzian (1999) gives an upper limit for the CO outgassing rate based on model results of less than 10^{26} molecules s^{-1}. Even assuming an abundance of CO and CO_2 molecules of 1%, the value of $d_{\max}$ would only be affected by about 2%. A value of about $(2.0 \pm 0.4) \cdot 10^{28}$ water molecules per second near perihelion seems to be a reasonable value for the gas production rate of 46P/Wirtanen (Fink & Combi 2004) although values as large as $4 \cdot 10^{28}$ (Jorda & Rickman 1995) and as small as $1 \cdot 10^{28}$ (A'Hearn et al. 1995) also appear in the literature.

In order to determine the value for v_g, I apply the expression for the thermal velocity $v_{\rm th}$ and $v_g = (1/2)v_{\rm th}$ (Wallis 1982) and then, $v_g = \sqrt{\frac{2RT}{\pi M}}$, where R the ideal gas constant, T the temperature and M the water molecular weight. Crifo & Rodionov (1997) report that total gas production rates of 4×10^{28} molecules per second or greater unquestionably produce hydrodynamical flows. A detailed discussion of the outflow speed of the gas is made by Ma, Williams, & Chen (2002), who argued that a fluid model is adequate for describing many of the phenomena associated with the cometary gas tail, but that an approach based on the kinetic theory of gases must be used for individual grain interactions. I use here the above expression for the gas velocity, which is the same thermal expansion velocity used by Nolan et al. (2006) (In the next section I compare our results with those obtained by Nolan et al. from radar measurements). Assuming a value for T of about 200 ± 100 K, I obtain $v_g = 240$ m s^{-1} with an upper limit of 300 m s^{-1} and a lower limit of 170 m s^{-1}. Taking into account the considerations shown above I estimate a value for $\dot{m}_g v_g$ between $0.8 \cdot 10^5$ and $21.5 \cdot 10^5$ kg m s^{-2} for an isotropic gas emission. Then, after considering equation (3), using $R = 600$ m and $\rho_d = 10^3$ kg m^{-3} I obtain values for $d_{\max}$ between 0.22 and 6.1 m.

Fulle (1997) also considered for 46P/Wirtanen an ejection varying as the third power of the cosine of the zenith angle, as indicated in the Halley case. If such a strongly anisotropic gas emission is assumed the upper limit for the diameter of the boulder could be several tens of meters. A representative value for $d_{\max}$ should be $d_{\max} = 0.4$ m, which is obtained for a total gas production rate of $2 \cdot 10^{28}$ water molecules per second when the comet was at ~ 1.1 AU of heliocentric distance, $v_g = 240$ m s^{-1}, $R = 600$ m, $\rho_d = 10^3$ kg m^{-3} and a 6 hour period, assuming an isotropic gas emission. If a strongly anisotropic emission is assumed (as the third power of the cosine of the zenith angle) our value would be $d_{\max} = 3.2$ m. An intermediate value could be obtained if the ejection varies with the cosine of the zenith angle (as assumed by Crifo & Rodionov 1997).

5. COMPARISON WITH OTHER COMETS OBSERVED BY RADAR

Radar observations have indicated the presence of large grains in several comets (see Harmon et al. 2004, and references therein). A firm detection of large grains from radar measurements was first published in Nolan et al. (2006), when they analyzed radar measurements of Comet C/2001 A2 (LINEAR). Besides this comet, Nolan et al. showed results for all comets for which a grain coma was detectable by radar. These comets are: C/2001 A2 (LINEAR), Halley, IRAS-Araki-Alcock, Hyakutake, and C/2002 O6, although the last comet was not modeled because the radar observations presented a low signal-noise ratio. They computed the Doppler spectra from the radial components of the terminal velocities of the entire ensemble of grains within the radar beam. They used a gas-drag model, first proposed by Whipple (1951) which postulates the dragging of particles by outflowing gases released by sublimation from the surface of the cometary nucleus. This model leads to an expression for the terminal ejection velocity of a spherical particle: $V_t = V_0(1 - a/a_m)^{1/2}$, where V_0 is the terminal velocity in the absence of gravity, a is the radius of the particle, and a_m is the radius of the largest grain that can be lifted (see Harmon et al. 1989, and references therein). Also, V_t is expressed by $V_t = C_v a^{-1/2}(1 - a/a_m)^{1/2}$ where $C_v = V_0 a^{1/2}$) is a velocity scale factor. Fitting the model to the radar Doppler measurements they obtained values for the factor C_v. From this model $C_v = (3C_D v_g Z R/4\rho_d)^{1/2}$, where Z is the mass gas flux at the surface; the model also leads to the equation (4) by Nolan et al. (2006),

$$a_m = \frac{9C_D v_g Z}{32\pi G R \rho_n \rho_d} = \frac{3{C_v}^2}{8\pi G R^2 \rho_n} . \qquad (4)$$

Nolan et al. get a good fit to the spectra with $C_v = 36$ cm$^{1/2}$ m s^{-1} for the comet C/2001 A2 LINEAR. They assumed $\rho_n = 1000$ kg m^{-3}, $\rho_d = 500$ kg m^{-3}, $R = 1$ km, and a temperature at the surface $T = 250$ K. Thus, they obtained a value for Z of $7 \cdot 10^{-4}$ g cm^2 s^{-1} and a value for $a_m = 10$ m. However, if $C_v = 36$ cm$^{1/2}$ m s^{-1} is inserted in their equation (4), other values, in fact, are obtained: $Z = 1.6 \cdot 10^{-3}$ g cm^2 s^{-1}, $a_m = 23.2$ m. For the moment I do not know the reason of such discrepancy.

Woodney, Schleicher, & Greer (2001) presented results from photometry and narrow band imaging of Comet C/2001 A2 (LINEAR) obtained at the Lowell Observatory 1.1 m Hall telescope. They studied the outward motion of the CN arcs and concluded that a 3 or 6 hour rotational period was possible, but they had too few data to obtain a unique solution (D. G. Schleicher, personal communication, May 19, 2009). If a 6 hour period is considered, then the inclusion of the rotational effects should enlarge the estimated maximum radius of the lifted particles by a factor of 1.43 (as in the case of comet 46P/Wirtanen). Therefore, the a_m estimated by Nolan et al. (2006) should be more than 14 m. I do not consider here the possible period of 3 h because it would be less than the critical period for a nucleus density of 1000 kg m^{-3} as can be seen in Figure 1, and for that value of the period, a high nucleus density ($\rho_n > 1200$ kg m^{-3}) should be assumed. Besides, the fastest cometary rotators observed have rotational periods larger than 5 hours (e.g., Meech 1996).

In order to compare the $d_{\max}$ values obtained from radar measurements with other techniques I consider the molecular abundances obtained by Magee-Sauer et al. (2008) on 10 July 2001 using the NIRSPEC instrument on the Keck-2 telescope at Mauna Kea. As the composition is not only water (although water molecules account for nearly 90% of the total molecular abundance), I must proceed in a similar way as for comet Halley. Thus, I take the average values for the July observations (Table 4 in Magee-Sauer et al. 2008): [402(H_2O), 6.3(C_2H_6), 16.6(CO), 13(CH_3OH), 5.5(CH_4), 1.6(C_2H_2), 2(HCN), 0.2(H_2CO)] $\cdot 10^{26}$ molecules per second at a heliocentric distance of $1.160 - 1.173$ AU. The result is $\dot{m}_g = 1.4 \cdot 10^3$ kg s^{-1}. This value is in agreement with that reported by Nolan et al. (2006) assuming isotropic grain ejection: $1 - 3 \cdot 10^3$ kg s^{-1}. It is an excellent result because both values were obtained using completely different techniques. Assuming a gas temperature of 250 K, I obtain a value of 270 m s^{-1} for v_g. Then, inserting $\dot{m}_g = 1.4 \cdot 10^3$ kg s^{-1} and $v_g = 270$ m s^{-1} in equation (2) and omitting the rotation term, I obtain $d_{\max} = 0.32$ m for isotropic ejection. If I consider an anisotropic ejection with third power of the cosine of the solar zenith angle and the fast rotation of the Comet C/2001 A2 (six hours period) I obtain a value $d_{\rm max} = 3.6$ m, which is a large value but much smaller than that the one reported by Nolan et al. (2006) using $C_{\rm v} = 36$ cm$^{1/2}$ m s^{-1}.

The other two comets mentioned above have a very different rotation period. IRAS-Araki-Alcock (comet IAA) is a very slow rotator. Feldman, A'Hearn, & Millis (1984) observed the ultraviolet emissions from comet IAA and showed that the rotation period must be ≥ 27 h. Harmon et al. (1989) derived a nucleus rotation period of 2–3 d from radar measurements. Then, $g_{\rm eff} = g$ and the value of $d_{\rm max}$ is unaffected by the rotation term of equation (3). Harmon et al. (1989) estimated values for the maximum radius $a_{\rm m}$ of the ejected particles of 3 cm from radar polarization measurements. They also applied a gas-drag model assuming an isotropic ejection and obtained $a_{\rm m} = 6 \times 10^{-4}$ m, which is inconsistent with the result obtained from the radar measurements. Then, they argued like Hanner et al. (1985) that is more likely that only 1% of the total surface area is active, and therefore a factor of 50 must be applied to the value $a_{\rm m} = 6 \times 10^{-4}$ m obtained for an isotropic emission on the illuminated hemisphere. Thus a value of $a_{\rm m} = 0.03$ m is found, which is consistent with the result derived from radar measurements.

On the other hand, I have used equation (2) of this paper and the assumption of an emission as $\cos^3(Z)$ and I obtained $d_{\rm max} = 5 \times 10^{-3}$ m. I have used $\rho_{\rm n} = \rho_{\rm d} = 10^3$ kg m^{-3}, $v_{\rm g} = 280$ m s^{-1}, $R = 5$ km, and the gas mass-loss rate of $6 \cdot 10^5$ g s^{-1} measured by Feldman et al. (1984) at 1.024 AU. All these values are those also used by Harmon et al. (1989). If I insert the value of $C_{\rm v} = 8$ cm$^{1/2}$ m s^{-1} as shown by Nolan et al. (2006) in their equation (4) I obtain a value of $a_{\rm m} = 0.06$ m, which is inconsistent with the value $a_{\rm m} = 6 \times 10^{-4}$ m reported by Harmon et al. (1989).

Comet Hyakutake (C/1996 B2) was also observed by radar on March 1996 by Harmon et al. (1997) at a heliocentric distance of $\simeq 1$ AU. They observed centimeter-sized grains in the coma of the comet. As the coma echo was asymmetric, they proposed that the asymmetry implied an anisotropy in the direction of grain ejection, and assumed that the grains were ejected in a 90°-wide cone. There are several estimations of the nucleus size of this comet based on infrared observations and on radio continuum measurements (see cited references in Harmon et al. 1997) and a value of about 2.4 km of radius is representative. Taking for the radius of the comet $R = 2.4$ km, $\rho_{\rm n} = 1000$ kg m^{-3}, and the same values as Harmon et al. (1997), $\rho_{\rm d} = 300$ kg m^{-3}, $v_{\rm g} = 290$ m s^{-1}, and $\dot{m}_{\rm g} = 5 \cdot 10^3$ kg s^{-1}, I obtain from equation (2) $d_{\rm max} = 0.15$ m if isotropic ejection is assumed. At first, two possible periods were attributed to Hyakutake (C/1996 B2). Schleicher et al. (1996) obtained a 6 h 14 min period from narrow-band photoelectric photometry and Larson et al. (1996) derived a rotation period of 12.5 h from observations made with the Hubble Space Telescope. However, Schleicher et al. (1998) presented a definitive determination of Comet Hyakutake's rotational period of 6.23 ± 0.03 h combining photometric data with CCD images. Then, and after adopting this last value, the rotation factor α is 39. I have also assumed (as Harmon et al. 1997) that the grains are ejected asymmetrically, although with a stronger asymmetry. I have maintained our assumption of an emission as $\cos^3(Z)$, for comparison, and then I obtain $d_{\rm max} = 1.7$ m. On the other hand, if the value $C_{\rm v} = 40$ given by Nolan el al. (2006) is inserted in their equation (4), then $a_{\rm m}$ near 5 m is found, which is not consistent with the results by Harmon et al. (1997).

6. COMET 67P/ CHURYUMOV-GERASIMENKO

This comet is the current target for the Rosetta mission. The Rosetta spacecraft will rendezvous and land upon the surface of comet Churyumov-Gerasimenko in late 2014. That is why it is important to consider the $d_{\rm max}$ obtained with the present model. Although first estimations favored a radius of about 3 km, more precise studies indicate a radius of about 2 km. Lamy et al. (2007) determined the size and shape of the nucleus of this comet from several visual light curves. They concluded that the comet is an irregular body with an effective radius of 1.72 km, and they found that it is rotating around a principal axis with a period of 12.4–12.7 hours. They estimated a nuclear density of 370 kg m^{-3} and densities between 100 and 500 kg m^{-3} were reported by Davidsson & Gutiérrez (2005). Tubiana et al. (2008) performed broad-band imaging of 67P/Churyumov-Gerasimenko in the visual range with a mosaic of two 2K$\times$4K MIT CCDs at the 8.2 m Very Large Telescope UT1 and determined a rotation period of 12.7407 ± 0.0011 h and an effective radius of 2.38 ± 0.04 km. Lamy et al. (2008) and Kelley et al. (2009) using the Multiband Imaging Photometry (MIPS) 24 μm channel of the Spitzer Space Telescope obtained a mean effective radius of $1.93 - 2.03$ km and 2.04 ± 0.11 km, respectively. Here, I adopt a value of 2 km for the radius of the nucleus of

TABLE 1

VALUES OF $d_{\max}$ FROM RADAR MEASUREMENTS COMPARED WITH THOSE FROM THIS WORK[a]

Comet	Radar measurements		This work		
	$d_{\max}$ (m)	r_c (AU)	$d_{\max}$ (m)	r_c (AU)	α
Halley	≥ 0.04[b]	1.59–1.47	0.17–1.06	0.89	$\simeq 0$
Hyakutake	10[c]	$\simeq 1$	1.7	$\simeq 1$	39
C/2001 A2	20[d]	$\simeq 1.14$	3.6	$\simeq 1.16$	43
IAA	0.06[e]	$\simeq 1$	0.005	$\simeq 1$	$\simeq 0$
Wirtanen			3.2	1.1	43
67P/C-G			0.3	1.34	29

[a]The last column shows the percentage relative increase in $d_{\max}$ due to cometary rotation (see text). [b]Campbell, Harmon, & Shapiro (1989). [c]Harmon et al. (1997). [d]Nolan et al. (2006). [e]Harmon et al. (1989).

the comet 67P/Churyumov-Gerasimenko. Lamy et al. (2007) carried out production rate measurements during both the 1982 and the 1996 apparition, and obtained approximate least-squares fitted analytical curves. I consider a gas production rate of $0.7 \cdot 10^{28}$ molecules per second, which is the maximum value of the above mentioned fitted curve near perihelion and, according to equation (4) of that paper it corresponds to a heliocentric distance of 1.34 AU. Agarwal, Müller, & Grün (2007) obtained terminal speeds of dust particles as functions of size at perihelion ($\simeq 1.29$ AU). Their values go from several hundreds of meters per second for submicrometer particles to a few meters per second for centimeter particles. Here I assume $v_{\rm g} = 270$ m s^{-1}, which is the value corresponding to a temperature of 250 K using the kinetic theory and of the same order as that used by Nolan et al. (2006, and references therein) for comparison. I assume the mean value of the interval mentioned by Davidsson & Gutiérrez (2005) for $\rho_{\rm n} = 300$ kg m^{-3}, $\rho_{\rm d} = \rho_{\rm n}$ in the absence of published information for $\rho_{\rm d}$, and $\tau = 12.7407$ h. Then, I obtain a value of $d_{\max} = 0.3$ m, if an ejection as the third power of the cosine of the zenith angle is considered. The centrifugal force due to the 12.7407 h rotation period increases the value of $d_{\max}$ as $\alpha = 28.8$. I show in Table 1 our $d_{\max}$ results together with those obtained from radar measurements (Nolan et al. 2006, and references therein) for comparison. I would like to point out that the values obtained for $d_{\max}$ are referred to a particular comet-to-Sun distance, because $\dot{m}_{\rm g} v_{\rm g}$ depends on $\vec{r}_{\rm c}$.

7. CONCLUSIONS

The standard model of planetary outgassing constitutes an useful way to estimate the maximum size $d_{\max}$ of the dust lifted from the surface of a comet. I have compared our results with those obtained from radar measurements for four comets: Halley, Hyakutake, C/2001 A2 (LINEAR) and IRAS-Araki-Alcock. In general, our results are smaller than those reported by Nolan et al. (2006, and references therein). Additionally, I have estimated values of $d_{\max}$ for comet 46P/Wirtanen and for comet 67P/Churyumov-Gerasimenko. The uncertainties in the quantities of equation (3) can considerably affect the estimated values of $d_{\max}$. Mainly, $\dot{m}_{\rm g} v_{\rm g}$ and R must be well known. The radius of the nucleus R appears as the third power in equation (3) and, on the other hand, the quantity $\dot{m}_{\rm g} v_{\rm g}$ is usually not well known. The discrepancy between the values of $v_{\rm g}$ obtained by using kinetic theory and those from the hydrodynamic models will be resolved when the GIADA (Grain Impact Analyser and Dust Accumulator) experiment measures the velocity of the grains from comet Churyumov-Gerasimenko. Independently of these uncertainties, $d_{\max}$ will be increased due to rotation of the nucleus. Thus, $d_{\max}$ increases by more than 40 percent due to rotation for fast comets with periods around 6 h. Therefore, the inertial forces, which introduce rotation terms in the equation of the cometary dust ejection, cannot be ignored, unless the comet is rotating with long a period (≥ 15 hours, $\alpha \leq 5$ for $\rho_{\rm n} = 10^3$ kg m^{-3}).

I have considered a strong anisotropy toward the Sun (as the third power of the cosine of the zenith angle) as proposed by Fulle (1997). This is equivalent to assuming an emission by an active area of about 12% of the total area, instead of assuming isotropic ejection. A more moderate assumption considering an anisotropy toward the Sun as the cosine of the zenith angle would lead to values of $d_{\max}$ just half of those estimated here. The dependence on the heliocentric distance, eccentricity of the orbit of the comet, true anomaly, obliquity and longitude of the place where the grain is lifted, will be studied in the future.

The author acknowledges the helpful comments of an anonymous referee which resulted in an improved version of this paper. This work was supported by contracts AY2007-6370, ESP2006-02934, and AYA2009-08190.

REFERENCES

Agarwal, J., Müller, M., & Gr̆un, E. 2007, Space Sci. Rev., 128, 79
A'Hearn, M., Millis, R. L., Schleicher, D. G., Osip, D. J., & Birch, P. V. 1995, Icarus, 118, 223
Babadzhanov, P. B. 2002, A&A, 384, 317
Beech, M. 1998, AJ, 116, 499
Belton, M. J. S., Mueller, B. E. A., Julian, W. H., & Anderson, A. J. 1991, Icarus, 93, 183
Burns, J. A., Lamy, P. L., & Soter, S. 1979, Icarus, 40, 1
Campbell, D. B., Harmon, J. K., & Shapiro, I. I. 1989, ApJ, 338, 1094
Crifo, J. F., & Rodionov, A. V. 1997, Icarus, 127, 319
Davidsson, B. J. R., & Gutiérrez, P. J. 2005, Icarus, 176, 453
Enzian, A. 1999, Space Sci. Rev., 90, 131
Feldman, P. D., A'Hearn, M. F., & Millis, R. L. 1984, AJ, 282, 799
Fink, U., & Combi, M. R. 2004, Planet. Space Sci., 52, 573
Finson, M. L., & Probstein, R. F. 1968, AJ, 154, 327
Fulle, M. 1997, A&A, 325, 1237
Groussin, O., & Lamy, P. 2003, A&A, 412, 879
Hanner, M. S., Aitken, D. K., Knacke, R., McCorckle, S., Roche, P. F., & Tokunaga, A. T. 1985, Icarus, 62, 97
Harmon, J. K., Cambpell, D. B., Hine, A. A., Shapiro, I. I., & Marsden, B. G. 1989, ApJ, 338, 1071
Harmon, J. K., Nolan, M. C., Ostro, S. J., & Campbell, D. B. 2004, in Comets II, ed. M. C. Festou, H. U. Keller, & H. A. Weaver (Tucson: University of Arizona Press), 265
Harmon, J. K., et al. 1997, Science, 278, 1921
Henderson, C. B. 1976, AIAA J., 14, 707
Ishiguro, M., et al. 2002, ApJ, 572, L117
Jorda, L., & Rickman, H. 1995, Planet. Space Sci., 43, 575
Kelley, M. S., Wooden, D. H., Tubiana, C., Boehnhardt, H., Woodward, C. E., & Harker, D. E. 2009, AJ, 137, 4633
Krankowsky, D., et al. 1986, Nature, 321, 326
Kuhrt, E., Knollenberg, J., & Keller, H. U. 1997, Planet. Space Sci., 45, 665
Lamy, P. L., Toth, I., Groussin, O., Jorda, L., Kelley, H. S., & Stansberry, J. A. 2008, A&A, 489, 777
Lamy, P., Toth, I., Jorda, L., Weaver, H. A., & A'Hearn, M. 1998, A&A, 335, 25
Lamy, P., et al. 2007, Space Sci. Rev., 128, 433
Larson, S., Brandt, J., Randall, C., & Niedner, M. 1996, BAAS, 28, 1088
Ma, Y., Williams, I. P., & Chen, W. 2002, MNRAS, 337, 1081
Magee-Sauer, K., Mumma, M. J., Disanti, M. A., Dello Russo, N., Gibb, E., Bonev, B. P., & Villanueva, G. L. 2008, Icarus, 194, 347
Meech, K. J. 1996, `http://www.ifa.hawaii.edu/~meech/papers/acm96.ps`
Molina, A., Moreno., F., & Jiménez-Fernández, F. J. 2008, Earth, Moon & Planets, 102, 521
Nolan, M. C., Harmon, J. K., Howell, E., Campbell, D. B., & Margot, J.-L. 2006, Icarus, 181, 432
Ortiz, J. L., Sada, P. V., Bellot-Rubio, L. R., Aceituno, F. J., Aceituno, J., Gutiérrez, P. J., & Thiele, U. 2000, Nature, 405, 921
Reach, W. T., Kelley, M. S., & Sykes, M. V. 2007, Icarus, 191, 298
Schleicher, D. G., Millis, R. L., Osip, D. J., & Lederer, S. M. 1996, BAAS, 28, 1089
________. 1998, Icarus, 131, 233
Schulz, R., & Schwehm, G. 1999, Space Sci. Rev., 90, 321
Sykes, M. V., Lebofsky, L. A., Hunten, D. M., & Low, F. 1986, Science, 232, 1115
Tubiana, C., Barrera, L., Drahus, M., & Boehnhardt, H. 2008, A&A, 490, 377
Wallis, M. K., 1982, in Comets, ed. L. L. Wilkening (Tucson: Univ. Arizona Press), 357
Whipple, F. L. 1951, ApJ, 113, 464
Woodney, L. M., Schleicher, D. G., & Greer, R. 2001, BAAS, 33, 1121

A. Molina: Departamento de Física Aplicada, Universidad de Granada, Facultad de Ciencias, Avenida Severo Ochoa s/n, 18071, Granada, Spain and Instituto de Astrofísica de Andalucía, CSIC, Camino Bajo de Huétor 50, 18008, Granada, Spain (amolina@iaa.es).

Revista Mexicana de Astronomía y Astrofísica, **46**, 331–338 (2010)

FUNCTIONAL RELATIONSHIPS FOR $T_{\rm eff}$ AND log g IN F-G SUPERGIANTS FROM $uvby - \beta$ PHOTOMETRY

A. Arellano Ferro

Instituto de Astronomía
Universidad Nacional Autónoma de México, Mexico

Received 2010 May 25; accepted 2010 July 2

RESUMEN

A partir de datos fotoeléctricos en el sistema $uvby - \beta$ y de valores precisos sintéticos y espectroscópicos de $T_{\rm eff}$ y log g en 50 supergigantes de tipos espectrales F-G, hemos calculado relaciones funcionales que permiten la estimación inicial de la temperatura efectiva y la gravedad en este tipo de estrellas. Se demuestra que aunque las calibraciones de $T_{\rm eff}$ fueron calculadas con los datos de estrellas supergigantes jóvenes y masivas, también son válidas para estrellas evolucionadas post-AGB y RV Tau de temperaturas similares. La gravedad superficial también puede calcularse a partir del índice $\Delta[c_1]$ con una precisión de 0.26 dex. Aunque se puede distinguir una correlación entre M_V y $\Delta[c_1]$, no hemos encontrado una correlación que prediga M_V de manera suficientemente precisa.

ABSTRACT

From photoelectric $uvby - \beta$ data and recent accurate synthetic and spectroscopic values of $T_{\rm eff}$ and log g for 50 F-G supergiants, we have calculated functional relationships that lead to initial estimates of effective temperature and gravities for these types of stars. It is shown that while the $T_{\rm eff}$ relationships are calculated using the data on young massive supergiants, they are also valid for evolved stars of similar temperatures like post-AGB and RV Tau stars. The gravity can also be predicted from the $\Delta[c_1]$ index with an uncertainty of about 0.26 dex. Although a clear and significant trend between M_V and $\Delta[c_1]$ is seen, no calibration is found that predicts accurate values of M_V.

Key Words: stars: AGB and post-AGB — supergiants — techniques: photometric

1. INTRODUCTION

Back in the mid 1990's we calculated a set of functional relationships between several reddening-free indices in the Strömgren $uvby-\beta$ system and the effective temperature for 41 supergiants of luminosity classes I and II and with spectral types between A0 and K0. The main goal of those relationships was to provide initial values of the effective temperature for our own spectroscopic work aimed at calculating detailed atmospheric abundances for stars of intermediate temperatures. At that time we used the temperatures calculated by Bravo-Alfaro, Arellano Ferro, & Schuster (1997) from 13-color photometry and the $uvby-\beta$ data from the catalogue of Arellano Ferro et al. (1998).

The relationships turned out to be quite useful for several problems related to the estimation of the temperature for these types of stars. However they remained unpublished mainly because the intrinsic scatter was rather large, probably due to the limited quality of the temperature data used.

Very recently a set of accurate temperatures, gravities and distances for 48 near ($d \leq 700$ pc) and 15 distant ($d \geq 700$ pc) A-G supergiants, were published (Lyubimkov et al. 2010). In the present paper functional relationships are worked out in view of these new values of physical parameters, with the aim of providing a tool to estimate initial values of $T_{\rm eff}$ and log g in yellow supergiants for subsequent spectroscopic work.

The paper is organized as follows: in § 2 the sources of the $uvby - \beta$ data are described, in § 3 the calibrations for the temperature as a function of the $[c_1]$, $[m_1]$ and Hβ photometric indices are dis-

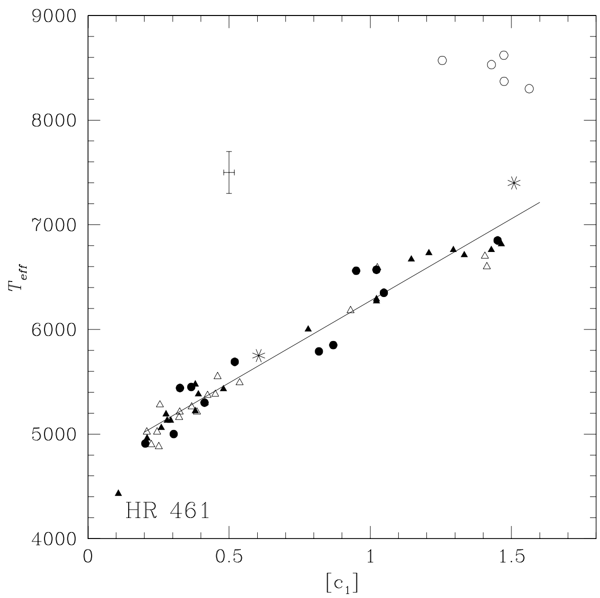

Fig. 1. Temperature dependence of the reddening free $[c_1]$ index. The open circles correspond to five A type stars which, along with the K1 star HR 461, are not included in the fit. The fit is valid for F-G type stars. Filled circles represent variable stars, empty triangles double stars and filled triangles non-variables. Asterisks correspond to two possible post-AGB stars in the sample of Lyubimkov et al. (2010). The error bars correspond to typical uncertainties of ± 200 K and ± 0.019 mag in $T_{\rm eff}$ and $[c_1]$, respectively.

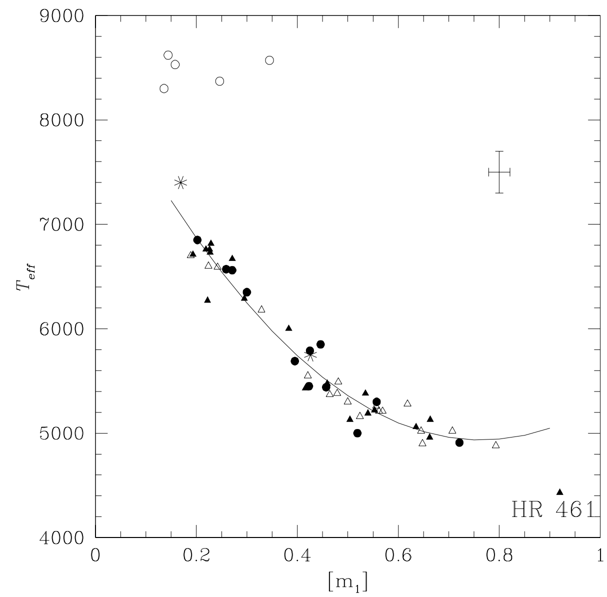

Fig. 2. Temperature dependence of the reddening free $[m_1]$ index. Symbols are as in Figure 1. The error bars correspond to typical uncertainties of ± 200 K and ± 0.021 mag in $T_{\rm eff}$ and $[m_1]$, respectively.

cussed, in § 4 the gravity calibration in terms of the $\Delta[c_1]$ index is calculated, in § 5 we discuss the validity of the calibrations for post-AGB and RV Tau stars, in § 6 the attempts at a calibration of the absolute magnitude and its limitations are presented, and in § 7 we summarize our conclusions.

2. THE PHOTOMETRIC $uvby-\beta$ DATA

The $uvby-\beta$ photometric data were taken from the catalogue of Arellano Ferro et al. (1998). For about a dozen of stars photometric data were not available in that source and their data were obtained from the sources given in the Simbad database. When several measurements exist a simple average was calculated. In Table 1 we present for the sample stars the reddening free indices $[c_1] = c_1 - 0.16(b-y)$ and $[m_1] = m_1 + 0.33(b-y)$, and values for their distance, effective temperature and gravity taken from Lyubimkov et al. (2010).

3. THE $T_{\rm eff}$ CALIBRATIONS

Plots of $T_{\rm eff}$ as a function of $[c_1]$ and $[m_1]$ are shown in Figures 1 and 2, respectively. Variable, double and non-variable stars have been plotted with different symbols to check whether their nature contributes to the scatter or if they appear as outliers. For the variable stars we used averages from rather scarce photometry not covering the full variational cycles; nevertheless, they follow the trends as well as the non-variable and double stars.

The $T_{\rm eff}$-$[c_1]$ correlation is good for F-G type stars. Five A-type stars included in the sample of Lyubimkov et al. (2010): HR 825, HR 1740, HR 2874, HR 3183 and HR 6081, identified with open circles, and the K1 star HR 461 (Yoss 1961) were not included in the fit. The line has the form:

$$T_{\rm eff} = 1566.6(\pm 50.7)[c_1] + 4704.0(\pm 40.5)\,, \qquad (1)$$

with a standard deviation of 152 K and a correlation coefficient of $R = 0.98$.

We can confirm from the models of Lester, Gray, & Kurucz (1986) that the c_1 index is temperature sensitive for $T_{\rm eff} \leq 7000$ K and that for hotter stars the sensitivity of the index changes and becomes more gravity dependent. This explains why the A-type stars do not follow the smooth correlation displayed by the F-G stars.

The $T_{\rm eff}$-$[m_1]$ correlation shows a non-linear form that can be represented by:

$$T_{\rm eff} = 6081.3(\pm 817.0)[m_1]^2 - 9294.9(\pm 731.8)[m_1] + 8486.7(\pm 149.5)\,. \qquad (2)$$

TABLE 1

PHYSICAL PARAMETERS AND PHOTOMETRIC INDICES FOR THE SAMPLE F-G SUPERGIANTS

Star	D (pc)	$T_{\rm eff}$ (K)	log g (dex)	$[c_1]$	$[m_1]$	Hβ	$E(b-y)$	M_V	$\Delta[c_1]$	Sp. T.	Comment
HR27	380	6270	2.10	1.022	0.222	2.668	0.100	−3.3	−0.236	F2 II	
HR 157	259	5130	2.15	0.293	0.504	2.585	−0.031	−1.5	−0.130	G2.5 IIa	
HR 207	935	5220	1.55	0.380	0.145	2.626	0.553	−3.9	0.000	G0 Ib	
HR 792	397	5020	2.09	0.245	0.645		0.034	−1.8	−0.062	G5 II	D
HR 849	538	5020	1.73	0.209	0.707	2.605	0.019	−8.6	−0.068	G5 Iab:	D
HR 1017	156	6350	1.90	1.048	0.300	2.681	0.097	−5.1	0.114	F5 Ib	V,S
HR 1135	170	6560	2.44	0.950	0.271	2.684	0.046	−2.6	−0.093	F5 II	V,RRL
HR 1242	629	6815	1.87	1.464	0.229	2.730	0.310	−5.3	0.236	F0 II	
HR 1270	427	5060	1.91	0.260	0.635	2.580	0.045	−2.1	−0.050	G8 IIa	
HR 1303	275	5380	1.73	0.451	0.479	2.609	0.097	−3.5	−0.018	G0 Ib	D,SB
HR 1327	98	5440	2.89	0.326	0.457	2.574	−0.024	+0.4	−0.183	G5 IIb	S
HR 1603	265	5300	1.79	0.414	0.500	2.607	0.002	−0.6	−0.009	G1 Ib-IIa	D
HR 1829	49	5450	2.60	0.366	0.423	2.576	0.007	−0.6	−0.232	G5 II	S
HR 1865	680	6850	1.34	1.451	0.202	2.730	0.121	−7.1	0.086	F0 Ib	V,S
HR 2000	224	5000	2.45	0.304	0.519	2.568	−0.045	−0.4	−0.105	G2 Ib-II	S
HR 2453	633	4900	1.70	0.224	0.648	2.582	−0.033	−2.4	−0.083	G5 Ib	D
HR 2597	935	6710	2.00	1.333	1.777	2.721	0.193	−4.3	−0.071	F2 Ib-II	
HR 2693	495	5850	1.00	0.869	0.446	2.660	0.013	−6.7	0.337	F8 Ia	V,S
HR 2786	386	5260	1.90	0.367	0.556	2.619	0.003	−2.7	−0.003	G2 Ib	D,S
HR 2833	375	5380	2.21	0.391	0.535	2.586	−0.010	−1.8	−0.005	G3 Ib	
HR 2881	461	5300	1.66	0.413	0.557	2.622	−0.029	−3.6	0.042	G3 Ib	S
HR 3045	370	4880	1.21	0.251	0.793	2.625	−0.030	−4.4	0.000	G6 Ia	D,S
HR 3073	338	6670	2.61	1.145	0.271	2.700	0.080	−2.2	0.106	F1 Ia	
HR 3102	161	5690	2.17	0.520	0.395	2.651	−0.005	−1.8	−0.144	F7 II	S
HR 3188	325	5210	1.75	0.325	0.569	2.589	−0.026	−3.1	−0.035	G2 Ib	D
HR 3229	267	5130	2.04	0.281	0.663	2.584	−0.003	−2.1	−0.016	G5 II	
HR 3291	900	6600	1.25	1.413	1.996	2.703	0.224	−7.2	0.165	F3 Ib	D
HR 3459	236	5370	2.08	0.424	0.464	2.609	0.005	−2.3	−0.072	G1 Ib	D
HR 4166	177	5475	2.36	0.380	0.459	2.586	−0.028	−1.4	−0.129	G2.5 IIa	
HR 5143	166	5190	2.75	0.277	0.540	2.543	−0.023	+0.2	−0.113	G5 II:	
HR 5165	253	5430	2.37	0.480	0.416	2.591	0.069	−1.7	−0.135	G0 Ib-IIa	
HR 6144	330	7400	1.80	1.509	2.277		0.169	−5.3	0.000	A7 Ib	pAGB?
HR 6536	117	5160	1.86	0.323	0.524	2.598	0.016	−2.6	−0.359	G2 Ib-IIa	D
HR 6978	649	6000	1.70	0.780	0.383	2.636	0.020	−4.4	0.075	F7 Ib	
HR 7014	1000	6760	1.66	1.429	2.043		0.226	−5.8	0.195	F2 Ib	
HR 7094	855	6730	1.75	1.208	1.460	2.711	0.227	−5.2	−0.026	F2 Ib	
HR 7264	156	6590	2.21	1.025	0.242	2.701	0.042	−3.2	−0.140	F2 II	D,S
HR 7387	880	6700	1.43	1.406	1.976	2.715	0.189	−6.7	0.015	F3 Ib	D
HR 7456	370	5550	2.06	0.459	0.421	2.611	0.087	−2.2	−0.143	G0 Ib	D
HR 7542	376	5750	2.15	0.605	0.426	2.633	0.185	−2.2	0.017	F8 Ib-II	pAGB?
HR 7770	960	6180	1.53	0.930	0.864	2.665	0.329	−5.4	0.080	F5 Ib	D
HR 7796	562	5790	1.02	0.818	0.425	2.645	0.026	−6.6	0.234	F8 Ib	V,S
HR 7823	1010	6760	1.92	1.294	1.674	2.729	0.219	−4.7	0.000	F1 II	
HR 7834	235	6570	2.32	1.022	0.259	2.691	0.060	−3.1	−0.078	F5 II	V
HR 7847	1040	6290	1.44	1.022	1.044	2.684	0.295	−5.9	0.077	F5 Iab	
HR 8232	165	5490	1.86	0.537	0.481	2.600	0.024	−3.3	0.076	G0 Ib	D
HR 8313	283	4910	1.58	0.203	0.721	2.593	−0.032	−2.8	−0.069	G5 Ib	V
HR 8412	284	5280	2.35	0.255	0.618	2.596	0.024	−1.0	−0.066	G5 Ia	D
HR 8414	161	5210	1.76	0.386	0.562	2.596	0.002	−3.1	0.020	G2 Ib	D
HR 8692	413	4960	1.90	0.210	0.662	2.597	−0.008	−1.8	−0.087	G4 Ib	

Comments code: V-variable, D-Double, S-$uvby-\beta$ from Simbad, pAGB?- possible post-AGB star, RRL- RR Lyrae, SB-Spectroscopic Binary.

As was done for equation (1) the five A-type stars and the K1 star HR 461 were not included. The standard deviation is 152 K, the correlation coefficient $R = 0.98$.

In order to explore a possible color dependence of the above calibrations, we have selected the dereddened color $(b-y)_0$. To calculate the reddenings for the F-G supergiants we used the calibration given by equation (5) of Arellano Ferro & Parrao (1990) which provides $E(b-y)$ from $(b-y)$, c_1 and m_1 indices with an accuracy of about ± 0.03 mag. The color excesses so calculated are given in Column 8 of Table 1. Since most of these supergiants have low reddening, and given the scatter in the reddening calibration, some small negative values are expected. These negative values should be taken as indicating zero reddening. The resulting equations with the color term included have slightly smaller standard deviations and higher correlation coefficients. They are:

$$T_{\rm eff} = 501.6(\pm 255.1)[c_1] - 1980.1(\pm 467.3)(b-y)_0 + 6252.0(\pm 367.0)\,, \quad (3)$$

with the standard deviation being 129 K and the correlation coefficient $R = 0.98$, and

$$T_{\rm eff} = 2244.0(\pm 958.6)[m_1]^2 - 2350.0(\pm 1407.1)[m_1] - 2244.0(\pm 454.7)(b-y)_0 + 7375.8(\pm 236.8)\,. \quad (4)$$

with the standard deviation being 119 K and the correlation coefficient $R = 0.99$.

At this point it is important to remark that since Lyubimkov et al. (2010) used $[c_1]$, among other indices, to estimate $T_{\rm eff}$, the correlations in Figures 1 and 2 are expected. Naturally, the calibrations of equations (1) to (4) are expressed in terms of the temperature scale of Lyubimkov et al. (2010). What it is offered here are functional relations that can be comfortably used to estimate $T_{\rm eff}$ in F-G supergiants from the c_1 photometry, with comparable accuracies.

The Hβ index is also linearly correlated with the temperature. For the linear fit between Hβ and $T_{\rm eff}$, using the 47 F-G stars with Hβ in Table 1, the standard deviation is 234 K and the correlation coefficient is $R = 0.93$. Since this calibration is of less quality than the four represented by equations (1) to (4), we have not illustrated it.

4. THE log g CALIBRATION

Calibrations of the surface gravity in yellow supergiants and bright giants have been performed in the past by Gray (1991) and Arellano Ferro & Mendoza (1993). The strategy was to use the $[m_1]$-$[c_1]$ plane, on which the locus of a "standard line", determined from F-G Ib supergiants exclusively, was defined by Gray (1991). Then, a vertical parameter; $\Delta[c_1] = [c_1] - [c_1](\textit{standard line})$, can be measured. It has been shown that $\Delta[c_1]$ is correlated with log g. Arellano Ferro & Mendoza (1993) used the spectroscopic gravities for 27 F-G supergiants given by Luck & Bond (1989) to calibrate the correlation. In this work we attempt a new calibration using the new values of log g given by Lyubimkov et al. (2010). The value of $\Delta[c_1]$ for each star in the sample is given in Column 10 of Table 1. Figure 3 shows the $\Delta[c_1]$ dependence on log g. As before, the five A type and the K1 star in the sample of Lyubimkov et al. (2010) have not been included. Among the F-G stars three outliers were noted in the $\Delta[c_1]$-log g plane; HR 1242 (F0 II) and HR 3073 (F1 Ia), both of which are non-variables, and the double star HR 6536. We have no ready explanation for their discordant position, and they were ignored. The remaining 47 stars display a clear relationship and the straight line has the form:

$$\log g = -2.836(\pm 0.349)\Delta[c_1] + 1.841(\pm 0.040), \quad (5)$$

with the standard deviation being 0.267 dex and the correlation coefficient $R = 0.77$.

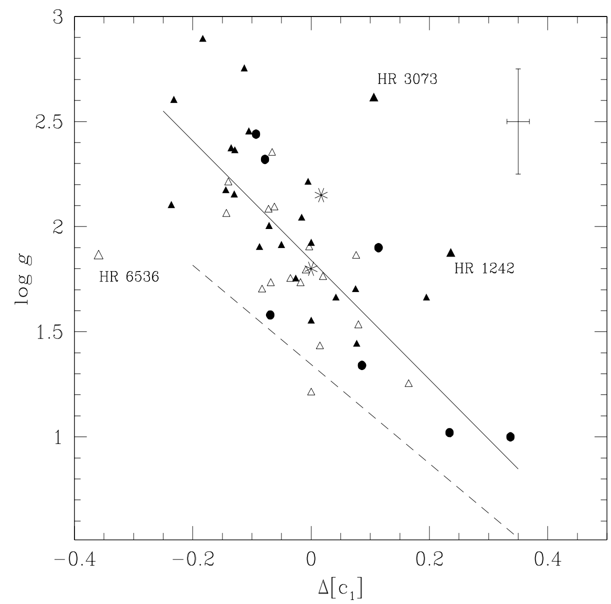

Fig. 3. Dependence of gravity on the index $\Delta[c_1]$. Symbols are as in Figure 1. The segmented line represents the calibration of Arellano Ferro & Mendoza (1993), shifted by 0.3–0.5 dex towards lower gravities. See text for discussion. The error bars correspond to typical uncertainties of ± 0.25 dex and ± 0.019 mag in log g and $\Delta[c_1]$, respectively.

TABLE 2

PHYSICAL PARAMETERS AND PHOTOMETRIC INDICES FOR A SAMPLE OF post-AGB AND RV TAU STARS

Star	$T_{\rm eff}$ (K)	log g (dex)	$[c_1]$	$[m_1]$	$\Delta[c_1]$	Sp. T.	Comment
HD 46703	6000	0.40	1.069	0.165	−0.463	F7 IVw	pAGB
HD 56126	7167	0.67	1.375	0.393	0.700	F5 Iab:	pAGB
HD 95767	7300	1.30	1.111	0.266	0.049	F3 II	pAGB
HD 107369	7600	1.50	1.575	0.119	−0.213	A2 II/III	pAGB
HD 108015	6800	1.25	1.187	0.237	0.000	F4 Ib/II	pAGB
HD 112374	6600	0.80	1.057	0.272	0.020	F3 Ia	pAGB
HD 148743	7200	0.50	1.509	0.169	0.000	A7 Ib	pAGB
HD 161796	6850	0.37	1.447	0.251	0.312	F3 Ib	pAGB
HD 163506	6550	0.60	1.309	0.193	−0.085	F2 Ibe	pAGB
HD 172481	7250	1.50	1.297	0.164	−0.257	F2 Ia0	pAGB
HD 179821	6775	0.90	1.003	0.601	0.675	G5 Ia	pAGB
HD 190390	6600	1.60	1.071	0.190	−0.338	F1 III	pAGB
HD 170756	5900	1.13	0.679	0.534	0.281	K0 III	RV Tau
AR Pup	6300	1.50	0.879	0.328	0.025	F0 Iab	RV Tau
IW Car	6700	2.00	1.211	0.270	0.160	A4 Ib/II	RV Tau
RU Cen	6000	1.00	0.741	0.457	0.234	F7/F8;A4 Ib	RV Tau
EN TrA	6150	1.25	0.968	0.312	0.074	F2 Ib	RV Tau

Since there are evidences that log g depends on $T_{\rm eff}$ for a given luminosity class (Straizys & Kuriliene 1981) we attempted to incorporate the color term $(b-y)_0$ but found it to be insignificant.

Equation (5), when compared with equation (5) of Arellano Ferro & Mendoza (1993), has smaller dispersion and a slightly higher correlation coefficient. However, we should note that the present calibration indicates lower gravities by 0.3–0.5 dex for a given $\Delta[c_1]$. This invited a comparison of the gravities used by Arellano Ferro & Mendoza (1993), taken from Luck & Bond (1989), with the gravities used in the present work from Lyubimkov et al. (2010) which are listed in Table 1. There are ten F and early G type stars in common; Figure 4 shows that the gravities of Luck & Bond (1989) are systematically smaller. Luck & Bond (1989) found that their spectroscopic gravities, obtained mostly from the ionization equilibrium condition on Fe I and Fe II lines, are systematically smaller by 0.3 dex than gravities derived via the membership of stars in clusters and their photometry. Similar discrepancies were found by Luck & Lambert (1985) for classical cepheids when spectroscopic gravities were compared with gravities obtained via PLC relationship. These authors forward a possible explanation as due to the fact that models built under the assumption of hydrostatic equilibrium may not be a good representation for the extended atmospheres of supergiant stars. The reader is referred to the detailed discussions on this point given in the above papers, and similar arguments might be invoked to explain the discrepancies displayed in Figure 4.

5. THE CASE OF post-AGB STARS

We often have wondered if the calibrations of physical parameters that have been worked out for young yellow supergiants would be equally valid for more evolved and less massive post-AGB stars of similar temperature and gravity. We found a few well known post-AGB and RV Tau stars in the catalogue of Stasińska et al. (2006) with reported values of effective temperature and gravity estimated by spectroscopic techniques, and with Strömgren photometry available in the Simbad database. These stars are listed in Table 2 and plotted in Figure 5 with blue and red symbols on the $[c_1]$-$T_{\rm eff}$ and $[m_1]$-$T_{\rm eff}$ planes of Figures 1 and 2. The stars are rather faint, and their spectral types may be difficult to determine with high accuracy. For this reason, and to avoid too small a sample we included several late

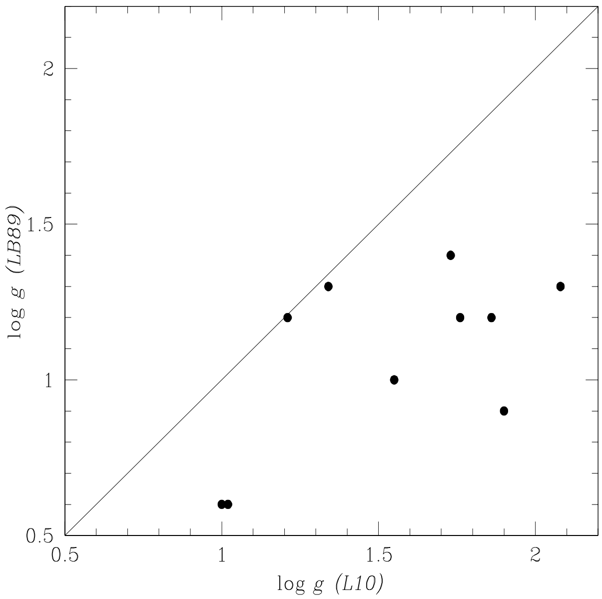

Fig. 4. Comparison of log g values for ten stars in common between Lyubimkov et al. (2010) and Luck & Bond (1989). See text for discussion.

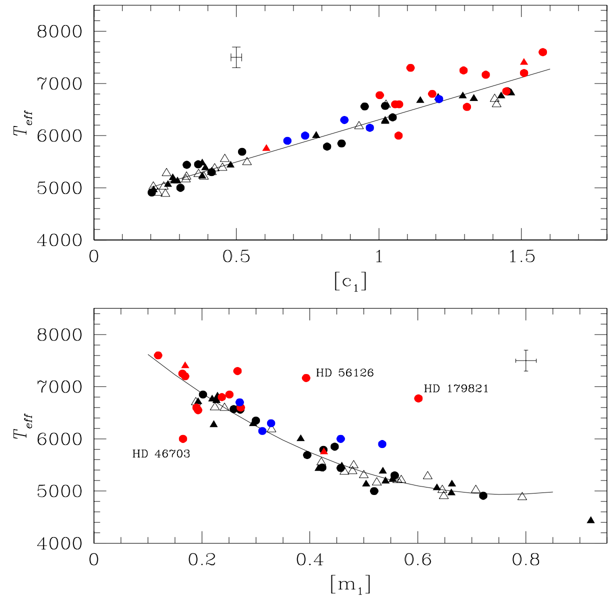

Fig. 5. Inclusion of post-AGB and RV Tau stars in the $T_{\rm eff}$ calibrations. The black symbols are as in Figure 1. The red circles are post-AGB stars and the blue circles are RV Tau stars. The red triangles are the two post-AGB candidate stars HR 6144 and HR 7542 plotted as asterisks in Figures 1, 2 and 3.

A stars and one K0 star. For the $[c_1]$ index the post-AGB and RV Tau stars follow very well the trend defined by the F-G supergiants and, therefore, it seems that the calibration is also valid for these types of stars stars. We have refrained from fitting the straight line with all points since the difference with equation (1) would be negligible. For the $[m_1]$ index the post-AGB's and RV Tau also follow the parabola of the F-G supergiants, except for three stars HD 46703 (F7 IVw), HD 56126 (F5 Iab:) and HD 179821 (G5 Ia). HD 46703 has the spectral type of a subgiant, which may explain its peculiar position. However, for HD 56126 and HD 179821 we have no explanation at hand.

Let us now explore, in a similar way, the role of post-AGB stars on the $\Delta[c_1]$-log g plane. As for the case of the young supergiants we started by plotting the stars on the $[m_1]$-$[c_1]$ diagram from which one can estimate $\Delta[c_1]$. Figure 6 illustrates both these planes. Except for the already noted outliers HD 46703, HD 56126 and HD 179821, both the post-AGB and the RV Tau stars follow the distribution on the $[m_1]$-$[c_1]$ plane. However, on the $\Delta[c_1]$-log g plane the post-AGB stars are at odds with the distribution of the supergiant stars. The five RV Tau stars (blue circles) seem to follow the supergiant trend rather well. With the available information we cannot say whether the post-AGB stars follow a completely different relationship, or if this is a result of the gravities reported by Stasińska et al. (2006) being anomalously too small. In either case it is clear that the relationship in equation (5) should be used only for the young supergiant stars.

6. COMMENTS ON THE DETERMINATION OF M_V

It would be desirable to posses a calibration that could predict the luminosity of young yellow supergiants given an observational parameter, such as for example a color index. Since these stars are luminous they could be used as distance indicators. We have attempted before to calculate such calibration (Arellano Ferro & Parrao 1990; Arellano Ferro & Mendoza 1993). However, an accurate result has been rather elusive. On the other hand a neat calibration of M_V from the intensity of the OI 7774 triplet, valid for a vast range of luminosities, was obtained by Arellano Ferro, Giridhar, & Rojo Arellano (2003), which predicts M_V with an uncertainty of 0.38 mag.

The distances provided by Lyubimkov et al. (2010) could in principle serve to explore a calibration of M_V in terms of a photometric index. The absolute magnitudes listed in Column 9 of Table 1 were calculated from the distances (Column 2) and the reddenings (Column 8). Since $\Delta[c_1]$ is correlated with log g one would expect a relationship between

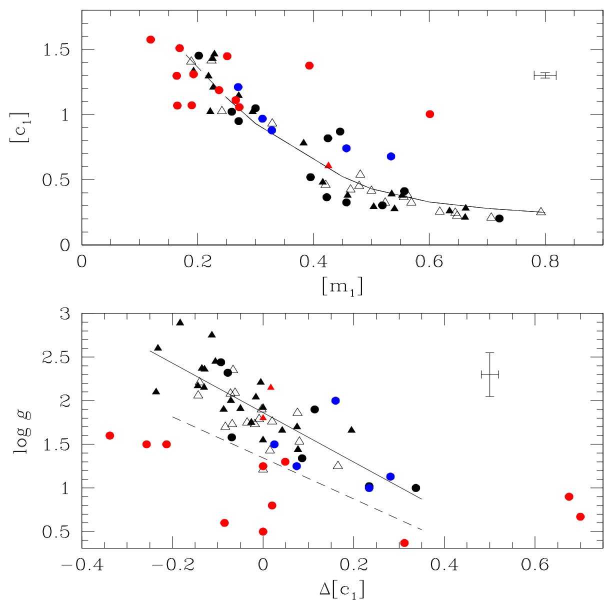

Fig. 6. Inclusion of post-AGB and RV Tau stars in the log g calibrations. The top panel shows the $[m_1]$-$[c_1]$ plane and the fiducial line definded by Gray (1991), relative to which the $\Delta[c_1]$ parameter is measured. The lower panel shows the distribution of the different groups of stars in the $\Delta[c_1]$- log g plane. Symbols are as in Figure 5. See text for discussion.

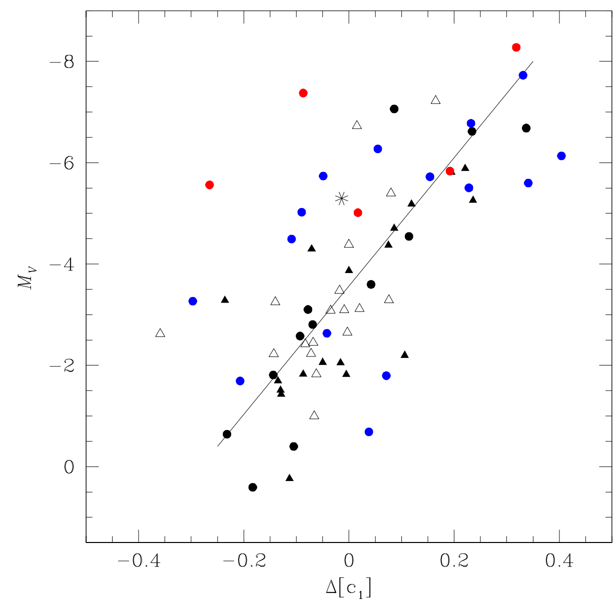

Fig. 7. Trend of M_V with $\Delta[c_1]$. The black symbols are as in Figure 1. The blue circles correspond to a sample of F-G supergiants and the red circles to a well documented post-AGB stars taken from Table 3 of Arellano Ferro et al. (2003), where values of M_V were calculated from the O I 7774 feature.

M_V and $\Delta[c_1]$. In Figure 7 the plot of $\Delta[c_1]$ vs M_V is shown. Although a trend is clearly seen, the scatter is large ($\sigma = 1.3$ mag). Inclusion of the color term, $(b-y)_0$ does not improve the relationship ($\sigma = 1.1$ mag).

We find of interest to consider a sample of F-G supergiants and 5 well documented post-AGB stars listed by Arellano Ferro et al. (2003) (their Table 3) for which values of M_V have been calculated from the O I 7774 calibration. $uvby-\beta$ photometry for all these stars is available in the *Simbad* data base and thus we can calculate their $\Delta[c_1]$ parameters. They are plotted in Figure 7 (blue and red symbols) along with the F-G supergiants of Table 1. We see that both groups of stars follow the same trend and display a similar scatter. One can conclude from this that while the distances in Lyubimkov et al. (2010) are consistent with the absolute magnitudes predicted from the strength of the O I 7774 feature in F-G supergiants, a reliable calibration of M_V in terms of a photometric index, for example $\Delta[c_1]$, is not foreseen.

7. CONCLUSIONS

New accurate values of $T_{\rm eff}$ and log g (Lyubimkov et al. 2010) lead to reliable functional relationships for the Strömgren reddening free indices $[c1]$ and $[m1]$, which allow to predict the effective temperature and gravity of F-G supergiants. The temperature calibrations are given in equations (1) and (2) which predict the effective temperature with an standard deviation of 152 K. If the reddening is available, alternative calibrations, given by equations (3) and (4) provide slightly smaller standard deviations (129 and 119 K respectively). These calibrations are valid for the more evolved post-AGB stars of similar temperature and gravity. Given the fact that RV Tau stars are variables of large amplitude, it is rewarding to see that the five RV Tau stars included follow the temperature trends very closely. Perhaps their mean temperature and photometric indices are not too different from the temperatures reported by Stasińska et al. (2006) and the mean photometric indices calculated here.

The stellar gravity can also be predicted from the $\Delta[c_1]$ index (Gray 1991) from the calibration given by equation (5), with an accuracy 0.28 dex. The color term was found to be insignificant. This equation is valid for F-G yellow supergiants and very likely for RV Tau stars. However, well known post-AGB stars of similar temperature and gravities (see Table 2) do not follow the calibration.

We have not been able to determine a reliable calibration that can predict the absolute magnitude M_V for F-G supergiant stars from photometric indices as accurately as from the strength of the OI 7774 feature.

Numerous comments and suggestions made by Prof. Sunetra Giridhar and an anonymous referee are thankfully acknowledged. This work was supported by DGAPA-Universidad Nacional Autónoma de México grant through project IN114309. This research has made extensive use of the *Simbad* data base operated at CDS, Strasbourg, France and of the NASA ADS Astronomy Query Form.

REFERENCES

Arellano Ferro, A., Giridhar, S., & Rojo Arellano, E. 2003, RevMexAA, 39, 3
Arellano Ferro, A., & Mendoza, E. E. 1993, AJ, 106, 2516
Arellano Ferro, A., & Parrao, L. 1990, A&A, 239, 205
Arellano Ferro, A., Rojo Arellano, E., González-Bedolla, S., & Rosenzweig, P. 1998, ApJS, 117, 167
Bravo-Alfaro, H., Arellano Ferro, A., & Schuster, W. H. 1997, PASP, 109, 958
Gray, R. O. 1991, A&A, 252, 237
Lester, J. P., Gray. R. O., & Kurucz, R. L. 1986, ApJS, 61, 509
Luck, R. E., & Bond, H. E. 1989, ApJS, 71, 559
Luck, R. E., & Lambert, D. L. 1985, ApJ, 298, 782
Lyubimkov, L. S., Lambert, D. L., Rostopchin, S. I., Rachkovskaya, T. M., & Poklad, D. B. 2010, MNRAS, 402, 1369
Stasińska, G., Szczerba, R., Schmidt, M., & Siódmiak, N. 2006, A&A, 450, 701
Straizys, V., & Kuriliene, G. 1981, Ap&SS, 80, 353
Yoss, K. M. 1961, ApJ, 134, 809

A. Arellano Ferro: Instituto de Astronomía, Universidad Nacional Autónoma de México, Apdo. Postal 70-264, México D.F. 04510, Mexico (armando@astro.unam.mx).

Revista Mexicana de Astronomía y Astrofísica, **46**, 339–348 (2010)

ATOMIC SPECIES IN THE SPECTRUM OF THE HG-MN STAR HD 53244

N. L. Maza,[1,2] H. Levato,[1,3] and Z. López-García[1,3]

Received 2009 December 29; accepted 2010 July 15

RESUMEN

Presentamos la identificación de líneas del espectro de la estrella Bp de Hg-Mn HD 53244 (γCMa) en el intervalo espectral $\lambda\lambda 3700 - 6700$ Å. Este objeto es miembro del cúmulo abierto austral Cr 121. La comparación de su espectro con otros de estrellas de Hg-Mn de campo muestra que comparte muchas de las anomalías espectrales pero también presenta algunas diferencias.

ABSTRACT

Line identifications are presented for the Hg-Mn Bp star HD 53244 (γCMa), in the spectral region $\lambda\lambda 3750 - 6700$ Å. This object is a member of the southern open cluster Cr 121. Comparison of the spectrum of HD 53244 with other field Hg-Mn stars shows that it shares many of their spectral anomalies but that also some differences exist.

Key Words: stars: chemically peculiar — stars: line identification — stars: individual (HD 53244)

1. INTRODUCTION

The identification of lines in stellar spectra is one of the basic operations in stellar spectroscopy. The main purpose of this task is to determine the element responsible for each observed spectral line. Today, complete identification studies in which one attempts to identify every absorption feature are rarely done but they are badly needed. This research is part of our current program for producing line identification lists and elemental abundances among southern chemically peculiar (CP) stars. For this paper we selected the Hg-Mn star HD 53244. It is a member of the open cluster Collinder 121 (Feinstein 1967). It was observed by Hipparcos (HIP 34045).

This peculiar star was classified as B8 II (Houk & Cowley 1975) and B8 III in several papers in the literature. In fact, HD 53244 is a Hg-Mn peculiar star or CP3 in the classification scheme of Preston (1974). It was first classified as a manganese star of the αAnd class by Morgan (1933). Some years later (Bidelman 1962a,b) identified the nature of the line λ 3984 Å as produced by Hg II and HD 53244 became a Hg-Mn star. It is included as such in the catalogues of Renson, Gerbaldi, & Catalano (1991) and Schneider (1981). *UBV* photoelectric fotometry was published by several authors; there are more than a dozen measurements in the literature. Also, *ubvy* photoelectric photometry has been provided by more than half a dozen sources. The most recent values for the *UBV* photometry are those provided by Fernie (1983), ($B - V = -0.13$ mag, $U - B = -0.45$ mag). The $ubvy - \beta$ photometry was taken from Hauck & Mermilliod (1998).

The radial velocity published by Wielen et al. (1999) is 32 km s^{-1} and the rotational velocity, 30 km s^{-1}, was derived by Abt, Levato, & Grosso (2002). Very recently Briquet et al. (2010) found variable line profiles of Hg line and they derived a rotation period of 6.16 days for HD 53244.

2. OBSERVATIONAL MATERIAL

The spectra of HD 53244 were obtained by NM with the Jorge Sahade 2.15 m telescope at Complejo Astrónomico El Leoncito (CASLEO) and the EBASIM bench echelle spectrograph with a Roper Scientific 1340 × 1310 CCD back illuminated detector with a pixel size of 20μ. Two spectra of the star were obtained covering the visual range $\lambda\lambda 3700 - 5500$ Å and another two covering the red portion $\lambda\lambda 4600 - 6700$ Å. The EBASIM spectrograph uses gratings as cross dispersers. We have used one grating with 226 lines mm^{-1}. The S/N ratio of

[1]Instituto de Ciencias Astronómicas, de la Tierra y del Espacio, San Juan, Argentina.

[2]Visiting astronomer Complejo Astronómico El Leoncito, Argentina.

[3]Consejo Nacional de Investigaciones Científicas y Técnicas, Argentina.

the spectra was around 300 and they were taken in March, 2008. The resolving power was 40000 at 5000 Å. There was no more than a 20% difference among the equivalent width measurements of the same lines in different orders of the echelle spectra. The spectra were reduced using IRAF[4] standard procedures for echelle spectra, and were normalized order by order with the CONTINUUM task of the same package. The resolution of the spectra was 0.04 Å/px. Extensive description of EBASIM spectrograph has been published by Simmons & Levato (1996) and by Pintado & Adelman (2003).

3. LINE IDENTIFICATIONS

The line identification techniques have been extensively reviewed by Cowley & Adelman (1990) and by Gulliver & Stadel (1990). Also the subject was addressed by Cowley (1995). Cowley & Adelman (1990) in particular compared the results of the classical technique for line identification with the WCS (wavelength coincidence statistics). As HD 53244 is an early type Bp star, we have used the classical technique for line identification based on the following precautions: (a) we use the highest resolution spectra on hand (EBASIM, 40000 resolving power), (b) we try to identify all the possible lines in the wavelength range, (c) we require that the strongest laboratory lines of each atomic species be present. The stellar lines were identified using the general compilation by Moore (1945) as well as the more specialized references: for Si II Shenstone (1961), for P II we used the NIST tables[5], for Ti II Huldt et al. (1982), for Mn II Iglesias & Velasco (1964), for Fe II Johansson (1978), Nave et al. (1994) and some few lines from Kurucz[6], while for the rare earths we have used the DREAM[7] database. We used a $\Delta\,\lambda$ interval of 0.15 Å to search for the possible contributors to each spectral feature. HD 53244 is not a very low rotator. The $v \sin i$ value derived from our EBASIM spectra is around 30 km s^{-1} and agrees with the Abt et al. (2002) determination. So we chose the interval ± 0.15 Å because the total width due to rotation for lines at 4000 Å is around 0.4 Å. Empirically, it is demonstrated that on our spectra one may note the presence of a companion line with less than half of that value. We have not used the synthetic computation of the spectra for line identification because that technique involves theory and several assumptions and simplifications of the real physical situation in Bp-Ap stars. The technique we have applied has been extensively justified in Cowley (1995).

Table 1 lists the line identifications. The first column shows the mean wavelength λ in Å as measured on HD 53244 and corrected by Doppler shift to the laboratory frame. The second column lists the equivalent width in Å measured in our spectra. The values are averages of two spectra. Column 3 lists the identification of the ion producing the line (the symbol ? means that the identification is doubtful). Column 4 provides the multiplet number or the source of the identification. The rest wavelengths are indicated in Column 5, while Column 6 provides the relative intensity of the line. The intensities are a measure of the depth of the line with respect to the continuum and they were estimated with a very rough scale in which lines (at the wavelength given) with a depth smaller than 4% correspond to intensity $I = 1$, those between 4% and 6% correspond to $I = 2$; 6% to 10%, to $I = 3$; 10% to 15%, to $I = 4$; 15% to 20%, to $I = 5$; 20% to 30%, to $I = 6$; 30% to 40%, to $I = 7$; 40% to 60%, to $I = 8$; 60% to 80%, to $I = 9$; and 80% to 100%, to $I = 10$.

In the vicinity of the Balmer lines, the intensities for the metal lines are measured with respect to the hydrogen line wings.The intensities for the Balmer lines are measured with respect to a continuum extrapolated across them.

Let us comment, next, the results for some atomic species:

- H I. The first line measured from the short wavelewngths region is λ3759.
- He I. There are several lines identified.
- C II. (Moore 1945) lines of multiplets 4 (λ3918 and λ3920) and λ4267 are present; lines of multiplet 2 (λ6578.05 and λ6582.88) were also found among the telluric lines present in the 6500 Å region.
- N I is not present.
- O I. We identified three lines of O I in the λ5300 region. They belong to multiplets 12 and 13 and one line of multiplet 3. We have also identified lines of multiplet 10 (λ6155.99 blended with λ6156.78) and also we found λ6158.19. We have also found the line of multiplet 9 λ6456.01. So the presence of O I is certain.
- O II. The identification is very doubtful, only one line is probably present.
- Ne I. There are several lines identified, multiplets 1, 3, 5, 6, 9, 11 and 13.
- Na I. There are many telluric lines present in the region, only λ5889 was identified.

[4]IRAF is distributed by the National Optical Astronomical Observatories which is operated by the Association of Universities for Research in Astronomy, Inc., under a cooperative agreement with the National Science Foundation.

[5]`http://physics.nist.gov/cgi-bin/AtData/lines.form`.

[6]`www.kurucz.havarard.edu/atoms/2601/gf2601.lines`.

[7]`http://www.umh.ac.be/astro/dream.shtml`.

TABLE 1

LINE IDENTIFICATION

		Identification			
λ [Å]	$W_{\rm eq}$	Element	Mult.	$\lambda_{\rm lab}$	Intensity
3700.00					
59.22	0.081	TiII	13	59.30	3
		FeII	154	59.46	
61.48	0.018	TiII	13	61.33	1
		CrII	11	61.66	
		TiII	107	61.88	
		CrII	11	61.85	
63.79	0.037	MnII	I	63.76	2
65.63	0.014	CrII	20	65.56	1
67.89	0.028	MnII	I	67.94	1
68.78	0.009	HeI	65	68.81	1/2
70.69		H11			7
78.32	0.054	MnII	I	78.32	2
79.62	0.019	FeII	23	79.58	1
83.33	0.100	FeII	14	83.35	3
84.23	0.092	CeIII ?			3
97.90		H10			7
98.28	0.049	FeII	14	98.28	2
3800.00					
01.38	0.022	MnII	I	01.63	1
		CrII	-	01.21	3
12.36	0.013	MnII	I	12.24	1
		MnII	I	12.52	
14.19	0.025	FeII	153	14.12	1
17.30	0.024	MnII	I	17.26	1
19.55	0.087	HeI			3
20.43	0.042	FeI	20	20.43	2
24.84	0.059	FeII	29	24.91	2
		MnII	I	25.04	
27.08	0.014	FeII	153	27.08	1
35.39		H9			8
38.80	0.024	MnII	I	39.05	1
41.79	0.019				
42.99	0.025	ZrII	7	43.03	1
43.26	0.010	MnII	I	43.32	1
44.10	0.022	MnII	I	44.17	1
45.17	0.072	FeII	127	45.18	2
48.24	0.059	MgII	5	48.24	2
49.51	0.035	NiII	11	49.58	2
50.95	0.034	OII	NI	51.03	1
		SII	50	50.93	
53.58	0.041	SiII	1	53.66	2
56.00	0.078	SiII	1	56.02	4
60.92	0.014	FeII	0	60.92	1
62.55	0.084	SiII	1	62.60	3
63.95	0.016	FeII		63.95	1
65.74	0.021	CrII	167	65.60	1
		CrII	130	65.99	
67.56	0.022	HeI	20	67.48	1
		HeI	20	67.63	
71.82	0.035	HeI	60	71.82	1
78.90	0.037	MnII	I	79.00	1
88.65	0.007	HeI	2	88.65	1/2
89.05		H8			6
3900.00					
00.48	0.028	TiII	34	00.56	1
05.94	0.075	FeII	173	06.04	2
		CrII	167	05.64	
11.76	0.018				
13.48	0.056	TiII	34	13.48	2
17.25	0.020	MnII	I	17.32	1
19.03	0.036	CII	4	18.98	1
20.66	0.048	CII	4	20.68	2
26.51	0.052	HeI	68	26.53	2
32.09	0.040	TiII	34	32.02	1
33.62	0.145	CaII			5
35.91	0.032	HeI	57	35.91	1
38.92	0.037	FeII	190	38.97	1
47.38	0.043	OI	3	47.29	1
50.40	0.027	YII	6	50.35	1
52.40	0.065	MnII	I	52.42	2
60.99	0.031	FeII	212	60.90	2
68.75		CaII			4
70.07		Hε			6
75.69	0.034	MnII	I	75.74	1
79.48	0.037	CrII	183	79.51	1
83.91	0.009	HgII		83.94	1
86.22	0.031				1
87.68	0.011	TiII	11	87.61	1
91.20	0.030	ZrII ?	30	91.14	1
95.31	0.014	MnII	I	95.32	1
99.84	0.013				1
4000.00					
00.02	0.006	MnII	I	00.04	1/2
02.58	0.030	FeII	190	2.54	1
		CrII	166	2.48	
03.62	0.013				1
04.69	0.021				1
09.35	0.042	HeI		09.25	1
12.45	0.019	TiII	11	12.40	1
		CrII	183	12.50	
15.50	0.037	NiII	12	15.50	2
18.24	0.018	ZrII ?	54	18.38	1
20.95	0.041				2
26.06		HeI			6
28.41	0.012	TiII	87	28.36	1
32.95	0.021	FeII	126	32.95	1
34.06	0.016	ZrII ?	42	34.10	1
37.91	0.032	CrII	194	37.98	1
40.26	0.018	ZrII	54	40.24	1
44.44	0.061	PII	30	44.49	2
48.81	0.032	FeII	172	48.83	1
50.60	0.027				
53.97	0.012	TiII	87	53.83	1
		CrII	19	54.09	
57.46	0.051	FeII	212	57.46	2
61.76	0.020	FeII	189	61.79	1
63.85	0.029				
64.48	0.028	FeII	29	64.57	1
		TiII	106	64.35	
65.40	0.015				1
66.94	0.054	NiII	11	67.05	2
69.96	0.014	FeII	188	69.88	1
72.48	0.027	CrII	26	72.56	1
73.76	0.031				1
75.43	0.028	SiII	3.01	75.45	1
78.50	0.013				1
80.94	0.080				2
83.63	0.100	MnII	I	83.66	3
4100.00					
01.76		Hδ			6
07.90	0.022				1
09.30	0.059	MnII ?	I	09.20	2
10.72	0.111	MnII	I	10.62	2
		CrII	18	11.01	
20.90	0.028	HeI			1
22.69	0.019	FeII	28	22.64	1
24.75	0.013	FeII	22	24.79	1
28.05	0.132	SiII	3	28.07	4
30.85	0.092	SiII	3	30.89	4
36.90	0.020	MnII	I	36.90	1
40.37	0.022	MnII	I	40.44	1
43.80	0.039	HeI			1
45.68	0.013	CrII	162	45.77	1
49.33	0.065	ZrII ?	41	49.22	2
53.20	0.010	SII	44	53.10	1
63.62	0.019	TiII	105	63.63	1
67.24	0.040	FeII	K88	67.30	1

TABLE 1 (CONTINUED)

		Identification			
λ [Å]	W_{eq}	Element	Mult.	λ_{lab}	Intensity
		FeIII	118	66.86	
71.54	0.039	MnII	I	71.51	2
73.59	0.090	FeII	27	73.45	2
		TiII	21	73.53	
78.67	0.058	FeII	28	78.86	2
		PII	S	78.46	
81.75	0.016	CrII	181	81.50	1
84.54	0.013	MnII	I	84.45	1
91.32	0.030				1
4200.00					
00.28	0.029	MnII	I	00.27	1
03.08	0.016	FeII	K88	02.99	1
05.37	0.034	MnII	I	05.38	1
06.31	0.056	MnII	I	06.37	2
22.26	0.012	CrII	180	22.00	1
24.62	0.032	CrII	31	24.08	1
		CrII	162	24.89	
33.14	0.057	FeII	27	33.17	2
		CrII	31	33.27	
35.16	0.012				1
35.62	0.027	YII	5	35.73	1
		FeII	K88	35.39	
37.95	0.014	MnII	I	37.87	1
38.80	0.022	MnII	I	38.79	1
42.36	0.056	MnII	I	42.33	1
		CrII	31	42.38	
44.23	0.023	MnII	I	44.25	1
46.55	0.073	ScII ?	7	46.83	2
		CrII	31	46.41	
50.44	0.013	FeII	K	50.44	1
51.73	0.043	MnII	I	51.74	2
52.97	0.045	MnII	I	52.96	2
54.47	0.004	CrII	D	54.52	1
59.07	0.029	MnII	I	59.20	1
61.99	0.022	CrII	31	61.92	1
63.89	0.012	FeII	J	63.90	1
67.19	0.061	CII	6	67.02,.27	2
70.84	0.014				1
73.31	0.019	FeII	27	73.32	1
75.59	0.029	CrII	31	75.57	1
78.38	0.008	SII	40	78.50	1/2
82.45	0.044	MnII	I	82.47	2
83.94	0.039	CrII	31	84.21	1
		MnII	I	83.77	
86.24	0.004	FeII	J	86.31	1/2
87.95	0.022	TiII	20	87.88	1
		MnII	I	88.07	
90.19	0.042	TiII	41	90.22	2
92.24	0.036	MnII	I	92.24	2
94.24	0.024	TiII	20	94.09	1
		SII	49	94.43	
96.57	0.026	FeII	28	96.57	1
4300.00					
00.08	0.037	TiII	41	00.06	2
03.10	0.044	FeII	27	00.17	2
07.96	0.047	MnII	I	08.16	2
		TiII	41	07.87	
09.52	0.003	YII	5	09.62	1
12.91	0.013	TiII	41	12.87	1
14.46	0.013	MnII	I	14.38	1
15.10	0.006	TiII	41	14.97	1
20.69	0.008	ScII	15	20.74	1
25.06	0.007	MnII	I	25.04	1
26.63	0.045	MnII	I	26.64	3
30.13	0.011	TiII	94	30.23	1
40.47		Hγ			6
43.92	0.054	MnII	I	43.98	2
48.42	0.030	MnII	I	48.40	1
51.79	0.053	FeII	27	51.77	2
56.62	0.018	MnII	I	56.62	1
63.22	0.019	MnII	I	63.26	1
65.22	0.030	MnII	I	65.22	1
67.69	0.011	TiII	105	67.65	1
69.36	0.006	FeII	28	69.40	1/2
73.03	0.018				1
74.59	0.016	TiII	93	74.84	1
		ScII	14	74.46	
		YII	13	74.94	
79.64	0.014	MnII	I	79.67	1
84.56	0.026	MgII	10	84.64	1
85.34	0.034	FeII	27	85.39	1
		PII	NI	85.31	
87.88	0.098	HeI		87.93	3
90.57	0.013	MgII	10	90.58	1
93.33	0.032	MnII	I	93.38	1
94.96	0.043	TiII	19	95.00	2
95.77	0.008	FeIII	4	95.78	1
99.80	0.026	TiII	51	99.79	1
4400.00					
00.74	0.020				1
07.74	0.004	TiII	51	07.68	1
09.49	0.007	TiII	61	09.51	1
11.10	0.009	TiII	115	11.10	1
11.99	0.003	TiII	61	11.92	1
15.20	0.003	FeI	41	15.12	1
16.80	0.035	FeII	27	16.83	1
17.76	0.002	TiII	40	17.72	1
19.41	0.007	FeIII	4	19.59	1
20.73	0.019	PII	NI	20.71	1
27.92	0.017	MgII	9	28.00	1
30.93	0.012	FeIII	4	30.95	1
34.03	0.019	MgII	9	33.99	1
		MnII	I	34.06	
37.51	0.017	HeI			1
41.84	0.007	TiII	40	41.73	1
43.76	0.039	TiII	19	43.78	1
50.43	0.015	TiII	19	50.50	1
51.53	0.008	FeII		51.55	1
55.26	0.009	FeII	J	55.27	1
61.93	0.015				1
63.07	0.017				1
68.49	0.043	TiII	31	68.52	1
71.51	0.182	HeI			5
75.24	0.013	PII	NI	75.26	1
78.64	0.026	MnII	I	78.64	1
81.17	0.187	MgII	4	81.13	6
		MgII	4	81.33	
89.14	0.028	FeII	37	89.18	1
		CrII	J	89.11	
91.38	0.029	FeII	37	91.40	1
93.68	0.011	TiII	18	93.53	1
		FeII	222	93.58	
99.31	0.029	PII	NI	99.24	1
4500.00					
01.31	0.037	TiII	31	01.27	1
08.24	0.038	FeII	38	08.28	2
15.29	0.039	FeII	37	15.34	2
18.99	0.012	MnII	I	18.96	1
20.20	0.030	FeII	37	20.22	1
22.57	0.046	FeII	38	22.63	2
24.83	0.018	SII	45	24.95	1
29.55	0.003	TiI	82	29.48	1
33.98	0.030	TiII	50	33.97	1
39.54	0.009	CrII	39	39.62	1
41.51	0.022	FeII	38	41.53	1
46.66	0.014	CrII	J	46.62	1
49.42	0.100	FeII	186	49.21	4
		FeII	38	49.47	
		TiII	82	49.62	
52.42	0.010	SiIII	2	52.62	1
		SII	48	52.38	
55.07	0.015	CrII	44	55.02	1

TABLE 1 (CONTINUED)

		Identification			
λ [Å]	W_{eq}	Element	Mult.	λ_{lab}	Intensity
55.92	0.013	FeII	37	55.89	2
58.56	0.048	CrII	44	58.66	2
63.77	0.024	TiII	50	63.72	1
65.74	0.010	CrII	30	65.77	1
67.87	0.008	SiIII	2	67.83	1/2
71.89	0.034	TiII	82	71.96	1
74.86	0.005	SiIII	2	74.76	1/2
76.39	0.029	FeII	38	76.33	1
79.58	0.007	FeII	J	79.52	1
82.87	0.020	FeII	37	82.84	1
83.80	0.074	FeII	38	83.83	2
88.13	0.027	PII	NI	88.04	3
		CrII	44	88.22	
89.83	0.031	CrII	44	89.89	1
		PII	NI	89.86	
92.03	0.023	CrII	44	92.07	1
96.02	0.021	FeII	D	96.02	1
98.39	0.013	FeII	219	98.53	1
4600.00					
02.04	0.034	P II	NI	02.08	1
00.44	0.029				1
16.60	0.022	CrII	44	16.64	1
18.78	0.023	CrII	44	18.82	1
20.56	0.017	FeII	38	20.52	1
21.65	0.023	SiII	7.05	21.42	1
				21.72	
25.86	0.002	FeII	186	25.91	1
29.26	0.037	FeII	37	29.34	1
31.99	0.003	FeII	219	31.90	1
34.12	0.020	CrII	44	34.16	1
35.27	0.022	FeII	186	35.32	1
40.91	0.004	FeII	J	40.84	1
56.99	0.007	FeII	43	56.98	1/2
58.36	0.011	PII	NI	58.31	1
66.70	0.008	FeII	37	66.75	1/2
70.13	0.010	FeII	25	70.18	1/2
73.16	0.017	SiII	7.15	73.27	1
4700.00					
08.72	0.043	NeI	11	08.85	2
13.18	0.045	HeI			2
16.16	0.008	SII	9	16.27	1/2
17.30	0.016	MnII	I	17.26	1
27.77	0.036	MnII	I	27.84	1
30.36	0.022	MnII	I	30.40	1
31.52	0.011	FeII	43	31.45	1
38.20	0.045	MnII	I	38.29	2
		MnII	I	38.29	
55.71	0.054	MnII	I	55.73	3
64.74	0.054	MnII	I	64.73	2
70.15	0.033				1
76.47	0.025				1
79.89	0.020	TiII	92	79.98	1
84.56	0.025				1
91.76	0.011	MnII	I	91.81	1
4800.00					
04.90	0.013	TiII	92	05.09	1
		FeII	J	04.73	
06.86	0.026	MnII	I	06.82	1
11.91	0.023	MnII	I	11.62	1
		CrII	30	12.36	
15.61	0.012	SII	9	15.55	1
24.08	0.032	CrII	30	24.13	2
26.63	0.017	FeII	J	26.68	1
30.17	0.011	MnII	I	30.06	1
36.13	0.008	CrII	30	36.22	1
47.67	0.019	MnII	I	47.61	1
48.28	0.017	CrII	30	48.24	1
61.33		Hβ			6
76.41	0.029	CrII	30	76.41	1
83.25	0.011	FeII	J	83.28	1

		Identification			
λ [Å]	W_{eq}	Element	Mult.	λ_{lab}	Intensity
4900.00					
01.60	0.013	CrII	190	01.65	1
11.13	0.015	TiII	114	11.18	1
13.29	0.020	FeII	J	13.29	1
21.77	0.133	HeI			3
23.87	0.063	FeII	42	23.93	2
31.30	0.018				1
43.51	0.021	PII	NI	43.53	1
48.80	0.010	FeII	J	48.80	1
51.52	0.014	FeII	J	51.59	1
54.18	0.011	FeII	J	53.98	1
69.63	0.039	PII	NI	69.71	1
76.95	0.019	FeII	J	77.04	1
77.50	0.038	FeII	J	77.03	1
		FeII	J	77.93	
80.14	0.006				1
84.49	0.010	FeII	J	84.49	1
90.59	0.012	FeII	J	90.51	1
91.66	0.010				1
93.36	0.003	FeII	J	93.35	1
5000.00					
01.90	0.034	FeII	J	01.92	2
04.22	0.025	FeII	J	04.20	1
07.40	0.030	FeII	J	07.45	1
09.54	0.012	SII	**7**	09.54	1
15.73	0.056	FeII	J	15.75	2
18.41	0.080	FeII	J	18.45	3
21.60	0.010	FeII	J	21.59	1
22.77	0.018	FeII	J	22.79	1
26.90	0.013	FeII	J	26.80	1
30.67	0.030	FeII	J	30.63	1
32.40	0.017	SII	**7**	32.41	1
35.68	0.027	FeII	J	35.71	1
40.96	0.086	SiII	5	41.02	3
47.66	0.029	FeII	J	47.64	1
		HeI			
56.16	0.122	SiII	5	55.98	4
		SiII	5	56.32	
61.64	0.018	FeII	J	61.72	1
67.79	0.018	FeII	J	67.89	1
75.74	0.024	FeII	J	75.76	1
82.22	0.013	FeII	J	82.23	1
89.17	0.012	FeII	J	89.21	1
93.54	0.023	FeII	J	93.56	1
97.24	0.018	FeII	J	97.27	1
5100.00					
00.72	0.056	FeII	J	00.74	2
02.47	0.029	MnII	I	02.52	1
03.30	0.004	SII	7	3.30	1/2
06.16	0.021	FeII	J	06.11	1
23.19	0.020	FeII	J	23.19	1
27.50	0.018	FeII	J	27.85	1
44.16	0.012	FeII	J	43.88	1
		FeII	J	44.36	
45.71	0.010	FeII	J	45.78	1
49.24	0.036	FeII	J	48.94	2
		FeII	J	49.46	
57.58	0.024	FeII	J	57.51	1
60.87	0.016	FeII	J	60.85	1
63.22	0.013	FeII	J	63.00	1
		FeII	J	63.58	
66.47	0.020	FeII	J	66.56	1
69.00	0.080	FeII	J	69.03	3
77.46	0.042	FeII	J	77.39	2
		MnII	I	77.65	
83.51	0.014	MgI	2	83.60	1
85.86	0.018	TiII	86	85.90	1
91.48	0.023	PII	NI	91.41	1
97.56	0.036	FeII		97.58	2
99.16	0.009	FeII	J	99.12	1

TABLE 1 (CONTINUED)

		Identification			
λ [Å]	W_{eq}	Element	Mult.	λ_{lab}	Intensity
5200.00					
01.00	0.012	FeII	J	00.81	1
02.40	0.010	SiII	23	02.41	1
		SiII	23	02.41	
03.69	0.018	FeII	J	03.64	1
12.70	0.001	SII	39	12.61	1
13.87	0.015	FeII	J	13.99	1
15.54	0.028	FeII	J	15.34	1
		FeII	J	15.82	
16.77	0.028	FeII	J	16.85	2
18.88	0.008	FeII		18.84	1
25.56	0.032	FeII	J	25.25	1
		FeII	J	25.36	
		FeII	J	25.98	
27.43	0.037	FeII	J	27.48	2
32.90	0.020	FeII	J	32.78	1
34.53	0.049	FeII	J	34.29	2
		FeII	J	34.62	
37.62	0.023	CrII	43	37.34	1
		FeII	J	37.95	
39.71	0.013	FeII	J	39.81	1
41.14	0.015	FeII	J	41.08	1
43.03	0.006	FeIII	113	43.3	1
45.12	0.015	FeII	J	45.08	1
46.75	0.003	CrII	23	46.75	1/2
47.94	0.021	FeII	J	47.95	1
49.40	0.017	CrII	23	49.40	1
51.32	0.027	FeII	J	51.23	1
53.46	0.068	FeII	J	53.64	2
		PII	NI	53.52	
54.77	0.010	FeII	J	54.64	1
57.25	0.020	FeII	J	57.11	1
60.25	0.041	FeII	J	60.26	2
64.34	0.043	FeII	J	64.18	2
		FeII	J	64.80	
69.98	0.015	FeII	J	70.03	1
72.35	0.018	FeII	J	72.40	1
75.91	0.060	FeII	J	75.99	2
79.79	0.023	CrII	43	79.88	1
84.14	0.025	FeII	J	84.11	1
91.91	0.040	FeII	J	91.67	2
		XeII	NI	92.22	
94.29	0.034	MnII	I	94.32	1
95.52	0.064	MnII	I	95.40	2
96.60	0.025				1
97.13	0.021	MnII	I	97.06	1
99.30	0.061	MnII	I	99.39	2
5300.00					
02.50	0.053	FeII	J	02.55	2
06.18	0.011	FeII	J	06.18	1
13.58	0.017	CrII	43	13.59	1
16.39	0.122	FeII	J	16.23	5
		FeII	J	16.62	
		FeII	J	16.78	
25.53	0.018	FeII	J	25.55	1
29.51	0.014	OI	12	29.10	1
		OI	12	29.68	
30.72	0.031	OI	12	30.74	1
		NeI	9	30.78	
34.85	0.013	CrII	43	34.88	1
36.73	0.032	TiII	69	36.78	1
39.55	0.040	FeII	J	39.59	2
44.68	0.035	PII	NI	44.71	1
46.23	0.017				1
62.84	0.047	FeII	J	62.87	2
66.25	0.014	FeII	J	66.21	1
70.34	0.010	FeII	J	70.30	1
72.36	0.022	XeII	NI	72.39	1
75.91	0.011	FeII	J	75.84	1
86.95	0.066	FeII	J	87.06	2
		PII	NI	86.88	
93.70	0.013	FeII	J	93.85	1
		FeII	J	93.59	
95.92	0.019	FeII	J	95.86	1
5400.00					
02.00	0.033	FeII	J	02.06	1
05.19	0.012	FeII	J	05.10	1
08.76	0.024	FeII	J	8.81	1
09.70	0.031	PII	NI	09.72	1
14.53	0.028	FeII	J	14.05	1
		FeII	J	14.84	
19.19	0.017	XeII	NI	19.15	1
21.92	0.015	MnII	I	21.92	1
25.82	0.067	FeII	J	25.82	2
		PII	NI	25.88	
27.70	0.008	FeII	J	27.82	1
29.90	0.014	FeII	J	29.99	1
32.85	0.019	SII	6	32.82	1
42.35	0.005	FeII		42.35	1/2
44.43	0.012	FeII	J	44.39	1
45.87	0.013	FeII	J	45.81	1
50.68	0.019	PII	NI	50.74	1
53.86	0.015	SII	6	53.83	1
66.40	0.050	SiII	7.03	66.43	2
72.84	0.014	FeII	J	72.86	1
75.79	0.009	FeII	J	75.83	1
82.30	0.019	FeII	J	82.31	1
87.66	0.023	FeII	J	87.62	1
92.14	0.018	FeII	J	92.08	1
		FeII	J	92.40	
93.66	0.011	FeII	J	93.63	1
98.53	0.015	FeII	J	98.57	1
99.77	0.033	PII	NI	99.73	1
5500.00					
02.99	0.024	FeII	J	02.68	1
		FeII	J	03.22	
06.27	0.036	FeII		06.20	2
10.69	0.055	FeII	J	10.67	2
		FeII	J	10.78	
28.93	0.004	FeII	J	29.06	1
29.74	0.005	FeII	J	29.92	1
31.99	0.008	FeII	J	32.09	1
34.86	0.025	FeII	J	34.83	1
44.66	0.019	FeII	J	44.76	1
		FeII	J	44.20	
48.65	0.015	FeII	J	48.21	1
59.06	0.030	SII	61	59.06	1
		MnII	I	59.05	
61.43	0.010	FeII	J	61.52	1
63.46	0.010	FeII	J	63.40	1
67.76	0.019	FeII	J	67.84	1
70.58	0.041				1
78.06	0.032	FeII	J	77.92	1
		MnII	I	78.15	
88.16	0.018	FeII	J	88.22	1
		FeII	J	88.05	
5600.00					
06.08	0.011	SII	11	06.15	1
39.96	0.022	SII	14	39.97	1
45.43	0.010	FeII	J	45.40	1
46.93	0.003	SII	14	47.03	1/2
48.80	0.008	FeII	J	48.90	1
51.56	0.006	FeII	J	51.54	1
55.32	0.005	FeII	J	55.36	1/2
57.86	0.003	FeII	J	57.92	1/2
60.18	0.014	FeII	J	60.15	1
64.70	0.009	SII	11	64.78	1
68.78	0.003	FeII	J	68.64	1/2
69.58	0.011	SiII	7.33	69.56	1
86.92	0.013				1
91.38	0.011	FeII	47	91.38	1

TABLE 1 (CONTINUED)

		Identification			
λ [Å]	W_{eq}	Element	Mult.	λ_{lab}	Intensity
5700.00					
16.51	0.007	FeII	J	16.58	1/2
48.30	0.006	NeI	13	48.30	1
80.18	0.021	FeII	J	80.13	1
83.79	0.014	FeII	J	83.63	1
5800.00					
26.30	0.020	FeII	J	26.11	1
		FeII	J	26.51	
52.38	0.012	NeI	6	52.48	1
75.62	0.168	HeI	11	75.62	6
		HeI	11	75.65	
78.57	0.013	FeII	J	78.53	1
79.84	0.017	FeII	K09	79.79	1
80.80	0.013	FeII	K09	80.84	1
81.87	0.019	NeI	1	81.89	1
82.82	0.022	FeII	K09	82.78	1
84.99	0.034	FeII	J	85.02	1
89.95	0.013	NaI	1	89.95	1
91.36	0.018	FeII	J	91.33	1
95.38	0.012	FeII	J	95.35	2
97.96	0.015	FeII	J	98.03	1
98.90	0.044	SiIII	K	98.79	2
5900.00					
01.25	0.010	FeII	J	01.39	2
02.60	0.029	FeII	J	02.82	1
11.86	0.022				1
14.50	0.018	FeII	J	14.53	1
21.39	0.025				1
27.18	0.016	SII	21	27.15	1
44.41	0.028	FeII	J	44.38	1
44.89	0.026	NeI	1	44.83	1
48.42	0.029	FeII	J	48.42	1
55.67	0.016	FeII	J	55.70	1
57.52	0.100	SiII	4	57.56	3
61.62	0.029	FeII	J	61.71	1
65.52	0.036	FeII	J	65.63	1
75.88	0.033	NeI	1	75.53	1
		XeII	NI	76.46	
78.97	0.048	SiII	4	78.97	2
83.96	0.015	FeII	J	83.86	1
6000.00					
24.16	0.064	PII	NI	24.18	2
34.00	0.049	PII	NI	34.04	2
43.04	0.074	PII	NI	43.12	3
45.50	0.012	FeII	J	45.46	1
49.49	0.007	FeII	J	49.45	1/2
60.93	0.021	FeII	J	60.99	1
69.63	0.006	FeII	J	69.67	1/2
71.43	0.009	FeII	J	71.42	1
74.41	0.012	NeI	3	74.34	1
84.19	0.006	FeII	J	84.11	1/2
87.76	0.030	PII	NI	87.82	1
89.76	0.004	CrII	87	89.69	1
96.29	0.017				1
6100.00					
05.33	0.006	MnII	K	05.27	1/2
22.55	0.032	MnII	K	22.45	1
28.91	0.023	MnII	K	29.04	1
43.01	0.021	NeI	1	43.06	1
47.77	0.016	FeII	J	47.77	1
49.19	0.018	FeII	J	49.25	1
56.57	0.040	OI	10	56.78	1
		OI	10	55.99	
58.18	0.031	OI	10	58.19	1
63.53	0.013	FeII	J	63.60	1
65.56	0.031	PII	NI	65.59	1
68.32	0.013	MnII	K	68.35	1
75.24	0.005	FeII	J	75.14	1/2
		FeII	J	75.44	
79.33	0.035	FeII	J	79.39	1
6200.00					
38.49	0.049	FeII	J	38.39	2
39.65	0.029	FeII	J	39.34	1
		FeII	J	39.90	
47.42	0.053	FeII	J	47.37	2
61.75	0.003	FeII	J	61.72	1/2
66.44	0.026	NeI	5	66.50	1
69.28	0.004	FeII	J	69.34	1/2
71.27	0.014	FeII	J	71.21	1
73.63	0.005	FeII	J	73.59	1/2
82.64	0.012	MnII	K	82.52	1
94.02	0.022	FeII	J	94.14	1
6300.00					
05.32	0.023	FeII	J	05.29	1
31.97	0.011	FeII	J	31.95	1
34.42	0.026	NeI	1	34.43	1
40.23	0.010	FeII	J	40.24	1
47.09	0.151	SiII	2	47.09	6
49.55	0.009	FeII	J	49.58	1/2
57.22	0.028	FeII	J	57.16	1
62.54	0.004	FeII	J	62.48	1/2
67.34	0.009	FeII	J	67.41	1/2
71.36	0.132	SiII	2	71.36	5
83.21	0.026	NeI	3	82.99	1
6400.00					
02.25	0.035	NeI	1	02.24	1
07.14	0.015	FeII	J	01.25	1
11.07	0.008	MnII	K	11.00	1/2
15.57	0.014	FeII	J	15.56	1
16.92	0.021	FeII	J	16.92	1
25.75	0.014	FeII	J	25.74	1
33.43	0.025				1
40.44	0.005	FeII	J	40.48	1/2
46.52	0.008	FeII	J	46.40	1/2
48.32	0.008	FeII	J	48.22	1/2
52.92	0.009	MnII	K	52.88	1/2
55.94	0.020	OI	9	56.01	1
56.38	0.046	FeII	J	56.38	2
58.62	0.013	MnII	K	58.56	1
59.93	0.031	PII	K	59.94	1
62.21	0.020	MnII	20	62.21	1
63.20	0.017	MnII	20	63.20	1
78.12	0.020	FeII	J	78.14	1
82.30	0.044	FeII	J	82.20	2
91.61	0.051	TiII	91	91.56	1
		FeII	J	91.67	
93.11	0.009	FeII	J	93.03	1
94.46	0.046	MnII	K	94.42	2
6500.00					
03.13	0.045				2
06.40	0.025	NeI	3	06.53	1
10.76	0.028	FeII	J	10.73	1
31.12	0.035	FeII	J	31.16	1
41.27	0.018	FeII	J	41.37	1
42.68	0.040	FeII	J	42.63	2
55.67	0.019	MnII	K	55.69	1
62.82		Hα			6
73.54	0.037	FeII	J	73.49	5
78.03	0.033	CII	2	78.05	1
82.84	0.012	CII	2	82.85	1
85.32	0.016	MnII	K	85.24	1
98.24	0.008	FeII	J	98.31	1/2
6600.00					
00.81	0.009				1
04.30	0.006	FeII	K09	04.30	1/2
11.32	0.005	FeII	K09	11.40	1
22.04	0.014	FeII	J	21.98	1
47.62	0.005	FeII	J	47.70	1/2

TABLE 2

COMPARISON OF HD 53244 WITH OTHER HG-MN STARS

Atomic Species	HD 53244	HD 175640	HD 186122	HD 144206	112 HerA	HR 7361	HR 7245	HR 7143
He I	Pres	Pres	Abs	Pres	Pres	Pres	...	...
Be II	...	Pres	...	...	...	...	...	...
B II	...	Abs	...	...	...	...	...	...
C I	Abs	Pres	Abs	Pres	Abs	Abs	Pres	Pres
C II	Pres	Pres	Abs	Pres	Pres	Pres	Pres	Pres
N II	Abs	Abs	Abs	...	...	...	...	...
O I	Pres	Pres	Pres	Pres	Pres	Pres	...	...
O II	Doub	Pres	Pres	Pres	Abs	Pres	...	...
Ne I	Pres	Pres	Pres	...	...	...	...	...
Na I	Pres	Pres	Pres	...	...	...	...	...
Mg I	Abs	Pres	Abs	Pres	Abs	Abs	Doub	Pres
Mg II	Pres	Pres	Pres	Pres	Pres	Pres	Pres	Pres
Al I,II	...	Abs	Pres	...	Pres	Abs	...	...
Si II	Pres	Pres	Pres	Pres	Pres	Pres	Pres	Pres
Si III	Pres	Pres	Abs	Pres	Pres	Pres	...	...
P II	Pres	Pres	Pres	Pres	Pres	Pres	Pres	Abs
S I	Abs	Pres	Abs	Pres	Pres	...	...	...
S II	Pres	Pres	Abs	Pres	Pres	...	...	...
Ca I	Abs	Pres	...	Pres	Pres	Pres	...	...
Ca II	Pres	Pres	...	Pres	Pres	Pres	...	...
Sc II	Pres	Pres	...	Pres	Pres	Pres	Doub	Abs
Ti II	Pres	Pres	Pres	Pres	Pres	Pres	Pres	Pres
Cr I	Abs	Pres	Pres	Pres	Abs	Abs	Abs	Pres
Cr II	Pres	Pres	Pres	Pres	Pres	Pres	Pres	Pres
Mn I	Abs	Pres	Pres	Pres	Abs	Pres	Pres	Pres
Mn II	Pres	Pres	Pres	Pres	Pres	Pres	Pres	Pres
Fe I	Abs	Pres	Pres	Pres	Pres	Pres	Pres	Pres
Fe II	Pres	Pres	Pres	Pres	Pres	Pres	Pres	Pres
Fe III	Pres	...	...	Pres	Pres	Pres	Pres	Pres
Co II	...	Doub	Pres	...	Abs	Abs	...	...
Ni II	Pres	Pres	Pres	Pres	Abs	Pres	...	...
Cu I	Abs	Pres	...	...	...	...	...	...
Cu II	Abs	...	Pres	...	...	...	...	...
Zn II	...	Abs	Pres	...	...	...	...	...
Ga I,II	Abs	Pres	Pres[a]	Pres	Pres	Pres	Pres	Pres
As II	...	Doub	Pres	...	...	...	...	...
Br II	...	Pres	...	...	...	...	...	...
Sr II	Abs	Pres	...	Pres	Pres	Doub	Pres	Pres
Y II	Pres	Pres	...	Pres	Doub	Pres	Pres	Pres
Zr II	Doub	Pres	...	Pres	Pres	Abs	Abs	Abs
Rh II	...	Pres	...	...	...	...	...	...
Pd I,II	...	Pres	...	...	...	...	...	...
Xe II	Pres	Pres	Pres	Abs	Pres	Pres	...	...
Ba II	...	Pres	...	Pres	Abs	Abs	...	...
Ce II	...	Pres	...	...	...	...	...	...
Ce III	...	Abs	...	...	...	...	...	...
Pr II	...	Abs	...	...	...	Abs	...	...
Pr III	...	Doub	...	...	...	Abs	...	...
Nd III	...	Pres	...	...	Abs	Abs	Abs	Abs
Yb II,III	...	Pres	...	...	...	...	...	...
Os II	...	Doub	...	...	...	...	...	...
Ir II	...	Pres	...	...	...	...	...	...
Pt II	Abs	Pres	...	...	Abs	Abs	Abs	Abs
Au II	Abs	Pres	...	...	Abs	Abs	Abs	Abs
Hg I	...	Pres	Pres	Pres	Abs	Abs	...	...
Hg II	Pres	Pres	Pres	Pres	Pres	Pres	Pres	Pres
$T_{\rm eff}$	13.781	12.050	13.000	12.000	13.450	13.650	12.293	12.050
$v \sin i$	30	20	20	20	20	15	15	20

Notes: Abs = Absent, Pres = Present, Doub = Doubtful.

[a]Castelli et al. (2009) did not observe Ga for this star on optical UVES spectra. Smith & Dworetsky (1993) studied the star in the ultraviolet using IUE spectra. Maybe also HD 53244 would show Ga in the ultraviolet.

- Mg I is not present.
- Mg II. We have identified lines of multiplets 4, 5, 9 and 10.
- Si II. Several lines were identified from multiplets. 1, 3, 4, 5, 7.03, 7.05, 7.33.
- Si III. Lines of Multiplet 1 are present.
- P II. Several lines were identified. We have used NIST tables.
- S I is not present.
- S II. A lot of lines were identified using Moore's tables (Moore 1945).
- Ca I is not present.
- Ca II $\lambda3933$ and $\lambda3968$ are present.
- Sc II. The most intense lines are identified using Moore Tables (Moore 1945); $\lambda4246$ blended with Cr II, $\lambda4320.74$ and $\lambda4374.46$ blended with Ti II.
- Ti II. We have identified a lot of lines. Very probably this element is overabundant.
- Cr II. A lot of lines were identified using Moore's tables. There are no lines of Cr I.
- Mn II. Using the tables from Iglesias & Velasco (1964) we have identified a lot of lines. Mn is very well represented.
- Fe I. There are no lines. Probably the effective temperature ($T_{\rm eff} = 13781$ K) is too high.
- Fe II. A lot of lines are present. We have used Moore's tables. For $\lambda > 4800$ Å we have used Johansson (1978) and the more recent table by Nave et al. (1994).
- Fe III. We have identified lines of multiplet 4.
- Ni II. We have identified only two lines, $\lambda4015.50$ and $\lambda4067.05$.
- Cu II is not present.
- Y II. We identified $\lambda3950.35$ (multiplet 6), $\lambda4235.73$, $\lambda4309.62$ (multiplet 5) and $\lambda4374.94$ (multiplet 13).
- Zr II. The most intense line $\lambda4149$ is ambiguously present although other weaker lines are identified $\lambda3843.03$ (multiplet 7), $\lambda3991.14$ (multiplet 30), $\lambda4018.38$, $\lambda4040.24$ (multiplet 54) and $\lambda4034.10$ (multiplet 42); we think that the presence of this element is doubtful.
- Xe II. The most intense lines are identified using the NIST tables.
- Hg II. The line $\lambda3983$ is definitely present.

We have not identified lines of Ga II and Sr II. We have not identified rare earths nor Au and Pt. The red regions of the spectra of HD 53244 have many telluric lines and it was difficult to identify with certainty some lines.

Thus, H I, He I, C II, O I, Ne I, Na I, Mg II, Si II, P II, S II, Ca II, Sc II, Ti II, Cr II, Mn II, Fe II, Fe III, Ni II, Y II, Xe II, Hg II are definitely present. O II and Zr II are doubtful. There are a number of unidentified lines. These are likely to be lines of atomic species which have been already identified.

4. COMPARISON WITH OTHER FIELD BP-AP STARS AND COMMENTS

Line identification lists have been published for several other HgMn stars. In Table 2 we have indicated the atomic species present in the blue, visual and red regions of HD 53244 The spectrum in the photographic region of HD 53244 is compared in the table with those of other Hg-Mn stars: HD 144206 (Adelman, Gulliver, & Rayle 2001), HD 186122 (Sadakane et al. 2001), HD 175640 (Castelli & Hubrig 2004), and 112HerA, HR 7361, HR 7245 and HR 7143 (Guthrie 1985).

Effective temperatures were obtained from Smith & Dworetsky (1993) for HD 144206, HD 186122, 112 HerA and HR 7361; Heacox (1979) for HR 7245; Cenarro et al. (2007) for HD 175640 and HR 7143. For HD 53244 we used $uvby-\beta$ mean colors from Hauck & Mermilliod (1998) and the TEMPLOGG program Rogers (1995) to obtain this parameter. The $v \sin i$ were taken from Abt et al. (2002).

As is usually the case, Hg-Mn stars seem to differ one from another. The Hg-Mn phenomenon seems to be heterogeneous with star to star diversity. Probably the absence of Ga I, II and Sr II is the distintive feature in HD 53244. It does not appear to be identical to any of the other stars in Table 2 although it shares many of their anomalies. Many of the atomic species which are present are represented by only a few lines. Differences in the magnetic field strength and configuration, apparent rotational velocity, effective temperature, surface gravity, elemental distributions on the stellar surface (see the recent paper by Briquet et al. 2010), and the exact wavelength region studied may well hide some of the underlying similarities.

There is no evidence in the spectra of HD 53244 of doubly ionized rare-earth lines. This lack of identifications may be due to the choice of the region studied (Adelman 1974).

The major similarity occur between HD 53244 and HD144206, which share almost the same anomalies except for the absence of Ga in the former. We conclude that HD 53244 appears to be a Hg-Mn star without Ga or rare earth elements.

The present work was partially supported through a grant from Consejo Nacional de Investigaciones Científicas y Técnicas de la República Argentina (CONICET PIP 1113). The authors thank the help provided by CASLEO personnel during the observing runs and an anonymous referee for helping to improve the presentation of this paper.

REFERENCES

Abt, H. A, Levato, H., & Grosso, M. 2002, ApJ, 537, 359
Adelman, S. J. 1974, ApJS, 28,51
Adelman, S. J., Gulliver, A. F., & Rayle, K. E. 2001, A&A, 367, 597
Bidelman, W. P. 1962a, AJ, 67, 111
_________. 1962b, S&T 23, 140
Briquet, M., Korhonen, H., González, J. F., Hubrig, S., & Hackman, T. 2010, A&A, 511, 71
Castelli, F., & Hubrig, S. 2004, A&A, 425, 263
Castelli, F., Kurucz, R., & Hubrig, S. 2009, A&A, 508, 401
Cenarro, A. J., et al. 2007, MNRAS, 374, 664
Cowley, C. R. 1995, in ASP Conf. Ser. 81, Workshop on Laboratory and Astronomical High Resolution Spectra, ed. A. J. Sauval, R. Blomme, & N. Grevesse (San Francisco: ASP), 467
Cowley, C. R., & Adelman, S. J. 1990, PASP, 102, 1077
Feinstein, A. 1967, ApJ, 149, 107
Fernie, J. D. 1983, ApJS, 52, 7
Gulliver, A. F., & Stadel, J. G. 1990, PASP, 102, 587
Guthrie, B. N. G. 1985, MNRAS, 216, 1
Hauck, B., & Mermilliod, M. 1998, A&AS, 129, 431
Heacox, W. D. 1979, ApJS, 41, 675
Houk, N., & Cowley, A. P. 1975, Michigan Catalogue of Two Dimensional Spectral Types for HD Stars, Vol. 1 (Ann Arbor: University of Michigan)
Huldt, S., Johansson, S., Litzen, U., & Wyart, J. F. 1982, Phys. Scr., 25, 401
Iglesias, L., & Velasco, R. 1964, Publ. Inst. Opt. Madrid, No. 23
Johansson, S. 1978, Phys. Scr., 18, 217
Moore, C. E., 1945, A Multiplet Table of Astrophysical Interest (Princeton: Princeton Univ. Obs.)
Morgan, W. W. 1933, ApJ, 77, 330
Nave, G., Johansson, S., Learner, R. C. M., Thorne, A. P., & Brault, J. W. 1994, ApJS, 94, 221
Pintado, O. I., & Adelman, S. J. 2003, A&A, 406, 987
Preston, G. W. 1974, ARA&A, 12, 257
Renson, P., Gerbaldi, M., & Catalano, F. A. 1991, A&AS, 89, 429
Rogers, N. Y. 1995, Comm. Asteroseismol., 78
Sadakane, K., et al. 2001, PASJ, 53, 1223
Shenstone, A. G. 1961, Proc. Roy. Soc. London A, 261, 153
Schneider, H. 1981, Bull. Inf. CDS, 20, 113
Simmons, J., & Levato, H. 1996, Bol. Asoc. Argent. Astron., 40, 44
Smith, K. C., & Dworetsky, M. M. 1993, A&A, 274, 335
Wielen, R., Schwan, H., Dettbarn, C., Lenhardt, H., Jehreiss, H., & Jahrling, R. 1999, Veröff. Astron. Rechen-Inst. Heidelberg, 35, 1

Natalia L. Maza: Instituto de Ciencias Astronómicas, de la Tierra y del Espacio, Av. España 1512 Sur, J5402DSP, San Juan, Argentina (nmaza@icate-conicet.gob.ar).
Hugo Levato: Consejo Nacional de Investigaciones Científicas y Técnicas de la República Argentina (hlevato@icate-conicet.gob.ar).
Zulema López-García: Visiting Astronomer of Instituto de Ciencias Astronómicas, de la Tierra y del Espacio, Av.España 1512 Sur, J5402DSP, San Juan, Argentina (zlgarcia@icate-conicet.gob.ar).

Revista Mexicana de Astronomía y Astrofísica, **46**, 349–356 (2010)

COMPACT RADIO SOURCES APPARENTLY ASSOCIATED WITH EXTENDED GALACTIC SOURCES

Alfonso Trejo and Luis F. Rodríguez

Centro de Radioastronomía y Astrofísica
Universidad Nacional Autónoma de México, Morelia, Michoacán, Mexico

Received 2010 January 12; accepted 2010 July 26

RESUMEN

Reportamos observaciones hechas con el VLA de la línea de 21 cm del HI hacia dos fuentes compactas que podrían estar asociadas con fuentes galácticas extendidas. En el caso de la nebulosa planetaria PHR 1735-333 observamos HI en absorción hacia una fuente de radio no térmica recientemente descubierta en la región, la cual se propuso estaba físicamente asociada con la nebulosa planetaria. Sin embargo, el análisis del espectro de HI en absorción sugiere una distancia mayor para esta fuente no térmica. En el caso del candidato a remanente de supernova SNR G3.8+0.3 obtuvimos espectros de HI en absorción hacia ella y hacia la fuente compacta de radio localizada en su centro. Concluimos que SNR G3.8+0.3 es más distante que la fuente compacta y que por lo tanto no están asociadas físicamente.

ABSTRACT

We report VLA radio observations of the 21 cm HI line toward two compact radio sources that could be associated with extended Galactic sources. In the case of the planetary nebula PHR 1735-333 we observed HI absorption against a non-thermal radio source recently discovered in the region, which was proposed to be physically associated with the planetary nebula. However, from the analysis of the HI absorption spectrum, we suggest a larger distance for this non-thermal source. In the case of the supernova remnant candidate SNR G3.8+0.3 we obtained HI absorption spectra towards it and towards a compact radio source located at its center. We conclude that SNR G3.8+0.3 is more distant than the compact radio source and that they are not physically associated.

Key Words: ISM: individual (SNR G3.8+0.3) — ISM: supernova remnants — planetary nebulae: individual (PHR 1735-333) — radio lines: ISM

1. INTRODUCTION

Compact radio sources sometimes appear associated in the plane of the sky with Galactic regions of extended emission. This association, if real, can be very important, since the compact source may be tracing the exciting source of the nebulosity or its interaction with other sources of energy such as the wind from a central star. On the other hand, we may just be dealing with a fortuitous line-of-sight alignment, with no real physical association. We have started a program of observations of such apparent associations using several techniques to determine the distance to the objects (Trejo & Rodríguez 2006, 2008, 2010), in an attempt to support or refute the association.

In this paper we present two cases of such an apparent association. One is the planetary nebula PHR 1735-333, and the other is the supernova remnant candidate SNR G3.8+0.3. In both cases we have been able to obtain HI absorption spectra that allow a determination of the distances to the sources and a better understanding of their nature. In both cases we favor a fortuitous line-of-sight alignment and propose that the compact source and the extended region of emission are not physically associated.

2. PHR 1735-333

The OH/IR star OH 354.88-0.54 (V1018 Sco) was detected as a mid-infrared point source in the Revised Air Force Geophysics Laboratory Rocket Sky

Survey of Price & Walker (1976) as source AFGL 5356. It was independently discovered as a strong 1612-MHz maser source during a survey of part of the Galactic plane (Caswell et al. 1981). Recently, Cohen, Parker, & Chapman (2005) discovered a planetary nebula around this star using data from the Anglo-Australian Observatory/United Kingdom Schmidt Telescope Hα Survey of the Southern Milky Way (Parker et al. 2005). This planetary nebula is named PHR 1735-333 in the MASH Planetary Nebula Catalog of Parker et al. (2006). There are several studies of this star involving different wavelengths. Green et al. (1999) found continuum emission associated with OH 354.88-0.54 in the first Molonglo Galactic Plane Survey at 843 MHz. The detected source was unresolved with a beam of approximately $1'$. Cohen et al. (2006) made a study of this source and its environment by means of 3, 6, 13 and 20 cm continuum and 1.3 cm line observations. These observations were taken with ATCA. Previously, only OH and SiO masers were reported in association with this source (e.g., Cohen et al. 2005; Nyman, Hall, & Bertre 1993), and Cohen et al. (2006) clearly detected water maser emission as well.

Cohen et al. (2006) found two non-thermal radio sources inside the planetary nebula (see Figure 1). Source A is relatively strong ($\sim$ 8 mJy at 20 cm) and partially resolved, while source B is weaker, unresolved and has no detection at 20 cm. The spectral indices of both sources are similar, -0.81 ± 0.01 and -0.95 ± 0.11, for A and B respectively. The sources lie at about the same projected angular distance from the central star. At 13 cm Cohen et al. found weak emission (2σ) apparently connecting both sources, but it is unclear if such extended emission is real. If confirmed, this connection would strengthen the possible association of sources A and B with the nebula.

It is well known that non-thermal emission can be found in massive stars (e.g., Abbott, Bieging, & Churchwell 1984; Persi et al. 1985). This non-thermal emission is believed to originate by embedded shocks in the stellar winds, as a faster component catches up with previous slower ejecta (White 1985). In a source such as PHR 1735-333, it can also be expected that the fast wind characteristic of the planetary nebula stage reaches and shocks the slow AGB wind, creating non-thermal emission.

In their study of PHR 1735-333, Cohen et al. (2006) proposed that the non-thermal radio sources were directly related to the nebula and not just line-of-sight alignments, since the probabilities of finding a single source at those positions are 1/500 and 1/200, for the observed 6 cm and 20 cm flux densities. The probability of finding two sources, if they are independent, will be much smaller ($\sim 10^{-5}$). The synchrotron emission would be generated, as they proposed, by the interaction between the slow AGB wind and the more recent fast wind from the nucleus of the PN. Since the presence of this type of interaction at relatively large distances from the star has not been reported in other sources and could be potentially very important, we tested the association of the non-thermal source A with the planetary nebula via HI absorption observations.

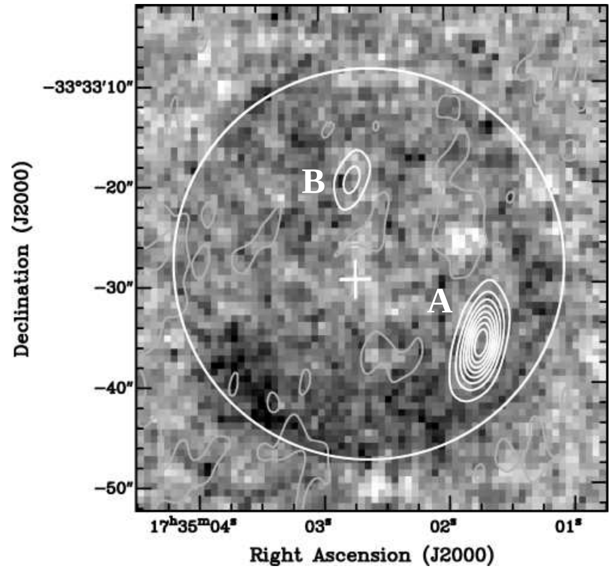

Fig. 1. Optical Hα image shown in grey, taken from the SuperCOSMOS database. The contours trace the 6 cm radio emission and show both non-thermal sources. The contours are 0.3, 0.5, 0.8, 1.1, 1.4, 1.6, 1.9, and 2.2 mJy beam^{-1}. The names of the sources (A & B) are as in Cohen et al. (2006). The cross marks the position of the star OH 354.88-0.54 and the white circle shows the approximate size of the PN candidate PHR 1735-333, which is visible in the optical image. This image is taken from Cohen et al. (2006).

2.1. *Observations*

We made observations of the 21 cm HI line using the NRAO[1] Very Large Array in its B configuration. A total of 26 antennas were used at the L band. We observed on 2008 March 6 under project AR661 with a total on-source time of about 1.5 hours. We used a bandwidth of 3.125 MHz with the 2IF mode (both circular polarizations). A total of 64 channels, each

[1]The National Radio Astronomy Observatory is a facility of the National Science Foundation operated under cooperative agreement by Associated Universities, Inc.

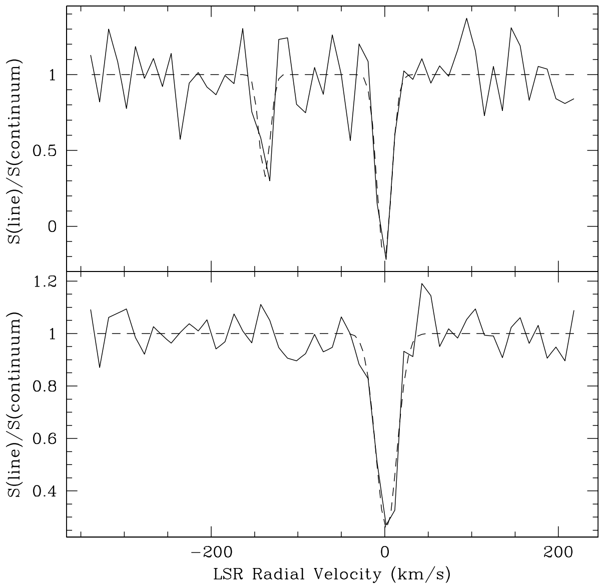

Fig. 2. Upper panel: Spectrum of the non-thermal source A seen in projection toward PHR 1735-333. The spectrum shows absorption at -140 km s^{-1}, which points to a farther location than that of the planetary nebula. Lower panel: Spectrum of a relatively strong Galactic source near the non-thermal source toward PHR 1735-333. It can be seen that the -140 km s^{-1} feature is not present in this last spectrum.

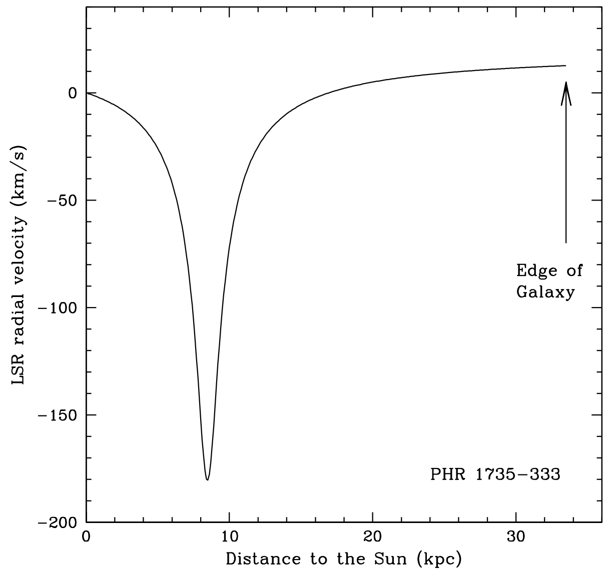

Fig. 3. LSR radial velocity as a function of distance to the Sun in the direction of PHR 1735-333. The positive values of the LSR radial velocity come from gas beyond the solar circle. The arrow marks the distance to the Sun where the edge of the Galaxy is located.

of 48.8 kHz wide, were used, which gave us a velocity resolution of 10.3 km s^{-1}.

We tried different weighting schemes in the task IMAGR, with ROBUST=0 (Briggs 1995) resulting as the best compromise between angular resolution and sensitivity. In order to avoid the emission of the Galactic plane we constructed images and spectra excluding baselines shorter that 0.7 Kλ (1 K$\lambda = 10^3$ wavelenghts), suppressing features more extended than $\sim 5'$. The data were processed in the standard manner, following the procedures of the AIPS Cookbook[2]. The beam had a half power full width of $34''\!.3 \times 12''\!.8$, PA$= 3^\circ\!.5$, with a positional accuracy of $\sim 3''$.

2.2. *Results and discussion*

The main goal of these observations was to obtain an HI absorption spectrum of the brighter non-thermal source (source A) seen toward the planetary nebula PHR 1735-333, with the purpose of constraining its distance and testing its association with the PN. As the target source turned out to be weak at the epoch of observation, we got a spectrum with modest signal to noise ratio (see top panel of Figure 2), with two absorption features. Since the continuum and the line are observed simultaneously and are perfectly aligned, we only need to determine the peak of the continuum emission and there take the spectra. The values for the HI absorption features are $S_{\rm L}/S_{\rm C} = -1.22 \pm 0.15$ (7.9σ), $V_{\rm LSR} = -0.6 \pm 1.4$ km s^{-1} and $\Delta V = 19.5 \pm 2.8$ km s^{-1} for one, and $S_{\rm L}/S_{\rm C} = -0.68 \pm 0.15$ (4.5σ), $V_{\rm LSR} = -138.3 \pm 2.7$ km s^{-1} and $\Delta V = 15.0 \pm 4.6$ km s^{-1} for the other, where S_L/S_C is the normalized ratio between line and continuum flux densities, $V_{\rm LSR}$ is the radial velocity of the component referred to the local standard of rest, and ΔV stands for the full width at half minimum of the fitting. In the case of the Galactic source near PHR 1735-333 (see lower panel of Figure 2), the HI absorption feature has $S_{\rm L}/S_{\rm C} = -0.75 \pm 0.04$ (18.8σ), $V_{\rm LSR} = +1.9 \pm 0.8$ km s^{-1} and $\Delta V = 28.7 \pm 1.9$ km s^{-1}. We considered as real only features above 4σ. Figure 2 shows the spectra and the fit superposed on it. The derived line widths are broadened by the instrumental resolution (10.3 km s^{-1}) and the deconvolved values are ~ 17 and ~ 11 km s^{-1} for the two absorption components shown in the upper panel of Figure 2, and ~ 27 km s^{-1} for the absorption shown in the lower panel of Figure 2. The HI absorption at a $V_{\rm LSR}$ near 0 km s^{-1} is attributed to nearby gas.

[2]http://www.aips.nrao.edu/cook.html.

TABLE 1

SOURCES IN THE FIELD OF PHR 1735-333 FOR WHICH HI SPECTRA WERE EXTRACTED

Source	Position α(J2000)	Position δ(J2000)	20 cm Flux Density (mJy)
OH 354.88-0.54 A	17 35 01.734	−33 33 36.36	2.7 ± 0.5
Galactic source	17 35 00.070	−33 24 17.10	20.5 ± 0.5

On the other hand, considering the rotation curve of the Galaxy (Brand & Blitz 1993) and assuming that the HI disk of the Galaxy has an outer radius of 25 kpc (Dickey et al. 2009), we show in Figure 3 the LSR velocity versus distance to the Sun for a source at the Galactic latitude and longitude of PHR 1735-333. From this figure we can see that if the non-thermal source A is associated with the PN, we expect HI absorption components with LSR radial velocities only in the 0 to -11 km s^{-1} range. In contrast, if the radio source is extragalactic we expect possible HI absorption components from 0 to -180 km s^{-1}. In addition, HI absorption at positive velocities (0 to $+13$ km s^{-1}) may be detected from gas outside the solar circle and located on the other side of the Galaxy.

Then, the absorption feature at approximately -140 km s^{-1} suggests that the gas responsible for that absorption is located at more than 8 kpc, according to Figure 3. We then propose that this non-thermal source is not related to the planetary nebula, which is located at a smaller distance of 3.2 kpc (Cohen et al. 2005). It should be noted, however, that the detection of the -140 km s^{-1} absorption feature is at the level of only 4.5σ level and that additional studies are required to be fully confident that the source A is more distant than the planetary nebula.

The position and flux density of this non thermal source is given in Table 1. For comparison, we plot in the lower panel of Figure 2 an example of a spectrum of another source present in the field observed. There is very little information on this source. It is detected in the NRAO VLA Sky Survey (Condon et al. 1998) with a 1.4 GHz flux density of 21.6$\pm$0.6 mJy, in good agreement with the value found by us (see Table 1). Since it shows HI absorption only near 0 km s^{-1}, we will assume it is a nearby Galactic source. We can see that the spectrum towards this source does not present the absorption feature at ~ -140 km s^{-1}.

Finally, Cohen et al. (2006) reported a 20 cm flux density of 7.68 ± 0.18 mJy for the non-thermal source A, from their 2005 March 24 observations. We found this flux to be of only 2.7 mJy (see Table 1) in our 2008 March 6 observations. As we noted before, source A could be an extragalactic object, such as a quasar. Then, a change in the flux density by a factor of ~ 3 is not unexpected for this type of sources. However, it should be noted that changes have also been observed in some planetary nebulae (Gómez et al. 2005; Zijlstra, van Hoof, & Perley 2008). This decrease in flux density was unfortunate, since it reduced the signal-to-noise ratio of the HI absorption spectrum toward source A. It will be interesting to study from the theoretical point of view if flux density changes of this order and timescale can be produced by the interaction of two winds.

3. SNR CANDIDATE G3.8+0.3

The radio continuum source SNR G3.8+0.3 is a supernova remnant candidate that was detected by Gray (1994) in the Molonglo Observatory Synthesis Telescope (MOST) Galactic center survey made at 843 MHz. As noted by Gray, this source shows an incomplete ring almost perfectly centered on a compact source (see Figure 4). The supernova remnant candidate has been studied by Bhatnagar (2002) at 327 MHz, who determined a spectral index of $\alpha = -0.6 \pm 0.1$ ($S_\nu \propto \nu^\alpha$) between 327 and 843 MHz. This result implies a synchrotron origin for the emission and strongly supports a supernova remnant nature for the extended radio source. Case & Bhattacharya (1998) used a radio surface brightness-to-diameter (Σ-D) relation to estimate a distance of 9.6 kpc to SNR G3.8+0.3, while Stupar et al. (2007) obtain a distance of 7.7 kpc from a different relation. We adopt an estimate of 8.7 ± 1.0 kpc for the distance to the SNR. Examination of available Hα survey imaging data such as for the AAO/UKST H-alpha survey (Parker et al. 2005) reveals no evidence of optical emission from the SNR candidate. There are no known X-ray sources or pulsars associated with this SNR candidate.

The compact radio source at the center of SNR candidate G3.8+0.3 is associated with the source

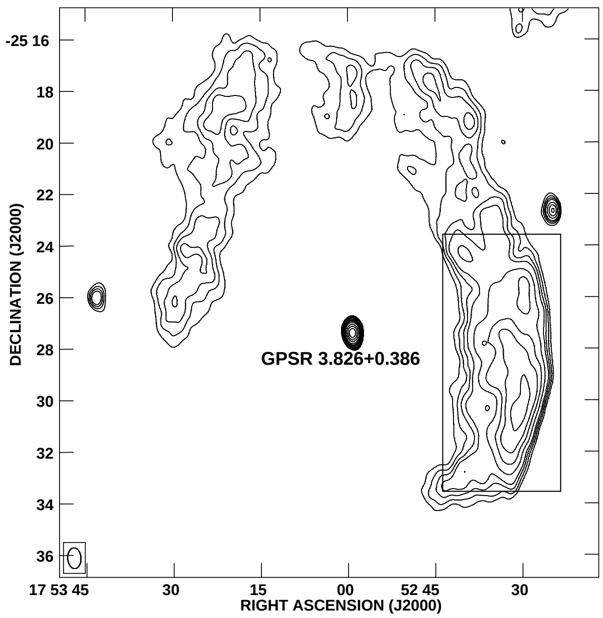

Fig. 4. VLA contour image of the continuum emission at 1.5 GHz of the supernova remnant candidate SNR G3.8+0.3. Contours are 3, 4, 5, 6, 8, 10, 12, 15, 20, 25, and 30 times 0.5 mJy beam^{-1}. The image is not corrected for the primary beam response (the observations were made centered at the position of the phase calibrator 1751–253 at $\alpha(2000) = 17^h\ 51^m\ 51\overset{s}{.}265; \delta(2000) = -25^\circ\ 23'\ 59\overset{''}{.}80$) and the eastern edge of the shell appears weaker in comparison to the western edge than it really is. The compact source GPSR 3.826+0.386 is labeled in the figure. The rectangle indicates the region over which the HI absorption spectrum of the SNR candidate was obtained. The half-power contour of the synthesized beam ($48\overset{''}{.}4 \times 30\overset{''}{.}8$; PA=3°) is shown in the bottom left corner of the image.

IRAS 17498–2526. This far-infrared source was proposed to be a possible planetary nebula by Preite-Martínez (1988) and Pottasch et al. (1988) on the basis of its IRAS colors. However, it should be noted that this association is uncertain. The radio source is listed in the catalog of small-diameter radio sources in the Galactic plane of Zoonematkermani et al. (1990) as GPSR 3.826+0.386 and we use this nomenclature to refer to it. These authors determine at 1.4 GHz a flux density of 45 mJy and an angular size of $2\overset{''}{.}3$ for the source. In their 5 GHz VLA survey of the Galactic plane, Becker et al. (1994) report the source with a flux density of 50.7 mJy and an angular size of $3\overset{''}{.}1$. The flat spectrum observed between 1.4 and 5.0 GHz is consistent with an optically-thin free-free source such as a planetary nebula or an HII region. The *a priori* probability of finding a ~ 50 mJy source at 5 GHz in a region with angular dimensions of $2' \times 2'$ (that approximately define the center of the SNR remnant candidate) is only ~ 0.0003 (Fomalont et al. 1991). The position of GPSR 3.826+0.386 is $\alpha(2000) = 17^h\ 52^m\ 59\overset{s}{.}28; \delta(2000) = -25^\circ\ 27'\ 24\overset{''}{.}7$. The images of the AAO/UKST Hα survey (Parker et al. 2005) show that this source is a strong and compact Hα emitter (see Figure 5) and that optical spectroscopy should be pursued.

3.1. *Observations*

SNR G3.8+0.3 has practically not been observed with the VLA. Fortunately, it is located at $\sim 15'$ from the well known VLA phase calibrator 1751–253 that has been extensively observed. We have then used data centered on 1751–253 to study SNR G3.8+0.3. Although the latter source is located at a position where the primary beam response at 20 cm of the 1751–253 observations is ~ 0.5 of that at the center, the observations can be used taking this factor into account.

In Figure 4 we show a 1.5 GHz image made with archive VLA data taken on 1984 May 31 as part of project AE32. The VLA was then in the C configuration and the absolute amplitude calibrator was 1331+305. The bootstrapped flux density of 1751–253 was 1.24 ± 0.01 Jy. The image shows the incomplete shell morphology of SNR G3.8+0.3 and the central location of GPSR 3.826+0.386.

The HI observations, made in 1989 October 21 as part of project AL201, were taken from the archive of the Very Large Array. The VLA was then in the C configuration, providing an angular resolution of about $40''$ for images made with natural weighting. The absolute amplitude calibrator was 1331+305 (with an adopted flux density of 14.73 Jy at 1.4 GHz). The bootstrapped flux density of 1751–253 was 1.02 ± 0.01 Jy. The data were edited and calibrated using the software package Astronomical Image Processing System (AIPS) of NRAO. The spectra consisted of two windows, one centered below in frequency (1419.406 MHz) and the other above in frequency (1421.406 MHz) of the HI rest frequency (1420.406 MHz). Each window had 127 channels of 24.4 kHz (5.2 km s^{-1}) each. In order to avoid the emission of the Galactic plane we made images and spectra excluding baselines shorter that 0.5 Kλ, supressing features more extended than $\sim 7'$. We analyzed separately each window and overlapped them to produce a single spectrum for the sources studied.

3.2. *Results and discussion*

In Figure 6 we show the HI absorption spectra toward three sources in the field: the phase calibrator 1751–253, the brightest part of the western shell

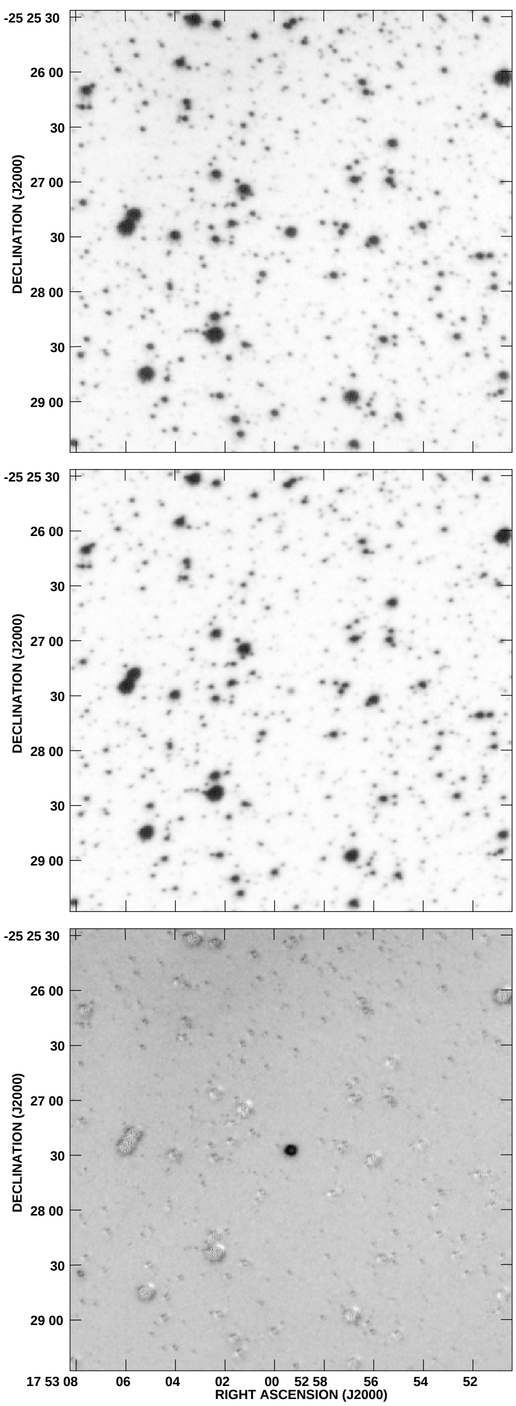

Fig. 5. 4 × 4 arcmin extracts of the AAO/UKST Hα SuperCOSMOS survey (Parker et al. 2005) around the compact source GPSR 3.826+0.386. Top: Hα emission; center: short red emission; bottom: Hα minus short red emission. Only GPSR 3.826+0.386 remains detectable in the bottom image, indicating it is a strong Hα emitter. The weaker features in this last image are the result of an imperfect subtraction.

of SNR G3.8+0.3, and the compact source GPSR 3.826+0.386.

To help in the discussion, we show in Figure 7 the LSR velocity versus distance to the Sun for a source at the Galactic latitude and longitude of GPSR 3.826+0.386, obtained as for the case of PHR 1735-333. The phase calibrator $1751-253$ is an extragalactic source and, as expected, its HI absorption spectrum confirms this. The spectrum shows strong absorption near 0 km s^{-1}, as expected since most of the gas in the direction of this region appears near the LSR radial velocity. In addition, the absorption spectrum shows a clear feature at +160 km s^{-1} that is coming from gas close to the subcentral point. Finally, this spectrum also shows absorption at -41 km s^{-1}, that is coming from beyond the solar circle. Our HI spectrum is in good agreement with that presented by Dickey et al. (1983), although these authors do not cover a sufficiently large velocity interval to include the +160 km s^{-1} feature.

The HI spectra of SNR G3.8+0.3 and GPSR 3.826+0.386 both show absorption around 0 km s^{-1}. However, the spectrum of SNR G3.8+0.3 clearly shows an absorption at +170 km s^{-1} which places this supernova remnant candidate beyond the subcentral point, at 8.5 kpc. This lower limit for the distance is consistent with the value estimated from the results of Case & Bhattacharya (1998) and Stupar et al. (2007), 8.7 ± 1.0 kpc. In contrast, GPSR 3.826+0.386 does not show this absorption, suggesting it is closer to us than the subcentral point. This upper limit for the distance is consistent with the value of 1.7 kpc estimated by Preite-Martínez (1988), from a modified Shklovski (statistical) method applied to all the planetary nebulae in his sample. We then conclude that the supernova remnant candidate and the compact source are most likely not associated.

4. CONCLUSIONS

We made HI line radio observations toward the planetary nebula PHR 1735-333 and analyzed archive data of the supernova remnant candidate SNR G3.8+0.3. Both sources are associated in the plane of the sky with compact radio sources that could be physically related to them. Our study shows that the distance to the non-thermal radio source recently found in apparent association with the planetary nebula PHR 1735-333 is at least two times larger than that of the nebula. We conclude that the radio source is most probably unrelated to the Galactic planetary nebula and we suggest an extragalactic nature for it. However, there are several arguments that favor the association as real: (i) the

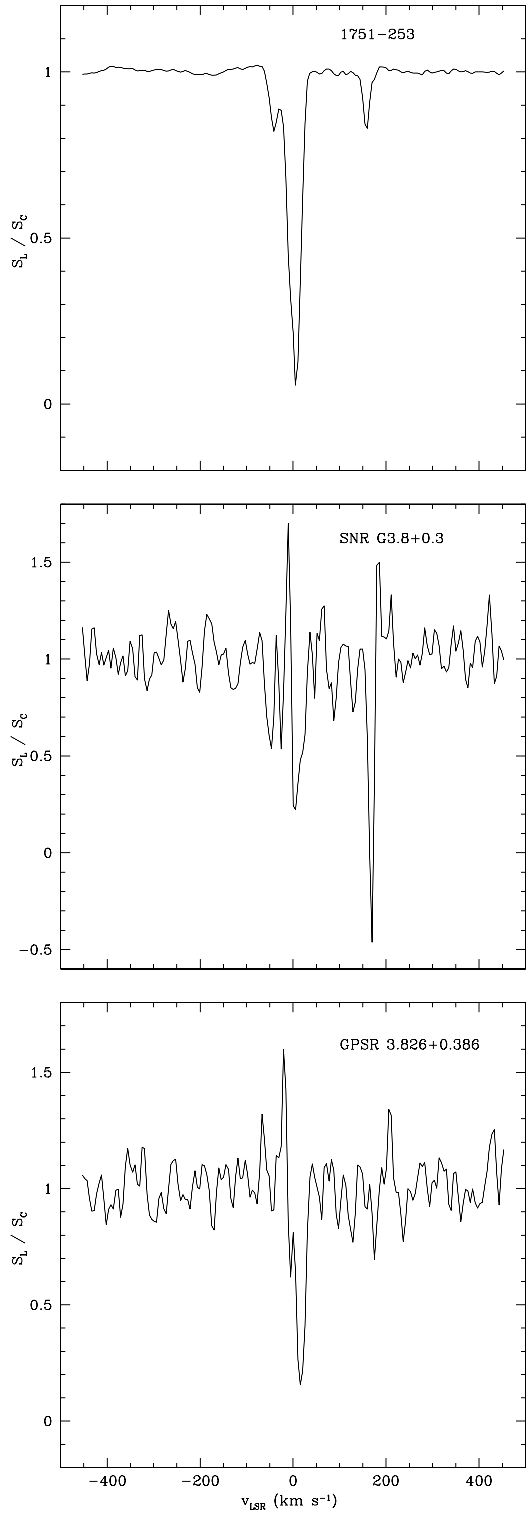

Fig. 6. 21 cm H I absorption spectra for the three sources discussed in the text, plotted as a function of LSR radial velocity. The measured spectra were divided by the continuum level ($-\tau_v$), where τ_v is the opacity as a function of velocity.

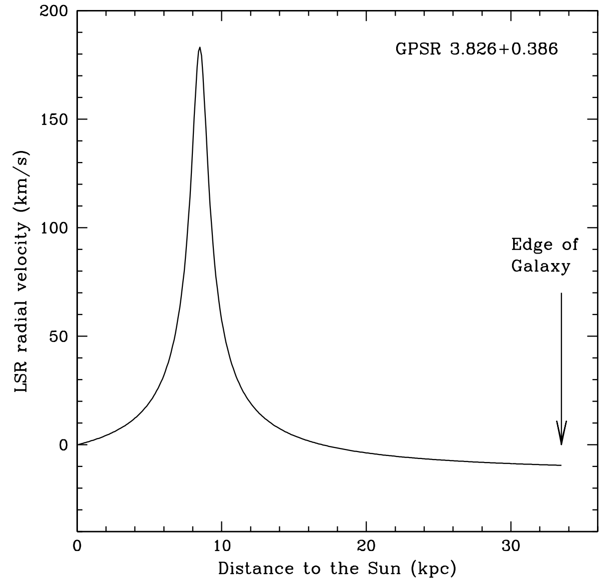

Fig. 7. LSR radial velocity as a function of distance to the Sun in the direction of GPSR 3.826+0.386. The negative values of the LSR radial velocity come from gas beyond the solar circle. The arrow marks the distance to the Sun where the edge of the Galaxy is located.

low probability of detection of two sources within the PN shell (see above), (ii) the possible link between them at 13 cm, (iii) the fact that the radio sources are equidistant from the compact central source, and (iv) the low signal-to-noise ratio of the HI detection at source A. Additional observations are clearly required.

In the case of the supernova remnant candidate SNR G3.8+0.3, we conclude that it is located beyond the subcentral point, at more than 8.5 kpc from the Sun, while the compact source GPSR 3.826+0.386 is located closer than the subcentral point and thus the two sources are not physically associated.

We thank the referee for many suggestions and for pointing out that the source GPSR 3.826+0.386 is a bright Hα source. AT is supported by a Conacyt scholarship. LFR acknowledges the support of DGAPA, Universidad Nacional Autónoma de México, and of Conacyt (Mexico). This research has made use of the SIMBAD database, operated at CDS, Strasbourg, France.

REFERENCES

Abbott, D. C., Bieging, J. H., & Churchwell, E. 1984, ApJ, 280, 671

Becker, R. H., White, R. L., Helfand, D. J., & Zoonematkermani, S. 1994, ApJS, 91, 347

Bhatnagar, S. 2002, MNRAS, 332, 1
Brand, J., & Blitz, L. 1993, A&A, 275, 67
Briggs, D. 1995, Ph.D. Thesis, New Mexico Inst. of Mining and Technology
Case, G. L., & Bhattacharya, D. 1998, ApJ, 504, 761
Caswell, J. L., Haynes, R. F., Goss, W. M., & Mebold, U. 1981, Aust. J. Phys., 34, 333
Cohen, M., Chapman, J., Deacon, R., Sault, R., Parker, Q., & Green, A. 2006, MNRAS, 369, 189
Cohen, M., Parker, Q. A., & Chapman, J. 2005, MNRAS, 357, 1189
Condon, J. J., Cotton, W. D., Greisen, E. W., Yin, Q. F., Perley, R. A., Taylor, G. B., & Broderick, J. J. 1998, AJ, 115, 1693
Dickey, J. M., Kulkarni, S. R., Heiles, C. E., & van Gorkom, J. H. 1983, ApJS, 53, 591
Dickey, J. M., et al. 2009, ApJ, 693, 1250
Fomalont, E. B., Windhorst, R. A., Kristian, J. A., & Kellerman, K. I. 1991, AJ, 102, 1258
Gómez, J. F., et al. 2005, MNRAS, 364, 738
Gray, A. D. 1994, MNRAS, 270, 847
Green, A. J., Cram, L. E., Large, M. I., & Ye, T. 1999, ApJS, 122, 207
Nyman, L. A., Hall, P. J., & Bertre, T. L. 1993, A&A, 280, 551
Parker, Q. A., et al. 2005, MNRAS, 362, 689
Parker, Q. A., et al. 2006, MNRAS, 373, 79
Persi, P., Ferrari-Toniolo, M., Tapia, M., Roth, M., & Rodríguez, L. F. 1985, A&A, 142, 263
Pottasch, S. R., Olling, R., Bignell, C., & Zijlstra, A. A. 1988, A&A, 205, 248
Preite-Martínez, A. 1988, A&AS, 76, 317
Price, S. D., & Walker, R. G. 1976, The AFGL Four Color Infrared Sky Survey: Catalog of Observations at 4.2, 11.0, 19.8, and 27.4 Î¼m (Hanscom AFB: Air Force Geophys. Lab., Opt. Phys. Div.)
Trejo, A., & Rodríguez, L. F. 2006, RevMexAA, 42, 147
———. 2008, AJ, 135, 575
———. 2010, RevMexAA, 46, 349
Stupar, M., Filipović, M. D., Parker, Q. A., White, G. L., Pannuti, T. G., & Jones, P. A. 2007, Ap&SS, 307, 423
White, R. L. 1985, ApJ, 289, 698
Zijlstra, A. A., van Hoof, P. A. M., & Perley, R. A. 2008, ApJ, 681, 1296
Zoonematkermani, S., Helfand, D. J., Becker, R. H., White, R. L., & Perley, R. A. 1990, ApJS, 74, 181

Alfonso Trejo and Luis F. Rodríguez: Centro de Radiostronomía y Astrofísica, Universidad Nacional Autónoma de México, Apdo. Postal 3-72, (Xangari), 58089 Morelia, Michoacán, Mexico (a.trejo, l.rodriguez@crya.unam.mx).

Revista Mexicana de Astronomía y Astrofísica, **46**, 357–361 (2010)

ON THE NATURE OF THE NON-THERMAL RADIO SOURCE AT THE CENTER OF THE ORION STREAMERS

Alfonso Trejo and Luis F. Rodríguez

Centro de Radioastronomía y Astrofísica
Universidad Nacional Autónoma de México, Morelia, Michoacán, Mexico

Received 2010 June 28; accepted 2010 July 27

RESUMEN

Presentamos un análisis de observaciones del VLA en el continuo a 20 y 6 cm hacia una fuente de radio no térmica en la región de las Serpentinas (*Streamers*) en Orión. Comparamos observaciones de archivo de 1991 con nuevas observaciones hechas por nosotros en 2008. Dicha fuente puede ser un objeto estelar joven o un objeto evolucionado, como un microcuasar, o incluso un jet de una radiogalaxia. Nuestro análisis muestra que no hay evidencia de cambio en la densidad de flujo, entre ambas épocas, arriba del 10%, y que la morfología permanece constante dentro del ruido. Tampoco hay indicio de movimientos propios mayores que 23 msa año^{-1}, a un nivel de 3σ, que a la distancia de Orión implican un límite superior a la velocidad en el plano del cielo de $\sim$ 45 km s^{-1}. A 6 cm detectamos emisión polarizada linealmente con un nivel de $\sim$ 5%, mientras que a 20 cm no se detecta esta emisión por encima de $\sim$ 2%. Concluimos que esta fuente de radio no térmica es muy probablemente una radiogalaxia vista por mera casualidad en la línea de visión hacia el centro del sistema de las Serpentinas de Orión.

ABSTRACT

We present VLA continuum observations at 20 and 6 cm toward a non-thermal radio source located at the *Streamers* region in Orion. We compare 1991 archive observations with new ones taken by us in 2008. The radio source could be a young stellar source or an evolved object like a microquasar or even a jet from a radio galaxy. Our analysis shows that there is no evidence of changes in the flux densities between both epochs at a level higher than 10%. Also, we set an upper limit at a 3σ level of 23 mas year^{-1} for the proper motions. At the distance of Orion this implies an upper limit to the velocity in the plane of the sky of 45 km s^{-1}. At 6 cm, we detect linearly polarized emission at a level of $\sim$ 5%, while at 20 cm we do not detect this emission above a level of $\sim$ 2%. We conclude that the non-thermal radio source most probably is a radio galaxy aligned by chance with the line of sight to the Streamers in Orion.

Key Words: ISM: individual (Orion Streamers, HH 222) — radiation mechanisms: non-thermal — radio continuum: ISM

1. INTRODUCTION

The system known as the Streamers in Orion is an elongated, arc-like optical structure in the L1641 cloud in Orion. It stretches in the sky for 5 arcmin in the NE-SW direction. The system has optical line emission (Cohen & Schwartz 1983) and is very close to the HH-34 system. There is a T Tauri star located at only 15 arcsec from the center of the system. On the basis of this association, the arc was suggested to be the result of an interaction from the wind of this star with the surrounding medium (Reipurth & Sandell 1985).

In 1990, Yusef-Zadeh et al. (1990) reported a non-thermal radio source detected with the VLA in that region. The source is linearly polarized at a level of 5% in the 6 cm emission and is located at the very center of the Streamers with its main axis approximately aligned with the axis of the system. These

TABLE 1

PARAMETERS OF THE OBSERVATIONS

	Flux Density (Jy) 0541-056		Image rms noise (μJy)	
Epoch	20 cm	6 cm	20 cm	6 cm
1991.64	1.20 ± 0.02	1.24 ± 0.03	80.6	26.7
2008.79	1.20 ± 0.10	1.27 ± 0.07	61.5	26.3

authors also found a 2-micron source at the position of the radio source and several low-mass young stars in the surroundings of it. They concluded that the non-thermal radio source could be a newly born star.

A different interpretation of this association was given by Castets, Reipurth, & Loinard (2004), who proposed that this radio source could be the result of a T Tauri star undergoing an energetic event or to emission from an X-ray binary system. However, using millimeter studies of the CO, ^{13}CO, C^{18}O and CS molecules emission around a region centered in the Streamers, Castets et al. (2004) found no evidence to link the radio source with any molecular outflow. Since the probability of finding this radio source to be just a fortuitous alignment is only 7.5×10^{-5} (Castets et al. 2004), the most probable interpretation was in terms of this source being an evolved galactic object.

In these cases, there always exists the possibility of a fortuitous alignment. We decided to test this hypothesis using new VLA observations. Since the source is at $\sim -20°$ of Galactic latitude, relatively far from the galactic plane, we found that the existing HI absorption observations were not useful to test the distance to the source, given the lack of line-of-sight gas in that direction. Thus our new observations were planned to study any possible flux variability, morphology changes and proper motions. To acomplish this, we used 1991 archive observations plus new observations performed by us.

At the distance of the Streamers, proper motions over two decades would be of the order of 2 arcsec for a velocity of 200 km s^{-1}, which is expected for Herbig-Haro objects. Typically, also flux variability would be present in these cases (Rodríguez et al. 2000). For the extended radio lobes of an extragalactic source we would not see any proper motion, perhaps only flux changes between both epochs, arising in a possible compact core located between the lobes.

We present this work as a part of a series of studies of non-thermal radio sources apparently associated with galactic star forming regions or nebulae. We have previously shown that an association on the plane of the sky is not always a physical association (Trejo & Rodríguez 2006, 2008, 2010).

2. OBSERVATIONS

We made our new observations with the VLA, an NRAO[1] telescope. The observations were planned for the A configuration and taken on October 16, 2008 (epoch 2008.79) under project AT 368. We matched the parameters of our observations to those of the August 20, 1991 (epoch 1991.64) archive observations made under project AY 037. Thus, the pointing center, the frequency, and the calibrators are the same. The rms noise is roughly the same in both data sets, as is the *uv* coverage, which allows a reliable comparison between both epochs.

A total of 26 antennas in the A configuration were present at the time of the observations, both in 1991 and 2008. The flux calibrator was 1331+305 at both epochs and for both frequencies. To calibrate the phase, the source 0541-056 was used, with bootstrapped flux densities at both epochs and wavelengths indicated in Table 1. At 20 cm, a total of 1.25 hours was spent on the source in 2008, and 1.96 hours in 1991. At 6 cm, the times were 1.15 hours for 2008 and of 2.00 hours for 1991.

Since the source is weak at 6 cm, we made the images setting the robust parameter of the task IMAGR to 0, which produces images with the best compromise between angular resolution and noise level. The 20 cm observations show a brighter source, and a scheme with uniform weighing (robust parameter set to -5) is used, since it allows the highest angular resolution possible. This is important to look for the existence of morphology changes and proper motions. The data at both frequencies were calibrated and imaged following the standard procedures listed in the AIPS Cookbook.

[1]The National Radio Astronomy Observatory is a facility of the National Science Foundation operated under cooperative agreement by Associated Universities, Inc.

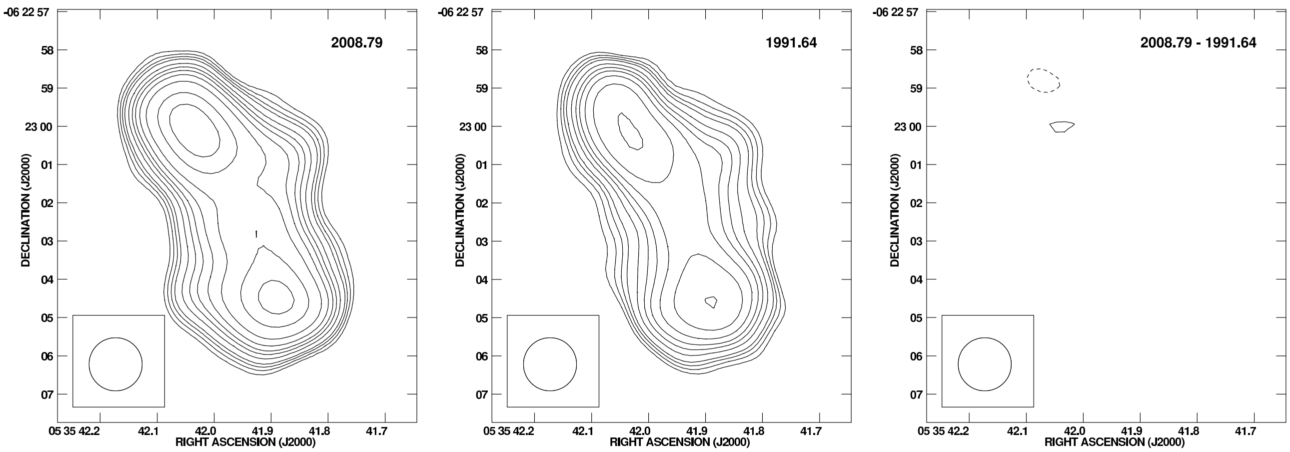

Fig. 1. 20 cm continuum images for the non-thermal source VLA J05354198–0623018. Left: 2008 image with an rms noise of 61.5 μJy. Center: 1991 image with an rms noise of 80.6 μJy. Right: Residual image 0.92 × 2008 - 1991, the rms noise is 95.7 μJy. The levels for all images are −3, −4, 3, 4, 5, 6, 8, 10, 12, 15, 20, 30, and 40 × the individual rms noise. The full-width half maximum of the restoring beam is 11.″39 × 1.″39 and is shown in the bottom left corner.

3. RESULTS AND DISCUSSION

We shifted the position of the phase calibrator in 1991 to that of 2008 to remove a small offset, which is necessary because of the continuous refinement of the calibrator positions made by NRAO personnel. Also, in order to reliably compare both data sets we made images convolved with a circular beam of 1.″39 for the 20 cm data, and of 0.″47 for the 6 cm data.

3.1. *20 cm*

After performing the normal imaging for the 20 cm observations, we still detected a small offset, of the order of 0.″03 in declination and 0.″17 in right ascension, between the 2008 and 1991 images. To test if the offset seen in the data was a real position change of the source or an observational problem, we measured the positions of four sources located inside the primary beam of the telescope. All of them showed roughly the same small offset between both epochs. We then conclude that the offset is most likely an observational problem, perhaps produced by the fact that the 1991 observations were made near solar maximum, which can affect the long wavelength observations and produce positional errors such as those observed (Kaplan et al. 1982). A phase cross-calibration was performed to the data to minimize the diferences in phase between both observations. We could then compare reliably the images and search for morphology changes and flux variations, if any. To subtract the images we used a scheme to minimize the rms noise of the difference image (Franco-Hernández & Rodríguez 2004). This is done by selecting the appropriate weight to one data set while making the subtraction. In this case we made the subtraction as 2008 image − 1.09×1991 image. This allows to correct any calibration error in the flux scale. We present in Figure 1 the maps for the 20 cm emission at both epochs, and also the difference image resulting from the subtraction, made as we just noted. The morphology is that of a well-defined double component source. We refer to the source as VLA J05354198–0623018, where the coordinates are those of the centroid of the source. The total flux density obtained is about 20 mJy. The right panel of Figure 1 shows there are no residuals above a 3σ level of 0.3 mJy. The average total flux density of the source from both epochs is 17.9 ± 0.6 mJy.

We also looked for proper motions by measuring the positions of the two lobes of the source at the two epochs. The analysis showed that there were no proper motions larger than 10 mas year^{-1} at a 3σ level. Taking the distance to Orion to be 414 pc (Menten et al. 2007), that limit implies velocities below 20 km s^{-1}. However, since the data at both epochs were aligned with the phase cross-calibration, we will use the more reliable upper limits obtained at 6 cm (see below).

To look for polarized emission at this frequency, several tests with different weighting schemes were applied to the data. We did not find any polarization in the data at a level larger than 2%.

3.2. *6 cm*

At 6 cm, VLA J05354198–0623018 is weaker which makes a cross-calibration harder to perform.

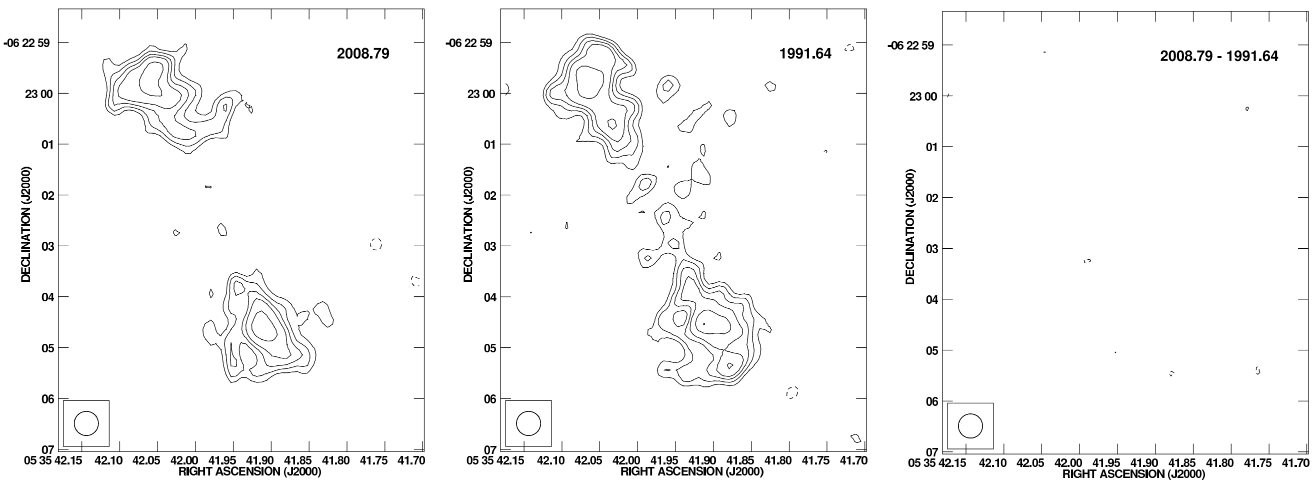

Fig. 2. 6 cm continuum images for the non-thermal source VLA J05354198–0623018. Left: 2008 image, the rms noise is 26.3 μJy. Center: 1991 image with an rms noise of 26.7 μJy. Right: Residual image 2008 – 1991, the rms noise is 36.8 μJy. The levels for all the images are −3, −4, 3, 4, 5, 6, 8, 10, 12, 15, 20, 30, and 40 × the individual rms noise. The full-width half maximum of the restoring beam is $0.''47 \times 0.''47$ and is shown in the bottom left corner.

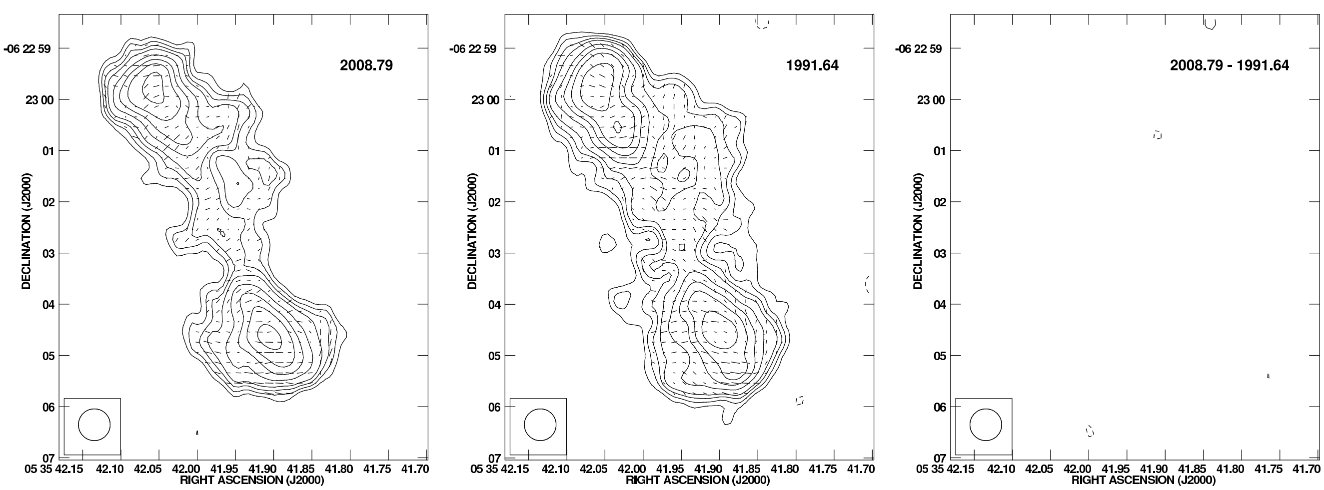

Fig. 3. 6 cm continuum images made with natural weighing showing polarized emission as vectors. A 0.5 arcsec line represents a polarization of 5%. Left: 2008 image with rms noise of 25.54 μJy. Center: 1991 image with rms noise of 23.30 μJy. Right: 2008 - 1991 image with rms noise of 32.33 μJy. Levels are as in previous figures. The full-width half maximum of the restoring beam is $0.''62 \times 0.''62$ and shown in the bottom left corner.

In addition, the data sets did not present the same small instrumental misalignment as did the 20 cm observations. Then, there was no need for a phase cross-calibration, apart from the shifting of the 1991 data for the refinement of the position of the phase calibrator. Neither was a scale correction in flux density needed. In Figure 2 we present both images for 2008 and 1991, as well as the subtracted image. At this resolution, the images clearly split into two main components. The average total flux density from both epochs is 7.7 ± 0.5 mJy. As can be seen in the right panel of Figure 2, the residual image shows no evidence of emission at all, at least not above a 3σ level of 0.1 mJy. The morphology remains essentially the same.

The spectral index from the 20 and 6 cm measurements is $\alpha = -0.67 \pm 0.06 (S_\nu \propto \nu^\alpha)$. This value is characteristic of extragalactic radio jets (Bridle & Perley 1984).

By measuring the peaks of the two main lobes of VLA J05354198–0623018 at the two epochs, we set an upper limit for proper motions of 3σ of

23 mas year^{-1}, equivalent to $\sim$ 45 km s^{-1} at the distance of Orion.

Contrary to the case of the 20 cm emission, we detected linearly polarized emission at 6 cm. In Figure 3 we show maps of the two epochs and also the residual image. The maps were made with natural weighting in order to have the lowest rms noise possible. The electrical vectors are shown with their length proportional to the degree of polarization. Yusef-Zadeh et al. (1990) reported a level of polarization of 5%, and we confirmed this value both with the 1991 archive data and with our new 2008 observations. The position angles for the electrical vectors in Figure 3 are consistent with those reported in their study at a lower angular resolution. The polarization level found in this source is within the range of 5% to 40% observed in most extragalactic radio jets (Bridle & Perley 1984).

The Faraday rotation measure in the direction of HH 222 is $\sim$ 20 radians per square meter (Johnston-Hollitt, Hollitt, & Ekers 2004). This implies rotations of order 0.07 radians ($\sim 4^\circ$) and 0.8 radians ($\sim 46^\circ$) at 6 and 20 cm, respectively. This difference in the expected rotations suggests that the non-detection of polarization at 20 cm could be due to Faraday depolarization.

Since the upper limit to the velocity implied by the proper motions at 6 cm is of the order of $\leq$ 45 km s^{-1}, we do not favor a galactic location for the non-thermal source. As we noted, HH objects have velocities of the order of 200 km s^{-1}. Microquasars have ejecta that move at relativistic speeds and we can rule them out. Also, the absence of significant residual emission and the fact that no essential morphological changes at both frequencies were observed support an extragalactic location. We propose this source to be a radio galaxy. The double lobe morphology seen at both frequencies is typical of radio galaxies.

4. CONCLUSIONS

We present 20 and 6 cm observations of the non-thermal source VLA J05354198–0623018 at the very center of the Streamers system in Orion. The probability of this source to be an alignment by chance is very low, as we noted. However, the upper limit to the velocity implied by the absence of detectable proper motions and the lack of significant morphology variation weigh against a physical association with the Orion region. The polarization is consistent with that present in radio galaxies. We conclude that the radio source is most probably an extragalactic one, apparently a radio galaxy in the line of sight to the Streamers.

AT is supported by a Conacyt scholarship. LFR acknowledges the support of DGAPA, Universidad Nacional Autónoma de México, and of Conacyt (Mexico). This research has made use of the SIMBAD database, operated at CDS, Strasbourg, France.

REFERENCES

Bridle, A. H., & Perley, R. A. 1984, ARA&A, 22, 319
Castets, A., Reipurth, B., & Loinard, L. 2004, A&A, 427, 895
Cohen, M., & Schwartz, R. D. 1983, ApJ, 265, 877
Franco-Hernández, R., & Rodríguez, L. F. 2004, ApJ, 604, L105
Johnston-Hollitt, M., Hollitt, C. P., & Ekers, R. D. 2004, in The Magnetized Interstellar Medium, ed. B. Uyaniker, W. Reich, & R. Wielebinski (Katlenburg-Lindau: Copernicus), 13
Kaplan, G. H., Josties, F. J., Angerhofer, P. E., Johnston, K. J., & Spencer, J. H. 1982, AJ, 87, 570
Menten, K. M., Reid, M. J., Forbrich, J., & Brunthaler, A. 2007, A&A, 474, 515
Reipurth, B., & Sandell, G. 1985, A&A, 150, 307
Rodríguez, L. F., et al. 2000, AJ, 119, 882
Trejo, A., & Rodríguez, L. F. 2006, RevMexAA, 42, 147
________. 2008, AJ, 135, 575
________. 2010, RevMexAA, 46, 341
Yusef-Zadeh, F., Cornwell, T. J., Reipurth, B., & Roth, M. 1990, ApJ, 348, L61

Alfonso Trejo and Luis F. Rodríguez: Centro de Radiostronomía y Astrofísica, Universidad Nacional Autónoma de México, Apdo. Postal 3-72, (Xangari), 58089 Morelia, Michoacán, Mexico (a.trejo, l.rodriguez@crya.unam.mx).

Revista Mexicana de Astronomía y Astrofísica, **46**, 363–373 (2010)

THE ABSOLUTE PARAMETERS FOR NSVS 11868841[1] AND THE OVERSIZED STARS IN LOW-MASS ECLIPSING BINARIES

Ö. Çakırlı,[2,3] C. İbanoğlu,[2] and A. Dervişoğlu[2]

Received 2010 April 12; accepted 2010 July 29

RESUMEN

Se han realizado observaciones espectroscópicas de la binaria eclipsante de baja masa NSV 11868841, y se han derivado las velocidades radiales de ambas componentes. Las masas y radios dererminados son $M_1 = 0.870 \pm 0.074\ M_\odot$, $M_2 = 0.607 \pm 0.053\ M_\odot$, $R_1 = 0.983 \pm 0.030\ R_\odot$, $R_2 = 0.901 \pm 0.026\ R_\odot$. Los radios de ambas componentes son, respectivamente, 10% y 57% mayores que los que corresponden a estrellas de la secuencia principal de edad cero y de las mismas masas. Esta discrepancia puede deberse a que ambas estrellas tienen una gran cobertura por manchas. Hemos reunido parámetros absolutos para 21 binarias eclipsantes de doble línea y de baja masa, para comparar sus posiciones en los diagramas masa-radio y masa-temperatura efectiva. Los valores altos de los radios y las bajas temperaturas efectivas encontradas no son debidos a diferencias en metalicidad o en longitud de mezcla. Las discrepancias encontradas para estrellas de baja masa pueden deberse a campos magnéticos que inhiben el transporte convectivo, lo cual propicia una gran cobertura de la superficie estelar por manchas magnéticas.

ABSTRACT

Spectroscopic observations of the low-mass eclipsing binary NSVS 11868841 have been obtained and the radial velocities were derived for both components. The masses and radii determined for the components are $M_1 = 0.870 \pm 0.074\ M_\odot$, $M_2 = 0.607 \pm 0.053\ M_\odot$ and $R_1 = 0.983 \pm 0.030\ R_\odot$, $R_2 = 0.901 \pm 0.026\ R_\odot$. Both the primary and secondary stars' radii are 10% and 57% larger than those of zero-age-main-sequence stars with the same masses. This discrepancy may arise from the large spot coverage of both stars. We collected absolute parameters of 21 low mass double-lined eclipsing binaries and compared their positions in the mass-radius and mass-effective temperature panels. The large radii and lower effective temperatures found for NSV 11868841 are solved neither with differences in metallicity nor in mixing length parameters. These discrepancies for low mass stars may be due to magnetic fields inhibiting the convective energy transport, which lead to a large magnetic spot coverage of the surface of such low mass stars.

Key Words: binaries: eclipsing — stars: activity — stars: fundamental parameters — stars: low-mass

1. INTRODUCTION

Eclipsing binaries are the best laboratories for determining the fundamental physical properties of stars. Detached, double-lined eclipsing binaries yield direct and accurate measures of the masses and radii of the component stars. Measuring these quantities has always been observationally challenging. Large-scale surveys, providing imaging and photometric catalogues for substantial fractions of the celestial sphere, are now available at a wide range of wavelengths. Over the last few years, these surveys have become invaluable research tools for investigating the properties of intrinsically rare objects. These surveys have proven most useful in searches for low-mass stars. Stars with masses less than 1 $M_\odot$ are regarded as low-mass stars and have late spectral types, namely G, K or M. We cannot vary the con-

[1]Based on spectroscopic observations collected at TÜBİTAK National Observatory, Turkey.

[2]Ege University, Science Faculty, İzmir, Turkey.

[3]Tübitak National Observatory, Akdeniz University Campus, Turkey.

ditions prevalent on an individual star, but observations of many individual stars can be combined to build up a picture of how stars of different mass and composition evolve. Since the intermediate- and high-mass stars are intrinsically bright sources, most studies have centered on them, with little consideration of M dwarfs with masses below 0.6 $M_\odot$. This reflects the availability of more precise observational constraints, and also greater analytic tractability in modelling higher-mass stars. Recently, however, the lower main-sequence has attracted more attention, with a series of detailed models extending past the hydrogen-burning limit to the boundary between low-mass brown dwarfs and giant planets. Understanding the structure and evolution of stars is a basic goal of stellar astronomy. Critical tests of the evolution theory for stars can be made on a small set of eclipsing binary stars (Baraffe et al. 1998; Girardi et al. 2002; Siess, Forestini, & Dougados 1997; Chabrier, Gallardo, & Baraffe 2007). While the results of stellar evolution models compare favorably to data for main-sequence stars with masses greater than that of the Sun, evidence has been growing that the models for stars on the lower main-sequence have problems when confronted with precise masses and radii from double-lined eclipsing binaries. As shown by Torres & Ribas (2002) the evolutionary models underestimate the radii and overestimate the effective temperatures of the low-mass stars. These discrepancies were confirmed in subsequent studies by Ribas (2003), Lopez-Morales & Ribas (2005), Torres et al. (2006), Morales et al. (2009a), Morales et al. (2009b), and others. Hints of the radius discrepancies have also been described by Popper (1997), Clausen, Hett, & Olsen (1999), and others. Recently, Mullan & MacDonald (2001), Torres et al. (2006), Morales, Ribas, & Jordi (2008) proposed a hypothesis based upon the effects of stellar activity to explain the discrepancies. Furthermore Stassun et al. (2009) called attention to the fact that low-mass stars appear older or younger in the mass-radius diagram depending on whether post- or pre-main-sequence models are used. As the number of low-mass eclipsing binaries studied carefully, both photometrically and spectroscopically, increases, a better comparison with the theoretical models can be made.

Light variability of NSVS 11868841 ($\alpha = 23^h17^m58^s$, $\delta = +19°17'03''$ (J2000), hereafter NSVS 1186) was detected by Wozniak et al. (2004) from data of the *Northern Sky Variability Survey*. They classified it as a detached eclipsing binary with combined median magnitude $V = 14^m.084 \pm 0.076$ and an orbital period of 0.60179 days. High-precision light curves in the Johnson V-, R-, and I-bandpass were obtained by Coughlin & Shaw (2007). Since the radial velocities of the components were not available they determined the radii of the stars by analyzing the V- and R-bandpass light curves. In this study we present the first radial velocities obtained for the components of the double-lined, short-period eclipsing binary NSVS 1186 and the physical parameters derived from the analyses of the radial velocities and the light curves. Both components show high level chromospheric activity, evidenced by Hα emission lines in their spectra. We discuss the properties of the binary and their relation to the discrepancies between empirical and theoretical mass-radius and mass-effective temperature relations for low-mass stars.

2. SPECTROSCOPIC OBSERVATIONS

2.1. *Spectroscopy*

Since wide-band light curves of NSVS 1186 are available we observed the star spectroscopically. Optical spectroscopic observations were obtained with the Turkish Faint Object Spectrograph Camera (TFOSC) attached to the 1.5 m telescope,[4] on August 23, 24, and 25, 2008 under good seeing conditions. The wavelength coverage of each spectrum was 4100–8100 Å in 11 orders, with a resolving power of $\lambda/\Delta\lambda \approx 7000$ at 6563 Å and an average signal-to-noise ratio (S/N) of ~ 150. We also obtained a high S/N spectrum of the M dwarfs GJ 740 (M0 V) and GJ 623 (M1.5 V) for use as templates in the derivation of the radial velocities (Nidever et al. 2002).

The electronic bias was removed from each image and we used the CRREJECT option for cosmic ray removal. The echelle spectra were extracted and wavelength calibrated using a Fe-Ar lamp source with help of the IRAF ECHELLE package. The stability of the instrument was checked by cross correlating the spectra of the standard star against each other using the FXCOR task in IRAF. The standard deviation of the differences between the velocities measured using FXCOR and the velocities in Nidever et al. (2002) was about 1.1 km s^{-1}.

2.1.1. *Spectral Types and Temperature Estimates*

We have used the spectra to reveal the spectral type of the primary component of NSVS 1186. For this purpose we have degraded the spectral resolution from 7000 to 3000, in order to use the calibrations by Hernández et al. (2004) by convolving the data with a Gaussian kernel of the appropriate width, and we have measured the equivalent

[4]Further details on the telescope and the spectrograph can be found at `http://www.tug.tubitak.gov.tr`.

TABLE 1

EQUIVALENT WIDTHS OF THE SELECTED LINES IN THE SPECTRA

Spectral lines	EW_p (Å)	EW_s (Å)
Ca I λ 4226	2.13±0.11	1.39±0.12
Fe I λ 5329	1.11±0.11	0.99±0.12
Fe I λ 4271	1.44±0.13	1.41±0.12
Ca I+Fe I λ 5270	2.91±0.21	2.11±0.21
Ca I λ 6162	1.99±0.42	1.11±0.09
Fe I λ 5079	0.79±0.07	0.47±0.11

widths (EW) of photospheric absorption lines for the spectral classification. We have followed the procedures described by Hernández et al. (2004), choosing metallic lines in the blue-wavelength region, where the contribution of the primary component is considerably larger than that of the secondary. From several spectra we measured equivalent widths of some spectral lines assuming the light contribution of the primary star is 0.6, as given in Table 1.

From the calibration relations of EW-Spectral-type given by Hernández et al. (2004), we have derived a spectral type of G9±1 for the primary component. The effective temperature deduced from the calibrations of Drilling & Landolt (2000), de Jager & Nieuwenhuijzen (1987) and Popper (1980) is, respectively, 5230±80, 5230±80, and 5330±141 K for the primary component. The mean effective temperature of the primary component deduced from the spectra is 5250±95 K .

NSVS 1186 is listed in several large photometric databases consolidated in the *Naval Observatory Merged Astronomical Dataset* (NOMAD-1.0, Zacharias et al. 2004), which provides optical magnitudes of $B = 14^m.77 \pm 0^m.02$, $V = 13^m.87 \pm 0^m.01$, $R = 13^m.94 \pm 0^m.01$, $I = 12^m.74 \pm 0^m.02$. Since the magnitudes collected from photographic measurements and the colors are inconsistent no attempt has been made to calculate the effective temperatures of the components. The infrared magnitudes are taken from 2MASS (Cutri et al. 2003) catalog as $J = 12^m.518 \pm 0^m.023$, $H = 12^m.069 \pm 0^m.021$, and $K = 11^m.995 \pm 0^m.019$. The observed infrared colours $J - H = 0^m.449 \pm 0^m.031$ and $H - K = 0^m.074 \pm 0^m.028$ correspond to a combined spectral type of G9±2, in a good agreement with that we derived by spectral lines alone. Using the depth of the eclipses in three bands we estimate the light contribution of the primary component as 0.60, 0.57, 0.55 and 0.56 in the V, J, H and K bands, respectively. Hence, the $V - K$, $J - H$ and $H - K$ colors of the primary component correspond to a spectral type of G9±2. We estimate a temperature of 5240±230 K from the calibrations of Tokunaga (2000). The temperature uncertainty of the primary component results from considerations of spectral type uncertainties, and calibration differences. The effective temperature of the primary star that we derived from infrared photometric measurements is in a good agreement with that we estimated from the spectra alone. The weighted mean of the effective temperature of the primary component is 5250±135 K.

2.1.2. *Rotational Velocities of the Components*

The width of the cross-correlation profile is a good tool for the measurement of $v \sin i$ (see e.g., Queloz et al. 1998). The rotational velocities ($v \sin i$) of the two components were obtained by measuring the FWHM of the CCF peaks in nine high-S/N spectra of NSVS 1186 acquired close to the quadratures, where the spectral lines have the largest Doppler-shifts. In order to construct a calibration curve FWHM-$v \sin i$, we used an average spectrum of HD 27962, acquired with the same instrumentation. Since the rotational velocity of HD 27962 is very low, but not zero ($v \sin i \simeq 11$ km s^{-1}, e.g., Royer, Zorec, & Gómez 2004, and references therein), it could be considered as a useful template for low-mass stars rotating faster than $v \sin i \simeq 10$ km s^{-1}. The spectrum of HD 27962 was synthetically broadened by convolution with rotational profiles of increasing $v \sin i$ in steps of 5 km s^{-1}, and the cross-correlation with the original one was performed at each step. The FWHM of the CCF peak was measured and the FWHM-$v \sin i$ calibration was established. The $v \sin i$ values of the two components of NSVS 1186 were derived from the FWHM of their CCF peaks and the aforementioned calibration relations, for few wavelength regions and for the best spectra. As a result, a projected rotational velocity of 77 ± 3 km s^{-1} for the primary star and of 62 ± 4 km s^{-1} for the secondary star were estimated. However, note that the spectral lines of the components could not be separated even at quadrature. Thus, the projected rotational velocities estimated in this way should involve larger uncertainties than those given here.

3. ANALYSIS

3.1. *The Orbital Configuration*

To derive the radial velocities for the components of binary system, the 16 TFOSC spectra of the eclipsing binary were cross-correlated against the spectrum of GJ 740, a single-lined M0V star,

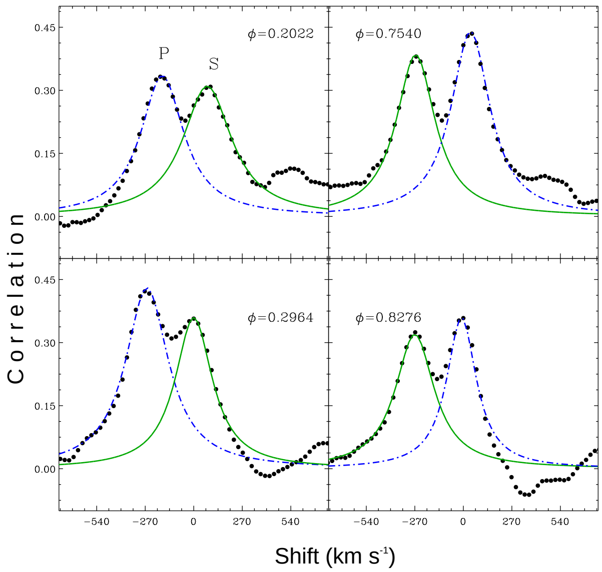

Fig. 1. Sample of cross correlation functions (CCFs) between NSVS 1186 and the radial velocity template spectrum around first and second quadrature.

on an order-by-order basis using the FXCOR package in IRAF[5]. The majority of the spectra showed two distinct cross-correlation peaks in quadrature, one for each component of the binary. Thus, to measure the velocity and errors of the individual components both peaks were fitted independently in quadrature with a Gaussian profile. If the two peaks appeared blended, a double Gaussian was applied to the combined profile using DE-BLEND function in the task. For each of the 16 observations we then determined a weighted-average radial velocity for each star from all orders without significant contamination by telluric absorption features. Here we used as weights the inverse of the variance of the radial velocity measurements in each order, as reported by FXCOR. In these data, we find no evidence for a third component, since the cross-correlation function showed only two distinct peaks. We adopted a two-Gaussian fit algorithm to resolve cross-correlation peaks near the first and second quadratures when spectral lines are visible separately. Figure 1 shows examples of cross-correlations obtained by using the largest FWHM at nearly first and second quadratures. The two peaks, non-blended, correspond to each component of NSVS 1186. The stronger peaks in each CCF correspond to the more luminous component, which has a larger weight into the observed spectrum.

[5]IRAF is distributed by the National Optical Observatory, which is operated by the Association of the Universities for Research in Astronomy, inc. (AURA) under cooperative agreement with the National Science Foundation.

TABLE 2

HELIOCENTRIC RADIAL VELOCITIES OF NSVS 1186[a]

HJD 2400000+	Phase	Star 1		Star 2	
		V_p	σ	V_s	σ
55069.4412*	0.0536	−120.0	14.3	...	...
55069.4855	0.1272	−162.0	9.2	...	...
55069.5284	0.1985	−193.6	4.3	80.6	4.2
55069.5727	0.2721	−198.1	3.9	85.6	6.3
55068.3810	0.2918	−183.7	3.2	80.0	8.4
55068.4258	0.3663	−171.6	3.0	47.2	8.6
55068.4707	0.4409	−128.7	13.2	...	...
55068.5134	0.5119	−68.2	14.9	...	...
55068.5578	0.5857	−28.6	11.1	...	...
55067.3674	0.6076	−6.0	7.3	−184.6	19.7
55068.6006	0.6568	19.2	3.3	−214.3	12.6
55067.4122	0.6820	28.3	3.1	−235.1	10.2
55067.4552	0.7534	40.0	1.4	−244.3	13.3
55067.4976	0.8240	19.9	9.2	−230.6	5.2
55067.5419	0.8975	1.1	2.4	...	...
55067.5846*	0.9684	−56.5	15.5	...	...

[a]The columns give the heliocentric Julian date, the orbital phase, the radial velocities of the two components and the corresponding standard deviations.
*These data were not used in the RV analysis.

The heliocentric radial velocities for the primary (V_p) and the secondary (V_s) components are listed in Table 2, along with the dates of observation and the corresponding orbital phases computed with the ephemerides given by Coughlin & Shaw (2007). The velocities in this table have been corrected to the heliocentric reference system by adopting a radial velocity of 9.5 km s^{-1} for the template star GJ 740. The radial velocities listed in Table 2 are the weighted averages of the values obtained from the cross-correlation of orders #4, #5, #6 and #7 of the target spectra with the corresponding order of the standard star's spectrum. A weight $W_i = 1/\sigma_i^2$ has been given to each measurement. The standard errors of the weighted means have been calculated on the basis of the errors (σ_i) of the radial velocity values for each order according to the usual formula (e.g., Topping 1972). The σ_i values are computed by FXCOR according to the fitted peak height, as described by Tonry & Davis (1979).

First we analysed the radial velocities given in Table 2 for the initial orbital parameters. We held fixed the orbital period and computed the eccentricity of the orbit, the systemic velocity and the semi-amplitudes of the radial velocities. The results of

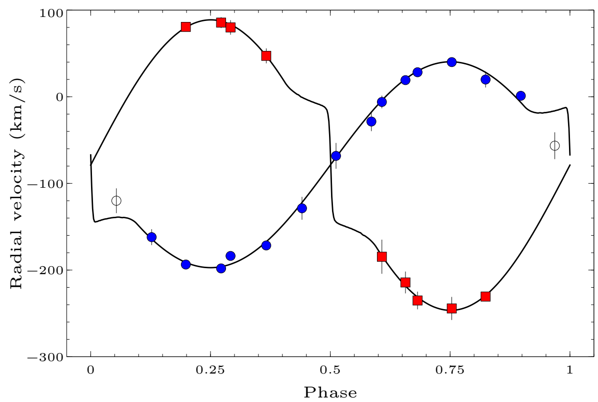

Fig. 2. Radial velocity curve folded on an orbital period of 0.601790 days, where phase zero is defined to be at primary mid-eclipse. Symbols with error bars show the RV measurements for two components of the system (primary: circles, secondary: squares). Open circles were excluded from the RV analysis.

the analysis performed with PHOEBE are as follows: $e = 0.002 \pm 0.001$, i.e. formally consistent with a circular orbit, $\gamma = -80 \pm 3$ km s^{-1}, $K_1 = 118 \pm 5$ and $K_2 = 169 \pm 6$ km s^{-1}. Using these values we estimated the projected orbital semi-major axis and the mass ratio as: $a \sin i = 3.412 \pm 0.093\ R_\odot$ and $q = M_2/M_1 = 0.70 \pm 0.04$. The observed and calculated radial velocities of both components are plotted in Figure 2 for comparison.

3.2. *Modelling the Light Curves*

As we mentioned in § 1 the V-, R- and I-bandpass light curves were obtained by Coughlin & Shaw (2007). The differential magnitudes and orbital phases were read out carefully by the method of DEXTER[6]. We used the most recent version of the eclipsing binary light curve modelling algorithm of Wilson & Devinney (1971, with updates), as implemented in the PHOEBE code of Prša & Zwitter (2005). The code needs some input parameters, which depend upon the physical structures of the component stars. In the light curve solution we fixed some parameters whose values can be estimated from global stellar properties, such as effective temperature of the primary component and mass ratio. The weighted mean of the effective temperature has been estimated to be 5250±135 K and the mass ratio 0.70±0.04. Using these values we adopted the linear limb-darkening coefficients from van Hamme (1993) as 0.39 and 0.28 for the primary and secondary components, respectively; the bolometric albedos from Lucy (1967) as 0.5, typical for a convective stellar

[6] http://dc.zah.uni-heidelberg.de/sdexter.

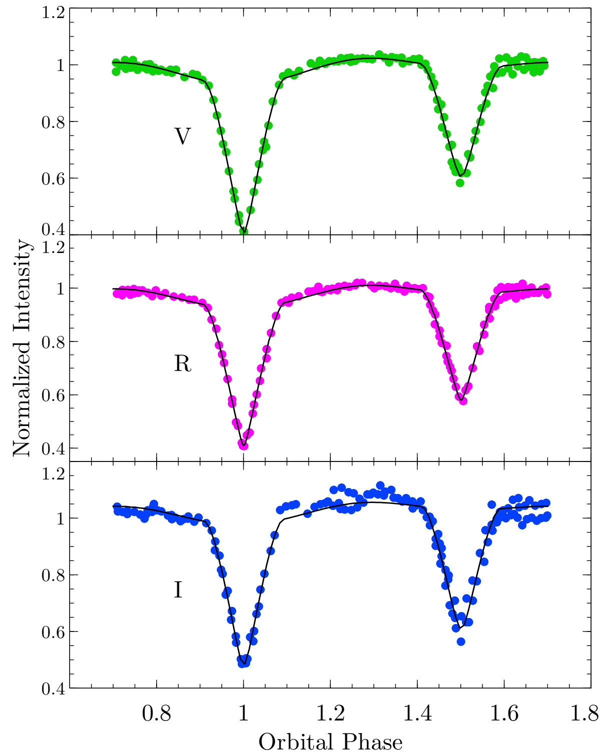

Fig. 3. The phase folded V-, R- and I-bandpass light curves for NSVS 1186. The best fitting solutions represented by the solid lines are also plotted for comparison (see text).

envelope, the gravity brightening coefficients as 0.32 for the both components. The components are assumed to be in synchronous rotation. We start with the adjustable parameters: the orbital inclination, i, the effective temperature of the less massive star, T_{eff_2}, the potential of the components, Ω_1 and Ω_2, and the monochromatic luminosity of the more massive star, L_1. Assuming it is a detached binary we used MODE-2 of the DC program for the individual solution. First we determined the preliminary elements and compared them with the observed light curves. Since the observed light curves show distortions we started with the two-spot solution, one on the primary and the other on the secondary component. The initial spot parameters were adopted from Coughlin & Shaw (2007). A best fit was obtained for each light curve using the same spots, and the corresponding parameters are given in Table 3. The parameter presented in the last column is the weighted mean of the parameters obtained from the individual light curves. The light curves along with the best-fitting solutions are shown in Figure 3.

TABLE 3

RESULTS OF THE V-, R- AND I-BANDPASS LIGHT CURVE ANALYSIS FOR NSVS 1186[a]

Parameters	V	R	I	Adopted
i°	87.0±0.5	88.6±0.2	88.3±0.2	88.0±0.4
T_{eff_1} (K)	5250[Fix]	5250[Fix]	5250[Fix]	5250[Fix]
T_{eff_2} (K)	5040±12	4990±14	5110±34	5020±16
Ω_1	4.242±0.049	4.274±0.049	4.260±0.072	4.262±0.052
Ω_2	3.810±0.026	3.739±0.020	3.989±0.054	3.790±0.026
r_1	0.289±0.004	0.288±0.004	0.286±0.006	0.288±0.004
r_2	0.263±0.003	0.267±0.002	0.250±0.005	0.264±0.003
$L_1/(L_1+L_2)$	0.604±0.009	0.586±0.009	0.591±0.013	···
$\sum(W(O-C)^2)$	0.041	0.026	0.131	···
Weight	3	5	1	···

[a]The adopted values are the weighted means of the values determined from the individual light curves.

Coughlin & Shaw (2007) analyzed only V- and R-light curves. Our analysis gives very different parameters when compared with those obtained by them. They estimate very low effective temperatures for the components with respect to their predicted masses. The fractional radii for the primary and secondary stars obtained by them are 15% and 20% smaller than those obtained by us using the same light curves. In contrast, the absolute radii are 5% and 3% larger than we found. The main difference is the location of the spots on the surface of the stars. The spot parameters given by them for the stars should be interchanged. One spot on the south pole of the primary and one spot on the north pole of the secondary represent well the three-color light curves. The spot coverage on the surface of the stars is about 8%.

3.3. *Absolute Parameters*

Combining the parameters obtained by radial velocity and light curve analyses we calculated the physical parameters of the components as listed in Table 4. We compared the locations of the components in the effective temperature-luminosity diagram, i.e., Hertzsprung-Russell diagram (Figure 4). While the location of the more massive primary star agrees well with that of a star having its mass, the secondary component appears to be more luminous, probably due to a larger effective temperature and radius. We also computed the radii of the components as $R_1 = 0.983 \pm 0.030\ R_{\odot}$ and $R_2 = 0.901 \pm 0.026\ R_{\odot}$ for the primary and secondary stars, respectively.

We computed the luminosities of the components using these radii and effective temperatures as $L_1 = 0.649 \pm 0.069\ L_{\odot}$ and $L_2 = 0.456 \pm 0.049\ L_{\odot}$ for the primary and secondary stars, respectively. We compared the positions of the components in the $L - T_e$ diagram with evolutionary tracks of pre- and post- main sequence evolution and as well as with the ZAMS, as shown in Figure 4. For constructing the solar metallicity ZAMS and evolutionary tracks, we used the Cambridge version of the the STARS code which was originally developed by Eggleton (1971) and substantially updated by Eldridge & Tout (2004). The current version is also capable of accounting for molecular contributions in the equation of state according to the Marigo (2002) approximation, which may be crucial for low mass stars. The less massive component seems to be hotter and more luminous with respect to the models. The physical parameters determined by us are very different from those obtained by Coughlin & Shaw (2007). While they estimate effective temperatures between 4370 and 5250 K from the observed colours they adopted an effective temperature of 3970 K for the more massive star. The masses of the components were estimated to be 0.94 $M_{\odot}$ and 0.87 $M_{\odot}$, the radii 1.03 $R_{\odot}$ and 0.93 $R_{\odot}$, and the effective temperature 3750 K for the secondary star. The locations of the component stars in the HR diagram correspond to stars having masses below 0.4 $M_{\odot}$. The J-,H-, and K- band extinctions in the direction of the variable were taken from Schlegel, Finkbeiner, & Davis (1998) as $A_J = 0.046$, $A_H = 0.030$ and $A_K = 0.019$ magnitudes. We computed the absolute

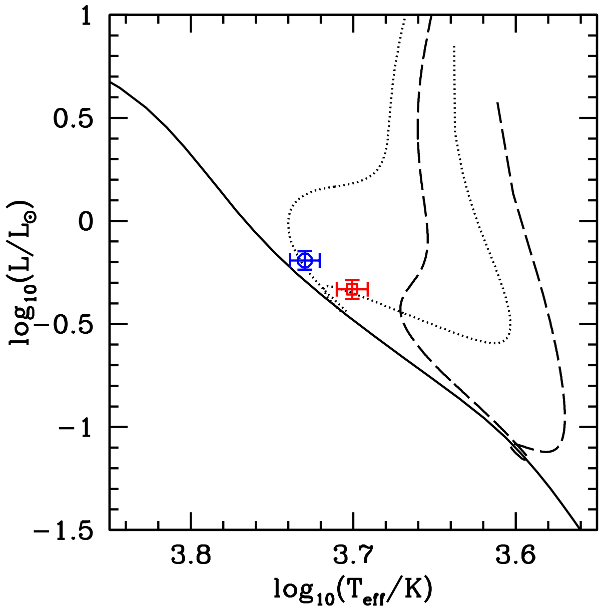

Fig. 4. Comparison between evolutionary models and the physical parameters of NSVS 1186 in the effective temperature-luminosity diagram with the luminosities determined from the light and radial velocity curves. Theoretical evolutionary tracks, both pre- and post-main sequence, for masses of 0.870 $M_\odot$ (dotted line) and 0.607 $M_\odot$ (dashed line) and ZAMS (solid line) with solar abundance were calculated with the STARS code. The circle and square denote the primary and secondary stars.

TABLE 4

FUNDAMENTAL PARAMETERS OF THE SYSTEM

Parameter	Primary	Secondary
Mass ($M_\odot$)	0.870±0.074	0.607±0.053
Radius ($R_\odot$)	0.983±0.030	0.901±0.026
log g (cgs)	4.392±0.019	4.311±0.021
$T_{\rm eff}$ (K)	5250±135	5 020±135
log ($L/L_\odot$)	-0.188 ± 0.045	-0.341 ± 0.046
$(v \sin\ i)_{\rm obs}$ (km s^{-1})	77±3	62±4
$(v \sin\ i)_{\rm calc}$ (km s^{-1})	83±3	76±2

magnitudes as $M_J = 3.96 \pm 0.10$, $M_H = 3.50 \pm 0.07$ and $M_K = 3.46 \pm 0.07$ for the primary star. Then using the JHK magnitudes given in § 2.1.1 we estimate the distance to the variable as 668±25, 689±24 and 678±22 parsec in the J, H, and K bands, respectively.

4. OVERSIZED STARS IN LOW-MASS ECLIPSING BINARIES

Abt (1963) and Duquennoy, Mayor, & Halbwachs (1991) report that binary stars are more common than single stars at masses above that of the Sun. In contrast, Reid & Gizis (1997) and Delfosse et al. (1999) suggest that binaries are not very common among low-mass stars, although approximately 75% of all stars in our Galaxy are low-mass dwarfs with masses smaller than 0.7 $M_\odot$. Due to the low binary fractions and their faintness very few low-mass eclipsing binary systems have been observed so far both photometrically and spectroscopically, yielding accurate physical parameters. Recently, in a pioneer study, Ribas (2003, 2006) collected the available masses and radii of the low-mass stars and compared with those obtained by stellar evolution models. Despite the small numbers of the sample, a total of eight double-lined eclipsing binaries with masses and radii determined with an accuracy of better than 3%, the comparison evidently revealed that the observed radii are systematically larger than those predicted by the models. However, the effective temperatures are cooler than in the theoretical calculations, the luminosities being in agreement with those of single stars of the same mass. This discrepancy between the models and observations has been explained by Mullan & MacDonald (2001), Torres et al. (2006), Ribas (2006) and Lopez-Morales (2007) and others by the high level magnetic activity in low-mass stars. They suggest that stellar activity may be responsible for the observed discrepancy through inhibition of convection or effects of a significant spot coverage. However, Berger et al. (2006) compared the interferometric radii of low-mass stars with those estimated from theory and found a correlation between an increase in metallicity and a larger-than-expected radius, i.e. the larger radii seem to be caused by differences in metallicity.

The number of double-lined low-mass eclipsing binaries having precise photometric and spectroscopic observations is now 21, as far as the authors know. Combining the results of the analysis of both photometric and spectroscopic observations accurate masses, radii, effective temperatures and luminosities of the components have been obtained. In Table 5 we list absolute parameters for the low-mass stars with their standard deviations. In Figure 5 we plot the radii of the low-mass stars in eclipsing binary systems as a function of mass. Theoretical mass-radius ($M-R$) diagrams for the zero-age main-sequence stars with solar abundance taken from the STARS code and Siess, Dufour, & Forestini (2000) are also plotted for comparison.

The stars below 0.3 $M_\odot$ appear to trace the theoretical $M-R$ diagram. However, larger mass stars, above 0.3 $M_\odot$, significantly deviate from the theo-

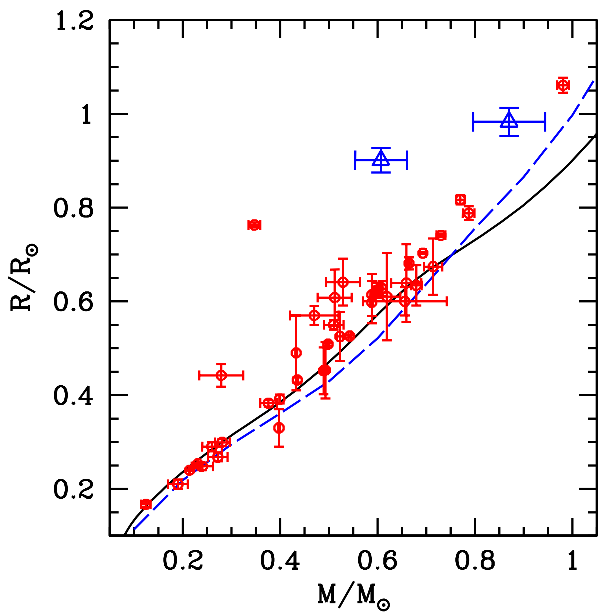

Fig. 5. Locations of the low-mass stars in the mass-radius diagram. The components of NSVS 1186 are shown by triangles. The solid and dashed lines represent the ZAMS models taken from the STARS code and Siess et al. (2000), respectively, with solar abundance.

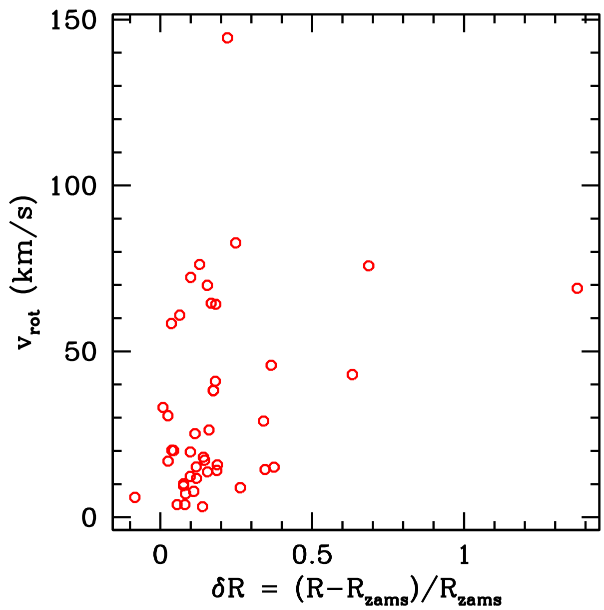

Fig. 6. The rotational velocities are plotted against the radius difference from the ZAMS at the same mass.

retical $M-R$ digram. We also computed projected rotational velocities of the components using their radii and orbital periods. Since the orbital periods are generally short, we assumed spin-orbit synchronization. The rotational velocities are plotted in Figure 6 as a function of the radius difference calculated as $(R_{\rm obs}-R_{\rm zams})/R_{\rm zams}$. This plot shows that as the rotational velocity increases, the difference in radius, gets larger for the stars given in Table 5.

A low-mass star has a convective atmosphere with a radiative core. The depth of the convective zone is about 0.28 R for a star of mass of about 0.9 $M_\odot$, and gradually increases to about 0.41 R for a star with a mass of about 0.4 $M_\odot$. Stars are thought to be fully convective below about 0.35 $M_\odot$. Therefore, the internal structure of such a low-mass star with a deep convective zone is tightly dependent on the mixing length parameter, α. In Figure 7a and b we compare locations of the low-mass stars in the $M-R$ and $M-T_{\rm eff}$ diagrams with the theoretical calculations for various α parameters. Convection is modelled by mixing length theory (Böhm-Vitense 1958) with the ratio of mixing length to pressure scale height (i.e., $\alpha = l/H_{\rm p}$). Theoretical models show that there is no significant separation in the $M-R$ relation for the stars below about 0.6 $M_\odot$, depending on the mixing length parameter. For masses above this value a separation is revealed. However, as the α parameter increases the computed effective temperature also increases. A separation is clearly seen even for the masses below 0.6 $M_\odot$. We also plotted empirical parameters for the low-mass stars in these diagrams. This comparison clearly exposes that the discrepancies in radii and effective temperatures could not be explained only by changing the α parameter as it is obvious in the $M-R$ and $M-T_{\rm eff}$ plots represented in Figure 7. On the other hand, Demory et al. (2009) showed that there is no significant correlation between metallicity and radius for the single, low-mass stars. An alternative explanation appears to be the magnetic activity responsible for the observed larger radii but cooler effective temperatures. As demonstrated by D'Antona, Ventura, & Mazzitelli (2000), Mullan & MacDonald (2001) and Chabrier et al. (2007) magnetic fields change the evolution of low-mass stars. Due to the high magnetic activity in fast-rotating dwarfs their surfaces are covered by dark spots. Spot coverage in active dwarfs yields larger radii and lower effective temperatures.

5. DISCUSSION

We obtained the radial velocity curves for the low-mass eclipsing binary NSVS 1186. We reanalysed the existing V-, R- and I-bandpass light curves. Since the light curves are distorted they are modelled assuming one spot located on each star. Then, combining the photometric and spectroscopic

TABLE 5

MASS, RADIUS, EFFECTIVE TEMPERATURE AND ORBITAL PERIOD OF THE LOW-MASS STARS IN DOUBLE-LINED ECLIPSING BINARIES

Object	Star	Mass/$M_\odot$	Radius/$R_\odot$	$T_{\rm eff}$/K	$P_{\rm orb}$/day	Refs
CM Dra	A	0.2310±0.0009	0.2534±0.0019	3130±70	1.276	1
	B	0.2141±0.0008	0.2398±0.0018	3120±70		
YY Gem	A	0.5992±0.0047	0.6194±0.0057	3820±100	0.820	2
	B	0.5992±0.0047	0.6194±0.0057	3820±100		
CU Cnc	A	0.4349±0.0012	0.4323±0.0055	3160±150	2.794	3
	B	0.3992±0.0009	0.3916±0.0094	3125±150		
GU Boo	A	0.6101±0.0064	0.6270±0.0160	3920±130	0.492	4
	B	0.5995±0.0064	0.6240±0.0160	3810±130		
TrES-Her0-07621	A	0.4930±0.0030	0.4530±0.0600	3500±···	1.137	5
	B	0.4890±0.0030	0.4520±0.0500	3395±···		
2MASS J05162881+2607387	A	0.7870±0.0120	0.7880±0.0150	4200±···	2.619	6
	B	0.7700±0.0090	0.8170±0.0100	4154±···		
UNSW-TR 2	A	0.5290±0.0350	0.6410±0.0500	···	2.144	7
	B	0.5120±0.0350	0.6080±0.0600	···		
NSVS 06507557	A	0.6560±0.0860	0.6000±0.0300	3960±80	0.520	8
	B	0.2790±0.0450	0.4420±0.0240	3365±80		
NSVS 02502726	A	0.7140±0.0190	0.6740±0.0600	4300±200	0.560	9
	B	0.3470±0.0120	0.7630±0.0050	3620±205		
T-Lyr1-17236	A	0.6795±0.0107	0.6340±0.0430	4150±···	8.430	10
	B	0.5226±0.0061	0.5250±0.0520	3700±···		
2MASS J01542930+0053266	A	0.6590±0.0310	0.6390±0.0830	3730±100	2.639	11
	B	0.6190±0.0280	0.6100±0.0930	3532±100		
GJ 3236	A	0.3760±0.0170	0.3828±0.0072	3310±110	0.770	12
	B	0.2810±0.0150	0.2992±0.0075	3240±110		
SDSS-MEB-1	A	0.2720±0.0200	0.2680±0.0090	3320±130	0.410	13
	B	0.2400±0.0220	0.2480±0.0080	3300±130		
BD -22 5866	A	0.5881±0.0029	0.6140±0.0450	···	2.211	14
	B	0.5881±0.0029	0.5980±0.0450	···		
NSVS 01031772	A	0.5428±0.0027	0.5260±0.0028	3615±72	0.368	15
	B	0.4982±0.0025	0.5088±0.0030	3513±31		
NSVS 11868841	A	0.8700±0.0740	0.9830±0.0300	5260±110	0.602	This paper
	B	0.6070±0.0530	0.9010±0.0260	5020±110		
GJ 2069A	A	0.4329±0.0018	0.4900±0.0800	···	2.771	16
	B	0.3975±0.0015	0.3300±0.0400	···		
2MASS J04463285+1901432	A	0.4700±0.0500	0.5700±0.0200	3320±150	0.630	18
	B	0.1900±0.0200	0.2100±0.0100	2910±150		
NSVS 6550671	A	0.5100±0.0200	0.5500±0.0100	3730±60	0.193	19
	B	0.2600±0.0200	0.2900±0.0100	3120±65		
IM Vir	A	0.9810±0.0120	1.0610±0.0160	5570±100	1.309	20
	B	0.6644±0.0048	0.6810±0.0130	4250±130		
RXJ0239.1	A	0.7300±0.0090	0.7410±0.0040	4645±20	2.072	21
	B	0.6930±0.0060	0.7030±0.0020	4275±15		

References: (1) Morales et al. (2009a), (2) Torres & Ribas (2002), (3) Ribas (2003), (4) López-Morales & Ribas (2005), (5) Creevey et al. (2005), (6) Bayless & Orosz (2006), (7) Young et al. (2006), (8) Çakırlı & Ibanoğlu (2010), (9) Çakırlı, Ibanoğlu, & Güngör (2009), (10) Devor et al. (2008), (11) Becker et al. (2008), (12) Irwin et al. (2009), (13) Blake et al. (2008), (14) Shkolnik et al. (2008), (15) López-Morales et al. (2006), (16) Delfosse et al. (1999), (17) Beatty et al. (2007), (18) Hebb et al. (2006), (19) Dimitrov & Kjurkchieva (2010), (20) Morales et al. (2009b), (21) López-Morales & Shaw (2007).

solutions, we derived the absolute physical parameters for both components. The standard deviations of the parameters have been determined using the JKTABSDIM code (Southworth & Clausen 2007). The less massive component appears to have a larger radius and a higher temperature than expected for its mass. On the other hand, the primary star seems to have a larger radius but the effective temperature is in agreement with that expected for its mass. We suppose that the larger radii of both components may be due to a higher activity in the system at the time that photometry is obtained. The locations of the components in the H-R diagram have been plotted and compared with theoretical models. The secondary component seems to be slightly brighter than expected for its mass.

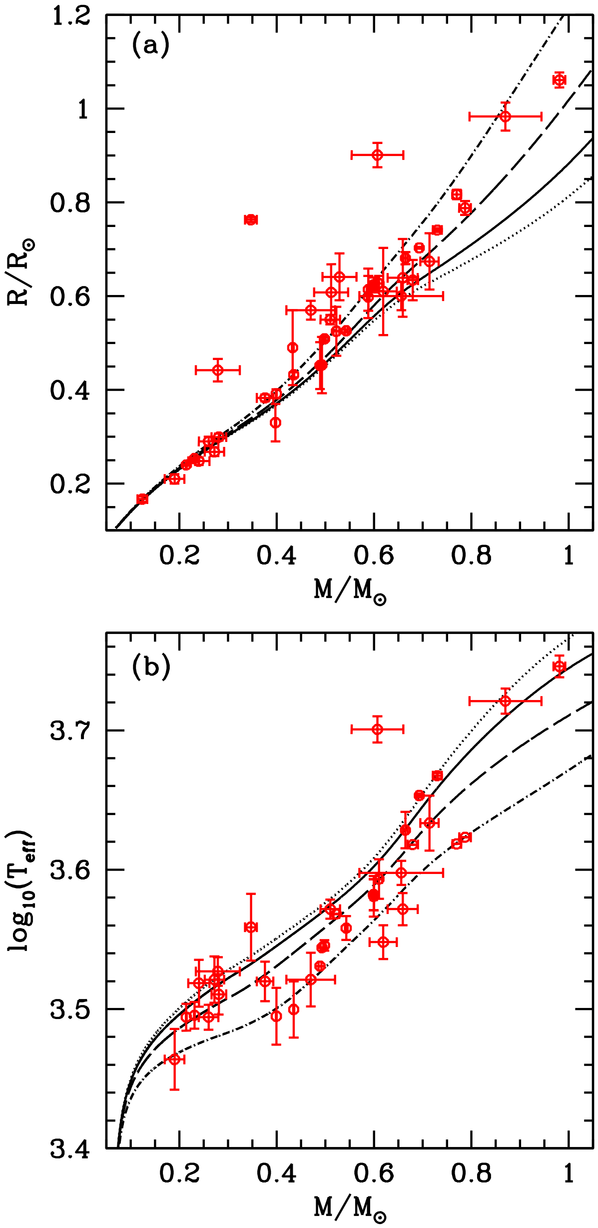

Fig. 7. Mass-radius (a) and mass-effective temperature (b) relationships for zero-age main-sequence low-mass stars calculated with the STARS code for values of the mixing length parameter $\alpha = 4$ (dotted line), $\alpha = 2$ (solid line), $\alpha = 1$ (dashed line) and $\alpha = 0.5$ (dot-dashed line). Values of the α parameter larger than 0.5 appear to affect the radius slightly for a star below 0.7 $M_{\odot}$. As α increases the effective temperatures also increase.

Basic physical parameters determined from double lined low mass binaries, such as mass, radius, effective temperature and orbital period, are collected. The locations of the low-mass stars in the mass-radius diagram are compared with the theoretical ZAMS models. Since the low-mass stars evolve very slowly, we prefer a comparison with the ZAMS models. Theoretical models tend to underestimate the radii at a given mass in the range of 0.3 and 0.6 $M_{\odot}$. Due to the evolutionary effect on the radius, we take into account only this mass range, preventing any confusion. Since low-mass stars have deeper convective layers in their atmospheres, we also computed the radii and temperatures for the abovementioned mass range for various mixing-length parameters. We find that the mixing-length parameter does not significantly affect the radii; on the contrary, it changes considerably the effective temperatures of the stars. Comparison with the observations shows that the observed larger radii of the late K and M dwarfs cannot be represented with the values of mixing-length parameters. These comparisons confirm that magnetic field induced inhibition of convection in fast-rotating low-mass stars with deep convective zones leads to larger radii and lower effective temperatures than those expected from theoretical models (D'Antona et al. 2000; Mullan & MacDonald 2001; Chabrier et al. 2007).

The authors acknowledge generous allotments of observing time at TÜBİTAK National Observatory (TUG) of Turkey. We also wish to thank the Turkish Scientific and Technical Research Council for supporting this work through grant Nr. 108T210 and EBİLTEM Ege University Science Foundation Project No:08/BİL/027. Dr. Esin Sipahi is acknowledged for the aid during the computation. We would like express our sincere gratitude to the anonymous referee, whose suggestions made the paper much clearer.

REFERENCES

Abt, H. A. 1963, ApJS, 8, 99

Baraffe, I., Chabrier, G., Allad, F., & Hauschildt, P. H. 1998, A&A, 337, 403

Bayless, A. J., & Orosz, J. A. 2006, ApJ, 651, 1155

Beatty, T. G., et al. 2007, ApJ, 663, 573

Becker, A. C., et al. 2008, MNRAS, 386, 416

Berger, D. H., et al. 2006, ApJ, 644, 475

Blake, C. H., Torres, G., Bloom, J. S., & Gaudi, B. S. 2008, ApJ, 684, 635

Böhm-Vitense, E. 1958, Zert. Astrophys., 46, 108

Chabrier, G., Gallardo, J., & Baraffe, I. 2007, A&A, 472, 17

Clausen, J. V., Helt, B. E., & Olsen, E. H. 1999, in ASP Conf. Ser. 173, Theory and Tests of Convection in Stellar Structure, ed. A. Giménez, E. F. Guinan, & B. Montesinos (San Francisco: ASP), 321

Coughlin, J. L., & Shaw, J. S. 2007, J. Southeastern Assoc. Res. Astron., 1, 7C

Creevey, O. L., et al. 2005, ApJ, 625, L127
Cutri, R. M., et al. 2003, The IRSA 2MASS All-Sky Point Source Catalog, NASA/IPAC Infrared Science Archive (Pasadena, CA: NASA/CalTech), http://irsa.ipac.caltech.edu/applications/Gator/
Çakırlı, Ö., & Ibanoğlu, C. 2010, MNRAS, 401, 1141
Çakırlı, Ö., Ibanoğlu, C., & Güngör, C. 2009, New Astron., 14, 496
D'Antona, F., Ventura, P., & Mazzitelli, I. 2000, ApJ, 543, L77
Delfosse, X., Forveille, T., Mayor, M., Burnet, M., & Perrier, C. 1999, A&A, 341, 63
de Jager, C., & Nieuwenhuijzen, H. 1987, A&A, 177, 217
Demory, B.-O., et al. 2009, A&A, 505, 205
Devor, J., et al. 2008, ApJ, 687, 1253
Dimitrov, D. P., & Kjurkchieva, D. P. 2010, MNRAS, 406, 2559
Drilling, J. S., & Landolt, A. U. 2000, in Allen's Astrophysical Quantities, ed. A. N. Cox (4th ed., New York: AIP/Springer), 381
Duquennoy, A., Mayor, M., & Halbwachs, J.-L. 1991, A&AS, 88, 281
Eggleton, P. P. 1971, MNRAS, 151, 351
Eldridge, J. J., & Tout, C. A. 2004, MNRAS, 348, 201
Girardi, L., Bressan, A., Bertelli, G., & Chiosi, C. 2002, A&AS, 141, 371
Hebb, L., Wyse, R. F. G., Gilmore, G., & Holtzman, J. 2006, AJ, 131, 555
Hernández, J., Calvet, N., Briceño, C., Hartmann, L., & Berlind, P. 2004, AJ, 127, 1682
Irwin, J., et al. 2009, ApJ, 701, 1436
López-Morales, M. 2007, ApJ, 660, 732
López-Morales, M., Orosz, J. A., Shaw, J. S., Havelka, L., Arévalo, M. J., McIntyre, T., & Lázaro, C. 2006, arXiv:astro-ph/0610225
López-Morales, M., & Ribas, I. 2005, ApJ, 631, 1120
López-Morales, M., & Shaw, J. S. 2007, in ASP Conf. Ser. 362, The Seventh Pacific Rim Conference on Stellar Astrophysics, ed. Y. W. Kang, H.-W. Lee, K.-C. Leung, & K.-S. Cheng (San Francisco: ASP), 26
Lucy, L. B. 1967, Zert. Astrophys., 65, 89
Marigo, P. 2002, A&A, 387, 507
Morales, J. C., Ribas, I., & Jordi, C. 2008, A&A, 478, 507
Morales, J. C., Torres, G., Marschall, L. A., & Brehm, W. 2009b, ApJ, 707, 671
Morales, J. C., et al. 2009a, ApJ, 691, 1400
Mullan, D. J., & MacDonald, J. 2001, ApJ, 559, 353
Nidever, D. L., Marcy, G. W., Butler, R. P., Fischer, D. A., & Vogt, S. S. 2002, ApJS, 141, 503
Popper, D. M. 1980, ARA&A, 18, 115
_________. 1997, AJ, 114, 1195
Prša, A., & Zwitter, T. 2005, ApJ 628, 426
Queloz, D., Allain, S., Mermilliod, J.-C., Bouvier, J., & Mayor, M. 1998, A&A, 335, 183
Reid, I. N., & Gizis, J. E. 1997, AJ, 114, 1992
Ribas, I. 2003, A&A, 398, 239
_________. 2006, Ap&SS, 304, 89
Royer, F., Zorec, J., & Gómez, A. 2004, in IAU Symp. 224, The A-Star Puzzle, ed. J. Zverko, J. Ziznovsky, S. J. Adelman, & W. W. Weiss (Cambridge: Cambridge Univ. Press), 109
Schlegel, D. J., Finkbeiner, D. P., & Davis, M. 1998, ApJ, 500, 525
Shkolnik, E., Liu, M. C., Reid, I. N., Hebb, L., Cameron, A. C., Torres, C. A., & Wilson, D. M. 2008, ApJ, 682, 1248
Siess, L., Dufour, E., & Forestini, M. 2000, A&A, 358, 593
Siess, L., Forestini, M., & Dougados, C. 1997, A&A, 324, 556
Southworth, J., & Clausen, J. V. 2007, A&A, 461, 1077
Stassun, K. G., Hebb, L., López-Morales, M., & Prša, A. 2009, arXiv:0902.2548
Tokunaga, A. T. 2000, in Allen's Astrophysical Quantities, ed. A. N. Cox (4th ed. New York: Springer), 143
Tonry, J., & Davis, M. 1979, AJ, 84, 1511
Topping, J. 1972, Errors of Observation & Their Treatment (London: Chapman & Hall Ltd.)
Torres, G., Lacy, C. H., Marschall, L. A., Sheets, H. A., & Mader, J. A. 2006, ApJ, 640, 1018
Torres, G., & Ribas, I. 2002, ApJ, 567, 1140
van Hamme, W. 1993, AJ, 106, 2096
Wilson, R. E., & Devinney, E. J. 1971, ApJ, 166, 605
Wozniak, P. R., et al. 2004, AJ, 127, 2436
Young, T. B., Hidas, M. G., Webb, J. K., Ashley, M. C. B., Christiansen, J. L., Derekas, A., & Nutto, C. 2006, MNRAS, 370, 1529
Zacharias, N., Monet, D. G., Levine, S. E., Urban, S. E., Gaume, R., & Wycoff, G. L. 2004, BAAS, 36, 1418

Ö. Çakırlı, C. İbanoğlu, and A. Dervişoğlu: Ege University, Science Faculty, Astronomy and Space Sciences Dept., 35100 Bornova, İzmir, Turkey (omur.cakirli@ege.edu.tr).

Revista Mexicana de Astronomía y Astrofísica, **46**, 375–383 (2010)

A REASSESSMENT OF THE KINEMATICS OF PV CEPHEI BASED ON ACCURATE PROPER MOTION MEASUREMENTS

L. Loinard,[1] L. F. Rodríguez,[1] L. Gómez,[2] J. Cantó,[3] A. C. Raga,[4] A. A. Goodman,[5] and H. G. Arce[6]

Received 2010 June 15; accepted 2010 August 2

RESUMEN

Presentamos dos observaciones de la estrella de pre-secuencia principal PV Cephei tomadas con el Very Large Array con una separación de 10.5 años. Estos datos implican que los movimientos propios de esta estrella son $\mu_\alpha \cos\delta = +10.9 \pm 3.0$ mas año^{-1}; $\mu_\delta = +0.2 \pm 1.8$ mas año^{-1}, muy similares a los ya conocidos para HD 200775, la estrella B2Ve que domina la iluminación de la cercana nebulosa de reflexión NGC 7023. Este resultado sugiere que PV Cephei no es una estrella desbocada con movimientos rápidos, como se había sugerido en anteriores estudios. La alta velocidad de PV Cep se había inferido de los desplazamientos sistemáticos hacia el este de los bisectores de pares sucesivos de objetos Herbig Haro a lo largo de su chorro. Estos desplazamientos sistemáticos podrían, en realidad, deberse a una asimetría en los mecanismos de eyección, o en la distribución del material circunestelar.

ABSTRACT

We present two Very Large Array observations of the pre-main-sequence star PV Cephei, taken with a separation of 10.5 years. These data show that the proper motions of this star are $\mu_\alpha \cos\delta = +10.9 \pm 3.0$ mas yr^{-1}; $\mu_\delta = +0.2 \pm 1.8$ mas yr^{-1}, very similar to those –previously known– of HD 200775, the B2Ve star that dominates the illumination of the nearby reflection nebula NGC 7023. This result suggests that PV Cephei is not a rapidly moving runaway star as suggested by previous studies. The large velocity of PV Cephei had been inferred from the systematic eastward displacement of the bisectors of successive pairs of Herbig Haro knots along its flow. These systematic shifts might instead result from an intrinsic asymmetry in the ejection mechanisms, or in the distribution of the circumstellar material.

Key Words: astrometry — ISM: individual (PV Cep) — ISM: jets and outflows — stars: pre-main sequence

1. INTRODUCTION

Compact stellar clusters as well as multiple stellar systems with three or more members can be dynamically unstable (e.g., Valtonen & Mikkola 1991; Poveda, Ruiz, & Allen 1967). Indeed, close few body encounters occurring within them can lead to the acceleration of one or more of the system members, which –if the acceleration is sufficient– can escape their birthplace and become runaway stars. It is important to search for direct observational evidence of these energetic events, because if they occurred with sufficient frequency during the earliest stages of star-formation, they could have a significant impact on the very outcome of the star-forming process (Reipurth 2000). Arguably the most promising case so far, is that of the BN/KL region in Orion where three stars (including BN itself) are moving away

[1]Centro de Radioastronomía y Astrofísica, Universidad Nacional Autónoma de México, Morelia, Mexico.

[2]Max-Planck-Institut für Radioastronomie, Bonn, Germany (Member of the International Max Planck Research School for Astronomy and Astrophysics at the Universities of Bonn and Cologne).

[3]Instituto de Astronomía, Universidad Nacional Autónoma de México, Mexico.

[4]Instituto de Ciencias Nucleares, Universidad Nacional Autónoma de México, Mexico.

[5]Harvard-Smithsonian Center for Astrophysics, Cambridge, USA.

[6]Yale University, New Haven, USA.

TABLE 1

CHARACTERISTICS OF PV CEP

Spectral type	A5
R-band magnitude	$R = 11.1$
Distance	$d = 430^{+155}_{-91}$ pc
Mean position (Equinox J2000,	$\alpha = 20^h45^m53\overset{s}{.}9550 \pm 0\overset{s}{.}0014$
Epoch 2002.26)	$\delta = 67°57'38\overset{''}{.}681 \pm 0\overset{''}{.}008$

at about 30 km s^{-1} from a common point of origin, which happens to be near the center of the massive KL outflow (Rodríguez et al. 2005; Gómez et al. 2005, 2008; Zapata et al. 2009). The dynamical disruption in that case, appears to have occurred a mere 500 years ago.

Goodman & Arce (2004, hereafter GA2004) have suggested that the star PV Cephei (hereafter PV Cep) might be another potential candidate. PV Cep (Table 1) is a Herbig Ae/Be star (Li et al. 1994) that drives a well-studied giant Herbig Haro (HH) flow (Reipurth, Bally, & Devine 1997; Gómez, Whitney, & Kenyon 1997; Arce & Goodman 2002a,b; GA2004). It is located about 1$\overset{\circ}{.}$5 west of the reflection nebula NGC 7023, and the centroid velocity of its CO emission is similar to that of the CO emission from NGC 7023 itself (Cohen et al. 1981). Because of this shared kinematics, it is very likely that PV Cep and NGC 7023 are at the same distance from the Sun. The measured trigonometric parallax of HD 200775 (MWC 361, $V = 7.4$ mag) the B2Ve star that dominates the illumination of NGC 7023 (Herbig 1960) yields a distance for the entire region of 430^{+155}_{-91} pc (Perryman et al. 1997). This value is consistent with the somewhat older estimate of 500 pc used by GA2004. NGC 7023 is associated with a compact cluster of young stars that contains a number of low luminosity pre-main-sequence objects (Lepine & Rieu 1974).

The suggestion by GA2004 that PV Cep might be a runaway star was based on a careful analysis of the kinematics and morphology of the gas surrounding PV Cep. The strongest argument follows from a study of the distribution of successive pairs of HH knots located at nearly equal distances from PV Cep along its jet. The segments joining such successive pairs of knots are expected to pass through the source driving the flow — if the latter is stationary. In the case of PV Cep, however, GA2004 found that the bisectors of the segments were systematically shifted eastward of the source, and increasingly more so, as older HH pairs were considered. This suggests that the source used to be somewhat to the east of its current position, and thus, that it is moving westward relative to its surroundings. Assuming that the HH knots along the flow are fully detached clumps, GA2004 estimated the velocity of the central source to be 22 km s^{-1} (see discussion in § 2). Most remarkably, the velocity vector obtained by GA2004 points almost exactly *away* from NGC 7023, as if PV Cep had been ejected from NGC 7023 about 10^5 yr ago (see their Figure 6). Thus, PV Cep might indeed provide us with an example of a runaway star dynamically ejected from its (still identifiable) parent cluster. Note, however, that the conclusions of GA2004 were based on an analysis of the kinematics and morphology of the gas surrounding PV Cep, and *not* on a direct measurement of the relative proper motion between PV Cep and NGC 7023. In the present paper (§§ 3 and 4), we will provide such a direct measurement, combining published optical proper motions of the brightest star in NGC 7023 and new radio measurements of the proper motion of PV Cep itself.

2. A RE-ANALYSIS OF THE BISECTOR RESULTS

Several theoretical models (both analytic and numerical) have been proposed to explain the curved morphology presented by some HH jets. Cantó & Raga (1995) have developed an analytical model that treats the problem of a *steady* jet interacting with a sidewind. More recently, Masciadri & Raga (2001) presented numerical simulations of a *variable* jet in a sidewind and identified two different regimes. For low-amplitude variability (caused by moderate changes in the jet ejection velocity), small working surfaces (i.e., HH knots) are created along the jet, and they travel following the path predicted by the steady jet model of Cantó & Raga (1995). On the other hand, large working surfaces created by larger changes in the jet ejection velocity eventually become detached "clumps" that travel on somewhat straighter trajectories.

2.1. *Analytic solution for fully detached clumps*

In their analysis of the bisectors of successive HH pairs, GA2004 assumed that the ejecta had become detached clumps, and integrated the equations of motion numerically to obtain the trajectory of the clumps. Recently, however, Cantó et al. (2008) showed that the idealized case of fully detached clumps has a completely analytic solution, which produces trajectories similar to those obtained in numerical simulation. To examine that analytic solution in the case of PV Cep, we assume (following GA2004) that PV Cep is moving relative to the ambient gas in a direction exactly perpendicular to that of its jet. The velocity of the star relative to the surroundings is taken to be v_*, and individual clumps of mass M are ejected at a velocity v_e (see Figure 1a for a schematic description). The trajectory is parametrized by a distance s_0 (Cantó et al. 2008) given by:

$$s_0 \equiv \frac{3}{4}\left(\frac{M v_0^4}{\xi \rho_0 c^4}\right)^{1/3} . \tag{1}$$

Here, ξ is a constant of integration whose numerical value is $\xi = 14$ (Cantó et al. 2008), c is the isothermal sound speed of the clump material, and ρ_0 is the density of the ambient gas. In the present case, where v_* and v_e are perpendicular, v_0 is simply

$$v_0 = \sqrt{v_*^2 + v_e^2}\,. \tag{2}$$

If one further defines the angle θ as

$$\tan\theta = \frac{v_e}{v_*}\,, \tag{3}$$

the equation of the trajectory is given analytically by:

$$x = \frac{y}{\tan\theta} - 4 s_0 \left(\frac{v_*}{v_0}\right)\left[1 - \left(1 - \frac{y}{s_0 \sin\theta}\right)^{1/4}\right] . \tag{4}$$

Following GA2004, we adopt $v_e = 350$ km s^{-1} and $\rho_0 = 1.5 \times 10^3$ cm^{-3}. A good fit to the data points (shown in Figure 1a) is obtained for $v_* = 22$ km s^{-1}, provided that $s_0 \approx 6.4 \times 10^{18}$ cm. This, in turn, implies $M \approx 2 \times 10^{-4}\ M_\odot$ if the value for c is taken to be 3.2 km s^{-1} as suggested by GA2004. A comparison between the analytic trajectory obtained using these parameters and the path obtained numerically by GA2004 (see their Figure 2) shows that the analytical and numerical trajectories agree extremely well.

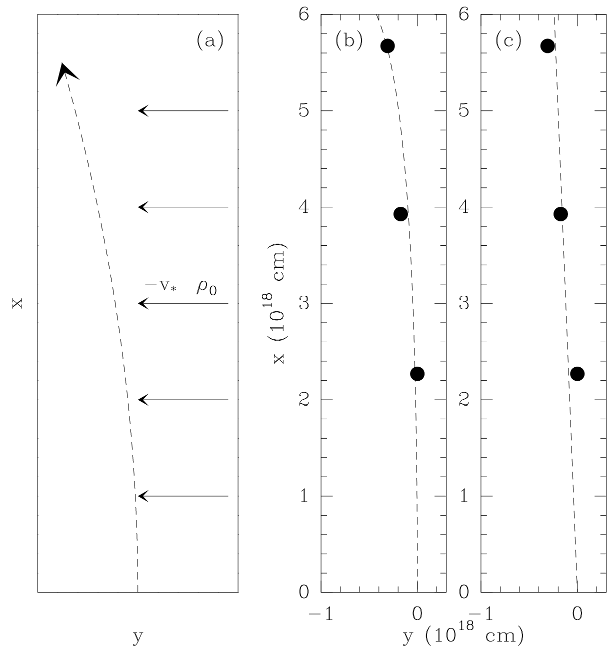

Fig. 1. (a) Schematic diagram of a star which ejects a bipolar outflow along the positive x-axis, in a direction perpendicular to the motion of the star with respect to the surrounding environment. In the frame of reference of the star, the environment moves towards the left along the y-axis, producing a curvature in the bipolar outflow system. (b) and (c) The black filled circles show the positions of the ejecta relative to the source according to the results of GA2004, and the dashed lines represent the best fit for fully detached clumps [Panel (b); see § 2.1] and for a continuous jet [Panel (c); see § 2.2].

It should be mentioned that c in equation (1) is the isothermal sound speed *of the ejecta*. Such ejecta are believed to be ionized, so the appropriate sound speed is $c \approx 10$ km s^{-1}. In their analysis, however, GA2004 used $c = 3.2$ km s^{-1}, the typical velocity dispersion of the *ambient* molecular gas. From equation (1), it is clear that to obtain a similar value of s_0 for $c = 10$ km s^{-1} without resorting to unreasonable assumptions for ρ_0 and v_0, one has to increase the mass of the ejecta by nearly two orders of magnitude, to about $1.5 \times 10^{-2}\ M_\odot$. Even if one allows v_e to increase to 400 km s^{-1} and ρ_0 to decrease to 1000 cm^{-3}, the ejecta must still have masses of order $10^{-2}\ M_\odot$. Moreover, the transverse velocity of the star must then be increased to about 40 km s^{-1} to obtain a good fit. We conclude that if the ejecta from PV Cep are indeed fully detached clumps of ionized gas, they must be very massive[7], and the velocity

[7]As a consequence, in this scenario, PV Cep must have undergone episodes of extremely high accretion/ejection.

of PV Cep might be even larger that the 22 km s^{-1} proposed by GA2004.

2.2. *The HH knots of PV Cep as part of an underlying continuous jet*

The trajectories considered in § 2.1 appropriately describe jets in which large amplitude perturbations leading to fully detached clumps have developed. As mentioned earlier, lower amplitude perturbations create HH knots that travel along different paths: those predicted by the analytical model of Cantó & Raga (1995). Moreover, the analysis of Masciadri & Raga (2001) shows that a smaller sidewind velocity is necessary to create a given jet curvature if the HH knots are such small perturbations along an underlying continuous jet than if they are fully detached clumps. Well-defined HH knots suggestive of detached clumps are certainly present along the jet driven by PV Cep (GA2004, and references therein). There is also evidence, however, for an underlying continuous jet which is always "on". Indeed, the very existence of steady, compact centimeter radio emission associated with PV Cep (which traces free-free emission from the base of an ionized flow; see § 3 below) demonstrates that such a continuous jet exists and that the ejection of matter is not fully episodic. The detection of water masers (Marvel 2005) and of high velocity entrained molecular gas (Arce & Goodman 2002b) in the immediate vicinity of PV Cep confirm the existence of such a steady jet. Let us, therefore, estimate the sidewind velocity that would be required to explain the bisector results of GA2004 in a steady wind scenario. The applicability of this model to the specific case of PV Cep will be discussed in § 5.

As shown by Cantó & Raga (1995), in the vicinity of the source, a bipolar flow in a sidewind approximately follows a parabolical shape[8] (with both the jet and the counterjet on the same parabola) described by

$$y = \frac{x^2}{2\lambda}\,, \tag{5}$$

where x is parallel to the initial outflow direction, and y is the coordinate perpendicular to x and parallel to the motion of the source (Figure 1a). This relation is valid for the case in which the motion of the source is perpendicular to the ejection. The distance λ in equation (5) is given by

$$\lambda \equiv \left(\frac{\dot{M}v_e^3}{\pi c^2 \rho_0 v_*^2}\right)^{1/2} = 7.8\times10^{18}\ \mathrm{cm} \times \left(\frac{\dot{M}}{10^{-7}\ M_\odot\ \mathrm{yr}^{-1}}\right)^{1/2} \left(\frac{v_e}{100\ \mathrm{km\,s^{-1}}}\right)^{3/2} \times \left(\frac{\rho_0}{10^3\ \mathrm{cm}^{-3}}\right)^{-1/2} \left(\frac{v_*}{1\ \mathrm{km\,s^{-1}}}\right)^{-1}, \tag{6}$$

where $\dot{M}$ is the mass-loss rate, and the other parameters have the same meaning as before. The best fit to the observed positions reported by GA2004 using equation (5) yields $\lambda = 4.64\times10^{19}$ cm. With this value, we can now use equation (6) to determine the required velocity for the environment:

$$\left(\frac{v_*}{1\,\mathrm{km\,s^{-1}}}\right) = 0.17\left(\frac{\dot{M}}{10^{-7}\ \mathrm{M_\odot yr^{-1}}}\right)^{1/2} \times \left(\frac{v_e}{100\ \mathrm{km\,s^{-1}}}\right)^{3/2} \left(\frac{\rho_0}{10^3\ \mathrm{cm}^{-3}}\right)^{-1/2}. \tag{7}$$

Finally, using the values $v_e = 350$ km s^{-1} and $\rho_0 = 1500$ cm^{-3} determined by GA2004, we obtain $v_* = 0.9$ km s^{-1}, assuming a mass loss rate $\dot{M} = 10^{-7}$ $M_\odot$ yr^{-1}. The corresponding trajectory is shown in Figure 1c.

Thus, a very modest relative motion –of the order of the typical stellar velocity dispersion in newborn stellar clusters– between PV Cep and its surroundings would be required to explain the bisector results of GA2004 in the case of a continuous jet. We will return to this point in § 5.

3. OBSERVATIONS

In this paper, we will make use of 3.6 cm continuum observations obtained on 1997 January 10 and 2007 July 2 with the Very Large Array (VLA) of the NRAO[9] in its most extended (A) configuration. This combination of wavelength and configuration provides an angular resolution of about 0.″3 for images with natural weighting. The absolute amplitude calibrator was 1331+305 (with an adopted flux density of 5.20 Jy at 8.4 GHz) and the phase calibrator was 2022+616, with bootstrapped flux densities of 3.36 ± 0.03 Jy and 3.07 ± 0.02 Jy, for the first and second epochs, respectively. For the first epoch only 14 of the 27 antennas of the VLA were used, with an

[8] Farther out, the jet moves on nearly straight trajectories aligned with the direction of the side wind (Cantó & Raga 1995). Since the knots in PV Cep are clearly not moving perpendicularly to the direction of the jet (GA2004), the portion of the jet considered here can be assumed to be parabolic.

[9] The National Radio Astronomy Observatory is operated by Associated Universities Inc. under cooperative agreement with the National Science Foundation.

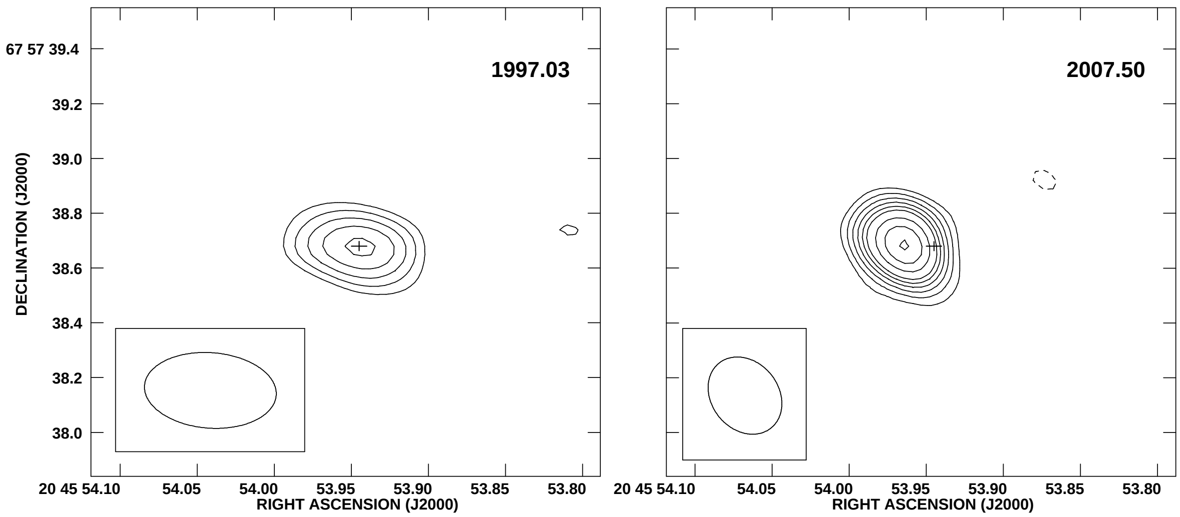

Fig. 2. VLA 3.6 cm images of PV Cep for 1997.03 (left) and 2007.50 (right). The contours are −3, 3, 4, 5, 6, 7, 8, 10, 12 and 14 times 19 and 12 μJy beam^{-1}, the rms noise of the first and second epochs, respectively. The cross marks the position and positional error at the 1997.03 epoch. The half-power synthesized beam for each epoch ($0''.48 \times 0''.28$; PA = +86° for 1997.03 and $0''.30 \times 0''.24$; PA = +39° for 2007.50) is shown in the bottom left corner of the images.

on-source integration time of 4.2 hours. For the second epoch we used 23 of the 27 antennas of the VLA, with an on-source integration time of 3.2 hours. The data were edited and calibrated using the Astronomical Image Processing System (AIPS) software package (Greisen 2003).

To ensure accurate astrometry, the position of the calibrator 2022+616 for the 1997 observations was updated to the refined position given in the VLA catalog of calibrators for 2007. The continuum images shown in Figure 2 were used to measure the positions and flux densities of PV Cep for the two epochs (Table 2). The source appears to be unresolved at both epochs, and the emission is most probably free-free radiation from ionized gas at the base of the outflow driven by PV Cep (i.e., Eislöffel et al. 2000). The small variation in flux density between the two epochs is common for this type of sources (e.g., Galván-Madrid, Ávila, & Rodríguez 2004), and most likely reflects moderate variability either of the mass-loss rate or of the velocity of the wind.

As can be seen in Figure 2 and Table 2, the source shows a small displacement (∼ $0''.11$ toward the east. The proper motions of the source measured over the 10.47 year time baseline of the observations are $\mu_\alpha \cos\delta = +10.9 \pm 3.0$ mas yr^{-1}; $\mu_\delta = +0.2 \pm 1.8$ mas yr^{-1}. The base of the jet driven by PV Cep (as traced by the radio emission) is expected to follow closely the motion of the star itself, because the emission is largely dominated by the highest density gas in the wind, which is located very close to the star since the gas density typically falls as $n(r) \propto r^{-2}$. The high accuracy with which VLA observations of free-free emission from young stars can trace the stellar motions themselves can be seen, for instance, from the multi-epoch observations of IRAS 16293-2422 (Loinard et al. 2007; Pech et al. 2010) or of T Tau N (Loinard, Rodríguez, & Rodríguez 2003). Thus, the proper motions measured here can safely be assumed to represent the motion of PV Cep.

4. RESULTS

To test the proposal of GA2004 that PV Cep might be moving at ∼ 22 km s^{-1} away from NGC 7023, one must compare the proper motion of PV Cep derived above with the proper motion of stars within NGC 7023. The only star of NGC 7023 (and indeed, the only star within a few degrees of PV Cep) for which we found reliable published proper motions is HD 200775, the bright star responsible for most of the illumination of NGC 7023 (see § 1). Since it is the brightest member of the cluster, HD 200775 is likely to be very near its center of mass, and its proper motion should provide a good estimate of the proper motion of the entire cluster. The most recent reported proper motion for HD 200775 can be found in Ducourant et al. (2005)[10]; they give $\mu_\alpha \cos\delta = +11 \pm 2$ mas yr^{-1};

[10]Indeed, Ducourant et al. (2005) also report proper motions for PV Cep. However, their values of $\mu_\alpha \cos\delta =$

TABLE 2

POSITIONS AND FLUX DENSITIES FOR PV CEP

Epoch	Position α(J2000)	Position δ(J2000)	3.6 cm Flux Density (mJy)
1997.03	$20^h45^m53\overset{s}{.}9449 \pm 0\overset{s}{.}0051$	$67°57'38\overset{''}{.}680 \pm 0\overset{''}{.}017$	0.14 ± 0.02
2007.50	$20^h45^m53\overset{s}{.}9651 \pm 0\overset{s}{.}0014$	$67°57'38\overset{''}{.}682 \pm 0\overset{''}{.}008$	0.18 ± 0.01

$\mu_\delta = +2 \pm 2$ mas yr^{-1}. HD 200775 is also contained in the Hipparcos catalog, where the reported proper motions are $\mu_\alpha \cos\delta = +6.74 \pm 0.64$ mas yr^{-1}; $\mu_\delta = -1.48 \pm 0.54$ mas yr^{-1}. These two values are consistent with one another at the 1.5σ level.

The relative motion between PV Cep and NGC 7023 (obtained by subtracting the proper motion of PV Cep measured above from that of NGC 7023) is

$$\Delta(\mu_\alpha \cos\delta) = +0.1 \pm 3.6 \text{ mas yr}^{-1}\,,$$
$$\Delta(\mu_\delta) = +1.8 \pm 2.7 \text{ mas yr}^{-1}\,,$$

if the values quoted by Ducourant et al. (2005) are used. Using the Hipparcos figures, we obtain:

$$\Delta(\mu_\alpha \cos\delta) = -4.2 \pm 3.1 \text{ mas yr}^{-1}\,,$$
$$\Delta(\mu_\delta) = -1.7 \pm 1.9 \text{ mas yr}^{-1}\,.$$

Recall that GA2004 predicted a relative velocity of 22 km s^{-1} toward the west, corresponding to a relative proper motion (almost entirely in right ascension) of $\Delta(\mu_\alpha \cos\delta) = +9.3$ mas yr^{-1}. The observed values are inconsistent at the 3σ level with this prediction,[11] and show that PV Cep is in fact very nearly stationary relative to NGC 7023 both in right ascension and declination. If anything, the Hipparcos value suggests a marginal motion of PV Cep *toward* NGC 7023. We conclude that PV Cep is very unlikely to have been ejected from NGC 7023 about 10^5 yr ago.

Strictly speaking, the analysis of GA2004 does not require PV Cep to be moving away from NGC 7023 at 22 km s^{-1}. It only requires PV Cep to be moving at that speed relative to its surrounding gas. The morphology of the jet driven by PV Cep could still be explained by the model proposed by GA2004 if the gas cloud in which PV Cep is embedded were moving at 22 km s^{-1} *toward the east* relative to both PV Cep and NGC 7023. We consider this possibility very unlikely, however, because (i) as mentioned in § 1, the radial velocities of the gas associated with NGC 7023 and with PV Cep are very similar, and (ii) it is not clear what physical mechanism could accelerate an entire molecular cloud to 22 km s^{-1}, particularly without also accelerating the stars that formed within it.

-3 ± 7 mas yr^{-1}; $\mu_\delta = -14 \pm 7$ mas yr^{-1} have significantly larger errors than our measurements.

[11] They are, of course, even more inconsistent with the relative velocity of 40 km s^{-1} obtained in the detached clump scenario assuming a sound speed of 10 km s^{-1} (see § 2.1).

5. DISCUSSION

Given that a relative velocity of 22 km s^{-1} between PV Cep and its surroundings appears to be inconsistent with the present observations, one must seek a different interpretation of the systematic eastward shift of the bisectors of successive HH pairs along the flow driven by PV Cep. One obvious alternative possibility is provided by the continuous jet model presented in § 2.2. In that scenario, a relative velocity between PV Cep and NGC 7023 of a few km s^{-1} would be sufficient to explain the bisector data, and such a small relative velocity would be fully consistent with the astrometry presented in § 3. We note, indeed, that continuous jet models have been used to explain the curved morphologies of other young stellar flows. Of particular relevance is the case of the jet driven by HH 30 (López et al. 1995) whose curved shape was interpreted by Cantó & Raga (1995) in terms of such a continuous flow in a sidewind.

It is important to note, however, that the flow driven by PV Cep does show clear signs of strong variability (GA2004, and references therein). A steady jet is clearly present in the system, but the knots considered by GA2004 in their bisector analysis have likely been created during episodes of significantly increased mass-loss.[12] To completely describe that situation, one should consider a steady, low-level (i.e., moderate mass-loss rate) underlying jet, periodically undergoing episodes of enhanced mass-loss. This is a case intermediate between the two

[12] Note that the flow in HH 30 appears overall more continuous than that in PV Cep, and does lend itself more naturally to a treatment based on the hypothesis of a steady jet.

idealized descriptions provided in § 2, so numerical simulations would in principle be needed to treat it in general. However, since the periodic mass-loss enhancements undergone by PV Cep seem particularly strong, the correct description for that specific source is almost certainly more similar to the case of detached bullets than to that of a continuous jet. In this situation, a relative velocity between PV Cep and its surroundings of at least 20 km s^{-1} would be needed to explain the bisector results of GA2004, and that appears to be inconsistent with our new measurements.

Another alternative interpretation of the bisector results of GA2004 would be to invoke asymmetries. The basic assumption behind the argumentation of GA2004 is that pairs of clumps ejected from a stationary star propagate symmetrically away from it, in such a way that the bisectors of such ejecta pairs intercept the driving source. This assumption would be violated, however, if the ejecta on the two sides of the star moved away at different speeds and/or not exactly in opposite directions, either because of an intrinsic asymmetry in the jet launching mechanism or because of an asymmetry in the density of the circumstellar material. Several jets (e.g., HH 1–2, Cepheus A, or HH 80; Rodríguez et al. 2000; Martí, Rodríguez, & Reipurth 1998; Curiel et al. 2006) are known to exhibit this kind of asymmetries. Arguably the clearest case is that of the very young low-mass protostar IRAS 16293-2422 (Pech et al. 2010). In this object, a bipolar pair of clumps has been ejected just a few years ago, and each clump has now moved (in projection) about 60 AU away from the central source. Multi-epoch radio observations have shown that the projected speed of the southern clump is two to three times larger than that of the northern clump and that –in at least one of the observations– the line joining the ejecta does not pass through the position of the driving source (Pech et al. 2010, particularly their Figure 2). In addition, the large-scale molecular outflow powered by that jet system is known to be highly asymmetric (e.g., Castets et al. 2001; Hirano et al. 2001), the northern lobe being much more conspicuous, massive, and extended that its southern equivalent. Interestingly, the molecular outflow in PV Cep happens to be equally asymmetric (e.g., Arce & Goodman 2002a) with a northern lobe about 2.5 times more massive and 1.5 times more extended than its southern counterpart. Could an asymmetry similar to that in IRAS 16293-2422 be at the origin of the PV Cep bisector results of GA2004?

Three pairs of HH groups have been identified along the jet driven by PV Cep: HH 315 A, B, and C towards the north-west, and HH 315 D, E, and F toward the south-east (e.g., Gómez et al. 1997, see Figure 3). They are believed to have been created during three episodes of enhanced accretion/ejection (Gómez et al. 1997; GA2004; Arce & Goodman 2002a). Moreover, these HH groups are not distributed along a straight line, but along an S-shaped structure, clearly resulting from precession in the underlying jet (Figure 3). A simple precessing jet model that reasonably accounts for that structure has been proposed by Gómez et al. (1997) and is reproduced in Figure 3a. This model (e.g., Hjellming & Johnston 1981) assumes that the jet axis precesses on the surface of a cone of opening angle θ, inclined by an angle i from the line of sight. The jet has constant ejection velocity v_e and precession velocity ω, and the position angle of the precession axis is ϕ. The black line on Figure 3a corresponds to $\theta = 22.5°$, $i = 80°$, $\omega = 1.5$ arcmin yr^{-1}, $v = 180$ km s^{-1}, and $\phi = -36.5°$ (Gómez et al. 1997). As discussed by Gómez et al. (1997), this model shows that successive episodes of enhanced mass-loss occurred in PV Cep roughly every 2000 years.

An asymmetry in the distribution of the HH groups is immediately apparent in Figure 3a. For instance, while the C-F pair is expected to have been created during the same enhanced mass-loss episode, the symmetric model shown in Figure 3a would ascribe to them ages differing by about 1000 yr. A similar situation occurs for the B-E pair. Of course, this age inconsistency is simply a different way of re-expressing the bisector conclusions of GA2004. Because of the asymmetry in the distribution of the HH groups, the segments joining C to F and B to E do not pass through the current position of the driving source. The situation can be significantly improved by relaxing slightly the symmetry of the jet. As an example, we show in Figure 3b a model identical to that of Gómez et al. (1997) for the northern part of the flow, but slightly different for the southern counterpart. Specifically, the velocity of the southern jet is 10% larger than that of the northern jet, and the southern half of the jet precesses around an axis misaligned by 10° relative to the symmetry axis of the northern jet. Such a model represents a somewhat better fit to the positions of the southern HH groups, and ascribes the same age to the B and E groups (4900 yr) and to the C and F groups (6900 yr). Moreover, the bisector of segments joining pairs of same-age positions on either sides of the jet are progressively displaced towards the east as larger ages are considered. In particular, the bisectors at ages 4900 yr and 6900 yr are very nearly coincident

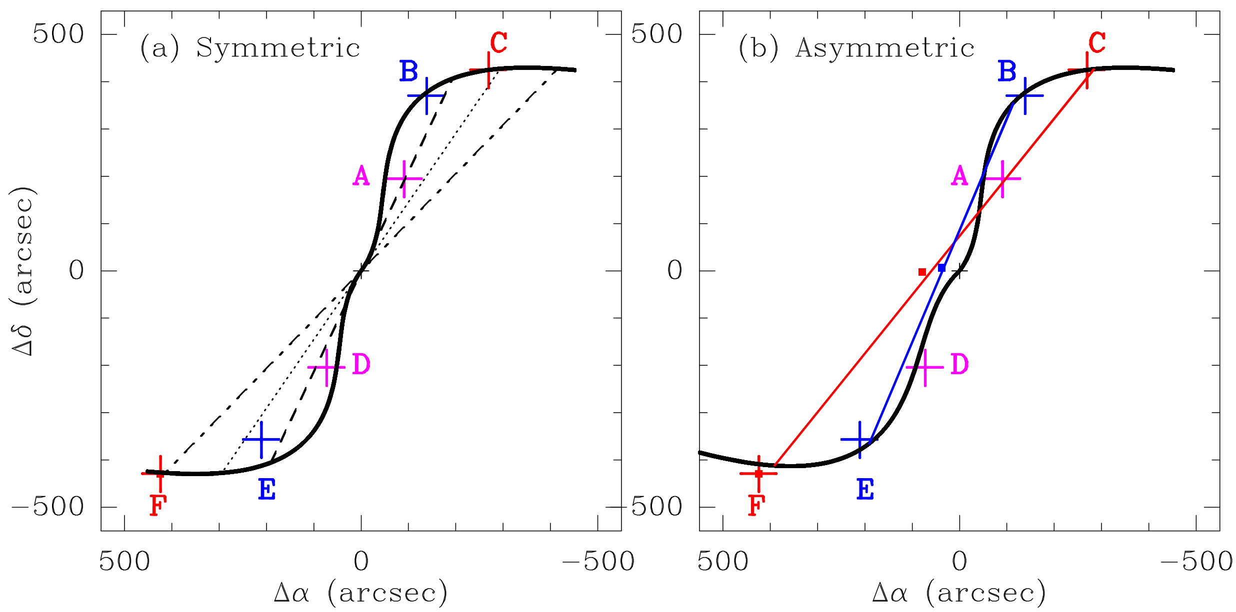

Fig. 3. Distribution of groups of HH knots around PV Cep. The three groups towards the north-west are labelled A, B, and C, and the three groups toward the south-east are D, E, and F. The positions are taken from Gómez et al. (1997). (a) Model based on a symmetric precessing jet following Gómez et al. (1997) with the parameters given in the text (solid black line). Lines joining the expected positions along the jet at times 6000, 7000, and 8000 yr are shown. (b) Model based on an asymmetric precessing jet with the parameters given in the text (solid black line). Lines joining the expected positions along the jet at 4900 and 6900 yr are shown. They intercept the positions of the bisectors of the B-E and C-F pairs (shown as blue and red squares).

with the measured bisectors of the B-E and C-F pairs (Figure 3b).

The model shown in Figure 3b certainly represents an oversimplification of the true structure of the jet in PV Cep, and is clearly not unique. It does demonstrate, however, that a slightly asymmetric jet can provide a better description of the structure of the flow than a symmetric one, and could readily explain the bisector results of GA2004 with no need for a large stellar velocity. It would be interesting to investigate more realistic numerical models of bipolar jets encountering asymmetric surroundings. In particular, it would be useful to know in what domain of the parameter space they can produce bisector results similar to those found in PV Cep by GA2004.

It is worth mentioning that the gas immediately south of PV Cep appears to be significantly denser than the gas immediately north of it (Arce & Goodman 2002a,b). Thus, one might expect the southern lobe to be slower than the northern lobe and not the other way around, as our asymmetric model would suggest. The distribution of the gas surrounding PV Cep, however, is likely to be quite asymmetric. For instance, knot C (to the north) is known to entrain a massive molecular gas shell, whereas no entrained gas is associated with its southern counterpart knot F (Arce & Goodman 2002a,b). This suggests that, on large scales, the density of molecular material north of PV Cep might be higher that south of it. This is reversed compared to the density distribution in the immediate surroundings of PV Cep.

In addition to their bisector results, GA2004 mention two pieces of evidence supporting the idea that PV Cep might be a runaway star. The first one is the existence of a tail of red-shifted gas located to the east of PV Cep. The second is the wiggling of the southern jet seen at small scales. These two effects have not been reported in other outflow systems, and it is unclear if they have a direct relation to the asymmetry of the jet in PV Cep. It certainly would be worthwhile to search for these effects in other outflow systems (symmetric or not) and to investigate numerically in what kind of situation they would tend to develop.

6. CONCLUSIONS

Comparing two VLA observations separated by 10.5 years, we have measured the proper motion of the young star PV Cep. This measurement shows that PV Cep is essentially stationary with respect to its surroundings, and is not a fast-moving runaway star, as suggested by GA2004. The jet morphological characteristics that led GA2004 to conclude that PV Cep might be a runaway star might instead result from an asymmetry in the jet itself. GA2004 had built a case against PV Cep reflected in the title of their paper: "PV Cephei: young star caught speeding?" Given the new evidence presented here, that accusation is now under question.

LFR, LL, JC and ACR acknowledge the support of DGAPA, Universidad Nacional Autónoma de México, and of Conacyt (Mexico). L. G. was supported for this research through a stipend from the International Max Planck Research School (IMPRS) for Astronomy and Astrophysics at the Universities of Bonn and Cologne. This research has made use of the SIMBAD database, operated at CDS, Strasbourg, France.

REFERENCES

Arce, H. G., & Goodman, A. A. 2002a, ApJ, 575, 928
———. 2002b, ApJ, 575, 911
Cantó, J., & Raga, A. C. 1995, MNRAS, 277, 1120
Cantó, J., Raga, A. C., Loinard, L., & Rodríguez, L. F. 2008, RexMexAA, 44, 381
Castets, A., Ceccarelli, C., Loinard, L., Caux, E., & Lefloch, B. 2001, A&A, 375, 40
Cohen, M., Kuhi, L. V., Spinrad, H., & Harlan, E. A. 1981, ApJ, 245, 920
Curiel, S., et al. 2006, ApJ, 638, 878
Ducourant, C., Teixeira, R., Périé, J. P., Lecampion, J. F., Guibert, J., & Sartori, M. J. 2005, A&A, 438, 769
Eislöffel, J., Mundt, R., Ray, T. P., & Rodríguez, L. F. 2000, in Protostars and Planets IV, ed. V. Mannings, A. P. Boss, & S. S. Russell (Tucson: Univ. Arizona Press), 815
Galván-Madrid, R., Ávila, R., & Rodríguez, L. F. 2004, RevMexAA, 40, 31
Gómez, L., Rodríguez, L. F., Loinard, L., Lizano, S., Poveda, A., & Allen, C. 2005, ApJ, 635, 1166
———. 2008, ApJ, 685, 333
Gómez, M., Whitney, B. A., & Kenyon, S. J. 1997, AJ, 114, 1138
Goodman, A. A., & Arce, H. G. 2004, ApJ, 608, 831 (GA2004)
Greisen, E. W. 2003, in Information Handling in Astronomy: Historical Vistas, ed. A. Heck (Dordrecht: Kluwer), 109
Herbig, G. 1960, ApJS, 4, 337
Hirano, N., Mikami, H., Umemoto, T., Yamamoto, S., & Taniguchi, Y. 2001, ApJ, 547, 899
Hjellming, R. M., & Johnston, K. J. 1981, ApJ, 246, L141
Lepine, J. R. D., & Rieu, N. Q. 1974, A&A 36, 469
Li, W., Evans, N. J., II, Harvey, P. M., & Colome, C. 1994, ApJ, 433, 199
Loinard, L., Chandler, C. J., Rodríguez, L. F., D'Alessio, P., Brogan, C., Wilner, D., & Ho, P. 2007, ApJ, 670, 1353
Loinard, L., Rodríguez, L. F., & Rodríguez, M. I. 2003, ApJ, 587, L47
López, R., Raga, A., Riera, A., Anglada, G., & Estalella, R. 1995, MNRAS, 274, L19
Martí, J., Rodríguez, L. F., & Reipurth, B. 1998, ApJ, 502, 337
Masciadri, E., & Raga, A. C. 2001, AJ, 121, 408
Marvel, K. B. 2005, AJ, 130, 2732
Pech, G., et al. 2010, ApJ, 712, 1403
Perryman, M. A. C., et al. 1997, A&A, 323, L49
Poveda, A., Ruiz, J., & Allen, C. 1967, Bol. Obs. Tonantzintla y Tacubaya, 4, 86
Reipurth, B. 2000, AJ, 120, 3177
Reipurth, B., Bally, J., & Devine, D. 1997, AJ, 114, 2708
Rodríguez, L. F., Poveda, A., Lizano, S., & Allen, C. 2005, ApJ, 627, L65
Rodríguez, L. F., et al. 2000, AJ, 119, 882
Valtonen, M., & Mikkola, S. 1991, ARA&A, 29, 9
Zapata, L. A., Schmid-Burgk, J., Ho, P. T. P., Rodríguez, L. F., & Menten, K. M. 2009, ApJ, 704, L45

Laurent Loinard and Luis F. Rodríguez: Centro de Radiostronomía y Astrofísica, Universidad Nacional Autónoma de México, Apdo. Postal 3-72 (Xangari), 58089 Morelia, Michoacán, Mexico (l.loinard, l.rodriguez@crya.unam.mx).
Laura Gómez: Max-Planck-Institut für Radioastronomie, Auf dem Hügel 69, 53121 Bonn, Germany (lgomez@mpifr.de).
Jorge Cantó: Instituto de Astronomía, Universidad Nacional Autónoma de México, Apdo. Postal 70-264, 04510 México, D. F., Mexico.
Alejandro C. Raga: Instituto de Ciencias Nucleares, Universidad Nacional Autónoma de México, Apdo. Postal 70-543, 04510 México, D. F., Mexico (raga@nucleares.unam.mx).
Alyssa A. Goodman: Harvard-Smithsonian Center for Astrophysics, 60 Garden Street, Cambridge, MA 02138, USA (agoodman@cfa.harvard.edu).
Hector G. Arce: Department of Astronomy, Yale University, P.O. Box 208101, New Haven, CT 06520, USA (hector.arce@yale.edu).

Revista Mexicana de Astronomía y Astrofísica, **46**, 385–430 (2010)

CCD *UBVRI* PHOTOMETRY OF THE GALACTIC OPEN CLUSTERS[1]: BE 89, RU 135, AND BE 10

İnci Akkaya,[2] William J. Schuster,[3] Raúl Michel,[3] Carlos Chavarría-K,[3] André Moitinho,[4] Roberto Vázquez,[3] and Yüksel Karataş[5]

Received 2009 May 15; accepted 2010 August 15

RESUMEN

Presentamos los parámetros fundamentales de enrojecimiento, metalicidad, edad y distancia de los cúmulos abiertos poco estudiados Be 89, Ru 135 y Be 10, derivados de la fotometría CCD *UBVRI*. Los enrojecimientos interestelares se midieron en el diagrama color-color, y las metalicidades fotométricas se derivaron del exceso de ultravioleta de las estrellas tipo F. Las distancias y edades se obtuvieron ajustando isocronas a las secuencias observadas en cinco diagramas color-magnitud diferentes. Los promedios ponderados de los módulos de distancia y distancias heliocéntricas $[(V_0 - M_V), d(\mathrm{kpc})]$ son: $(11\overset{\mathrm{m}}{.}90 \pm 0\overset{\mathrm{m}}{.}06, 2.4 \pm 0.06)$ para Be 89, $(9\overset{\mathrm{m}}{.}58 \pm 0\overset{\mathrm{m}}{.}07, 0.81 \pm 0.03)$ para Ru 135 y $(11\overset{\mathrm{m}}{.}16 \pm 0\overset{\mathrm{m}}{.}06, 1.7 \pm 0.05)$ para Be 10, mientras que los promedios ponderados para las edades $[\log(A), A(\mathrm{Gyr})]$ son: $(9.58 \pm 0.06, 3.8 \pm 0.6)$ para Be 89, $(9.58 \pm 0.06, 3.8 \pm 0.7)$ para Ru 135 y $(9.06 \pm 0.05, 1.08 \pm 0.08)$ para Be 10.

ABSTRACT

The fundamental parameters of reddening, metallicity, age, and distance are presented for the poorly studied open clusters Be 89, Ru 135, and Be 10, derived from their CCD *UBVRI* photometry. The interstellar reddenings, $E(B–V)$, were measured in the two-color diagram, and the photometric metallicities, [Fe/H], from the ultraviolet excesses of the F-type stars. By fitting isochrones to the observed sequences of the clusters in five different color-magnitude diagrams, the weighted averages of distance moduli and heliocentric distances $[(V_0–M_V), d(\mathrm{kpc})]$ are $(11\overset{\mathrm{m}}{.}90 \pm 0\overset{\mathrm{m}}{.}06, 2.4 \pm 0.06)$ for Be 89, $(9\overset{\mathrm{m}}{.}58 \pm 0\overset{\mathrm{m}}{.}07, 0.81 \pm 0.03)$ for Ru 135, and $(11\overset{\mathrm{m}}{.}16 \pm 0\overset{\mathrm{m}}{.}06, 1.7 \pm 0.05)$ for Be 10, and the weighted averages of the ages $[\log(A), A(\mathrm{Gyr})]$ are $(9.58 \pm 0.06, 3.8 \pm 0.6)$ for Be 89, $(9.58 \pm 0.06, 3.8 \pm 0.7)$ for Ru 135, and $(9.06 \pm 0.05, 1.08 \pm 0.08)$ for Be 10.

Key Words: open clusters and associations: individual (Be10, Be89, Ru135) — stars: fundamental parameters — stars: Hertzsprung-Russell and C-M diagrams — techniques: photometric

1. INTRODUCTION

Galactic open clusters, which contain a few tens to a few tens of thousands of stars and are a few parsecs across, are sparsely populated, loosely concentrated, and gravitationally bound systems. With systematic image searches and follow-up photometric surveys, new open clusters are currently being discovered. By fitting the photometric observations of open clusters to synthetic photometry resulting from stellar models (i.e., theoretical isochrones), which include the newest input physics, stellar structure, and differing heavy-element abundances, fun-

[1]Based on observations carried out at the San Pedro Mártir National Astronomical Observatory (SPM), operated by Instituto de Astronomía, Universidad Nacional Autónoma de México, Ensenada, B. C., Mexico.

[2]Department of Astronomy and Space Sciences, Erciyes University, Kayseri, Turkey.

[3]Instituto de Astronomía, Universidad Nacional Autónoma de México, Ensenada, B. C., Mexico.

[4]SIM/IDL, Facultade de Ciencias da Universidade de Lisboa, Lisboa, Portugal.

[5]Istanbul University, Science Faculty, Department of Astronomy and Space Sciences, Turkey.

damental parameters such as interstellar reddening, metallicity, distance modulus, and age can be precisely and accurately determined. These parameters have great importance concerning the age-metallicity relation and the metal-abundance gradient in the Galactic disk (e.g., Cameron 1985; Carraro & Chiosi 1994; Friel 1995), as well as the luminosity and mass functions of the open clusters (Piskunov et al. 2008). Open clusters are also very useful for testing the stellar evolutionary models, given that their stars were formed at the same time, out of the same cloud, and under similar environmental conditions. Thus, open clusters are ideal entities for the study of stellar evolution since physical properties are tightly constrained, being mainly distinguished by the stellar mass, so that theoretical models of stellar formation and evolution can be compared with real clusters without excessive complications. For these analyses, the fundamental parameters such as interstellar reddening, metallicity, distance modulus, and age should be determined as precisely and accurately as possible.

In Galactic studies, one of the more severe observational limitations is due to the absence of photometric data for nearly half of the approximately 1500 open clusters known. Furthermore, there is a lack of homogeneity in the observations and analyses of the clusters studied. The catalogue of Lyngå (1987), that resulted from a collection of data from many different sources and which includes 422 open clusters, constituted the observational basis for a large number of astronomical studies, led to important conclusions about the Galactic disk, and has been very useful for planning subsequent observations by other astronomers. However, this catalogue has been built from parameters obtained by various authors, with diverse observing techniques, distinct calibrations, and different criteria for determining the stellar ages, rendering it very inhomogeneous and limited for studies requiring precision in the measurement of these fundamental parameters. As an example of the precision and accuracy that one can expect due to the effects of these inhomogeneities, we refer to Janes & Adler (1982), who found that distance moduli of a given cluster obtained by two or more authors have a mean difference of $0\overset{m}{.}55$.

Within the Sierra San Pedro Mártir, National Astronomical Observatory (hereafter SPM) open cluster project (cf. Schuster et al. 2007; Michael et al. 2010, in preparation), the aims are the following:

1. A common *UBVRI* photometric scale for open clusters.
2. An atlas of color-color and color-magnitude diagrams for these clusters.
3. A homogeneous set of cluster reddenings, distances, ages, and, if possible, metallicities.
4. An increased number of old, significantly reddened, or distant, open clusters.
5. A selection of interesting clusters for further study.

The open clusters for the present study were selected from the large (and most complete) catalogue, "Optically visible open Clusters and Candidates" (Dias et al. 2002), which is now also available at the Centre de Données Astronomiques de Strasbourg (CDS)[6]. This work aims to provide the fundamental parameters of reddening, metallicity, distance modulus and age for the open clusters Be 89, Ru 135, and Be 10. Our final intention is to publish a set of homogeneous photometric *UBVRI* data for over 300 Galactic clusters (Schuster et al. 2007; Tapia et al. 2010).

This paper is organized as follows: § 2 describes the observations and reduction techniques. § 3 contains the derivation from the *UBVRI* photometry of reddening and metallicity of the clusters from two-color diagrams, and the inference of distance moduli and ages from color-magnitude diagrams. Their uncertainties are also discussed. Comparisons of these parameters with previous results from the literature are made in § 4, and the conclusions are given in § 5.

2. OBSERVATION AND REDUCTION TECHNIQUES

2.1. *The observations*

This CCD *UBVRI* project of northern open clusters has been undertaken at SPM using always the same instrumental setup (telescope, CCD-detector, and filters), observing procedures, reduction methods, and system of standard stars (Landolt 1983, 1992). A par focal set of *UBVRI* Johnson-Cousins filters was used for our observations. The 0.84 m f/13 Cassegrain telescope hosted the filter-wheel "Mexman" provided with the SITE#1 (SI003) CCD camera, which has a 1024×1024 square pixel array and a 24 μm $\times$ 24 μm pixel size; this CCD has non-linearities less than 0.45% over a wide dynamical range, no evidence for fringing even in the I band, and Metachrome II and VISAR coverings to increase sensitivity in the blue and near ultraviolet. The sky-projected pixel size was $0\overset{''}{.}393$, and the field of view

[6] `http://www.astro.iag.usp.br/~wilton/`.

TABLE 1

LANDOLT'S FIELDS OF STANDARD STARS

July 2001		February 2002	
Region	N_{stds}	Region	N_{stds}
PG1528+062	3	PG0918+029	5
PG1530+057	3	PG0942-029	5
PG1633+099	5	PG1047+003	4
PG1657+078	4	PG1323-086	5
PG2213-006	4	PG1528+062	3
PG2331+055	3	SA 95	5
MARK A	4	SA104	4
		SA107	4
TOTAL	26	TOTAL	35

of the detector was 6.73×6.73 arcmin^2. Here the results of *UBVRI* images for the open clusters Be 89, Ru 135, and Be 10 are presented, which were acquired in July 2001 (Be 89 and Ru 135) and February 2002 (Be 10). The exposure times were typically 3×240 seconds for the U filter, 3×180 for B, 3×100 for V, 3×100 for R, and 3×120 for I. Several standard-star fields from Landolt (1992) were observed nightly to permit the derivation of the photometric transformations to the Johnson-Cousins' system and the atmospheric extinction coefficients. For the July 2001 observing run, seven Landolt groups were used, containing 26 different standard stars with color ranges, $-0\overset{\mathrm{m}}{.}25 \leq (B-V) \leq +1\overset{\mathrm{m}}{.}14$, $-1\overset{\mathrm{m}}{.}09 \leq (U-B) \leq +1\overset{\mathrm{m}}{.}14$, and $-0\overset{\mathrm{m}}{.}30 \leq (V-I) \leq +1\overset{\mathrm{m}}{.}14$. Sixteen to twenty-five observations of these Landolt standards were made per night. For the February 2002 run, eight Landolt groups were employed, containing 35 different standard stars with color ranges, $-0\overset{\mathrm{m}}{.}30 \leq (B-V) \leq +1\overset{\mathrm{m}}{.}42$, $-1\overset{\mathrm{m}}{.}18 \leq (U-B) \leq +1\overset{\mathrm{m}}{.}27$, and $-0\overset{\mathrm{m}}{.}28 \leq (V-I) \leq +1\overset{\mathrm{m}}{.}77$. Fifty-two to seventy-two observations of these Landolt standards were made per night, except one night cut short by clouds, when only 15 observations were managed. The standard-star fields have been observed with exposures of 1×240 seconds for the U filter, 1×120 for B, 1×60 for V, 1×60 for R, and 1×60 for I. The observed Landolt fields and the number of associated stars in each one are summarized in Table 1.

Usually one or more Landolt fields were reobserved nightly with an air-mass range of at least 0.70 in order to measure the coefficients of the atmospheric extinction of the SPM site, which has excellent sky conditions. To improve the accuracy, precision, and efficiency of the photometric observations when required, the filters were observed in forward and backward sequences (i.e., *UBVRI* − *IRVBU*), especially for the large air-mass observations.

2.2. *Data reduction*

The usual (night and run) calibrations for CCD photometry were done during each of our observing periods (i.e., bias, twilight-sky flat fields, and dark-current determinations) to determine the (night and run) mean correcting frames. Standard data reduction procedures have been used within IRAF,[7] the CCDRED and DAOPHOT tasks (aperture and PSF photometry, see Howell 1989, 1990; Stetson 1987, 1990). More details concerning the instrumentation and the observing and reduction procedures of this project will be given in the near future in the succeeding paper of this project (Michel et al. 2010, in preparation, and references therein). To obtain the magnitudes and colors on the standard system for the stars associated with these clusters, we followed Jordi et al. (1995), and Rosselló et al. (1988, and references therein). We proceeded twofold: (i)

The natural magnitude of the filter N is defined as: $\lambda_{Nn} = -2.5 \cdot \log{(ADU's)_N}$, where λ_N stands for the corresponding filters U, B, V, R, and I, $ADU's$ for the analog-to-digital counts, and the subscript n for the corresponding quantity in the natural photometric system. The atmospheric extinction coefficients for a given filter have been estimated by transforming the nightly λ_{Nn}'s to the corresponding magnitudes in the standard system, λ_{Ns}'s, with the following equation:

$$\lambda_{Ns} - \lambda_{Nn} = (\mathrm{zero\ point})_{\mathrm{N}} - \kappa_{\mathrm{N}}^{'} \cdot \mathrm{X_{Nn}} - \kappa_{N,12}^{''} \cdot X_{Nn} \cdot (\lambda_1 - \lambda_2)_s \,, \tag{1}$$

where X_{Nn} is the air-mass when measuring λ_{Nn}. The subscript $N, 12$ indicates that the color $(\lambda_1 - \lambda_2)_s$ was used to determine the second-order extinction coefficient of filter N. Here we follow the convention that the effective wavelength $\lambda_{1\mathrm{eff}} < \lambda_{2\mathrm{eff}}$ to construct the color $(\lambda_1 - \lambda_2)$. Finally, for a proper determination of $\kappa_N^{'}$ and $\kappa_{N,12}^{''}$ by a least squares solution, sufficiently large ranges in the air masses and colors of the standard stars ($\Delta X_N \geq 0.7$ and $\Delta(\lambda_1 - \lambda_2)_n \geq 0.8$ for SPM) must be obtained. Note that the standard magnitudes and colors are known to an accuracy of about two percent, reflected in the

[7]IRAF is distributed by NOAO (operated by the Association of Universities for Research in Astronomy, Inc.) under cooperative agreement with NSF.

TABLE 2

ATMOSPHERIC EXTINCTION AND TRANSFORMATION COEFFICIENTS

Color	λ_1	λ_2	λ_3	$\kappa_1^{'}$	$\kappa_{1,12}^{''}$	$\kappa_{0,12}$	β_{12}	γ_{12}	rms
					July 2001				
$(U-B)$	U	B	V	0.472	−0.056	+1.625	0.711	+0.263	0.028
$(B-V)$	B	V	–	0.243	−0.050	+0.409	1.016	−0.050	0.010
V	V	R	–	0.106	+0.079	+2.375	0.033	−0.008	0.016
$(V-R)$	V	R	–	0.104*	+0.030*	+0.027	0.973	+0.011	0.012
$(V-I)$	V	I	–	0.087*	−0.035*	−0.151	0.923	+0.070	0.010
					February 2002				
$(U-B)$	U	B	V	0.325	−0.056	+1.765	0.751	+0.313	0.037
$(B-V)$	B	V	–	0.212	−0.050	+0.470	0.979	−0.023	0.018
V	V	R	–	0.082	+0.079	+2.455	0.035	−0.054	0.027
$(V-R)$	V	R	–	0.054*	+0.030*	−0.000	1.023	−0.008	0.012
$(V-I)$	V	I	–	0.056*	−0.035*	−0.165	1.038	+0.004	0.014

*Indicates that extinction coefficients refer to λ_2, otherwise to λ_1.

errors of the final transformations of the (bright) standard stars, and that the observed magnitudes and air masses are measured quantities that can have an even better precision. To further simplify the equations, the extra-atmospheric instrumental magnitudes were then introduced using the extinction coefficients of the night:

$$\lambda_{Ni} = \lambda_{Nn} - \kappa_N^{'} \cdot X_{Nn} - \kappa_{N,12}^{''} \cdot X_{Nn} \cdot (\lambda_1 - \lambda_2)_s \,. \quad (2)$$

An instrumental color is the subtraction of two instrumental magnitudes with different passbands,

$$(\lambda_1 - \lambda_2)_i = \lambda_{1i} - \lambda_{2i} \,.$$

(ii) Once the atmospheric extinction coefficients $\kappa_N^{'}$ and $\kappa_{N,12}^{''}$ have been determined and applied, the nightly transformation coefficients are calculated (i.e., β_{12} and γ_{12}) with the following relations for the colors:

$$(\lambda_1 - \lambda_2)_i = \kappa_{0,12} + \beta_{12} \cdot (\lambda_1 - \lambda_2)_s + \gamma_{12} \cdot (\lambda_1 - \lambda_2)_s^2 \,. \quad (3)$$

Due to the Balmer discontinuity that lies in both the U and B passbands, a better transformation for the $U-B$ color has been achieved by substituting the quadratic term on the right side of the above equation with a linear term in the color $B-V$, obtaining the following expression:

$$(\lambda_1 - \lambda_2)_i = \kappa_{0,12} + \beta_{12} \cdot (\lambda_1 - \lambda_2)_s + \gamma_{12} \cdot (\lambda_2 - \lambda_3)_s , \quad (4)$$

where $\lambda_{1\mathrm{eff}} < \lambda_{2\mathrm{eff}} < \lambda_{3\mathrm{eff}}$. For the case of the magnitude V, equation (3) has been used as follows:

$$V_i - V_s = \kappa_{01} + \beta_{12} \cdot (\lambda_1 - \lambda_2)_s + \gamma_{12} \cdot (\lambda_1 - \lambda_2)_s^2 \,. \quad (5)$$

For equations (3)–(5), $\kappa_{0,12}$ and κ_{01} are the zero-points of the transformations of the colors $(\lambda_1 - \lambda_2)_s$, i.e., $U-B$, $B-V$, $V-R$, $V-I$, etc., and of the V magnitude, respectively. The coefficients β_{12} and γ_{12} are the respective first- and second-order transformation coefficients.

In general, the second-order atmospheric extinction coefficient $\kappa_{VR}^{''}$ is expected to be close to zero due to the nearly constant level (ozone-band contribution) of the atmospheric extinction curve at SPM near 5500 Å (Schuster & Parrao 2001). The second-order extinction and linear-transformation coefficients for correcting to extra-atmospheric standard magnitudes and colors are very similar from night to night, and also from run to run, because, (i) the SPM has excellent sky conditions, and (ii) the same instrumental setup, observing techniques, and data reduction procedures were used for all nights during both observing runs. In Table 2 the mean zero-point corrections, atmospheric extinction, and transformation coefficients are given.

In Tables 3, 4, and 5 are given the final transformed CCD *UBVRI* photometric values for the open clusters, Be 89, Ru 135, and Be 10, respectively. In these tables Columns 1 and 2 give the X and Y (pixels) the position of a star in the CCD field; Columns 3, 5, 7, 9, and 11 the magnitude and color indices V, $(B-V)$, $(U-B)$, $(V-R)$, and $(V-I)$, respectively (in magnitudes); and Columns 4, 6, 8, 10, and 12 the respective photometric errors, $\sigma_V, \sigma_{B-V}, \sigma_{U-B}, \sigma_{V-R}$, and σ_{V-I} (in magnitudes), as provided by IRAF.

TABLE 3

CCD *UBVRI* PHOTOMETRY OF BE 89

X	Y	V	σ_V	$(B-V)$	σ_{B-V}	$(U-B)$	σ_{U-B}	$(V-R)$	σ_{V-R}	$(V-I)$	σ_{V-I}
767.7	538.3	11.261	0.006	0.441	0.009	0.002	0.007	0.315	0.009	99.999	99.999
466.5	496.2	12.118	0.011	1.362	0.018	1.191	0.011	0.742	0.013	1.399	0.013
511.7	742.6	12.172	0.008	0.443	0.011	0.268	0.005	0.296	0.011	0.569	0.017
213	99.5	12.333	0.006	0.791	0.009	0.359	0.007	0.378	0.012	99.999	99.999
741.7	403.2	12.911	0.005	1.193	0.007	0.855	0.008	0.629	0.008	1.182	0.01
113.3	465.7	13.309	0.004	0.658	0.006	−0.019	0.006	0.351	0.005	0.705	0.006
678.3	596.5	13.754	0.006	1.921	0.014	1.75	0.024	1.058	0.009	2	0.012
464.6	338.7	13.761	0.006	0.706	0.01	0.07	0.01	0.396	0.008	0.725	0.007
834.1	610.2	13.972	0.004	0.735	0.007	0.113	0.009	0.403	0.007	0.777	0.006
701.2	578.9	13.98	0.005	0.875	0.009	0.333	0.011	0.508	0.01	0.932	0.008
254.5	280.4	14.089	0.004	0.819	0.007	0.176	0.009	0.463	0.006	0.897	0.006
198	28.1	14.141	0.016	1.317	0.025	0.695	0.015	0.871	0.019	1.663	0.017
312.4	276.8	14.279	0.004	1.948	0.014	2.029	0.041	1.023	0.006	1.985	0.007
541.6	770.5	14.368	0.01	1.818	0.059	1.688	0.058	0.95	0.015	1.842	0.015
334.6	31.2	14.416	0.006	0.779	0.01	0.179	0.012	0.425	0.009	0.853	0.008
842.2	789.4	14.475	0.004	2.238	0.012	99.999	99.999	1.33	0.006	2.632	0.011
592.1	526.6	14.528	0.006	0.79	0.011	0.104	0.011	0.422	0.009	0.858	0.009
560.7	782.1	14.593	0.006	0.868	0.009	0.25	0.013	0.454	0.007	0.902	0.007
613.3	190.6	14.663	0.006	1.711	0.018	99.999	99.999	0.907	0.01	1.785	0.008
675.9	887.1	14.669	0.005	0.846	0.009	0.241	0.013	0.481	0.006	0.929	0.006
360.9	268.5	14.678	0.004	1.717	0.011	1.441	0.032	0.901	0.006	1.683	0.006
482.7	702.4	14.727	0.005	1.649	0.011	1.23	0.029	0.895	0.007	1.752	0.007
645.6	248.1	14.744	0.006	0.691	0.009	0.366	0.013	0.353	0.008	0.787	0.007
268.8	739	14.759	0.005	1.001	0.01	0.655	0.015	0.55	0.007	1.024	0.007
399.4	206.7	14.83	0.006	0.914	0.01	0.308	0.015	0.518	0.007	0.95	0.007
323	88.8	14.851	0.006	0.726	0.009	0.131	0.013	0.409	0.007	0.829	0.007
791.4	99.7	14.862	0.005	1.574	0.012	1.299	0.033	0.872	0.008	1.696	0.007
416.2	595.1	14.916	0.006	0.829	0.012	0.256	0.015	0.443	0.008	0.878	0.008
219.1	264.4	14.92	0.004	0.83	0.008	0.184	0.014	0.481	0.006	0.913	0.006
758.7	277.5	15.017	0.003	1.582	0.01	1.294	0.035	0.868	0.006	1.68	0.005
385.7	51	15.02	0.005	1.059	0.01	0.974	0.022	0.612	0.007	1.092	0.007
797.4	412.5	15.033	0.004	1.676	0.012	1.436	0.042	0.916	0.007	1.763	0.006
196	157.7	15.054	0.004	1.644	0.013	1.39	0.041	0.89	0.007	1.715	0.006
365.3	316	15.062	0.006	0.687	0.01	0.347	0.013	0.363	0.007	0.79	0.007
338.1	499.2	15.082	0.029	1.49	0.048	99.999	99.999	0.897	0.037	1.713	0.032
579.6	621.2	15.095	0.006	1.553	0.018	1.32	0.046	0.874	0.012	1.684	0.013
738.4	183	15.1	0.005	0.983	0.01	0.543	0.024	0.495	0.006	0.986	0.006
640.5	610.8	15.128	0.006	1.618	0.015	1.289	0.042	0.917	0.01	1.726	0.009
535.4	889.9	15.137	0.004	1.647	0.01	1.373	0.041	0.884	0.006	1.718	0.006
521.7	859.9	15.181	0.004	1.652	0.012	1.448	0.042	0.909	0.007	1.733	0.007
923.2	159.1	15.185	0.007	0.816	0.015	0.248	0.02	0.465	0.01	0.974	0.009
648.5	469.9	15.227	0.006	1.596	0.015	1.371	0.044	0.878	0.01	99.999	99.999
620.5	76.6	15.257	0.006	0.906	0.011	0.312	0.018	0.508	0.007	0.998	0.007
408.6	525	15.258	0.006	0.705	0.012	0.313	0.017	0.408	0.009	0.884	0.007
574.2	818	15.283	0.004	1.718	0.013	1.414	0.049	0.914	0.007	1.785	0.007
697.8	177.7	15.297	0.005	1.225	0.012	0.75	0.027	0.643	0.007	1.283	0.007
916.7	274.2	15.308	0.004	1.523	0.012	1.284	0.037	0.818	0.007	1.602	0.006
601.1	523.6	15.338	0.007	0.671	0.012	0.251	0.015	0.403	0.01	0.884	0.01
53	615	15.445	0.008	1.002	0.016	0.516	0.026	0.527	0.011	1.011	0.01
350.5	182.5	15.466	0.006	0.911	0.011	0.326	0.025	0.5	0.008	1.006	0.007
112.3	890.9	15.494	0.011	0.863	0.019	0.22	0.022	0.521	0.016	0.961	0.024
389.8	609.1	15.51	0.006	0.807	0.011	0.09	0.016	0.456	0.008	0.885	0.007
803	547.1	15.534	0.005	1.337	0.012	1.052	0.041	0.763	0.008	1.397	0.007
538	360.7	15.571	0.007	1.071	0.014	0.379	0.02	0.641	0.009	1.239	0.008
925.7	533.9	15.576	0.006	0.997	0.011	0.578	0.026	0.537	0.007	1.01	0.007
594.4	466.9	15.658	0.007	0.873	0.013	0.559	0.023	0.471	0.01	1.031	0.009
653.4	273.1	15.665	0.006	0.77	0.012	0.357	0.02	0.456	0.008	0.952	0.008
299.5	235.1	15.713	0.006	1.038	0.012	0.406	0.026	0.609	0.008	1.23	0.007
298.7	224.4	15.766	0.006	0.979	0.011	0.271	0.024	0.542	0.008	1.115	0.007
330	898.6	15.832	0.007	2.318	0.023	99.999	99.999	1.272	0.009	2.36	0.007
969	823.5	15.875	0.007	1.662	0.018	1.08	0.063	0.982	0.01	1.87	0.008
328.6	933.5	15.876	0.008	0.839	0.015	0.127	0.02	0.491	0.011	0.959	0.01
281.7	565.7	15.921	0.006	0.979	0.014	0.506	0.03	0.497	0.008	0.976	0.009

TABLE 3 (CONTINUED)

X	Y	V	σ_V	$(B-V)$	σ_{B-V}	$(U-B)$	σ_{U-B}	$(V-R)$	σ_{V-R}	$(V-I)$	σ_{V-I}
337.1	623.4	15.964	0.033	1.211	0.052	0.477	0.035	0.656	0.047	1.349	0.035
375.5	847.5	15.993	0.007	0.994	0.015	0.453	0.031	0.542	0.009	1.044	0.009
110.4	961	16.023	0.012	0.917	0.022	0.315	0.027	0.567	0.018	1.051	0.034
713.7	22.8	16.05	0.014	0.946	0.023	0.373	0.035	0.559	0.034	1.207	0.023
451	508.7	16.078	0.006	1.176	0.016	0.392	0.041	0.679	0.009	1.366	0.009
369.5	170.1	16.087	0.006	1.074	0.014	0.431	0.03	0.641	0.008	1.262	0.007
162.3	731	16.115	0.008	1.018	0.016	0.458	0.031	0.582	0.01	1.158	0.009
271.3	105.4	16.162	0.008	0.983	0.016	0.297	0.029	0.551	0.01	1.104	0.01
471.7	585.8	16.185	0.006	1.207	0.015	0.464	0.037	0.655	0.01	1.359	0.008
356.9	708	16.191	0.006	1.081	0.016	0.463	0.029	0.634	0.008	1.33	0.007
476.4	570.8	16.2	0.012	1.113	0.024	0.451	0.037	0.639	0.029	1.285	0.026
181.2	944.2	16.211	0.009	1.182	0.021	0.455	0.036	0.724	0.016	1.34	0.027
802	593.9	16.212	0.007	0.882	0.015	0.252	0.029	0.494	0.009	0.956	0.009
22.8	76.8	16.24	0.012	0.897	0.022	0.305	0.032	0.57	0.017	1.103	0.015
276.6	796	16.241	0.007	2.443	0.026	99.999	99.999	1.332	0.009	2.534	0.008
512.7	161.5	16.248	0.007	1.015	0.015	0.379	0.035	0.588	0.01	1.206	0.008
234.9	633.8	16.28	0.006	1.634	0.019	1.317	0.087	0.901	0.008	1.712	0.007
329	471.8	16.291	0.011	1.307	0.024	1.078	0.055	0.727	0.019	1.429	0.026
489.9	562.9	16.304	0.007	0.927	0.016	0.405	0.031	0.53	0.01	1.098	0.009
733.2	794.9	16.312	0.006	1.208	0.016	0.617	0.04	0.717	0.009	1.435	0.008
305.2	840.3	16.322	0.005	1.173	0.016	0.614	0.045	0.694	0.008	1.378	0.008
437	570.1	16.329	0.008	1.223	0.019	0.526	0.04	0.682	0.012	1.393	0.01
535.2	540.7	16.358	0.008	1.619	0.022	1.143	0.081	0.92	0.011	1.736	0.01
918.4	181.7	16.358	0.008	1.065	0.018	0.713	0.056	0.585	0.012	1.102	0.009
800.1	734.7	16.359	0.006	1.084	0.015	0.722	0.042	0.595	0.009	1.122	0.008
550.3	660.5	16.378	0.007	0.987	0.016	0.35	0.027	0.531	0.01	1.121	0.009
32.2	883.4	16.394	0.015	0.99	0.028	0.285	0.037	0.585	0.02	99.999	99.999
985.1	387.1	16.407	0.008	2.525	0.035	99.999	99.999	1.364	0.01	2.644	0.008
31.9	844.7	16.409	0.015	1.148	0.028	0.624	0.051	0.631	0.02	99.999	99.999
172.4	134.1	16.413	0.008	1.067	0.019	0.538	0.044	0.613	0.011	1.262	0.01
196.1	310.2	16.421	0.007	1.047	0.016	0.436	0.037	0.558	0.009	1.102	0.009
624	463.7	16.428	0.008	0.975	0.016	0.5	0.043	0.533	0.011	1.055	0.012
860.7	116.4	16.432	0.007	1.057	0.019	0.44	0.039	0.643	0.012	1.289	0.009
555.2	346.8	16.457	0.012	1.537	0.022	1.151	0.074	0.851	0.011	1.67	0.009
659.5	820.6	16.457	0.007	1.293	0.019	0.622	0.052	0.739	0.01	1.471	0.009
502.4	82.9	16.467	0.007	1.077	0.017	0.407	0.038	0.648	0.01	1.279	0.01
797.1	496.5	16.472	0.007	1.024	0.016	0.397	0.035	0.625	0.011	1.275	0.008
89.5	532.4	16.492	0.008	1.681	0.023	99.999	99.999	0.924	0.011	1.786	0.009
852.3	148.8	16.501	0.01	0.886	0.021	0.361	0.035	0.551	0.014	1.051	0.029
602.7	723.9	16.515	0.008	2.703	0.043	99.999	99.999	1.587	0.01	3.138	0.008
910.3	744.4	16.523	0.007	1.097	0.018	0.384	0.033	0.679	0.01	1.35	0.009
474.6	116.8	16.527	0.007	1.121	0.019	0.381	0.041	0.642	0.01	1.271	0.009
155.5	37.2	16.538	0.01	1.145	0.021	0.705	0.05	0.638	0.014	1.212	0.03
667.2	46.2	16.554	0.007	1.143	0.016	99.999	99.999	0.569	0.01	1.123	0.009
340	851.1	16.556	0.008	1.061	0.018	0.213	0.041	0.605	0.011	1.195	0.01
612.5	514.7	16.565	0.008	1.09	0.018	0.459	0.04	0.618	0.012	1.301	0.011
638.7	75.3	16.576	0.007	1.082	0.019	0.376	0.041	0.626	0.011	1.26	0.01
121.6	104.7	16.587	0.01	2.263	0.036	99.999	99.999	1.248	0.013	2.36	0.011
148.3	445.5	16.587	0.008	1.048	0.018	0.335	0.036	0.6	0.01	1.217	0.009
566.6	490.7	16.594	0.011	1.077	0.025	0.411	0.049	0.656	0.019	1.314	0.014
489.2	177	16.597	0.007	1.148	0.019	0.428	0.05	0.623	0.01	1.271	0.009
190.8	98.6	16.61	0.009	1.016	0.02	0.394	0.043	0.528	0.012	1.074	0.011
16.9	777.2	16.621	0.013	1.13	0.027	0.337	0.046	0.646	0.018	1.275	0.017
634.9	654.1	16.621	0.009	1.07	0.019	0.304	0.039	0.622	0.013	1.25	0.012
366.6	579.9	16.632	0.007	1.145	0.02	0.421	0.043	0.691	0.011	1.383	0.01
481.7	654.7	16.632	0.008	1.155	0.021	0.491	0.048	0.649	0.012	1.371	0.01
951.4	209.9	16.633	0.012	1.097	0.025	0.623	0.05	0.594	0.02	1.104	0.029
809.9	321.1	16.646	0.007	1.114	0.019	0.429	0.042	0.645	0.011	1.276	0.009
479	327.2	16.669	0.008	1.193	0.021	0.889	0.064	0.626	0.012	1.168	0.011
540.8	337.6	16.68	0.013	1.412	0.024	1.014	0.08	0.819	0.013	1.583	0.011
804.6	180.9	16.684	0.018	1.015	0.036	0.396	0.063	0.421	0.049	1.112	0.043
705.8	675	16.7	0.008	1.016	0.019	0.349	0.036	0.609	0.011	1.254	0.011
126.4	135.2	16.706	0.008	1.022	0.018	0.358	0.038	0.564	0.012	1.127	0.011
70.3	281.9	16.71	0.007	1.154	0.021	0.568	0.055	0.678	0.012	1.367	0.011
231.1	990	16.711	0.009	1.063	0.023	0.424	0.05	0.65	0.016	1.302	0.014

TABLE 3 (CONTINUED)

X	Y	V	σ_V	$(B-V)$	σ_{B-V}	$(U-B)$	σ_{U-B}	$(V-R)$	σ_{V-R}	$(V-I)$	σ_{V-I}
699.6	149.3	16.725	0.008	1.137	0.02	0.445	0.05	0.629	0.011	1.279	0.01
521.1	506	16.726	0.007	1.203	0.022	0.423	0.051	0.69	0.012	1.379	0.01
535.5	304.3	16.752	0.014	99.999	99.999	99.999	99.999	0.548	0.05	99.999	99.999
228.4	593.8	16.755	0.008	1.067	0.018	0.297	0.049	0.643	0.012	1.264	0.012
457.6	417.9	16.765	0.008	1.084	0.02	0.501	0.049	0.612	0.011	1.239	0.01
341.7	150.6	16.767	0.007	1.055	0.02	0.343	0.05	0.632	0.011	1.209	0.01
117.5	677.4	16.768	0.007	1.098	0.021	0.412	0.056	0.699	0.012	1.341	0.009
609.1	701.3	16.776	0.008	0.944	0.018	0.242	0.044	0.574	0.012	1.171	0.01
285.2	586.1	16.781	0.008	1.19	0.02	0.556	0.058	0.709	0.011	1.379	0.01
137	372.4	16.781	0.008	1.079	0.021	0.407	0.05	0.629	0.012	1.224	0.011
283.5	57.3	16.786	0.008	1.033	0.021	0.301	0.041	0.611	0.011	1.225	0.01
875.4	230.6	16.791	0.009	1.686	0.025	99.999	99.999	0.932	0.012	1.824	0.01
646	637.8	16.793	0.008	0.941	0.018	0.255	0.046	0.579	0.01	1.061	0.01
950.4	189.7	16.796	0.009	1.119	0.022	0.444	0.047	0.617	0.014	1.303	0.012
702.9	955.9	16.802	0.008	1.073	0.021	0.389	0.051	0.648	0.013	1.277	0.011
791.6	205.4	16.805	0.007	1.029	0.018	0.396	0.041	0.571	0.01	1.208	0.009
444.9	34.3	16.806	0.011	1.078	0.029	0.605	0.058	0.661	0.019	1.244	0.032
27.9	886.1	16.809	0.015	1.125	0.031	0.408	0.055	0.581	0.042	99.999	99.999
346.7	344	16.846	0.009	1.112	0.021	0.456	0.059	0.63	0.012	1.311	0.012
865	505.3	16.847	0.007	1.166	0.022	0.525	0.047	0.705	0.012	1.397	0.01
528.3	698.1	16.851	0.008	1.096	0.019	0.392	0.05	0.634	0.012	1.291	0.01
796.7	158.7	16.856	0.009	2.059	0.037	99.999	99.999	1.138	0.012	2.192	0.009
89	808.1	16.857	0.012	2.062	0.037	99.999	99.999	1.105	0.017	2.137	0.014
875.6	485.8	16.857	0.008	1.21	0.025	0.575	0.055	0.599	0.014	1.234	0.011
337.5	763	16.858	0.011	1.084	0.025	0.489	0.057	0.571	0.018	1.149	0.016
363.3	573.6	16.872	0.009	0.991	0.019	0.256	0.047	0.583	0.012	1.194	0.011
345	253.6	16.885	0.007	1.132	0.02	0.474	0.047	0.657	0.011	1.347	0.011
397.1	845.7	16.891	0.008	1.041	0.02	0.36	0.048	0.628	0.012	1.278	0.01
559.6	440	16.897	0.008	1.09	0.022	0.364	0.051	0.616	0.013	1.282	0.011
737.7	258.6	16.903	0.011	0.866	0.021	0.513	0.05	0.515	0.014	1.087	0.013
64.4	175.6	16.906	0.009	1.845	0.032	99.999	99.999	1.05	0.013	2.038	0.011
441.6	469.4	16.912	0.008	1.121	0.022	0.537	0.056	0.677	0.013	1.294	0.012
621.1	540.1	16.914	0.01	1.047	0.023	0.406	0.055	0.601	0.013	1.146	0.012
548.5	711.8	16.916	0.008	1.117	0.024	0.302	0.054	0.642	0.013	1.285	0.011
393.8	473.8	16.919	0.015	1.134	0.034	0.38	0.052	0.726	0.045	1.456	0.019
960.9	931.9	16.927	0.008	1.093	0.022	0.691	0.061	0.649	0.015	1.345	0.013
474.1	552.7	16.932	0.008	1.165	0.023	0.553	0.069	0.649	0.012	1.333	0.012
228.6	274.8	16.936	0.01	0.965	0.023	0.636	0.06	0.559	0.013	1.093	0.012
490.7	545	16.941	0.01	1.693	0.03	99.999	99.999	0.94	0.013	1.866	0.011
507.7	216	16.978	0.007	1.122	0.023	0.517	0.061	0.646	0.012	1.27	0.011
907.1	680	16.98	0.008	1.142	0.021	0.464	0.067	0.631	0.011	1.326	0.01
763.3	911.5	16.987	0.008	1.076	0.025	0.419	0.05	0.654	0.012	1.322	0.012
199.4	13.4	16.989	0.01	1.065	0.025	0.363	0.056	0.597	0.016	1.266	0.015
431	371.1	16.995	0.009	2.693	0.051	99.999	99.999	1.471	0.012	2.801	0.009
465.3	114.7	17.017	0.014	1.188	0.03	99.999	99.999	0.744	0.021	1.357	0.036
307.3	234.8	17.022	0.01	2.23	0.043	99.999	99.999	1.252	0.012	2.387	0.011
539	303.5	17.023	0.017	99.999	99.999	99.999	99.999	0.508	0.06	99.999	99.999
723.5	743	17.031	0.01	1.928	0.035	99.999	99.999	1.046	0.012	2.081	0.011
676.3	716.3	17.037	0.006	1.093	0.02	0.316	0.056	0.613	0.011	1.253	0.01
960.1	844.3	17.038	0.011	1.191	0.026	0.519	0.067	0.719	0.015	1.408	0.012
462.5	542.5	17.054	0.011	0.865	0.023	0.454	0.054	0.557	0.014	1.073	0.012
644.8	122.5	17.064	0.012	1.052	0.031	0.46	0.063	0.596	0.019	1.226	0.014
938.6	483.7	17.065	0.009	1.026	0.022	0.48	0.059	0.607	0.012	1.3	0.012
910.1	919.8	17.07	0.008	1.079	0.023	0.349	0.065	0.646	0.013	1.281	0.013
473	611.3	17.076	0.009	1.165	0.026	0.467	0.064	0.676	0.014	1.342	0.012
110.2	642.8	17.086	0.01	1.142	0.024	0.466	0.065	0.645	0.014	1.319	0.013
743.3	347.4	17.09	0.01	1.134	0.023	0.465	0.058	0.615	0.014	1.292	0.013
139.5	848.1	17.095	0.012	0.986	0.025	0.325	0.06	0.594	0.018	1.171	0.015
444.2	599.1	17.101	0.008	1.133	0.025	0.35	0.06	0.66	0.012	1.338	0.012
802.7	294.5	17.103	0.006	1.031	0.022	0.533	0.068	0.613	0.011	1.164	0.01
262.2	983.6	17.11	0.01	1.12	0.025	0.45	0.066	0.61	0.015	1.226	0.013
30.5	544.8	17.116	0.009	1.1	0.026	0.282	0.06	0.629	0.015	1.3	0.013
352.4	618.3	17.135	0.008	1.107	0.025	0.372	0.07	0.609	0.012	1.285	0.011
588	777.6	17.138	0.008	1.07	0.024	0.36	0.067	0.618	0.012	1.226	0.011
328.1	375.7	17.139	0.011	1.051	0.026	0.389	0.066	0.578	0.015	1.176	0.014

TABLE 3 (CONTINUED)

X	Y	V	σ_V	$(B-V)$	σ_{B-V}	$(U-B)$	σ_{U-B}	$(V-R)$	σ_{V-R}	$(V-I)$	σ_{V-I}
483.7	613.6	17.148	0.009	1.14	0.026	0.647	0.083	0.666	0.015	1.34	0.013
863.8	539.9	17.151	0.01	1.026	0.025	0.254	0.058	0.562	0.014	1.119	0.012
433.7	875.2	17.155	0.009	1.105	0.022	0.388	0.068	0.587	0.012	1.241	0.011
659.9	385.8	17.156	0.008	2.042	0.036	99.999	99.999	1.122	0.012	2.142	0.01
6.8	313.8	17.16	0.013	1.108	0.028	0.39	0.061	0.616	0.017	1.308	0.016
798.5	918.2	17.16	0.009	1.403	0.024	99.999	99.999	0.821	0.012	1.626	0.01
500.4	607.6	17.163	0.009	1.122	0.025	0.462	0.061	0.631	0.014	1.316	0.013
122.5	981.5	17.164	0.011	1.112	0.03	0.407	0.066	0.646	0.02	1.298	0.017
105.6	945.9	17.172	0.012	1.529	0.034	99.999	99.999	0.865	0.018	1.588	0.034
228.4	154.3	17.183	0.011	1.112	0.028	0.403	0.062	0.645	0.016	1.287	0.015
422.2	539.7	17.183	0.008	1.046	0.026	0.412	0.073	0.636	0.012	1.299	0.012
370.6	439	17.184	0.009	1.051	0.027	0.351	0.055	0.638	0.014	1.285	0.012
234.2	343.7	17.186	0.011	1.187	0.026	99.999	99.999	0.655	0.017	1.367	0.016
227.1	821.9	17.192	0.008	1.085	0.023	0.339	0.062	0.65	0.014	1.322	0.012
465.7	248.2	17.192	0.009	1.103	0.027	0.514	0.08	0.649	0.014	1.316	0.012
939.4	176.1	17.192	0.01	1.276	0.026	99.999	99.999	0.68	0.013	1.285	0.011
698.4	981.9	17.203	0.009	1.132	0.023	0.379	0.073	0.675	0.013	1.323	0.012
577.4	617	17.206	0.017	1.051	0.04	0.388	0.076	0.648	0.026	1.316	0.023
841.5	346.2	17.211	0.011	0.902	0.023	0.442	0.052	0.545	0.013	1.135	0.012
191.2	676.1	17.226	0.012	1.195	0.026	0.488	0.083	0.723	0.014	1.361	0.012
433.9	990.1	17.239	0.007	1.035	0.024	0.315	0.066	0.632	0.013	1.306	0.011
990.5	723.5	17.239	0.009	1.11	0.027	0.497	0.071	0.661	0.014	1.364	0.013
256.6	669.7	17.24	0.009	1.123	0.024	0.443	0.09	0.653	0.014	1.331	0.012
72.1	429.1	17.242	0.01	1.236	0.026	0.365	0.079	0.65	0.016	1.36	0.014
718.7	71.2	17.242	0.011	1.323	0.03	99.999	99.999	0.798	0.013	1.492	0.013
78.1	850.3	17.252	0.012	1.131	0.032	0.516	0.081	0.644	0.02	1.243	0.017
18.5	219.1	17.275	0.01	1.147	0.025	0.244	0.067	0.65	0.018	1.289	0.014
155.1	955.3	17.275	0.012	1.127	0.032	0.594	0.094	0.648	0.021	1.242	0.018
167	21.9	17.281	0.015	1.143	0.035	99.999	99.999	0.647	0.021	1.348	0.018
295.3	505.3	17.283	0.011	1.932	0.042	99.999	99.999	1.1	0.014	2.109	0.012
828.6	353.3	17.287	0.01	1.08	0.025	0.365	0.065	0.631	0.014	1.299	0.013
225.2	114.1	17.3	0.013	1.36	0.038	99.999	99.999	0.828	0.017	1.567	0.015
768.4	225	17.306	0.01	1.067	0.028	0.302	0.072	0.631	0.016	1.253	0.013
756.9	386.8	17.307	0.008	1.145	0.025	0.255	0.07	0.664	0.013	1.308	0.011
441.8	494.7	17.311	0.011	1.193	0.026	0.398	0.069	0.7	0.015	1.36	0.014
838.2	847.6	17.316	0.009	1.105	0.027	0.333	0.056	0.676	0.013	1.354	0.012
916	358.1	17.327	0.01	1.089	0.026	0.611	0.096	0.652	0.015	1.349	0.013
900.7	93.4	17.331	0.01	1.051	0.029	0.715	0.082	0.687	0.017	1.401	0.012
273.2	622.7	17.333	0.007	1.028	0.022	0.578	0.072	0.642	0.012	1.301	0.011
537.3	569.2	17.337	0.011	1.088	0.026	0.335	0.074	0.69	0.015	1.322	0.014
292.2	742.1	17.348	0.011	1.107	0.025	0.443	0.086	0.686	0.015	1.348	0.016
522.9	33.2	17.354	0.01	1.308	0.031	99.999	99.999	0.678	0.014	1.315	0.012
520.8	847.5	17.357	0.011	1.113	0.028	99.999	99.999	0.657	0.016	1.275	0.014
331.5	821.6	17.364	0.008	1.062	0.025	0.413	0.065	0.648	0.014	1.246	0.013
491.6	464.3	17.373	0.01	1.119	0.027	0.275	0.068	0.644	0.016	1.314	0.014
496.6	132.8	17.374	0.011	1.092	0.029	0.496	0.105	0.671	0.016	1.317	0.014
715.5	758.5	17.381	0.012	1.233	0.03	99.999	99.999	0.667	0.015	1.335	0.014
560.8	66.1	17.383	0.012	1.208	0.032	99.999	99.999	0.683	0.016	1.405	0.013
649.7	229.5	17.384	0.01	2.199	0.048	99.999	99.999	1.168	0.014	2.263	0.011
451.4	513.5	17.391	0.016	1.191	0.036	99.999	99.999	0.661	0.02	1.423	0.018
27.4	448.9	17.395	0.01	1.132	0.029	0.41	0.093	0.671	0.014	1.359	0.013
91.2	632.9	17.397	0.009	1.184	0.029	0.378	0.088	0.638	0.015	1.274	0.013
694.9	797.3	17.397	0.01	1.134	0.028	0.531	0.075	0.656	0.016	1.364	0.016
282.6	702.2	17.406	0.011	1.08	0.028	0.427	0.082	0.688	0.013	1.344	0.013
729.7	314.3	17.419	0.011	1.022	0.029	0.365	0.078	0.576	0.015	1.232	0.013
480.3	645.2	17.432	0.013	2.001	0.045	99.999	99.999	1.109	0.016	2.17	0.014
719.4	230.2	17.447	0.014	1.186	0.03	0.51	0.098	0.709	0.016	1.38	0.014
863.8	60.3	17.447	0.01	2.317	0.056	99.999	99.999	1.247	0.015	2.393	0.012
915.3	33.9	17.455	0.011	1.029	0.03	0.333	0.081	0.667	0.017	1.35	0.014
885.8	159.6	17.46	0.009	1.176	0.029	0.371	0.078	0.619	0.014	1.301	0.012
368.6	506.4	17.463	0.013	1.159	0.033	99.999	99.999	0.704	0.021	1.269	0.036
475.2	921.3	17.465	0.011	1.088	0.026	99.999	99.999	0.629	0.015	1.249	0.013
813.4	464.2	17.469	0.01	1.595	0.032	99.999	99.999	0.876	0.014	1.738	0.012
421.9	770	17.474	0.009	1.131	0.03	0.577	0.098	0.638	0.014	1.316	0.012
937	240.9	17.488	0.011	1.094	0.027	0.427	0.116	0.673	0.016	1.328	0.014

TABLE 3 (CONTINUED)

X	Y	V	σ_V	$(B-V)$	σ_{B-V}	$(U-B)$	σ_{U-B}	$(V-R)$	σ_{V-R}	$(V-I)$	σ_{V-I}
98.1	961.1	17.492	0.016	1.336	0.041	99.999	99.999	0.827	0.022	1.519	0.02
295	455.6	17.506	0.01	1.227	0.027	99.999	99.999	0.679	0.014	1.31	0.012
786.1	494.9	17.507	0.011	1.211	0.032	0.568	0.098	0.639	0.017	1.222	0.015
301	57	17.508	0.011	1.831	0.044	99.999	99.999	0.982	0.015	1.973	0.012
201.2	626.5	17.51	0.011	1.173	0.028	99.999	99.999	0.721	0.016	1.443	0.014
393.9	344.5	17.53	0.01	1.082	0.026	0.392	0.082	0.628	0.017	1.285	0.013
550.5	185.3	17.535	0.012	1.089	0.031	0.378	0.092	0.645	0.017	1.254	0.016
299	296.1	17.553	0.013	2.269	0.062	99.999	99.999	1.24	0.017	2.391	0.013
252.5	767.4	17.554	0.012	1.231	0.034	0.417	0.095	0.673	0.015	1.299	0.014
515	472	17.566	0.015	1.214	0.034	0.3	0.074	0.692	0.019	1.306	0.018
298.1	519.4	17.569	0.011	1.054	0.031	99.999	99.999	0.68	0.016	1.282	0.013
697.3	560	17.573	0.011	0.994	0.031	0.284	0.079	0.618	0.016	1.299	0.015
600.6	109.6	17.593	0.012	1.082	0.033	0.214	0.082	0.586	0.018	1.201	0.015
264.2	721.5	17.612	0.013	1.205	0.036	99.999	99.999	0.656	0.017	1.379	0.015
590	536.8	17.625	0.011	1.03	0.032	0.499	0.108	0.633	0.017	1.281	0.015
343	560.6	17.628	0.013	1.189	0.033	99.999	99.999	0.655	0.017	1.359	0.015
868.5	185.7	17.632	0.01	2.19	0.063	99.999	99.999	1.318	0.014	2.502	0.011
420.9	615.5	17.638	0.015	1.232	0.037	99.999	99.999	0.666	0.022	1.389	0.02
947.8	483.3	17.65	0.01	1.645	0.039	99.999	99.999	0.95	0.014	1.785	0.012
777.9	17.2	17.662	0.015	1.007	0.037	0.514	0.095	0.606	0.021	1.248	0.02
355.5	944.5	17.688	0.013	1.041	0.036	99.999	99.999	0.673	0.017	1.31	0.015
265.5	580.4	17.689	0.027	1.214	0.037	0.376	0.124	0.738	0.017	1.422	0.016
167.8	837.6	17.694	0.016	1.051	0.036	99.999	99.999	0.663	0.023	1.347	0.02
693.8	599.4	17.698	0.01	1.03	0.032	0.395	0.097	0.617	0.017	1.289	0.016
156.8	336.5	17.698	0.011	1.012	0.031	0.427	0.123	0.652	0.016	1.296	0.015
477.9	777.1	17.701	0.013	1.133	0.035	99.999	99.999	0.714	0.018	1.397	0.014
150.4	402.6	17.702	0.014	1.175	0.037	99.999	99.999	0.689	0.018	1.349	0.016
797.1	769.8	17.709	0.013	1.872	0.053	99.999	99.999	1.037	0.016	2.009	0.014
460.4	236.6	17.71	0.013	1.162	0.032	99.999	99.999	0.635	0.016	1.296	0.015
332.4	289.9	17.714	0.01	1.195	0.034	99.999	99.999	0.679	0.015	1.28	0.013
637.3	500	17.715	0.014	1.079	0.031	0.282	0.086	0.667	0.019	1.323	0.018
654.7	130.4	17.717	0.014	1.059	0.031	99.999	99.999	0.657	0.018	1.295	0.015
270.3	570.8	17.736	0.011	1.018	0.028	99.999	99.999	0.62	0.016	1.215	0.013
773.2	789.6	17.756	0.013	1.221	0.031	99.999	99.999	0.629	0.018	1.279	0.015
947.8	510.1	17.757	0.014	1.173	0.039	99.999	99.999	0.684	0.018	1.383	0.016
848.4	634.6	17.758	0.013	1.104	0.031	99.999	99.999	0.674	0.017	1.372	0.015
271.4	293.9	17.762	0.013	1.327	0.04	99.999	99.999	0.748	0.017	1.501	0.014
599.7	480.7	17.762	0.013	1.08	0.035	99.999	99.999	0.648	0.018	1.341	0.014
396.1	530.2	17.764	0.014	1.121	0.035	99.999	99.999	0.686	0.018	1.344	0.015
171.3	697	17.768	0.012	1.24	0.032	99.999	99.999	0.697	0.017	1.339	0.014
473.7	619.3	17.771	0.014	1.16	0.037	99.999	99.999	0.711	0.018	1.336	0.017
352.8	601.4	17.775	0.015	2.14	0.075	99.999	99.999	1.231	0.02	2.34	0.017
644.7	501.5	17.781	0.013	1.382	0.039	99.999	99.999	0.856	0.017	1.499	0.015
495.8	754.9	17.782	0.011	99.999	99.999	99.999	99.999	1.138	0.015	2.198	0.012
612	731.4	17.783	0.015	1.084	0.031	99.999	99.999	0.647	0.02	99.999	99.999
594.3	135	17.786	0.015	1.1	0.035	99.999	99.999	0.658	0.019	1.315	0.018
894.3	258.4	17.786	0.013	1.11	0.033	99.999	99.999	0.624	0.017	1.396	0.014
176.1	418.4	17.787	0.012	1.145	0.036	99.999	99.999	0.692	0.017	1.318	0.014
37	537	17.798	0.012	1.108	0.035	0.296	0.108	0.65	0.019	1.301	0.017
202.8	614.2	17.816	0.015	1.15	0.037	99.999	99.999	0.699	0.021	1.325	0.0 2
100.3	831.9	17.817	0.018	1.254	0.044	99.999	99.999	0.781	0.023	1.535	0.02
349.5	443.3	17.818	0.014	1.244	0.035	99.999	99.999	0.722	0.019	1.46	0.016
620	710.2	17.823	0.016	0.953	0.032	99.999	99.999	0.526	0.021	1.116	0.019
697.3	808.6	17.825	0.012	1.166	0.036	99.999	99.999	0.667	0.016	1.332	0.015
702.2	313.4	17.826	0.01	0.929	0.032	0.337	0.083	0.635	0.016	1.224	0.015
901.3	624.2	17.829	0.013	1.18	0.037	99.999	99.999	0.674	0.017	1.351	0.015
40	988.9	17.831	0.017	1.087	0.044	99.999	99.999	0.642	0.027	1.285	0.023
853.3	284.8	17.831	0.013	1.142	0.031	99.999	99.999	0.652	0.016	1.301	0.015
395.1	491.5	17.841	0.016	1.121	0.037	99.999	99.999	0.713	0.022	1.415	0.019
701.8	917.8	17.841	0.014	1.113	0.034	99.999	99.999	0.565	0.019	1.197	0.016
680.3	990.6	17.844	0.014	1.105	0.034	99.999	99.999	0.66	0.018	1.341	0.015
18	523.6	17.853	0.016	1.836	0.056	99.999	99.999	0.99	0.021	2.025	0.018
454.2	604.3	17.875	0.014	1.13	0.04	99.999	99.999	0.661	0.018	1.306	0.016
808	847.1	17.901	0.014	1.144	0.037	99.999	99.999	0.671	0.018	1.37	0.016
423.7	945.2	17.902	0.015	1.178	0.039	99.999	99.999	0.662	0.019	1.354	0.017

TABLE 3 (CONTINUED)

X	Y	V	σ_V	$(B-V)$	σ_{B-V}	$(U-B)$	σ_{U-B}	$(V-R)$	σ_{V-R}	$(V-I)$	σ_{V-I}
934.4	643.1	17.907	0.023	1.1	0.035	0.362	0.103	0.697	0.018	1.411	0.016
158.7	860.2	17.909	0.014	1.164	0.037	99.999	99.999	0.593	0.02	1.298	0.018
933.2	454.9	17.915	0.014	1.82	0.054	99.999	99.999	1.113	0.017	2.093	0.014
212.8	312.1	17.918	0.017	1.966	0.062	99.999	99.999	1.062	0.022	2.11	0.017
423.1	473.2	17.923	0.014	1.285	0.042	99.999	99.999	0.678	0.021	1.334	0.018
256.8	290	17.926	0.022	1.18	0.053	99.999	99.999	0.746	0.031	1.418	0.026
768.3	456.2	17.927	0.015	1.095	0.04	99.999	99.999	0.767	0.019	1.477	0.017
800.6	29.4	17.937	0.014	1.333	0.038	99.999	99.999	0.755	0.019	1.517	0.015
408.6	342.1	17.938	0.011	1.383	0.041	99.999	99.999	0.851	0.018	1.676	0.013
819.9	70.2	17.941	0.015	1.177	0.038	99.999	99.999	0.699	0.02	1.347	0.017
619.3	600.4	17.942	0.015	1.16	0.038	99.999	99.999	0.718	0.02	1.414	0.018
685	318.2	17.947	0.022	1.167	0.045	0.338	0.145	0.653	0.031	99.999	99.999
759.6	596.5	17.949	0.015	1.039	0.037	99.999	99.999	0.669	0.02	1.294	0.019
631.4	957.1	17.954	0.015	1.155	0.038	99.999	99.999	0.665	0.02	1.334	0.017
103.3	152.3	17.956	0.012	1.875	0.057	99.999	99.999	1.035	0.018	2.017	0.013
168.4	572.7	17.957	0.015	1.202	0.038	99.999	99.999	0.657	0.02	1.305	0.018
232	672.9	17.957	0.014	1.076	0.035	99.999	99.999	0.659	0.019	1.312	0.016
833.2	591.5	17.963	0.015	1.228	0.041	99.999	99.999	0.677	0.02	1.362	0.018
540.5	391.8	17.966	0.014	2.186	0.077	99.999	99.999	1.34	0.018	2.453	0.015
732.5	883	17.971	0.014	1.174	0.042	99.999	99.999	0.655	0.019	1.271	0.016
598.9	30.6	17.974	0.014	1.311	0.043	99.999	99.999	0.739	0.019	1.44	0.018
740.2	383.7	17.987	0.014	1.058	0.036	99.999	99.999	0.683	0.018	1.383	0.018
802	146.5	17.987	0.017	1.962	0.08	99.999	99.999	1.105	0.021	2.155	0.018
885.8	577.4	17.992	0.014	1.125	0.039	99.999	99.999	0.768	0.019	1.429	0.017
532.5	462.6	18	0.017	1.157	0.045	99.999	99.999	0.687	0.021	1.312	0.021
894.3	338.5	18.007	0.015	2.014	0.058	99.999	99.999	1.14	0.019	2.213	0.016
515.8	864.9	18.019	0.014	1.205	0.045	99.999	99.999	0.741	0.021	1.374	0.022
795	576.5	18.019	0.015	1.112	0.036	99.999	99.999	0.618	0.021	1.33	0.018
149.5	240.8	18.021	0.016	1.349	0.048	99.999	99.999	0.756	0.02	1.502	0.018
920.5	611.5	18.024	0.014	1.123	0.037	99.999	99.999	0.71	0.019	1.44	0.017
305.1	181.3	18.027	0.018	1.35	0.044	99.999	99.999	0.735	0.023	1.521	0.02
61.8	47.7	18.035	0.015	1.319	0.054	99.999	99.999	0.737	0.021	1.495	0.018
365.8	415.3	18.037	0.021	1.221	0.049	99.999	99.999	0.707	0.034	1.434	0.027
802.9	423	18.046	0.015	1.632	0.051	99.999	99.999	0.922	0.019	1.883	0.016
357.9	121.2	18.047	0.014	1.069	0.036	99.999	99.999	0.601	0.02	1.27	0.016
227.5	614.8	18.05	0.015	1.885	0.061	99.999	99.999	1.044	0.019	2.069	0.016
221.6	732.1	18.058	0.016	1.354	0.044	99.999	99.999	0.726	0.02	1.401	0.018
668.8	333	18.073	0.016	1.1	0.043	99.999	99.999	0.621	0.021	1.31	0.019
675.5	609.9	18.074	0.016	1.119	0.041	99.999	99.999	0.69	0.022	1.268	0.043
531.4	458.6	18.077	0.018	1.193	0.047	99.999	99.999	0.62	0.023	1.33	0.02
613.9	660.8	18.087	0.015	1.106	0.04	99.999	99.999	0.646	0.019	1.327	0.017
224.7	288.7	18.089	0.016	2.236	0.074	99.999	99.999	1.198	0.021	2.306	0.017
493.7	688.9	18.093	0.014	1.382	0.048	99.999	99.999	0.768	0.019	1.521	0.017
761.6	179.8	18.096	0.016	1.225	0.046	99.999	99.999	0.584	0.021	1.25	0.019
163.1	475.8	18.108	0.015	1.132	0.043	99.999	99.999	0.694	0.022	1.307	0.019
729.5	255.7	18.112	0.018	2.025	0.085	99.999	99.999	1.153	0.023	2.206	0.019
438.5	375.8	18.12	0.014	1.361	0.043	99.999	99.999	0.788	0.019	1.495	0.016
619.9	803.7	18.129	0.017	1.054	0.042	99.999	99.999	0.69	0.02	1.349	0.019
653.4	98.1	18.137	0.018	1.188	0.044	99.999	99.999	0.709	0.024	1.439	0.021
536.9	405.5	18.143	0.015	1.175	0.04	99.999	99.999	0.652	0.021	1.362	0.018
447.6	730.4	18.145	0.016	1.235	0.049	99.999	99.999	0.675	0.02	1.375	0.019
701.6	478.9	18.146	0.017	1.485	0.055	99.999	99.999	0.956	0.021	1.982	0.018
15.4	93.9	18.154	0.018	1.272	0.051	99.999	99.999	0.727	0.026	1.413	0.021
598.9	253.9	18.159	0.015	1.367	0.045	99.999	99.999	0.74	0.02	1.453	0.017
877.5	267.3	18.166	0.016	1.282	0.044	99.999	99.999	0.71	0.022	1.41	0.018
791.9	189.1	18.168	0.014	1.401	0.05	99.999	99.999	0.802	0.02	1.445	0.017
388.8	719	18.172	0.017	1.161	0.049	99.999	99.999	0.669	0.022	1.362	0.019
621	585.4	18.177	0.015	1.159	0.042	99.999	99.999	0.707	0.021	1.377	0.018
641.8	476.2	18.178	0.02	1.327	0.055	99.999	99.999	0.689	0.027	1.43	0.022
462.2	293.6	18.192	0.017	1.472	0.051	99.999	99.999	0.753	0.023	1.451	0.019
472.3	832.6	18.197	0.015	1.195	0.046	99.999	99.999	0.692	0.021	1.398	0.017
905.9	445	18.2	0.016	1.039	0.041	99.999	99.999	0.664	0.021	1.325	0.019
530.1	781.7	18.206	0.014	1.257	0.042	99.999	99.999	0.708	0.019	1.351	0.019
240.9	511.2	18.21	0.016	1.105	0.043	99.999	99.999	0.597	0.02	1.258	0.018
959.8	257.1	18.213	0.015	1.313	0.052	99.999	99.999	0.776	0.021	1.546	0.018

TABLE 3 (CONTINUED)

X	Y	V	σ_V	$(B-V)$	σ_{B-V}	$(U-B)$	σ_{U-B}	$(V-R)$	σ_{V-R}	$(V-I)$	σ_{V-I}
237.3	582.9	18.223	0.014	2.026	0.087	99.999	99.999	1.101	0.019	2.082	0.016
621.9	282.1	18.223	0.016	1.277	0.041	99.999	99.999	0.678	0.022	1.307	0.019
883.9	455.7	18.224	0.019	1.351	0.054	99.999	99.999	0.85	0.024	1.542	0.021
205.8	201.7	18.229	0.018	1.372	0.049	99.999	99.999	0.748	0.023	1.478	0.021
787.6	590.6	18.231	0.016	1.22	0.042	99.999	99.999	0.746	0.022	1.435	0.019
634.7	113.5	18.232	0.016	1.209	0.048	99.999	99.999	0.629	0.021	1.333	0.019
558.8	400.5	18.24	0.016	1.086	0.043	99.999	99.999	0.621	0.023	1.283	0.019
572.2	773.6	18.241	0.016	1.268	0.044	99.999	99.999	0.692	0.021	1.355	0.02
850.5	399.2	18.255	0.015	1.172	0.05	99.999	99.999	0.708	0.02	1.416	0.018
516.6	271.4	18.261	0.018	1.145	0.049	99.999	99.999	0.648	0.024	1.328	0.021
554.8	69.2	18.261	0.019	1.212	0.049	99.999	99.999	0.727	0.024	1.418	0.021
892.2	366.9	18.263	0.017	1.127	0.048	99.999	99.999	0.693	0.022	1.381	0.021
17.4	245.4	18.266	0.017	1.784	0.084	99.999	99.999	0.979	0.022	1.973	0.019
439.4	832.7	18.267	0.017	1.143	0.045	99.999	99.999	0.64	0.022	1.311	0.021
810.8	114.7	18.271	0.02	1.284	0.054	99.999	99.999	0.644	0.026	1.307	0.023
463.5	323	18.272	0.015	1.095	0.044	99.999	99.999	0.692	0.02	1.321	0.018
930.3	154.4	18.274	0.02	1.912	0.086	99.999	99.999	1.08	0.025	2.096	0.021
86.9	655	18.281	0.019	1.068	0.049	99.999	99.999	0.676	0.023	1.321	0.022
907	828.6	18.284	0.017	0.973	0.041	99.999	99.999	0.632	0.023	1.337	0.02
367	705.1	18.289	0.016	1.188	0.05	99.999	99.999	0.645	0.022	1.337	0.019
244.2	136.1	18.29	0.02	1.204	0.046	99.999	99.999	0.637	0.026	1.301	0.022
781	975.6	18.292	0.023	1.174	0.055	99.999	99.999	0.759	0.031	1.466	0.058
208.4	499.8	18.293	0.016	1.255	0.05	99.999	99.999	0.683	0.022	1.44	0.02
597.4	714.8	18.304	0.018	99.999	99.999	99.999	99.999	1.101	0.023	2.184	0.02
891.4	673.7	18.314	0.015	1.836	0.074	99.999	99.999	1.029	0.021	2.029	0.016
361.8	962.8	18.317	0.015	1.698	0.058	99.999	99.999	0.964	0.02	1.999	0.017
351.6	639.1	18.324	0.019	1.153	0.053	99.999	99.999	0.711	0.024	1.358	0.021
546.2	74.2	18.326	0.019	1.496	0.065	99.999	99.999	0.798	0.025	1.659	0.021
935.6	741	18.335	0.014	1.212	0.05	99.999	99.999	0.717	0.02	1.436	0.017
12.2	735.5	18.349	0.019	1.903	0.078	99.999	99.999	1.045	0.026	2.07	0.021
625.1	494.4	18.351	0.018	1.22	0.049	99.999	99.999	0.739	0.025	1.368	0.022
278.9	767.7	18.355	0.02	1.338	0.057	99.999	99.999	0.674	0.027	1.465	0.024
520	986.4	18.365	0.019	1.278	0.051	99.999	99.999	0.655	0.026	1.351	0.022
563	579.2	18.371	0.018	1.01	0.049	99.999	99.999	0.689	0.025	1.32	0.021
332.9	348.7	18.375	0.019	1.35	0.063	99.999	99.999	0.77	0.026	1.454	0.022
469.5	563	18.393	0.02	1.21	0.051	99.999	99.999	0.665	0.027	1.433	0.024
403.8	125.3	18.394	0.02	99.999	99.999	99.999	99.999	0.786	0.025	1.588	0.022
411.4	552.6	18.397	0.021	1.344	0.059	99.999	99.999	0.7	0.027	1.409	0.024
321.3	465.6	18.414	0.02	1.148	0.046	99.999	99.999	0.687	0.027	1.394	0.025
387	641	18.416	0.017	1.798	0.092	99.999	99.999	1.077	0.022	2.111	0.019
36.1	704.7	18.421	0.019	1.391	0.069	99.999	99.999	0.777	0.025	1.478	0.022
820.9	571	18.421	0.017	1.227	0.058	99.999	99.999	0.847	0.022	1.556	0.02
951.9	619	18.425	0.017	1.454	0.063	99.999	99.999	0.869	0.023	1.771	0.019
666.2	213	18.428	0.019	1.053	0.048	99.999	99.999	0.724	0.025	1.362	0.022
570.6	947.2	18.43	0.017	1.142	0.058	99.999	99.999	0.69	0.022	1.348	0.02
803.1	989.2	18.43	0.015	1.456	0.061	99.999	99.999	0.852	0.024	1.572	0.022
679.4	847.1	18.434	0.017	1.176	0.053	99.999	99.999	0.729	0.021	1.46	0.019
600.5	568.2	18.438	0.02	1.13	0.053	99.999	99.999	0.671	0.027	1.408	0.023
720.7	449.5	18.457	0.02	1.203	0.051	99.999	99.999	0.648	0.028	1.373	0.023
725.9	703.4	18.469	0.017	1.391	0.063	99.999	99.999	0.782	0.022	1.621	0.019
827.4	880.4	18.475	0.02	1.186	0.055	99.999	99.999	0.699	0.025	1.394	0.023
15.9	411.4	18.476	0.022	1.653	0.083	99.999	99.999	0.955	0.028	1.799	0.024
56.8	736.7	18.477	0.022	1.117	0.055	99.999	99.999	0.74	0.028	1.402	0.025
888.8	854.7	18.479	0.019	1.084	0.052	99.999	99.999	0.742	0.025	1.398	0.022
981.2	553.4	18.483	0.018	1.378	0.059	99.999	99.999	0.669	0.024	1.418	0.021
406	258.3	18.484	0.017	99.999	99.999	99.999	99.999	0.853	0.024	1.547	0.02
406.2	35.9	18.485	0.02	1.315	0.059	99.999	99.999	0.651	0.026	1.365	0.023
441.8	798.6	18.485	0.02	1.262	0.059	99.999	99.999	0.635	0.025	1.376	0.022
172.9	502.5	18.486	0.019	1.209	0.058	99.999	99.999	0.679	0.024	1.426	0.023
173.6	727.2	18.486	0.019	1.394	0.065	99.999	99.999	0.737	0.025	1.377	0.022
426.2	354.7	18.488	0.019	1.768	0.08	99.999	99.999	1.056	0.025	2.073	0.02
734.2	470.6	18.491	0.019	1.138	0.052	99.999	99.999	0.681	0.024	1.388	0.024
888	539.8	18.496	0.019	1.882	0.097	99.999	99.999	1.103	0.026	2.092	0.022
105.8	106.7	18.498	0.019	1.485	0.075	99.999	99.999	0.969	0.026	1.861	0.022
634.7	659.3	18.507	0.02	1.102	0.05	99.999	99.999	0.679	0.027	1.355	0.023

TABLE 3 (CONTINUED)

X	Y	V	σ_V	$(B-V)$	σ_{B-V}	$(U-B)$	σ_{U-B}	$(V-R)$	σ_{V-R}	$(V-I)$	σ_{V-I}
839.3	690.7	18.507	0.021	1.326	0.063	99.999	99.999	0.729	0.027	1.398	0.024
433.4	812.5	18.524	0.021	1.128	0.06	99.999	99.999	0.67	0.027	1.37	0.025
775.2	917	18.527	0.018	1.191	0.054	99.999	99.999	0.719	0.024	1.444	0.021
6.7	420.3	18.529	0.02	1.166	0.054	99.999	99.999	0.681	0.027	1.455	0.023
733.6	48.3	18.529	0.022	1.287	0.063	99.999	99.999	0.807	0.029	1.576	0.024
162.1	236.6	18.53	0.022	1.199	0.063	99.999	99.999	0.774	0.028	1.415	0.026
879.8	393.4	18.531	0.021	1.074	0.053	99.999	99.999	0.756	0.028	1.521	0.024
95.3	992.1	18.532	0.029	1.219	0.068	99.999	99.999	0.763	0.043	1.484	0.06
297.4	334.9	18.546	0.02	1.262	0.069	99.999	99.999	0.782	0.026	1.46	0.024
671.1	823.1	18.552	0.014	1.87	0.088	99.999	99.999	1.144	0.021	2.197	0.016
426	601.5	18.57	0.021	99.999	99.999	99.999	99.999	1.114	0.028	2.175	0.023
88	649.9	18.573	0.02	1.128	0.059	99.999	99.999	0.669	0.028	1.364	0.024
561.4	469.1	18.58	0.019	1.143	0.051	99.999	99.999	0.789	0.025	1.397	0.024
494	329.9	18.582	0.02	1.125	0.058	99.999	99.999	0.703	0.026	1.409	0.024
220.3	609.4	18.592	0.019	1.201	0.059	99.999	99.999	0.699	0.025	1.389	0.021
929.4	100.7	18.599	0.019	1.093	0.053	99.999	99.999	0.664	0.028	1.359	0.023
657.5	710.9	18.6	0.019	1.262	0.068	99.999	99.999	0.692	0.026	1.453	0.022
658.8	425.5	18.601	0.02	1.083	0.066	99.999	99.999	0.678	0.027	1.41	0.023
692.9	956	18.601	0.021	1.256	0.062	99.999	99.999	0.746	0.027	1.446	0.025
797.3	787.9	18.606	0.02	1.412	0.07	99.999	99.999	0.799	0.028	1.499	0.024
225	319.2	18.609	0.019	1.77	0.088	99.999	99.999	1.011	0.025	2.037	0.02
394.2	560.6	18.624	0.023	1.181	0.061	99.999	99.999	0.727	0.029	1.445	0.026
186.5	176.4	18.626	0.022	1.727	0.106	99.999	99.999	0.997	0.028	2.076	0.024
402.9	759.5	18.633	0.024	1.173	0.064	99.999	99.999	0.713	0.029	1.385	0.027
465.6	176.8	18.636	0.021	1.256	0.062	99.999	99.999	0.695	0.028	1.427	0.024
272.8	725.2	18.637	0.02	1.18	0.06	99.999	99.999	0.796	0.026	1.482	0.025
693.1	7.2	18.64	0.018	1.077	0.054	99.999	99.999	0.672	0.025	1.38	0.022
458.4	752.8	18.646	0.022	1.182	0.062	99.999	99.999	0.718	0.029	1.406	0.025
93.2	893.1	18.649	0.024	1.155	0.07	99.999	99.999	0.708	0.033	1.411	0.028
591.8	234.8	18.655	0.021	1.091	0.058	99.999	99.999	0.764	0.027	1.435	0.024
280.8	895.1	18.659	0.02	1.236	0.071	99.999	99.999	0.705	0.027	1.473	0.023
935.1	711.8	18.659	0.018	1.458	0.068	99.999	99.999	0.767	0.024	1.442	0.021
930.1	130.4	18.66	0.02	1.181	0.063	99.999	99.999	0.724	0.028	1.447	0.026
595	258.4	18.662	0.023	1.292	0.067	99.999	99.999	0.708	0.029	1.431	0.027
614.2	792.3	18.663	0.023	1.322	0.069	99.999	99.999	0.802	0.03	1.562	0.026
794.7	868.4	18.668	0.02	1.37	0.066	99.999	99.999	0.803	0.025	1.627	0.022
721	157.3	18.671	0.021	99.999	99.999	99.999	99.999	1.159	0.028	2.278	0.022
654.6	611.3	18.675	0.022	1.265	0.067	99.999	99.999	0.76	0.027	1.418	0.026
907.4	893.5	18.676	0.021	1.916	0.089	99.999	99.999	1.021	0.027	2.031	0.022
65.7	578.3	18.677	0.02	1.256	0.077	99.999	99.999	0.863	0.026	1.654	0.023
430.1	567.4	18.696	0.021	1.289	0.073	99.999	99.999	0.785	0.029	1.55	0.025
275.2	459.6	18.699	0.021	1.168	0.063	99.999	99.999	0.695	0.028	1.415	0.026
117.1	252.6	18.706	0.022	1.209	0.076	99.999	99.999	0.789	0.03	1.522	0.025
238.7	332.1	18.707	0.022	1.273	0.063	99.999	99.999	0.733	0.028	1.485	0.024
608.8	898.4	18.709	0.02	1.311	0.068	99.999	99.999	0.724	0.026	1.422	0.023
523.2	129.9	18.712	0.022	1.091	0.069	99.999	99.999	0.694	0.028	1.379	0.026
245.7	564	18.717	0.023	1.195	0.071	99.999	99.999	0.704	0.029	1.447	0.025
726.4	51.2	18.719	0.024	1.101	0.066	99.999	99.999	0.705	0.03	1.403	0.027
859.9	211.4	18.721	0.024	1.136	0.064	99.999	99.999	0.705	0.032	1.363	0.03
565.1	651.9	18.722	0.022	1.177	0.065	99.999	99.999	0.762	0.029	1.448	0.027
277.8	299.6	18.725	0.021	1.394	0.087	99.999	99.999	0.764	0.029	1.512	0.023
238.2	140.8	18.727	0.02	1.25	0.07	99.999	99.999	0.833	0.025	1.588	0.024
809.9	303.2	18.729	0.024	1.082	0.06	99.999	99.999	0.712	0.031	1.371	0.027
55.8	807.8	18.73	0.024	1.373	0.081	99.999	99.999	0.753	0.032	1.572	0.027
395.8	103.6	18.735	0.023	1.215	0.068	99.999	99.999	0.762	0.03	1.615	0.026
268.8	801.9	18.741	0.025	1.145	0.065	99.999	99.999	0.722	0.03	1.479	0.029
591.5	119.9	18.743	0.021	1.159	0.07	99.999	99.999	0.688	0.028	1.442	0.024
891.8	212.7	18.744	0.019	1.225	0.076	99.999	99.999	0.692	0.028	1.445	0.023
912.1	684.9	18.745	0.026	1.251	0.063	99.999	99.999	0.76	0.032	1.482	0.028
198.7	828.7	18.75	0.024	1.297	0.075	99.999	99.999	0.737	0.031	1.449	0.028
125.7	224.4	18.75	0.026	1.297	0.082	99.999	99.999	0.807	0.034	1.508	0.029
347.4	581.8	18.756	0.025	1.258	0.072	99.999	99.999	0.607	0.031	1.328	0.028
942.1	673.1	18.757	0.02	1.201	0.076	99.999	99.999	0.755	0.027	1.421	0.023
741.3	946.6	18.763	0.021	99.999	99.999	99.999	99.999	0.716	0.026	1.432	0.025
140.3	207.4	18.763	0.026	1.45	0.094	99.999	99.999	0.749	0.034	1.548	0.029

TABLE 3 (CONTINUED)

X	Y	V	σ_V	$(B-V)$	σ_{B-V}	$(U-B)$	σ_{U-B}	$(V-R)$	σ_{V-R}	$(V-I)$	σ_{V-I}
351.4	347.3	18.765	0.027	1.316	0.083	99.999	99.999	0.734	0.034	1.465	0.031
150.3	363.3	18.767	0.026	1.226	0.074	99.999	99.999	0.669	0.034	1.386	0.029
466.5	652.6	18.778	0.023	1.82	0.121	99.999	99.999	1.079	0.028	2.077	0.024
8.9	594.7	18.778	0.027	1.061	0.075	99.999	99.999	0.738	0.035	99.999	99.999
50.1	352.3	18.779	0.025	1.284	0.071	99.999	99.999	0.813	0.03	1.49	0.029
545.7	421.9	18.779	0.023	1.144	0.07	99.999	99.999	0.749	0.032	1.417	0.027
511.5	47.3	18.785	0.025	1.352	0.084	99.999	99.999	0.81	0.033	1.668	0.027
702.3	563.3	18.786	0.023	1.173	0.074	99.999	99.999	0.646	0.032	1.373	0.029
356.5	291.2	18.787	0.026	1.23	0.069	99.999	99.999	0.8	0.036	1.585	0.03
64.4	558.1	18.787	0.025	1.204	0.074	99.999	99.999	0.64	0.035	1.327	0.028
540.5	58.1	18.787	0.018	99.999	99.999	99.999	99.999	1.115	0.025	2.121	0.019
262.6	9	18.8	0.025	1.289	0.076	99.999	99.999	0.687	0.033	1.436	0.028
486.4	693.1	18.802	0.027	1.422	0.082	99.999	99.999	0.813	0.036	1.446	0.07
335.1	469.9	18.806	0.023	1.31	0.08	99.999	99.999	0.737	0.029	1.485	0.028
150	217.5	18.809	0.023	1.1	0.065	99.999	99.999	0.74	0.031	1.425	0.026
277.6	883.6	18.81	0.021	99.999	99.999	99.999	99.999	1.061	0.028	2.08	0.023
901.4	713.3	18.811	0.022	1.186	0.072	99.999	99.999	0.747	0.029	1.417	0.026
24.7	696.2	18.817	0.027	99.999	99.999	99.999	99.999	1.196	0.034	2.237	0.029
2.7	814.9	18.819	0.026	1.34	0.088	99.999	99.999	0.887	0.037	1.718	0.03
43	43.5	18.827	0.023	1.423	0.076	99.999	99.999	0.798	0.033	1.607	0.027
857.4	830.6	18.835	0.023	1.187	0.073	99.999	99.999	0.724	0.03	1.417	0.026
512.6	419.2	18.836	0.024	1.339	0.087	99.999	99.999	0.725	0.032	1.482	0.028
664.9	298.5	18.842	0.024	1.202	0.073	99.999	99.999	0.67	0.032	1.509	0.026
948.2	586.2	18.844	0.023	1.339	0.074	99.999	99.999	0.766	0.03	1.627	0.026
172.3	532.8	18.847	0.027	1.233	0.079	99.999	99.999	0.734	0.035	1.491	0.031
691.2	336.4	18.848	0.025	1.257	0.076	99.999	99.999	0.777	0.032	1.472	0.029
751.7	942.3	18.849	0.023	1.518	0.102	99.999	99.999	0.92	0.031	1.642	0.025
34.1	957.5	18.852	0.027	99.999	99.999	99.999	99.999	1.154	0.036	2.21	0.029
777.4	446.8	18.853	0.027	1.112	0.072	99.999	99.999	0.722	0.034	1.419	0.03
239.2	294.5	18.854	0.025	1.475	0.09	99.999	99.999	0.824	0.033	1.601	0.029
944.3	845.7	18.857	0.022	1.698	0.112	99.999	99.999	1.066	0.028	2.034	0.024
152.8	972.9	18.863	0.027	1.678	0.128	99.999	99.999	0.828	0.034	1.571	0.033
860.9	341.8	18.871	0.027	1.232	0.081	99.999	99.999	0.713	0.034	1.414	0.029
310	334.4	18.875	0.023	1.18	0.073	99.999	99.999	0.766	0.032	1.471	0.027
632.8	988.9	18.877	0.023	1.259	0.076	99.999	99.999	0.65	0.029	1.361	0.028
348.4	561.9	18.884	0.024	1.366	0.078	99.999	99.999	0.694	0.033	1.428	0.028
550.6	206.7	18.886	0.027	1.425	0.085	99.999	99.999	0.775	0.035	1.492	0.031
387.7	486.7	18.891	0.027	99.999	99.999	99.999	99.999	0.776	0.038	1.552	0.032
466.4	687.2	18.892	0.025	1.241	0.068	99.999	99.999	0.698	0.034	1.474	0.028
169.6	66.9	18.895	0.025	1.265	0.092	99.999	99.999	0.831	0.035	1.658	0.028
614.7	642.8	18.897	0.025	1.108	0.075	99.999	99.999	0.671	0.033	1.356	0.029
560.2	617.6	18.902	0.024	1.239	0.086	99.999	99.999	0.713	0.031	1.356	0.029
536.2	155.9	18.906	0.023	99.999	99.999	99.999	99.999	1.01	0.029	2.009	0.025
545	735.4	18.907	0.024	1.326	0.079	99.999	99.999	0.697	0.03	1.403	0.028
556.1	395.7	18.909	0.021	1.159	0.068	99.999	99.999	0.652	0.03	1.387	0.025
181.3	621.1	18.925	0.026	99.999	99.999	99.999	99.999	0.949	0.034	2.001	0.027
623.1	451.9	18.927	0.03	99.999	99.999	99.999	99.999	0.757	0.038	1.411	0.035
485.2	430.9	18.929	0.029	1.186	0.086	99.999	99.999	0.69	0.037	1.424	0.034
975.5	386.4	18.929	0.023	1.439	0.092	99.999	99.999	0.841	0.032	1.603	0.027
597.1	413.6	18.935	0.026	1.276	0.085	99.999	99.999	0.801	0.036	1.533	0.03
275.3	424.3	18.939	0.024	99.999	99.999	99.999	99.999	0.835	0.033	1.705	0.027
412.9	240.8	18.945	0.021	1.414	0.098	99.999	99.999	0.897	0.028	1.598	0.023
979.6	659.5	18.946	0.026	1.298	0.08	99.999	99.999	0.671	0.034	1.435	0.028
488.9	460.3	18.947	0.025	1.098	0.083	99.999	99.999	0.745	0.036	1.487	0.031
171.6	458.6	18.957	0.029	1.238	0.082	99.999	99.999	0.721	0.038	1.393	0.033
693.7	910.9	18.96	0.025	1.233	0.085	99.999	99.999	0.685	0.033	1.352	0.031
668.4	472.2	18.964	0.027	1.578	0.112	99.999	99.999	1.063	0.035	1.967	0.033
184.3	299.9	18.965	0.028	1.151	0.084	99.999	99.999	0.721	0.035	1.468	0.032
50	754.7	18.968	0.025	99.999	99.999	99.999	99.999	1.12	0.034	2.201	0.027
576.4	740.5	18.974	0.026	1.053	0.068	99.999	99.999	0.751	0.035	1.385	0.03
757.6	779.7	18.975	0.027	1.537	0.106	99.999	99.999	0.785	0.037	99.999	99.999
376.1	876.9	18.976	0.027	1.212	0.075	99.999	99.999	0.743	0.034	1.388	0.03
349.6	294.8	18.98	0.027	1.006	0.073	99.999	99.999	0.731	0.035	1.503	0.031
929.2	388.7	18.983	0.028	1.214	0.085	99.999	99.999	0.774	0.038	1.525	0.032
198.4	796.7	18.998	0.027	99.999	99.999	99.999	99.999	0.89	0.033	1.83	0.029

TABLE 3 (CONTINUED)

X	Y	V	σ_V	$(B-V)$	σ_{B-V}	$(U-B)$	σ_{U-B}	$(V-R)$	σ_{V-R}	$(V-I)$	σ_{V-I}
861.5	155.3	18.999	0.025	1.493	0.093	99.999	99.999	0.986	0.032	2.153	0.027
670.2	608.5	19	0.03	1.249	0.086	99.999	99.999	0.84	0.04	1.502	0.042
734.8	350.9	19	0.027	1.318	0.09	99.999	99.999	0.799	0.036	1.665	0.03
579	230.4	19.007	0.029	1.608	0.127	99.999	99.999	1.03	0.038	1.896	0.032
19.5	529.3	19.011	0.03	1.088	0.084	99.999	99.999	0.788	0.038	1.405	0.035
17.1	340.5	19.012	0.024	1.449	0.089	99.999	99.999	0.673	0.033	1.466	0.029
667.3	366.7	19.013	0.024	1.272	0.079	99.999	99.999	0.735	0.032	1.523	0.027
981	611.8	19.017	0.025	1.456	0.095	99.999	99.999	0.832	0.033	1.692	0.029
229.2	141.3	19.019	0.024	1.331	0.095	99.999	99.999	0.709	0.033	1.439	0.029
562.9	592.9	19.023	0.029	1.216	0.079	99.999	99.999	0.77	0.045	1.399	0.033
173.4	175	19.029	0.026	1.172	0.097	99.999	99.999	0.727	0.034	1.476	0.03
949.5	891.4	19.032	0.024	1.401	0.096	99.999	99.999	1.036	0.031	2.1	0.025
937.4	618.2	19.033	0.024	1.579	0.102	99.999	99.999	0.961	0.032	1.736	0.027
698	721.7	19.037	0.025	1.131	0.083	99.999	99.999	0.798	0.032	1.517	0.028
271.4	750.5	19.039	0.03	1.18	0.094	99.999	99.999	0.798	0.04	1.538	0.035
317.9	576.3	19.052	0.027	99.999	99.999	99.999	99.999	1.027	0.035	1.91	0.029
413.3	647.7	19.059	0.026	1.327	0.092	99.999	99.999	0.813	0.034	1.487	0.03
771	820.2	19.065	0.025	1.461	0.106	99.999	99.999	1.017	0.033	1.909	0.027
224	687.2	19.071	0.029	99.999	99.999	99.999	99.999	0.996	0.037	1.9	0.032
233.9	766.3	19.071	0.024	99.999	99.999	99.999	99.999	1.115	0.032	2.141	0.027
722.2	846.2	19.079	0.023	1.334	0.094	99.999	99.999	0.736	0.031	1.433	0.028
402.4	260.7	19.086	0.035	99.999	99.999	99.999	99.999	0.653	0.045	1.487	0.039
232.1	186.3	19.087	0.027	99.999	99.999	99.999	99.999	0.82	0.036	1.7	0.03
213.3	389.2	19.094	0.031	1.402	0.111	99.999	99.999	0.75	0.04	1.547	0.035
501.3	143	19.098	0.023	1.22	0.084	99.999	99.999	0.76	0.033	1.525	0.027
276.2	643.8	19.104	0.026	1.214	0.089	99.999	99.999	0.813	0.035	1.49	0.032
831	73.2	19.106	0.028	1.2	0.088	99.999	99.999	0.866	0.037	1.63	0.032
570.2	460.2	19.108	0.025	1.488	0.102	99.999	99.999	0.769	0.034	1.474	0.031
507.6	642.2	19.109	0.028	1.337	0.094	99.999	99.999	0.792	0.037	1.581	0.031
760.9	778.7	19.12	0.032	1.369	0.113	99.999	99.999	0.808	0.043	99.999	99.999
534.9	478.8	19.126	0.025	1.333	0.113	99.999	99.999	0.818	0.031	1.616	0.029
226.9	6.4	19.132	0.033	1.37	0.106	99.999	99.999	0.767	0.041	1.659	0.036
104.2	808	19.132	0.028	99.999	99.999	99.999	99.999	0.704	0.039	1.455	0.032
429.2	419.6	19.134	0.029	1.172	0.089	99.999	99.999	0.663	0.038	1.421	0.033
594.5	788.4	19.134	0.03	1.297	0.09	99.999	99.999	0.77	0.038	1.507	0.034
769.1	613.9	19.134	0.027	99.999	99.999	99.999	99.999	1.019	0.035	1.987	0.03
558.6	731.8	19.145	0.029	99.999	99.999	99.999	99.999	1.156	0.037	2.132	0.031
668.6	771.5	19.148	0.034	1.164	0.096	99.999	99.999	0.729	0.044	1.504	0.038
39.4	213.1	19.151	0.029	1.171	0.09	99.999	99.999	0.72	0.038	1.532	0.033
558.4	911.3	19.161	0.029	1.171	0.098	99.999	99.999	0.749	0.039	1.4	0.033
168.9	230.6	19.169	0.027	99.999	99.999	99.999	99.999	0.767	0.037	1.501	0.032
327.9	155	19.174	0.026	1.198	0.105	99.999	99.999	0.791	0.036	1.43	0.03
201	656.9	19.182	0.03	1.24	0.1	99.999	99.999	0.777	0.038	1.452	0.034
990.9	145.5	19.19	0.04	1.174	0.092	99.999	99.999	0.722	0.048	1.437	0.044
900.6	979.6	19.195	0.029	99.999	99.999	99.999	99.999	1.066	0.038	2.435	0.03
506.9	504.6	19.215	0.028	1.373	0.121	99.999	99.999	0.739	0.038	1.539	0.032
479.8	341.5	19.217	0.033	1.648	0.129	99.999	99.999	0.834	0.042	1.604	0.038
296.1	587.5	19.223	0.034	99.999	99.999	99.999	99.999	0.91	0.043	1.79	0.037
334.8	580	19.229	0.024	99.999	99.999	99.999	99.999	0.73	0.033	1.572	0.029
629.2	158.7	19.232	0.028	0.98	0.087	99.999	99.999	0.856	0.037	1.648	0.032
135.9	886.4	19.233	0.026	99.999	99.999	99.999	99.999	1.038	0.036	2.093	0.028
252.3	695.7	19.244	0.027	1.307	0.122	99.999	99.999	0.86	0.036	1.625	0.032
941.5	249.1	19.261	0.027	1.269	0.095	99.999	99.999	0.778	0.037	1.555	0.032
11.8	120	19.268	0.031	99.999	99.999	99.999	99.999	0.784	0.043	1.513	0.038
89.6	298.8	19.273	0.034	1.246	0.133	99.999	99.999	0.778	0.042	1.471	0.038
352.1	224.3	19.274	0.025	99.999	99.999	99.999	99.999	0.782	0.037	1.467	0.032
871.6	626.3	19.274	0.032	99.999	99.999	99.999	99.999	0.807	0.04	1.532	0.036
658.1	13.8	19.275	0.031	1.184	0.125	99.999	99.999	0.72	0.043	1.577	0.038
851.6	854.6	19.276	0.028	1.402	0.11	99.999	99.999	0.702	0.038	1.452	0.034
781.8	587.7	19.277	0.038	1.023	0.09	99.999	99.999	0.686	0.047	1.484	0.043
837.6	23.8	19.279	0.036	99.999	99.999	99.999	99.999	0.929	0.046	1.625	0.042
172.2	822.1	19.293	0.035	99.999	99.999	99.999	99.999	0.766	0.045	1.491	0.039
25.1	391.8	19.299	0.033	1.18	0.104	99.999	99.999	0.739	0.044	1.511	0.037
400.3	121.8	19.307	0.035	99.999	99.999	99.999	99.999	0.778	0.047	1.509	0.039
443.6	558.8	19.309	0.035	99.999	99.999	99.999	99.999	0.808	0.045	1.626	0.039

TABLE 3 (CONTINUED)

X	Y	V	σ_V	$(B-V)$	σ_{B-V}	$(U-B)$	σ_{U-B}	$(V-R)$	σ_{V-R}	$(V-I)$	σ_{V-I}
444.7	621.8	19.309	0.034	1.228	0.103	99.999	99.999	0.781	0.042	1.514	0.039
456.8	550	19.309	0.039	1.448	0.128	99.999	99.999	0.735	0.053	1.484	0.05
728.4	917.1	19.314	0.025	99.999	99.999	99.999	99.999	0.919	0.033	1.728	0.03
462.2	411.7	19.318	0.029	99.999	99.999	99.999	99.999	0.947	0.039	1.675	0.034
277.9	409.2	19.319	0.032	1.394	0.111	99.999	99.999	0.763	0.043	1.523	0.034
56.8	911.5	19.322	0.032	99.999	99.999	99.999	99.999	0.757	0.044	1.532	0.038
677.5	105.9	19.326	0.03	99.999	99.999	99.999	99.999	1.054	0.04	2.148	0.031
27	900.4	19.329	0.024	99.999	99.999	99.999	99.999	0.744	0.035	1.549	0.031
622.8	122.7	19.334	0.032	99.999	99.999	99.999	99.999	0.893	0.04	1.6	0.037
602.8	732.5	19.338	0.032	99.999	99.999	99.999	99.999	0.845	0.042	1.981	0.039
938.8	787	19.339	0.031	0.058	0.049	−0.805	0.068	−0.014	0.051	99.999	99.999
63	668.3	19.342	0.035	99.999	99.999	99.999	99.999	0.932	0.045	1.785	0.039
825.8	224.6	19.344	0.03	1.391	0.128	99.999	99.999	0.923	0.039	1.644	0.036
275.4	629	19.345	0.033	1.179	0.127	99.999	99.999	0.694	0.042	1.487	0.037
391.1	897.3	19.346	0.025	99.999	99.999	99.999	99.999	0.81	0.034	1.552	0.03
637.1	836.8	19.347	0.034	1.119	0.105	99.999	99.999	0.795	0.045	1.547	0.039
436.3	498.3	19.349	0.034	99.999	99.999	99.999	99.999	0.921	0.044	1.863	0.038
539.7	616	19.352	0.036	0.989	0.112	99.999	99.999	0.747	0.046	1.48	0.041
464.9	20.1	19.357	0.034	99.999	99.999	99.999	99.999	1.036	0.042	2.132	0.036
294.7	203	19.359	0.036	99.999	99.999	99.999	99.999	0.842	0.046	1.649	0.039
849.2	313.5	19.359	0.031	99.999	99.999	99.999	99.999	0.809	0.041	1.512	0.035
666.8	410.8	19.361	0.034	99.999	99.999	99.999	99.999	0.856	0.043	1.542	0.038
466.8	965.6	19.366	0.035	1.287	0.116	99.999	99.999	0.752	0.046	1.431	0.04
388.6	817.6	19.374	0.031	99.999	99.999	99.999	99.999	0.997	0.04	1.83	0.037
735.7	421.1	19.378	0.027	99.999	99.999	99.999	99.999	0.789	0.038	1.559	0.034
882.1	491.4	19.378	0.039	1.297	0.121	99.999	99.999	0.777	0.049	1.575	0.043
635.9	714.2	19.385	0.046	99.999	99.999	99.999	99.999	0.773	0.057	1.455	0.052
668.2	864.9	19.387	0.042	99.999	99.999	99.999	99.999	0.798	0.054	1.537	0.048
330.7	54.1	19.388	0.032	99.999	99.999	99.999	99.999	0.757	0.043	1.49	0.036
215.4	168.8	19.389	0.034	99.999	99.999	99.999	99.999	0.647	0.047	1.336	0.04
560.4	642.7	19.391	0.032	99.999	99.999	99.999	99.999	0.851	0.042	1.644	0.036
290.7	346.6	19.396	0.035	99.999	99.999	99.999	99.999	0.905	0.046	1.718	0.038
141	482	19.4	0.038	99.999	99.999	99.999	99.999	0.794	0.047	1.655	0.041
603.6	656.6	19.401	0.04	99.999	99.999	99.999	99.999	0.641	0.05	1.385	0.044
477.4	62.9	19.402	0.032	99.999	99.999	99.999	99.999	0.887	0.043	1.788	0.036
119	76	19.402	0.036	99.999	99.999	99.999	99.999	0.741	0.047	1.436	0.042
280	985.5	19.406	0.031	99.999	99.999	99.999	99.999	0.661	0.043	1.476	0.039
819	832.4	19.407	0.034	1.239	0.139	99.999	99.999	0.802	0.042	1.491	0.038
475.8	228.1	19.408	0.034	1.075	0.103	99.999	99.999	0.794	0.044	1.474	0.041
119.9	860.2	19.408	0.033	99.999	99.999	99.999	99.999	0.897	0.044	1.647	0.038
858	819.3	19.417	0.032	99.999	99.999	99.999	99.999	0.891	0.042	1.776	0.035
264.9	442.4	19.421	0.032	99.999	99.999	99.999	99.999	0.712	0.044	1.467	0.036
512.4	862.4	19.422	0.034	99.999	99.999	99.999	99.999	0.923	0.045	1.66	0.042
666.2	195.5	19.422	0.039	99.999	99.999	99.999	99.999	0.661	0.051	1.418	0.045
457.7	270.4	19.423	0.036	99.999	99.999	99.999	99.999	0.959	0.044	1.946	0.038
882	94.6	19.431	0.035	1.163	0.121	99.999	99.999	0.73	0.045	1.481	0.04
483.8	917.2	19.433	0.035	1.173	0.108	99.999	99.999	0.729	0.046	1.489	0.041
180.5	491	19.434	0.031	99.999	99.999	99.999	99.999	0.755	0.044	1.516	0.037
929.2	603.3	19.434	0.033	1.238	0.123	99.999	99.999	0.708	0.046	1.439	0.039
266.8	795.7	19.441	0.037	99.999	99.999	99.999	99.999	0.876	0.046	1.742	0.042
473	738.9	19.446	0.04	99.999	99.999	99.999	99.999	0.744	0.051	1.498	0.045
640	382.5	19.446	0.034	99.999	99.999	99.999	99.999	0.864	0.045	1.681	0.039
561.2	888.2	19.448	0.038	1.073	0.101	99.999	99.999	0.778	0.049	1.55	0.043
209.9	849.7	19.449	0.038	99.999	99.999	99.999	99.999	0.862	0.049	1.65	0.041
188.3	892.2	19.457	0.044	99.999	99.999	99.999	99.999	0.768	0.056	1.594	0.048
517.8	221	19.462	0.043	99.999	99.999	99.999	99.999	0.717	0.054	1.517	0.049
320.9	870.5	19.486	0.039	99.999	99.999	99.999	99.999	0.874	0.05	1.501	0.045
358	176.4	19.49	0.036	99.999	99.999	99.999	99.999	0.887	0.049	1.506	0.042
666.5	985.4	19.495	0.04	99.999	99.999	99.999	99.999	0.724	0.051	1.451	0.045
938.4	939	19.496	0.032	99.999	99.999	99.999	99.999	0.802	0.045	1.625	0.035
408.2	250.5	19.52	0.036	99.999	99.999	99.999	99.999	0.803	0.051	1.662	0.042
77.9	68.8	19.522	0.037	99.999	99.999	99.999	99.999	0.736	0.052	1.391	0.043
589	948.4	19.524	0.037	99.999	99.999	99.999	99.999	0.729	0.049	1.413	0.042
852.4	637.8	19.524	0.037	99.999	99.999	99.999	99.999	0.835	0.047	1.611	0.043
463.8	163.5	19.53	0.043	99.999	99.999	99.999	99.999	0.707	0.054	1.526	0.047

TABLE 3 (CONTINUED)

X	Y	V	σ_V	$(B-V)$	σ_{B-V}	$(U-B)$	σ_{U-B}	$(V-R)$	σ_{V-R}	$(V-I)$	σ_{V-I}
75.8	40	19.53	0.048	99.999	99.999	99.999	99.999	0.659	0.064	1.378	0.06
908.5	71	19.532	0.034	99.999	99.999	99.999	99.999	0.783	0.044	1.484	0.041
103	212.9	19.533	0.038	99.999	99.999	99.999	99.999	0.821	0.051	1.507	0.045
77.8	159.4	19.539	0.037	99.999	99.999	99.999	99.999	0.745	0.05	1.469	0.044
121	789.5	19.557	0.038	99.999	99.999	99.999	99.999	0.818	0.05	1.575	0.043
259.3	467.2	19.559	0.042	99.999	99.999	99.999	99.999	0.8	0.054	1.578	0.048
925.9	666.9	19.575	0.041	99.999	99.999	99.999	99.999	0.746	0.055	1.606	0.049
131.7	412.9	19.58	0.031	99.999	99.999	99.999	99.999	1.095	0.041	2.149	0.033
767.5	963.8	19.594	0.032	1.055	0.111	99.999	99.999	0.717	0.044	1.519	0.037
302.2	521.8	19.614	0.045	99.999	99.999	99.999	99.999	0.999	0.061	2.143	0.046
95.2	29.1	19.614	0.036	99.999	99.999	99.999	99.999	0.718	0.05	1.589	0.045
899.7	502.3	19.631	0.035	1.345	0.184	99.999	99.999	0.998	0.046	1.983	0.039
486.9	320.5	19.638	0.042	99.999	99.999	99.999	99.999	0.709	0.056	1.443	0.05
649.4	871.7	19.639	0.039	99.999	99.999	99.999	99.999	0.946	0.049	1.839	0.043
916.2	643.2	19.64	0.041	99.999	99.999	99.999	99.999	1.102	0.053	2.141	0.043
498	253.8	19.654	0.045	99.999	99.999	99.999	99.999	0.997	0.059	1.877	0.052
194.4	621.4	19.66	0.047	99.999	99.999	99.999	99.999	0.891	0.061	1.646	0.051
844	421.1	19.66	0.043	99.999	99.999	99.999	99.999	0.928	0.055	1.806	0.047
737.2	608.8	19.688	0.04	99.999	99.999	99.999	99.999	0.894	0.052	1.663	0.046
581.6	705.3	19.693	0.041	99.999	99.999	99.999	99.999	0.659	0.053	1.452	0.047
229.5	337.6	19.697	0.046	99.999	99.999	99.999	99.999	0.924	0.059	1.842	0.049
469.2	856.7	19.7	0.05	99.999	99.999	99.999	99.999	1.015	0.063	1.862	0.054
46.7	803	19.714	0.045	99.999	99.999	99.999	99.999	0.774	0.057	1.553	0.05
592.9	612.6	19.716	0.043	99.999	99.999	99.999	99.999	0.834	0.056	1.589	0.049
178.3	404.1	19.721	0.043	99.999	99.999	99.999	99.999	0.788	0.057	1.674	0.049
503.6	544.1	19.729	0.046	99.999	99.999	99.999	99.999	0.819	0.058	1.774	0.05
712.3	14.6	19.732	0.045	99.999	99.999	99.999	99.999	0.794	0.063	1.554	0.055
961	523.3	19.732	0.045	99.999	99.999	99.999	99.999	0.903	0.058	1.805	0.049
299.2	702.9	19.736	0.041	99.999	99.999	99.999	99.999	0.807	0.054	1.557	0.047
752.7	202.8	19.736	0.046	99.999	99.999	99.999	99.999	0.796	0.062	1.516	0.053
180.5	340.6	19.737	0.048	99.999	99.999	99.999	99.999	0.872	0.065	1.657	0.055
436.2	340.9	19.738	0.042	0.991	0.154	99.999	99.999	0.61	0.057	1.383	0.049
750.6	306.8	19.739	0.036	99.999	99.999	99.999	99.999	0.737	0.049	1.497	0.041
173.4	566.1	19.75	0.048	99.999	99.999	99.999	99.999	0.803	0.064	1.464	0.056
411.3	299.1	19.753	0.041	99.999	99.999	99.999	99.999	0.809	0.054	1.547	0.047
792.5	268.9	19.765	0.036	99.999	99.999	99.999	99.999	0.826	0.05	1.767	0.042
161.2	795.5	19.767	0.054	99.999	99.999	99.999	99.999	0.793	0.067	1.646	0.057
991.4	267.2	19.77	0.036	99.999	99.999	99.999	99.999	0.628	0.049	1.346	0.043
467.9	142.5	19.782	0.049	99.999	99.999	99.999	99.999	0.799	0.063	1.71	0.052
128	626	19.803	0.044	99.999	99.999	99.999	99.999	0.748	0.058	1.63	0.049
14.1	894.9	19.814	0.051	99.999	99.999	99.999	99.999	0.889	0.068	1.702	0.058
865	526.6	19.817	0.046	99.999	99.999	99.999	99.999	0.823	0.059	1.599	0.053
392.3	593.1	19.849	0.051	99.999	99.999	99.999	99.999	0.767	0.068	1.598	0.057
365.9	301.3	19.911	0.047	99.999	99.999	99.999	99.999	1.17	0.063	2.019	0.052
588.6	395.2	19.94	0.049	99.999	99.999	99.999	99.999	0.713	0.068	1.476	0.056
579.9	668.7	19.969	0.048	99.999	99.999	99.999	99.999	1.129	0.06	2.104	0.052
558.7	713.5	19.985	0.053	99.999	99.999	99.999	99.999	1.096	0.068	2.086	0.058
354.3	350.4	19.988	0.058	99.999	99.999	99.999	99.999	1.099	0.074	2.062	0.063
593.7	641.3	19.992	0.057	99.999	99.999	99.999	99.999	1.104	0.073	2.013	0.063
552.9	428.6	20	0.062	99.999	99.999	99.999	99.999	0.999	0.078	1.859	0.068
892.1	376.9	20.015	0.049	99.999	99.999	99.999	99.999	0.983	0.066	1.759	0.058
554	864.7	20.018	0.05	99.999	99.999	99.999	99.999	0.999	0.064	1.977	0.055
761.4	639.3	20.019	0.053	99.999	99.999	99.999	99.999	0.965	0.07	1.771	0.058
714.2	712.7	20.025	0.056	99.999	99.999	99.999	99.999	0.95	0.071	1.773	0.061
765.7	728.1	20.037	0.06	99.999	99.999	99.999	99.999	1.167	0.075	2.653	0.061
226.7	516.2	20.043	0.053	99.999	99.999	99.999	99.999	0.954	0.069	1.796	0.06
746.9	729.5	20.045	0.051	99.999	99.999	99.999	99.999	1.082	0.065	2.086	0.055
709.1	884.1	20.051	0.06	99.999	99.999	99.999	99.999	0.939	0.075	1.743	0.066
569.3	542.4	20.07	0.054	99.999	99.999	99.999	99.999	0.836	0.071	1.621	0.062
591.2	654.5	20.073	0.04	99.999	99.999	99.999	99.999	0.869	0.054	1.614	0.049
880.7	884.8	20.073	0.064	99.999	99.999	99.999	99.999	0.873	0.081	1.621	0.073
367.8	97.3	20.092	0.049	99.999	99.999	99.999	99.999	0.823	0.067	1.563	0.058
950.8	985.3	20.096	0.062	99.999	99.999	99.999	99.999	0.843	0.08	1.656	0.069
934.6	609.6	20.102	0.062	99.999	99.999	99.999	99.999	0.85	0.079	1.701	0.068
764.4	625.4	20.103	0.061	99.999	99.999	99.999	99.999	0.842	0.079	1.731	0.068

TABLE 3 (CONTINUED)

X	Y	V	σ_V	$(B-V)$	σ_{B-V}	$(U-B)$	σ_{U-B}	$(V-R)$	σ_{V-R}	$(V-I)$	σ_{V-I}
417.5	218.9	20.105	0.058	99.999	99.999	99.999	99.999	0.879	0.075	1.816	0.063
88.7	573.6	20.105	0.056	99.999	99.999	99.999	99.999	0.838	0.072	1.649	0.063
964.3	194.1	20.109	0.052	99.999	99.999	99.999	99.999	0.865	0.067	1.622	0.061
473.2	382.4	20.111	0.05	99.999	99.999	99.999	99.999	0.936	0.067	1.724	0.057
583	379.1	20.113	0.058	99.999	99.999	99.999	99.999	0.89	0.077	1.741	0.066
849.2	940.4	20.113	0.058	99.999	99.999	99.999	99.999	0.874	0.079	1.723	0.065
635	683.9	20.117	0.055	99.999	99.999	99.999	99.999	0.834	0.071	1.764	0.061
686.7	646.6	20.118	0.062	99.999	99.999	99.999	99.999	0.834	0.081	1.697	0.069
831.9	651.2	20.122	0.053	99.999	99.999	99.999	99.999	0.99	0.068	2.078	0.057
285.4	96.9	20.127	0.058	99.999	99.999	99.999	99.999	0.826	0.078	1.626	0.067
506.3	66.5	20.128	0.078	99.999	99.999	99.999	99.999	0.871	0.097	1.794	0.083
503.3	964.5	20.132	0.063	99.999	99.999	99.999	99.999	0.841	0.081	1.593	0.071
788	246.9	20.132	0.063	99.999	99.999	99.999	99.999	1.038	0.08	1.841	0.07
645.4	973.6	20.144	0.061	99.999	99.999	99.999	99.999	0.765	0.081	1.65	0.069
158	173.2	20.15	0.063	99.999	99.999	99.999	99.999	0.85	0.081	1.721	0.075
252.2	787	20.154	0.054	99.999	99.999	99.999	99.999	0.763	0.075	1.564	0.062
969.6	273.4	20.161	0.056	99.999	99.999	99.999	99.999	0.731	0.078	1.694	0.062
322.6	825.9	20.165	0.064	99.999	99.999	99.999	99.999	1.02	0.084	99.999	99.999
909.1	870.4	20.172	0.053	99.999	99.999	99.999	99.999	0.764	0.072	1.539	0.061
853.6	959.5	20.174	0.056	99.999	99.999	99.999	99.999	0.913	0.071	1.708	0.064
512.3	830.4	20.185	0.068	99.999	99.999	99.999	99.999	0.781	0.088	1.463	0.077
981.4	802.5	20.196	0.049	99.999	99.999	99.999	99.999	1.012	0.064	2.157	0.053
605.7	36.3	20.21	0.055	99.999	99.999	99.999	99.999	0.826	0.074	1.676	0.065
147.8	580.8	20.217	0.074	99.999	99.999	99.999	99.999	0.757	0.094	1.442	0.085
805.1	669.4	20.219	0.063	99.999	99.999	99.999	99.999	0.787	0.082	1.687	0.07
754.5	909.6	20.221	0.066	99.999	99.999	99.999	99.999	1.162	0.082	1.901	0.073
475.5	443.1	20.225	0.066	99.999	99.999	99.999	99.999	1.036	0.083	1.813	0.073
419.7	609.3	20.226	0.062	99.999	99.999	99.999	99.999	1.068	0.079	1.914	0.071
880	326.8	20.227	0.081	99.999	99.999	99.999	99.999	0.744	0.1	1.675	0.088
253	170.9	20.236	0.064	99.999	99.999	99.999	99.999	0.642	0.089	1.399	0.077
825.6	339.4	20.239	0.08	99.999	99.999	99.999	99.999	0.861	0.102	1.667	0.088
533.3	500.4	20.24	0.053	99.999	99.999	99.999	99.999	0.827	0.075	1.543	0.063
870	192.3	20.24	0.074	99.999	99.999	99.999	99.999	1.169	0.095	2.122	0.081
584.9	751.6	20.244	0.073	99.999	99.999	99.999	99.999	0.869	0.093	1.801	0.079
971.2	349.6	20.246	0.064	99.999	99.999	99.999	99.999	0.994	0.083	1.929	0.069
568.3	359.6	20.252	0.074	99.999	99.999	99.999	99.999	0.787	0.096	1.691	0.081
901.7	900.1	20.253	0.055	99.999	99.999	99.999	99.999	0.945	0.075	1.747	0.061
990.6	313.4	20.254	0.059	99.999	99.999	99.999	99.999	0.836	0.079	1.78	0.064
784.3	437.1	20.266	0.062	99.999	99.999	99.999	99.999	0.913	0.08	1.661	0.072
404.5	364	20.27	0.069	99.999	99.999	99.999	99.999	0.76	0.089	1.6	0.078
809.9	811.1	20.283	0.071	99.999	99.999	99.999	99.999	1.089	0.089	2.181	0.075
109.2	527.1	20.284	0.091	99.999	99.999	99.999	99.999	0.771	0.115	1.674	0.097
726.7	99.4	20.286	0.066	99.999	99.999	99.999	99.999	0.689	0.085	1.695	0.073
833.3	120.9	20.29	0.075	99.999	99.999	99.999	99.999	0.811	0.098	1.545	0.082
993.4	453.6	20.302	0.067	99.999	99.999	99.999	99.999	0.825	0.084	1.805	0.071
961.8	444.3	20.321	0.068	99.999	99.999	99.999	99.999	0.888	0.089	1.768	0.073
605.6	244.7	20.342	0.074	99.999	99.999	99.999	99.999	0.794	0.096	1.636	0.082
666.7	741.3	20.364	0.064	99.999	99.999	99.999	99.999	0.884	0.082	1.768	0.072
795.7	224.1	20.365	0.074	99.999	99.999	99.999	99.999	0.871	0.097	1.794	0.08
960.8	103.9	20.395	0.082	99.999	99.999	99.999	99.999	0.832	0.105	1.804	0.087
941.4	45.4	20.398	0.074	99.999	99.999	99.999	99.999	0.766	0.1	1.65	0.084
943.9	654.6	20.409	0.072	99.999	99.999	99.999	99.999	0.899	0.094	1.637	0.082
871.2	251.2	20.423	0.072	99.999	99.999	99.999	99.999	0.918	0.095	1.676	0.082
889.1	833.8	20.445	0.099	99.999	99.999	99.999	99.999	1.046	0.126	1.884	0.112
606.2	427.6	20.516	0.091	99.999	99.999	99.999	99.999	1.033	0.117	2.15	0.096

2.3. *The data inspection tools* ELIPSE *and* SAFE

Since the stellar density of a cluster increases towards its center with respect to the field stars, an AWK macro (ELIPSE, Moitinho 2003, private communication) was used to extract the data of the central region of a given cluster, as defined by visual inspection in a visual (V) or red (R) image, thus increasing the contrast of the cluster with respect to the surrounding field stars. An ellipse was fitted visually to the image in order to extract the photometric data of the central region of the cluster. To further support the analyses of the clusters, a Java-based computer program (SAFE, McFarland 2010) was developed and

TABLE 4

CCD *UBVRI* PHOTOMETRY OF RU 135

X	Y	V	σ_V	$(B-V)$	σ_{B-V}	$(U-B)$	σ_{U-B}	$(V-R)$	σ_{V-R}	$(V-I)$	σ_{V-I}
862.7	231.5	11.132	0.003	0.597	0.004	0.212	0.002	0.36	0.01	99.999	99.999
237.1	325.4	11.689	0.003	0.71	0.003	0.364	0.003	0.387	0.014	0.86	0.011
294	387.3	11.871	0.008	0.742	0.003	0.405	0.004	0.45	0.038	0.895	0.014
753.2	283.1	12.258	0.002	0.742	0.004	0.405	0.005	0.45	0.002	99.999	99.999
219.7	343	12.337	0.004	0.789	0.003	0.409	0.005	0.47	0.015	0.97	0.01
251.1	263.2	12.691	0.005	0.734	0.004	0.418	0.005	0.431	0.014	0.886	0.003
914.4	595.1	12.697	0.005	0.729	0.004	0.383	0.004	0.433	0.014	0.915	0.003
905.1	237	12.769	0.004	0.768	0.003	0.401	0.006	0.447	0.01	0.956	0.003
244	620.7	12.8	0.004	0.755	0.003	0.378	0.006	0.439	0.01	0.867	0.003
765.1	218	12.809	0.005	0.686	0.005	0.426	0.005	0.414	0.012	0.861	0.003
754.6	654.7	13.162	0.002	2.372	0.006	2.415	0.033	1.276	0.002	2.387	0.01
312	509.4	13.221	0.002	0.995	0.011	0.399	0.007	0.549	0.003	1.099	0.007
929	857.1	13.228	0.002	1.885	0.009	1.897	0.024	1.003	0.003	1.88	0.01
311.8	534.8	13.467	0.002	1.023	0.005	0.446	0.008	0.579	0.002	1.125	0.003
240.7	741.6	14.015	0.003	0.818	0.005	0.444	0.01	0.462	0.02	0.976	0.003
375.8	871.1	14.124	0.003	1.035	0.006	0.31	0.012	0.63	0.003	1.266	0.003
170	549.7	14.153	0.003	0.835	0.005	0.345	0.01	0.483	0.017	1.001	0.004
900.7	200.3	14.153	0.005	1.018	0.01	0.422	0.013	0.592	0.008	99.999	99.999
59.6	527.3	14.168	0.003	0.831	0.006	0.403	0.012	0.462	0.024	0.995	0.004
469.5	207.9	14.189	0.003	0.859	0.006	0.494	0.011	0.494	0.004	1.025	0.004
853.8	605.3	14.221	0.004	1.196	0.008	0.529	0.014	0.693	0.005	1.353	0.005
809.4	224	14.231	0.003	1.853	0.011	1.838	0.038	0.993	0.003	1.896	0.004
811.6	155.8	14.256	0.003	1.446	0.008	1.047	0.02	0.811	0.003	1.556	0.003
655.4	41.7	14.441	0.005	0.948	0.009	0.543	0.013	0.552	0.005	1.138	0.005
900.3	424.6	14.467	0.003	2.276	0.011	2.269	0.088	1.236	0.003	2.373	0.003
153.8	339.4	14.601	0.003	1.895	0.013	1.697	0.049	1.004	0.004	1.915	0.005
989.5	613.4	14.68	0.004	1.226	0.008	0.502	0.021	0.715	0.005	1.464	0.004
472.4	387.8	14.741	0.004	0.969	0.008	0.442	0.017	0.556	0.004	1.137	0.005
61.3	781.1	14.918	0.005	1.098	0.01	0.407	0.02	0.654	0.006	1.297	0.006
501.1	703.7	14.956	0.005	1.036	0.009	0.428	0.019	0.627	0.005	1.253	0.005
183.2	500.2	14.976	0.004	0.99	0.008	0.385	0.019	0.602	0.004	1.212	0.004
818.7	932	14.986	0.003	2.001	0.012	1.942	0.079	1.115	0.004	2.156	0.004
351.3	365.8	14.994	0.004	0.999	0.009	0.384	0.017	0.585	0.004	1.193	0.005
379.3	444	15.06	0.003	2.422	0.017	99.999	99.999	1.301	0.004	2.513	0.004
343.8	97.8	15.111	0.004	1.031	0.009	0.352	0.02	0.571	0.005	1.177	0.005
68.5	51	15.134	0.006	1.088	0.014	0.459	0.025	0.632	0.009	1.309	0.008
706.7	842.4	15.192	0.004	1.84	0.014	1.504	0.079	1.03	0.005	1.986	0.004
150.3	825.4	15.197	0.004	1.112	0.01	0.388	0.023	0.657	0.006	1.316	0.005
313.6	726.9	15.205	0.004	2.212	0.017	99.999	99.999	1.223	0.005	2.286	0.004
375.9	803.3	15.224	0.003	2.564	0.018	99.999	99.999	1.531	0.004	3.096	0.003
799.1	572.3	15.23	0.004	2.175	0.017	99.999	99.999	1.197	0.005	2.282	0.005
903.7	670.2	15.288	0.005	0.988	0.01	0.556	0.022	0.573	0.006	1.197	0.005
864.3	948.6	15.3	0.004	1.032	0.011	0.343	0.023	0.632	0.006	1.293	0.005
521.4	250.4	15.316	0.005	1.04	0.01	0.404	0.023	0.609	0.006	1.242	0.005
892.6	117	15.322	0.004	1.195	0.011	0.554	0.031	0.706	0.006	1.405	0.005
461.7	756.4	15.425	0.005	1.084	0.011	0.441	0.025	0.609	0.006	1.244	0.005
76.8	106.8	15.463	0.006	1.174	0.015	0.552	0.029	0.651	0.008	1.321	0.007
695.9	568.1	15.488	0.006	1.072	0.014	0.396	0.025	0.65	0.009	1.255	0.027
463	662.2	15.506	0.005	1.279	0.011	0.749	0.034	0.735	0.006	1.424	0.006
203.7	486	15.517	0.007	2.078	0.021	99.999	99.999	1.127	0.008	2.196	0.006
360.7	317	15.546	0.005	1.068	0.012	0.374	0.028	0.643	0.007	1.261	0.007
470.2	605.9	15.559	0.004	1.315	0.012	0.62	0.035	0.747	0.006	1.489	0.005
247.4	882.8	15.6	0.004	2.152	0.019	99.999	99.999	1.191	0.005	2.26	0.004
548	109.8	15.611	0.004	1.321	0.012	0.62	0.033	0.743	0.006	1.479	0.005
140.3	606.1	15.616	0.005	1.837	0.016	1.35	0.085	1.014	0.006	1.982	0.005
188.1	270.2	15.655	0.005	1.176	0.013	0.437	0.029	0.689	0.007	1.392	0.006
209.3	281.9	15.658	0.005	1.184	0.014	0.464	0.031	0.693	0.006	1.377	0.006
328.2	15.2	15.663	0.006	1.1	0.014	0.398	0.029	0.659	0.008	1.325	0.007
88	309.4	15.683	0.005	1.884	0.018	1.365	0.119	1.005	0.006	1.983	0.005
211	583.4	15.74	0.004	1.191	0.013	0.571	0.033	0.699	0.006	1.372	0.005
627.1	302.6	15.745	0.005	1.194	0.013	0.591	0.034	0.717	0.006	1.432	0.006
358.2	286.1	15.779	0.004	1.274	0.014	0.588	0.037	0.737	0.007	1.462	0.006
333.6	329.6	15.836	0.008	1.821	0.024	99.999	99.999	0.987	0.012	1.85	0.027
444	138.8	15.841	0.005	1.097	0.014	0.394	0.031	0.614	0.006	1.263	0.006

TABLE 4 (CONTINUED)

X	Y	V	σ_V	$(B-V)$	σ_{B-V}	$(U-B)$	σ_{U-B}	$(V-R)$	σ_{V-R}	$(V-I)$	σ_{V-I}
184.3	820	15.872	0.006	2.283	0.023	99.999	99.999	1.231	0.007	2.301	0.006
290.3	303.8	15.937	0.005	1.284	0.016	0.499	0.038	0.723	0.007	1.418	0.007
185.1	234.9	16.002	0.006	2.123	0.027	99.999	99.999	1.139	0.007	2.165	0.006
752.2	402	16.035	0.005	1.217	0.016	0.546	0.043	0.715	0.008	1.418	0.007
882.7	333.3	16.039	0.006	1.919	0.021	99.999	99.999	1.051	0.007	2.013	0.006
752.8	733.8	16.051	0.004	1.208	0.015	0.579	0.042	0.727	0.006	1.435	0.006
366.3	480.5	16.091	0.006	2.366	0.027	99.999	99.999	1.308	0.007	2.527	0.006
768.8	543	16.107	0.006	2.45	0.028	99.999	99.999	1.312	0.008	2.477	0.006
338.2	90.7	16.112	0.006	1.23	0.017	0.653	0.05	0.762	0.009	1.471	0.008
824.9	64.7	16.124	0.006	2.435	0.032	99.999	99.999	1.381	0.008	2.598	0.006
886.1	231.2	16.133	0.006	1.304	0.019	99.999	99.999	0.718	0.008	1.438	0.007
306.2	824.7	16.141	0.006	1.819	0.02	99.999	99.999	0.921	0.008	1.676	0.006
191.6	669.5	16.186	0.005	1.206	0.016	0.543	0.044	0.708	0.008	1.429	0.007
92	678	16.2	0.006	1.869	0.025	99.999	99.999	0.999	0.008	1.928	0.006
415.8	968.1	16.235	0.006	1.435	0.019	0.716	0.063	0.793	0.008	1.576	0.007
413.4	213.4	16.237	0.007	2.121	0.028	99.999	99.999	1.122	0.008	2.164	0.007
95.5	889.5	16.243	0.006	1.18	0.017	0.262	0.04	0.649	0.009	1.354	0.008
24.3	299.1	16.3	0.006	1.182	0.018	0.353	0.047	0.701	0.01	1.439	0.008
815.3	887.9	16.324	0.006	1.194	0.02	0.593	0.054	0.76	0.009	1.495	0.008
813.1	638.1	16.356	0.006	1.982	0.024	99.999	99.999	1.103	0.008	2.116	0.007
515.2	188.3	16.388	0.007	1.684	0.025	99.999	99.999	0.941	0.008	1.798	0.007
610.2	294	16.405	0.006	1.342	0.022	0.947	0.081	0.769	0.009	1.516	0.008
282.9	830.9	16.434	0.006	1.129	0.018	0.392	0.045	0.709	0.008	1.405	0.008
630.8	635.4	16.465	0.007	1.319	0.021	0.568	0.059	0.785	0.01	1.499	0.009
344.2	162.9	16.467	0.007	1.347	0.021	0.765	0.07	0.768	0.009	1.506	0.008
79.3	270.1	16.506	0.008	1.229	0.021	99.999	99.999	0.74	0.01	1.461	0.008
572.8	213.6	16.526	0.021	1.805	0.034	99.999	99.999	1.028	0.067	99.999	99.999
129.5	127	16.538	0.006	1.239	0.021	0.392	0.059	0.714	0.01	1.408	0.009
737.2	811.1	16.557	0.013	1.498	0.023	0.822	0.107	0.862	0.01	1.671	0.009
264.5	777.8	16.594	0.007	2.012	0.031	99.999	99.999	1.095	0.008	2.074	0.007
934.5	237.7	16.614	0.009	2.107	0.038	99.999	99.999	1.144	0.012	2.187	0.01
760.6	550.9	16.634	0.008	1.309	0.022	0.639	0.071	0.777	0.009	1.533	0.009
61.3	553.6	16.652	0.007	1.884	0.03	99.999	99.999	1.057	0.009	2.061	0.008
746.1	114.2	16.664	0.008	2.049	0.033	99.999	99.999	1.109	0.01	2.11	0.008
137	235.2	16.673	0.007	1.193	0.022	0.559	0.074	0.743	0.01	1.437	0.009
490.8	408.2	16.687	0.008	1.758	0.029	99.999	99.999	1.029	0.01	2.007	0.008
409.1	283.6	16.709	0.008	1.326	0.023	0.727	0.077	0.763	0.011	1.498	0.01
95.7	22.9	16.717	0.01	1.954	0.034	99.999	99.999	1.103	0.012	2.117	0.011
354.4	941.2	16.733	0.007	1.144	0.023	0.481	0.064	0.698	0.01	1.407	0.01
812.7	355.6	16.742	0.007	1.902	0.031	99.999	99.999	1.057	0.009	2.031	0.008
505.7	194.2	16.752	0.009	1.286	0.025	0.652	0.098	0.752	0.012	1.481	0.011
863.5	537.6	16.767	0.008	1.727	0.03	99.999	99.999	1.082	0.01	2.244	0.008
972.6	730.3	16.781	0.009	1.918	0.033	99.999	99.999	1.026	0.011	2.028	0.009
2.1	118.5	16.789	0.009	2.02	0.04	99.999	99.999	1.077	0.012	2.098	0.01
391.1	830.6	16.817	0.009	1.322	0.026	0.71	0.095	0.76	0.011	1.488	0.01
873.1	206.6	16.842	0.01	1.587	0.032	99.999	99.999	0.878	0.012	1.721	0.011
586.2	658.1	16.85	0.008	1.634	0.031	99.999	99.999	0.874	0.01	1.742	0.009
290	63.5	16.873	0.009	2.045	0.036	99.999	99.999	1.175	0.011	2.249	0.009
725.5	100.3	16.877	0.008	1.24	0.025	0.451	0.082	0.718	0.011	1.433	0.01
555	250.4	16.887	0.008	1.771	0.034	99.999	99.999	0.988	0.011	1.947	0.009
854	771.5	16.893	0.013	1.408	0.027	0.58	0.111	0.796	0.012	1.58	0.011
461.8	176.8	16.913	0.008	1.371	0.028	99.999	99.999	0.773	0.011	1.49	0.01
905.1	15.1	16.923	0.011	1.366	0.029	0.665	0.088	0.772	0.013	1.539	0.011
456.4	781.6	16.941	0.007	2.022	0.036	99.999	99.999	1.123	0.009	2.116	0.008
99.2	770.3	16.949	0.01	99.999	99.999	99.999	99.999	1.036	0.013	2.123	0.039
927.5	475	16.953	0.009	1.58	0.03	99.999	99.999	0.939	0.011	1.806	0.01
680.8	105.6	16.967	0.008	1.871	0.036	99.999	99.999	1.029	0.01	2.015	0.009
213.2	622.9	16.969	0.009	1.477	0.03	99.999	99.999	0.851	0.012	1.668	0.01
406.4	861.7	16.987	0.009	1.7	0.035	99.999	99.999	0.979	0.011	1.894	0.009
419	210.8	16.995	0.011	1.88	0.043	99.999	99.999	1.037	0.014	2.012	0.014
586.2	482.6	17.031	0.01	1.26	0.025	0.761	0.103	0.741	0.012	1.467	0.01
794.2	705.6	17.04	0.009	1.926	0.043	99.999	99.999	1.098	0.011	2.084	0.009
678.4	942	17.043	0.012	2.349	0.061	99.999	99.999	1.293	0.016	2.421	0.013
849.3	61.4	17.07	0.01	1.88	0.04	99.999	99.999	1.07	0.012	2.077	0.01
365.7	892.8	17.073	0.01	1.297	0.03	99.999	99.999	0.828	0.013	1.58	0.011
156.4	570	17.083	0.008	1.268	0.026	99.999	99.999	0.764	0.011	1.493	0.009

TABLE 4 (CONTINUED)

X	Y	V	σ_V	$(B-V)$	σ_{B-V}	$(U-B)$	σ_{U-B}	$(V-R)$	σ_{V-R}	$(V-I)$	σ_{V-I}
368.6	275.1	17.086	0.009	2.122	0.051	99.999	99.999	1.196	0.011	2.257	0.009
445.4	296.3	17.104	0.011	1.301	0.029	99.999	99.999	0.746	0.014	1.485	0.012
218.5	564.4	17.138	0.009	1.362	0.033	99.999	99.999	0.757	0.012	1.519	0.01
476.3	271.1	17.139	0.01	1.332	0.028	99.999	99.999	0.758	0.013	1.494	0.011
822	108.5	17.151	0.01	2.077	0.049	99.999	99.999	1.21	0.013	2.301	0.011
906.3	510.2	17.165	0.01	1.756	0.039	99.999	99.999	0.991	0.013	1.952	0.01
482.2	595.9	17.168	0.009	1.926	0.045	99.999	99.999	1.131	0.012	2.12	0.01
237.5	120.7	17.173	0.009	2.32	0.052	99.999	99.999	1.267	0.012	2.38	0.01
527.7	735.7	17.181	0.009	1.942	0.045	99.999	99.999	1.052	0.011	1.994	0.009
906.9	842.3	17.183	0.011	1.385	0.034	99.999	99.999	0.8	0.014	1.585	0.012
201.5	732.9	17.184	0.009	1.217	0.031	99.999	99.999	0.8	0.012	1.525	0.011
925.6	149.5	17.197	0.015	99.999	99.999	99.999	99.999	0.83	0.022	1.654	0.019
466	902.1	17.217	0.009	1.854	0.043	99.999	99.999	0.993	0.011	1.949	0.009
446.9	492.6	17.218	0.014	99.999	99.999	99.999	99.999	1.086	0.019	99.999	99.999
745.3	579.2	17.219	0.011	1.391	0.034	99.999	99.999	0.881	0.014	1.718	0.012
751.7	152.2	17.219	0.011	1.897	0.053	99.999	99.999	1.078	0.015	2.063	0.012
607.5	572.6	17.223	0.011	1.342	0.033	99.999	99.999	0.786	0.014	1.55	0.012
753.5	233.6	17.224	0.011	1.803	0.038	99.999	99.999	1.094	0.014	2.079	0.012
319.2	878.6	17.236	0.01	1.311	0.031	99.999	99.999	0.75	0.013	1.474	0.011
810	904	17.241	0.011	1.403	0.035	99.999	99.999	0.861	0.015	1.66	0.013
110.2	933.7	17.245	0.011	1.413	0.035	99.999	99.999	0.787	0.015	1.558	0.013
357.8	451.6	17.249	0.01	1.513	0.034	99.999	99.999	0.825	0.013	1.591	0.011
328.3	762.8	17.26	0.01	1.815	0.041	99.999	99.999	1.021	0.013	1.969	0.011
818.2	740.1	17.263	0.01	1.784	0.041	99.999	99.999	1.012	0.013	1.956	0.011
611.8	964.6	17.306	0.011	1.419	0.035	99.999	99.999	0.804	0.015	1.572	0.014
508	75.8	17.31	0.012	1.431	0.035	99.999	99.999	0.81	0.014	1.613	0.013
971.1	836.7	17.322	0.011	1.909	0.05	99.999	99.999	1.064	0.014	2.097	0.012
919.6	70.5	17.327	0.012	1.279	0.038	99.999	99.999	0.767	0.015	1.542	0.013
547.2	231.7	17.357	0.011	1.756	0.048	99.999	99.999	1.025	0.014	1.975	0.012
824.3	986.5	17.382	0.011	1.823	0.052	99.999	99.999	1.022	0.014	1.953	0.012
7.8	319.3	17.389	0.013	2.027	0.051	99.999	99.999	1.085	0.016	2.095	0.013
869.9	635.1	17.397	0.01	1.69	0.046	99.999	99.999	1.029	0.013	1.973	0.011
974.9	118.1	17.418	0.009	2.62	0.081	99.999	99.999	1.382	0.012	2.67	0.01
792.6	311.8	17.424	0.015	1.873	0.055	99.999	99.999	1.034	0.019	1.989	0.016
31.4	739.7	17.429	0.013	2.082	0.063	99.999	99.999	1.137	0.016	2.149	0.013
518.1	429.3	17.43	0.012	1.284	0.037	99.999	99.999	0.757	0.016	1.542	0.014
334.7	347.9	17.448	0.013	1.36	0.036	99.999	99.999	0.796	0.016	1.521	0.014
87.4	480.8	17.453	0.011	2.005	0.058	99.999	99.999	1.093	0.014	2.092	0.012
87.5	256.5	17.459	0.012	2.073	0.068	99.999	99.999	1.098	0.015	2.116	0.012
469.8	867.5	17.461	0.012	1.473	0.041	99.999	99.999	0.854	0.015	1.673	0.013
655.5	726.6	17.461	0.011	1.536	0.039	99.999	99.999	0.858	0.014	1.66	0.012
528.4	217.8	17.463	0.012	2.028	0.067	99.999	99.999	1.127	0.016	2.086	0.013
137.2	585.6	17.469	0.011	1.984	0.051	99.999	99.999	1.097	0.014	2.082	0.012
111.4	515.9	17.476	0.014	1.968	0.058	99.999	99.999	1.092	0.019	2.107	0.015
201.9	138.1	17.485	0.012	2.028	0.063	99.999	99.999	1.17	0.016	2.187	0.013
7.3	466.3	17.487	0.011	1.361	0.035	99.999	99.999	0.78	0.016	1.54	0.012
164.5	186.9	17.489	0.013	1.42	0.037	99.999	99.999	0.789	0.017	1.548	0.015
229.5	520.9	17.505	0.011	1.33	0.042	99.999	99.999	0.812	0.015	1.523	0.013
167.3	429.6	17.511	0.012	1.653	0.053	99.999	99.999	1.014	0.015	1.966	0.013
608.8	72.8	17.522	0.012	1.609	0.046	99.999	99.999	0.846	0.015	1.679	0.013
72.4	217.1	17.532	0.013	1.351	0.043	99.999	99.999	0.77	0.017	1.537	0.015
434.2	710.5	17.534	0.012	1.447	0.054	99.999	99.999	0.914	0.015	1.728	0.014
734.2	460.8	17.542	0.012	1.702	0.047	99.999	99.999	0.974	0.015	1.843	0.013
659.9	85.5	17.547	0.013	2.064	0.052	99.999	99.999	1.102	0.017	2.127	0.014
468.6	705.9	17.551	0.012	1.368	0.038	99.999	99.999	0.812	0.015	1.61	0.013
690.6	801.2	17.57	0.012	1.328	0.04	99.999	99.999	0.828	0.017	1.662	0.014
795.7	485.1	17.582	0.014	99.999	99.999	99.999	99.999	1.103	0.018	2.119	0.015
205.9	514	17.583	0.014	2.232	0.07	99.999	99.999	1.212	0.018	2.285	0.015
879.8	929.6	17.584	0.012	1.381	0.044	99.999	99.999	0.803	0.015	1.618	0.013
873.3	723.2	17.587	0.011	1.898	0.05	99.999	99.999	1.123	0.014	2.092	0.012
714.3	66.9	17.594	0.013	1.376	0.044	99.999	99.999	0.8	0.017	1.574	0.015
601.7	607.3	17.623	0.012	2.037	0.073	99.999	99.999	1.104	0.015	2.101	0.013
24.5	766.4	17.627	0.015	1.367	0.045	99.999	99.999	0.758	0.018	1.545	0.016
331.1	211.7	17.632	0.014	1.393	0.045	99.999	99.999	0.835	0.018	1.554	0.016
768.7	25.7	17.642	0.012	2.137	0.077	99.999	99.999	1.201	0.016	2.278	0.013
282.8	367.4	17.643	0.014	99.999	99.999	99.999	99.999	1.004	0.018	1.968	0.016

TABLE 4 (CONTINUED)

X	Y	V	σ_V	$(B-V)$	σ_{B-V}	$(U-B)$	σ_{U-B}	$(V-R)$	σ_{V-R}	$(V-I)$	σ_{V-I}
271	201.8	17.667	0.013	99.999	99.999	99.999	99.999	1.113	0.018	2.15	0.014
410.2	815.2	17.667	0.015	2.004	0.065	99.999	99.999	1.171	0.02	2.15	0.016
174.1	880.8	17.669	0.014	1.98	0.065	99.999	99.999	1.109	0.019	2.12	0.016
451.2	656.3	17.669	0.015	1.413	0.045	99.999	99.999	0.727	0.019	1.478	0.016
310.9	206.9	17.67	0.012	1.611	0.051	99.999	99.999	0.882	0.016	1.75	0.014
654.1	576.7	17.672	0.013	2.396	0.086	99.999	99.999	1.263	0.017	2.388	0.014
789.2	702.1	17.683	0.014	1.487	0.048	99.999	99.999	0.826	0.019	1.652	0.016
775.5	886.6	17.685	0.014	1.056	0.037	99.999	99.999	0.658	0.019	1.364	0.017
348.7	659.8	17.694	0.013	1.294	0.041	99.999	99.999	0.753	0.018	1.529	0.015
210.8	480.9	17.701	0.013	2.119	0.077	99.999	99.999	1.122	0.017	2.14	0.014
544.3	696.3	17.701	0.015	1.373	0.045	99.999	99.999	0.831	0.019	1.64	0.016
323.4	401.1	17.708	0.014	2.048	0.074	99.999	99.999	1.048	0.018	1.956	0.015
902.9	681.7	17.715	0.012	2.119	0.066	99.999	99.999	1.185	0.016	2.209	0.013
296.1	529.6	17.717	0.014	1.454	0.05	99.999	99.999	0.817	0.019	1.569	0.016
356	482.3	17.728	0.013	1.282	0.045	99.999	99.999	0.818	0.017	1.611	0.014
779.3	599.5	17.733	0.015	1.307	0.062	99.999	99.999	0.778	0.02	1.535	0.017
363.4	109.5	17.74	0.014	1.812	0.06	99.999	99.999	1	0.018	1.911	0.016
547.8	846.7	17.756	0.015	1.413	0.049	99.999	99.999	0.831	0.019	1.632	0.017
780.8	604.5	17.761	0.016	1.361	0.063	99.999	99.999	0.879	0.024	1.686	0.02
203	36.2	17.767	0.015	1.781	0.067	99.999	99.999	1.064	0.019	2.072	0.016
92.1	990.2	17.767	0.017	1.47	0.049	99.999	99.999	0.797	0.024	1.56	0.02
702.2	601.4	17.768	0.014	1.339	0.041	99.999	99.999	0.828	0.018	1.609	0.016
662.5	917.2	17.769	0.014	1.962	0.062	99.999	99.999	1.058	0.018	2.044	0.015
725.8	623	17.775	0.013	1.525	0.05	99.999	99.999	0.897	0.017	1.742	0.014
877.3	477.7	17.777	0.013	2.019	0.067	99.999	99.999	1.091	0.017	2.078	0.014
985.6	318.6	17.784	0.016	1.468	0.054	99.999	99.999	0.825	0.023	1.595	0.019
218.7	812.3	17.789	0.014	1.235	0.043	99.999	99.999	0.789	0.018	1.573	0.016
951.4	441	17.796	0.013	1.41	0.05	99.999	99.999	0.79	0.017	1.571	0.015
275.4	536.2	17.799	0.015	1.899	0.074	99.999	99.999	1.156	0.019	2.143	0.016
555.7	140.9	17.803	0.012	1.857	0.064	99.999	99.999	1.158	0.016	2.171	0.013
246	723.6	17.818	0.014	1.866	0.078	99.999	99.999	1.13	0.018	2.125	0.015
850.1	803.5	17.819	0.014	1.613	0.051	99.999	99.999	0.868	0.018	1.65	0.016
129.8	227.8	17.822	0.015	1.398	0.049	99.999	99.999	0.868	0.018	1.63	0.017
768.6	616.3	17.826	0.015	1.358	0.049	99.999	99.999	0.833	0.02	1.656	0.02
226.9	302.7	17.83	0.015	2.57	0.116	99.999	99.999	1.193	0.019	2.303	0.015
848.3	122.4	17.842	0.019	99.999	99.999	99.999	99.999	1.086	0.024	2.079	0.02
624.2	13.8	17.843	0.015	1.392	0.049	99.999	99.999	0.844	0.02	1.607	0.018
656.1	636.9	17.859	0.016	1.834	0.074	99.999	99.999	1.18	0.02	2.467	0.016
924.3	881	17.873	0.015	2.234	0.144	99.999	99.999	1.974	0.02	4.023	0.016
485.3	54.3	17.878	0.015	1.752	0.07	99.999	99.999	0.986	0.019	1.968	0.017
776.4	547.5	17.878	0.016	1.894	0.074	99.999	99.999	1.086	0.02	2.068	0.017
626.6	918.6	17.891	0.015	1.644	0.061	99.999	99.999	0.991	0.019	1.87	0.016
169.6	332.3	17.892	0.018	1.62	0.066	99.999	99.999	0.904	0.023	1.844	0.02
475.8	951.5	17.894	0.014	1.815	0.075	99.999	99.999	1.039	0.018	2.036	0.015
615.9	635.6	17.927	0.016	1.859	0.074	99.999	99.999	1.086	0.021	2.107	0.018
668.5	725.7	17.93	0.016	1.474	0.055	99.999	99.999	0.858	0.02	1.685	0.018
981.7	950.3	17.934	0.017	1.544	0.055	99.999	99.999	0.887	0.023	1.728	0.02
88.4	816.2	17.936	0.014	1.761	0.074	99.999	99.999	1.037	0.019	1.989	0.016
473.4	164.6	17.939	0.015	1.801	0.072	99.999	99.999	1.124	0.019	2.07	0.016
695.6	330.1	17.943	0.019	1.944	0.083	99.999	99.999	1.13	0.026	99.999	99.999
125.4	340	17.946	0.016	1.876	0.073	99.999	99.999	1.089	0.02	2.093	0.017
71.7	473.4	17.949	0.015	2.197	0.096	99.999	99.999	1.098	0.02	2.188	0.016
781.7	480.8	17.958	0.016	1.83	0.074	99.999	99.999	0.997	0.021	1.972	0.017
19.2	716.9	17.964	0.015	1.341	0.055	99.999	99.999	0.781	0.019	1.552	0.016
384.2	612.5	17.968	0.014	1.563	0.058	99.999	99.999	0.882	0.019	1.744	0.015
71.3	314.4	17.97	0.019	1.929	0.075	99.999	99.999	1.103	0.023	2.052	0.02
293.6	642.1	17.974	0.017	1.661	0.071	99.999	99.999	0.979	0.022	1.907	0.019
234.5	252.3	17.978	0.017	1.8	0.074	99.999	99.999	0.975	0.021	1.939	0.018
794.2	761	17.983	0.02	2.19	0.101	99.999	99.999	1.16	0.026	2.207	0.021
686.7	183.9	17.991	0.015	1.378	0.06	99.999	99.999	0.862	0.02	1.676	0.018
381.4	217.1	17.995	0.016	2.145	0.103	99.999	99.999	1.202	0.02	2.232	0.017
262.2	294.3	17.997	0.018	2.129	0.102	99.999	99.999	1.164	0.022	2.223	0.018
240.9	236.3	17.999	0.017	99.999	99.999	99.999	99.999	1.041	0.022	1.954	0.018
732.9	758.2	18.004	0.015	1.675	0.065	99.999	99.999	0.916	0.02	1.793	0.016
452.9	189.2	18.011	0.018	1.444	0.065	99.999	99.999	0.852	0.023	1.645	0.021
564.3	495.4	18.017	0.016	1.859	0.069	99.999	99.999	1.2	0.02	2.208	0.017

TABLE 4 (CONTINUED)

X	Y	V	σ_V	$(B-V)$	σ_{B-V}	$(U-B)$	σ_{U-B}	$(V-R)$	σ_{V-R}	$(V-I)$	σ_{V-I}
784.2	128.7	18.022	0.015	2.148	0.088	99.999	99.999	1.192	0.02	2.261	0.015
86	981.2	18.029	0.016	1.98	0.088	99.999	99.999	1.055	0.021	2.044	0.017
559.1	342.8	18.031	0.016	1.299	0.06	99.999	99.999	0.839	0.022	1.645	0.019
621.8	401.8	18.038	0.017	1.493	0.064	99.999	99.999	0.887	0.022	1.685	0.019
89.1	656.5	18.039	0.022	99.999	99.999	99.999	99.999	0.807	0.031	1.608	0.028
565.2	744.2	18.053	0.017	1.386	0.057	99.999	99.999	0.855	0.022	1.639	0.019
770	383.1	18.055	0.022	1.488	0.072	99.999	99.999	0.853	0.031	1.702	0.026
936	416.7	18.057	0.015	1.618	0.061	99.999	99.999	0.909	0.02	1.789	0.017
64.9	663.2	18.068	0.017	1.828	0.09	99.999	99.999	1.04	0.022	2.018	0.018
561.6	865.9	18.07	0.016	1.428	0.06	99.999	99.999	0.836	0.021	1.62	0.018
339.2	141.5	18.074	0.017	1.326	0.058	99.999	99.999	0.741	0.023	1.488	0.02
29.4	688.4	18.1	0.019	99.999	99.999	99.999	99.999	1.057	0.024	2.019	0.02
639.4	780.1	18.101	0.019	2.005	0.086	99.999	99.999	1.115	0.024	2.153	0.019
942.9	270	18.101	0.018	1.596	0.071	99.999	99.999	0.899	0.024	1.693	0.02
660	510.9	18.104	0.023	1.76	0.09	99.999	99.999	1.015	0.03	99.999	99.999
538.7	10.3	18.109	0.017	1.532	0.074	99.999	99.999	0.813	0.022	1.646	0.019
534	206.9	18.114	0.019	1.979	0.087	99.999	99.999	1.072	0.024	2.005	0.02
104.2	768.2	18.117	0.023	99.999	99.999	99.999	99.999	0.851	0.031	99.999	99.999
702.1	852.9	18.118	0.018	1.589	0.074	99.999	99.999	0.917	0.024	1.785	0.02
634.1	309.7	18.123	0.018	1.809	0.081	99.999	99.999	0.98	0.023	1.95	0.019
18.8	612.5	18.126	0.018	1.946	0.082	99.999	99.999	1.028	0.023	2.036	0.019
301.3	286.2	18.13	0.018	99.999	99.999	99.999	99.999	0.833	0.025	1.548	0.02
154.6	58.7	18.143	0.018	1.457	0.065	99.999	99.999	0.845	0.023	1.665	0.019
180.2	599.2	18.148	0.018	1.716	0.076	99.999	99.999	0.924	0.022	1.912	0.019
384.4	351.1	18.155	0.02	1.228	0.061	99.999	99.999	0.854	0.028	1.574	0.024
367.9	577.9	18.17	0.019	1.586	0.071	99.999	99.999	0.804	0.024	1.66	0.021
321.6	180.6	18.174	0.02	1.019	0.054	99.999	99.999	0.532	0.026	1.198	0.024
617	889.7	18.182	0.018	1.43	0.065	99.999	99.999	0.894	0.023	1.689	0.02
396.5	755.3	18.187	0.018	99.999	99.999	99.999	99.999	1.183	0.023	2.231	0.019
243.6	499.2	18.188	0.017	1.309	0.065	99.999	99.999	0.848	0.022	1.596	0.02
708.6	913	18.197	0.02	1.445	0.066	99.999	99.999	0.877	0.027	1.683	0.024
424.6	215.9	18.198	0.022	1.574	0.076	99.999	99.999	0.844	0.029	1.611	0.036
253.4	805.6	18.204	0.02	0.938	0.049	99.999	99.999	0.491	0.027	1.119	0.023
112.5	255.6	18.207	0.022	1.442	0.067	99.999	99.999	0.795	0.029	1.616	0.024
389.1	792.5	18.211	0.017	1.574	0.071	99.999	99.999	0.838	0.024	1.67	0.022
298.2	225.2	18.214	0.021	1.365	0.073	99.999	99.999	0.802	0.027	1.571	0.025
423.5	27.7	18.215	0.021	99.999	99.999	99.999	99.999	1.157	0.027	2.236	0.022
922.1	394.6	18.22	0.022	1.356	0.078	99.999	99.999	0.835	0.031	1.643	0.028
361	686.7	18.225	0.022	99.999	99.999	99.999	99.999	1.07	0.028	1.994	0.024
111	342.2	18.225	0.019	1.185	0.062	99.999	99.999	0.773	0.025	1.57	0.021
398.2	318.1	18.237	0.019	1.697	0.089	99.999	99.999	1.03	0.025	2.009	0.022
405.6	308	18.237	0.017	1.904	0.102	99.999	99.999	1.024	0.022	1.998	0.019
363.4	868	18.238	0.02	1.409	0.074	99.999	99.999	0.799	0.027	1.622	0.024
472.3	304.8	18.245	0.019	1.863	0.099	99.999	99.999	1.07	0.025	2.073	0.02
508.4	17.4	18.246	0.019	1.405	0.064	99.999	99.999	0.88	0.024	1.716	0.02
532.6	313.5	18.246	0.02	1.317	0.069	99.999	99.999	0.785	0.025	1.582	0.021
440.5	448.8	18.253	0.021	1.903	0.098	99.999	99.999	1.11	0.027	2.102	0.023
320.9	42.3	18.257	0.019	1.64	0.078	99.999	99.999	0.884	0.024	1.748	0.021
986.6	232.2	18.258	0.019	1.978	0.104	99.999	99.999	0.952	0.025	1.912	0.02
450	290	18.265	0.021	1.365	0.064	99.999	99.999	0.834	0.028	1.655	0.023
316.1	846.9	18.267	0.023	99.999	99.999	99.999	99.999	0.861	0.032	1.686	0.029
372.5	958.6	18.267	0.02	1.298	0.069	99.999	99.999	0.757	0.025	1.512	0.022
783.9	820.6	18.271	0.016	1.419	0.073	99.999	99.999	0.872	0.022	1.663	0.018
829.5	860.4	18.278	0.024	1.401	0.077	99.999	99.999	0.818	0.034	1.638	0.029
705.8	462.1	18.284	0.02	1.89	0.088	99.999	99.999	1.043	0.025	2.021	0.021
464.5	233.2	18.285	0.023	1.72	0.107	99.999	99.999	0.866	0.031	1.69	0.027
813.9	651.7	18.287	0.016	1.365	0.068	99.999	99.999	0.826	0.023	1.684	0.018
19.2	121.5	18.293	0.019	1.905	0.102	99.999	99.999	1.126	0.026	2.129	0.021
512.9	118.8	18.315	0.021	1.412	0.071	99.999	99.999	0.875	0.026	1.69	0.023
222.8	499.6	18.32	0.021	1.965	0.102	99.999	99.999	1.152	0.027	2.143	0.023
600.4	429	18.32	0.02	1.612	0.087	99.999	99.999	1.006	0.025	1.89	0.021
540.9	912.4	18.325	0.019	1.841	0.106	99.999	99.999	0.941	0.025	1.843	0.021
636.8	506.6	18.335	0.019	1.504	0.075	99.999	99.999	0.853	0.025	1.648	0.022
21.3	444.2	18.338	0.021	1.371	0.066	99.999	99.999	0.874	0.028	1.735	0.024
889.9	539.7	18.343	0.02	1.877	0.088	99.999	99.999	1.076	0.026	2.048	0.022
21.5	597.5	18.346	0.022	1.346	0.072	99.999	99.999	0.774	0.028	1.577	0.025

TABLE 4 (CONTINUED)

X	Y	V	σ_V	$(B-V)$	σ_{B-V}	$(U-B)$	σ_{U-B}	$(V-R)$	σ_{V-R}	$(V-I)$	σ_{V-I}
639.9	912.8	18.351	0.02	99.999	99.999	99.999	99.999	1.076	0.026	2.029	0.022
122.9	438.9	18.356	0.019	2.021	0.128	99.999	99.999	1	0.025	2.035	0.02
127.3	48.8	18.363	0.021	1.369	0.075	99.999	99.999	0.876	0.028	1.682	0.024
540.9	740.8	18.372	0.021	1.293	0.079	99.999	99.999	0.876	0.028	1.654	0.025
978.6	104	18.374	0.02	1.343	0.078	99.999	99.999	0.858	0.027	1.618	0.024
659	782.1	18.377	0.019	1.354	0.066	99.999	99.999	0.858	0.026	1.646	0.021
104	207.9	18.382	0.023	1.993	0.102	99.999	99.999	1.042	0.029	2.059	0.024
770.3	966.7	18.389	0.021	1.532	0.085	99.999	99.999	0.95	0.026	1.793	0.022
899.1	688.8	18.391	0.02	1.712	0.09	99.999	99.999	0.834	0.028	1.676	0.024
180.3	472.9	18.395	0.021	1.473	0.081	99.999	99.999	0.985	0.029	1.814	0.025
345	502.8	18.395	0.022	1.844	0.108	99.999	99.999	0.988	0.03	1.964	0.024
980.7	395.9	18.404	0.024	99.999	99.999	99.999	99.999	1.021	0.031	1.913	0.026
406.1	164.1	18.405	0.021	1.656	0.103	99.999	99.999	0.986	0.027	1.937	0.023
303.4	159.3	18.409	0.023	1.512	0.083	99.999	99.999	0.835	0.029	1.619	0.025
515.2	91.2	18.409	0.022	1.413	0.091	99.999	99.999	0.943	0.028	1.806	0.025
396.6	620.2	18.411	0.021	1.497	0.084	99.999	99.999	0.958	0.027	1.759	0.023
823.8	537.1	18.411	0.021	1.484	0.088	99.999	99.999	0.87	0.027	1.662	0.024
432.4	593.6	18.415	0.021	1.636	0.095	99.999	99.999	0.937	0.027	1.814	0.023
52	700.1	18.424	0.024	1.852	0.122	99.999	99.999	1.044	0.032	2.025	0.026
215.9	235.4	18.429	0.021	99.999	99.999	99.999	99.999	1.16	0.027	2.277	0.022
375.3	600.2	18.433	0.022	1.477	0.081	99.999	99.999	0.993	0.028	1.941	0.023
260	848.6	18.439	0.022	1.408	0.083	99.999	99.999	0.955	0.028	1.775	0.025
267.9	915.8	18.443	0.022	1.594	0.093	99.999	99.999	1.07	0.029	2.051	0.024
154.6	810.4	18.445	0.022	1.359	0.083	99.999	99.999	0.827	0.029	1.625	0.025
206.2	388.7	18.451	0.02	1.383	0.081	99.999	99.999	0.923	0.025	1.776	0.022
221.3	943.6	18.458	0.024	2.053	0.139	99.999	99.999	1.143	0.03	2.151	0.025
814.4	882.2	18.472	0.031	99.999	99.999	99.999	99.999	0.913	0.041	1.728	0.034
785.2	358.9	18.485	0.023	99.999	99.999	99.999	99.999	1.052	0.029	2.032	0.025
376.4	573	18.486	0.025	1.586	0.094	99.999	99.999	1.068	0.031	2.026	0.026
60.1	85.2	18.488	0.026	1.612	0.107	99.999	99.999	0.917	0.033	1.739	0.028
173.3	748.6	18.492	0.024	99.999	99.999	99.999	99.999	1.101	0.03	2.03	0.026
757.7	317	18.494	0.023	1.46	0.088	99.999	99.999	0.794	0.03	1.602	0.025
130.9	109.1	18.496	0.023	1.187	0.075	99.999	99.999	0.861	0.03	1.633	0.025
508.9	918.3	18.501	0.023	1.763	0.114	99.999	99.999	0.975	0.029	1.954	0.024
14.3	826.2	18.505	0.02	1.176	0.071	99.999	99.999	0.799	0.027	1.56	0.023
839.1	774.3	18.515	0.028	1.266	0.076	99.999	99.999	0.899	0.036	1.744	0.032
143.1	282.5	18.52	0.025	1.335	0.09	99.999	99.999	0.843	0.035	1.668	0.03
777.5	523.5	18.521	0.023	1.276	0.076	99.999	99.999	0.872	0.03	1.668	0.026
980.3	451	18.522	0.021	1.768	0.124	99.999	99.999	0.952	0.027	1.888	0.023
667.4	220.8	18.526	0.023	1.723	0.102	99.999	99.999	1.005	0.031	1.975	0.025
262.9	39.2	18.527	0.025	1.252	0.075	99.999	99.999	0.896	0.033	1.68	0.028
484.1	551	18.53	0.021	99.999	99.999	99.999	99.999	0.968	0.028	1.913	0.023
367.6	877.7	18.541	0.025	1.708	0.118	99.999	99.999	0.853	0.035	1.63	0.031
823	324.7	18.549	0.022	1.38	0.079	99.999	99.999	0.899	0.029	1.813	0.024
303.9	589.4	18.551	0.023	1.505	0.087	99.999	99.999	0.856	0.03	1.702	0.026
516.4	894.4	18.557	0.024	99.999	99.999	99.999	99.999	0.88	0.031	1.712	0.026
799.6	652.7	18.561	0.023	1.459	0.089	99.999	99.999	0.834	0.031	1.653	0.026
855.3	665	18.564	0.025	1.465	0.102	99.999	99.999	0.853	0.032	1.697	0.027
197.1	930	18.566	0.023	99.999	99.999	99.999	99.999	1.085	0.03	2.083	0.025
403.5	623.1	18.566	0.025	1.69	0.105	99.999	99.999	1.072	0.032	2.093	0.026
818.2	83.4	18.57	0.025	1.54	0.098	99.999	99.999	0.942	0.033	1.782	0.031
704.8	960.7	18.576	0.022	1.553	0.083	99.999	99.999	0.872	0.028	1.689	0.025
28.5	126.4	18.578	0.027	99.999	99.999	99.999	99.999	1.05	0.034	2.069	0.029
165.3	308.2	18.585	0.027	1.856	0.136	99.999	99.999	1.183	0.035	2.167	0.029
22.7	787.2	18.589	0.024	1.583	0.122	99.999	99.999	0.921	0.032	1.721	0.028
185.4	44.3	18.598	0.026	1.487	0.102	99.999	99.999	0.992	0.033	1.901	0.028
621.6	79.5	18.607	0.028	1.828	0.145	99.999	99.999	1.004	0.035	2.002	0.03
330.4	36.6	18.61	0.026	1.31	0.092	99.999	99.999	0.876	0.035	1.657	0.031
315.5	662.9	18.627	0.024	1.479	0.098	99.999	99.999	0.808	0.032	1.629	0.028
53.7	504.4	18.634	0.027	99.999	99.999	99.999	99.999	0.998	0.034	1.951	0.028
439.8	228.9	18.634	0.023	1.46	0.084	99.999	99.999	0.796	0.032	1.656	0.03
5.5	523.6	18.636	0.023	1.511	0.105	99.999	99.999	0.871	0.03	1.685	0.026
980.2	401.1	18.638	0.033	99.999	99.999	99.999	99.999	1.007	0.044	1.948	0.038
680.5	293.2	18.643	0.024	1.658	0.116	99.999	99.999	0.973	0.033	1.796	0.028
541.5	879.7	18.646	0.027	99.999	99.999	99.999	99.999	0.996	0.035	2.026	0.029
512.2	846.2	18.648	0.026	99.999	99.999	99.999	99.999	1.068	0.033	2.021	0.028

TABLE 4 (CONTINUED)

X	Y	V	σ_V	$(B-V)$	σ_{B-V}	$(U-B)$	σ_{U-B}	$(V-R)$	σ_{V-R}	$(V-I)$	σ_{V-I}
843.5	66.1	18.651	0.025	99.999	99.999	99.999	99.999	1.124	0.032	2.155	0.028
551.7	960.8	18.656	0.026	1.477	0.101	99.999	99.999	0.911	0.035	1.761	0.03
563.2	503.2	18.666	0.026	1.485	0.096	99.999	99.999	0.844	0.032	1.699	0.028
153.6	563.6	18.674	0.03	99.999	99.999	99.999	99.999	0.914	0.041	1.751	0.034
677.8	429.4	18.675	0.026	99.999	99.999	99.999	99.999	1.028	0.033	1.99	0.028
673.5	800	18.676	0.025	1.295	0.081	99.999	99.999	0.854	0.032	1.717	0.027
447	635.2	18.68	0.023	99.999	99.999	99.999	99.999	1.093	0.029	1.996	0.026
171.2	179.8	18.682	0.027	1.598	0.117	99.999	99.999	0.988	0.035	1.847	0.03
111.4	715.1	18.688	0.025	99.999	99.999	99.999	99.999	1.106	0.032	2.015	0.027
897.7	829.8	18.689	0.028	1.507	0.123	99.999	99.999	0.825	0.035	1.728	0.031
438.2	606	18.694	0.022	99.999	99.999	99.999	99.999	1.154	0.029	2.162	0.024
728.5	738.8	18.694	0.023	1.754	0.122	99.999	99.999	0.985	0.029	1.828	0.025
526.3	242.4	18.7	0.032	99.999	99.999	99.999	99.999	0.879	0.041	1.758	0.035
493.5	172.3	18.71	0.03	1.57	0.114	99.999	99.999	1.146	0.039	2.108	0.032
971.6	311.4	18.713	0.023	99.999	99.999	99.999	99.999	1.165	0.029	2.188	0.025
953.2	469.3	18.715	0.023	1.178	0.076	99.999	99.999	0.831	0.03	1.629	0.026
956.6	93.3	18.717	0.025	1.625	0.129	99.999	99.999	1.071	0.032	2.083	0.027
573.8	722.6	18.722	0.027	99.999	99.999	99.999	99.999	1.178	0.035	2.152	0.029
335.5	821.2	18.725	0.028	1.439	0.1	99.999	99.999	0.748	0.036	1.537	0.031
668.1	847.1	18.727	0.024	1.679	0.134	99.999	99.999	0.917	0.032	1.763	0.027
708.8	372.7	18.727	0.03	99.999	99.999	99.999	99.999	1.073	0.038	2.178	0.031
885.7	830.7	18.738	0.026	1.609	0.108	99.999	99.999	1.009	0.035	1.961	0.028
406.5	489	18.739	0.028	99.999	99.999	99.999	99.999	1.123	0.036	2.148	0.031
481.8	464.8	18.74	0.026	1.557	0.097	99.999	99.999	0.899	0.033	1.728	0.029
616	294.4	18.741	0.031	99.999	99.999	99.999	99.999	1.123	0.039	2.12	0.033
62.7	607.4	18.742	0.026	1.334	0.095	99.999	99.999	0.781	0.033	1.621	0.029
727.2	225.2	18.743	0.028	99.999	99.999	99.999	99.999	0.975	0.036	1.983	0.03
231.5	800.9	18.756	0.025	1.347	0.11	99.999	99.999	0.956	0.034	1.771	0.028
891.7	47.4	18.758	0.031	99.999	99.999	99.999	99.999	1.105	0.04	2.104	0.033
407.4	719.7	18.76	0.024	1.447	0.089	99.999	99.999	0.872	0.033	1.685	0.027
228.8	163.8	18.763	0.028	1.479	0.116	99.999	99.999	1.011	0.036	1.865	0.031
453.3	952.2	18.765	0.03	99.999	99.999	99.999	99.999	0.998	0.037	1.977	0.032
388	228.9	18.767	0.03	1.289	0.093	99.999	99.999	0.883	0.04	1.665	0.036
630	728.3	18.768	0.026	99.999	99.999	99.999	99.999	1.048	0.033	2.059	0.027
195.9	842.3	18.772	0.031	99.999	99.999	99.999	99.999	1.055	0.043	1.995	0.035
204.1	638.4	18.775	0.028	1.74	0.146	99.999	99.999	0.999	0.037	1.905	0.031
323.9	106.6	18.778	0.028	99.999	99.999	99.999	99.999	0.803	0.036	1.586	0.03
698.5	703.8	18.779	0.029	99.999	99.999	99.999	99.999	1.076	0.038	2.062	0.031
121.7	623.8	18.781	0.027	1.666	0.128	99.999	99.999	0.991	0.036	1.895	0.03
603.2	270.6	18.783	0.028	1.429	0.095	99.999	99.999	0.896	0.036	1.646	0.032
414.9	714.9	18.79	0.028	99.999	99.999	99.999	99.999	1.095	0.037	2.058	0.031
624.4	101.3	18.791	0.028	1.47	0.135	99.999	99.999	1.07	0.036	2.058	0.03
674.2	204.7	18.791	0.029	1.497	0.108	99.999	99.999	0.918	0.039	1.723	0.032
809.2	752.9	18.803	0.026	1.589	0.117	99.999	99.999	0.921	0.036	1.763	0.03
111.2	882.9	18.81	0.03	99.999	99.999	99.999	99.999	0.981	0.038	1.802	0.033
641.6	926.8	18.827	0.029	99.999	99.999	99.999	99.999	1.019	0.036	1.981	0.031
706.7	788.2	18.834	0.025	1.265	0.101	99.999	99.999	0.813	0.034	1.643	0.028
162.7	433.5	18.835	0.031	99.999	99.999	99.999	99.999	0.866	0.042	1.667	0.037
33	905.9	18.841	0.031	99.999	99.999	99.999	99.999	1.079	0.039	2.028	0.033
786.1	2.5	18.847	0.032	1.372	0.131	99.999	99.999	0.977	0.04	1.836	0.035
426.4	625.7	18.849	0.029	0.984	0.09	99.999	99.999	0.704	0.038	1.467	0.033
439.5	710.4	18.849	0.031	99.999	99.999	99.999	99.999	0.84	0.041	1.577	0.038
71.7	287.8	18.849	0.028	99.999	99.999	99.999	99.999	0.971	0.037	1.853	0.031
567.8	948.9	18.855	0.03	99.999	99.999	99.999	99.999	0.93	0.038	1.76	0.033
709.3	427.2	18.855	0.028	99.999	99.999	99.999	99.999	1.011	0.037	1.898	0.031
20.2	423.8	18.862	0.029	99.999	99.999	99.999	99.999	0.888	0.038	1.73	0.033
207.7	655.7	18.873	0.03	1.327	0.096	99.999	99.999	0.859	0.04	1.688	0.033
488.5	348.6	18.873	0.027	1.502	0.116	99.999	99.999	0.87	0.036	1.696	0.031
386.1	88.4	18.885	0.029	99.999	99.999	99.999	99.999	0.988	0.039	1.954	0.032
961.5	305.3	18.901	0.028	1.321	0.11	99.999	99.999	0.772	0.036	1.62	0.031
254.6	839.7	18.904	0.03	1.582	0.133	99.999	99.999	1.062	0.04	2.02	0.033
879	274.3	18.904	0.033	99.999	99.999	99.999	99.999	0.866	0.042	1.709	0.037
13.3	125.9	18.904	0.032	1.273	0.126	99.999	99.999	0.88	0.04	1.704	0.036
295	239.5	18.906	0.026	99.999	99.999	99.999	99.999	1.079	0.035	2.038	0.029
849.6	504.2	18.906	0.033	99.999	99.999	99.999	99.999	0.955	0.041	1.862	0.035
168.7	806.8	18.917	0.029	99.999	99.999	99.999	99.999	1.066	0.039	2.091	0.031

TABLE 4 (CONTINUED)

X	Y	V	σ_V	$(B-V)$	σ_{B-V}	$(U-B)$	σ_{U-B}	$(V-R)$	σ_{V-R}	$(V-I)$	σ_{V-I}
832.4	227.2	18.917	0.034	99.999	99.999	99.999	99.999	1.13	0.043	2.156	0.037
446.1	669.5	18.919	0.031	99.999	99.999	99.999	99.999	1.101	0.041	1.936	0.035
37.5	479.3	18.92	0.033	99.999	99.999	99.999	99.999	0.871	0.042	1.787	0.037
808.3	302.7	18.92	0.032	99.999	99.999	99.999	99.999	0.826	0.042	1.61	0.036
591.6	730.9	18.926	0.034	99.999	99.999	99.999	99.999	0.971	0.044	1.788	0.038
890.1	733.4	18.932	0.035	1.506	0.149	99.999	99.999	0.821	0.045	1.69	0.038
256.4	755	18.938	0.029	1.337	0.141	99.999	99.999	0.834	0.039	1.652	0.035
599.7	249.7	18.946	0.033	1.331	0.104	99.999	99.999	0.883	0.042	1.747	0.036
529.8	978.5	18.95	0.032	1.47	0.124	99.999	99.999	0.912	0.042	1.734	0.036
467.2	562.9	18.951	0.034	99.999	99.999	99.999	99.999	0.946	0.043	1.884	0.037
534.2	423	18.951	0.031	99.999	99.999	99.999	99.999	0.821	0.04	1.681	0.035
970.9	901.3	18.952	0.031	99.999	99.999	99.999	99.999	0.999	0.039	1.955	0.034
3.7	773.8	18.959	0.031	99.999	99.999	99.999	99.999	0.989	0.04	1.947	0.033
349.1	285.4	18.961	0.03	99.999	99.999	99.999	99.999	0.868	0.038	1.734	0.034
557.9	39.3	18.965	0.037	99.999	99.999	99.999	99.999	1.045	0.046	1.992	0.04
186.3	279	18.969	0.035	99.999	99.999	99.999	99.999	1.031	0.045	1.951	0.038
586.5	607.7	18.973	0.034	1.471	0.151	99.999	99.999	0.898	0.044	1.765	0.038
785.8	525.9	18.98	0.029	99.999	99.999	99.999	99.999	1.059	0.038	1.987	0.031
444.9	392.6	18.982	0.033	99.999	99.999	99.999	99.999	1.231	0.043	2.186	0.036
59.1	848.2	18.984	0.034	1.293	0.142	99.999	99.999	0.887	0.044	1.723	0.038
364.8	400.4	18.995	0.032	99.999	99.999	99.999	99.999	1.143	0.041	2.128	0.034
401.7	374.8	18.997	0.029	99.999	99.999	99.999	99.999	0.923	0.04	1.765	0.034
534.8	32.3	18.997	0.033	99.999	99.999	99.999	99.999	1.202	0.043	2.196	0.035
986.6	77.2	19.001	0.033	99.999	99.999	99.999	99.999	0.964	0.043	1.821	0.036
488.6	556.3	19.008	0.034	99.999	99.999	99.999	99.999	1.172	0.044	2.098	0.036
514.2	836.6	19.015	0.041	99.999	99.999	99.999	99.999	0.704	0.053	1.486	0.046
175.8	646.1	19.019	0.033	1.58	0.158	99.999	99.999	0.873	0.043	1.701	0.036
841.3	28.8	19.019	0.04	99.999	99.999	99.999	99.999	1.047	0.056	1.925	0.043
247.6	412.4	19.02	0.031	99.999	99.999	99.999	99.999	0.922	0.039	1.768	0.036
850.1	365.6	19.028	0.029	99.999	99.999	99.999	99.999	0.935	0.039	1.816	0.032
263.3	603.1	19.031	0.047	99.999	99.999	99.999	99.999	1.062	0.062	2.053	0.051
138.2	688.8	19.037	0.036	99.999	99.999	99.999	99.999	0.994	0.046	1.891	0.039
141.4	365.1	19.039	0.033	99.999	99.999	99.999	99.999	0.921	0.044	1.784	0.037
214.2	363.3	19.043	0.036	99.999	99.999	99.999	99.999	1.058	0.047	2.001	0.04
69.6	857.8	19.043	0.037	99.999	99.999	99.999	99.999	0.992	0.047	1.921	0.04
420.3	632.8	19.044	0.03	99.999	99.999	99.999	99.999	1.027	0.039	1.861	0.034
915.2	778.7	19.044	0.034	99.999	99.999	99.999	99.999	0.74	0.045	1.495	0.04
410.9	352.7	19.045	0.036	99.999	99.999	99.999	99.999	0.869	0.046	1.784	0.039
316.2	29.8	19.048	0.04	99.999	99.999	99.999	99.999	1.112	0.05	2.124	0.043
403.4	251.8	19.05	0.035	99.999	99.999	99.999	99.999	1.015	0.045	1.91	0.039
593.6	279.8	19.05	0.035	99.999	99.999	99.999	99.999	0.966	0.046	1.784	0.039
676.9	240.2	19.056	0.033	99.999	99.999	99.999	99.999	0.983	0.043	1.85	0.036
285.4	736.2	19.057	0.037	99.999	99.999	99.999	99.999	0.863	0.048	1.815	0.039
286.7	960	19.057	0.033	99.999	99.999	99.999	99.999	0.966	0.041	1.86	0.036
233.6	276.2	19.058	0.035	99.999	99.999	99.999	99.999	1.032	0.047	2.015	0.038
512.6	742.4	19.062	0.035	99.999	99.999	99.999	99.999	0.921	0.044	1.742	0.038
242.3	279.1	19.069	0.042	99.999	99.999	99.999	99.999	0.719	0.057	1.553	0.048
926	569.8	19.069	0.032	99.999	99.999	99.999	99.999	1.189	0.041	2.15	0.034
722.6	206.6	19.077	0.034	99.999	99.999	99.999	99.999	1.005	0.044	2.004	0.037
34.2	928.4	19.084	0.041	99.999	99.999	99.999	99.999	1.018	0.055	2.027	0.045
651	25.9	19.084	0.032	99.999	99.999	99.999	99.999	0.944	0.042	1.788	0.036
836.3	636.9	19.084	0.04	99.999	99.999	99.999	99.999	0.974	0.05	1.909	0.042
43.8	36.4	19.085	0.037	99.999	99.999	99.999	99.999	0.971	0.049	1.842	0.041
73.1	861.1	19.085	0.041	99.999	99.999	99.999	99.999	1.031	0.053	2.106	0.044
983.4	742.3	19.085	0.037	99.999	99.999	99.999	99.999	0.861	0.048	1.718	0.041
494.7	53.5	19.09	0.037	99.999	99.999	99.999	99.999	0.966	0.047	1.921	0.04
320.2	656.5	19.098	0.036	99.999	99.999	99.999	99.999	0.885	0.047	1.73	0.041
325.6	344	19.101	0.037	99.999	99.999	99.999	99.999	0.959	0.048	1.798	0.042
161.5	370.8	19.103	0.038	99.999	99.999	99.999	99.999	0.94	0.05	1.783	0.042
449.4	759.5	19.105	0.036	1.435	0.172	99.999	99.999	1.045	0.047	1.886	0.04
880.9	593.5	19.107	0.034	99.999	99.999	99.999	99.999	0.996	0.045	1.839	0.037
336.7	768.1	19.118	0.034	99.999	99.999	99.999	99.999	0.849	0.045	1.713	0.039
928.6	885.5	19.121	0.038	99.999	99.999	99.999	99.999	1.093	0.049	99.999	99.999
76.9	119.6	19.133	0.039	99.999	99.999	99.999	99.999	1.02	0.049	1.982	0.041
34.9	210.5	19.139	0.034	99.999	99.999	99.999	99.999	1.047	0.044	2.03	0.036
943.4	779.2	19.14	0.04	99.999	99.999	99.999	99.999	0.876	0.053	1.764	0.044

TABLE 4 (CONTINUED)

X	Y	V	σ_V	$(B-V)$	σ_{B-V}	$(U-B)$	σ_{U-B}	$(V-R)$	σ_{V-R}	$(V-I)$	σ_{V-I}
531.2	900.2	19.146	0.035	99.999	99.999	99.999	99.999	0.933	0.046	1.736	0.04
573.9	235.7	19.152	0.039	99.999	99.999	99.999	99.999	0.957	0.049	1.839	0.042
167.8	394.8	19.153	0.043	99.999	99.999	99.999	99.999	0.721	0.056	1.646	0.047
742.1	70.2	19.154	0.035	99.999	99.999	99.999	99.999	1.082	0.044	2.094	0.038
131.4	559.3	19.156	0.039	99.999	99.999	99.999	99.999	0.93	0.05	1.817	0.043
254.2	283.7	19.161	0.047	99.999	99.999	99.999	99.999	0.986	0.06	1.986	0.051
325.1	500.9	19.161	0.042	99.999	99.999	99.999	99.999	0.853	0.058	1.738	0.046
123.8	717.4	19.167	0.035	99.999	99.999	99.999	99.999	1.078	0.045	2.006	0.038
712	860.4	19.169	0.036	99.999	99.999	99.999	99.999	0.955	0.046	1.834	0.04
138.6	125.4	19.172	0.035	99.999	99.999	99.999	99.999	0.916	0.045	1.796	0.038
308	749.5	19.173	0.039	99.999	99.999	99.999	99.999	0.839	0.05	1.674	0.045
413.7	652.5	19.178	0.04	99.999	99.999	99.999	99.999	0.776	0.052	1.618	0.045
694.2	164.3	19.179	0.034	99.999	99.999	99.999	99.999	1.148	0.044	2.102	0.037
791.7	876.4	19.18	0.036	99.999	99.999	99.999	99.999	0.943	0.049	1.83	0.041
92.9	368.4	19.187	0.034	99.999	99.999	99.999	99.999	0.936	0.045	1.797	0.039
746.4	31.5	19.19	0.039	99.999	99.999	99.999	99.999	1.141	0.049	2.147	0.042
806.8	851.7	19.194	0.04	99.999	99.999	99.999	99.999	0.904	0.052	1.744	0.044
188.5	851.8	19.204	0.041	99.999	99.999	99.999	99.999	0.953	0.053	1.758	0.045
342.8	414.4	19.206	0.038	99.999	99.999	99.999	99.999	0.949	0.048	1.786	0.042
150	833.7	19.214	0.046	99.999	99.999	99.999	99.999	0.971	0.059	1.846	0.051
431.9	777.5	19.214	0.034	99.999	99.999	99.999	99.999	1.122	0.046	2.029	0.038
79.9	764.1	19.219	0.033	99.999	99.999	99.999	99.999	0.775	0.047	1.618	0.039
74.2	879	19.22	0.036	99.999	99.999	99.999	99.999	1.032	0.046	2.034	0.038
195.8	326.2	19.222	0.044	99.999	99.999	99.999	99.999	0.993	0.058	1.984	0.047
313.9	624.6	19.225	0.042	99.999	99.999	99.999	99.999	0.988	0.053	1.887	0.046
122.9	640	19.227	0.04	99.999	99.999	99.999	99.999	0.908	0.054	1.713	0.047
447.3	274.1	19.228	0.038	99.999	99.999	99.999	99.999	1.149	0.053	2.101	0.043
786.7	978.3	19.229	0.037	99.999	99.999	99.999	99.999	0.881	0.048	1.723	0.042
49.7	856	19.233	0.043	99.999	99.999	99.999	99.999	0.823	0.056	1.624	0.048
462.2	742.5	19.233	0.042	99.999	99.999	99.999	99.999	1.042	0.053	2.05	0.045
816.8	116.7	19.234	0.043	99.999	99.999	99.999	99.999	0.919	0.057	1.797	0.049
335.6	798.7	19.239	0.035	99.999	99.999	99.999	99.999	0.881	0.047	1.678	0.042
529.1	938.4	19.25	0.034	99.999	99.999	99.999	99.999	0.839	0.046	1.695	0.038
127.2	668.9	19.25	0.035	99.999	99.999	99.999	99.999	0.869	0.046	1.749	0.039
373.5	717.6	19.256	0.043	99.999	99.999	99.999	99.999	0.904	0.056	1.726	0.047
545.3	746.5	19.258	0.036	99.999	99.999	99.999	99.999	0.985	0.048	1.863	0.041
869.2	36.7	19.258	0.045	99.999	99.999	99.999	99.999	0.746	0.057	1.591	0.049
946	704.9	19.259	0.042	99.999	99.999	99.999	99.999	0.913	0.053	1.826	0.045
817.1	251.3	19.265	0.044	99.999	99.999	99.999	99.999	1.169	0.056	2.164	0.047
433	989.5	19.266	0.046	99.999	99.999	99.999	99.999	0.883	0.059	1.641	0.052
169	221.6	19.272	0.04	99.999	99.999	99.999	99.999	1.081	0.051	2	0.045
627.9	410.5	19.272	0.045	99.999	99.999	99.999	99.999	1.076	0.058	2.036	0.048
407.8	195.7	19.274	0.039	99.999	99.999	99.999	99.999	0.969	0.053	99.999	99.999
190.4	612.7	19.275	0.041	99.999	99.999	99.999	99.999	0.979	0.054	1.796	0.046
521.2	511.6	19.276	0.039	99.999	99.999	99.999	99.999	1.096	0.049	2.113	0.042
955.9	461.1	19.277	0.043	99.999	99.999	99.999	99.999	0.787	0.055	1.58	0.049
308	175.1	19.282	0.036	99.999	99.999	99.999	99.999	0.964	0.046	1.81	0.043
811.5	848.3	19.285	0.038	99.999	99.999	99.999	99.999	1.021	0.049	1.972	0.041
662.4	949.2	19.289	0.036	99.999	99.999	99.999	99.999	0.951	0.048	1.808	0.041
567.6	126	19.29	0.041	99.999	99.999	99.999	99.999	1.019	0.055	1.891	0.045
275.9	620.7	19.292	0.04	99.999	99.999	99.999	99.999	0.962	0.052	1.768	0.045
320.2	922.2	19.292	0.046	99.999	99.999	99.999	99.999	0.852	0.061	1.663	0.053
547.3	323.5	19.294	0.038	99.999	99.999	99.999	99.999	0.912	0.05	1.726	0.042
583.3	393.4	19.294	0.05	99.999	99.999	99.999	99.999	0.741	0.062	1.518	0.056
869.8	64.6	19.299	0.046	99.999	99.999	99.999	99.999	0.953	0.059	1.822	0.051
257.1	148.2	19.304	0.043	99.999	99.999	99.999	99.999	0.924	0.054	1.754	0.048
696.3	493.3	19.304	0.041	99.999	99.999	99.999	99.999	0.87	0.054	1.695	0.047
561.9	187.3	19.308	0.038	99.999	99.999	99.999	99.999	0.714	0.051	1.496	0.047
837.7	366.4	19.308	0.041	99.999	99.999	99.999	99.999	0.975	0.055	1.77	0.047
440	614.4	19.309	0.042	99.999	99.999	99.999	99.999	0.908	0.055	1.891	0.045
714.5	256.1	19.319	0.043	99.999	99.999	99.999	99.999	0.926	0.056	1.76	0.049
856.5	310.3	19.32	0.045	99.999	99.999	99.999	99.999	0.938	0.058	1.788	0.049
965.3	600.1	19.323	0.042	99.999	99.999	99.999	99.999	0.918	0.054	1.789	0.046
429	162.8	19.324	0.043	99.999	99.999	99.999	99.999	0.993	0.057	1.875	0.05
616.2	504.1	19.327	0.042	99.999	99.999	99.999	99.999	1.033	0.053	2.053	0.045
105.3	984.4	19.328	0.044	99.999	99.999	99.999	99.999	0.877	0.057	1.755	0.048

TABLE 4 (CONTINUED)

X	Y	V	σ_V	$(B-V)$	σ_{B-V}	$(U-B)$	σ_{U-B}	$(V-R)$	σ_{V-R}	$(V-I)$	σ_{V-I}
522	825.8	19.33	0.047	99.999	99.999	99.999	99.999	1.049	0.06	1.921	0.051
854.9	956.3	19.331	0.043	99.999	99.999	99.999	99.999	0.987	0.055	1.853	0.046
91.4	319.3	19.332	0.046	99.999	99.999	99.999	99.999	0.94	0.059	1.942	0.049
80.9	819.9	19.334	0.046	99.999	99.999	99.999	99.999	0.839	0.058	1.667	0.051
609.4	303.9	19.34	0.041	99.999	99.999	99.999	99.999	1.101	0.055	2.041	0.044
535.1	329.2	19.344	0.039	99.999	99.999	99.999	99.999	0.957	0.052	1.934	0.043
142	157.2	19.352	0.041	99.999	99.999	99.999	99.999	0.979	0.055	1.869	0.046
234.7	697.3	19.352	0.045	99.999	99.999	99.999	99.999	1.004	0.056	1.963	0.049
576.9	548.7	19.352	0.042	99.999	99.999	99.999	99.999	0.927	0.055	1.784	0.046
265.2	901.1	19.355	0.045	99.999	99.999	99.999	99.999	0.972	0.059	1.942	0.049
484.4	851.3	19.362	0.041	99.999	99.999	99.999	99.999	1.076	0.052	2.053	0.045
863	798.4	19.367	0.046	99.999	99.999	99.999	99.999	1.187	0.059	2.081	0.05
952.6	283	19.369	0.041	99.999	99.999	99.999	99.999	0.885	0.053	1.827	0.046
423.5	221.9	19.371	0.048	99.999	99.999	99.999	99.999	0.875	0.064	1.673	0.062
875.3	527.4	19.374	0.042	99.999	99.999	99.999	99.999	0.978	0.054	1.745	0.048
725	383.6	19.375	0.038	99.999	99.999	99.999	99.999	0.86	0.051	1.695	0.044
101.1	109.3	19.381	0.049	99.999	99.999	99.999	99.999	0.784	0.066	1.49	0.061
458.5	264.4	19.382	0.041	99.999	99.999	99.999	99.999	0.99	0.054	1.942	0.046
209.6	859.9	19.385	0.043	99.999	99.999	99.999	99.999	0.859	0.055	1.651	0.048
22	191.8	19.386	0.049	99.999	99.999	99.999	99.999	0.883	0.063	1.815	0.053
740.2	583.8	19.388	0.042	99.999	99.999	99.999	99.999	0.915	0.056	1.752	0.048
213.7	176.1	19.389	0.045	99.999	99.999	99.999	99.999	1.037	0.058	1.973	0.049
804	958.7	19.393	0.042	99.999	99.999	99.999	99.999	1.018	0.053	1.744	0.048
581.8	575.3	19.397	0.039	99.999	99.999	99.999	99.999	1.01	0.052	1.891	0.042
771.5	105.9	19.398	0.043	99.999	99.999	99.999	99.999	0.902	0.057	1.716	0.049
636.8	551.3	19.402	0.048	99.999	99.999	99.999	99.999	0.997	0.061	1.819	0.053
878.9	86.3	19.402	0.045	99.999	99.999	99.999	99.999	1.071	0.06	2.068	0.05
471.6	39.2	19.408	0.043	99.999	99.999	99.999	99.999	0.824	0.058	1.693	0.046
691.4	295.5	19.41	0.052	99.999	99.999	99.999	99.999	0.991	0.066	1.879	0.058
351.3	551.2	19.415	0.043	99.999	99.999	99.999	99.999	0.898	0.057	1.819	0.049
691.6	260.6	19.417	0.054	99.999	99.999	99.999	99.999	0.992	0.068	1.836	0.059
418.6	797.3	19.418	0.043	99.999	99.999	99.999	99.999	1.03	0.056	2.015	0.046
674.6	861.3	19.418	0.049	99.999	99.999	99.999	99.999	0.969	0.062	1.889	0.053
283.6	326.6	19.42	0.05	99.999	99.999	99.999	99.999	0.97	0.063	1.946	0.053
876.5	381.7	19.428	0.048	99.999	99.999	99.999	99.999	0.907	0.062	1.724	0.053
489.4	954.1	19.429	0.042	99.999	99.999	99.999	99.999	0.917	0.055	1.69	0.049
821.5	201.3	19.433	0.052	99.999	99.999	99.999	99.999	0.957	0.068	1.826	0.058
844.3	771	19.434	0.042	99.999	99.999	99.999	99.999	0.848	0.056	1.764	0.047
924	43.5	19.435	0.043	99.999	99.999	99.999	99.999	1.099	0.057	2.106	0.047
823.5	190.9	19.436	0.049	99.999	99.999	99.999	99.999	0.868	0.067	1.654	0.058
457.9	304.7	19.44	0.044	99.999	99.999	99.999	99.999	1.021	0.06	1.885	0.049
673	123.3	19.441	0.048	99.999	99.999	99.999	99.999	0.844	0.062	1.715	0.053
783.8	80.5	19.444	0.044	99.999	99.999	99.999	99.999	0.974	0.058	1.951	0.048
254.4	396.2	19.445	0.056	99.999	99.999	99.999	99.999	1.024	0.071	2.03	0.06
586.7	798.9	19.445	0.054	99.999	99.999	99.999	99.999	0.874	0.07	1.746	0.061
317.8	648.7	19.446	0.05	99.999	99.999	99.999	99.999	1.044	0.064	2.039	0.054
436.8	981.3	19.447	0.046	99.999	99.999	99.999	99.999	0.83	0.059	1.718	0.05
604.8	709.5	19.447	0.044	99.999	99.999	99.999	99.999	1.068	0.057	2.055	0.048
693.5	953.8	19.447	0.044	99.999	99.999	99.999	99.999	0.881	0.058	1.648	0.05
818.4	496.8	19.448	0.046	99.999	99.999	99.999	99.999	0.965	0.058	1.907	0.05
891.9	457	19.448	0.052	99.999	99.999	99.999	99.999	0.843	0.066	1.699	0.057
648.6	812	19.451	0.043	99.999	99.999	99.999	99.999	0.995	0.056	2.095	0.049
355.5	988.2	19.452	0.046	99.999	99.999	99.999	99.999	0.751	0.059	1.502	0.053
198.1	413.6	19.453	0.05	99.999	99.999	99.999	99.999	0.904	0.068	1.767	0.057
6.3	591.5	19.453	0.041	99.999	99.999	99.999	99.999	0.862	0.055	1.805	0.045
970.5	498.7	19.454	0.049	99.999	99.999	99.999	99.999	0.868	0.064	1.694	0.054
561.3	532.2	19.457	0.039	99.999	99.999	99.999	99.999	0.955	0.052	1.828	0.044
461.6	339.1	19.459	0.051	99.999	99.999	99.999	99.999	0.956	0.069	1.788	0.06
700.3	262.3	19.461	0.048	99.999	99.999	99.999	99.999	0.958	0.061	1.9	0.053
277.2	208.1	19.464	0.05	99.999	99.999	99.999	99.999	0.933	0.063	1.714	0.056
107.9	142.1	19.474	0.048	99.999	99.999	99.999	99.999	0.833	0.061	1.788	0.053
868.5	871.5	19.477	0.047	99.999	99.999	99.999	99.999	0.815	0.061	1.739	0.052
162.4	718.3	19.479	0.06	99.999	99.999	99.999	99.999	0.951	0.079	1.847	0.067
216.5	495.2	19.48	0.049	99.999	99.999	99.999	99.999	1.033	0.066	99.999	99.999
588.3	340.1	19.48	0.05	99.999	99.999	99.999	99.999	0.96	0.064	1.785	0.055
485.5	581.3	19.482	0.048	99.999	99.999	99.999	99.999	0.896	0.063	1.758	0.054

TABLE 4 (CONTINUED)

X	Y	V	σ_V	$(B-V)$	σ_{B-V}	$(U-B)$	σ_{U-B}	$(V-R)$	σ_{V-R}	$(V-I)$	σ_{V-I}
733.2	573.2	19.483	0.054	99.999	99.999	99.999	99.999	0.944	0.068	1.815	0.058
188.1	797.7	19.49	0.044	99.999	99.999	99.999	99.999	1.041	0.057	1.99	0.048
241.6	767.1	19.49	0.072	99.999	99.999	99.999	99.999	1.021	0.091	1.979	0.077
336.6	835.3	19.492	0.046	99.999	99.999	99.999	99.999	1.05	0.059	1.884	0.051
123.8	569.2	19.493	0.048	99.999	99.999	99.999	99.999	0.858	0.062	1.746	0.055
271.4	485.6	19.496	0.05	99.999	99.999	99.999	99.999	1.046	0.063	1.924	0.054
272.9	688.4	19.5	0.049	99.999	99.999	99.999	99.999	0.916	0.064	1.731	0.055
479.4	377.8	19.501	0.055	99.999	99.999	99.999	99.999	0.839	0.072	1.665	0.061
40.7	395.6	19.506	0.046	99.999	99.999	99.999	99.999	0.926	0.06	1.796	0.051
521.9	932.5	19.513	0.043	99.999	99.999	99.999	99.999	0.955	0.058	1.777	0.048
445.2	244.8	19.519	0.05	99.999	99.999	99.999	99.999	0.862	0.063	1.726	0.056
404.4	657.8	19.523	0.054	99.999	99.999	99.999	99.999	0.929	0.07	1.776	0.061
706.5	360.4	19.524	0.045	99.999	99.999	99.999	99.999	0.861	0.061	1.766	0.05
479.3	412.5	19.532	0.055	99.999	99.999	99.999	99.999	0.992	0.078	1.753	0.063
274.8	721.5	19.533	0.051	99.999	99.999	99.999	99.999	1.014	0.065	1.944	0.055
681.5	737.3	19.533	0.056	99.999	99.999	99.999	99.999	0.973	0.071	1.792	0.063
42.7	866.7	19.535	0.054	99.999	99.999	99.999	99.999	0.984	0.07	1.839	0.059
743.6	422.6	19.54	0.046	99.999	99.999	99.999	99.999	0.836	0.06	1.651	0.054
364.5	72.2	19.545	0.05	99.999	99.999	99.999	99.999	0.935	0.064	1.769	0.055
801.8	622.5	19.545	0.054	99.999	99.999	99.999	99.999	0.942	0.068	1.757	0.059
147	624.1	19.547	0.048	99.999	99.999	99.999	99.999	0.89	0.063	1.712	0.054
699.5	552.8	19.55	0.059	99.999	99.999	99.999	99.999	0.952	0.076	1.714	0.064
770.9	247.1	19.551	0.048	99.999	99.999	99.999	99.999	0.882	0.065	1.673	0.055
12.4	438.3	19.555	0.048	99.999	99.999	99.999	99.999	0.702	0.064	1.608	0.053
102.6	841.7	19.557	0.05	99.999	99.999	99.999	99.999	1.002	0.065	1.8	0.056
255.3	777.6	19.559	0.047	99.999	99.999	99.999	99.999	0.993	0.063	1.81	0.054
288.1	417.9	19.56	0.044	99.999	99.999	99.999	99.999	0.905	0.059	1.741	0.052
781.3	771.4	19.561	0.052	99.999	99.999	99.999	99.999	0.893	0.068	1.77	0.057
512.4	673.6	19.564	0.058	99.999	99.999	99.999	99.999	0.783	0.073	1.765	0.062
536	237.2	19.568	0.062	99.999	99.999	99.999	99.999	0.936	0.077	99.999	99.999
608.4	883.8	19.568	0.065	99.999	99.999	99.999	99.999	0.865	0.082	1.697	0.071
236.3	764	19.572	0.054	99.999	99.999	99.999	99.999	0.913	0.069	1.728	0.06
963.2	975.4	19.582	0.054	99.999	99.999	99.999	99.999	1.102	0.07	1.999	0.059
353.3	781.1	19.586	0.056	99.999	99.999	99.999	99.999	0.975	0.073	1.731	0.064
415.2	384.8	19.59	0.049	99.999	99.999	99.999	99.999	0.91	0.065	1.821	0.055
421.8	576.3	19.593	0.054	99.999	99.999	99.999	99.999	0.875	0.07	1.671	0.062
337.1	622.5	19.596	0.046	99.999	99.999	99.999	99.999	0.941	0.062	1.661	0.056
942.6	783.6	19.599	0.055	99.999	99.999	99.999	99.999	0.945	0.073	1.789	0.06
357.5	735.8	19.6	0.058	99.999	99.999	99.999	99.999	0.848	0.075	1.715	0.064
305.1	291	19.604	0.05	99.999	99.999	99.999	99.999	0.879	0.069	1.627	0.058
124.5	394.4	19.61	0.061	99.999	99.999	99.999	99.999	0.703	0.077	1.571	0.068
634.3	810.2	19.613	0.059	99.999	99.999	99.999	99.999	0.839	0.076	1.718	0.065
305.6	975.8	19.616	0.057	99.999	99.999	99.999	99.999	0.993	0.075	1.891	0.064
758	429.6	19.62	0.056	99.999	99.999	99.999	99.999	0.875	0.072	1.725	0.064
302.2	192.3	19.629	0.052	99.999	99.999	99.999	99.999	0.839	0.068	1.73	0.061
614	741.7	19.637	0.061	99.999	99.999	99.999	99.999	0.925	0.079	1.762	0.068
98.1	710.2	19.646	0.055	99.999	99.999	99.999	99.999	0.868	0.072	1.799	0.06
382.1	974.2	19.675	0.05	99.999	99.999	99.999	99.999	0.824	0.066	1.602	0.06
489.2	372.2	19.681	0.064	99.999	99.999	99.999	99.999	0.796	0.081	1.629	0.07
552	807.5	19.683	0.052	99.999	99.999	99.999	99.999	0.765	0.069	1.598	0.059
382.4	941.8	19.693	0.059	99.999	99.999	99.999	99.999	0.672	0.077	1.541	0.066
897	613.9	19.707	0.054	99.999	99.999	99.999	99.999	0.811	0.074	1.623	0.064
666.9	571.6	19.711	0.065	99.999	99.999	99.999	99.999	1.076	0.082	1.893	0.071
958.8	258.5	19.72	0.068	99.999	99.999	99.999	99.999	0.823	0.085	1.605	0.078
46.7	519.8	19.735	0.067	99.999	99.999	99.999	99.999	0.921	0.086	1.911	0.072
696.3	668.3	19.737	0.069	99.999	99.999	99.999	99.999	1.204	0.089	2.166	0.075
68.7	355.7	19.746	0.06	99.999	99.999	99.999	99.999	1.169	0.077	2.212	0.064
796.6	933.4	19.796	0.073	99.999	99.999	99.999	99.999	1.062	0.092	2.041	0.079
334.2	698.1	19.804	0.056	99.999	99.999	99.999	99.999	1.069	0.072	2.015	0.062
675.3	679.1	19.819	0.063	99.999	99.999	99.999	99.999	1.033	0.081	1.913	0.07
811.8	19.6	19.819	0.06	99.999	99.999	99.999	99.999	0.978	0.076	2.086	0.064
677.6	61.9	19.857	0.066	99.999	99.999	99.999	99.999	0.903	0.09	1.797	0.072

TABLE 5 CCD *UBVRI* PHOTOMETRY OF BE 10

X	Y	V	σ_V	$(B-V)$	σ_{B-V}	$(U-B)$	σ_{U-B}	$(V-R)$	σ_{V-R}	$(V-I)$	σ_{V-I}
374.5	153.4	11.244	0.004	0.433	0.004	0.246	0.002	0.22	0.005	0.5	0.004
528.6	217.9	12.352	0.002	1.483	0.004	1.346	0.009	0.851	0.003	1.631	0.003
804.6	881.2	12.746	0.003	0.738	0.014	0.231	0.004	0.44	0.014	0.873	0.005
102.5	174.5	13.562	0.002	0.771	0.012	0.174	0.008	0.499	0.006	0.971	0.003
85.1	74.1	13.573	0.003	0.794	0.009	0.213	0.008	0.493	0.01	0.994	0.005
400.8	856.8	13.729	0.002	0.823	0.004	0.227	0.007	0.548	0.003	1.047	0.002
491.8	510.5	13.945	0.003	1.083	0.006	1.061	0.013	0.631	0.005	1.185	0.004
213.6	723.9	14.418	0.003	0.861	0.006	0.496	0.012	0.568	0.004	1.152	0.003
206.6	867.4	14.437	0.003	1.655	0.009	0.976	0.029	0.93	0.004	1.859	0.004
517.1	851.9	14.542	0.003	1.759	0.009	1.117	0.039	0.991	0.004	1.963	0.004
508.4	866.6	14.555	0.003	0.95	0.006	0.52	0.014	0.584	0.004	1.217	0.003
444.3	880.9	14.646	0.004	1.57	0.009	0.914	0.029	0.973	0.004	1.898	0.003
908.6	351.2	14.664	0.005	1.603	0.009	0.96	0.032	0.953	0.005	1.87	0.004
407.5	366.4	14.681	0.005	1.387	0.008	0.694	0.02	0.834	0.005	1.638	0.004
633.4	848	14.681	0.004	0.876	0.007	0.567	0.018	0.578	0.005	1.191	0.004
741.7	698.6	14.689	0.005	1.573	0.009	1.054	0.034	0.982	0.004	1.911	0.004
31.6	851.7	14.741	0.004	0.975	0.007	0.547	0.013	0.599	0.005	1.275	0.004
589.3	431.3	14.783	0.004	1.062	0.009	0.579	0.018	0.677	0.005	1.376	0.004
863.5	657.2	14.814	0.004	0.925	0.008	0.572	0.016	0.598	0.005	1.217	0.004
519.3	148.1	14.868	0.004	1.009	0.008	0.572	0.017	0.65	0.005	1.353	0.004
567.4	597.2	14.908	0.005	0.907	0.01	0.476	0.019	0.605	0.007	1.248	0.006
450.5	539.8	14.955	0.004	1.024	0.009	0.557	0.018	0.618	0.006	1.289	0.005
706.6	23.4	14.967	0.005	0.99	0.01	0.642	0.019	0.632	0.007	1.313	0.006
639.9	578.8	15.018	0.004	1.656	0.011	1.017	0.043	0.994	0.005	1.986	0.004
622.6	800.4	15.028	0.004	0.907	0.008	0.535	0.018	0.557	0.005	1.161	0.004
586.6	361.2	15.161	0.005	1.029	0.01	0.61	0.021	0.658	0.006	1.357	0.005
595.8	449.5	15.205	0.005	0.964	0.01	0.523	0.02	0.594	0.006	1.256	0.006
209.6	597	15.27	0.004	0.846	0.009	0.512	0.021	0.534	0.005	1.113	0.005
751.6	369	15.352	0.005	1.04	0.011	0.567	0.027	0.668	0.006	1.397	0.005
616.3	399.1	15.353	0.004	1.037	0.01	0.552	0.026	0.649	0.006	1.337	0.005
177.9	451.3	15.365	0.007	0.988	0.014	99.999	99.999	0.606	0.008	1.262	0.007
567.3	534.7	15.391	0.005	0.948	0.011	0.545	0.026	0.577	0.006	1.264	0.006
116.4	346	15.472	0.007	1.739	0.015	1.021	0.07	1.084	0.005	2.128	0.004
541.2	770.4	15.507	0.005	0.894	0.01	0.568	0.025	0.581	0.006	1.198	0.005
841	133	15.568	0.006	1.184	0.012	0.646	0.034	0.715	0.007	1.381	0.006
483.6	451.3	15.593	0.005	1.022	0.012	0.542	0.027	0.62	0.007	1.29	0.006
603.6	643.9	15.598	0.005	1.042	0.011	0.518	0.026	0.635	0.007	1.345	0.006
104.1	201.2	15.609	0.006	1.105	0.012	0.655	0.032	0.707	0.007	1.358	0.006
371.1	561.6	15.696	0.005	0.952	0.012	0.478	0.028	0.51	0.007	1.169	0.006
468.5	477	15.712	0.006	1.048	0.012	0.583	0.027	0.602	0.007	1.329	0.006
379.1	857.6	15.732	0.005	1.139	0.012	0.41	0.029	0.697	0.006	1.421	0.005
688.2	56.5	15.734	0.006	0.99	0.013	0.576	0.026	0.614	0.007	1.293	0.006
100.7	7.4	15.771	0.007	2.373	0.022	99.999	99.999	1.413	0.009	2.839	0.007
607.3	180.7	15.78	0.007	1.302	0.015	1.238	0.059	0.82	0.007	1.523	0.006
432.8	785.3	15.8	0.006	1.125	0.012	0.44	0.033	0.732	0.006	1.487	0.005
752.4	40.7	15.804	0.006	0.955	0.012	0.708	0.037	0.643	0.007	1.324	0.006
176.1	445.9	15.804	0.009	1.002	0.02	99.999	99.999	0.621	0.01	1.271	0.01
761.4	451.7	15.818	0.005	0.987	0.012	0.53	0.03	0.597	0.007	1.253	0.006
334.6	223.5	15.869	0.006	1.027	0.013	0.597	0.032	0.622	0.007	1.392	0.006
483.1	963.5	15.918	0.006	0.987	0.012	0.511	0.033	0.608	0.007	1.281	0.006
852.3	189.3	15.93	0.009	1.355	0.015	1.184	0.056	0.929	0.007	1.81	0.006
470.5	507.4	15.934	0.006	1.941	0.019	99.999	99.999	1.128	0.007	2.184	0.006
103.4	84.9	15.943	0.009	1.465	0.016	0.72	0.053	0.88	0.007	1.831	0.006
743.2	35.5	15.994	0.007	1.005	0.017	0.68	0.04	0.594	0.008	1.265	0.008
423.8	387.4	16.024	0.007	1.058	0.016	0.558	0.037	0.612	0.008	1.298	0.007
214.1	792.8	16.045	0.006	0.904	0.013	0.538	0.033	0.598	0.007	1.216	0.006
650.9	521.1	16.106	0.007	0.969	0.015	0.555	0.035	0.579	0.008	1.209	0.007
310.3	345.1	16.106	0.007	1.112	0.016	0.539	0.041	0.665	0.008	1.41	0.007
578.3	415.5	16.194	0.007	1.084	0.015	0.575	0.041	0.649	0.009	1.363	0.008
299.7	814.6	16.248	0.01	1.415	0.018	0.792	0.063	0.881	0.008	1.775	0.007
390	775.1	16.254	0.007	0.972	0.015	0.5	0.042	0.552	0.008	1.22	0.008
459.5	58.4	16.259	0.007	1.014	0.017	0.63	0.046	0.645	0.008	1.339	0.008
530.2	848.3	16.284	0.008	1.025	0.017	0.572	0.047	0.629	0.009	1.317	0.008
173.2	655	16.373	0.008	0.949	0.017	0.514	0.041	0.599	0.01	1.235	0.008
644.8	610.1	16.383	0.007	1.153	0.018	0.455	0.05	0.708	0.008	1.467	0.007
637.7	392.2	16.4	0.008	1.081	0.018	0.596	0.05	0.653	0.009	1.351	0.008

TABLE 5 (CONTINUED)

X	Y	V	σ_V	$(B-V)$	σ_{B-V}	$(U-B)$	σ_{U-B}	$(V-R)$	σ_{V-R}	$(V-I)$	σ_{V-I}
884.7	48.6	16.466	0.008	1.086	0.02	0.582	0.055	0.682	0.01	1.432	0.009
208.4	805.8	16.475	0.008	1.024	0.018	0.511	0.047	0.643	0.009	1.329	0.008
503	790.6	16.51	0.008	1.006	0.019	0.488	0.046	0.611	0.009	1.271	0.008
341.8	333.4	16.511	0.008	1.129	0.02	0.472	0.055	0.625	0.009	1.327	0.008
848.8	423.3	16.524	0.008	1.026	0.017	0.602	0.052	0.665	0.009	1.333	0.008
56.6	322.6	16.606	0.01	1.935	0.029	99.999	99.999	1.089	0.01	2.228	0.008
511.8	242.7	16.662	0.011	1.341	0.025	0.556	0.072	0.801	0.01	1.702	0.009
461.4	238.9	16.689	0.009	1.125	0.022	0.507	0.053	0.705	0.01	1.466	0.009
890.3	254.8	16.715	0.009	1.14	0.023	0.518	0.063	0.672	0.011	1.401	0.009
127.6	688.2	16.715	0.009	1.047	0.022	0.381	0.087	0.643	0.011	1.34	0.009
830.3	571.3	16.725	0.01	1.637	0.028	99.999	99.999	1.015	0.011	2.004	0.009
706.8	653.2	16.785	0.01	1.056	0.023	0.478	0.059	0.659	0.012	1.354	0.01
857.7	686.4	16.872	0.011	1.904	0.035	99.999	99.999	1.129	0.011	2.153	0.009
313	474.9	16.925	0.012	1.122	0.025	0.556	0.076	0.74	0.013	1.505	0.011
407.9	892.1	16.949	0.012	1.302	0.028	0.395	0.079	0.792	0.012	1.595	0.01
213.7	569.5	16.953	0.013	1.287	0.028	99.999	99.999	0.719	0.016	1.445	0.014
898.4	763.7	17.005	0.011	1.021	0.025	0.351	0.064	0.677	0.013	1.353	0.011
889.5	213.6	17.022	0.011	1.114	0.029	0.542	0.081	0.686	0.012	1.397	0.011
365.8	56.9	17.048	0.016	1.443	0.031	0.552	0.113	0.878	0.014	1.739	0.012
715.2	204.4	17.055	0.013	1.254	0.028	0.469	0.093	0.821	0.012	1.633	0.011
357.7	727	17.073	0.011	1.263	0.028	99.999	99.999	0.83	0.012	1.682	0.011
784.3	880.8	17.087	0.012	1.403	0.035	99.999	99.999	0.875	0.014	1.728	0.012
181.3	413	17.117	0.012	1.17	0.029	0.525	0.095	0.737	0.013	1.513	0.011
522.8	437.4	17.118	0.012	1.295	0.03	0.428	0.099	0.75	0.013	1.565	0.011
455.4	6.7	17.126	0.012	1.307	0.028	0.36	0.099	0.759	0.013	1.594	0.011
536.7	965.8	17.159	0.012	1.075	0.028	0.559	0.088	0.685	0.014	1.419	0.012
572.6	539.7	17.166	0.013	1.082	0.029	99.999	99.999	0.733	0.015	1.476	0.013
574.3	574	17.175	0.011	1.081	0.026	0.412	0.076	0.688	0.013	1.421	0.011
855.7	929.1	17.194	0.013	1.31	0.031	99.999	99.999	0.855	0.015	1.567	0.013
96.4	221.9	17.246	0.012	1.057	0.029	0.576	0.089	0.629	0.014	1.387	0.012
440.9	474.2	17.249	0.013	1.181	0.032	99.999	99.999	0.733	0.016	1.521	0.014
292.2	905.7	17.372	0.014	0.91	0.03	0.391	0.082	0.518	0.018	1.134	0.015
149.1	325.6	17.39	0.016	1.512	0.042	99.999	99.999	0.98	0.016	1.856	0.014
371.1	428.8	17.396	0.017	1.202	0.035	0.396	0.105	0.785	0.017	1.635	0.014
349.9	730.6	17.412	0.017	1.324	0.044	99.999	99.999	0.801	0.027	99.999	99.999
607	409.2	17.414	0.014	1.71	0.048	99.999	99.999	1.005	0.015	2.008	0.012
423.8	676.4	17.521	0.014	1.159	0.037	99.999	99.999	0.74	0.015	1.539	0.014
441.5	467.7	17.548	0.018	1.225	0.042	0.274	0.119	0.766	0.02	1.565	0.017
36.8	252.1	17.565	0.016	1.302	0.042	99.999	99.999	0.791	0.018	1.631	0.015
715.7	474.9	17.578	0.015	1.21	0.04	99.999	99.999	0.723	0.017	1.521	0.015
144.7	66.3	17.578	0.016	1.36	0.042	99.999	99.999	0.811	0.017	1.647	0.016
802.6	738.1	17.587	0.014	1.354	0.042	99.999	99.999	0.812	0.015	1.655	0.014
774.7	680.8	17.64	0.016	1.149	0.038	0.329	0.115	0.762	0.017	1.505	0.015
191.5	383.9	17.646	0.017	1.286	0.042	99.999	99.999	0.797	0.018	1.64	0.016
514.3	656.5	17.666	0.015	1.21	0.039	99.999	99.999	0.705	0.018	1.437	0.015
99	636.6	17.676	0.016	1.118	0.039	99.999	99.999	0.783	0.018	1.49	0.015
893.2	772	17.676	0.017	1.512	0.047	99.999	99.999	0.942	0.018	1.802	0.015
12.1	285.9	17.685	0.017	2.008	0.066	99.999	99.999	1.197	0.018	2.364	0.015
39.7	492.9	17.708	0.018	1.833	0.061	99.999	99.999	1.07	0.018	2.129	0.015
474.5	639	17.72	0.018	1.213	0.045	99.999	99.999	0.778	0.02	1.545	0.017
409	384.8	17.738	0.018	1.276	0.047	99.999	99.999	0.802	0.02	1.637	0.018
243.4	985.8	17.772	0.02	1.189	0.05	99.999	99.999	0.769	0.022	1.614	0.019
887.8	66	17.774	0.018	1.255	0.047	99.999	99.999	0.771	0.021	1.636	0.017
327.7	808.9	17.787	0.017	1.19	0.047	99.999	99.999	0.798	0.02	1.576	0.017
513.6	755.5	17.796	0.018	1.189	0.047	99.999	99.999	0.753	0.021	1.546	0.017
260.1	268.5	17.802	0.015	1.352	0.05	99.999	99.999	0.797	0.018	1.668	0.015
523.4	410	17.822	0.02	1.218	0.049	99.999	99.999	0.765	0.022	1.563	0.019
114.3	942.4	17.856	0.019	1.384	0.051	99.999	99.999	0.872	0.02	1.692	0.018
866.3	423.4	17.867	0.019	1.156	0.052	99.999	99.999	0.716	0.021	1.514	0.019
290.3	127.4	17.882	0.018	1.424	0.055	99.999	99.999	0.944	0.019	1.89	0.016
14.3	632	17.885	0.018	1.144	0.045	99.999	99.999	0.675	0.021	1.487	0.018
564.4	466.8	17.917	0.02	1.354	0.054	99.999	99.999	0.742	0.023	1.599	0.019
730.8	894.1	17.936	0.022	1.58	0.064	99.999	99.999	1.026	0.022	1.892	0.019
261.7	687.5	17.968	0.019	1.199	0.047	99.999	99.999	0.668	0.022	1.44	0.018
706.4	601.3	17.993	0.02	1.141	0.054	99.999	99.999	0.783	0.022	1.586	0.019
802	334	18.008	0.021	1.223	0.053	99.999	99.999	0.781	0.023	1.527	0.021

TABLE 5 (CONTINUED)

X	Y	V	σ_V	$(B-V)$	σ_{B-V}	$(U-B)$	σ_{U-B}	$(V-R)$	σ_{V-R}	$(V-I)$	σ_{V-I}
535.4	613.7	18.015	0.019	1.177	0.052	99.999	99.999	0.788	0.022	1.584	0.019
1.8	843.6	18.024	0.026	99.999	99.999	99.999	99.999	0.806	0.028	1.643	0.025
131.7	267.7	18.042	0.021	1.376	0.058	99.999	99.999	0.868	0.023	1.751	0.02
299.4	501.5	18.047	0.019	1.43	0.063	99.999	99.999	0.826	0.021	1.707	0.018
849.6	729.5	18.062	0.024	1.465	0.073	99.999	99.999	0.929	0.025	1.84	0.021
689.8	859.2	18.094	0.023	1.259	0.069	99.999	99.999	0.719	0.026	1.5	0.022
534.8	528.8	18.117	0.02	1.365	0.068	99.999	99.999	0.8	0.023	1.617	0.019
292.6	554.1	18.124	0.024	1.263	0.063	99.999	99.999	0.682	0.026	1.553	0.023
282.5	893.1	18.183	0.023	1.156	0.061	99.999	99.999	0.77	0.026	1.535	0.022
714.4	700.2	18.208	0.023	1.247	0.066	99.999	99.999	0.868	0.026	1.672	0.022
858.6	508	18.238	0.025	1.095	0.063	99.999	99.999	0.785	0.027	1.553	0.024
839.7	656.6	18.259	0.025	1.207	0.065	99.999	99.999	0.754	0.028	1.515	0.024
648.3	735.1	18.272	0.024	1.333	0.087	99.999	99.999	0.811	0.026	1.597	0.023
171.7	905.5	18.286	0.023	1.402	0.07	99.999	99.999	0.868	0.025	1.748	0.022
841	620.1	18.289	0.025	99.999	99.999	99.999	99.999	0.782	0.028	1.521	0.024
166.7	606.4	18.324	0.023	1.254	0.077	99.999	99.999	0.723	0.027	1.533	0.023
451.1	430	18.348	0.026	1.444	0.08	99.999	99.999	0.854	0.027	1.735	0.025
405.4	637.9	18.352	0.028	1.482	0.08	99.999	99.999	0.829	0.031	1.693	0.026
545	575.8	18.401	0.03	1.26	0.08	99.999	99.999	0.82	0.032	1.674	0.028
263.3	242.9	18.407	0.027	1.567	0.091	99.999	99.999	1.028	0.028	1.917	0.024
628	293.8	18.446	0.028	1.358	0.088	99.999	99.999	0.842	0.03	1.735	0.026
836.7	425.5	18.459	0.029	1.248	0.081	99.999	99.999	0.762	0.031	1.58	0.028
212.6	459.4	18.459	0.029	1.188	0.076	99.999	99.999	0.814	0.031	1.606	0.028
183.9	340.2	18.474	0.029	1.357	0.085	99.999	99.999	0.844	0.031	1.728	0.028
412	648	18.491	0.028	1.274	0.077	99.999	99.999	0.961	0.03	1.855	0.025
394.7	881.8	18.494	0.028	1.647	0.103	99.999	99.999	0.942	0.029	1.849	0.026
474	96.9	18.5	0.029	1.768	0.109	99.999	99.999	0.954	0.03	1.854	0.026
418.6	440.8	18.501	0.031	1.587	0.092	99.999	99.999	0.877	0.033	1.756	0.028
867.5	598	18.507	0.031	99.999	99.999	99.999	99.999	1.092	0.03	2.078	0.027
533.3	252	18.551	0.033	99.999	99.999	99.999	99.999	0.875	0.035	1.784	0.031
833.6	631.9	18.578	0.031	1.44	0.097	99.999	99.999	0.827	0.035	1.644	0.029
785	971.5	18.581	0.032	99.999	99.999	99.999	99.999	0.907	0.033	1.75	0.03
147.5	315.8	18.593	0.032	1.31	0.09	99.999	99.999	0.876	0.034	1.779	0.03
923.2	618.1	18.603	0.03	1.326	0.091	99.999	99.999	0.934	0.031	1.832	0.028
751.8	244	18.632	0.033	1.431	0.098	99.999	99.999	1.016	0.034	1.964	0.029
318.5	481.2	18.654	0.039	1.68	0.14	99.999	99.999	0.96	0.04	1.868	0.035
396.5	260.3	18.673	0.033	1.371	0.101	99.999	99.999	0.732	0.036	1.642	0.032
468.1	232.5	18.694	0.031	99.999	99.999	99.999	99.999	0.83	0.034	1.744	0.03
896.9	706.3	18.702	0.034	99.999	99.999	99.999	99.999	0.731	0.037	1.609	0.033
396.9	404.3	18.707	0.033	99.999	99.999	99.999	99.999	0.918	0.035	1.794	0.031
348.2	679.7	18.707	0.032	1.097	0.089	99.999	99.999	0.824	0.035	1.644	0.031
113.9	727	18.714	0.035	1.267	0.105	99.999	99.999	0.865	0.037	1.666	0.032
123.9	544.8	18.716	0.036	1.283	0.1	99.999	99.999	0.822	0.04	1.598	0.034
188.5	861	18.72	0.03	1.243	0.101	99.999	99.999	0.822	0.034	1.635	0.03
459.8	343.8	18.732	0.036	1.533	0.136	99.999	99.999	0.796	0.04	1.679	0.034
916.2	835.9	18.735	0.036	1.225	0.1	99.999	99.999	0.833	0.039	1.65	0.034
497	118.9	18.745	0.03	99.999	99.999	99.999	99.999	0.813	0.033	1.769	0.029
368.5	578.8	18.757	0.036	1.458	0.126	99.999	99.999	0.905	0.037	1.844	0.033
776.1	687.7	18.758	0.033	1.258	0.101	99.999	99.999	0.745	0.038	1.586	0.032
170.7	934.1	18.838	0.036	99.999	99.999	99.999	99.999	1.064	0.036	2.07	0.032
148.2	394.9	18.877	0.036	99.999	99.999	99.999	99.999	0.93	0.039	1.791	0.033
189.2	460.1	18.887	0.047	99.999	99.999	99.999	99.999	1.111	0.045	2.138	0.04
378.7	407.8	18.897	0.037	99.999	99.999	99.999	99.999	0.891	0.039	1.749	0.034
263.5	664.5	18.899	0.039	99.999	99.999	99.999	99.999	0.788	0.042	1.58	0.037
104.9	695	18.934	0.042	1.154	0.116	99.999	99.999	0.819	0.045	1.632	0.039
24.9	681.5	18.938	0.038	1.184	0.113	99.999	99.999	0.763	0.042	1.529	0.037
422.7	449.4	18.968	0.037	99.999	99.999	99.999	99.999	0.884	0.039	1.783	0.035
306.5	767.3	18.971	0.042	99.999	99.999	99.999	99.999	0.797	0.045	1.645	0.04
277.9	498.6	18.973	0.043	99.999	99.999	99.999	99.999	0.826	0.047	1.69	0.04
186	556.3	18.978	0.045	1.271	0.133	99.999	99.999	0.804	0.049	1.638	0.043
533.3	407.9	18.983	0.044	99.999	99.999	99.999	99.999	0.866	0.045	1.76	0.04
253.5	678.5	19.008	0.04	1.121	0.103	99.999	99.999	0.69	0.045	1.423	0.041
715.4	275.5	19.048	0.04	99.999	99.999	99.999	99.999	0.815	0.042	1.766	0.038
712.4	485.8	19.074	0.046	99.999	99.999	99.999	99.999	0.977	0.048	1.808	0.041
448.1	839.3	19.079	0.043	99.999	99.999	99.999	99.999	0.803	0.046	1.624	0.041
609.2	585.4	19.098	0.052	99.999	99.999	99.999	99.999	1.169	0.049	2.38	0.043

TABLE 5 (CONTINUED)

X	Y	V	σ_V	$(B-V)$	σ_{B-V}	$(U-B)$	σ_{U-B}	$(V-R)$	σ_{V-R}	$(V-I)$	σ_{V-I}
167	666.8	19.103	0.045	99.999	99.999	99.999	99.999	0.722	0.049	1.51	0.043
660.7	542.1	19.15	0.054	99.999	99.999	99.999	99.999	0.909	0.055	1.812	0.049
840.5	711	19.152	0.043	99.999	99.999	99.999	99.999	0.855	0.046	1.658	0.041
747.2	514.5	19.16	0.045	99.999	99.999	99.999	99.999	0.911	0.047	1.802	0.042
791.4	338.5	19.163	0.047	1.091	0.134	99.999	99.999	1.029	0.048	1.882	0.043
884.2	936	19.165	0.051	99.999	99.999	99.999	99.999	0.982	0.051	1.883	0.046
799.2	629.2	19.181	0.052	0.898	0.122	99.999	99.999	0.858	0.054	1.651	0.049
315.9	924	19.202	0.05	99.999	99.999	99.999	99.999	0.923	0.052	1.83	0.046
325.3	790.9	19.204	0.052	99.999	99.999	99.999	99.999	0.875	0.055	1.748	0.048
425	25.3	19.212	0.044	99.999	99.999	99.999	99.999	0.935	0.046	1.814	0.041
151.9	459	19.217	0.047	99.999	99.999	99.999	99.999	0.799	0.05	1.651	0.046
568.2	3.8	19.221	0.054	99.999	99.999	99.999	99.999	0.835	0.056	1.794	0.05
75.1	753.4	19.235	0.048	99.999	99.999	99.999	99.999	0.765	0.051	1.586	0.047
660.3	809	19.244	0.052	99.999	99.999	99.999	99.999	0.846	0.054	1.677	0.049
277.2	874.9	19.248	0.057	99.999	99.999	99.999	99.999	0.866	0.058	1.697	0.053
636.9	698.1	19.254	0.045	99.999	99.999	99.999	99.999	0.738	0.05	1.543	0.043
854.3	293.3	19.257	0.055	99.999	99.999	99.999	99.999	0.83	0.057	1.646	0.052
170.4	418.7	19.273	0.055	99.999	99.999	99.999	99.999	0.856	0.058	1.768	0.051
740	805.2	19.313	0.051	99.999	99.999	99.999	99.999	0.914	0.053	1.897	0.046
305.6	336.1	19.324	0.057	99.999	99.999	99.999	99.999	0.888	0.062	1.794	0.053
861.4	623.4	19.326	0.058	99.999	99.999	99.999	99.999	0.985	0.059	2.026	0.051
780.4	105.5	19.33	0.055	99.999	99.999	99.999	99.999	0.838	0.058	1.746	0.051
891.1	150.2	19.334	0.055	1.12	0.15	99.999	99.999	0.772	0.062	1.6	0.053
384.8	755.5	19.344	0.055	99.999	99.999	99.999	99.999	0.848	0.058	1.678	0.051
637.2	613.8	19.358	0.055	99.999	99.999	99.999	99.999	0.871	0.058	1.628	0.052
680.1	860.1	19.359	0.059	99.999	99.999	99.999	99.999	0.798	0.061	1.688	0.056
50	455.1	19.363	0.055	99.999	99.999	99.999	99.999	0.807	0.058	1.878	0.051
215.8	223.9	19.368	0.058	99.999	99.999	99.999	99.999	0.845	0.06	1.786	0.053
10.3	605.8	19.382	0.057	99.999	99.999	99.999	99.999	0.799	0.061	1.702	0.055
537.4	942.8	19.389	0.064	99.999	99.999	99.999	99.999	0.841	0.066	1.734	0.059
255.4	599.4	19.402	0.059	99.999	99.999	99.999	99.999	0.946	0.059	1.764	0.054
49	671.7	19.409	0.064	99.999	99.999	99.999	99.999	1.089	0.062	2.069	0.055
847.1	541.9	19.419	0.062	99.999	99.999	99.999	99.999	0.748	0.066	1.66	0.059
550.9	454.9	19.421	0.057	99.999	99.999	99.999	99.999	0.939	0.058	1.903	0.051
576.3	687.7	19.428	0.055	99.999	99.999	99.999	99.999	0.747	0.063	1.659	0.054
680	429	19.428	0.067	99.999	99.999	99.999	99.999	0.844	0.068	1.673	0.063
751.4	450.8	19.432	0.055	99.999	99.999	99.999	99.999	0.942	0.057	1.76	0.052
429.8	251.6	19.437	0.061	99.999	99.999	99.999	99.999	0.739	0.066	1.616	0.058
394.7	367	19.449	0.07	99.999	99.999	99.999	99.999	0.955	0.071	1.734	0.064
249.1	983.9	19.45	0.074	99.999	99.999	99.999	99.999	1.107	0.071	2.083	0.063
295.1	657	19.451	0.058	99.999	99.999	99.999	99.999	1.154	0.057	2.063	0.05
340.6	456.9	19.502	0.06	99.999	99.999	99.999	99.999	0.86	0.064	1.765	0.055
863.5	383.3	19.553	0.066	99.999	99.999	99.999	99.999	0.812	0.071	1.646	0.062
376.6	539.7	19.579	0.066	99.999	99.999	99.999	99.999	0.706	0.074	1.493	0.065
732.4	168.4	19.58	0.067	99.999	99.999	99.999	99.999	0.877	0.068	1.819	0.062
673.3	587.1	19.593	0.073	99.999	99.999	99.999	99.999	1.04	0.072	1.947	0.064
136.6	393.6	19.593	0.067	99.999	99.999	99.999	99.999	0.855	0.069	1.816	0.061
892.5	688.9	19.595	0.067	99.999	99.999	99.999	99.999	0.782	0.072	1.72	0.064
284.6	219.6	19.607	0.067	99.999	99.999	99.999	99.999	0.787	0.074	1.794	0.063
466.8	246.1	19.614	0.067	99.999	99.999	99.999	99.999	0.828	0.071	1.802	0.063
669.1	739.3	19.63	0.066	99.999	99.999	99.999	99.999	0.834	0.072	1.711	0.062
187.3	543.2	19.651	0.074	99.999	99.999	99.999	99.999	0.59	0.081	1.558	0.074
595.7	889.6	19.668	0.077	99.999	99.999	99.999	99.999	0.868	0.079	1.744	0.073
630.9	198.8	19.671	0.075	99.999	99.999	99.999	99.999	0.842	0.08	1.804	0.069
340.1	373	19.671	0.067	99.999	99.999	99.999	99.999	0.813	0.074	1.711	0.063
915.1	27.4	19.683	0.075	99.999	99.999	99.999	99.999	1.065	0.074	2.101	0.066
607.4	290.5	19.686	0.073	99.999	99.999	99.999	99.999	0.876	0.074	1.854	0.067
512.5	302.7	19.723	0.087	99.999	99.999	99.999	99.999	1.044	0.083	2.022	0.076
500.5	973.7	19.725	0.077	99.999	99.999	99.999	99.999	0.659	0.085	1.552	0.076
645.4	154.5	19.733	0.08	99.999	99.999	99.999	99.999	0.884	0.08	1.757	0.073
280.7	123.8	19.778	0.08	99.999	99.999	99.999	99.999	0.997	0.08	1.972	0.071
636.5	933	19.805	0.095	99.999	99.999	99.999	99.999	0.729	0.098	1.584	0.088
64.8	500.9	19.82	0.096	99.999	99.999	99.999	99.999	1.05	0.092	2.009	0.082
111.6	32.8	19.867	0.104	99.999	99.999	99.999	99.999	1.086	0.102	2.178	0.088
819.8	718.2	19.902	0.083	99.999	99.999	99.999	99.999	0.717	0.092	1.592	0.08
65.4	714.9	19.921	0.083	99.999	99.999	99.999	99.999	0.707	0.094	1.598	0.082

used to help us in the visualization and analysis of the photometric data (e.g., Schuster et al. 2007). These programs facilitate the elimination of field and apparent non-member stars of a given cluster from the diagnostic diagrams used to enhance the apperception of cluster features. Once a satisfactory first estimate of the parameters was obtained, a full-frame solution was also consulted and refined.

SAFE is capable of displaying simultaneously in different color-color (CC) and color-magnitude (CM) diagrams the cluster's data and has an interactive way to identify a (group of) star(s) in one particular diagram and to see where it falls in the other diagrams. This program is capable of displaying up to 16 different diagrams for a given cluster and is very useful for the determination of a cluster's physical parameters. Figure 1a-c presents the DSS red-filter images of Be 89 (Panel a), Ru 135 (Panel b) and Be 10 (Panel c), with the regions analyzed in this work enclosed by ellipses. The central (X, Y) pixel coordinates of the nearly circular regions in Figure 1a-c, which are considered for the photometric analyses are the following: (584, 488) pixels for Be 89, (542, 504) for Ru 135, and (517, 493) for Be 10. The diameters in arcminutes $(\Delta X,\ \Delta Y)$ of nearly circular regions in Figure 1a-c are the following: (2.27, 2.65) for Be 89, (2.62, 2.67) for Ru 135, and (3.12, 2.34) for Be 10.

3. ANALYSES OF THE OPEN CLUSTERS BE 89, RU 135, AND BE 10

The $(U-B, B-V)$, two-color or CC, diagram, and five CM diagrams have been used together with the zero-age-main-sequence (ZAMS) intrinsic-color calibrations of Schmidt-Kaler (1982, hereafter SK82) and with the Padova isochrones (Girardi et al. 2000, hereafter GBBC; Bertelli et al. 2008; Marigo et al. 2008, hereafter MGBG) to obtain reddenings, metallicities, distance moduli, and ages for these clusters.

Our analysis technique for our program clusters places particular emphasis upon the fit of the ZAMS intrinsic colors and Padova isochrones to the observational data of the clusters, and this depends in turn upon important characteristics of the CM and CC diagrams for open clusters (e.g., Paunzen & Netopil 2006, their § 3), which are summarized as follows:

1. A procedure for eliminating non-members.

2. A determination of the interstellar reddening as accurately as possible.

3. Visibility of the turn-off.

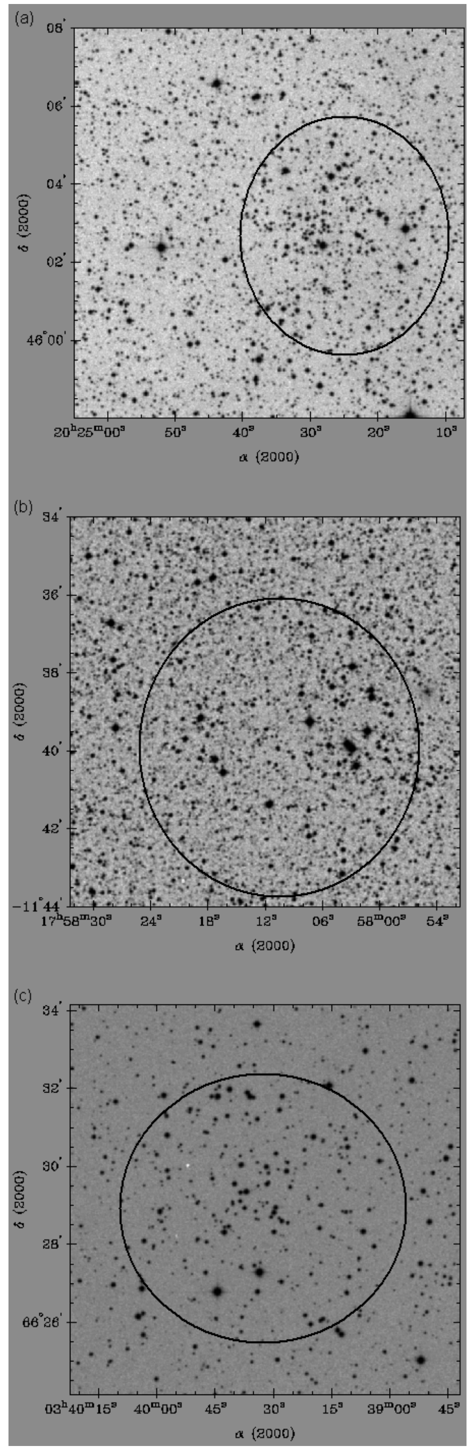

Fig. 1. DSS red-filter images of the Galactic open clusters Be 89 (Panel a), Ru 135 (Panel b), and Be 10 (Panel c). The regions analyzed with the ELIPSE inspection tool, to derive first estimates for the fundamental parameters, are enclosed by ellipses. Orientation as usual: north is up, and east to the left.

4. Compensation for binary stars which tend to widen the main-sequence distribution.

5. Consideration of the red-clump stars (if present) to improve the isochrone fit.

6. An appropriate choice of the isochrone which corresponds to the correct heavy-element abundance (Z).

Regarding the locus of the main sequence in a CM diagram, and independent of any cosmic dispersion, the main-sequence strips or bands in the CM diagrams are affected by the contamination of binary and multiple stars; particularly, the mid-points are shifted to brighter magnitudes and the colors to redder values due to this contamination, and also sometimes due to variable intercluster extinction. For this reason, the SK82 ZAMS and the MGBG isochrones have been fitted to the blue- and faint-most concentrations within the observed broad main-sequence bands whenever possible, assuming that these concentrations reflect the single-star distribution (e.g., Carney 2001), and that most stars observed red- and bright-ward of these are in fact binary, or multiple, systems.

In the absence of proper-motion/radial-velocity measurements to insure cluster membership, and to minimize the effects of field-star contamination, we have concentrated more on the central regions of the clusters rather than using the full-frame CCD images; this has been accomplished by using the ELIPSE or SAFE programs, described above. These have been used to select an elliptical, or polygonal area (with as many as 10 sides), centered on the open cluster as seen in a V or R image, excluding stars outside this area from further analyses. (See Figure 1). These interactive analyses greatly increase the contrast of cluster members with respect to the field stars, and thus the scatter in the CM and CC diagrams is significantly reduced.

Also, the observational errors, e.g., $\sigma_{(U-B)}$, of these three clusters have been considered as a criterion in selecting the more reliable data for further analyses. The values of $\sigma_{(U-B)}$ are almost always larger than the ones of $\sigma_{(B-V)}$ due to the smaller sensitivity of the CCD in the ultraviolet, and the errors $\sigma_{(R-I)}$, $\sigma_{(V-I)}$, and $\sigma_{(V-R)}$ are among the smallest. The observational errors, such as $\sigma_{(U-B)}$, $\sigma_{(B-V)}$, and $\sigma_{(B-R)}$, have been selected to be less than $\approx 0\overset{\mathrm{m}}{.}10$ (and sometimes $\lesssim 0\overset{\mathrm{m}}{.}05$) in some of the diagnostic diagrams presented in the analyses to follow, such as the $(U-B,\ B-V)$, $(V,\ B-V)$, and $(V,\ B-R)$ diagrams.

Interstellar reddenings of the program clusters have been estimated from shifts of the intrinsic-color sequences of SK82 in the $(U-B,\ B-V)$ diagram, until the best fit to the data of the clusters was achieved: along the $U-B$ axis by $0.72\ E(B-V) + 0.05\ E(B-V)^2$ and along the $(B-V)$ axis by $E(B-V)$. For this, F-type stars have been fitted above the main sequence of SK82 [i.e., blue-ward in $(U-B)$], and simultaneously the red-clump stars above the red-giant colors of SK82 with consistent ultraviolet excesses according to the normalizations of Sandage (1969). The two-color sequence of SK82 has been constructed from the intrinsic colors of SK82 for zero-age dwarfs [$(B-V)_0 \lesssim 0\overset{\mathrm{m}}{.}75$] and for giants [$(B-V)_0 \gtrsim 0\overset{\mathrm{m}}{.}75$].

Once the two-color sequence of SK82 has been fixed as indicated above, to determine the photometric metal abundance, [Fe/H], one first locates the F-type stars in the $(U-B,\ B-V)$ diagram and compares their location with that of their counterparts of known metallicity (e.g., the SK82's ZAMS calibration). Deviations between the two are due mainly to their differences in metal content, an ultraviolet excess, $\delta(U-B)$, being caused by differences in line blanketing. The metal-deficient F-type cluster stars, if present, lie blue-ward of the "hump region" of the ZAMS sequence, where an eyeball-fitted osculating curve similar to "the hump" has been fitted to the data points of the F-stars (i.e., the thick line above the hump of the F-star region in Figures 2, 5, and 8) and, simultaneously, to the red-clump stars (if present), since they also will lie blue-ward of the red-giant colors of SK82 with a corresponding ultraviolet excess. This ultraviolet excess is correlated with the photometric metallicity of the cluster. Then, a metallicity value, [Fe/H], for a cluster can be derived from the empirical calibration, [Fe/H]-$\delta(U-B)_{0.6}$, of Karataş & Schuster (2006), allowing the determination of [Fe/H] independently of the isochrones to be fitted to the data, thus reducing from three to two the free parameters to be derived from the CM diagrams. Heavy-element abundances (Z) of the three clusters have been obtained from the photometric metal abundances [Fe/H] with the expression

$$Z = Z_{\odot} \cdot 10^{[\mathrm{Fe/H}]}, \quad Z_{\odot} = +0.019\,. \qquad (6)$$

Finally, the appropriate isochrones of MGBG were computed online in terms of the resulting heavy-element abundance for further analyses of the clusters (distances and ages).

To estimate the the age of a cluster (A) and the true distance modulus ($DM = V_0 - M_V$) in a CM diagram, for example the $(V,\ B-V)$ dia-

TABLE 6

ADOPTED INTERSTELLAR EXTINCTION LAW

$\frac{E(V-I)}{E(B-V)}$	$\frac{E(R-I)}{E(B-V)}$	$\frac{E(V-R)}{E(B-V)}$	$\frac{E(B-R)}{E(B-V)}$
1.25	0.69	0.56	1.56

gram, the absolute magnitudes, M_V, of the MGBG isochrones have been shifted by $DM + 3.1\ E(B-V)$ along the magnitude axis and their corresponding colors, $(B-V)_0$, reddened by adding the color excess $E(B-V)$ until some DM value provides a good fit of the appropriate isochrone to the faint/blue concentration of the observed lower main sequence of the cluster and, if present, of the red-clump stars. One has to take into account when determining the DM that metal-poor stars are sub-luminous as compared with their solar-like counterparts by determining a reliable value for Z from the CC diagram. To infer the age of the cluster, the (logarithm of the) age of the isochrones, log A, has been varied until a good match with the observed sequences, i.e., the upper main-sequence (MS), the turn-off (TO) stars, and, if present, the red-clump (RC) stars, has been achieved. A fine tuning of the DM has been made if necessary. The uncertainties of $E(B-V)$, Z, DM, and log A are discussed in § 3.4.

Following a similar procedure to that outlined above, the distance moduli and cluster ages have also been derived from analyses of four other CM diagrams for each of the clusters. The corresponding color excesses applied in the diagrams were iterated starting with the previously derived color excess estimates, $E(B-V)$, and the results were intercompared by means of the standard interstellar extinction law adopted (see Table 6; also cf. Dean, Warren, & Cousins 1978; Mathis 1990; Straižys 1995) until satisfactory solutions were obtained for all the CM diagrams. The derived extinction laws do not differ significantly from that of Table 6.

3.1. *Be 89*

The $(U-B,\ B-V)$ diagram of Be 89 is shown in Figure 2. An interstellar reddening of $(B-V) = 0\overset{\mathrm{m}}{.}60 \pm 0\overset{\mathrm{m}}{.}09$ has been derived by shifting the intrinsic two-color stellar sequence of SK82 along the reddening vector as described in the previous section. (Another possibility, to fit the stars by $E(B-V) \simeq 0\overset{\mathrm{m}}{.}73$ to the blue (B-star) branch of the ZAMS curve, would leave many stars far from a good fit). Six stars apparently in the cluster are noticed with $(B-V) \approx 1\overset{\mathrm{m}}{.}6$ and $(U-B) \approx 1\overset{\mathrm{m}}{.}4$

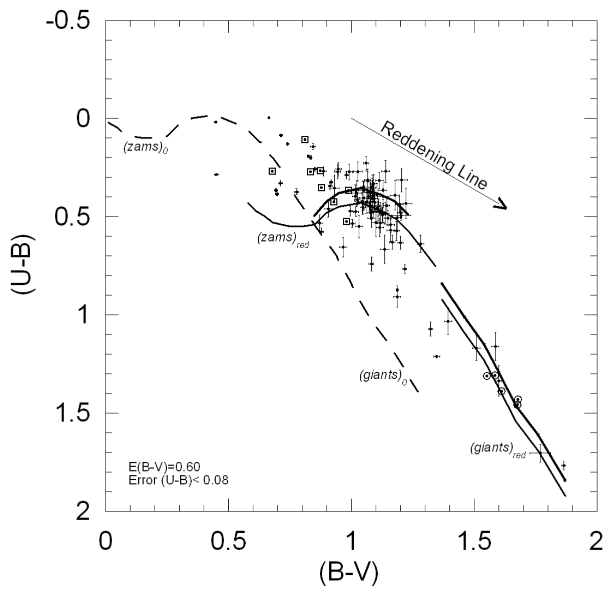

Fig. 2. The $(U-B,\ B-V)$ diagram of Be 89. The "S" curves (upper parts, ZAMS, and lower parts, red giants) have been taken from the two-color relations of SK82 and are displayed for the interstellar reddening values $E(B-V) = 0\overset{\mathrm{m}}{.}00$ and $0\overset{\mathrm{m}}{.}60$ (the bluer and redder versions, respectively). A reddening vector is also shown as an arrow, and big open circles mark the six RC candidates, and open squares, the blue-straggler ones. A heavy solid curve represents our best fit to the data; this has been adjusted to the main-sequence F-type stars above (i.e., blue-ward of) the ZAMS colors of SK82 and, simultaneously, to the RC stars above the red-giant colors of SK82. This fit has been used to estimate the heavy-element abundance of the cluster, which is shown in Table 7.

(big open circles in Figure 2) lying near, but above (i.e., blue-ward of) the giant sequence of SK82, the expected location of the RC stars; their subsequent locations in the CM diagrams confirm this classification (see Figures 3 and 4). A seventh candidate falls further from the expected RC locus in four of the five CM diagrams.

The F-type and RC stars of Be 89 (cf. Figure 2, $(B-V) \approx 1\overset{\mathrm{m}}{.}0$ and $\approx 1\overset{\mathrm{m}}{.}6$, respectively) lie above the (reddened) ZAMS two-color calibration of SK82 by $\delta(U-B) \simeq 0\overset{\mathrm{m}}{.}1$. Our best eyeball fit to the data is shown as the heavy solid curve in Figure 2. In the dereddened two-color diagram, the heavy line gives a value of $(U-B)_0 = -0\overset{\mathrm{m}}{.}10 \pm 0\overset{\mathrm{m}}{.}02$ at $(B-V)_0 = 0\overset{\mathrm{m}}{.}44$, and at this same color index, the highest point of the SK82 hump has $(U-B)_0 = -0\overset{\mathrm{m}}{.}02$. The resulting ultraviolet excess, $\delta(U-B) = +0\overset{\mathrm{m}}{.}08 \pm 0\overset{\mathrm{m}}{.}02$, has been converted to $\delta(0.6) = +0\overset{\mathrm{m}}{.}10 \pm 0\overset{\mathrm{m}}{.}02$ at

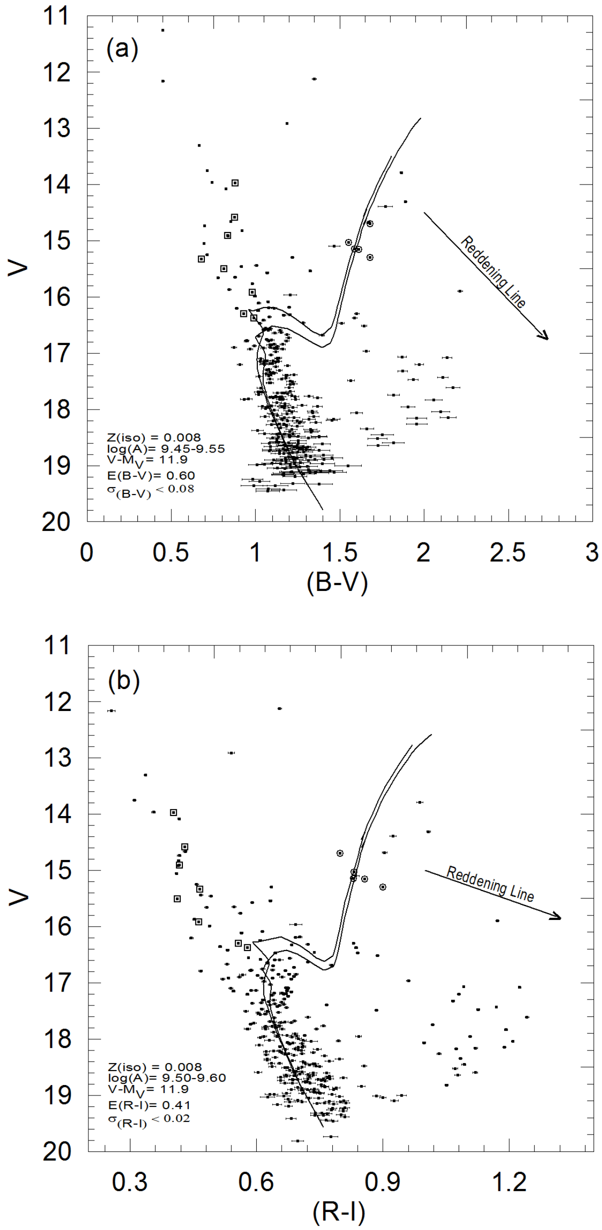

Fig. 3. CM diagrams, $(V,\ B-V)$ and $(V,\ R-I)$, for Be 89. Solid lines show the interpolated $Z = +0.008$ isochrones of MGBG (cf. Table 7 for the inferred metallicity). Big open circles denote the RC candidates, and open squares, the blue-straggler ones. See the text and Table 8 for the inferred values of the distance modulus and age.

$(B-V) = +0\overset{\mathrm{m}}{.}60$ with the normalization ratios given by Sandage (1969, his Table 1A). These values have been listed in Table 7, together with the corresponding photometric metallicity [Fe/H]$= -0.35 \pm 0.02$ dex derived with help of the calibration [Fe/H]-$\delta(0.6)$ of

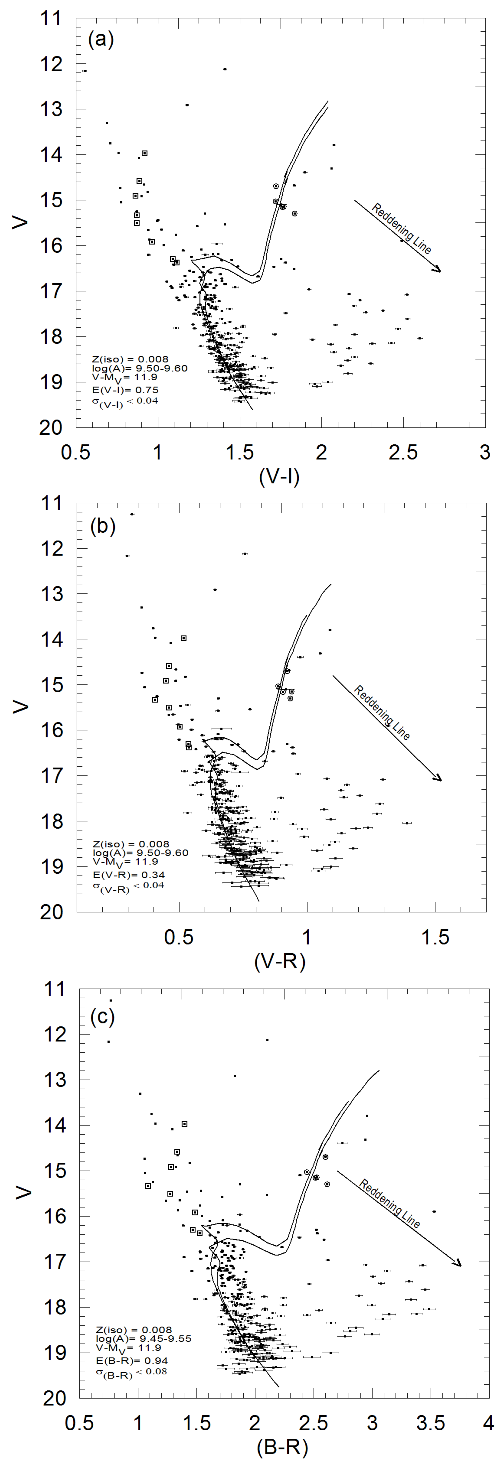

Fig. 4. CM diagrams, $(V,\ V-I)$, $(V,\ V-R)$, and $(V,\ B-R)$, (top, center and bottom panels, respectively) for Be 89. The isochrone curves and the symbols have the same meaning as in Figure 3. See the text and Table 7 for the inferred values of reddening and metallicity, and Table 8 for the distance modulus and age.

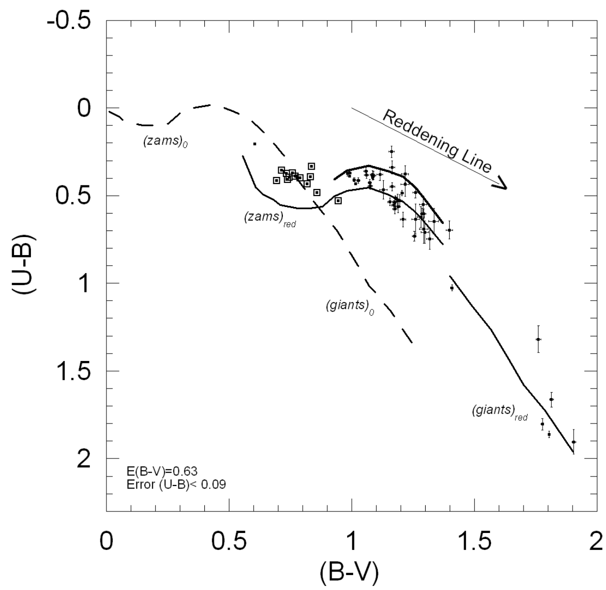

Fig. 5. The CC diagram of Ru135. The SK82 curves and the symbols have the same meaning as in Figure 2. See the text and Table 7 for the inferred values of the reddening and metallicity.

Karataş & Schuster (2006). Note that the $\delta(0.6)$ in the notation of the latter authors corresponds to delta(0.6) in the notation of Sandage (1969). Applying the above relation between [Fe/H] and Z, where [Fe/H] has been estimated as -0.35 ± 0.02 dex, gives $Z = +0.008 \pm 0.0003$. The online isochrones of MGBG have been iterated using this metal abundance when further analyzing Be 89.

In Figures 3 and 4, the isochrones of MGBG for $Z = +0.008$ have been over-plotted in five CM diagrams: $(V,\ B-V)$, $(V,\ R-I)$, $(V,\ V-I)$, $(V,\ V-R)$, and $(V,\ B-R)$ after reddening the isochrones along the color axis with a color excess corresponding to $E(B-V) = 0\overset{\mathrm{m}}{.}60$, converted with help of Table 6, and adding a visual extinction of $A_{\mathrm{V}} = 3.1 \cdot E(B-V) = 1\overset{\mathrm{m}}{.}86$ to the absolute magnitudes of the isochrones. The isochrones have then been shifted vertically to obtain the best fit to the observed lower-MS and and RC sequences. This vertical shift is the (true) distance modulus, $DM = (V_0 - M_{\mathrm{V}})$. The best fit for Be 89 is $DM = 11\overset{\mathrm{m}}{.}90 \pm 0\overset{\mathrm{m}}{.}06$ ($d = 2.4 \pm 0.06$ kpc, cf. Table 8).

To derive an age estimate for Be 89, the isochrones of MGBG for $Z = +0.008$ have been shifted in the CM planes as above, i.e., $M_V + 3.1E(B-V) + DM$ and $C_0(\lambda_1 - \lambda_2) + E[C(\lambda_1 - \lambda_2)]$, respectively, where the latter color excesses have been computed from $E(B-V)$ with help of Table 6, and then the isochrone ages have been varied until a satisfactory fit to the data has been obtained through the observed upper-MS, TO, and RC sequences of the cluster (cf. Figures 3–4). The resulting inferred mean age of Be 89 is $\log(A) = 9.58 \pm 0.06$ dex ($A = 3.8 \pm 0.6$ Gyr).

For all of these CM diagrams of Be 89, two isochrones have been plotted to provide a means for appreciating the uncertainties of the derived distances and ages. In Table 8 the range in ages provided by these isochrone pairs, the final values for the distances and ages from each CM diagram, and the mean values for each cluster are given. Error estimates of $(V_0 - M_{\mathrm{V}})$ and $\log(A)$ are discussed in § 3.4 below, and the mean results given in Table 8 have been calculated with equations (8) and (9) inserting the corresponding parameters summarized in the table.

3.2. *Ru 135*

The same procedures outlined in § 3, and § 3.1 for Be 89, have also been used for the clusters Ru 135 and Be 10. A reddening of $E(B-V) = 0\overset{\mathrm{m}}{.}63 \pm 0\overset{\mathrm{m}}{.}12$ has been derived for Ru 135 (cf. Figure 5). However, a clump of A-type stars at $(B-V) \simeq 0\overset{\mathrm{m}}{.}8$ and $(U-B) \simeq 0\overset{\mathrm{m}}{.}4$ seems to be present, with a horizontal-like distribution which does not fit satisfactorily the reddened two-color ZAMS curve of SK82. These stars (Sp $\approx$ A-types) are probably less reddened than Ru 135 by $\simeq 0\overset{\mathrm{m}}{.}3$ in $E(B-V)$, nearer, and most probably not cluster members (cf. the open squares in the CC and CM diagrams of Figures 5, 6, and 7), or they could be blue stragglers belonging to the cluster. For this latter case, they would be peculiar because of an ultraviolet-flux excess present in their spectral energy distributions (SEDs), and only a spectroscopic study with good signal-to-noise ratios would reveal more about their true nature.

Ru 135 contains a considerable number of F- and later-type stars, and appears to have its blue-most turn-off limit at $(B-V) \approx +1\overset{\mathrm{m}}{.}0$ and $(U-B) \approx 0\overset{\mathrm{m}}{.}4$, corresponding to a dereddened $(B-V) \approx +0\overset{\mathrm{m}}{.}43$ (i.e., Sp $\approx$ F5V). The best fit to the observed F-hump sequence in the $(U-B,\ B-V)$ diagram is the solid curve shifted blue-ward with respect to the two-color SK82 curve (cf. Figure 5). From the ultraviolet excess of these cluster F stars and following the procedure outlined at the beginning of § 3, [Fe/H]$= -0.71 \pm 0.02$ dex ($Z = +0.004 \pm 0.0002$) has been derived. The isochrones of MGBG with this metallicity have been computed on line and used in the following analyses.

TABLE 7

NORMALIZED (U-B) EXCESSES AND DERIVED METALLICITIES

Cluster	$(U-B)_{\rm SK82}$ [mag]	$(U-B)_{0,\rm fit}$ [mag]	$\delta(U-B)$ [mag]	$\delta(0.6)$ [mag]	[Fe/H] [dex]	Z
Be 89	-0.02	-0.10	0.08	0.10	-0.35	0.008
Ru 135	-0.02	-0.16	0.14	0.14	-0.71	0.004
Be 10	-0.02	-0.09	0.07	0.11	-0.49	0.006
error	$\leq \pm0.01$	±0.02	±0.02	±0.02	±0.02	$\leq \pm0.001$

TABLE 8

DISTANCE AND AGE ESTIMATES OF THE CLUSTERS

Color	(V_0-M_V) [mag]	d [kpc]	$\log(A)$ range	$\log(A)$	A [Gyr]
	Be 89: $E(B-V)=0.60\pm0.09$ & $Z=+0.008\pm0.001$				
$(B-V)$	11.90 ± 0.10	2.4 ± 0.1	9.45–9.55	9.55 ± 0.15	3.6 ± 1.4
$(R-I)$	11.90 ± 0.20	2.4 ± 0.2	9.50–9.60	9.60 ± 0.20	4.0 ± 2.3
$(V-I)$	11.90 ± 0.15	2.4 ± 0.2	9.50–9.60	9.60 ± 0.20	4.0 ± 2.3
$(V-R)$	11.90 ± 0.10	2.4 ± 0.1	9.50–9.60	9.60 ± 0.15	4.0 ± 1.6
$(B-R)$	11.90 ± 0.20	2.4 ± 0.2	9.45–9.55	9.55 ± 0.10	3.6 ± 0.9
Mean	11.90 ± 0.06	2.4 ± 0.06		9.58 ± 0.06	3.8 ± 0.6
	Ru 135: $E(B-V)=0.63\pm0.12$ & $Z=+0.004\pm0.001$				
$(B-V)$	9.50 ± 0.15	0.75 ± 0.05	9.60–9.70	9.60 ± 0.15	4.0 ± 1.6
$(R-I)$	9.70 ± 0.15	0.87 ± 0.06	9.55–9.65	9.55 ± 0.15	3.6 ± 1.5
$(V-I)$	9.60 ± 0.20	0.83 ± 0.08	9.55–9.65	9.55 ± 0.15	3.6 ± 1.5
$(V-R)$	9.60 ± 0.15	0.83 ± 0.06	9.55–9.65	9.60 ± 0.15	4.0 ± 1.5
$(B-R)$	9.50 ± 0.20	0.75 ± 0.07	9.60–9.70	9.60 ± 0.15	4.0 ± 1.6
Mean	9.58 ± 0.07	0.81 ± 0.03		9.58 ± 0.06	3.8 ± 0.7
	Be 10: $E(B-V)=0.75\pm0.09$ & $Z=+0.006\pm0.001$				
$(B-V)$	11.20 ± 0.11	1.7 ± 0.1	9.05–9.15	9.05 ± 0.10	1.1 ± 0.3
$(R-I)$	11.10 ± 0.20	1.7 ± 0.2	9.10–9.20	9.10 ± 0.10	1.3 ± 0.3
$(V-I)$	11.15 ± 0.15	1.7 ± 0.1	9.05–9.15	9.05 ± 0.15	1.1 ± 0.3
$(V-R)$	11.15 ± 0.20	1.7 ± 0.2	9.05–9.15	9.05 ± 0.10	1.1 ± 0.3
$(B-R)$	11.20 ± 0.10	1.7 ± 0.1	9.05–9.15	9.05 ± 0.05	1.1 ± 0.1
Mean	11.16 ± 0.06	1.70 ± 0.05		9.06 ± 0.05	1.08 ± 0.08

The five CM diagrams, $(V,\ B-V)$ through $(V,\ B-R)$, of Ru 135 are displayed in Figures 6 and 7 together with the reddened isochrones that best fit the data for the derived color excess and metallicity, $E(B-V) = 0\overset{\rm m}{.}63$ and $Z = +0.004$. The distance moduli, $(V_0 - M_V)$, and ages, A, found from these five CM diagrams and their respective isochrone fittings are given in Table 8.

In these CM diagrams a significant number of stars are seen extending to brighter magnitudes and red-ward from the fainter and redder observational limits of the main sequences, i.e., the stars extending red-ward and upward from $(V,\ B-V) \approx (18\overset{\rm m}{.}5, 1\overset{\rm m}{.}5)$ or $(V,\ R-I) \approx (18\overset{\rm m}{.}5, 0\overset{\rm m}{.}9)$ (cf. Figure 6). These are probably field red-giant stars contributed by the Galactic bulge, as suggested by the Galactic longitude and latitude of Ru 135, $\ell \simeq 16.4°$ and $b \simeq +6.2°$ (see Binney & Merrifield 1998; Stanek et al. 1996, Figures 3.5 and 2, respectively). The fact that Ru 135 lies near the direction of the Galactic central region also explains the significant number of brighter and bluer foreground stars seen in its CC and CM diagrams.

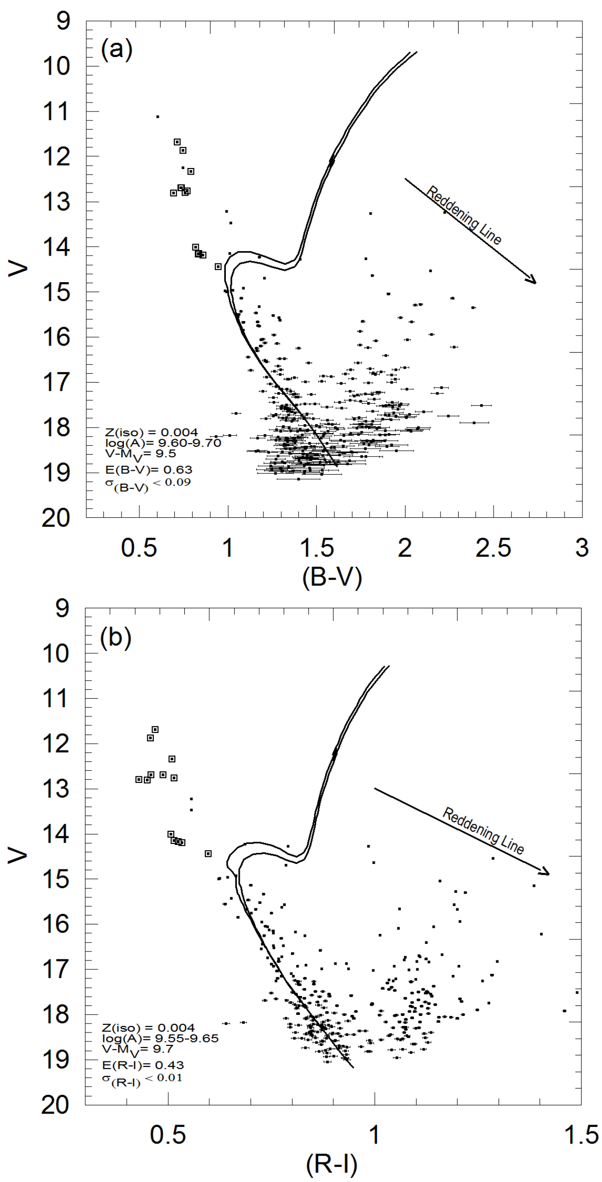

Fig. 6. The $(V,\ B-V)$ and $(V,\ R-I)$ diagrams for Ru 135. Solid lines show the isochrones of MGBG interpolated to $Z=+0.004$. See the text, and Tables 7 and 8, for the inferred values of reddening, metallicity, distance modulus, and age. Stars shown with open-square symbols are most likely field, or blue-straggler, stars.

3.3. *Be 10*

In Figure 8 the loci of stars observed in the direction of Be 10 are shown in the $(U-B,\ B-V)$ diagram, together with the standard interstellar reddening vector and the two-color curve of SK82, shifted along this vector to procure the best fit to the data. From the fits along the $(B-V)$ and $(U-B)$ axes, $E(B-V)=0\overset{\mathrm{m}}{.}75\pm0\overset{\mathrm{m}}{.}09$ and ([Fe/H],

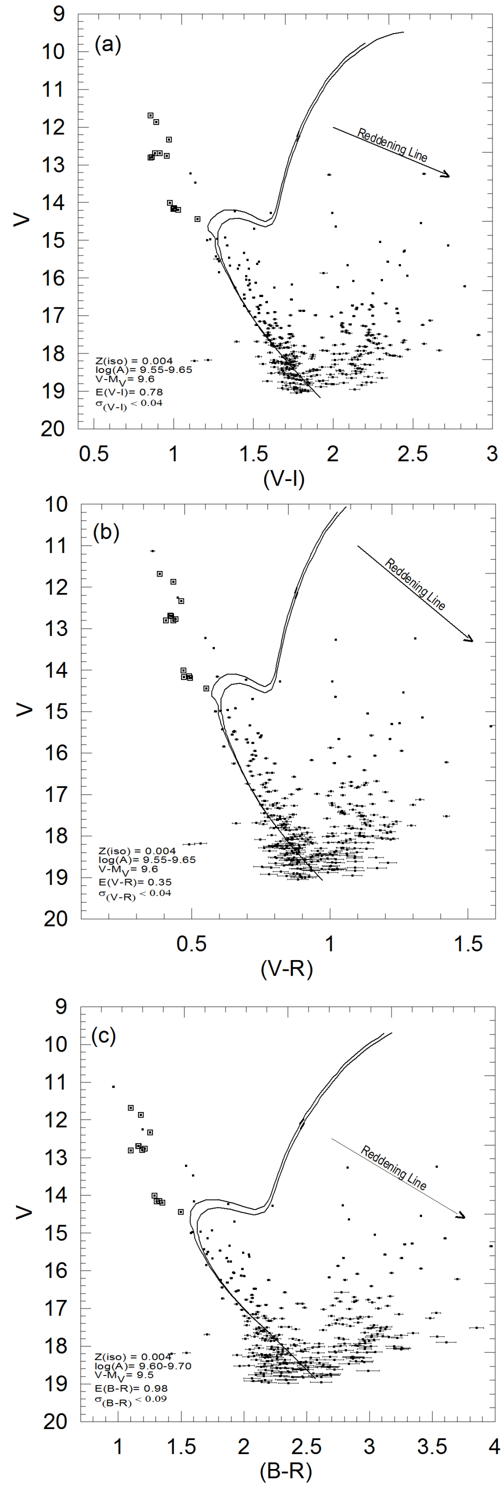

Fig. 7. The $(V,\ V-I)$, $(V,\ V-R)$ and $(V,\ B-R)$ diagrams for Ru 135. The symbols are the same as in Figure 6. See the text, and Tables 7 and 8, for the inferred values of reddening, metallicity, distance modulus, and age.

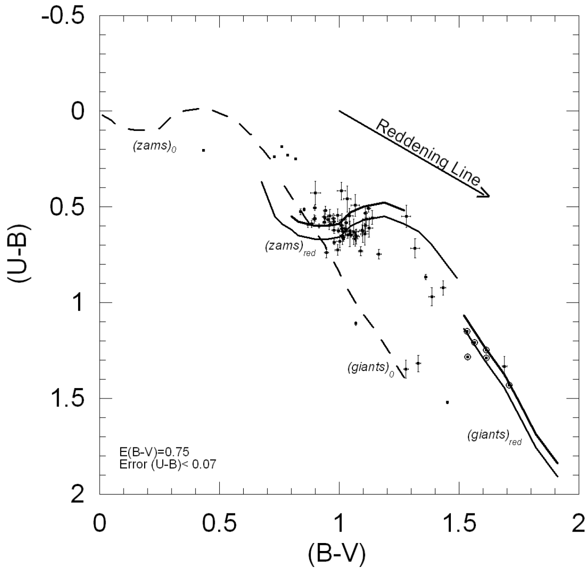

Fig. 8. The $(U-B,\ B-V)$ plot of Be 10. The symbols and the curves are the same as in Figure 2.

$Z) = (-0.49 \pm 0.02$ dex, $+0.006 \pm 0.0003)$ are found, following the procedures described in § 3 and § 3.1 (see Table 8 for partial and mean results). Again, the appropriate isochrones of MGBG have been computed online with this corresponding metallicity and are used below for further analyses of Be 10.

For Be 10, $DM = (V - 3.1 \cdot E(B-V) - M_V) = 11^{\mathrm{m}}.16 \pm 0^{\mathrm{m}}.06$, the distance, $d = 1.7 \pm 0.05$ kpc, the metallicity, $Z = +0.006 \pm 0.0003$, $\log(A) = 9.06 \pm 0.05$, and the age, $A = 1.08 \pm 0.08$ Gyr have been measured. Our results are listed in Tables 7 and 8. The resulting (best) isochrone fitting to the corresponding Be 10 data in the $(V,\ B-V)$, $(V,\ R-I)$, $(V,\ V-I)$, $(V,\ V-R)$ and $(V,\ B-R)$ diagrams are displayed in Figures 9 and 10, where one can see that the isochrones reproduce well the observed lower and upper MS, the TO, and RC sequences of this cluster.

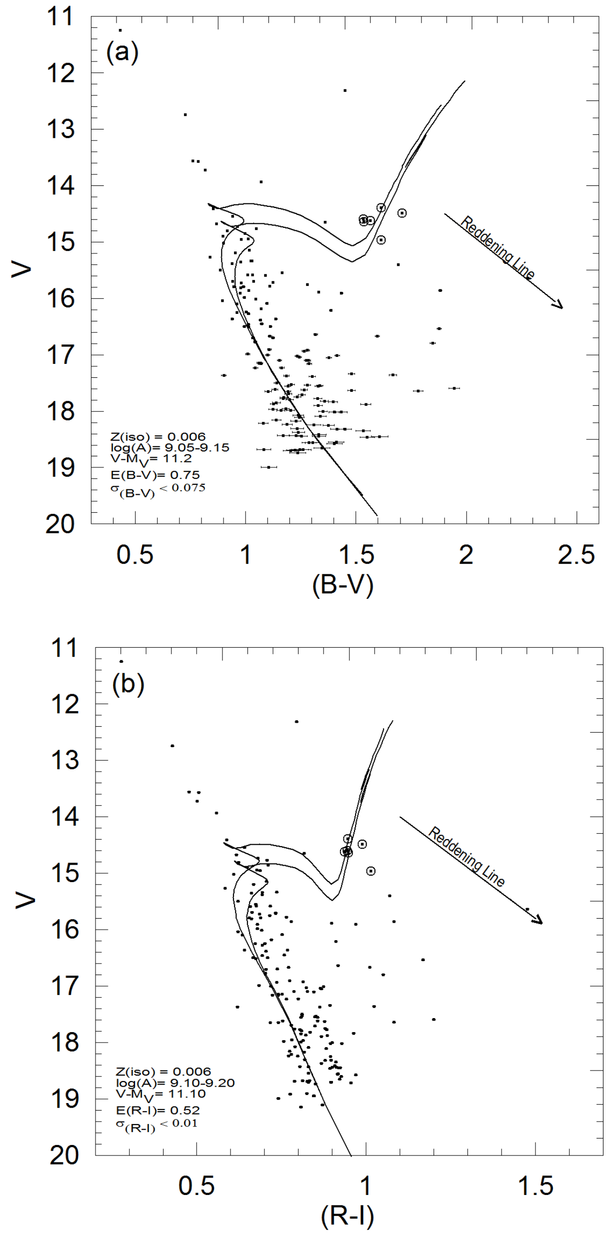

Fig. 9. The $(V,\ B-V)$ and $(V,\ R-I)$ diagrams for Be 10. Solid lines show the isochrones of MGBG interpolated to $Z = +0.006$. The larger open circles identify the RC candidates. See the text, and Tables 7 and 8, for the inferred values for reddening, metallicity, distance modulus, and age.

3.4. *Estimated errors and weighted averages*

In Table 7, the ultraviolet excesses and the metallicities are given for Be 89, Ru 135, and Be 10, and in Table 8, the mean values for the distance moduli, heliocentric distances, logarithmic ages, and ages, together with the corresponding estimates of precision. The errors were calculated in a straightforward manner (cf. Bevington & Robinson 2003, and references therein). In the following the details of this error analysis are presented.

3.4.1. *Errors in $E(B-V)$ and Z*

The random errors in the color excess $E(B-V)$ and photometric metallicity [Fe/H] were estimated as follows:

(i) By moving the two-color curve of SK82 backward and forward along the standard reddening

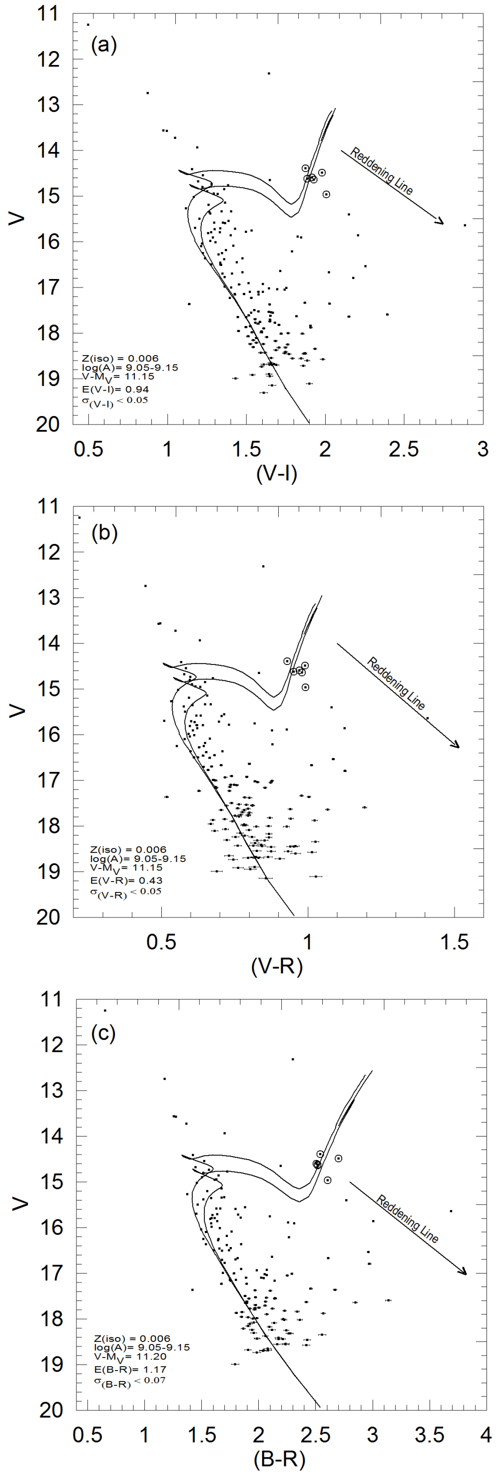

Fig. 10. The $(V,\ V-I)$, $(V,\ V-R)$ and $(V,\ B-R)$ diagrams for Be 10. The symbols are the same as in Figure 9. See the text, and Tables 7 and 8, for the inferred values for reddening, metallicity, distance modulus, and age.

vector in the $(U-B,\ B-V)$ diagram until a good fit with the observed GK-type, RC, and F-hump sequences was achieved. (No BA-type sequences were present for these clusters.) The precision of the determinations also depends on the scatter of the data points (cf. Figure 5 of Ru 135 and Figure 8 of Be 10 for good and fair cases, respectively). The uncertainties given in Tables 7 and 8 reflect this. Following this procedure, a typical error in $E(B-V)$ for the quality of the reduced data of our clusters is (conservatively) $\approx 0\overset{\text{m}}{.}04$. The systematic error in $E(B-V)$ depends on the color calibration used. In the case of SK82, the uncertainty can be safely assumed to be, at the most, of the order of the difference between two adjacent spectral subclasses.

(ii) The random photometric-metallicity uncertainty has then been estimated from the parabolic (eyeball) fit to the data of the maximum characterizing the ultraviolet flux excess of the stars at the dereddened color $(B-V)_0 \simeq 0\overset{\text{m}}{.}44$ (Sp $\simeq$ F5) and then following Sandage's (1969) normalization procedure.

The uncertainty of the metal content Z was determined from the relation (e.g., Bevington & Robinson 2003):

$$\sigma_Z = \ln\ 10\ \times Z\ \times \sigma_{[\mathrm{Fe/H}]}\,. \qquad (7)$$

$\sigma_{[\mathrm{Fe/H}]}$ has been estimated from the uncertainty in the ultraviolet excess $\delta(U-B)$ at the F hump between the observed and the SK82 two-color curves and is typically $\pm 0\overset{\text{m}}{.}02$. Assuming $\langle Z\rangle = 0.006$ (the mean of the three clusters) $\mid \sigma_Z \mid \leq\ 0.0003$ is obtained with equation (7) above. Assuming an error of about 0.001 for Z is, in our case, a quite conservative estimate.

(iii) On the other hand, the deviation of the assumed reddening vector from the "true" one depends on the quotient $E(U-B)/E(B-V)$, which can strongly deviate locally from its canonical value of 0.72 (see Chavarría, de Lara, & Hasse 1987; Johnson 1977). This uncertainty may produce errors larger than the precision quoted above. For a crude estimate, using the extremes of the cited values of $E(U-B)/E(B-V)$ and a typical color excess of $E(B-V) = 0\overset{\text{m}}{.}50$, the uncertainty in $\delta(U-B)$ could be as large as $0\overset{\text{m}}{.}15$-$0\overset{\text{m}}{.}20$. However, since our displacements of the SK82 curve in the CM-diagrams are consistent with the canonical value for the interstellar extinction law, we assume that this error contribution is negligible statistically.

(iv) Another systematic uncertainty results from the two-color calibration of SK82: from the uncertainty of $(U-B)$ or $(B-V)$ in the two-color calibration curve of SK82, which is expected to be of the order of the difference between two typical spectral subclasses (in our case $\lesssim 0\overset{\mathrm{m}}{.}05$) for the (U-B) index; and from the fit of the whole curve to a cluster data set, of the order $\lesssim \left(0\overset{\mathrm{m}}{.}05/\sqrt{N}\right)$, where there are N pivotal points considered when adjusting the SK2 two-color curve (the BA-type, the F-hump, the GK-type, and the RC sequences; i.e., $N \gtrsim 3$). Summarizing, the systematic uncertainty in $\delta(U-B)$ should be less than roughly three times that given by the precision of the flux measurements.

3.4.2. *Errors in the distance moduli and ages*

(i) The uncertainties σ_{DMi} for the moduli given in Table 8 that result from fitting the appropriate isochrones to the data in the CM diagrams depend on the photometric uncertainties (flux measurement and standard-transformation errors), the absolute magnitude and intrinsic color calibration errors (see for example, SK82), the color excess uncertainty of a given color [which depends on $E(B-V)$], and on the reddening law adopted. We assume that the isochrones only contain the errors of the absolute magnitude and intrinsic-color calibrations and that the photometric and transformation errors are small ($\approx 0\overset{\mathrm{m}}{.}03$) when compared to the other sources of error. In our case, the largest contribution to the distance modulus uncertainty is due to the uncertainty in the absolute-magnitude scale, followed by the uncertainty in the slope of the reddening vector, and the color-excess error, about $0\overset{\mathrm{m}}{.}3$, $0\overset{\mathrm{m}}{.}15$ and $0\overset{\mathrm{m}}{.}12$, respectively, which combine to give an expected total uncertainty as large as $\sigma_{\mathrm{DMi}} \cong 0\overset{\mathrm{m}}{.}25$.

The moduli resulting from the CM diagrams of each object and the mean moduli for the three clusters are given in Table 8, and the mean of the moduli has been derived from the five moduli, weighted with their respective (usually unequal) precisions, with the following expression:

$$\overline{DM} = \frac{\Sigma (DM)_i/\sigma^2_{DMi}}{\Sigma\left[1/\sigma^2_{DMi}\right]};\ (i = 1, ..., 5), \qquad (8)$$

and the associated mean uncertainty is estimated from the individual uncertainties of the five CM-diagrams of a given cluster by the relation:

$$\frac{1}{(\sigma_{\mathrm{mean}})^2} = \sum \frac{1}{(\sigma_{DM})^2_i} \qquad (9)$$

The combined error is the square root of the sum of the squared uncertainties and is expected to be about $0\overset{\mathrm{m}}{.}15$, or even less.

(ii) The uncertainty in the $\log(A)$ has a random error due to the (eyeball) fit of the isochrone with the appropriate metallicity to a given CM diagram of a cluster in question, and a quantitative estimate is obtained by jiggling brightward and faint-ward the isochrone curve until a good fit of the lower main sequence produces the DM. Then the age of the isochrone is varied until a good fit to the upper main sequence, the TO, and the RC sequences is achieved. The two isochrones shown in the CM diagrams of the program clusters give a quantitative estimate of this last error. Several different authors have computed isochrones as function of the metallicity, and the physics behind seems to be well understood. One does not expect a large variation in the $\log(A)$ error due to any uncertainty in the physics, and the uncertainties of $E(B-V)$ and (V_0-M_V) play a secondary role because the age errors depend more on the form of the isochrone curve and how it embraces the data (i.e., the the upper main-sequence and TO regions and the RC sequence) and, less significantly, on the reddening law (except perhaps the blue and near-ultraviolet filters). More problematic is the case when the TO region is not well defined (i.e., isolated from field stars) and/or the RC sequence is not present. In our case, the errors for the different colors of Table 8 reflect these uncertainties.

4. COMPARISON OF FUNDAMENTAL PARAMETERS OF THE THREE CLUSTERS

The reddening values of our three clusters have been compared to ones derived from the dust maps of Schlegel, Finkbeiner & Davis (1998; hereafter, SFD); these are based on the COBE/DIRBE and IRAS/ISSA maps, and take into account the dust absorption all the way to infinity. $E(B-V)(\ell, b)_\infty$ values of our three clusters have been taken from SFD maps using the web pages of NED[8]. These $E(B-V)(\ell, b)_\infty$ values are $0\overset{\mathrm{m}}{.}99$ for Be 89, and $1\overset{\mathrm{m}}{.}06$ for both Ru 135 and Be 10. However, Arce &

[8]http://nedwww.ipac.caltech.edu/forms/calculator.html.

TABLE 9

FUNDAMENTAL PARAMETERS OF BE 89, RU 135, AND BE 10

Cluster	(l°, b°)	$E(B-V)$ [mag]	[Fe/H] [dex]	Z	$(V_0 - M_V)$ [mag]	d [kpc]	log(A)	Isochrone	$R_{\rm GC}$ [kpc]	Reference
Be 89	83.16, +4.82	0.60	−0.35	+0.008	11.90	2.40	9.58	m8†	8.55	this work
		1.03	–	solar	12.40	3.00	8.93	b4	–	Tadross 2008a
		1.05	–	solar	11.54	2.04	9.02	g0	–	Subramaniam et al. 2010
Ru 135	16.42, +6.23	0.63	−0.71	+0.004	9.58	0.81	9.58	m8	7.72	this work
		1.10	–	solar	11.33	1.85	8.70	b4	–	Tadross 2008b
Be 10	138.62, +8.88	0.75	−0.49	+0.006	11.16	1.70	9.06	m8	9.84	this work
		0.87	–	+0.008	11.80	2.30	8.80	g2	–	Lata et al. 2004
		0.71	–	solar	11.26	1.79	9.00	B4	–	MN07

†Isochrone sources: B4 = Bertelli et al. (1994); b4 = Bonatto et al. (2004); g0 = GBBC; g2 = Girardi et al. (2002); m8 = MGBG.

Goodman (1999) caution that SFD reddening maps overestimate the reddening values when the color excess $E(B-V)$ is more than $\approx 0\overset{\rm m}{.}15$. For the revision of SFD reddening estimates, the equations of Bonifacio, Monai & Beers (2000) and Schuster et al. (2004) have been adopted. Then the final reddening, $E(B-V)_A$, for a given star is reduced compared to the total reddening $E(B-V)(\ell,b)_\infty$ by a factor $\{1 - \exp[-d \sin\ |b|/H]\}$, where b, d, and H are the Galactic latitude (Column 2 of Table 9), the distance from the observer to the object (Column 7 of Table 9), and the scale height of the dust layer in the Galaxy, respectively; here we have assumed $H = 125$ pc (Bonifacio et al. 2000). Note that Galactic latitudes of our three clusters are less than 10°. These reduced final reddenings are $E(B-V)_A = 0\overset{\rm m}{.}54$ for Be 89, $0\overset{\rm m}{.}36$ for Ru 135, and $0\overset{\rm m}{.}64$ for Be 10.

For Be 89, our reddening value of $0\overset{\rm m}{.}60$ is in good agreement with the value of $0\overset{\rm m}{.}54$ obtained from the dust maps of SFD. For Be 10 our reddening value of $E(B-V) = 0\overset{\rm m}{.}75$ is within about 1σ of the value $0\overset{\rm m}{.}64$ derived from the SFD dust maps, and for Ru 135, our reddening value of $0\overset{\rm m}{.}63$ differs by about 2σ from the value of $0\overset{\rm m}{.}36$ obtained from these SFD maps. These reddening values derived by different methods are in reasonable agreement with each other, giving confidence to our results.

As can be seen from the summarized results given in Table 9, the reddening value $0\overset{\rm m}{.}60$ found here for Be 89 is smaller than the $E(B-V) = 1\overset{\rm m}{.}03$ of Tadross (2008a; hereafter T08a), and than the $E(B-V) = 1\overset{\rm m}{.}05$ of Subramaniam, Carraro, & Janes (2010, hereafter S10). Our derived distance modulus and distance for Be 89, $[(V_0 - M_V), d(\text{kpc})] = (11\overset{\rm m}{.}90 \pm 0\overset{\rm m}{.}06, 2.4 \pm 0.06)$, are smaller than the values of $(12\overset{\rm m}{.}39, 3.00)$ of T08a and larger than the $(11\overset{\rm m}{.}54, 2.04)$ of S10. Our inferred age $[\log(A), A(\text{Gyr})] = (9.58,\ 3.8\ \text{Gyr})$ for this cluster is considerably older than $(8.93, 0.85\ \text{Gyr})$ given by T08a and larger than the estimate $(9.02, 1.06\ \text{Gyr})$ by S10. For the analysis of Be 89, T08a used JHK photometry and the isochrones of Bonatto, Bica, & Girardi (2004) with a solar metallicity. This is, partially, the origin of the disagreement between the two age estimates, since our lower metallicity for Be 89 will necessarily lead to a larger age for a given TO. Also, most probably, the differences are partially due to the different procedural approaches for estimating the fundamental parameters; we derive in a straightforward manner the estimates for the interstellar extinction and metallicity: by fitting SK82's ZAMS to the data in the $(U-B, B-V)$ diagram, by then measuring the ultraviolet excess of the F-type stars to derive a cluster metallicity, and finally using the appropriate isochrones in CM diagrams to estimate the true distance modulus and age of Be 89. Two parameters (reddening and metallicity) are estimated in a CC diagram separately from the other two parameters (distance and age) from the CM diagrams. S10 have also assumed a solar metallicity ($Z_\odot$) for their isochrones (from GBBC) and have used only CM diagrams to estimate the reddening, distance, and age of Be 89.

Previous results in the literature for Ru 135 are found in the work by Tadross (2008b; hereafter T08b), and for Be 10 in the papers by Lata et al. (2004; L04) and Maciejewski & Niedzielski (2007; MN07). Our reddening value $E(B-V) = 0\overset{\rm m}{.}63 \pm 0\overset{\rm m}{.}12$ for Ru 135 is significantly smaller compared to the reddening value of $1\overset{\rm m}{.}10$ given by T08b. Also, our derived distance modulus and distance, $[(V_0 - M_V), d(\text{kpc})] = (9\overset{\rm m}{.}58, 0.81)$, for Ru 135 are significantly smaller than $(11\overset{\rm m}{.}33, 1.85)$, and our inferred age $[\log(A), A] = (9.58, 3.80\ \text{Gyr})$ is considerably older than $(8.70, 0.50\ \text{Gyr})$, values by T08b.

In defense of the present results, our value for $E(B-V)$ ($0\overset{m}{.}63$) falls between the value derived from SFD ($0\overset{m}{.}36$) and the value of T08b ($1\overset{m}{.}10$); our value is in much better agreement with SFD. T08b used the solar-metallicity isochrones of Bonatto et al. (2004), and his results are based on the comparison of isochrones to observed data in the $J,(J-H)$ and $K,(J-K)$ planes of infrared photometry. These differences between our values and those of T08b are probably due mainly to the largely different values for the interstellar reddening, but also to the difference in the assumed metallicities, to the use of different stellar models and isochrone sets, which make use of differing input physics and colour-temperature transformations, and to distinct photometric data sets.

For the Be 10 open cluster, our reddening value $E(B-V) = 0\overset{m}{.}75$ is in reasonable agreement with the value of $E(B-V) = 0\overset{m}{.}87$ given by L04, and in good agreement with $E(B-V) = 0\overset{m}{.}71$ by MN07. For the metallicity of the Be 10 cluster, L04 adopt the $Z = +0.008$ isochrones of Girardi et al. (2002), and MN07 adopt the solar isochrones of Bertelli et al. (1994). From our two-color diagram, $Z = +0.006$ has been derived (see § 3.3), which is in agreement, within the error bars, with the value of L04. Our distance modulus and distance for Be 10, $[(V_0 - M_V), d(\mathrm{kpc})] = (11\overset{m}{.}16, 1.70)$ differ from the values $(11\overset{m}{.}8, 2.3)$ of L04, but very little from the values of MN07, $(11\overset{m}{.}26, 1.79)$. Our inferred age $[\log(A),\ A] = (9.06, 1.08$ Gyr) for this cluster disagrees by almost a factor of two (0.5 Gyr) with L04, but is in good agreement with MN07, (9.00, 1.00 Gyr). Again, our interstellar reddening for Be 10, $E(B-V) = 0\overset{m}{.}75$ falls between the value derived from SFD ($0\overset{m}{.}64$) and the value $0\overset{m}{.}87$ by L04.

The age values in Table 9 have been compared to ages estimated with the (age, ΔV) calibration given by Carraro & Chiosi (1994; their equation 3). Note that this last calibration does not consider the metal abundance of the cluster. Here, ΔV means the magnitude difference between the RC and TO, which is well known as an age indicator. Both open clusters Be 89 and Be 10 have RC candidates (see the CM plots for these two clusters, Figures 3–4, and Figures 9–10, respectively). TO values occur at $V \approx 16\overset{m}{.}5$ for Be 89 and $V \approx 14\overset{m}{.}8$ for Be 10, whereas the RCs occur at $V \approx 15\overset{m}{.}3$ and $V \approx 14\overset{m}{.}7$, respectively. From this age-ΔV calibration of Carraro & Chiosi (1994), ages have been estimated as $\log(A) = 9.1$ (1.3 Gyr) for Be 89 and $\log(A) = 8.6$ (0.4 Gyr) for the Be 10.

The average age values given by us, $\log(A) = 9.58$ (3.8 Gyr) for Be 89 and $\log(A) = 9.06$ (1.08 Gyr) for Be 10 are somewhat older than the ones estimated from this relation of Carraro & Chiosi (1994). However, these age differences are at least partially explained by the sub-solar metallicities of these two clusters ([Fe/H]= -0.35 dex for Be 89 and -0.49 dex for Be 10; see § 3.1, § 3.3, and Table 9). Lower metallicities require larger ages for the same TO.

In Table 9 our results are summarized for Be 89, Ru 135, and Be 10: Columns 1 and 2 contain the cluster name and Galactic coordinates, respectively. The resulting reddening, $E(B-V)$, is given in Column 3. The metallicity and heavy-element abundances, [Fe/H] and (Z), are given in Columns 4 and 5, respectively. True distance modulus values, $(V_0 - M_V)$, and their corresponding heliocentric distances to the observer are given in Columns 6 and 7, respectively. Column 8 gives the average age (i.e., $\log(A)$; where A is in years), as derived from the five CM diagrams. Different isochrones used by us and by other authors are referenced in Column 9. Average Galactocentric distances are listed in Column 10. The corresponding references from the literature are listed in Column 11.

5. CONCLUSIONS

CCD *UBVRI* photometry of three poorly studied Galactic open clusters, Be 89, Ru 135, and Be 10, has been analyzed, based on new SPM observations. The fundamental parameters of reddening, metallicity, age, and distance of these open clusters have been inferred and presented in Tables 7–9.

The interstellar reddenings and metallicities of these three clusters have been determined from two-color, $(U-B,\ B-V)$, diagrams prior to the use of the CM diagrams. Heavy element abundances, Z, of the three clusters have been found from the ultraviolet excess, $\delta(U-B)$, of the F-stars by comparison with the two-color curve of SK82 ($Z_{\mathrm{SK82}} = Z_{\odot}$), by using the normalizations of Sandage (1969), and by applying the calibration, [Fe/H]-$\delta(0.6)$, of Karataş & Schuster (2006), with the advantage of reducing by two the number of free parameters of the isochrones when fitting to the data in the CM diagrams. When necessary, we have iterated slightly afterwards for a better, more consistent, solution for the four cluster parameters (reddening, metallicity, distance, and age). Deeper U frames would improve our determinations employing this method, which allows us to estimate the reddening and metallicity independently using a CC diagram, in contrast to the exclusive fitting of isochrones to CM diagrams and the use of the solar metallicity, which are the more common techniques used in the literature.

The present adjustments of the SK82, CC relations to the MS and RC stars, and of the MGBG isochrones to MS, TO, and RC stars in the CM diagrams show good consistency and appropriate fits for all three open clusters, in the one CC diagram and all five CM diagrams. Good consistency is seen in the Figures 2–4 for Be 89, Figures 5–7 for Ru 135, and Figures 8–10 for Be 10.

The CC and CM diagrams of Be 89 and Ru 135 suggest that they are metal-poor and old for their location in the Galaxy, compared to other open clusters.

For Be 89, stars with $V < 16\overset{\mathrm{m}}{.}2$ and $(B-V) \leq 0\overset{\mathrm{m}}{.}9$ are most likely foreground or blue-straggler stars. The blue-straggler and RC candidates in the field of Be 89 need spectroscopic and/or astrometric observations to test their cluster membership and to elucidate their nature.

Similar candidates for blue-straggler or bright foreground stars are seen in the CC and CM diagrams of Ru 135 and Be 10, Figures 5–7 and 8–10, respectively. In the case of Ru 135 and for stars with V fainter than about $14\overset{\mathrm{m}}{.}2$, the onset of the cluster sequence in the CM diagrams is clearly seen. Objects brighter than this limit and with $(B-V) \leq 0\overset{\mathrm{m}}{.}9$ are probably blue stragglers or bright foreground stars.

Despite its similar age to Be 89, no RC stars are noticeable in the CM diagrams of Ru 135. On the other hand, the CC and CM diagrams of Be 10 show clear evidence for an RC grouping, although it is somewhat younger than the other two clusters. The lack of any RC stars in the CM diagrams of Ru 135, contrasting with Be 89 and Be 10, may result either from relative differences in mass segregation and our emphasis on the inner regions of these clusters, or from the poorness of these cluster fields and small-number statistics. Ru 135, being closer to the Galactic center, may be more perturbed and less dynamically relaxed than the other two clusters. Also, Be 89 and Be 10 each show only eight, or fewer, RC candidate stars, and it is not clear that all of these are in fact cluster members.

For the typical accuracy of photometric observations (and we are no exception), the final error estimates are fixed by the accuracy of the cluster parameters as given by the systematic uncertainties in the absolute-magnitude, intrinsic-color, and reddening-vector calibrations, for example, the adequacies, or not, of the SK82 colors, the MGBG isochrones, and the standard interstellar-reddening curve.

Finally, further radial velocity and proper motion information for these clusters will allow us to clean with more assurance most non-members from the CC and CM diagrams in order to obtain better determinations of their physical parameters and to better understand the nature of the blue-straggler and red-clump candidates in these three open clusters. Deeper photometric observations, especially in the U and B bands, will provide clearer, cleaner, and more precise solutions from the CC diagram.

This work was supported by the Conacyt projects 33940, 45014, 49434 and PAPIIT-Universidad Nacional Autónoma de México IN111500 (Mexico). İA acknowledges a grant from the Mexican Government (Secretaría de Relaciones Exteriores). YK acknowledges financial support of the Scientific and Technical Research Council of Turkey (TUBITAK, BIDEB-2219). This research made use of the WEBDA open cluster database of J.-C. Mermilliod. We also thank an anonymous referee for valuable suggestions and comments that helped improve this work substantially.

REFERENCES

Arce, H. G., & Goodman, A. A. 1999, ApJ, 512, L135

Bertelli, G., Bressan, A., Chiosi, C., Fagotto, F., & Nasi, E. 1994, A&AS, 106, 275

Bertelli, G., Girardi, L., Marigo, P., & Nasi, E. 2008, A&A, 484, 815

Bevington, P. R., & Robinson, D. K. 2003, Data Reduction and Error Analysis for the Physical Sciences (3th ed.; Boston: McGraw-Hill)

Binney, J., & Merrifield, M. 1998, Galactic Astronomy (Princeton: Princeton Univ. Press)

Bonatto, Ch., Bica, E., & Girardi, L. 2004, A&A, 415, 571

Bonifacio, P., Monai, S., & Beers, T. C. 2000, AJ, 120, 2065

Cameron, L. M. 1985, A&A, 147, 47

Carney, B. 2001, in Star Clusters, ed. L. Labhardt & B. Binggeli (Berlin: Springer-Verlag), 1

Carraro, G., & Chiosi, C. 1994, A&A, 287, 761

Chavarría-K, C., de Lara, E., & Hasse, G. 1987, A&A, 171, 216

Dean, J. F., Warren, P. R., & Cousins, A. W. J. 1978, MNRAS, 183, 569

Dias, W. S., Alessi, B. S., Moitinho, A., & Lépine, J. R. D. 2002, A&A, 389, 871

Friel, E. D. 1995, ARA&A, 33, 381

Girardi, L., Bressan, A., Bertelli, G., & Chiosi, C. 2000, A&AS, 141, 371 (GBBC)

Girardi, L., et al. 2002, A&A, 391, 195

Howell, S. B. 1989, PASP, 101, 616

__________. 1990, in ASP Conf. Ser. 8, CCDs in Astronomy, ed. G. H. Jacoby (San Francisco: ASP), 312

Janes, K. A., & Adler, D. 1982, ApJS, 49, 425
Johnson, H. L. 1977, RevMexAA, 2, 175
Jordi, C., Galadí-Enríquez, D., Trullols, E., & Lahulla, F. 1995, A&AS, 114, 489
Karataş, Y., & Schuster, W. J. 2006, MNRAS, 371, 1793
Landolt, A. U. 1983, AJ, 88, 439
_________. 1992, AJ, 104, 340
Lata, S., Mohan, V., Pandey, A. K., & Sagar, R. 2004, Bull. Astron. Soc. India, 32, 59 (L04)
Lyngå, G. 1987, Computer Based Catalogue of Open Cluster Data (5th ed.; Strasbourg: CDS)
Maciejewski, G., & Niedzielski, A. 2007, A&A, 467, 1065 (MN07)
Marigo, P., Girardi, L., Bressan, A., Groenewegen, M. A. T., Silva, L., & Granato, G. L. 2008, A&A, 482, 883 (MGBG)
Mathis, J. 1990, ARA&A, 28, 37
McFarland, J. 2010, PhD Thesis, Universidad Autónoma de Baja California, Mexico
Paunzen, E., & Netopil, M. 2006, MNRAS, 371, 1641
Piskunov, A. E., Kharchenko, N. V., Schilbach, E., Röser, S., Scholz, R. D., & Zinnecker, H. 2008, A&A, 487, 557
Rosselló, G., Figueras, F., Jordi, C., Núñez, J., Paredes, J. M., Sala, F., & Torra, J. 1988, A&AS, 75, 21
Sandage, A. 1969, ApJ, 158, 1115
Schlegel, D. J., Finkbeiner, D. P., & Davis, M. 1998, ApJ, 500, 525 (SFD)
Schmidt-Kaler, Th. 1982, in Landolt Bornstein New Series, Group VI, Vol. 2b, Stars and Stars Clusters, ed. K. Schaifers & H. H. Voigt (Berlin: SpringerVerlag), 14 (SK82)
Schuster, W. J., Beers, T. C., Michel, R., Nissen, P. E., & García, G. 2004, A&A, 422, 527
Schuster, W. J., & Parrao, L. 2001, RevMexAA, 37, 187
Schuster, W. J., et al. 2007, in IAU Symp. 235, Galaxy Evolution Across the Hubble Time, ed. F. Combes & J. Palouš (Cambridge, Cambridge Univ. Press), 331
Stanek, K. Z., Mateo, M., Udalski, A., Szymański, M., Kałużny, J., Kubiak, M., & Krzemiński, W. 1996, in IAU Symp. 169, Unsolved Problems of the Milky Way, ed. L. Blitz & P. Teuben (Dordrecht: Kluwer), 103
Stetson, P. B. 1987, PASP, 99, 191
_________. 1990, PASP, 102, 932
Straižys, V. 1995, Multicolor Stellar Photometry, Astronomy and Astrophysics Series, Vol. 15, ed. A. G. Pacholczyk (Tucson, Arizona: Pachart Pub. House)
Subramaniam, A., Carraro, G., & Janes, K. A. 2010, MNRAS, 404, 1385 (S10)
Tadross, A. L. 2008a, MNRAS, 389, 285 (T08a)
_________. 2008b, New Astron., 13, 370 (T08b)
Tapia, M. T., Schuster, W. J., Michel, R., Chavarría-K, C., Dias, W. S., Vázquez, R., & Moitinho, A. 2010, MNRAS 401, 621

İnci Akkaya: Department of Astronomy and Space Sciences, Faculty of Arts and Sciences, Erciyes University, Talas Yolu, 38039, Kayseri, Turkey (iakkaya@erciyes.edu.tr).
William J. Schuster, Raúl Michel, Carlos Chavarría-K, and Roberto Vázquez: Observatorio Astronómico Nacional, Instituto de Astronomía, Universidad Nacional Autónoma de México, Apdo. Postal 877, 22800 Ensenada, B. C., Mexico (schuster, rmm, chavarri, vazquez@astrosen.unam.mx).
André Moitinho: SIM/IDL, Facultade de Ciencias da Universidade de Lisboa, Ed. C8, Campo Grande, 1749-016, Lisboa, Portugal (andre@sim.ul.pt).
Yüksel Karataş: Istanbul University, Science Faculty, Department of Astronomy and Space Sciences, 34119, Üniversite-Istanbul, Turkey (karatas@istanbul.edu.tr).

Revista Mexicana de Astronomía y Astrofísica, **46**, 431–438 (2010)

STAR IMAGE SHAPE TRANSFORMER FOR ASTRONOMICAL SLIT SPECTROSCOPY

O. Cardona, A. Cornejo-Rodríguez, and P. C. García-Flores

Instituto Nacional de Astrofísica, Óptica y Electrónica, Puebla, Mexico

Received 2010 June 15; accepted 2010 August 15

RESUMEN

Presentamos un nuevo transformador de la forma de las imágenes estelares para espectroscopía astronómica de rendija que consiste de una lente plano convexa pegada a una placa rectangular plana paralela de vidrio en uno de sus lados menores con el fin de mejorar el desempeño de los sistemas espectrométricos. El sistema cambia la forma de los objetos a la forma rectangular con el propósito de llenar con luz la abertura de entrada de la rendija en los sistemas espectroscópicos. La placa se pone de lado con la lente como la abertura de entrada y la abertura de salida es la rendija iluminada vista por el sistema espectrométrico. El objetivo de este transformador es también el de mantener las características del haz de luz, la resolución intrínseca del espectrómetro y de mejorar la eficiencia de los sistemas espectrométricos y detectores.

ABSTRACT

We present a new star image shape transformer for astronomical slit spectroscopy that consists of a plano-convex lens attached to a plane-parallel rectangular glass plate on one of the small sides, with the aim of improving the performance of spectrometric systems. The system transforms the shape of the objects into a rectangular form with the purpose of filling with light the entrance slit aperture in spectroscopic systems. The plate is set sidewise with the lens as the entrance aperture and the exit aperture of the plate is the illuminated slit seen by the spectrometric system. The aim of this transformer is also to maintain the beam characteristics, the intrinsic resolution of the spectrometers and to improve the throughput of the spectrometer and detector systems.

Key Words: instrumentation: miscellaneous — stars: imaging — techniques: imaging spectroscopy — techniques: spectroscopic

1. INTRODUCTION

The main purpose of spectroscopy is to collect the maximum possible radiant power from the given source, and to disperse and detect it appropriately and efficiently. The slit spectrometers used in stellar astronomy consist of an entrance slit, a collimator, a dispersing element, a camera, and a detector. The camera is used to demagnify and focus the slit on the detector. The image produced by the optical system or telescope on the entrance slit of the spectrometers is in general not a sharp point and its size is larger than the optimum slit width. This is a common problem in astronomical spectroscopy where the stellar image is distorted by the earth atmosphere, the seeing, producing in general greater images than the required slit width. For that reason the light lost is great and is necessary to address this problem especially if one observes faint objects. For instance, if the width of the slit of the spectrometer is opened to accept, say, one second of arc in the given telescope and the seeing is of the order 2.5 seconds of arc, one is loosing fifty percent of the stellar light. Therefore, it is essential to find the way to introduce all the star light into the spectrometer. This can be accomplished by changing the shape of the image while trying to maintain the beam properties. This is realized converting the star circular image shape into a rectangular one, with the required size to maintain the resolution and to improve the throughput of the spectrometric systems.

The intrinsic resolution of spectrometers and the intensity transmitted by the slit are interconnected. Assuming perfect illumination and that the light from the source fills or overfills the spectrometer solid angle, then the resolving power, the intensity at the peak of a spectral line, and the slit width are interrelated. The maximum of the product of resolution and intensity is of the order of the wavelength of the incoming radiation times the aperture ratio of the spectrometer. This product becomes the optimum slit width of the spectrometer (Jacquinot 1954; Davis 1970; Thorne 1974) and is given by

$$w = \lambda \frac{f_s}{D_s} , \tag{1}$$

where w is the slit width, λ is the wavelength of the incoming radiation, f_s and D_s are the focal length and diameter of the collimator of the spectrometer.

To make full use of a spectroscopic instrument, the dispersion at the receptor must be matched to the resolution. The match between the size of the detector elements (pixels) and the projected slit width on the detector, based on the Nyquist criterion for discrete sampling, is that the slit width should cover two pixel, required to recover the resolution of the images, that are just resolved according to the Rayleigh criterion (Schroeder 2000).

There have been several solutions for changing the form of the circular stellar images into rectangular ones using image slicers (Bowen 1938; Richardson 1968), optical image transformers (Benesch & Strong 1951), fiber optics systems (Furenlid & Cardona 1988; Avila & Singh 2008); and some other systems for beam shaping (O'Shea 1985). In this work we propose a new system, different from the ones mentioned before, for changing the form of the stellar images to fit the entrance slit of the spectrometric systems without changing the F number of the exit beam of light in any direction with respect to the F number of the entrance beam from the telescope.

Of course, when one uses active and adaptive optics instruments in the telescope it is not necessary to have the instruments mentioned before for changing the form of the image (Lena et al. 1998; Hardy 1998). But these systems are expensive and complicated, and also, one cannot use them all the time because of the lack of useful guiding stars. The system presented here can be used in any observational situation and in any telescope-spectrometer system.

In what follows, § 2 introduces the historical background for transforming the shape of stars in spectrometric systems that sets the basics of the development of the transformer. The conception of the transformer is introduced in § 3. In § 4 the design of the transformer is described. Finally in § 5 some conclusions are presented.

2. HISTORICAL BACKGROUND

In the image slicers, the image is cut into slices, which are then arranged end-to-end to fit the entrance slit of the spectrometer system. Basically there are two types of slicers, the one designed by Bowen (1938) and the other by Richardson (1968), but there exist also several other types (Strong & Stauffer 1964; Simmons et al. 1982; Diego 1993; Suto & Takami 1997). The Bowen slicer, properly used, can result in a large advantage, especially for telescopes with large focal ratios. One of the difficulties with an image slicer is the minute scale, because the field to be sliced is very small in diameter. Benesch & Strong (1951) describe some of the problems of a Bowen slicer in an f/10 beam. The Bowen slicer is composed of a stack of glass plates, aluminized in some predesignated regions. The light is reflected by ninety degrees to align end-to-end the slices on the slit. However they are not in the same plane: they are arranged in steps like in a staircase. This is the principal reason for limiting the focal-ratio to values greater than 30 (Hunten 1974).

A modification of the Bowen slicer was introduced by (Walraven & Walraven 1972). The Bowen-Walraven image slicer in which the mirrors were replaced by total internal reflections inside a thin parallel plate where the seeing disk is sliced by a tilted edge of a prism in contact with the plate. In practice, the non-uniform illumination of the spectrograph collimator led to substantial problems and they were not extensively used.

A modified version of the Bowen-Walraven slicer that overcomes most of the problems of this type of slicers is the Confocal Image Slicer, which delivers a large number of slices, all in focus (Diego 1994). These new developments are very useful for high-resolution spectrography. These system are more complicated and difficult to construct in comparison with the transformer reported in this article.

The Richardson slicer resembles a confocal cavity composed of two concave mirrors one in front of the other. Each concave mirror is divided into two symmetric parts producing a slit between the parts. The two parts of each concave mirror are slightly tilted in opposite directions around the perpendicular to the slit. One of the concave mirrors is rotated by ninety degrees around the optical axis. In this way, the slits of each concave mirror are aligned perpendicular to each other in order to reflect the entrance image in the four inclined mirrors several times and exits through one of the slits forming a long slit with the desired size. This slicer is difficult to construct and the multiple reflections diminish the amount of light in the system. In this type of slicer all the slices are in focus.

To avoid some of the problems of the Bowen slicer in a fast system Benesch & Strong (1951) introduced an alternative, the optical image transformer, a redirector of rays. The slices are diverted to the sides by small plane mirrors, except the central one, and reflected back by concave mirrors to a central small plane mirror above or below the central slice, and are deflected through the slit. The concave mirrors refocus each slice back on the slit. In this way, there is no limitation on the focal-number of the system. The problem of many reflections and the alignment of tiny mirrors make it difficult to implement this system.

A scheme proposed by Fastie (1967) is appropriate for segmented mirror telescopes composed of several independent mirrors. The individual images may be aligned along the slit, and the pencils superposed on the grating by tiny individual prisms.

To solve the image-slicer problem Kapany (1958) suggested that a fiber optic system would help and gave a detailed exposition of that possibility but no description of a working unit was given. One can use a fiber bundle arranged in a round profile at the focal plane of a telescope and then ordered linearly in the exit of the bundle to become the entrance slit of the spectrometer. The size of the circular entrance aperture can be made to cover several seconds of arc to match the distorted star image produced by the seeing in the telescope. The exit of the fiber bundle is composed of individual fibers to form the slit with the required dimensions to be projected onto two pixels (Furenlid & Cardona 1988). This fiber bundle is very efficient and the light loses are only due to the light lost in the inter bundle holes and in the cladding of the individual fibers, and also by the absorption of light in the long fiber bundles. The individual fibers in this linear array should have a diameter that covers two pixel sizes when demagnified by the optics, as mentioned before. For a spectrometer where the magnification is $m = -1$, like in an Ebert-Fastie spectrometer, this imposes a very restrictive design parameter.

All the systems mentioned above increase the signal to noise ratio of the spectrometric system because the length of the slit is defined by the number of slices or fibers in the entrance slit of the spectrometer, thus covering more pixels in the perpendicular direction to the dispersion of the detector.

O'Shea (1985) has described several techniques to change the light distribution in one direction using cylindrical lens telescopes and the prism beam compressors that can be used in spectroscopy. The problem with these systems is that the beam becomes anamorphic, that is, they produce a beam with different divergences in two orthogonal directions. The system reported in this work overcomes most of the problems mentioned before and is introduced in the following section.

3. CONCEPTION OF THE SYSTEM

One of the objectives of the design of the shape transformer is to produce a slit with a width w and length l having the aspect ratio $r = l/w$ equal to at least six or any other desirable number. This is with the purpose of producing an image on the detector that, when projected, covers two pixels in the dispersion direction and at least twelve in the perpendicular one, that at the same time obeys the sampling theorem of Shannon and improves the signal to noise ratio, when one sums up all the pixels in the direction perpendicular to the dispersion direction. In order to take into account the imperfections, the intrinsic noise and different responses of the pixels of the detector (CCD), and the statistics of the arriving photons, it is necessary to obtain all the parameters that describe the distribution as well as the mean and the standard deviation. A Gaussian of a data set is recovered when one has more than ten values of the function, by the law of large numbers in statistics (Bevington & Robinson 2002).

The location of the shape transformer in the observational set up is shown in Figure 1, which displays the flow of light from the star to the detector passing through the telescope, the shape transformer, the demagnifying optics that forms the slit, the spectrometer, and the detector.

The simplest image shape transformer is a thin glass plate seen edgewise, which can be used to change the form of a circular image into a more or less rectangular one, shown in Figures 2 and 3 for the design and for the glass plate in the laboratory. The width w of the plate is fixed to accept the entire image that comes directly from the telescope, or from an optical fiber bundle. The light beam, after bouncing back and forth inside the plate with total internal reflections, exits on the opposite side of the plate forming an illuminated strip of length l. The form of the image is flat in the upper and lower sides of the plate and round at the sides and that becomes the slit of the spectrometer. The plate does not change the F number of the entrance beam in any direction,

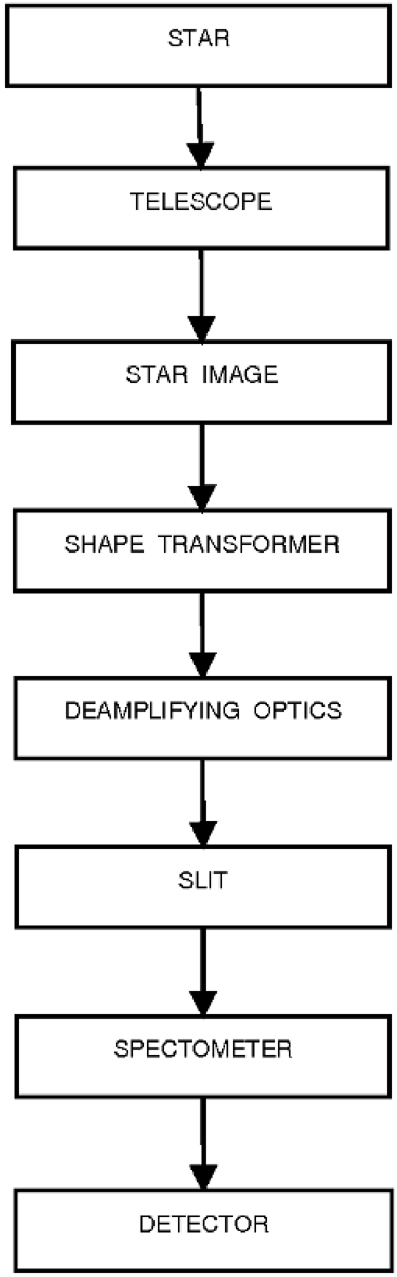

Fig. 1. The flow of light from the star to the detector, passing through the shape transformer.

but it scrambles the light rays inside it. This system can be analyzed using the unfolding ray trace technique for plates (Cardona, Cornejo-Rodríguez, & Flores-García 2010). In order to fulfill the condition imposed by the aspect ratio given above, the plate must be large in the direction of propagation, depending on the entrance aperture ratio. This distance depends in the F number of the entrance beam of the star light produced by the telescope. The size

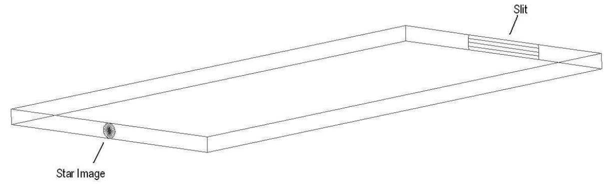

Fig. 2. Plate shape transformer showing the round entrance star image on the front face and the slit formed on the back face of the plate.

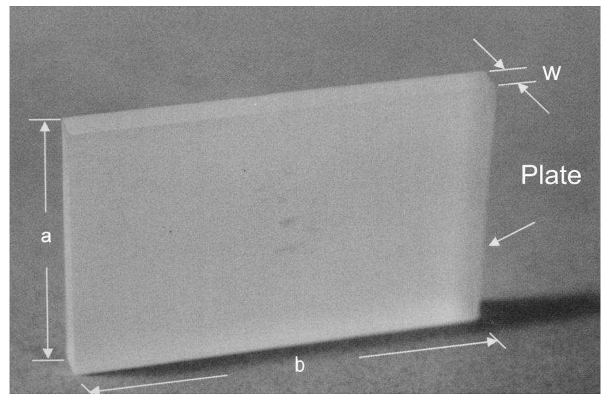

Fig. 3. Real glass plate showing the dimensions and the width w of the plate in the laboratory.

of the image produced by a telescope is given by the plate scale in seconds of arc per millimeter as

$$s = \frac{206.265}{f(m)} \, ('' \mathrm{mm}^{-1}) \, , \tag{2}$$

and the F number or focal ratio is defined as

$$F = \frac{f}{D} \, , \tag{3}$$

where f is the focal length, and D the diameter of the telescope in meters.

Equation (1) defines the width of the slit of the spectrometer when the average seeing disc of the star is given. The width in general should be larger because in order to funnel all the star light into the slit when the seeing disc of the star is larger than, say 2.5 seconds of arc. Then, for example, a telescope of 2.1 m diameter with focal ratio of 12, would produce, using equations (1) and (2), a star diameter of about 300 μm, for the seeing mentioned above. Thus, the width of the plate should have this dimensions and must be demagnified by around 7.5 times by the optics for a detector with square 20 μm pixels. The plate would be long and it would lose much light due to the distance traveled by the rays inside the plate. For this demagnification it is necessary to

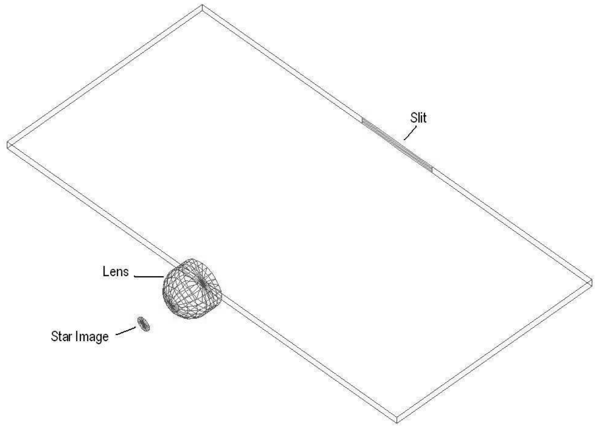

Fig. 4. Design of the shape transformer showing the star image from the telescope, the magnifying lens, the plate, and the exit slit.

employ fast cameras that, in general, are expensive and difficult to construct.

The same problems exist in a normal slit spectrometer for a slit opened to 300 μm in order to gather all the star light. For an existing spectrometer-telescope system the demagnification should not be great, because the image produced by the existing optics of the spectrometer is already used to reduce the size of the image produced by the slit, in general opened to accept star images of one second of arc, that becomes the entrance slit of the optics of the spectrometer. But the main problem is that the F number is changed and is difficult to convert back that number to the one necessary for the system. This plate can also be used with an optical fiber bundle that for the case considered here should have a diameter of 300 μm and should be connected directly to the plate. This plate does not fulfill the necessary requirements due to the problems mentioned above.

The system proposed in this work is similar to the one described before but has a small plano-convex lens attached to one of the smaller sides of the plate to overcome the problems of the single plate mentioned above. The design is shown in Figure 4. This system permits decreasing the width and the length of the plate compared to the case of the single plate.

Figure 5 shows a meridional ray trace for the system using a commercial package. The transformer is put in front of the image produced by the telescope or by an optical fiber bundle at a given distance of the lens to magnify the image to the required size and therefore the aspect ratio. The lens is used to magnify the image to give the desired aspect ratio of the slit with respect to the width of the plate, as

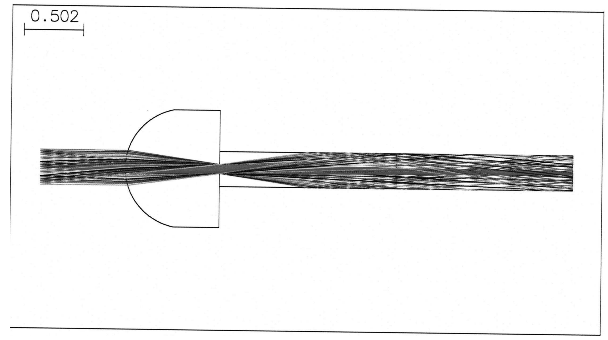

Fig. 5. Meridional ray trace of the transformer showing the waist of the beam and the internal reflections.

mentioned before; also, due to the bending of the rays by the lens the plate can be reduced in width depending on the characteristics of the lens and size of the object. The rays inside the plate are reflected between the upper and lower faces of the plate by total internal reflections; therefore, no light is lost (Figure 5) and the entrance beam F number is not changed in the plate, only its form. The light absorption in the plate is due only to the distance traveled inside of material and in this case is small.

When a wide rectangular glass plate set sidewise is used as a waveguide it behaves as an optical fiber in one dimension when the input end is one of the small sides and the light is transported inside the plate. In a fiber, from theoretical grounds, the focal ratio degradation (FRD) is proportional to the square root of the length of the fiber (Gloge 1972; Carrasco & Parry 1994; Poppett & Allington-Smith 2010). From the experimental side, the FRD slightly increases with the length of the fiber (Murphy et al. 2008). The output f-ratio for an input f-ratio of less than 5 shows little to no appreciable FRD (Murphy et al. 2008; Crause, Bershady, & Buckley 2008; Ramsey 1988). The experiments with fiber immersion show that the end effects diminish drastically the FRD for all the input f-ratios (Murphy et al. 2008). Fiber immersion involves contacting the input end of the fiber to an anti-reflective cover plate. The fiber-glass interface is made with an index matching gel.

In a plate there are no problems of macro and micro bending that produce part of the FRD in a fiber because it is a rigid piece of glass. When the length of the plate is small compared with the fibers considered in the experiments mentioned above, one expects little or no appreciable FRD. In the shape transformer, as the lens is attached to the plate it diminishes the end effects of the entrance surface of

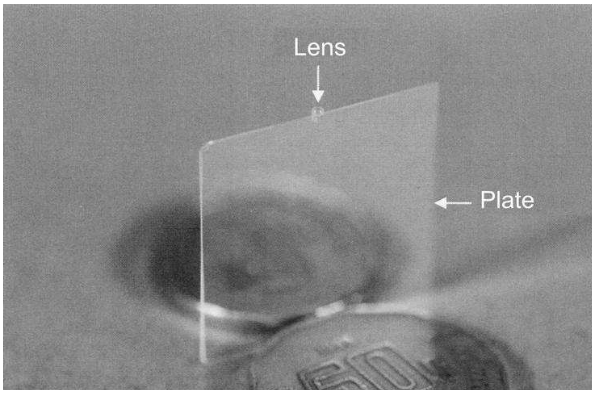

Fig. 6. Star shape transformer in the laboratory, composed of a one-millimeter diameter lens and a glass plate.

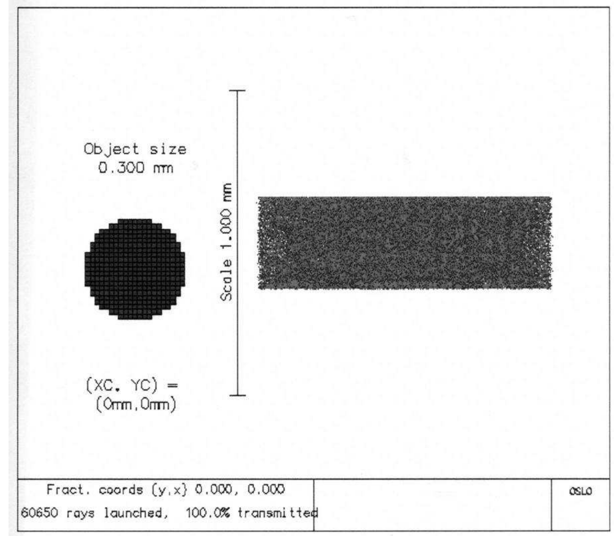

Fig. 7. Ray trace of the system for a round entrance image that produces the illuminated strip on the back side of the plate.

the plate. The lens magnifies the image of the object producing a beam faster than the beam coming from the object. The beams that enter the plate are fast and in most of the applications have an f-ratio of less than 5. Also, far from the plate the output beam that leaves the plate is symmetrical around the optical axis, showing that FRD does not occur in the plate, as can be seen in the experimental results of Flores-García (2006). Therefore, the shape transformer proposed preserves the f-ratio, as required.

If one desires a projected slit width on the detector of two pixels one has to demagnify the image of the illuminated side of the transformer maintaining the entrance F number of the original beam. To accomplish this it is necessary to magnify the image with the lens by the same amount as that of the necessary demagnification. Therefore, we fulfill all the requirements on the projected slit width, the aspect ratio of the slit, and the beam characteristics. The F number of the entrance beam to the plate is not changed inside it, and therefore the beam characteristics are not changed in the system, by the Lagrange optical invariant, since the magnification produced by the first lens is equal to the demagnification produced by the demagnifying optics. As was the case for the single plate, this system also scrambles the light rays inside the plate. Therefore this shape transformer is very efficient for astronomical spectroscopy with telescopes of any size.

4. TRANSFORMER DESIGN

We present the design of the shape transformer for some special cases in order to show the main ideas and peculiarities of the system. We have designed the transformer for a spectrometer for a $f = 8$ beam and a star image of 300 μm diameter.

The transformer is composed of a commercial plano-convex lens one millimeter in diameter and an effective focal length of 0.6 millimeters, with an index of refraction of 1.85 and a radius of curvature of the convex side of 0.51 millimeters. The plate has dimensions of five millimeters by five millimeters and a width of 0.160 millimeters, and has an index of refraction of 1.458. The lens is cemented on one of the thin sides of the plate as shown in Figure 5. Then, for a detector with 13.3 μm square pixel size, one has to demagnify the illuminated image on the side opposite to the lens on the plate (the slit of the spectrometer) by six times. For a detector with 20 μm pixel size one has to demagnify the image size by four times to fit two pixels on the detector. To maintain the beam parameters for the spectrometric system one has to magnify the image with the entrance lens by six and four times respectively for the cases given above. In the first case the image is formed on the rear face of the transformer, in the second, inside the plate. In this second case the beam of light continues traveling to the rear face of the plate forming a longer illuminated slit. For the two cases mentioned the slit length on the back of the plate will be of order of 1.8 millimeters and it will cover 22 pixels in the direction perpendicular to the dispersion of the spectrometer, for a five millimeter plate. For the second case one can use a plate of 3.38 millimeters, and therefore the length of the illuminated strip will be 1.2 millimeters in length, giving 15 pixels in the direction perpendicular to the dispersion. The demagnifying optics should be focused near the back

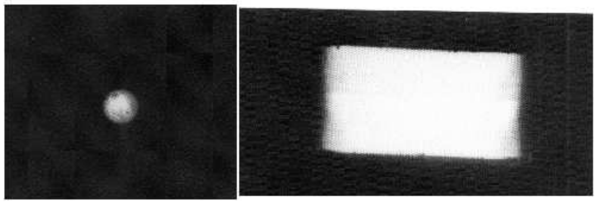

Fig. 8. The laboratory round entrance image (left) used to produce the illuminated strip (right) seen with a microscope.

side of the plate illuminated by the beam of light, in order not to show the imperfections of the rear face of the plate.

The number of pixels in the direction perpendicular to the dispersion is small, but larger than ten to have a good average, as was mentioned above, and to increase the signal to noise ratio. In the fiber bundle of 34 fibers covering 68 pixels of the Ebert-Fastie spectrometer in the direction perpendicular to the dispersion, the signal to noise ratio is large (Furenlid & Cardona 1988).

In Figure 6 we show one of the implementations of the transformer in the laboratory (Flores-García 2006). Figure 7 shows a ray trace with a commercial ray trace package for a round image as the input that produces a strip (slit) in the output. Figure 8 shows the illuminated side of the glass plate, seen in the laboratory with a microscope, produced by an illuminated circular image. Figure 9 shows the transformer with two three-mm diameter commercial lenses with focal lengths of two mm, for the demagnifying optics. This simple demagnifying optics does not absorb much light, resulting in a very efficient system.

Of course, the transformer can be changed in its dimensions and type of lens used, to be adjusted to any telescope and application, not only for astronomy. The transformer is simple and easy to construct and to implement in a laboratory, and for any telescope-spectrometer system. From the observational side, the first lens has a field of view larger than the star images, permitting the entrance of light from the surrounding sky into the spectrometer, which can be used for calibration purposes. Of course, when the light from the telescope is piped through an optical fiber bundle one encounters, as is usual, the problem of sky light subtraction. The scrambling of the light rays inside the plate makes the illumination of the slit of the transformer independent of slight changes in the position of the stars around the optical axis. Therefore, no problems of guiding the stars arise at the telescope.

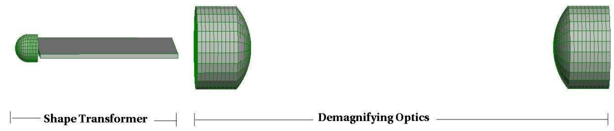

Fig. 9. Design of the shape transformer with the auxiliary demagnifying optics composed of two 3-mm diameter lenses.

5. CONCLUSIONS

We have designed a simple image shape transformer for astronomical slit spectroscopy that changes the circular images of stars into a rectangular form by using a lens and a glass plate set edgewise. The exit or back side of the plate becomes the slit for the spectrometer with the required aspect ratio for the width and length to comply with the sampling theorem and, at the same time, increases the efficiency of the spectrometric systems and the signal to noise ratio, with low light losses. The system reported here overcomes most of the problems of other systems known. This transformer is easy to construct and implement for any telescope and spectrometer system.

The authors acknowledge the technical support of María de los Ángeles López Castillo.

REFERENCES

Avila, G., & Singh, P. 2008, in Proc. SPIE, 7018, 70184W
Benesch, W., & Strong, J. 1951, J. Opt. Soc. Am., 41, 252
Bevington, P. R., & Robinson, D. K. 2002, Data Reduction and Error Analysis for the Physical Sciences (New York: McGraw-Hill)
Bowen, I. S. 1938, ApJ, 88, 113
Cardona, O., Cornejo-Rodríguez, A., & Flores-García, P. C. 2010, Rev. Mex. Fis., 56, 14
Carrasco, E., & Parry, I. R. 1994, MNRAS, 271, 1
Crause, L., Bershady, M., & Buckley, D. 2008, Proc. SPIE, 7014, 70146C
Davis, S. P. 1970, Diffraction Grating Spectrographs (New York: Holt, Rinhart & Winston)
Diego, F. 1993, Appl. Opt., 32, 31
__________. 1994, Proc. SPIE, 2198, 525
Fastie, W. G. 1967, Appl. Opt. 6, 397
Flores-García, P. C. 2006, PhD Thesis, INAOE, Mexico
Furenlid, I., & Cardona, O. 1988, PASP, 100, 1001
Gloge, D. 1972, Bell Syst. Tech. J., 51, 1767
Hardy, J. 1998, Adaptive Optics for Astronomical Telescopes (Oxford: Oxford Univ. Press)
Hunten, D. M. 1974, in Methods of Experimental Physics, Vol. 12, Part A, Astrophysics: Optical and Infrared, ed. N. Carleton (New York: Academic Press), 193

Jacquinot, P. 1954, J. Opt. Soc. Am., 44, 761
Kapany, N.S. 1958, in Concepts of Classical Optics, ed. J. Strong (San Francisco: Freeman), 553
Lena, P., Lebrun, F., Mignard, F., & Lyle, S. 1998, Observational Astrophysics (New York : Springer)
Murphy, J. D., et al. 2008, Proc. SPIE, 7018E, 70182T
O'Shea, D.C. 1985, Elements of Modern Optical Design (New York: Wiley & Sons)
Poppett, C.'L., & Allington-Smith, J. R. 2010, MNRAS, 404, 1349
Ramsey, L. W. 1988, in ASP Conf. Ser. 3, Fiber Optics in Astronomy, ed. S. C. Barden (San Francisco: ASP), 26
Richardson, E. H. 1968, JRASC, 62, 313
Schroeder, D. J. 2000, Astronomical Optics (2nd ed.; San Diego: Academic Press)
Simmons, J., et al. 1982, Proc. SPIE, 331, 427
Strong, J., & Stauffer, F. 1964, Appl. Opt., 3, 761
Suto, H., & Takami, H. 1997, Appl. Opt. 36, 4582
Thorne, A. P. 1974, Spectraphysics (London: Chapman & Hall)
Walraven, Th., & Walraven, J. H., 1972, in ESO/CERN Conference on Auxiliary Instrumentation for Large Telescopes, ed. S. Lausten & A. Reiz (Geneva: ESO/CERN), 175

Octavio Cardona, Alejandro Cornejo-Rodríguez and Perla C. García-Flores: Instituto Nacional de Astrofísica, Óptica y Electrónica, Apdo. Postal 51 y 216, 72000 Puebla, Pue., Mexico (ocardona@inaoep.mx).

AUTHOR INDEX